

# High efficiency laser-doped silicon solar cells with advanced hydrogenation

**Author:**

Hallam, Brett

**Publication Date:**

2014

**DOI:**

<https://doi.org/10.26190/unsworks/2643>

**License:**

<https://creativecommons.org/licenses/by-nc-nd/3.0/au/>

Link to license to see what you are allowed to do with this resource.

Downloaded from <http://hdl.handle.net/1959.4/53959> in <https://unsworks.unsw.edu.au> on 2024-05-04

# High Efficiency Laser-Doped Silicon Solar Cells with Advanced Hydrogenation

BRETT JASON HALLAM

School of Photovoltaic and Renewable Energy Engineering  
Faculty of Engineering



UNSW  
A U S T R A L I A

A thesis in fulfilment of the requirements for the degree of  
Doctor of Philosophy

July 2014



*“We’ll never know our full potential unless we push ourselves to find it.”*

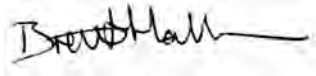
Travis Rice



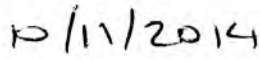
# CERTIFICATE OF ORIGINALITY

‘I hereby declare that this submission is my own work and to the best of my knowledge it contains no materials previously published or written by another person, or substantial proportions of material which have been accepted for the award of any other degree or diploma at UNSW or any other educational institution, except where due acknowledgment is made in the thesis. Any contribution made to the research by others, with whom I have worked at UNSW or elsewhere is explicitly acknowledged in the thesis. I also declare that the intellectual content of the thesis is the product of my own work, except to the extent that assistance from others in the projects design and conception or in style, presentation and linguistic expression is acknowledged.’

Signed:



Date:

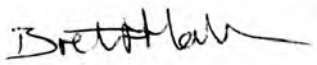


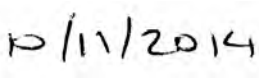
## COPYRIGHT STATEMENT

'I hereby grant the University of New South Wales or its agents the right to archive and to make available my thesis or dissertation in whole or part in the University libraries in all forms of media, now or here after known, subject to the provisions of the Copyright Act 1968. I retain all proprietary rights, such as patent rights. I also retain the right to use in future works (such as articles or books) all or part of this thesis or dissertation.

I also authorise University Microfilms to use the 350 word abstract of my thesis in Dissertation Abstract International (this is applicable to doctoral theses only).

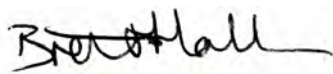
I have either used no substantial portions of copyright material in my thesis or I have obtained permission to use copyright material; where permission has not been granted I have applied/will apply for a partial restriction of the digital copy of my thesis or dissertation.'

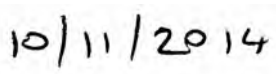
Signed: 

Date: 

## AUTHENTICITY STATEMENT

'I certify that the Library deposit digital copy is a direct equivalent of the final officially approved version of my thesis. No emendation of content has occurred and if there are any minor variations in formatting, they are the result of the conversion to digital format.

Signed: 

Date: 

# Abstract

Atomic hydrogen is widely used to passivate recombination active defects in silicon solar cells, yet the passivation mechanisms are poorly understood. Consequently, conventional silicon solar cells do not have effective hydrogenation. Crystallographic and impurity related defects can be incorporated into the silicon during crystal growth, subsequent processes (e.g. oxidation-induced stacking faults), or form under illumination (e.g. boron-oxygen complexes). Processes such as laser doping are of significant interest for high efficiency solar cell fabrication due to the localised nature and industrial applicability, but the introduction of laser-induced defects typically degrades electrical performance. This thesis aims to provide an improved understanding of, and develop an advanced hydrogenation process for silicon solar cells. In addition, this thesis will present new and novel contact structures for silicon solar cells fabricated using laser doping.

This thesis begins with an overview of hydrogen passivation, boron-oxygen defect formation and laser doping for silicon solar cells. An advanced hydrogenation process is then developed based on theoretical calculations to enhance minority hydrogen charge state concentrations using minority carrier injection. Open circuit voltages over 680 mV and pseudo-efficiencies of 23 % are demonstrated on standard commercial grade boron-doped Czochralski silicon through hydrogen passivation of boron-oxygen defects. The same hydrogenation process is then used to passivate oxidation-induced stacking faults. Implied open circuit voltages over 700 mV on large area multi-crystalline silicon and improvements in bulk lifetime from 90  $\mu$ s to 3.4 ms on n-type Czochralski silicon are also demonstrated.

The formation of advanced laser doped structures is then presented to allow deep junction formation ( $> 10 \mu$ m), utilise dopants from aluminium oxide layers, allow contact to buried layers in silicon solar cells and form transistors. After hydrogen passivation of the laser-induced defects, efficiencies of 20.7 % for p-type and 21.2 % for n-type Czochralski silicon are demonstrated for large area devices featuring such contacts.

Whilst substantial efficiency enhancements can be foreseen for solar cells fabricated on a whole array of silicon materials, a significant amount of further research is required to fully understand and exploit the potential of hydrogen passivation and laser doping.



# On the Assistance of Completing a PhD in Photovoltaic Engineering

Brett Hallam<sup>a)</sup>, Mr. Underpants, Brett von Surfátot, Big Pig (大猪), Garbage Guts, Stuart Wenham

*School of Photovoltaic and Renewable Energy Engineering, University of New South Wales, Kensington NSW 2052, Australia*

(Received 10 July 2014; accepted 4 November 2014; published online 24 November 2014)

This paper reports on the appreciation of various individuals and groups who have greatly supported the completion of a PhD in photovoltaic engineering, both directly and indirectly through many complex interactions and interdependencies. With such assistance, a great deal of knowledge has been obtained in relation to the fabrication of laser doped solar cells and hydrogen passivation. In addition, a vast array of insights have been gained about the wider photovoltaic community and numerous other aspects of life. © 2014 Journal of Applied Photovoltaics.

## I. INTRODUCTION

A PhD typically requires a great deal of dedication and work by the candidate over several years in order to achieve satisfactory completion, by demonstrating ‘a significant contribution to the knowledge or understanding of a field of study’.<sup>1</sup> In recent years, a leading university in New Zealand has suggested that the primary reason for undertaking a PhD should be one’s own commitment to a particular research interest.<sup>2</sup> With various studies reporting an increased rate of PhD completion in the field of sciences rather than that in humanities and social sciences,<sup>3-4</sup> this may suggest a higher level of interest in the research of PhD candidates in the field of sciences. However many other factors reported as essential for successful completion of a PhD, such as intelligence, research aptitude and tenacity may also be involved.<sup>2,5</sup>

In addition, there is often a large support network behind the candidate providing supervision, maintenance of equipment, process development and financial support.<sup>5</sup> This work reports on such provided assistance and knowledge acquisition for the completion of a PhD in photovoltaic engineering.

## II. METHODOLOGY

The assistance provided and experiences gained throughout a PhD appear remarkably similar to the steps required to develop and commercialise the laser doped selective emitter (LDSE) solar cell technology. Hence in this paper, we step through the processes of development and fabrication of an LDSE solar cell and how it relates to the lessons learnt and assistance provided throughout a PhD in photovoltaic engineering. As shown in Fig. 1, we discuss several aspects associated with concept development from the background

understanding of semiconductor physics through to the patenting process. We then discuss the ongoing technological developments through collaborations with industry, before moving on to the external requirements such as silicon/wafer and equipment development, to allow the pilot production of the technology including cell fabrication, module assembly and reliability testing.

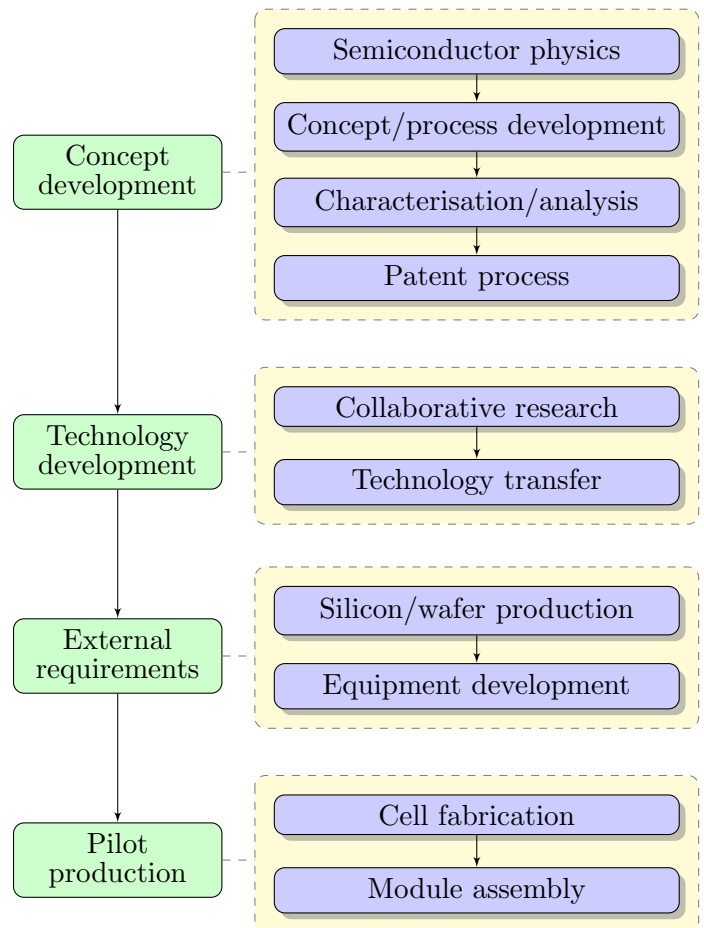


FIG. 1. (Color online) Process flow for developing and transferring the LDSE solar cell technology into pilot production.

<sup>a)</sup>Electronic mail: [brettjhallam@gmail.com](mailto:brettjhallam@gmail.com)

In following sections, a staggered process flow acts to guide the reader through the development and fabrication process, providing insights to the lessons learnt and assistance provided. Processes and attributes will be presented in the blue blocks, whilst a generic description of the process or attribute will be shown in the adjacent red blocks (see Fig. 2). The subsequent text describes the lessons learnt and/or appreciation acquired throughout my PhD.

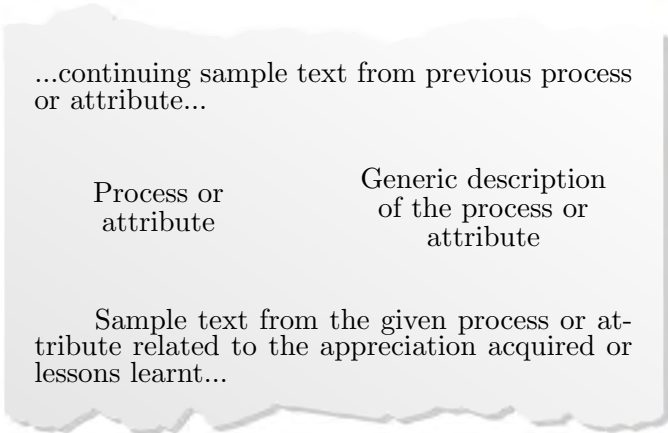
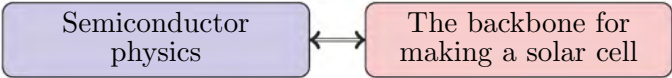
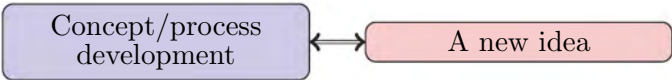


FIG. 2. (Color online) Guide for the process/attribute and associated description for the remainder of the text.

### III. CONCEPT DEVELOPMENT



I should begin with Jeff Cotter, Kate Fisher, Florence Chen and Malcolm Abbott, who introduced me to research and taught me many of the processing/characterisation skills I’ve used over the last few years. I may not have worked with most of you during my PhD, but you have helped me endlessly in getting me to where I am today. Mal, it’s a pleasure to be working with you again, you have strengthened the work in this thesis greatly. Thanks for numerous chats over a caramel latte.



Throughout my various international trips, I’ve been exposed to so many new interesting and exotic foods. Fig. 3 highlights my most memorable dishes such as protein enriched steamed egg whites and pork.

Ali, Amanda and Monica, you have all taught me so much! I don’t need to elaborate in any case, but I don’t feel like I’m missing out at all. From knowing you in the last few years I feel like I’ve pretty much experienced everything!

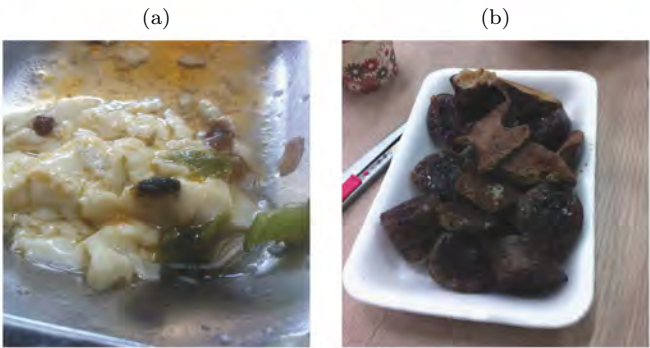
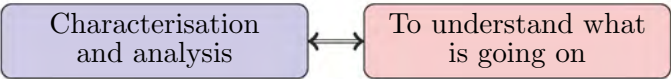
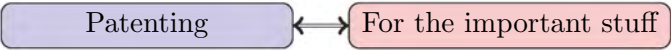


FIG. 3. (Color online) (a) Protein enriched steamed egg whites and (b) pork.



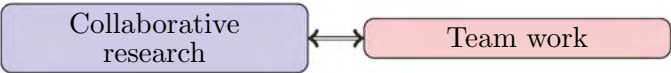
Alison Lennon, our resident chemist, thank you for the many chats in relation to the finer details plating and chemical reactions. Thank you also for your critical thinking.



Amanda, you are a true lady; a true flower; almost kissable. You may not be the ‘Perfect Angel’, but I think you’re pretty close! You’re in this section, because you’re not only my best friend, but you’ve become family. Your name pops up a few times throughout this paper for a couple of reasons. Firstly, your memory is quite poor, but secondly and most importantly, you mean the world to me. You have really taught me how valuable a friendship can be.

Aku, kiitos for your kind hospitality on numerous occasions. Over the last couple of years you have become a good friend.

### IV. TECHNOLOGY DEVELOPMENT



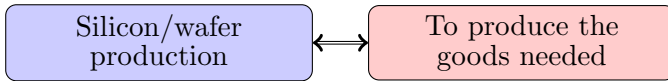
Thank you to the many people, past and present who I’ve been so lucky to work with at UNSW in the School of Photovoltaic and Renewable Energy Engineering (SPREE), and have supported me along the way. There are many people too numerous to mention in the administration of SPREE who have helped me over many years - thank you!



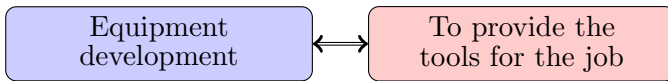
To the team at Newport/Spectra Physics, thanks for continuously developing such good lasers! In particular Jim Bovatsek, Raj Patel, Rainer Schramm and

Ravichandar Balasubramanian, thanks for teaching me a thing or two about lasers.

## V. EXTERNAL REQUIREMENTS



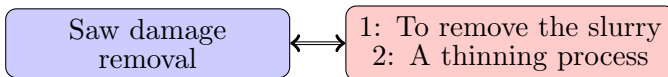
Dad, thanks for getting me interested in solar, if it wasn't for you installing solar hot water systems I may have ended up studying law! It has always amazed me at the many things you can do well. Mum, thanks for the many amazing varieties of cakes and biscuits that have always been on the table. Thanks also for taking the time when I was a little tacker to make sure I can read. I still might not like it, but at least I can. Thank you both for your support over many years and for loving me for who I am. I love you.



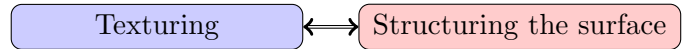
A big thank you to Moninya Roughan for introducing me to  $\text{\LaTeX}$  and the experience you gave me in modelling. Readers may have various misguided interpretations from the preceeding sentence, as has occurred on numerous occasions when engaging in conversations on such topics. Hence, it should be noted that  $\text{\LaTeX}$  is pronounced /'lətɛk/ or /'lɑ:tɛk/ and associated with document preparation system used in this work<sup>6</sup> and not the milky exudate from certain plants which coagulates on exposure to air (pronounced /'lətɛks/) and often used to make rubber products.<sup>7</sup> Similarly, modelling refers to the numerical simulation in MATLAB and FORTRAN associated with the dispersion of marine pests in Sydney Harbour and along the East Australian Coast, not modeling commonly seen in the fashion industry. The skills I learnt whilst working with you several years ago have proved invaluable in this thesis.

## VI. PILOT PRODUCTION

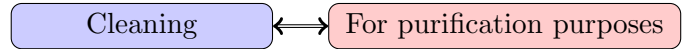
### A. Cell fabrication



Chris and Max, you fit into this category for many reasons. Thank you both for adding some logic into my life when feelings get in the way, and thank you for making my house feel even more like home. It's so pleasant to be able to come home to good friends. Chris, I'm not sure why but for some reason, the letters F. A. and T. come to mind, but I still love you (and you too Max)!

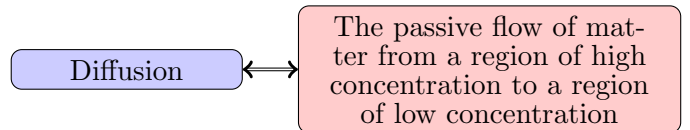


Mama and Papa, thank you for the many wonderful fishing trips, freshly baked scones and laughs over the years. Many people have called me a joker and if only they knew you both, they would see it really isn't my fault....it's genetic and also infectious. If there was a medical term for it, I'm pretty sure it would be called '*Cane Syndrome*'.



Michael, you've been such a reliable surfing buddy, I look forward to many more waves with you in the future to take my mind off making solar cells. Amanda and Evan, thanks for the many enjoyable moments both in and out of the water. I'm looking forward to many more bacon and egg rolls after a sunrise wave with you at Green Hills or over in Margs.

Also a big thank you to the good friends and colleagues that I've been able to do yoga with in various locations such as the Physics Lawn or on the back of a ship in the Pacific at sunset. Katrien Marent en het team van Flowing Yoga, ik dank u voor het openen van mijn geest en schouders, en leert me Nederlands.

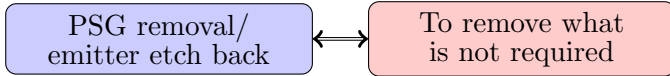


For the immense support of my supervisor Stuart Wenham (aka my younger brother, and here after referred to as Stuart), what can I say but thank you. You have given me so many wonderful opportunities that have really opened me up to the wonderful world of photovoltaics beyond just turning a silicon wafer into a solar cell in the lab. Thank you for giving me the opportunity to run with ideas and see where they lead. Your understanding of solar cells constantly amazes me. It is so pleasant to see your excitement for every new invention and result our group comes across, even after your many years in the industry. If there was a diffusion coefficient to describe the rate at which you can disseminate ideas and knowledge, it would be very large and could perhaps be likened to the diffusion coefficient of various impurities in liquid silicon compared to that in the solid silicon,<sup>8</sup> or similarly to the diffusion coefficient of  $\text{H}^0$  compared to that of  $\text{H}^+$ .<sup>9</sup> You have taught me so much more than just some of the fine intricate details about solar cells, including many skills in how to do one's laundry when on a business trip, and perhaps more importantly, what not to do.

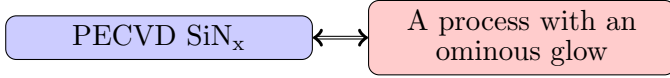
I would also like to acknowledge the support of my co-supervisor Allen Barnett for numerous discussions



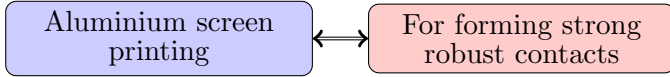
on my work. I look forward to working more closely with you in the future.



To the many people all over the world who have always been there to remind me when it is time to shave or go for a haircut - thank you - and especially to you Neil!

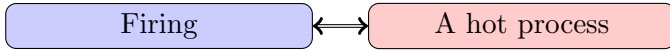


Stuart, your kind, caring nature and consideration has also been very much appreciated over the past few years. I would especially like to thank both you and Alison Lennon for your awareness of my ignorance to relevant world events in the Asia Pacific region, even if it did cut my snowboarding trip short.

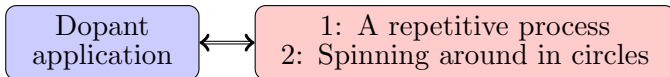


Thank you to the team at Roth & Rau in Hohenstein-Ernstthal for sharing your expertise and welcoming nature during my visits, especially Rico Böhme. From the Australian end, Linda Koschier, it's enjoyable every time I get to work with you or see you around the world, you've become a good friend.

Tine Uberg Nærland, Jordi Veirman and Dominik Lausch, you would have to fit into this category too. It has been a pleasure to spend a little bit of time with you all. Of the many conferences I've been able to attend, the time with all of you have been the most memorable, so much so it even left me breathless!



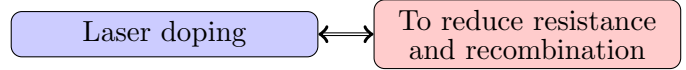
A big thank you to Apollon Solar (Roland Einhaus, Jed Kraiem, Julien Degoulange and Maxime Forster) for donating many great samples which have become such a big part of my thesis. It has been a pleasure working with you and visiting your facilities. In particular, the visit to FerroPem was a very warming experience!



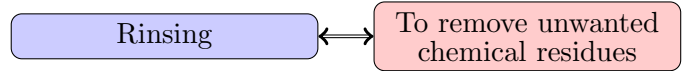
Thank you to the Bayside Swimming Club, past/present coaches too numerous to mention who have helped me achieve my goals, both inside and outside the pool. You have become an extended family to

me over many years. In particular, to Jon Shaw, thank you for always believing in me.

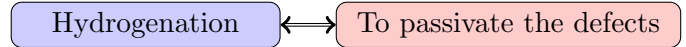
To Ashley Delaney, thank you for giving me someone to look up to, even if I do prefer the days when I could still beat you. I just hope one day I can be as successful developing solar cells as you have been in the pool. Sue would be so proud of you!



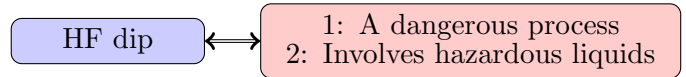
Thorsten Trupke, the photoluminescence (PL) guru, thank you for the many conversations we've had in regards to how to incorporate PL into my work and your insightful inputs.



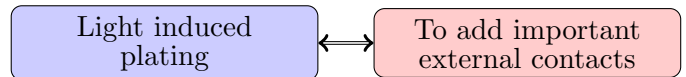
Brad, Ro, and Sophie, it is rare I get to see you but every time I do, it is always memorable. Andrew, I hope there is enough physics in here for you to look down at me proudly. Little Sophie, thank you for the cold wet lap you gave me just before an international flight, and Stuart/Mark Griffin thanks for the advice on how to get Platinum status, that shower was very much appreciated.



To the tireless efforts of the entire lab development team, thank you for helping maintain the equipment required for this work and in particular Kian Fong Chin for your work on the laser system.

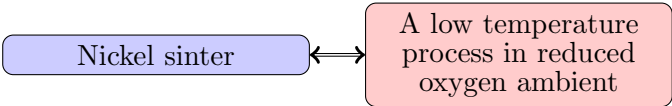


Chesty, Ash, Skinner and Skip, it is only fitting that you go in this section. I don't think there was ever a moment around any of you without either motorbikes or hazardous liquids present. Skinner and Skip, it has been great checking out the beaches in Newy and going for a surf, even though you never managed to stand up. Chesty, thank you for your support through some trying times. You have all become valued friends.



For the the numerous solar cell manufacturers I've been so fortunate to do research together with, thank you. At Suntech, I would like to give a special thank you for the support of Zhengrong Shi, Jingjia Ji, the

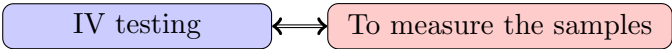
Pluto team in Wuxi and the Australian R&D team (especially Renate Egan, Rhett Evans and Oliver Kunz). At Shinsung, I would like to thank the numerous Lee's (Prof., Dr, Mr. and Mrs.). Also, a special thank you to Jisoo Kim and Kyeongyeon Cho for the many wonderful and exciting experiences with you such as snowboarding after work mid-week.



To the many people I've gone through my undergraduate and/or a PhD together with, it has been so nice to be able to work with so many talented students. In particular, Catherine Chan, Phill Hamer, Alison Wenham, Ly Mai, Budi Tjahjono, Nicole Kuepper, Adeline Sugianto, Doris (aka Little Pig) Pei Hsuan Lu, GuangQi Xu and Yu Yao who I've worked most closely with, thanks for the many contributions to aspects of this work and the company on numerous overseas trips. Furthermore, many of you have become good friends, including but not limited to those depicted in Fig. 4.

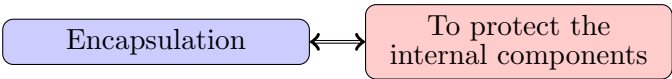


FIG. 4. (Color online) From left: Victor Ta, Doris Lu, Alison Wenham, Ivana Surduki, Brett Hallam and Jason Cui.



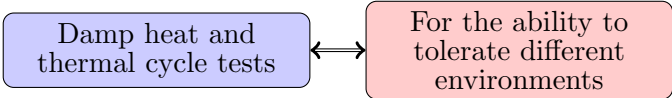
A big thank you to the many undergraduate students who I've been able to work with and have assisted me in my research (Ned Western, Mitchell Eadie, John Durrant, Nan Gao and Lei Chang). It was a pleasure to be involved with your research.

**B. Module assembly**



I would like to thank New South Innovations and FB Rice for the support of my work throughout the last

few years, in particular Neil Simpson, Athena Pribb, Tanya Motaldo and Chris Owens. Your dedication and efforts in protecting our ideas is very much appreciated. Thank you for giving me the opportunity to learn the patenting process. Neil, thank you for the numerous days we've spent around boats whether that be boat races at a Korean BBQ or sailing on Sydney Harbour amongst colleagues and friends. Amanda, thanks for being my date on awards night, I couldn't think of anyone I would have rather come with me and look stunning.

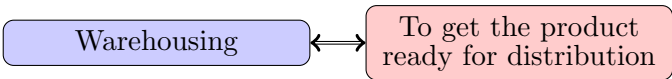


Like making a solar cell, no life during a PhD is complete without durability testing. The ability to work in diverse laboratory environments is reported to be a key factor for a successful career in science. Working under a different scientific mentor and in different environments with access to a broad academic and social culture can greatly expand learning opportunities throughout a PhD;<sup>10</sup> and could there be a better place to develop an eurokous nature than Europe?

Thank you to all the team at Imec and KU Leuven who I have worked with and for your assistance, but in particular Joachim John, Jozef Szlufcik, Jef Poortmans, and Filip Duerinckx for making the internship possible. Even more particularly, thank you to Richard Russell, Loic Tous, Emanuele Cornagliotti, Stefano Granata, Patrick Choulat, Monica Aleman, Angel Urueña and again Joachim who I've worked most closely with and for making me feel so welcome.

It has been a great year for me both inside and outside the lab, opening up a whole new array of cultural experiences and giving me the opportunity for some occasional travel and taste more of my three favourite food groups - beer, chocolate and waffles. Many of these I was lucky enough to taste during various memorable Friday night seminars/adventures hosted by Joachim and Ruth. I really felt as though I had a front row seat with a great view to see what it is like to be a part of a Belgian family.

A big thank you to the KU Leuven swim team for many enjoyable training sessions and evenings around Leuven. Renate and Willem, thanks for putting up with me over many months, I look forward to having you visit me in the warmer parts of the world.



Thank you to all the members of the Technology Transfer Team and in particular David Jordan,

for sharing your industrial experience and efforts in establishing the Solar Industrial Research Facility. Also, Danny Chen, thank you for your many efforts in sorting out my paperwork, you are a champion!

## VII. CONCLUSIONS

In this work, the lessons learnt and support provided throughout my PhD were presented, with an uncanny resemblance to the steps required to develop and commercialise the LDSE solar cell technology. However, it is also apparent that it is very much like yoga: *'It isn't about touching your toes; it's about what you learn on the way down'*.<sup>11</sup>

Whilst doing the research alone could have left many voids in potential experiences and learning opportunities throughout my PhD similar to that which can occur in laser doped regions processed at approximately 0.5 m/s (see Fig. 5), my interactions with all of you have made my time during a PhD feel complete.

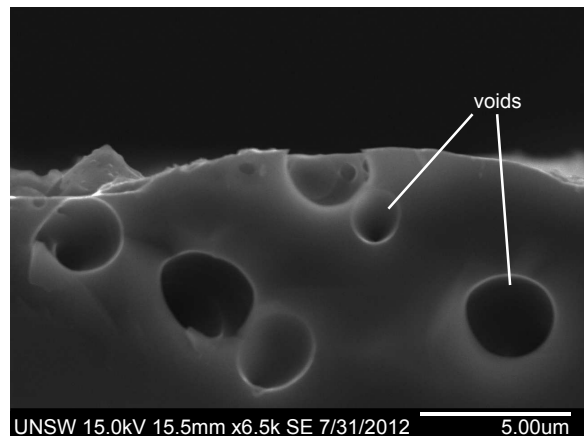


FIG. 5. SEM image of voids in an n-type laser doped region.

In Fig. 6, a custom made LDSE solar cell with an intentionally thick layer of  $105 \pm 5$  nm of PECVD hydrogenated silicon nitride ( $\text{SiN}_x\text{:H}$ ) is shown. During fabrication, a final message is inscribed using the direct etching method and a touch of love, to locally thin the  $\text{SiN}_x\text{:H}$  to a desired thickness of approximately 75 nm, prior to laser doping and metallisation. Processing details for the LDSE solar cell fabrication and direct etching method can be found elsewhere.<sup>12-13</sup>

## ACKNOWLEDGEMENTS

This work was supported by the Australian Government through the Australian Renewable Energy Agency (ARENA). Responsibility for the views, information or advice expressed herein is not accepted by the Australian Government. The authors would like to acknowledge the support of Tom Puzzer and the staff at the UNSW Electron Microscope Unit, a division of the Australian Microscope and Microanalysis Research

Facility (AMMRF) for the assistance with SEM, EBIC and FIB images produced in this thesis, particularly Jenny Norman and Katie Levick. A special thank you also to the Chief Executive Editorial Board consisting of Ian Skinner, Nicole Kuepper and Rowena Thompson, and the assistant to the editors, Dallas Verrills for corrections in this work.



FIG. 6. (Color online) Image of a custom made LDSE solar cell with final message of appreciation.

- <sup>1</sup>K. A. Corballis and R. P. Sutherland, *The New Zealand PhD-who wants it*, Citeseer, 2001.
- <sup>2</sup>Victoria University of Wellington, *Graduate English handbook*. Wellington: School of English, Film & Theatre, Victoria University of Wellington, 1998.
- <sup>3</sup>A. L. Booth and S. E. Satchell, *Journal of the Royal Statistical Society. Series A (Statistics in Society)* pp.297-318 (1995).
- <sup>4</sup>W. G. Bowen, N. L. Rudenstine and J. A. Sosa, *In pursuit of the PhD*, Princeton University Press Princeton, NJ, 1992.
- <sup>5</sup>T. Wright and R. Cochrane, *Studies in Higher Education* **25** (2), 181 (2000).
- <sup>7</sup>D. Wahler, C. S. Grovner, C. Richter, F. Foucu, R. M. Twyman, B. M. Moerschbacher, R. Fischer, J. Muth and D. Prüfer, *Plant physiology* **151** (1), 334 (2009).
- <sup>8</sup>K. Tang, E. J. Øvrelid, G. Tranell and M. Tangstad, *Crystal Growth of Si for Solar Cells*, pp. 219-251 (2009).
- <sup>9</sup>D. Mathiot, *Physical Review B* **40** (8), 5867 (1989).
- <sup>10</sup>D. Carter, M. Stat, L. Campbell and S. Blair, *Synergy* **23**, 3 (2006).
- <sup>11</sup>J. H. Lasater, *A Year of Living Your Yoga: Daily Practices to Shape Your Life*, Rodmell Press, 2006.
- <sup>12</sup>B. Hallam, S. Wenham, A. Sugianto, L. Mai, C. Chong, M. Edwards, D. Jordan and P. Fath, *IEEE Journal of Photovoltaics* **1**, 43 (2011).
- <sup>13</sup>A. J. Lennon, A. W. Y. Ho-Baillie and S. R. Wenham, *Solar Energy Materials and Solar Cells* **93** (10), 1865 (2009).



# Contents

Abstract . . . . .	v
Acknowledgements . . . . .	vii
<b>1 Introduction</b>	<b>1</b>
1.1 Motivation . . . . .	1
1.2 Towards an Industrial Passivated Emitter, Rear and Locally Diffused Solar Cell . . . .	2
1.3 Thesis Objectives . . . . .	5
1.4 Thesis Outline . . . . .	6
<b>2 Light-Induced Degradation, Hydrogenation and Laser Doping for Silicon Solar Cells</b>	<b>8</b>
2.1 Light-Induced Degradation in Boron-Doped Czochralski Silicon . . . . .	9
2.2 Hydrogen in Silicon . . . . .	15
2.3 Laser Doping for Silicon Solar Cells . . . . .	24
2.4 Chapter Summary . . . . .	34
<b>3 Advanced Hydrogenation for Silicon Solar Cells</b>	<b>36</b>
3.1 Increased Generation of Neutrally Charged Hydrogen in Silicon . . . . .	37
3.2 Hydrogen Passivation of B-O Defects . . . . .	53
3.3 Advanced Hydrogen Passivation for Upgraded Metallurgical Grade Silicon . . . . .	70
3.4 Passivation of Oxidation-Induced Stacking Faults . . . . .	82
3.5 Hydrogen Passivation for Defected n-type Silicon . . . . .	87
3.6 Hydrogenation for Multi-Crystalline and Seeded-Cast Quasi Mono-Crystalline Silicon	96
3.7 Hydrogenation for Finished Solar Cells . . . . .	113

3.8	Chapter Summary	121
<b>4</b>	<b>Advanced Laser-Doped Structure Formation</b>	<b>125</b>
4.1	Continuous Wave Laser Doping for Deep Junction Formation	127
4.2	Modelling Diffusion in Laser-Doped Regions	142
4.3	Laser Doping with Aluminium Oxide	168
4.4	Contacting Buried Layers in Silicon Solar Cells	191
4.5	Chapter Summary	213
<b>5</b>	<b>Hydrogen Passivation of Laser-Induced Defects</b>	<b>216</b>
5.1	Defects Generated during Continuous Wave Laser Doping	217
5.2	Hydrogen Passivation of LasID	223
5.3	Chapter Summary	247
<b>6</b>	<b>Development of High Efficiency Laser-Doped Solar Cells with Advanced Hydrogenation</b>	<b>249</b>
6.1	An Improved Firing Process to Avoid Localised Recombination	250
6.2	Avoidance of Parasitic Plating for LDSE Solar Cells	257
6.3	Edge Junction Isolation Methods for LDSE Silicon Solar Cells	265
6.4	Advanced Hydrogenation for LDSE1 Solar Cells	277
6.5	Efficiency Enhancements for Passivated Emitter and Rear Cell Through the Addition of an LDSE Structure	286
6.6	The Pathway to Improved Hydrogen Passivation for n-PERT Cells	308
6.7	Chapter Summary	330
<b>7</b>	<b>Conclusions and Outlook</b>	<b>332</b>
	<b>Appendix A Physical Constants, Symbols and Abbreviations</b>	<b>339</b>
	Physical Constants	339
	Symbols	340
	Abbreviations	343
	<b>Appendix B Publications List</b>	<b>346</b>

Refereed Journal Papers . . . . .	346
Conference Proceedings . . . . .	348
Patents and Patent Applications . . . . .	352



# Chapter 1

## Introduction

### 1.1 Motivation

In recent years the atmosphere and ocean have warmed; snow cover, ice sheets and glaciers have shrunk almost worldwide and sea levels have risen. Each of the past three decades has been successively warmer than any decade prior to 1950. Many of the observed changes are well beyond the natural variations observed over thousands of years. The largest cause of these changes is due to anthropogenically induced increases in greenhouse gas concentrations, primarily carbon dioxide. The levels of atmospheric greenhouse gas concentrations are now greater than that at any time within the previous 800,000 years and continuing to rise at alarming rates [[IPCC 13](#)].

To mitigate further increases in atmospheric greenhouse gas concentrations and the associated risks to human health and the environment, it is essential to uptake a widespread usage of renewable energy sources to replace polluting fossil fuels. Whilst global demand for renewable energy sources is continuing to rise, renewables only account for 19 % of global energy consumption [[REN2 13](#)]. However, many countries around the world have conducted studies with a feasible usage of 100 % renewables using commercially available and proven technologies such as wind, solar photovoltaics (PV), solar thermal and hydroelectricity sources [[Lund 09](#); [Elli 12](#); [Comm 11](#)].

Despite the promise of such technologies, a number of factors currently exist that limit the



## 1.2. TOWARDS AN INDUSTRIAL PASSIVATED EMITTER, REAR AND LOCALLY DIFFUSED SOLAR CELL

---

widespread usage of renewables worldwide, such as government policies, public perception, market barriers and cost [Pain 01; Verb 10]. However with time, many of these barriers are diminishing. Government policies to encourage the use of renewables now exist in more than 120 countries, many companies and residential households have opted for the voluntary use of renewable energy, and electricity markets around the world are adapting to allow a greater penetration of renewables [REN2 13]. In addition, the costs of renewable energy sources such as solar PV and wind have continued to fall dramatically in the last decade. Subsequently, they are now seen as viable technologies, able to compete against fossil fuel based technologies without subsidies in various locations around the world [IEA 13]. However, in order to reduce the cost of renewable energy sources such as PV further, the development of new techniques and an improved understanding of processes currently used within the industry are of critical importance to increase cell efficiencies as well as reduce the reliance on high cost processes.

The requirements for localised processing on solar cells to achieve high efficiencies lends itself towards the use of laser processing. This is due to the ability of lasers to form fine feature sizes at a high throughput. However many laser processes can introduce laser-induced defects (LasID) into the solar cell, causing increases in recombination. A whole range of other defects can also be introduced into the silicon during crystal growth or subsequent processes. In order to avoid performance degradation caused by such defects, the defects must either be subsequently removed chemically, or the recombination activity of such defects altered using hydrogen passivation.

## 1.2 Towards an Industrial Passivated Emitter, Rear and Locally Diffused Solar Cell

The passivated emitter, rear and locally diffused (PERL) solar cell was developed at the University of New South Wales (UNSW) to edge closer towards the theoretical efficiency limit for silicon solar cells of 29 % [Gree 95]. However the fabrication sequence of the PERL solar cell uses a series of complex, high cost processes common to the semiconductor industry such as photolithography. PERL cells also rely on expensive PV grade float-zone (FZ) wafers. Hence large scale production of the PERL cell for the current commercial market of silicon solar cells appears unviable. As shown

in Fig. 1.1, PERL cells exhibit a number of features which have allowed such a high efficiency to be achieved. To avoid bulk recombination and the formation of oxygen related defects in the device, PERL cells are fabricated on high lifetime  $1 \Omega \cdot \text{cm}$  p-type FZ silicon wafers.

PERL cells have multiple features to enhance the optical properties. An inverted pyramid structure with a double layer antireflection coating of evaporated  $\text{MgF}_2/\text{ZnS}$  is used on the front surface to reduce reflection. On the rear surface, the full area layer of evaporated aluminium (Al) acts as a mirror. This structure results in an average path length enhancement for light of approximately 40 times [Camp 87]. To further increase the short circuit current density ( $J_{SC}$ ), relatively thick wafers ( $400 \mu\text{m}$ ) are used to increase the absorption of photons, as well as very fine contact line widths of  $2 \mu\text{m}$  to reduce shading [Zhao 96].

High quality diffusions are performed using  $\text{PBr}_3$  and  $\text{BBr}_3$  to reduce surface damage in comparison to diffusions performed using solid sources [Zhao 96]. A lightly doped phosphorus emitter with a sheet resistance of approximately  $150 \Omega/\square$  is applied to reduce the surface recombination velocity (SRV) at the front surface. This also avoids the loss of blue response as commonly suffered by screen-printed solar cells which have a much more heavily doped emitter with a sheet resistance of  $40 - 60 \Omega/\square$  [Neuh 07].

Trichloroethane grown thermal silicon dioxide ( $\text{SiO}_2$ ) layers are used on both surfaces as surface passivating dielectrics, however high quality surface passivation is not achieved until atomic hydrogen is introduced. To do so, Al is evaporated onto both surfaces and an alneal process is performed in forming gas (FG) ambient [King 90]. During the alneal process, the Al reacts with hydroxyl ions in the  $\text{SiO}_2$  layer to form atomic hydrogen, which can then migrate to the Si/ $\text{SiO}_2$  interface to passivate dangling bonds [Zhao 96].

Reduced recombination losses at the metal/Si interface are achieved through a reduced metal/Si interface contact area and very heavy phosphorous or boron diffusions underneath the contacts. To minimise the metal/Si interface contact area on the rear surface, the localised heavy boron diffusions are performed in a point contact structure. This allows PERL cells to achieve high open circuit voltages ( $V_{OC}$ ) over 700 mV and an efficiency of 25 % [Zhao 96; Zhao 99].

Many newer solar cell technologies have developed alternative processes to take advantages

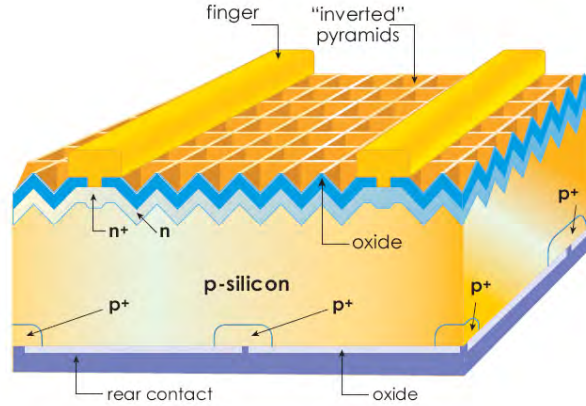


Figure 1.1: Structure of the world record holding PERC cell [UNSW 07].

of such features, often using novel processing techniques to avoid the high costs associated with the production of PERC cells. Commercial silicon solar cells are typically fabricated on lower quality wafers such as commercial grade Czochralski (CZ) grown or multi-crystalline silicon wafers. However, the use of these lower quality substrates introduces bulk defects into the solar cells, particularly due to the formation of boron-oxygen (B–O) complexes and the inclusion of impurities and crystallographic defects during crystal growth [Fisc 73].

Recent advancements in solar cell processing have seen the widespread use of plasma enhanced chemical vapor deposition (PECVD) for the growth of layers such as hydrogenated silicon nitride ( $\text{SiN}_x\text{:H}$ ). This has led to substantial improvements in the efficiency of solar cells fabricated on low quality materials such as multi-crystalline silicon due to improved defect passivation at the silicon surface and within the bulk [Aber 01]. The use of the improved hydrogen passivation realised by the release of atomic hydrogen from the PECVD films can effectively raise the electronic quality of the silicon material and avoid the need to introduce atomic hydrogen using expensive gases such as FG.

Advances in laser processing such as the development of laser doping for silicon solar cells can allow the formation of localised, heavily diffused regions of dimensions similar to that achieved using expensive patterning methods like photolithography. Furthermore, such regions can be formed in a self-aligned manner in which the dielectric is opened to define the contact area. At the same time, the underlying silicon is heavily diffused leading to substantial process simplifications compared to

conventional methods based on patterning and thermal diffusions [Wenh 02].

The following chapter discusses hydrogen passivation mechanisms, B–O defect formation as well as the laser doping process for silicon solar cells. If an improved understanding of such processes and limitations could be achieved, many of the high efficiency attributes of the world record PERL cells could be incorporated into low-cost commercial silicon solar cells.

### 1.3 Thesis Objectives

This thesis explores the use of laser doping and hydrogen passivation to increase the performance and reduce manufacturing costs of silicon solar cells. It focuses on several different aspects such as: (1) understanding mechanisms of hydrogen passivation in silicon solar cells; (2) developing new hydrogenation approaches; (3) developing new laser doped contact structures; (4) exploring the passivation of LasID using hydrogen; and (5) integrating advanced hydrogenation methods into laser doped solar cells.

The objectives of this thesis are to:

1. Understand hydrogen passivation mechanisms in silicon solar cells.
2. Develop advanced hydrogenation approaches to improve the electrical quality of a whole range of commercial grade silicon materials through the passivation of bulk defects.
3. Develop new contacting structures using laser doping to allow increased electrical performance of solar cells in an industrially applicable manner.
4. Understand diffusion mechanisms during the laser doping process.
5. Develop methods to avoid performance degradation from LasID generated during laser doping using hydrogen passivation.
6. Demonstrate that the benefits of advanced hydrogenation techniques can be retained by using laser doped contacts at the metal/Si interface.

7. Develop improved device designs to increase the effectiveness of hydrogen passivation in laser doped silicon solar cells.
8. Incorporate advanced hydrogenation methods into laser doped silicon solar cells.

## 1.4 Thesis Outline

This thesis is comprised of 7 chapters. In Chapter 1, the motivation, objectives and outline of this thesis are presented.

In Chapter 2, a literature review of B–O defects, diffusion and passivation mechanisms of hydrogen in silicon, and the laser doping process are presented.

In Chapter 3, new insights into the passivation mechanisms of hydrogen in silicon solar cells are presented. The fractional charge state concentrations of hydrogen within the silicon are observed to have a major influence on the passivation of defects such as B–O complexes. Furthermore, defect passivation can be reversed during subsequent processes at elevated temperatures if adequate charge state control is not maintained. Hydrogen passivation of various bulk defects such as dislocations, oxidation-induced stacking faults (OSF), slip-lines and impurities are explored on many different silicon materials used in commercial production. Remarkable increases in the electrical qualities of all materials are observed with increases in 1-sun implied open circuit voltages ( $iV_{OC}$ ) of up to 180 mV. Independently confirmed  $V_{OC}$  over 680 mV with pseudo efficiencies ( $p\text{-}\eta$ ) of 23 % are demonstrated on silicon solar cells fabricated on standard commercial grade boron-doped CZ (B-CZ) silicon wafers.

In Chapter 4, several advanced laser doped structures are presented. Due to the properties of continuous wave (CW) and quasi-continuous wave (Q-CW) lasers, deep molten silicon regions of more than 10  $\mu\text{m}$  depth can be formed. Such properties can enable electrical contact to buried layers within the solar cell or allow the formation of transistors. Furthermore, Al atoms from passivating aluminium oxide ( $\text{AlO}_x$ ) layers can be used as a dopant source to form localised heavily doped p-type regions in a self-aligned manner without the requirement for additional dopant sources. Fill factors ( $FF$ )  $> 80$  % on large area devices are presented featuring laser doped Al  $p^{++}$  regions.

In Chapter 5, hydrogen passivation of LasID is explored. This is an essential process for fabricating high efficiency laser doped solar cells. Increases in  $iV_{OC}$  of up to 50 mV are demonstrated on test structures, and efficiency increases of more than 0.7 % absolute to 20.7 % are achieved on n-type solar cells with a passivated rear, totally diffused boron emitter (n-PERT).

In Chapter 6, the development of high efficiency laser doped solar cells with advanced hydrogenation is presented. Several processes are explored to improve the performance of laser doped selective emitter (LDSE) solar cells through: (1) improved firing to avoid localised recombination; (2) emitter etch-back processes to avoid parasitic plating; and (3) edge junction isolation methods to avoid shunting when using self-aligned plated contacts. An independently confirmed efficiency of 19.6 % on a large area device with a LDSE structure and full area Al back surface field (Al-BSF) is obtained. This is achieved by using a rear phosphorus layer to assist in hydrogen retention in the device and an advanced firing process (AFP) with enhanced minority carrier injection.

In Chapter 7, the conclusions drawn from this thesis and recommendations for future work are presented.

## Chapter 2

# Light-Induced Degradation, Hydrogenation and Laser Doping for Silicon Solar Cells

In order to fabricate low-cost high efficiency solar cells, recombination mechanisms must be well understood to allow such losses to be overcome, either by avoiding the formation of the recombination site, or through defect passivation. In particular, an improved understanding of passivation processes is required for recombination sites which occur due to impurities within the bulk silicon, such as B–O complexes. With such knowledge, less stringent constraints could be placed on purification processes, leading to cost reductions. In addition to improved passivation, laser processes (such as laser doping) are of great importance for silicon solar cell fabrication, due to the compatibility with high-throughput fabrication and ability to create high efficiency solar cell structures at low cost.

In this chapter, the understanding of mechanisms associated with the formation and passivation of B–O defects, hydrogen diffusion and passivation in silicon, as well as the laser doping process are reviewed.

## 2.1 Light-Induced Degradation in Boron-Doped Czochralski Silicon

Due to the expense of high quality FZ wafers, CZ grown wafers dominate commercial mono-crystalline PV applications with a market share of almost 40 % of the entire PV market [ITRP 11]. Commercially manufactured mono-crystalline silicon solar cells are almost exclusively produced on B-CZ substrates, however there are substantial limitations to the lifetimes and hence efficiencies which can be obtained using such wafers due to a reduced quality when compared to FZ wafers. Lifetimes in B-CZ silicon are widely reported to degrade after illumination, carrier injection in the dark or thermal annealing [Reis 96; Fisc 73; Knob 95; Knob 96; Schm 97].

### 2.1.1 Formation of B–O Defects in Czochralski Silicon

Lifetime degradation in B-CZ silicon can occur due to the formation of boron associated recombination centres such as B–O complexes. However the degradation is fully reversible after annealing at temperatures above 170 °C [Fisc 73; Knob 95; Knob 96; Schm 97; Graf 81; Lim 08b]. Whilst the degradation associated with the formation of B–O complex is often referred to as light-induced degradation (LID), the defect generation rate only weakly depends on illumination intensity for intensities greater than 1 mW/cm<sup>2</sup> [Knob 95; Rein 03] and can occur in the dark for temperatures above 300 K in the absence of an applied bias [Both 03]. Furthermore, the defect formation rate is determined by the total recombination rate, and hence dependent on the total minority carrier concentration ( $n$ ) rather than the excess minority carrier concentration ( $\Delta n$ ) [Both 03]. It is also reported that the B–O defect related effective minority carrier lifetime ( $\tau_{eff}$ ) in silicon shows a strong injection-level dependence, particularly over the range of ( $\Delta n$ ) from  $1 \times 10^{14} - 2 \times 10^{16}$  /cm<sup>3</sup> [Schm 98].

For lifetime degradation in p-type silicon doped solely with boron, Bothe *et al.* 2006 observed a fast-forming recombination centre (FRC) and slow-forming recombination centre (SRC) process occurring in parallel. The FRC process occurs in the first few minutes, whilst the SRC process can take several hours. Initially these two processes show two different states, however for longer times



a subsequent reaction appears to transform both into a final state of the SRC asymptotic process [Both 06]. This observation suggests multiple stable states of the B–O complex, in agreement with theoretical predictions [Adey 04]. At the time, Bothe *et al.* 2003 attributed the formation of the recombination active form of the SRC defect to substitutional boron ( $B_s$ ) and an interstitial oxygen dimer ( $O_{2i}$ ), whereby the formation of the B–O complex is a recombination enhanced diffusion process [Week 75]. In this model, the minority carriers are not directly involved in the defect formation, but rather the energy released from minority carriers during the recombination process activates the diffusion of the  $O_{2i}$  which is then captured by a  $B_s$  atom, forming a  $B_s$ – $O_{2i}$  complex [Both 03]. It was also observed that the defect density of both the FRC and SRC processes were proportional to the  $B_s$  concentration and the square of the interstitial oxygen ( $O_i$ ) concentration, and the defect generation rate for both processes was proportional to the square of the  $B_s$  concentration. However the Bourgoin-Corbett mechanism [Bour 72] relies on two different charge states of  $O_{2i}$ , namely the neutral  $O_{2i}^0$  and the double positively charged  $O_{2i}^{2+}$  species. Whilst  $O_{2i}$  has been observed in optical absorption spectra, to date,  $O_{2i}^{2+}$  has not been observed. This has raised questions regarding the likelihood of this mechanism [Muri 11].

Another model based on the involvement of  $B_s$  suggests the presence of a latent  $(B_s-O_{2i})^-$  complex prior to illumination. In this case degradation proceeds through the transformation of a latent defect into a recombination-active state  $(B_s-O_{2i})^+$  [Bour 00]. In this model, the grown-in concentrations of  $(B_s-O_{2i})^-$  are also proportional to the boron dopant density ( $N_a$ ). However, in compensated p-type silicon, the introduced recombination active concentration for the SRC is proportional to the hole concentration ( $p$ ) rather than  $N_a$ , and the rate constant is proportional to the square of  $p$  [Macd 09; Macd 11]. Hence it would appear unlikely that  $B_s$  is involved in the SRC process.

To explain the dependence of the defect density on  $p$  and therefore effective dopant density ( $N_{eff}$ ), it was proposed that interstitial boron ( $B_i$ ) could be involved [Voro 10]. In this model,  $O_{2i}$  bind to  $B_i$  during ingot cooling and are therefore fixed at room temperature. Subsequently, the concentration of  $B_iO_{2i}$  is dependent on the  $B_i$  at the freeze-in temperature, and following on, dependent on  $N_{eff}$  and hence  $p$ . It is thought that this  $B_iO_{2i}$  defect is latent, and can be transformed into a recombination active defect with minority carrier injection. An alternative model involving  $B_i$  was proposed by MacDonald *et al.* 2011, in which the  $B_i$  binds to mobile  $O_{2i}$  at room

temperature [Macd 11]. Both models predict a defect density which is inversely proportional to the  $N_{eff}$  in n-type silicon and independent of  $\Delta n$ . However, more recently it has been demonstrated in compensated n-type silicon, that the defect density appears to be independent of  $N_{eff}$ , but strongly dependent on the  $\Delta n$  during illumination [Roug 11]. Hence it has been proposed that the defect concentration is fixed at room temperature by the Fermi level ( $E_F$ ) in p-type silicon and the quasi-Fermi level for holes ( $E_{Fp}$ ) in n-type silicon.

In contrast, in n-type silicon the FRC appears to be the dominant recombination mechanism [Voro 11]. Similarly to the SRC process, the generation rate for the FRC process is proportional to the square of  $p$ . As holes are the minority carrier in n-type silicon, the kinetics are several orders of magnitude lower than that of the FRC in p-type silicon. In studies to date, the SRC has not been observed in n-type silicon, however this may be due to the substantially increased time scale of the SRC mechanism which is also dependent on  $p$ . Furthermore, for the FRC process, as the remaining  $p$  is dependent on the FRC, the kinetics are non-linear [Voro 11].

The most recent understanding is that both  $B_s$  and  $B_i$  are involved in the formation [Voro 11]. It now appears that the SRC process is caused by  $B_i$  and the FRC process is caused by  $B_s$ . The FRC exists in three charge states (-1, 0, +1) with two energy levels. The FRC emerges by a reconstruction of a latent  $B_s-O_{2i}$  complex [Voro 11]. The current model of the reconfiguration through an intermediate state takes into account the dependence of the generation rate on  $p$ , which in some instances can be reduced to a dependence on the square of  $p$ .

Whilst much further study is required to fully understand the mechanisms behind the generation of B–O defects, the degradation of solar cell performance caused by B–O complexes is clear and must be avoided.

### 2.1.2 Avoidance of B–O Defect Formation

In order to reduce or avoid the effect of B–O related recombination centres, many different approaches can be taken. One such approach is to reduce  $B_s$  or  $B_i$  by using more lightly doped material or replacing the boron with other dopants such as phosphorus or gallium. However due to the lower segregation coefficients of phosphorus and in particular gallium, large resistivity varia-

## 2.1. LIGHT-INDUCED DEGRADATION IN BORON-DOPED CZOCHRALSKI SILICON

---

tions are observed throughout phosphorus- and gallium-doped CZ grown ingots, which may result in large variations for the efficiencies obtained using a given cell structure [Mori 03; Davi 80; Fors 11; Meem 06; Glun 01b].

Furthermore, moving to n-type wafers introduces the need to form a p-type layer to create the device junction. This is typically achieved using boron dopants through thermal diffusions or ion implantation [Cous 10; Vesc 11; Beni 08; Bate 11]. However LID has been observed in both n- and p-type compensated silicon [Schu 10; Macd 09; Lim 10b] and hence it would raise questions over the stability of solar cells fabricated with boron emitters. Alternatively, the junction may be formed on the rear of the device using conventional screen-printing approaches to form an alloyed Al junction [Schm 06]. However by forming the junction on the rear of the device, higher lifetimes are required in order to collect minority carriers, as the majority car generated near the front surface of the device.

Other approaches opt for reducing the oxygen concentration during the crystal growth process, such as by using the more expensive FZ growth method to virtually eliminate oxygen from the silicon material altogether [Glun 00b]. Modifications to the CZ growth process have also been used by applying magnetic fields to suppress turbulent convection in the silicon melt to decrease and control oxygen incorporation in the magnetically confined CZ (MCZ) material and reduce LID effects [Wata 02; Hosh 80; Hosh 85; Glun 00b; Sait 01]. Crucible walls can also be coated with layers such as silicon nitride ( $\text{SiN}_x$ ) to reduce oxygen contamination into the molten silicon [Zule 83; Schm 97].

However all of these processes are costly. As a result, most solar cells in commercial production still contain relatively large concentrations of both boron and oxygen, and hence suffer from B–O complex generation. Therefore, it is crucial to develop approaches to deactivate the recombination activity of B–O complexes.

### 2.1.3 Recovery and Permanent Deactivation of B–O Defects

Whilst annealing in the dark at temperatures above 170 °C is reported to fully reverse the effects of LID [Fisc 73; Knob 95; Knob 96; Schm 97; Graf 81; Lim 08b], the lifetimes prior to degradation

reported in literature are typically substantially lower than that of boron-doped FZ (B-FZ) or gallium-doped CZ (Ga-CZ) wafers [Glun 00b; Glun 01a; Lim 08b]. Furthermore, after the B–O<sub>2i</sub> complex dissociates through annealing in the dark, the B and O<sub>2i</sub> are still typically present in the silicon and therefore, can once again form a B–O<sub>2i</sub> complex under further minority carrier injection [Lim 08b].

Several approaches have been observed to increase the stable lifetime of B-CZ wafers through permanent deactivation of B–O defects. High temperature oxidation and annealing processes are reported by many groups to reduce the effect of LID if processing is performed in the correct manner [Glun 01b; Schm 04; Glun 01a; Lee 01; Nage 00; Sait 01; Knob 96]. However if not performed in the correct manner, a substantial degradation of the stable  $\tau_{eff}$  may result [Glun 01b].

Phosphorus diffusions are also reported to increase the stable lifetime of B-CZ wafers and accelerate the deactivation process of B–O defects [Both 05; Lim 08a; Lim 08c]. However other reports suggest phosphorus gettering has no direct impact on LID, with the same reduction in metastable defect concentration occurring from high temperature oxidations [Both 02]. In such high temperature processes, interstitial oxygen cluster formation and O<sub>2i</sub> dissociation are reported to reduce the available O<sub>2i</sub> concentration for B–O defect formation [Roug 11]. Alternatively annealing at 450 °C for over 30 h is reported to yield the same results as achieved from high temperature processes, through a reduction in O<sub>2i</sub> concentration and thermal donor creation [Both 02]. Annealing has also been performed at intermediate temperatures in the range of 500 – 700 °C, leading to a permanent decrease in the defect density, potentially due to O<sub>2i</sub> dissociation or changes to B<sub>i</sub> clusters [Roug 11].

Just as the formation of B–O complexes can be enhanced with illumination, the rate of B–O defect passivation can be enhanced by minority carrier injection from illumination. Recent work with simultaneous 1-sun illumination and thermal annealing at temperatures of 70 – 160 °C is reported to permanently deactivate the B–O complex and suggest the presence of a third regenerated state of the B–O complex [Herg 06; Herg 08]. In some instances however, prolonged exposure to simultaneous heating and illumination can lead to subsequent reductions in  $V_{OC}$ . Several possible causes for this subsequent reduction were hypothesised, including the presence of a fourth state of the B–O defect, however the reasons remain unclear [Herg 09]. The regenerated state of lifetime

can also be destabilised if subsequent annealing is performed over 200 °C without minority carrier injection [Herg 10].

Lim *et al.* 2006 also reported the permanent deactivation of the B–O complex using higher temperatures in the range of 160–215 °C [Lim 08b]. A theoretical model was introduced suggesting the presence of an unknown atom **X** which forms a recombination-inactive complex with the  $O_{2i}$ , ( $XO_{2i}$ ). The dissociation of the  $B_s-O_{2i}$  complex and subsequent formation of the  $XO_{2i}$  complex appeared to show different regimes occurring in parallel with a fast and slow process, similar to that observed by Bothe *et al.* 2006 [Both 06].

Whilst it has been reported that hydrogen plays no role in the deactivation process [Glun 01b], recent studies have observed that wafers passivated by PECVD of  $SiN_x:H$  show degradation upon exposure to illumination and the subsequent regeneration of  $\tau_{eff}$  though exposure to simultaneous heating and illumination, whilst wafers passivated by low pressure chemical vapor deposition of  $SiN_x$  not containing hydrogen show degradation but no subsequent regeneration [Munz 09]. Hence hydrogen plays a critical role in the regeneration process for B–O complexes. This effect has also been observed by other authors with a strong correlation between the hydrogen content in the  $SiN_x:H$  layer and the regeneration process [Dubo 12; Krug 11].

However Lim *et al.* 2010 indicate that hydrogen content in the dielectric layer alone does not influence the deactivation process, but the rate of deactivation is inversely proportional to the  $O_{2i}$  concentration and is adversely affected by the presence of thermal donors [Lim 10a]. Furthermore, the saturation value of the recovered lifetime decreases with increasing  $O_i$  concentration. This, in conjunction with earlier reports of lower lifetimes in the non-degraded state of B-CZ silicon compared to B-FZ and Ga-CZ wafers suggests that B–O defects may still be present in what is widely referred to as the non-degraded or regenerated states.

Whilst the formation of B–O defects occurs under illumination, simultaneous illumination and heating can lead to the permanent deactivation of the defects. Hydrogen passivation is reported to play a critical role during this process, however the mechanisms are not fully understood. Hence its role must be investigated further.

### 2.1.4 Summary of Light-Induced Degradation in Boron-Doped CZ Silicon

Many contradictions are reported in the literature for light-induced degradation in silicon in relation to the formation, recovery and permanent deactivation of B–O complexes. Conventional approaches to avoid the formation of B–O complexes often increase the cost of production of solar cells such as by using more expensive n-type CZ wafers, and hence typical solar cells still suffer from B–O generation. Simultaneous illumination and heating can lead to the permanent deactivation of B–O defects, with hydrogen playing a vital role in the process. However, the role of hydrogen is not fully understood. As a result, further work is required to improve the understanding of the passivation process, and reduce the recombination activity of B–O defects.

## 2.2 Hydrogen in Silicon

The properties and interactions of hydrogen in silicon has been widely studied over multiple decades with beneficial effects shown as early as 1976 [Paul 76]. However the diffusion and passivation mechanisms of hydrogen in silicon, and dependence on material parameters appear to be poorly understood with many contradictory theories and variations in the results and subsequent interpretations reported in the literature [Sopo 92; Sopo 96; Seag 87; Sopo 01; Seag 88]. The complications arise in that: (1) atomic hydrogen interacts with the lattice and virtually all impurities and defects within the silicon [Sopo 02]; (2) that hydrogen can be incorporated into films unintentionally during a variety of processing steps; and (3) the difficulty of measurement/detection of hydrogen in silicon [Quei 98; Seag 87]. Even a dilute HF dip at room temperature can result in large amounts of atomic hydrogen diffusing several microns into the silicon [Sopo 01].

### 2.2.1 Hydrogen Diffusion in Silicon

The diffusion of hydrogen in silicon has been studied by many authors and is complicated by effects of temperature, electric fields, crystallographic defects and the type and concentration of almost all

impurities and defects within the silicon [Sopo 01; Sopo 96; Sopo 03; Davi 96; Pear 91; Pank 91; Corb 88; John 85; Ichi 68]. As a result, many experiments and theories yield conflicting results [Sopo 01] and an uncertainty in the diffusivity of hydrogen [Seag 88]. However earlier studies of the effective diffusivity of hydrogen by Wieringen *et al.* 1956, are often seen as an upper limit to hydrogen diffusion in silicon (see Fig. 2.1) [Van 56]. As shown through experiments, factors which influence the mobility of hydrogen can lead to variations in hydrogen diffusivity of more than five orders of magnitude for a given temperature [Sopo 01; Sopo 92; Capi 87; John 85; Klee 06].

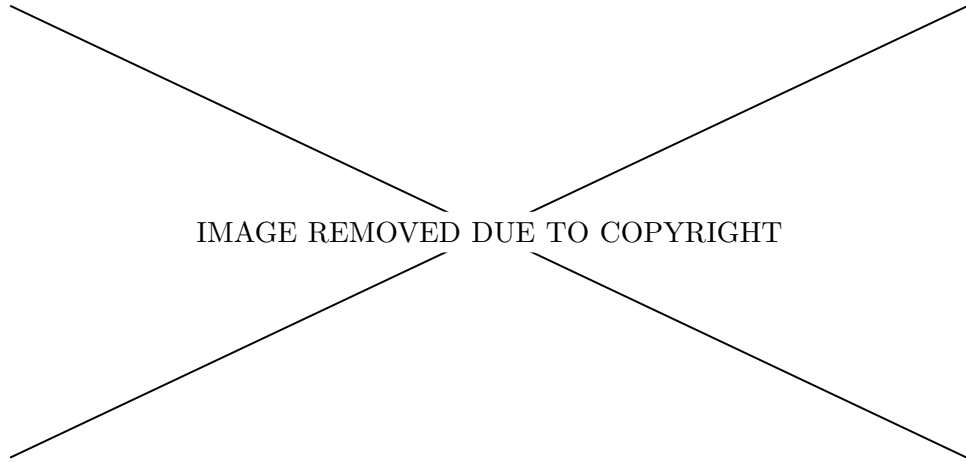


Figure 2.1: Hydrogen diffusivity in silicon from various studies. Image sourced from [Sopo 01].

The primary mechanism for the diffusion of hydrogen in silicon is via interactions with the lattice [Sopo 01]. Hence to understand the diffusion of hydrogen in silicon, such interactions must be understood. A lack of understanding of hydrogen diffusivity in silicon has resulted in a large variation in the reported times which are required to passivate bulk defects. For example, some researchers have reported that hydrogen passivation processes require only a few minutes, whilst others using somewhat similar conditions reported that a duration of several hours appears to be too short [Sopo 92; Seag 87; John 86; Hans 84; Jeng 88; Dube 84; Roha 86]. Such information does not appear to match hydrogen diffusivity data available in the literature, which is primarily based on mono-crystalline silicon. Surprisingly, in some studies, higher diffusivities have been

reported in cast ingots or silicon sheets of multi-crystalline silicon than in mono-crystalline CZ or FZ silicon, contrary to a widespread belief that the diffusivity should be lower due to interactions with defects [Sopo 92]. The higher diffusivity observed in multi-crystalline silicon may be due to a higher diffusion in grain boundaries than within the grains [Elga 98]. However, Jackson *et al.* 1992 presented conflicting data which suggests that grain boundaries do not enhance hydrogen diffusion but rather act as efficient hydrogen traps and conclude that hydrogen diffusion in multi-crystalline silicon is substantially lower than that of mono-crystalline material [Jack 92].

Many theories on hydrogen diffusion mechanisms have been proposed, however such theories neglect key factors which influence the diffusion of hydrogen. For example, Borenstein *et al.* 1988 proposed a model which highlights the effects of dopant type and concentration on hydrogen diffusivity, but neglects the influence of both built-in electric fields and the dissociation of boron-hydrogen complexes [Bore 88; Bore 93; Math 89]. The influence of dopants on hydrogen diffusivity is widely acknowledged in many other publications but with conflicting conclusions [Nick 98; Math 89; John 85; John 86]. Nickel *et al.* 1998 report an enhancement of hydrogen diffusivity in the presence of phosphorus, whilst Mathiot *et al.* 1989 indicate that hydrogen diffusivity is reduced by interactions with dopant atoms [Nick 98; Math 89].

Hydrogen diffusivity is affected by the concentration of binding sites [Pank 84], reduced by the formation of hydrogen molecules [Math 89] and it has been suggested that surface damage enhances the diffusion of hydrogen into silicon, which could assist in bulk passivation [Sopo 96]. Several authors have also reported interesting interactions between oxygen and hydrogen in silicon. For example the diffusivity of hydrogen is reduced by oxygen, whilst the diffusion of oxygen is greatly enhanced by the presence of hydrogen [Sopo 92; Estr 90; Newm 91; Capa 99; Elga 98]. It has also been reported that high carbon concentrations can lead to an enhancement of hydrogen diffusivity [Sopo 92], whilst others have not observed a correlation between carbon concentration and hydrogen diffusivity [Elga 98].

Perhaps one of the most underestimated properties of hydrogen in silicon is its ability to assume different charge states depending on the material's dominant conductivity [Herr 01]. Hence hydrogen can take on a positive ( $H^+$ ) neutral ( $H^0$ ) or negative ( $H^-$ ) charge state [Zhu 90; Math 89; Seag 88; Herr 01]. As highlighted by Herring *et al.* 2001, when in thermal equilibrium in p-type



silicon, almost all atomic hydrogen is  $\text{H}^+$  due to a deficiency of electrons, whilst in n-type silicon almost all hydrogen is  $\text{H}^-$  due to an abundance of electrons. Furthermore, under equilibrium conditions in both n- and p-type silicon,  $\text{H}^0$  never reaches a large relative concentration compared to the dominant charge species (see Fig. 2.2) [Herr 01]. However by changing the position of  $E_F$  relative to the middle of the band-gap ( $E_m$ ), the fraction of hydrogen in the various charge states can be altered by changing the number of electrons available to bond with the atomic hydrogen, and therefore the relative concentrations of the minority hydrogen charge species can be greatly enhanced.

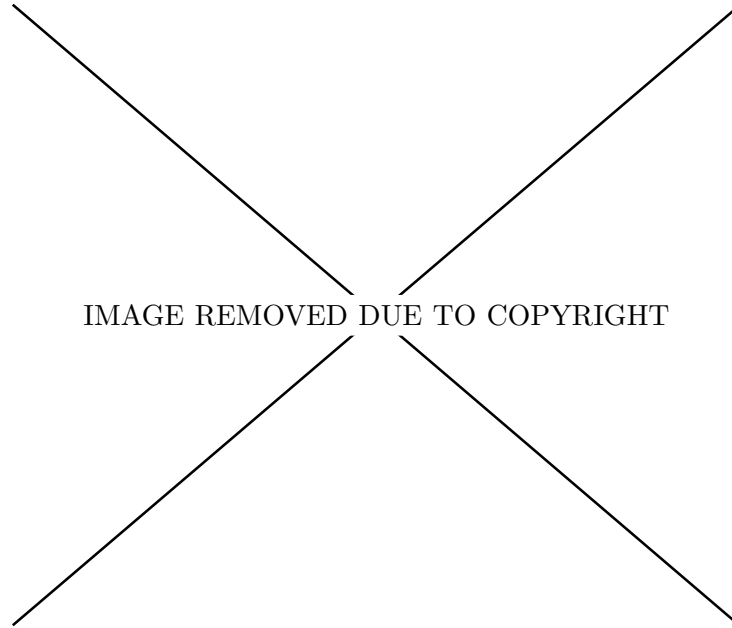


Figure 2.2: Relative concentrations of hydrogen charge states in equilibrium in relation to the position of  $E_F$  within the band-gap at 150 °C. Top diagram: Ratio of the population of  $\text{H}^+$  and  $\text{H}^-$  to that of  $\text{H}^0$ . Bottom diagram: Fraction of the total hydrogen concentration for each of the three charge states. Image sourced from [Herr 01].

Due to interactions with the lattice, impurities and defects within silicon, large differences have

been observed for the mobility of the various charge states. For example,  $H^0$  is not affected by electric fields and charge effects within the silicon [Herr 01], and has a diffusivity five orders of magnitude higher than that of  $H^+$  [Job 98]. Furthermore, the diffusivity of  $H^+$  is substantially smaller than that of  $H^-$  (see Table 2.1) [Math 89].

Such results may lead to the conclusions that it is easier to hydrogen passivate n-type silicon than p-type silicon due to a substantial increase in hydrogen diffusivity of the dominant charge species in thermal equilibrium. However many other factors can also influence the effectiveness of hydrogen passivation in silicon.

Table 2.1: Diffusion coefficients ( $D$ ) of the various charge states of hydrogen in silicon at 150 °C. Values obtained from [Math 89].

Charge state	$D$ at 150 °C (cm <sup>2</sup> /s)
$H^+$	$6 \times 10^{-13}$
$H^-$	$3 \times 10^{-10}$
$H^0$	$1.4 \times 10^{-8}$

### 2.2.2 Hydrogen Passivation of Defects and Impurities in Silicon

The mechanisms of hydrogen passivation in silicon are once again controversial, with many conflicting theories and results reported in the literature. Hydrogen is extremely electronically active in silicon, with the ability to interact with almost all impurities and defects [Sopo 02]. It therefore has important applications in improving the electrical qualities of silicon through defect passivation. Even in a perfect silicon lattice, hydrogen is reported to influence the electrical and optical properties [Sopo 01].

Particularly in the fabrication of multi-crystalline silicon solar cells, use of hydrogen containing antireflection coatings such as PECVD  $\text{SiN}_x\text{:H}$  has been reported to be essential for enhanced

bulk and surface passivation [Aber 01; Sopp 05]. Through the passivation of metallic impurities (including Fe, Ni, Cu, Cr, Au and Ag) to reduce their associated carrier recombination in silicon, and the passivation of crystallographic defects within the material, substantial improvements in  $\tau_{eff}$  and hence internal quantum efficiency (IQE) can be obtained [Lude 99; Sopp 05; Chen 94; Duer 02; Einh 99; Geer 03; Sing 86; Tave 00; Nick 93]. Subsequently, reports on the fabrication of p-type multi-crystalline silicon solar cells have indicated gains to the  $V_{OC}$  of 20 mV and an increase of 10 – 15 % relative cell performance through the use of hydrogen containing dielectrics over non-hydrogen containing dielectrics [Sopp 05]. However the effectiveness of hydrogen passivation can vary throughout the cast ingot presumably due to interactions with impurities and defects and subsequent variations in hydrogen diffusivity [Sheo 08].

Hydrogen passivation also plays an important role in mono-crystalline silicon solar cells, by passivating B–O defects (as detailed in Section 2.1.3). Furthermore, an ‘aleneal’ process can lead to hydrogen passivation of Si/SiO<sub>2</sub> interface defect states and is noted as a crucial process for the development of PERL cells with record efficiencies [Zhao 96].

Recent studies by Karzel *et al.* 2009 have mapped hydrogen related bond energies for a number of impurities and defects in silicon. The work covered a wide range of hydrogen bonds associated with: dopants; vacancy-oxygen complexes; LasID; metallic impurities; grain boundaries; and dislocations; hence showing the versatility of hydrogen passivation in silicon (see Table 2.2) [Karz 09]. Furthermore, important insights were obtained into the reactivation of hydrogen-defect complexes, which highlight the importance of cool-down procedures during hydrogenation processes to ensure defects are not unintentionally reactivated.

The mechanisms for hydrogen passivation in silicon, in general, appear to be poorly understood. Some reports indicate that a large fraction of iron-boron pairs can be passivated by hydrogen [Geer 03], whilst other studies do not support significant passivation of Fe by hydrogen [Tan 08]. Furthermore, several authors have questioned the effectiveness of hydrogen passivation of defects in silicon [Jian 03; Glun 01b]. The likelihood of bulk passivation of silicon from hydrogen has also been questioned due to the majority of the hydrogen in dielectric layers leaving the system rather than diffusing into the silicon [Boeh 00].

Simultaneous annealing of the SiN<sub>x</sub>:H layer during the formation of the Al back surface field

Table 2.2: Hydrogen bond energies for various impurities and defects in silicon. Values sourced from [Karz 09].

Impurity / Defect	Hydrogen bond energy (eV)
B	1.1
Fe	1.5
Ga	1.6
Al, Vacancy-O, Laser	1.9
In, S, Se, Te	2.1
Zn, Ag	2.2
Au, Pt	2.3
Pt	2.3
Pd	2.4
Cu, Ni, Grain Boundary	2.5
Dislocation, Plastic Deformation	3.1

(Al-BSF) has been reported to have positive effects for hydrogen passivation of the bulk silicon. The role of the formation of the Al-BSF in the hydrogenation process is unclear [Duer 02; Roha 02; Sopo 96; Nick 98; Hong 03], however the formation of the Al-BSF changes the optimal temperature for hydrogen passivation of the bulk [Roha 02].

Whilst hydrogen is often thought to have beneficial effects in silicon, hydrogen can also be detrimental to semiconductor devices [Davi 96]. For example, in hydrogenated amorphous silicon (a-Si:H), hydrogen can aid in defect formation under carrier injection, whilst in crystalline silicon, hydrogen can lead to the formation of structural defects, or enhance the diffusion of oxygen [Davi 96; John 91; Corb 89; Estr 90; Sopo 92; Jeng 88; Sopo 01].

Interactions between hydrogen and oxygen complexes in silicon are still a matter of discussion, however it has been observed that attaching atomic hydrogen to a pre-existing cluster of oxygen can change the electrical activity of the oxygen cluster. Hydrogen can also play a role in the generation

of thermal donors [Job 98; Rash 01]. Importantly Rashkeev *et al.* 2001 noted the reversibility of hydrogen passivation and activation of oxygen complexes [Rash 01], which suggests that the hydrogen passivation of other defects and impurities in silicon may also be reversible.

The ability of hydrogen to assume different charge states has important implications for the passivation of impurities and defects within silicon. Certain defects can only be passivated by a specific charge state of hydrogen and require the presence of electrons to allow the passivation process to occur. A number of authors have offered interpretations of hydrogen passivation mechanisms in silicon. However attempts to explain observed results have led to a number of contradictory assumptions of the charge state of hydrogen and hence the passivation reactions which take place [Sah 83; Pank 84; Pank 85; John 86]. However some authors highlight the importance of a specific charge state in certain chemical reactions, such as the role of  $H^0$  in the generation of thermal donors in both n- and p-type silicon [Job 98]. Subsequently, hydrogen can act as a donor or an acceptor depending on its charge state by reacting with ionised dopants to neutralise either acceptor or dopant atoms within the silicon and counteract the initial conductivity of the material [Wall 06; Capi 87; Sopo 02; Math 89; Hans 84; Sah 83; Pank 84; Herr 01]. For example,  $H^+$  can interact with ionised boron atoms ( $B^-$ ) to form neutral boron-hydrogen ( $B-H$ ) complexes. Similarly,  $H^-$  can interact with ionised phosphorus atoms ( $P^+$ ) to form neutral phosphorus-hydrogen ( $P-H$ ) complexes (see Eq. 2.1-2.2) [Math 89]. The neutralisation of acceptors such as boron in silicon is reported to be a very efficient process presumably due to the large capture radius of the Coulombic attraction between the  $B^-$  and  $H^+$ , in which more than 99 % of acceptor atoms can be passivated [Pank 84]. It has also been suggested that hydrogen passivation of acceptors ( $A$ ) can occur through the formation of an  $A^-OH^+$  complex [Hans 84].

The importance of minority carriers for hydrogen related reactions in silicon has been highlighted in several studies, such as for the dissociation of hydrogen-dopant complexes [Herr 01; John 92; Seag 91]. In these studies, the introduction of minority carriers has been experimentally shown to destabilise the  $P-H$  complex at much lower temperatures than those required to thermally dissociate the complexes, and also enhance the dissociation of  $B-H$  complexes. For the dissociation processes in Eq. 2.1-2.2, the Coulombic attraction between the ionised hydrogen and dopant atoms would not allow the hydrogen to escape, and hence a rapid reformation of the hydrogen-dopant complex is likely. As a result, before escape is possible, the dissociated hydrogen atoms must

be neutralised to allow the  $H^0$  to diffuse away from the ionised dopant atoms, unhindered by Coulombic attraction [Seag 91]. Eq. 2.3-2.4 show minority carrier mediated dissociation reactions of hydrogen-dopant complexes to generate  $H^0$  directly, where  $e^-$  is an electron and  $h^+$  is a hole [Herr 01].



Seager *et al.* 1991 suggest a two-step process for dissociation of B–H complexes, which follows Eq. 2.1, and the subsequent absorption of an  $e^-$  by  $H^+$  to form  $H^0$  (see Eq. 2.5). Similar reactions between the different charge states of hydrogen are shown in Eq. 2.6-2.7 for the absorption of an electron by  $H^0$  to generate  $H^-$ , or the absorption of two electrons by  $H^+$  to generate  $H^-$  [Seag 91].



Whilst literature regarding minority carrier enhanced dissociation of P–H complexes is consistent [Herr 01], there are conflicting reports regarding that for B–H complexes. Unlike the observations from Seager *et al.* 1991, Zundel *et al.* 1991 conclude that the dissociation rate is determined by the generation of molecular hydrogen by interactions from  $H^0$  and  $H^+$ , with no dependence on the minority carrier concentration [Seag 91; Zund 91]. Herring *et al.* 2001 notes that the suggestions of a two-step reaction for the dissociation of B–H complexes by Seager *et al.* 1991 seemed reasonable at the time of publication when the location of the  $H^+:H^0$  donor level was not known and assumed to be near  $E_m$ . However this two-step process requires the hydrogen to remain in the neutral charge state for sufficient time to diffuse away from the  $B^-$ . For the autoionisation of  $H^0$  to  $H^+$  in Eq. 2.5, the transition time is in the order of nanoseconds and is therefore very dominant over the reverse reaction. In contrast, the release of an electron by  $H^-$  to form  $H^0$  in Eq. 2.6 has a transition time in the order of one second. Subsequently, any  $H^0$  generated will revert back to  $H^+$

and be drawn back to the  $B^-$  well before it has had time to diffuse a sufficient distance to escape the  $B^-$ . On the other hand, for the dissociation of P–H complexes, the autoionisation of the  $H^0$  to form  $H^+$  will cause the atomic hydrogen to be repelled by the  $P^+$  and aid in the dissociation process [Herr 01]. Hence for the dissociation of B–H complexes, a two-step process seems unlikely unless there is a sufficient minority carrier concentration to result in an appreciable fraction of  $H^0$  being converted to  $H^-$  prior to the autoionisation process occurring, which would then be repelled from the  $B^-$  and assist in the dissociation process [Herr 01].

Importantly, Herring *et al.* 2001 conclude that the asymmetric positioning of the donor and acceptor levels of hydrogen enable a natural explanation for many previously unexplained phenomenon about the behaviour of hydrogen in silicon. For example, the differences between the dissociation of B–H and P–H complexes, and the difficulty in passivating phosphorus-doped silicon compared to boron-doped silicon [Herr 01].

### 2.2.3 Summary of Hydrogen in Silicon

Discrepancies with the reported literature highlight that in general, the diffusion and passivation mechanisms of hydrogen in silicon are poorly understood. As a result, more research needs to be done to improve the understanding of such mechanisms and enable more effective passivation to be achieved. However, it appears that the charge state of hydrogen can greatly influence the mobility, reactivity and therefore the effectiveness of hydrogen passivation.

## 2.3 Laser Doping for Silicon Solar Cells

Laser doping has been widely used for semiconductor processing, with early demonstrations dating back prior to 1970 [Fair 68]. Many different approaches have been used to deposit the dopant source, including ion implantation and phosphosilicate glass (PSG) growth through thermal diffusions, where the following laser doping process serves to redistribute the dopant atoms within the silicon [Whit 78; Stoc 90]. Alternatively, the dopant atoms can be introduced into the silicon during the laser doping process, by depositing dopant layers the silicon (i.e. by means of vacuum deposition,

## CHAPTER 2. LIGHT-INDUCED DEGRADATION, HYDROGENATION AND LASER DOPING FOR SILICON SOLAR CELLS

---

or through the application of spin on dopant (SOD) sources) prior to the laser doping process, in a process termed laser-induced melting of pre-deposited impurity doping (LIMPID) [Wong 93; Foga 81; Same 87]. Dopants may also be introduced during the laser doping process through gas-immersion laser doping or laser chemical processing (LCP) [Bent 88; Kray 08a].

To date, the application of laser doping to the fabrication of crystalline silicon solar cells has been quite limited. This may seem surprising due to a number of factors such as the compatibility of laser processes with high-throughput environments [Schn 03], and the ability to provide localised heating by the laser (therefore allowing the rest of the solar cell to remain at room temperature) [Abbo 06b; Tjah 08]. The low temperature processing capability is of particular importance for commercial solar cells fabricated on CZ or multi-crystalline wafers, in which the lifetimes are reported to degrade during high temperature processes [Macd 00].

*“Laser doping is the most under utilised of all laser processes currently used in solar cell fabrication.”* [Abbo 06b]

In recent applications laser doping has been used for the fabrication of crystalline silicon solar cells for the formation of selective and large area emitters [Wenh 02; Rmat 09; Eise 09; Pavi 11]. Whilst laser doping presents the potential to use a low cost solution to create high efficiency cell structures (such as a selective emitter), several challenges arise through the incorporation of laser doping in solar cell fabrication. These include the integration of the laser doping process with the deposition of surface dielectric and metal layers, due to the generation of defects during the laser doping process, and issues associated with aligned or plated contacts. In addition, typical lasers used for laser doping processes limit the depth to which dopants can diffuse, and hence limit junction depths and structures obtainable.

For solar cell applications, a recent review by Colville *et al.* 2007 reported that gas-immersion and wet laser doping processes tend to impose challenges associated with the complexity of laser systems, costs and the associated throughput in production environments [Neuh 07]. Therefore, it was concluded that dry laser processing methods such as LIMPID, used in conjunction with high speed scanners were seen as the most viable option for laser doping [Colv 09].



### 2.3.1 Laser-Induced Defects

Until recently, laser-induced defects (LasID) introduced during laser doping have limited the efficiency of commercially relevant laser-doped solar cells to below 19 % [Rode 10; Sugi 07; Tjah 08; Hopm 09; Sugi 10; Tjah 10; Kray 10a; Kray 10b]. To date, the majority of research groups have typically used conventional 532 nm wavelength Q-switched lasers with nanosecond pulse-lengths, with some studies using the LCP method investigating the use of infrared lasers with microsecond pulse-lengths.

Defects have been shown to form in silicon upon laser illumination with non-optimal processing conditions [Ohme 11]. LasID have been widely studied for laser doping applications over several decades. Early work using deep level transient spectroscopy indicated that the majority of defects are concentrated at the surface, however could extend up to 10  $\mu\text{m}$  from the surface [Moon 78], with some reports indicating that such defects could be observed in transmission electron microscope images [Nara 78]. More recent work by Hameiri *et al.* 2011 indicated that the recrystallisation occurs epitaxially with defects concentrated at the surface but no defect generation in deep regions [Hame 11b].

The generation of LasID in silicon is a complex process dependent on a number of factors. For example defect generation is affected by the orientation of the silicon whereby the use of a Q-switched ruby laser (694 nm) with a pulse-length of 15 ns is reported to generate defects in (111) orientated silicon, whilst (100) orientated silicon is defect free [Youn 79]. Given that most mono-crystalline wafers are grown on (100) orientated silicon wafers and are textured to expose the (111) planes, this would suggest that defects could form around the textured pyramids when laser doping. The recrystallisation velocity can also affect defect generation with a reduction in defect generation for reduced recrystallisation velocities [Youn 81; Liu 79; Bent 80]. One source of degradation caused by rapid recrystallisation velocities is reported to be electrically active point defects [Moon 78]. The purity of the SOD sources and introduction of oxygen into the molten silicon can also affect the performance of laser-doped solar cells. High oxygen concentrations are observed to cause the generation of micro-defects, and lead to increased dark saturation current densities ( $J_{0d}$ ) [Kish 79; Amet 07; Jour 08; Hame 11b].

## CHAPTER 2. LIGHT-INDUCED DEGRADATION, HYDROGENATION AND LASER DOPING FOR SILICON SOLAR CELLS

---

For Q-switched lasers, two critical laser power level thresholds exist in relation to LasID. One of these is related to the generation of bulk defects and the other for visible changes in surface morphology, with bulk defect generation occurring at lower power levels than that which induce visible changes of the surface [Park 83]. The pulse-length and wavelength of Q-switched lasers also affects defect generation. Laser doping using a wavelength of 532 nm has been observed to result in higher lifetimes than that observed when using a wavelength of 1064 nm [Okan 09]. In addition, longer pulses induce less mechanical damage to pyramids, but require higher energy pulses. It is also observed that increasing the energy density can lead to higher recombination rates [Kray 08b], with high laser powers causing micro cracks. This can lead to discontinuities in doping and potentially induce shunts [Hame 11b], or decrease the pseudo  $FF$  ( $p$ - $FF$ ) and  $V_{OC}$  [Hopm 09]. Hopman *et al.* 2009 attributed the sharp drops in efficiency with high fluencies leading to the evaporation of silicon and laser induced damage exceeding the depth of either the thermally diffused or selective emitter, with transmission electron microscope images indicating damage to depths of 1  $\mu\text{m}$  [Hopm 09].

Thermal stress appears to be one of the most likely causes of laser induced damage in silicon [Aror 96]. The energy threshold to induce surface damage is dependent on both the pulse-length and the number of pulses applied to a given area, with an increasing number of pulses decreasing the energy threshold. Furthermore, whilst damage induced using repetition frequencies below 1 kHz is reversible, higher repetition frequencies can lead to irreversible damage [Aror 96]. Thermally induced stress can create cracks at the surface [Kray 05] and it has been observed that increasing the number of passes over a laser-doped region can result in a higher defect density and further performance degradation [Sugi 07].

Subsequently, it appears that thermal expansion mismatch between the dielectric layer and the silicon contributes significantly to the generation of LasID immediately next to the laser-melted regions. Hence, minimal passes should be made over a solar cell [Sugi 07]. As  $\text{SiN}_x\text{:H}$  is typically used as a front surface dielectric, the use of a thin thermal  $\text{SiO}_2$  layer or another layer underneath the  $\text{SiN}_x\text{:H}$  with a lower thermal expansion coefficient has been observed to reduce defect generation, increase the  $V_{OC}$  and decrease the ideality factor [Wenh 11; Tjah 07; Sugi 07; Hame 11b]. When laser doping is performed through a dielectric layer, Sugianto *et al.* 2007 observed two types of LasID; holes adjacent to the laser-doped line, and dislocations at the interface between the laser-doped region and pyramids. However such defects were not observed if laser doping was performed

on bare silicon [Sugi 07]. Other groups have also observed a reduction in defect generation and improved  $p$ - $FF$  and  $V_{OC}$  by performing laser doping prior to the deposition of the dielectric layer [Kray 08a; Jaeg 09], and hence laser doping on bare silicon appears to be a more effective method to minimise LasID formation than the use of a thin oxide layer under the  $\text{SiN}_x\text{:H}$  to reduce thermal expansion mismatch [Hame 11b].

When performing laser doping on bare silicon, the focus of the laser beam can also be used to suppress defect formation. In particular, linear focused laser beams can avoid defect formation [Amet 05; Wern 07; Eise 09; Rode 10]. To do so, the width should be less than 10  $\mu\text{m}$ , however this width is dependent on the surface orientation with (111) orientated surfaces requiring narrower widths than (100) orientated surfaces [Ohme 11].

However, by performing laser doping prior to the deposition of a dielectric layer, metal contacts must be aligned to the laser-doped region. This is very challenging and introduces more complex processing steps, which therefore increases processing costs. Subsequently, self-aligned approaches should be explored to simplify the processing sequence.

### 2.3.2 Self-Aligned versus Aligned Contacts for Laser-Doped Solar Cells

Although performing laser doping through a dielectric layer can lead to increased defect generation, doing so can allow for elegant self-aligned metallisation schemes to be used such as light-induced plating (LIP) [Durk 79; Alla 07]. A self-aligning metallisation scheme in conjunction with laser doping was first proposed by Wenham and Green, in which the laser doping process simultaneously opens a dielectric layer selectively and incorporates dopants into the underlying silicon [Wenh 02]. This avoids the need to align contacts to the heavily doped layer during metallisation and vastly simplifies processing complexity.

The LDSE solar cell overcomes many of the fundamental limitations of conventional screen-printed solar cells. The laser doping process creates a heavily doped region to achieve low contact resistance whilst also minimising the metal/Si interface. It also allows the use of a lightly doped

## CHAPTER 2. LIGHT-INDUCED DEGRADATION, HYDROGENATION AND LASER DOPING FOR SILICON SOLAR CELLS

---

emitter to avoid the loss of  $J_{SC}$  due to a poor short wavelength response present in standard screen-printed solar cells with a heavily doped emitter, hence enabling a higher  $V_{OC}$  and  $J_{SC}$  on finished devices. In conjunction with LIP, fine finger contacts with widths less than 30  $\mu\text{m}$  are obtainable, which further increase the  $J_{SC}$  of finished devices compared to that of standard screen-printed solar cells (with finger widths of 120  $\mu\text{m}$ ) due to lower shading losses [Sugi 10]. The structure of an LDSE solar cell is shown in Fig. 2.3.

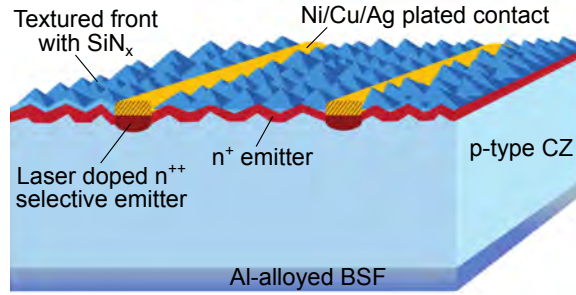


Figure 2.3: Structure of an LDSE solar cell. Image adapted from [UNSW 09].

However, when performing laser doping through a dielectric layer, Kray *et al.* 2008 observed a  $p$ - $FF$  that was 2–9 % absolute lower when using self-aligned LIP contacts than that obtained when precisely aligning photolithographically defined Ti/Pd/Ag evaporated contacts onto the laser-doped region [Kray 08a]. In addition, when performing laser doping prior to the deposition of a dielectric layer, a higher  $FF$  and  $p$ - $FF$  were observed for narrow contacts formed using techniques such as photolithography and aerosol printing rather than wider screen-printed contacts [Besu 97; Jaeg 09]. However, Röder *et al.* 2010 have demonstrated a  $p$ - $FF$  of 82 % using aligned screen-printed contacts to a laser-doped region formed using a laser beam with a width of 225  $\mu\text{m}$  [Rode 10]. This suggests that the loss of  $FF$  from structures with both self-aligned plated contacts and aligned contacts may be due to metal contacting a defected region alongside the laser-doped region [Sugi 07].

Whilst performing laser doping prior to the deposition of the dielectric layer in conjunction with aligned contacts reduces performance degradation from LasID, doing so introduces several

challenges and limitations to the performance of the finished devices. As misalignments between the metal and heavily doped selective emitter structure can degrade cell performance through increased series resistance [Meis 10], the laser-doped region must be wider than the metallised region, and processing must also ensure that metal does not contact the defected region alongside the laser-doped line. However, the most commercially relevant approach, screen-printing, fails to achieve narrow metal line widths, and hence such cells do not see the full potential of the selective emitter structure, as can be obtained using narrower LIP contacts due to increased shading [Rode 10; Kray 10a]. Furthermore, the use of a wide laser-doped region, which may be in the vicinity of 200 – 300  $\mu\text{m}$  [Rmat 09], reduces the fractional area of the cell with a good blue response and leads to a further reduction in the  $J_{SC}$  of the device. The laser doping approach used can also limit the width of the metal fingers using self-aligned laser doping approaches, and therefore limit the  $J_{SC}$  of the device. For example, Kyeong *et al.* 2012 observed that using LIMPID approaches the metal finger width of LIP contacts was primarily determined on the focus size of the laser beam with laser-doped line widths of 15  $\mu\text{m}$ , whilst when using the LCP approach, the laser-doped line width was determined by the liquid jet diameter, resulting in a line width of 35  $\mu\text{m}$ . Hence it appears that LIMPID approaches are ultimately capable of higher efficiencies than LCP approaches due to physical limitations on the widths of the liquid jet [Kyeo 12].

LDSE solar cells with self-aligned LIP contacts appear to be capable of higher efficiencies than achievable through aligned contacts formed using commercially relevant approaches. In recent years several groups have demonstrated efficiencies on large area devices in the range of 18.5 – 19 % using laser doping in conjunction with self-aligned LIP contacts [Sugi 10; Tjah 10; Kray 10a; Kray 10b; Bova 11], compared to efficiencies in the range of 18 % for aligned screen-printed contacts [Rode 10]. For the self-aligned approaches, differences in the laser processing speed of several orders of magnitude have been reported depending on the processing method used. Wet LCP methods have reported speeds in the vicinity of 1 mm/s, too slow for commercial production, whilst the dry laser doping approach adopted by UNSW has been performed at speeds as high as 5 m/s whilst still achieving higher efficiencies [Kray 10a; Hall 11d]. However, using such high processing speeds requires the use of galvanometer scanners and hence introduces challenges in maintaining adequate focus over the entire area of the wafer [Tjah 10]. On the other hand, LCP approaches are reported to induce more damage than LIMPID approaches and care must be taken with the fabrication

sequence to passivate the LasID [Kyeo 12].

The use of a self-aligned laser doping process in conjunction with plated contacts greatly simplifies the processing sequence for laser-doped solar cells. However careful attention must be made to minimise LasID generation. Another aspect of laser doping which should be considered is the dopant profile, which can affect recombination at the metal/Si interface.

### 2.3.3 Doping Profiles and Junction Depths

Due to the wide array of parameters used for laser doping, there is a large difference in the doping profiles and junction depths reported in the literature. When laser doping from a limited source, Gaussian dopant profiles are typical, with impurities such as oxygen and carbon following the same profile as dopants such as phosphorus [Foga 83; Foss 09]. Early work using Q-switched lasers with pulse-lengths of 10 – 30 ns resulted in junction depths of 200 – 300 nm. The work indicated that the junction depth did not depend on the number of pulses, but rather the junction depth was limited by the depth of the molten region, with additional pulses simply leading to a more uniform distribution of the dopants within the molten silicon [Same 87; Wong 93]. Using slightly increased pulse-lengths of 60 ns, White *et al.* 1978 indicated that the silicon was molten to a depth of approximately 1  $\mu\text{m}$ , with junction depths of up to 0.7  $\mu\text{m}$  and impurity profiles matching expected theoretical diffusion profiles [Whit 78].

Palina *et al.* 2011 have indicated that picosecond pulse-lengths are not sufficient for laser doping. In contrast, nanosecond pulse-lengths are sufficient to melt silicon on planar and textured surfaces to a depth of up to 2  $\mu\text{m}$  and 5  $\mu\text{m}$  respectively [Pali 11]. The pulse-length of the laser has a large influence on the maximum depth of molten silicon obtainable. Short pulse-lengths lead to very high temperatures being reached and can result in the evaporation of the silicon if the temperature exceeds 2900 K, whilst longer pulses have a higher energy threshold to melt the silicon. Due to the enhanced diffusion of heat into the silicon, such pulses can also tolerate higher energy densities before evaporation of the silicon occurs. Subsequently longer pulse-lengths are less efficient at forming shallow molten regions than short pulses (see Fig. ??) [Kohl 09].

For pulse energy densities above the threshold to melt the silicon, the junction depths and

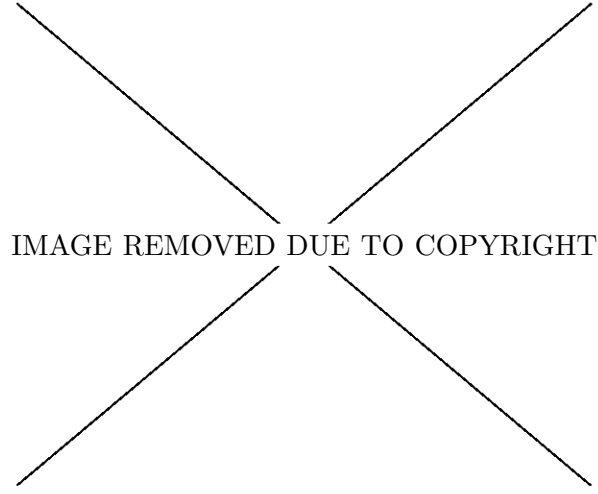


Figure 2.4: The depth of molten silicon for various pulse-lengths and pulse energy densities below the maximum depth when the temperature of the surface of the wafer exceeds the boiling temperature of silicon (2900 K). Image sourced from [Kohl 09].

presumably the depth of molten silicon obtained increase approximately linearly with the laser energy density [Li 12b; Kohl 09]. Whilst the absorption depth of light with a wavelength of 532 nm is approximately 1  $\mu\text{m}$  at room temperature, simulations have shown that although using a 65 ns pulse-length can result in melt depths of up to 1  $\mu\text{m}$ , almost complete absorption of the laser irradiation occurs within 50 nm of the surface. Therefore, the increase in melt depth is suggested to be due to heat conduction [Rode 10; Kohl 09]. Jellison *et al.* 1987 observed increases in the absorption coefficient in liquid silicon of several orders of magnitude compared to that in solid silicon at room temperature [Jell 87; Sze 07]. Hence heat transfer is essential to obtain deep molten regions, and therefore long pulse-lengths should be used to avoid evaporation of the silicon and/or dopant sources, which would lead to increased sheet resistances [Pali 11; Kohl 09; Pavi 11]. In some instances, high pulse energy densities have led to the formation of grooves to a depth of 20  $\mu\text{m}$ , although doping only extends to depths of approximately 4  $\mu\text{m}$  from the newly formed silicon surface within the groove. For slightly lower powers which do not result in groove formation, junction depths were limited to approximately 1.5  $\mu\text{m}$  [Hame 11b].

It appears that even when using lasers with a substantially longer pulse-length of 2  $\mu\text{s}$  and applying multiple pulses, junction depths are still limited to 2  $\mu\text{m}$ . Recently, 532 nm CW Nd:YVO<sub>4</sub> lasers have been used for laser doping applications with multiple reports of junction depths in the range of 2 – 5  $\mu\text{m}$  which can be controlled by processing speed or laser power. Whilst processing speeds using a 5 W laser are reported as 1 – 6 cm/s, processing speeds using a higher powered 15 W laser are substantially higher and in the order of 1 – 10 m/s [Sugi 10; Hira 09; Ogan 08]. Through enhanced diffusion of dopants due to the silicon remaining in the molten state for periods greater than 1  $\mu\text{s}$ , laser doping performed using CW lasers can result in sheet resistances below 4  $\Omega/\square$  [Sugi 10].

The dopant profile and junction depth of laser-doped regions greatly depends on the laser parameters used. To increase the junction depth, a laser with long pulse-lengths should be used to avoid ablation of the silicon, or more preferably, a CW laser.

### 2.3.4 Summary of Laser Doping for Silicon Solar Cells

Laser doping is an elegant process which can locally dope silicon. However its use for photovoltaics has been limited. This is due to difficulties in incorporating it into the solar cell sequence, primarily due to the generation of LasID. The generation of LasID can be reduced by laser doping on bare silicon, however this results in the need to align metal contacts to the laser-doped region which increases processing complexity. A self-aligned process can also be used for laser doping through a dielectric layer, however may require the use of a thin thermal SiO<sub>2</sub> layer under the SiN<sub>x</sub> to reduce defect generation. Both approaches lead to increased processing costs. The junction depth of laser doped regions greatly depends on the laser parameters. In order to form a deep molten region, a CW laser should be used to avoid ablation of the silicon. Doing so can also reduce LasID generation.



## 2.4 Chapter Summary

In this chapter, the formation and passivation of B–O defects, diffusion and passivation mechanisms of hydrogen in silicon, and laser doping process were reviewed. Whilst a vast amount of literature is available on such topics, there are many contradictory theories and variations in the information reported.

**Light-induced degradation:** The permanent deactivation of B–O defects has received great amounts of attention in recent years due to the important implications in overcoming fundamental lifetime and efficiency limitations of solar cells fabricated on p-type multi-crystalline and CZ substrates due to light-induced degradation. The most recent advancements suggest that hydrogen plays a key role in the permanent deactivation of such defects, contrary to earlier reports that hydrogen does not play a role. However reports indicate that hydrogen content alone is not sufficient to influence the deactivation process.

**Hydrogen in silicon:** In general, the diffusion and passivation mechanisms of hydrogen in silicon appear to be poorly understood. This is largely due to the fact that hydrogen interacts with almost all impurities and defects in silicon. As a result, the mobility of hydrogen reported in the literature can vary by more than five orders of magnitude, which has led to many conflicting theories on hydrogen diffusion. Similarly, reports on the requirements to passivate defects and the effectiveness of hydrogen passivation have yielded conflicting results. Perhaps the most underestimated aspect of hydrogen in silicon is its ability to assume different charge states. Taking into account the possible interactions of the different hydrogen charge states in silicon enables a natural explanation of many previously unexplained or incorrectly explained phenomena. The importance of  $E_F$  and hence  $\Delta n$  in changing the fractional charge state concentrations of hydrogen was highlighted, which can assist in passivation processes requiring a given hydrogen charge state which may be present in insufficient quantities in thermal equilibrium. To gain further insights into hydrogen passivation mechanisms in silicon, Chapter 3 explores theoretical calculations and methods to increase the generation of the minority hydrogen charge species in silicon. Subsequently, the advanced hydrogenation methods are used on a range of commercial grade silicon materials to

improve lifetime.

**Laser doping for silicon solar cells:** Laser doping has been used widely in the semiconductor industry, however its use in PV has been quite limited until recent times. The generation of LasID appears to be a key factor limiting the laser doping for selective emitter applications. LasID have been shown to be caused by a number of factors such as repetition frequency, and the thermal expansion mismatch between silicon and the overlying dielectric layers. Defect formation can be reduced by using dielectric layers with lower thermal expansion coefficients than  $\text{SiN}_x$  such as  $\text{SiO}_2$ , although laser doping on bare silicon is more effective at minimising defect generation. However, doing so requires precise alignment of metal contacts to the laser-doped region and loses the full  $J_{SC}$  potential of selective emitter structures, by having wider heavily doped regions than can be obtained using laser doping through a dielectric layer in conjunction with self-aligned LIP contacts.

The depth of molten regions formed by laser doping is greatly dependent on the pulse-length with increasing pulse-lengths allowing greater depths before the surface temperature of the silicon exceeds the boiling point. As a result it would appear that CW lasers pose a large potential to increase junction depth of laser-doped regions with junction depths of  $2 - 5 \mu\text{m}$  reported by several groups. In Chapter 4, deep junction formation is investigated using CW lasers to allow the fabrication of a range of advanced laser-doped structures.

## Chapter 3

# Advanced Hydrogenation for Silicon Solar Cells

To enable more effective passivation of defects in silicon using hydrogen, the mechanisms for hydrogen passivation must be understood in greater detail, particularly in relation to the involvement of the different hydrogen charge species. With an improved understanding, new methods to manipulate hydrogen in silicon may be developed, leading to increases in the effective quality of the silicon material. Doing so could allow the fabrication of high efficiency silicon solar cells on very low cost wafers (typically seen as reject wafers) with initial lifetimes too low to fabricate high efficiency devices using conventional processes.

In this chapter, theoretical calculations for the fractional charge state concentrations of hydrogen within silicon are presented. Subsequently, an advanced hydrogenation process is developed incorporating minority carrier injection. In the latter sections of this chapter, different hydrogenation processes are applied to a range of commercial grade silicon wafer materials including boron-doped and phosphorus-doped CZ, multi-crystalline and upgraded metallurgical grade (UMG) silicon. The results support the hypothesis that more effective passivation of defects by hydrogen can be achieved through increasing the minority hydrogen charge state concentrations, and that hydrogenation is not necessarily a one-step process.

## 3.1 Increased Generation of $H^0$ in Silicon

As described in Chapter 2, the fractional concentration of hydrogen in each of the charge states greatly depends on the position of  $E_F$  in relation to  $E_m$  [Herr 01]. As different defects and impurities in silicon require different charge states of hydrogen for passivation, it is preferable to have sufficient quantities of hydrogen in the positive, neutral and negative charge states. Hence the fractional concentration of  $H^0$  ( $f_0$ ) should be maximised, which in turn, allows equal fractional concentrations of  $H^+$  and  $H^-$ , denoted by  $f_+$  and  $f_-$  respectively.

### 3.1.1 Development of a Model for the Generation of $H^0$

Hydrogenation processes in silicon have been reported over a wide range of temperatures from room temperature to well above 800 °C [Munz 09; Duer 02]. Subsequently, the effect of temperature as well as the position of  $E_F$  should be considered. In this section, a model was developed which included the temperature dependence of the intrinsic carrier concentration ( $n_i$ ) through band-gap narrowing at elevated temperatures, and the temperature dependence of the density of states in the conduction ( $N_C$ ) and valence ( $N_V$ ) bands (see Eq. 3.1 - 3.4) [Sze 07], where  $m_{de}$  and  $m_{dh}$  are the mass of electrons and holes respectively (for density of states calculations),  $k$  is the Boltzmann constant,  $T$  is the absolute temperature,  $h$  is the Planck constant and  $E_g$  is the band-gap energy.

$$N_C = 2 \left( \frac{2\pi \cdot m_{de} \cdot kT}{h^2} \right)^{\frac{3}{2}} \quad (3.1)$$

$$N_V = 2 \left( \frac{2\pi \cdot m_{dh} \cdot kT}{h^2} \right)^{\frac{3}{2}} \quad (3.2)$$

$$E_g = 1.16 - \frac{7.02 \times 10^{-4} T^2}{T + 1108} \quad (3.3)$$

$$n_i = \sqrt{N_C N_V} \cdot e^{\left(-\frac{E_g}{2kT}\right)} \quad (3.4)$$

Assuming thermal equilibrium, the concentration of holes ( $p_0$ ) and electrons ( $n_0$ ) are given by Eq. 3.5-3.8 respectively where  $p_{p0}$  and  $n_{p0}$  are the concentration of holes and electrons respectively in p-type silicon,  $p_{n0}$  and  $n_{n0}$  are the concentration of holes and electrons respectively in n-type silicon,

### 3.1. INCREASED GENERATION OF NEUTRALLY CHARGED HYDROGEN IN SILICON

---

and  $N_a$  and  $N_d$  are the concentration of acceptor and donor dopants respectively. Illumination can generate excess carriers ( $\Delta n = \Delta p$ ), which increase the total hole and electron concentrations as shown in Eq. 3.9 and Eq. 3.10 respectively. In this model, due to the importance of electrons in binding to  $H^+$  to generate  $H^0$  or  $H^-$ , the  $E_F$  was represented by the electron quasi-Fermi level ( $E_{Fn}$ ) (see Eq. 3.11).

$$p_{p0} = 0.5 \left( (N_a - N_d) + \sqrt{(N_a - N_d)^2 + 4n_i^2} \right) \quad (3.5)$$

$$n_{p0} = \frac{n_i^2}{p_{p0}} \quad (3.6)$$

$$n_{n0} = 0.5 \left( (N_d - N_a) + \sqrt{(N_d - N_a)^2 + 4n_i^2} \right) \quad (3.7)$$

$$p_{n0} = \frac{n_i^2}{n_{n0}} \quad (3.8)$$

$$p = p_0 + \Delta p \quad (3.9)$$

$$n = n_0 + \Delta n \quad (3.10)$$

$$E_{Fn} = kT \cdot \ln \left( \frac{n}{n_i} \right) \quad (3.11)$$

Subsequently the  $f_0$  is calculated using Eq. 3.12 as adapted from Herring *et al.* 2001, where:  $v_i$  is the number of possible configurations in the unit cell for hydrogen species with charge state  $i$ ;  $Z_i$  is the corresponding vibrational partition function; and  $E_d$  and  $E_a$  are the donor and acceptor energies of hydrogen respectively. Similarly, Eq. 3.13 and Eq. 3.14 show the fractional concentration of  $H^+$  and  $H^-$  respectively. Table 3.1 shows the values of the constant used in the model where  $m_0$  is the electron mass. It was assumed that the relative positions of  $E_d$  and  $E_a$  within the band gap with respect to  $E_m$  are independent of temperature.

For this model:  $v_+$  takes on a bond centre site;  $v_0$  takes on a bond centre site with either spin; and  $v_-$  takes on a tetrahedral site where the unit cell consists of two silicon atoms. As the temperature dependence of the partition functions is unknown [Herr 01], the low temperature approximation of unity was used in each case. However, this makes it difficult to predict the fractional concentrations precisely.

$$f_0 = \left( 1 + \left( \frac{v_+ Z_+}{v_0 Z_0} \right) \cdot e^{\left( \frac{E_d - E_{Fn}}{kT} \right)} + \left( \frac{v_- Z_-}{v_0 Z_0} \right) \cdot e^{\left( \frac{E_{Fn} - E_a}{kT} \right)} \right)^{-1} \quad (3.12)$$

$$f_+ = f_0 \left( \frac{v_+ Z_+}{v_0 Z_0} \right) \cdot e^{\left( \frac{E_d - E_{Fn}}{kT} \right)} \quad (3.13)$$

$$f_- = f_0 \left( \frac{v_- Z_-}{v_0 Z_0} \right) \cdot e^{\left( \frac{E_{Fn} - E_a}{kT} \right)} \quad (3.14)$$

Table 3.1: Values of constants used in Eq. 3.12 -3.14 to determine the fractional hydrogen charge state concentrations.

Constant	Value
$m_{de}$	0.33 $m_0$
$m_{dh}$	0.56 $m_0$
$E_d - E_m$ at 310 K	0.4 eV
$E_m - E_a$ at 310 K	0.07 eV
$v_+$	4
$v_0$	8
$v_-$	2
$Z_+$	1
$Z_0$	1
$Z_-$	1

It was observed from Eq. 3.12, 3.13 and 3.14, that the maximum  $f_0$  for a given temperature occurred when  $f_-$  and  $f_+$  were equal. Furthermore, at this optimal  $f_0$  value, the value of  $f_-$  and  $f_+$  were always higher than  $f_0$ , and hence  $H^0$  was never the dominant charge species of hydrogen in the silicon. Therefore, given its importance in enhancing mobility, to ensure adequate concentrations of all hydrogen charge species in the silicon, the concentration of  $H^0$  should be maximised. Hence figures in this section are shown in relation to  $f_0$ .

Both temperature and the  $E_{Fn}$  have a dramatic influence on  $f_0$ . It was observed that for all

### 3.1. INCREASED GENERATION OF NEUTRALLY CHARGED HYDROGEN IN SILICON

temperatures, the maximum  $f_0$  occurs for  $E_{Fn} - E_m \approx 0.15$  eV, although a slight decrease in value of  $E_{Fn} - E_m$  was observed with increasing temperatures from  $E_{Fn} - E_m = 0.17$  eV at 300 K to  $E_{Fn} - E_m = 0.14$  eV at 1100 K (see Fig. 3.1). Increasing the temperature from 300 K to 1100 K results in approximately three orders of magnitude increase in maximum obtainable  $f_0$  for a given temperature highlighting the importance of elevated temperatures in generating sufficient fractional concentrations of the minority hydrogen charge states. The strong influence of  $E_{Fn}$  was also noted, particularly for lower temperatures which can result in variations of twelve orders of magnitude in  $f_0$  at 300 K, whilst its effect was reduced at higher temperatures, resulting in two orders of magnitude variation in  $f_0$  at 1100 K.

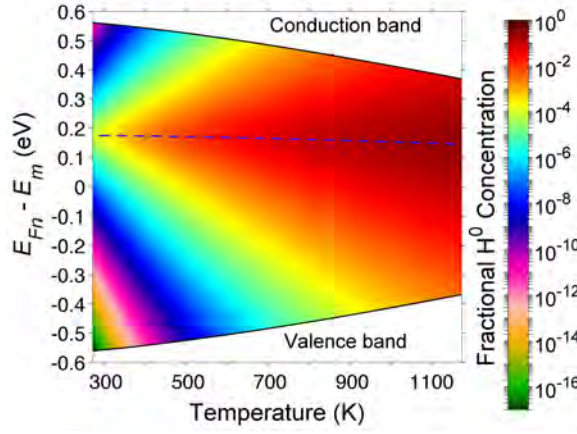


Figure 3.1: Fractional  $H^0$  concentrations in silicon highlighting the importance of  $E_{Fn}$  and  $T$  to increase  $H^0$  generation. The blue dashed line represents the maximum  $H^0$  concentration for a given temperature.

The  $E_{Fn}$  is determined by temperature,  $\Delta n$  and  $N_{eff}$  of the silicon. Therefore wafers with different  $N_{eff}$  can respond differently to hydrogenation processes, purely due to differences in the fractional concentration of the hydrogen charge species, before any differences in hydrogen mobility are considered. Furthermore,  $\Delta n$  was determined by the generation of light-induced electron-hole pairs ( $G$ ) and  $\tau_{eff}$  (see Eq. 3.15). Subsequently, both  $G$  and  $\tau_{eff}$  in the silicon can affect the

fractional hydrogen charge state concentrations.

$$\Delta n = G \cdot \tau_{eff} \quad (3.15)$$

A model was developed which suggested that the generation of  $H^0$  greatly depended on the  $E_{Fn}$ , which is affected by  $\Delta n$  and  $N_{eff}$  of the silicon. Furthermore, the  $\Delta n$  can be influenced by  $G$  and  $\tau_{eff}$  of the silicon. Therefore, such parameters should be investigated for both n-type and p-type silicon, to look at their direct relevance for hydrogenation processes in silicon solar cells.

### 3.1.2 Effect of Temperature and Minority Carrier Injection on $H^0$ Generation in p-type Silicon

Temperature and  $\Delta n$  have a strong influence on the position of  $E_{Fn}$  in relation to  $E_m$ , and therefore  $f_0$ . Fig. 3.2-3.3 show these influences for p-type silicon with different  $N_{eff}$ . It was observed that variations in  $E_{Fn}$  for different  $N_{eff}$  values only occurred when the given  $\Delta n$  and temperature resulted in an  $E_{Fn}$  below  $E_m$ . To achieve  $f_0$  values independent of  $N_{eff}$ ,  $E_{Fn}$  should be above  $E_m$ . To do so, higher  $\Delta n$  values were required for increasing temperatures (see Fig. 3.2). For each given temperature, an optimal  $\Delta n$  value was found to exist that result in the desired  $E_{Fn}$  of approximately 0.15 eV above  $E_m$  and therefore maximise  $f_0$ . With increasing temperature, this optimum  $\Delta n$  value increased. As this  $E_{Fn}$  was above  $E_m$ , this function of local maxima in  $f_0$  (denoted by the blue dashed lines in Fig. 3.3) was primarily independent of  $N_{eff}$  for all practical ranges of doping in crystalline silicon solar cells from  $N_a = 1 \times 10^{15} \text{ /cm}^3$  for lightly doped bulk material, to  $N_a = 1 \times 10^{20} \text{ /cm}^3$  for heavily diffused regions.

For all  $N_{eff}$ , a too high  $\Delta n$  value for a given temperature caused the  $E_{Fn}$  to be too far above  $E_m$  and hence reduced  $H^0$  generation. On the other hand, a too low  $\Delta n$  for a given temperature also reduced the  $f_0$  and if sufficiently low, the  $f_0$  became strongly dependent on the  $N_{eff}$  due to the  $E_{Fn}$  being below  $E_m$ . In such regimes, the  $E_{Fn}$  and therefore  $f_0$  became primarily dependent on temperature. As a result, at low  $\Delta n$ , the  $E_{Fn}$  could be increased towards  $E_m$  by increasing the temperature. However with increasing  $N_{eff}$ , higher temperatures were required for the  $E_{Fn}$  to



approach  $E_m$ .

Hence to increase  $H^0$  generation in p-type silicon, it becomes increasingly important to use methods such as illumination to inject minority carriers as the  $N_{eff}$  is increased. With sufficient illumination, lower temperatures to be used to generate the same  $f_0$  during the hydrogenation process as that achieved using a hydrogenation process at a higher temperature in the dark. Therefore, illumination can be used to reduce the thermal budget and cost of hydrogenation processes in p-type silicon, whilst potentially improving the effectiveness of passivation. In the next section, the influence of temperature and minority carrier injection in n-type silicon is explored.

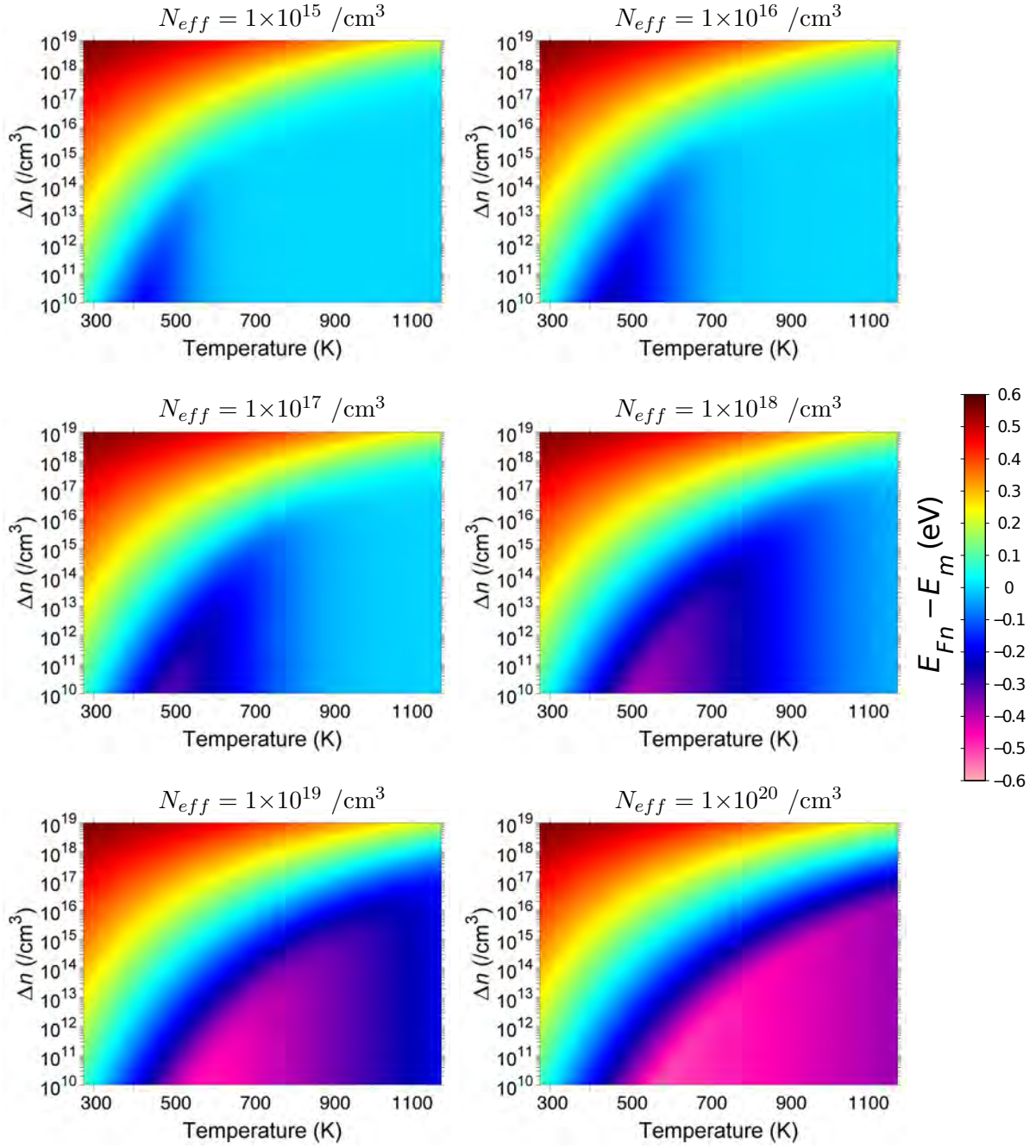


Figure 3.2: Effect of temperature and  $\Delta n$  on the position of  $E_{Fn}$  above  $E_m$  in p-type silicon, highlighting the importance of  $\Delta n$  in controlling  $E_{Fn}$ .

### 3.1. INCREASED GENERATION OF NEUTRALLY CHARGED HYDROGEN IN SILICON

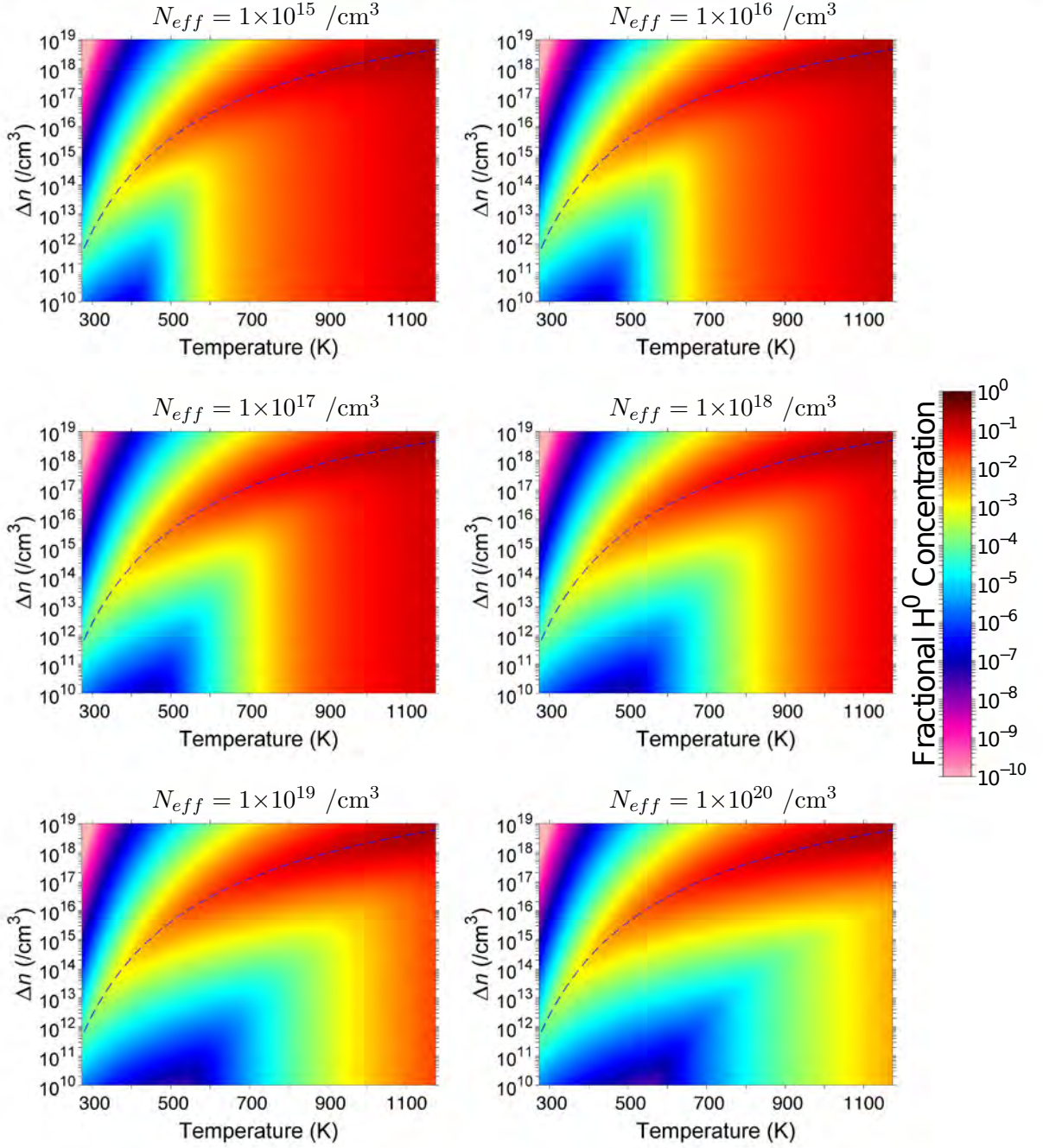


Figure 3.3: Dependence of the fractional  $H^0$  concentration on temperature and  $\Delta n$  in p-type silicon, highlighting the importance of  $\Delta n$  for maximising  $H^0$  generation. The blue dashed line represents the maximum  $H^0$  concentration for a given temperature.

### 3.1.3 Effect of Temperature and Minority Carrier Injection on $H^0$ Generation in n-type Silicon

In contrast, n-type silicon showed a very different response to minority carrier injection when compared with p-type silicon. In n-type silicon, for  $\Delta n$  values below the  $N_{eff}$  of the wafers, the  $E_{Fn}$  and  $f_0$  were predominately dependent on the temperature of the silicon (see Fig. 3.4-3.5). Hence in n-type silicon, minority carrier injection has a reduced impact on  $f_0$  with increasing  $N_{eff}$ . Furthermore, the desired  $E_{Fn}$  of 0.15 eV above  $E_m$  could only be achieved by elevating the temperature, which for example, requires at least 400 K for lightly doped silicon ( $N_{eff} = 1 \times 10^{15} / \text{cm}^3$ ). With increasing  $N_{eff}$  in n-type silicon, it becomes increasingly difficult to achieve  $E_{Fn}$  down to 0.15 eV above  $E_m$ , due to the increasing presence of free electrons. Subsequently, lightly doped n-type silicon shows advantages of illumination in terms of increased  $H^0$  generation. However as the  $N_{eff}$  increases,  $f_0$  was more strongly determined by temperature, and higher temperatures were shown to be required to increase  $H^0$  generation.

For heavily doped n-type silicon, unlike for p-type silicon, illumination does not appear to assist in the generation of  $H^0$ , and hence  $H^0$  is lost during the cool down process. Therefore, it appears that the use of illumination during thermal treatments is key for p-type silicon to generate sufficient concentrations of  $H^0$ , whilst for n-type silicon, illumination can be beneficial for lightly doped silicon, but of little or no benefit for heavily doped silicon. For such material, rapid cooling processes should be used to maintain high  $H^0$  concentrations for as long as possible while the material is above a critical temperature which can allow the reactivation of a given defect.

It should be noted that whilst Fig. 3.2-3.5 show  $\Delta n$  up to  $1 \times 10^{19} / \text{cm}^3$ , Auger recombination would pose a limitation on the  $\Delta n$  obtainable [Kerr 02]. For example, in  $1 - 2 \Omega \cdot \text{cm}$  p-type material, to obtain a  $\Delta n = 1 \times 10^{16} / \text{cm}^3$  with a corresponding  $\tau_{eff} = 1$  ms, an illumination intensity of approximately 1 sun is required. In contrast, increasing the  $\Delta n$  by one order of magnitude to  $1 \times 10^{17} / \text{cm}^3$  reduces the Auger lifetime to approximately 100  $\mu\text{s}$ , resulting in a required illumination intensity of approximately 100 suns.

Hence for n-type silicon, illumination can only increase  $H^0$  generation in lightly doped silicon with  $N_{eff} < 1 \times 10^{16} / \text{cm}^3$ . However, as typical n-type silicon wafers used for silicon solar cells have

### 3.1. INCREASED GENERATION OF NEUTRALLY CHARGED HYDROGEN IN SILICON

---

bulk doping densities less than this, an enhancement in  $H^0$  generation could be achieved through the use of illumination. For heavily doped n-type silicon,  $H^0$  generation is entirely dependent on temperature, and hence high temperatures should be used to maximise the  $f_0$ . Furthermore, a rapid cooling process should be used to minimise the loss of  $H^0$  during the cool down.

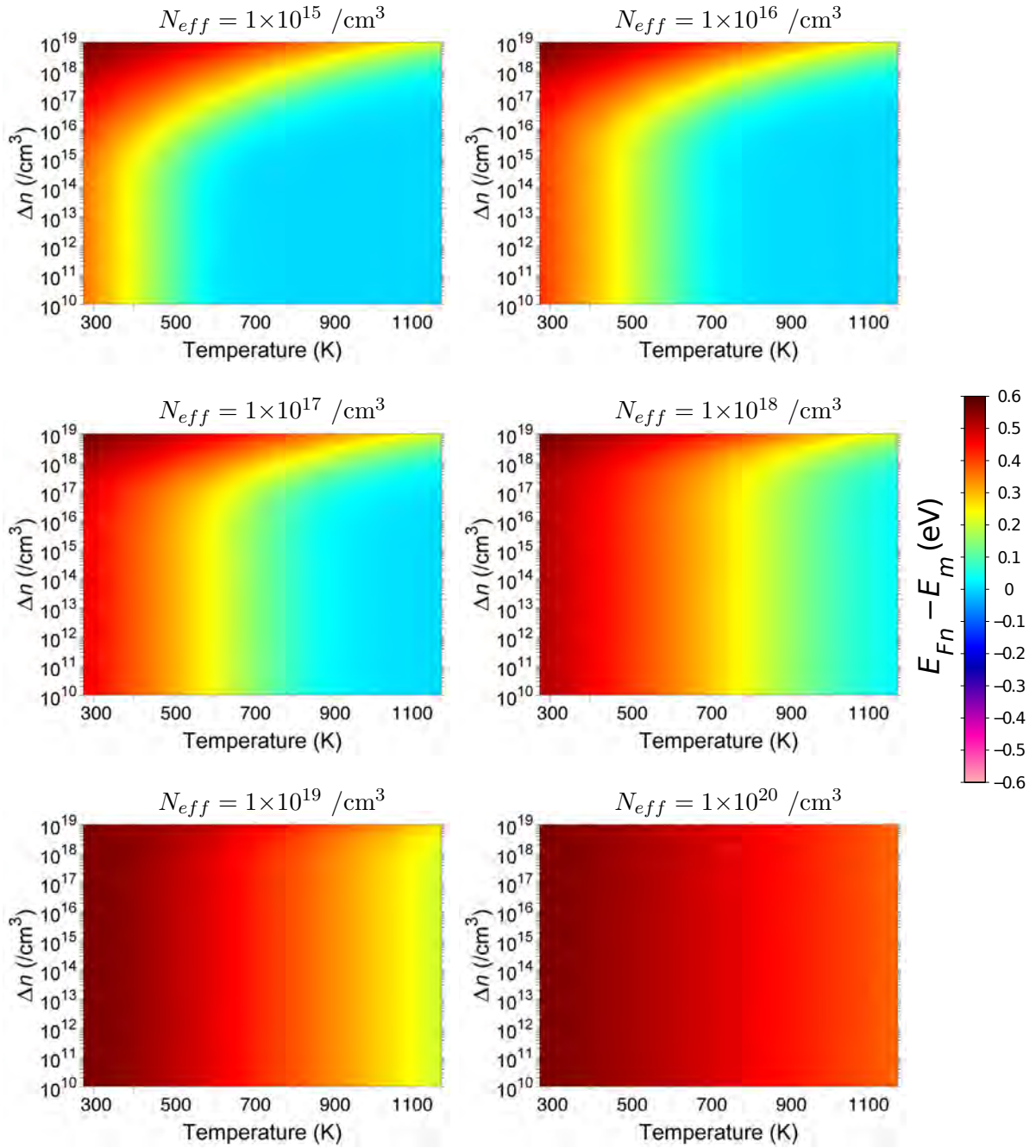


Figure 3.4: Effect of temperature and  $\Delta n$  on the position of  $E_{Fn}$  above  $E_m$  in n-type silicon, highlighting the dominance of temperature in determining  $E_{Fn}$ .



### 3.1. INCREASED GENERATION OF NEUTRALLY CHARGED HYDROGEN IN SILICON

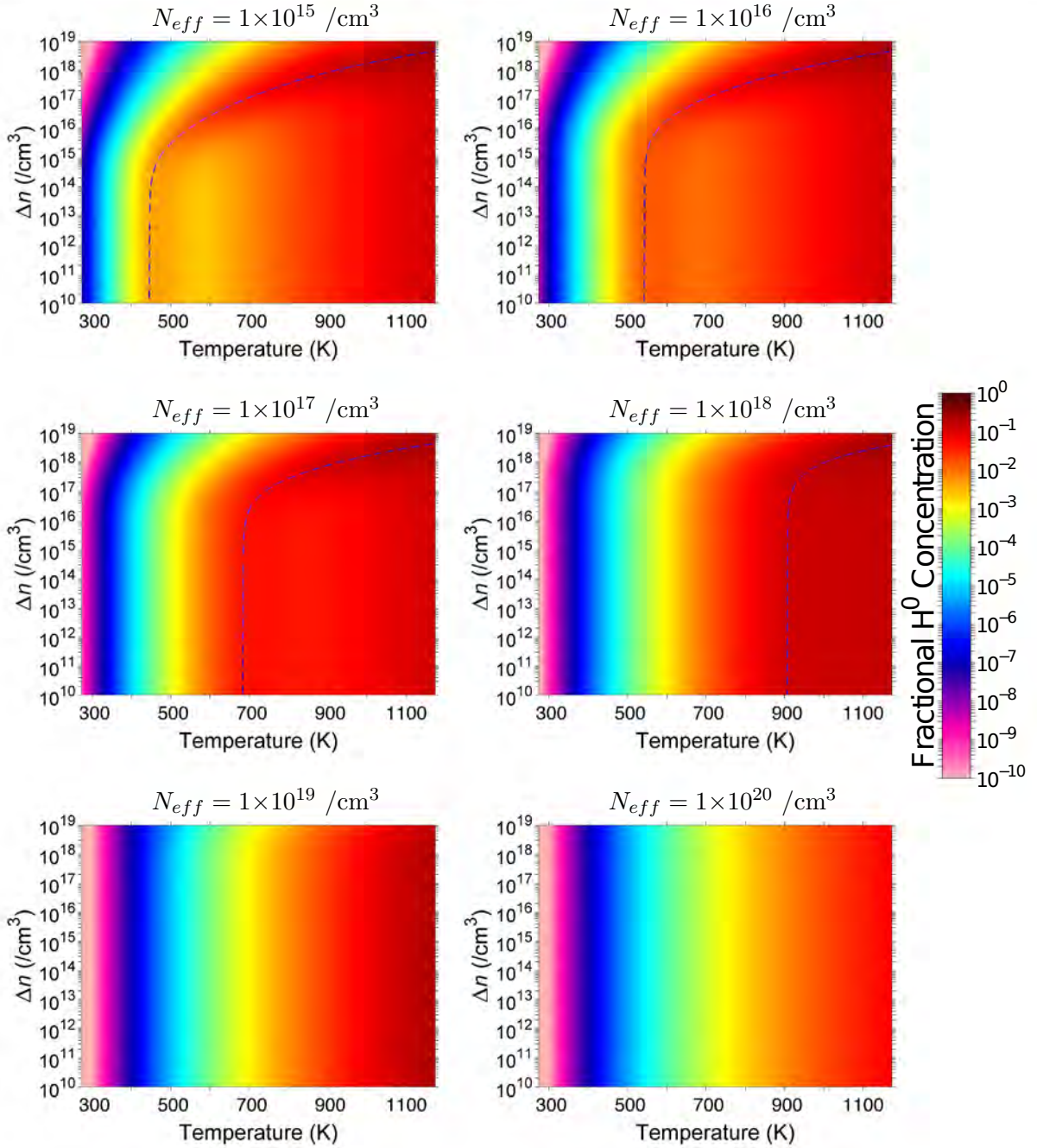


Figure 3.5: Dependence of the fractional  $H^0$  concentration on temperature and  $\Delta n$  in n-type silicon, highlighting the dominance of temperature in determining  $H^0$  concentrations. The blue dashed line represents the maximum  $H^0$  concentration for a given temperature.

### 3.1.4 An Advanced Hydrogenation Process for p-type Silicon Solar Cells

Due to the dependence of  $\Delta n$  on  $\tau_{eff}$ , for any hydrogenation process which operates at conditions in which the  $f_0$  is dependent on the  $\Delta n$ , such as in p-type silicon, or n-type silicon in high injection at low temperatures, the passivation of defects which leads to a change in  $\tau_{eff}$  can also lead to a change in  $E_{Fn}$  and subsequently  $f_0$ . Therefore, to maintain optimal  $H^0$  generation throughout a hydrogenation process, either  $G$  should be altered to maintain sufficient  $H^0$  quantities, or the hydrogenation process should operate in a window which can tolerate such changes in  $\tau_{eff}$  (without leading to substantial changes to  $E_{Fn}$  and subsequent changes to  $f_0$ ).

The benefits of illumination for generating  $H^0$  in p-type silicon (observed in Fig. 3.3), suggest that improvements to the effectiveness of hydrogenation processes could be achieved through careful control of illumination during thermal processing, such as fast-firing during the formation of an Al-BSF. Fig. 3.6 shows the fractional concentrations of  $H^0$  and  $H^-$  in p-type silicon for various  $N_{eff}$ . It was observed that for a conventional hydrogen process (CHP) with no minority carrier injection (Process A), the fractional concentration of the minority charge species greatly depends on  $N_{eff}$ , particularly at lower temperatures. However by using an advanced hydrogenation process (AHP) with appropriate minority carrier injection (Process B), which corresponds to the dashed blue line of optimal  $H^0$  generation in Fig. 3.3, the fractional charge state concentrations of both  $H^0$  and  $H^-$  are greatly enhanced and become independent of  $N_{eff}$ . Using Process B,  $f_-$  becomes predominantly independent of temperature. In Fig. 3.6 an  $N_{eff}$  of  $1 \times 10^{16} / \text{cm}^3$  is used for Process B, however values vary by less than 0.05 % by changing the  $N_{eff}$  over the range indicated in the legend.

For optimal  $H^0$  generation, a single  $\Delta n$  value should not be targeted for the entire thermal process. As the temperature varies throughout a thermal process, based on Eq. 3.12 the optimal  $E_{Fn}$  also changes slightly, meaning that the  $\Delta n$  required to maintain optimum  $H^0$  generation also varies. Fig. 3.7 shows fractional concentrations of  $H^0$  and  $H^-$  for p-type silicon with  $N_{eff} = 1 \times 10^{16} / \text{cm}^3$  at different  $\Delta n$  values, including a pure thermal process (Process A) with  $\Delta n = 0$  and the optimal case (Process B). It can be seen that for each given  $\Delta n$  shown in Fig. 3.7, when



### 3.1. INCREASED GENERATION OF NEUTRALLY CHARGED HYDROGEN IN SILICON

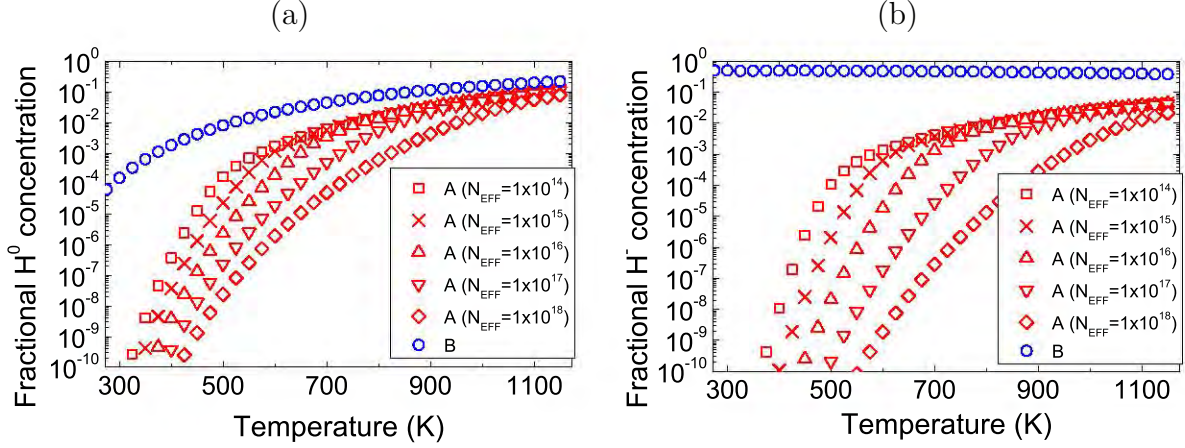


Figure 3.6: Theoretical fractional concentrations in p-type silicon with various  $N_{eff}$  (in  $/\text{cm}^3$ ) for (a)  $\text{H}^0$  and (b)  $\text{H}^-$  highlighting the importance of minority carrier injection. Process A has no excess minority carrier injection ( $\Delta n = 0$ ) and Process B has optimal excess minority carrier injection to maximise  $\text{H}^0$  generation.

decreasing from very high temperatures a reduction in both  $f_0$  and  $f_-$  are observed. However with further reductions in temperature, both the  $f_0$  and  $f_-$  increase. For the case of  $\text{H}^0$ , further reductions can then result in a substantial loss of  $\text{H}^0$ , whilst  $\text{H}^-$  remains in high concentrations due to an abundance of electrons, resulting in  $E_{Fn}$  being too far above  $E_m$ . It should also be noted that operating with  $E_{Fn}$  too high above  $E_m$  results in the loss of  $\text{H}^+$ , which may be required to passivate certain defects and would therefore appear undesirable.

Hydrogenation processes are typically carried out at elevated temperatures to increase hydrogen mobility. Whilst high minority charge state concentrations may be achieved at the elevated temperatures with either no illumination, or a given illumination level, as the silicon cools down the minority charge state concentrations will revert back to  $\text{H}^+$  if sufficient charge minority carrier injection is not applied. Hence it is expected that during cool down and subsequent thermal processes, a careful relationship between  $\Delta n$  and temperature should be maintained for any temperatures which provide thermal energies above the reactivation energy of the defects of interest.

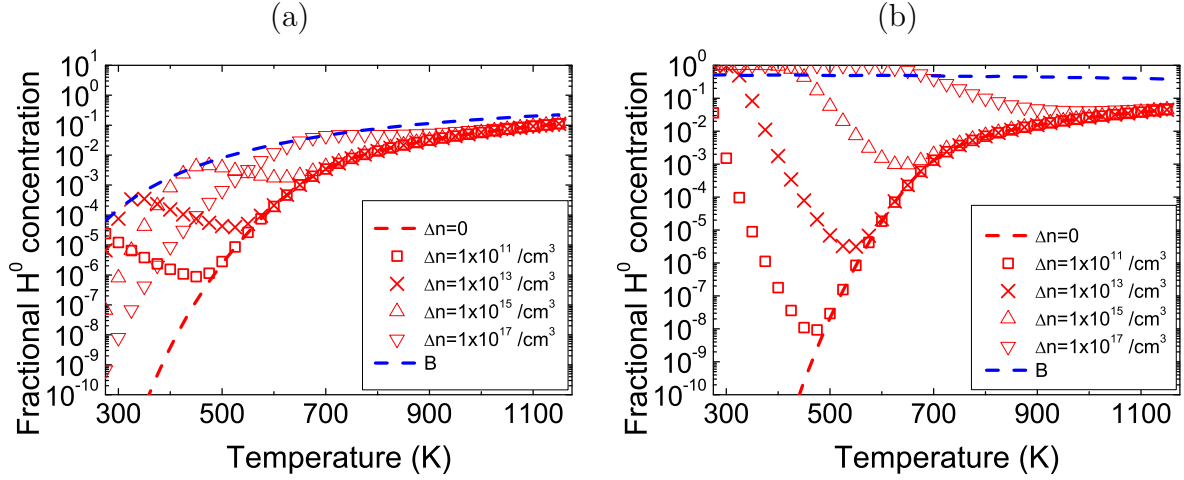


Figure 3.7: Theoretical fractional hydrogen concentrations in p-type silicon with  $N_{eff} = 1 \times 10^{16} \text{ /cm}^3$  for various  $\Delta n$  for (a)  $H^0$  and (b)  $H^-$ , highlighting the importance of varying  $\Delta n$  with temperature. Process B uses optimal  $\Delta n$  to maximise  $H^0$  generation.

Doing so, could avoid a net reactivation of the defects passivated by hydrogen. Eq. 3.16 shows the optimal  $\Delta n$  as a function of temperature ( $\Delta n_{opt}(T)$ ) for p-type silicon (denoted as Process B) where the values of the constants  $A_i$  are given in Table 3.2, correct to  $\pm 4 \%$  of  $\Delta n$  value predicted in the model.

Hence, for p-type silicon, an optimal function of  $\Delta n$  versus temperature was observed to maximise  $H^0$  generation independent of  $N_{eff}$ , with the value of  $\Delta n$  increasing for increasing temperatures. Assuming a constant  $\tau_{eff}$ , as the wafers cools, a decreasing illumination level should be used to maintain optimal  $H^0$  generation. Applying optimal  $\Delta n$  during the cool down process led to increases in  $f_0$  of several orders of magnitude compared to a process in the absence of minority carrier injection.

$$\Delta n_{opt}(T) = e^{(A_1 T^6 + A_2 T^5 + A_3 T^4 + A_4 T^3 + A_5 T^2 + A_6 T + A_7)} \quad (3.16)$$

Table 3.2: Values of constants used in Eq. 3.16 for the temperature dependent  $\Delta n$  required for optimal  $H^0$  generation in p-type silicon.

Constant	Value
$A_1$	$-1.36846 \times 10^{-16}$
$A_2$	$6.55636 \times 10^{-13}$
$A_3$	$-1.30667 \times 10^{-9}$
$A_4$	$1.40373 \times 10^{-6}$
$A_5$	$-8.79231 \times 10^{-4}$
$A_6$	$3.23537 \times 10^{-1}$
$A_7$	$-1.81684 \times 10^1$

### 3.1.5 Summary for Increased $H^0$ Generation in Silicon

A model was developed to calculate the generation of  $H^0$  in both n-type and p-type silicon. The position of  $E_{Fn}$  above  $E_m$  had a profound influence on  $H^0$  generation. Hence  $N_{eff}$ , temperature and  $\Delta n$  can all affect  $f_0$ . For p-type silicon, minority carrier injection was essential to increase  $f_0$  at lower temperatures, and became increasingly important for increasing  $N_{eff}$ . In n-type silicon, minority carrier injection only led to increases in  $f_0$  for lightly doped silicon ( $N_{eff} < 1 \times 10^{16} / \text{cm}^3$ ), whilst for higher  $N_{eff}$ ,  $H^0$  generation was primarily dependent on the temperature.

An optimal function of  $\Delta n$  versus temperature to maximise  $H^0$  generation was determined for p-type silicon independent of  $N_{eff}$ . During the cool down, a decreasing illumination level should be used to maintain optimal  $H^0$  generation, and led to increases in  $f_0$  of several orders of magnitude compared to a process without minority carrier injection.

## 3.2 Hydrogen Passivation of B–O Defects

As discussed in Section 2.1.3, there are contradictory theories relating to the role of hydrogen in the passivation of B–O defects. Hence further work to understand the role of hydrogen is required.

### 3.2.1 Lifetime Test Structures for the Passivation of B–O Defects

#### 3.2.1.1 Aim

In this experiment, the role of hydrogen is further explored for the passivation of B–O defects. In particular, the effectiveness and reversibility of the passivation of B–O defects is investigated for different hydrogenation processes.

#### 3.2.1.2 Experimental Procedures

In this experiment a range of wafers were used to investigate the passivation of B–O defects. The following wafers were used: (1)  $2\ \Omega \cdot \text{cm}$  standard commercial grade B-CZ wafers containing boron and oxygen; (2)  $2\ \Omega \cdot \text{cm}$  standard commercial grade Ga-CZ wafers containing oxygen but no boron; (3)  $1\ \Omega \cdot \text{cm}$  B-FZ wafers containing boron but negligible oxygen; and (4)  $2\ \Omega \cdot \text{cm}$  compensated boron-doped p-type CZ (CB-CZ) wafers containing boron and oxygen. The CB-CZ wafers were from an experimental ingot with a boron dopant concentration of approximately  $1 \times 10^{17} / \text{cm}^3$  and phosphorus compensation to result in a resistivity of approximately  $2\ \Omega \cdot \text{cm}$  grown by Apollon Solar and purified using the PHOTOSIL process [Einh 06].

Each pseudo square  $125 \times 125\ \text{mm}$  B-CZ, Ga-CZ and CB-CZ wafer was cleaved into 9 pieces with dimensions of approximately  $42 \times 42\ \text{mm}$  with one diagonal corner to assist with laboratory processing. The round  $100\ \text{mm}$  B-FZ wafers were also cleaved into 4 pieces of similar dimensions. Prior to the deposition of the dielectric passivation layer, wafers were saw-damage etched (SDE) (to create wafers with a resultant thickness of approximately  $150\ \mu\text{m}$ ), given the Radio Corporation

of America (RCA) clean and HF dipped.

Hydrogenated silicon oxynitride ( $\text{SiON}_x\text{:H}$ ) layers with a refractive index of 2.3 and hydrogen content of approximately 14.2 % [Hall 12b] were deposited using a laboratory type Roth & Rau AK400 remote microwave PECVD system. Subsequently, the passivation quality was determined through photoluminescence (PL) imaging [Trup 05a; Trup 06] obtained using a BTi luminescence imaging system. The quasi-steady-state photoconductance (QSS-PC) and quasi-steady-state PL (QSS-PL) measurement techniques [Sint 96b; Sint 96a; Trup 05b] were used to obtain injection-level-dependent  $\tau_{eff}$  curves, 1-sun  $\tau_{eff}$  and 1-sun  $iV_{OC}$ . Due to the unknown doping densities of both phosphorus and boron in the CB-CZ silicon wafers, the doping density used for the determination of the electron and hole mobilities (and therefore the  $\Delta n$  and  $\tau_{eff}$ ) were the  $N_{eff}$  values obtained from dark conductance measurements on the samples. This does not take into account the effect of the reduction in mobility of the minority carriers due to compensation, and therefore lifetimes presented in this section were underestimated [Roug 10].

To eliminate surface effects from the QSS-PC and QSS-PL measurements, the minority carrier bulk lifetime ( $\tau_{bulk}$ ) was extracted at  $\Delta n = 1 \times 10^{16} \text{ /cm}^3$  by removing the Auger and  $J_{0d}$  lifetime components associated with the surfaces [Cuev 04]. For Auger correction, the Kerr-Cuevas model was used with Auger contribution ( $C_A$ ) given by Eq. 3.17 [Kerr 02]. Hence the  $\tau_{eff}$  after removing the Auger contribution as measured by QSS-PL or QSS-PC ( $\tau_{eff}^*$ ) is given by Eq. 3.18. The lifetime components related to the  $J_{0d}$  ( $\tau_{J_{0d}}$ ) and Shockley-Read-Hall (SRH) recombination ( $\tau_{SRH}$ ) are shown by Eq. 3.19 and Eq. 3.20 respectively where  $W$  is the wafer thickness (in cm),  $q$  is the elementary charge,  $n_1$  and  $p_1$  are the equilibrium concentrations of electrons and holes respectively when  $E_F$  is the energy level of the recombination centre ( $E_T$ ) shown by Eq. 3.21-3.22 [Macd 03; Shoc 52; Hall 52]. Subsequently the total lifetime determined by the model ( $\tau_{total}$ ), which excludes Auger recombination, is given by Eq. 3.23 where  $\tau_{bulk_0}$  is a single valued lifetime (injection-level independent) attributed to the bulk of the wafer. The  $\tau_{bulk}$  was then extracted from Eq. 3.24 taking into account  $\tau_{bulk_0}$  and  $\tau_{SRH}$ . Fig. 3.8 shows a sample extraction of the lifetime parameters for a B-FZ wafer after a CHP with the relevant values for the model shown in Table 3.3. It should be noted that discrepancies between the lifetime measured in low injection and the model were due to localised and/or edge recombination, and the inversion layer formed on the surface by using a positively charged dielectric [Chen 07; Chen 08; Abbo 06a; Ruhl 12].

$$C_A = 3.79 \times 10^{-31} \left( \frac{\Delta n + 3.8 \times 10^{17}}{\Delta n + 6 \times 10^{16}} \right) \quad (3.17)$$

$$\frac{1}{\tau_{eff}^*} = \frac{1}{\tau_{eff}} - C_A \quad (3.18)$$

$$\frac{1}{\tau_{J_{0d}}} = \frac{J_{0d} \cdot (N_a + \Delta n)}{q \cdot W \cdot n_i^2} \quad (3.19)$$

$$\frac{1}{\tau_{SRH}} = \frac{(n_0 + \Delta n) \cdot (p_0 + \Delta n) - n_i^2}{\Delta n \cdot (\tau_n \cdot (p_0 + \Delta n + p_1) + \tau_p \cdot (n_0 + \Delta n + n_1))} \quad (3.20)$$

$$n_1 = N_C \cdot e^{\left(-\frac{q}{kT} \cdot (E_C - E_T)\right)} \quad (3.21)$$

$$p_1 = N_V \cdot e^{\left(-\frac{q}{kT} \cdot (E_T - E_V)\right)} \quad (3.22)$$

$$\frac{1}{\tau_{total}} = \frac{1}{\tau_{bulk_0}} + \frac{1}{\tau_{J_{0d}}} + \frac{1}{\tau_{SRH}} \quad (3.23)$$

$$\frac{1}{\tau_{bulk}} = \frac{1}{\tau_{bulk_0}} + \frac{1}{\tau_{SRH}} \quad (3.24)$$

Table 3.3: Extracted lifetime parameters for a B-FZ wafer after a conventional hydrogenation process shown for the example outlined in Fig. 3.8 to demonstrate the lifetime analysis performed in this experiment.

Parameter	Value
$\tau_{bulk_0}$	6000 $\mu$ s
$J_{0d}$	6.3 fA/cm <sup>2</sup>
$\tau_n$	90000 $\mu$ s
$\tau_p$	250000 $\mu$ s
$E_T$	0.78 eV
$W$	0.015 cm
$N_a$	$1.5 \times 10^{16}$ /cm <sup>3</sup>

To assess the passivation of B–O defects by hydrogen, two different hydrogenation processes were applied in this section. A CHP was used with no attempt to control the hydrogen charge state, resulting in insufficient  $f_-$  and  $f_0$  to passivate defects such as the B–O complex. CHP

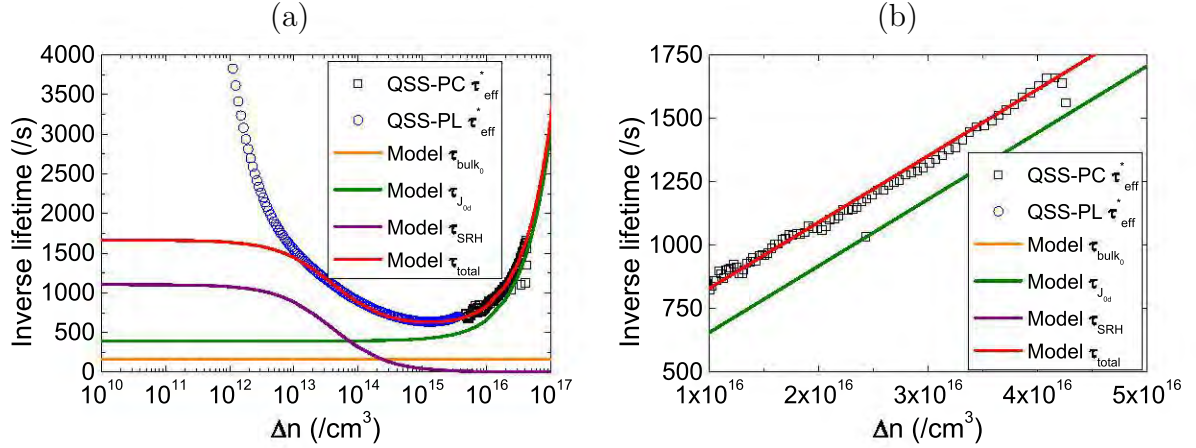


Figure 3.8: Determination of the lifetime components on a B-FZ wafer to demonstrate the analysis used in this experiment, showing (a) all injection-levels on a logarithmic scale and (b) high injection-levels on a linear scale to determine  $J_{0d}$  contributions.

such as those implemented via atomic hydrogen being generated through an alneal process for the world-record PERL cells are typically performed at approximately 400 °C for 5 – 30 min in the dark [Zhao 96], and in this work, consisted of 400 °C for 5 min. In contrast, industrial processes used for the firing of screen-printed contacts fortuitously implement conditions somewhat better for controlling the charge state of hydrogen, but because the lamps primary function is for heating rather than illumination, conditions are usually far from optimal, plus no illumination is provided during cool down.

An AHP was used where the charge state of the hydrogen was controlled to enhance passivation by minority carrier injection through increases in temperature and the addition of illumination. The AHP was performed in a conventional fast firing furnace with a peak set temperature of 700 °C and belt speed of 4600 mm/ min with a modification of power distribution throughout the furnace and incorporation of illumination into the cooling zone. Table 3.4 shows the set up and measurements for the conventional method for such a process with the same power applied to both the top and bottom lamps in all zones, where  $Z_i$  is the  $i^{th}$  zone. It should be noted that differences between

the “actual temperature” and the “additional measurement” were due to the placement of the different thermocouples within the furnace. Data logging performed using this firing configuration indicated that the peak temperature on the wafer of 620 °C was in close agreement with the “additional measurement” in Z5. For the AHP, all of the lamps in Z4 were turned off by setting the maximum allowed power to the lamps to 0%. In addition, the bottom lamps in Z5 and Z6 were also disabled. After this modification, to maintain temperature in Z5 and Z6 and also supply energy to Z4, the top lamps in Z5 and Z6 required a higher power than the combined power of the top and bottom lamps of the corresponding zones using the conventional approach. Due to the blackbody spectrum, this enhanced the illumination level using the modified heat distribution in the peak firing zones and cooling zone. Due to the more efficient emission of light above the Si band-gap, a slight reduction in the peak wafer temperature (620 °C) was observed (and similarly for the “additional measurements”) in Z5 and Z6 (see Table 3.5). One additional benefit for using single sided illumination in the peak firing zones is to place the illumination on what is typically the light-receiving surface of the solar cell, such that if the solar cell has a full area rear metallisation scheme, significant illumination levels can still enter the wafer to allow more effective  $H^0$  generation, rather than being reflected or absorbed by the metal contact.

Table 3.4: Standard configuration for a conventional fast firing hydrogenation process with a peak set temperature of 700 °C.

	<b>Z1</b>	<b>Z2</b>	<b>Z3</b>	<b>Z4</b>	<b>Z5</b>	<b>Z6</b>
<b>Set temperature (°C)</b>	400	450	500	550	700	700
<b>Actual temperature (°C)</b>	400	450	500	551	700	700
<b>Additional measurement (°C)</b>	-	-	-	-	657	613
<b>Top lamps maximum power (%)</b>	80	80	80	80	80	80
<b>Top lamps actual power (%)</b>	13	10	37	36	20	21
<b>Bottom lamps maximum power (%)</b>	80	80	80	80	80	80
<b>Bottom lamps actual power (%)</b>	11	8	32	36	20	21

---



Table 3.5: Configuration for an advanced fast firing hydrogenation process with increased illumination and a peak set temperature of 700 °C. Notable differences between the standard and enhanced configuration are featured in red.

	<b>Z1</b>	<b>Z2</b>	<b>Z3</b>	<b>Z4</b>	<b>Z5</b>	<b>Z6</b>
<b>Set temperature (°C)</b>	400	450	500	550	700	700
<b>Actual temperature (°C)</b>	400	450	500	356	700	700
<b>Additional measurement (°C)</b>	-	-	-	-	637	600
<b>Trim top (%)</b>	80	80	80	0	80	80
<b>Control output top (%)</b>	13	10	50	0	56	50
<b>Trim bottom (%)</b>	80	80	80	0	0	0
<b>Control output bottom (%)</b>	13	10	50	0	0	0

For both processes, atomic hydrogen from identical dielectric layers of PECVD SiON<sub>x</sub>:H were the only source of hydrogen for the passivation process. After the CHP and AHP, the wafers were re-measured using the aforementioned techniques. The process flow for this section is given in Fig. 3.9, showing the order of the hydrogenation processes in which the CHP is initially applied followed by the AHP. Additional hydrogenation treatments were then performed to demonstrate the reversibility of the hydrogenation process.

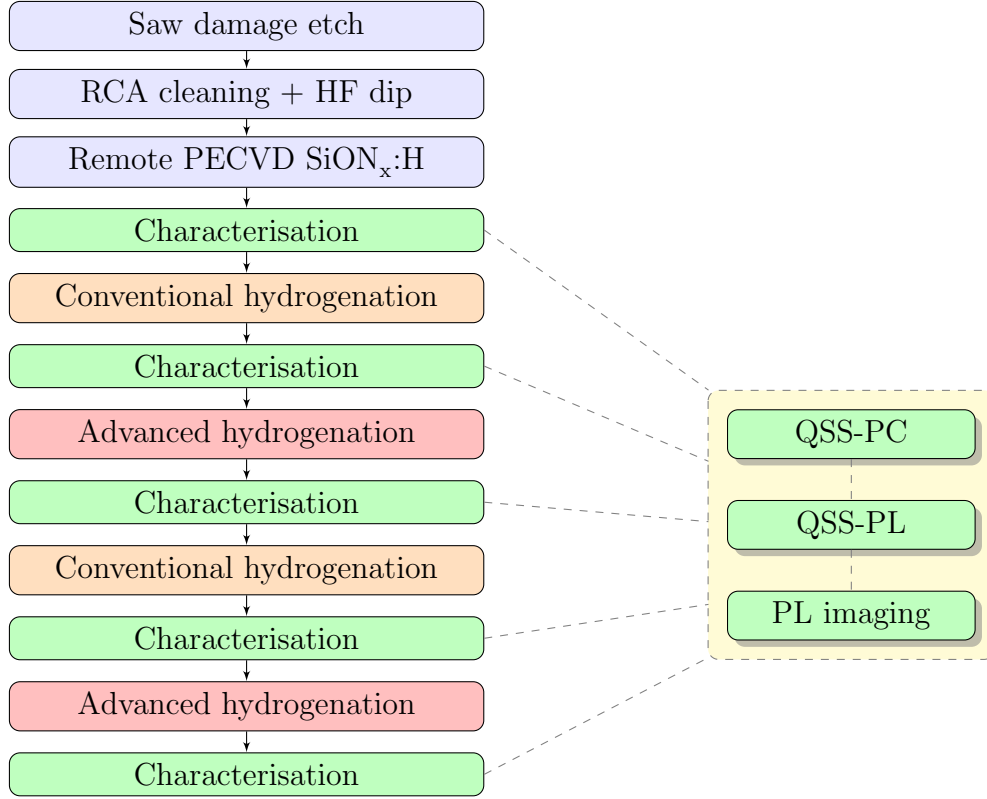


Figure 3.9: Process flow for lifetime studies on the hydrogen passivation of B–O defects.

### 3.2.1.3 Improved Passivation of B–O Defects through Advanced Hydrogenation on Lifetime Test Structures

A summary of the results showing the benefits of different hydrogenation processes for the various wafer types is shown in Table 3.6, highlighting the additional benefits of an AHP for wafers containing both boron and oxygen.

**B-FZ silicon:** B-FZ wafers contain boron, but negligible oxygen. Therefore, B-FZ silicon is not subject to the formation of B–O defects. Directly after the deposition of SiON<sub>x</sub>:H, the B-FZ wafers displayed  $\tau_{eff}$  of up to 700  $\mu$ s with only a weak injection-level dependence (see Fig. 3.10(a)). After a CHP, a large increase in  $\tau_{eff}$  was observed to values of approximately 1.7 ms, indicating improvements in both bulk and surface passivation. After the AHP was implemented by controlling

Table 3.6: Summary of the benefits obtained by various wafer types for a CHP and AHP highlighting substantial improvements for boron and oxygen containing wafers from an AHP.

Wafer type	B-FZ	Ga-CZ	B-CZ	CB-CZ
Contains boron	✓	✗	✓	✓
Contains oxygen	✗	✓	✓	✓
Significant benefit from a CHP	✓	✓	✗	✗
Significant benefit from an AHP	✗	✗	✓	✓

the charge state of the atomic hydrogen to enhance its mobility and reactivity, no improvement in  $\tau_{eff}$  was observed on the B-FZ wafers. In fact, the  $\tau_{eff}$  of such wafers slightly reduced for  $\Delta n < 1 \times 10^{16} / \text{cm}^3$ , due to an increase in localised and/or edge recombination [Chen 07; Chen 08; Abbo 06a; Ruhl 12], caused by the formation of pinholes in the dielectric layer during the AHP.

**Ga-CZ silicon:** Ga-CZ wafers contain oxygen, but no boron. Therefore, Ga-CZ silicon is not subject to the formation of B–O defects. Directly after the deposition of  $\text{SiON}_x\text{:H}$ , the Ga-CZ wafers displayed  $\tau_{eff}$  of up to 400  $\mu\text{s}$ , however the wafers suffered from a strong injection-level dependence (see Fig. 3.10(b)). This have have been due to localised and/or edge recombination. After the CHP, a substantial improvement in  $\tau_{eff}$  was observed for all injection levels, with improvements in both bulk and surface passivation. After the AHP, only a small increase in  $\tau_{eff}$  was observed for  $\Delta n$  in the range of  $1 \times 10^{12} - 1 \times 10^{16} / \text{cm}^3$ , indicating only a small benefit of performing an AHP for the Ga-CZ wafers.

**B-CZ silicon:** B-CZ wafers contain both boron and oxygen. Therefore, B-CZ silicon is subject to the formation of B–O defects. Directly after the deposition of  $\text{SiON}_x\text{:H}$ , the B-CZ wafers displayed  $\tau_{eff}$  of up to 400  $\mu\text{s}$ , however the wafers suffered from a strong injection-level dependence, with substantially lower  $\tau_{eff}$  in the range in  $\Delta n$  of  $1 \times 10^{14} - 1 \times 10^{15} / \text{cm}^3$  when compared to the Ga-CZ

wafers (see Fig. 3.10(c)). Furthermore, the  $\tau_{eff}$  of the B-CZ wafers was substantially lower than the B-FZ wafers over all injection levels. After a CHP, only a small increase in  $\tau_{eff}$  was observed for  $\Delta n > 1 \times 10^{13} / \text{cm}^3$ , suggesting the CHP was ineffective at passivating the defects in the B-CZ material. However after an AHP, a substantial increase in  $\tau_{eff}$  was observed over all injection levels, suggesting a greatly improved level of passivation achieved using the AHP when compared to that from a CHP.

**CB-CZ silicon:** CB-CZ wafers contain both boron and oxygen. Therefore, CB-CZ silicon is subject to the formation of B–O defects. Directly after the deposition of  $\text{SiON}_x\text{:H}$ , the CB-CZ wafers displayed  $\tau_{eff}$  of up to 100  $\mu\text{s}$ , which was substantially smaller than all of the other wafer types. Furthermore, the  $\tau_{eff}$  in low injections was less than 20  $\mu\text{s}$  (see Fig. 3.10(d)). The reduced lifetime of the CB-CZ wafers may be caused by an increased B–O defect concentration due to a higher B concentration in the CB-CZ material when compared to standard B-CZ material. After a CHP, the  $\tau_{eff}$  of the CB-CZ was slightly reduced for  $\Delta n < 1 \times 10^{16} / \text{cm}^3$ . This suggests that the CHP was of no benefit for the CB-CZ material, and in fact detrimental. After the AHP, the  $\tau_{eff}$  substantially increased with values of up to 300  $\mu\text{s}$ , and values in low injections over 40  $\mu\text{s}$ . This suggested that an AHP was essential for the CB-CZ material to improve lifetimes.

**Discussion:** The PECVD system used in this work incorporated a thermal process after the deposition of the dielectric layer. This process started at the deposition temperature of 400 °C and ramped down to a temperature of 250 °C over approximately 20 min before the samples were unloaded. According to literature, the thermal treatment above 170 °C should have resulted in the lifetime of the B-CZ and CB-CZ wafers being in a non-degraded state [Schm 97]. However directly after the deposition of  $\text{SiON}_x\text{:H}$ , the shape of the  $\tau_{eff}$  curves on B-CZ and CB-CZ wafers greatly varied from that obtained on Ga-CZ or B-FZ wafers (see Fig. 3.10). After a CHP at 400 °C, the  $\tau_{eff}$  of wafers not subject to the formation of B–O defects (i.e. B-FZ and Ga-CZ silicon) greatly improved, whereas the  $\tau_{eff}$  of wafers subject to the formation of B–O defects saw little improvement or were reduced. In contrast, after an AHP, wafers not subject to the formation of B–O defects saw little improvement or were reduced, whereas the  $\tau_{eff}$  of wafers subject to the formation of B–O defects saw a substantial improvement.

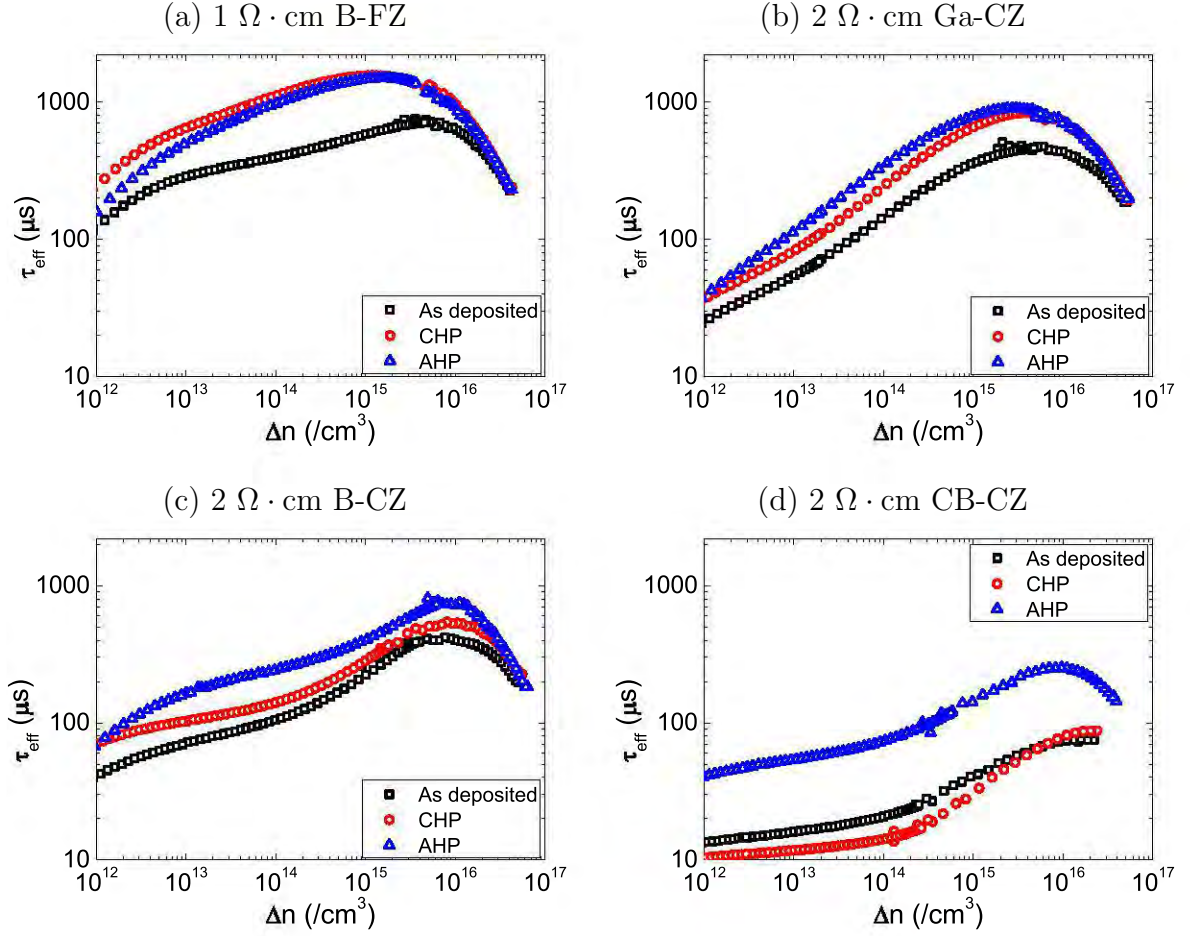


Figure 3.10:  $\tau_{eff}$  curves of various wafer types before and after hydrogenation, highlighting the large improvements in lifetime through the passivation of B–O defects.

These results suggests that recombination active B–O defects were still present in the wafers after the deposition of  $\text{SiON}_x\text{:H}$  and after the CHP. However after an AHP, the recombination active concentration of such defects was greatly reduced. Hence it appears that the AHP deactivated a number of B–O defects which a CHP failed to deactivate. This suggests that the charge state of hydrogen is of significant importance to passivating B–O defects. In recent work on the regeneration process for B–O defects by Wilking *et al.* 2013, minority carrier injection was also used with the authors eluding to the possibility of a change in charge state of hydrogen assisting with the

passivation process [Wilk 13]. Hence for wafers subject to the formation of B–O defects (i.e. the majority of wafers used in commercial production), an AHP should be used, whereas for wafers not subject to the formation of B–O defects, a CHP is sufficient. At this stage it remains unclear whether  $H^0$  or  $H^-$  is assisting in the passivation process. However one of the recent understandings for the recovery of the SRC of the B–O complex is through the capture of an electron [Voro 10]. This may suggest the capture of  $H^-$  to form a neutral complex.

Previous work by Glunz *et al.* 2001 reported substantial reductions in the normalised defect density and increased stabilised lifetimes through optimised processing during thermal oxidations. Whilst not explicitly reported, the improvements also resulted in higher lifetimes prior to degradation [Glun 01b]. Although light soaking will be required to confirm whether or not any increase in stabilised lifetime can be achieved, the results by Glunz *et al.* 2001 would suggest the possibility of an increase in stabilised lifetime in this work through the application of the AHP. However, this needs to be explored with further experimentation.

#### 3.2.1.4 Reversibility of passivation of B–O defects by hydrogen

Passivation stability is of utmost importance when investigating hydrogenation processes for commercial silicon solar cells. Hence the stability of the passivation provided by the CHP and AHP was investigated. Whilst other papers report permanent deactivation of B–O defects through hydrogenation [Krug 11; Munz 09; Lim 10a], it was observed that the hydrogen passivation of the B–O defects was indeed reversible. From the  $\tau_{eff}$  obtained from applying the AHP, subsequent processing with a CHP reverted the lifetime back to the previous  $\tau_{eff}$  determined after the initial CHP, whilst a further anneal using the AHP once again passivated the B–O defects and led to substantial increases in  $\tau_{eff}$ .

Hydrogen passivation of B–O defects appears to be a two-way process in which B–O defect deactivation and reactivation are occurring simultaneously. If conditions during subsequent processing result in the atomic hydrogen being in an unsuitable state to re-passivate a sufficient quantity of defects which are reactivated during such processes, a net reactivation of the B–O defects may result. Hence careful attention must be given to ensure the right mobility and reactivity of the

hydrogen throughout the process to result in a net passivation of the B–O and presumably other defects within the silicon. Fig. 3.11(a) shows the injection-level dependent  $\tau_{eff}$  curves of B–O defects in B-CZ wafers subjected to additional hydrogenation processes (with the legend indicating the sequential order of the processes), showing complete reversibility between the  $\tau_{eff}$  obtained after the CHP and AHP. Fig. 3.11(b) indicates that the changes in  $\tau_{eff}$  were due to changes in the  $\tau_{bulk}$  of the B-CZ wafers. Hence the passivation of bulk defects by applying additional hydrogenation treatments (CHP and AHP) was shown to be reversible. For B-CZ wafers, after an initial  $\tau_{bulk}$  of 500  $\mu$ s, the  $\tau_{bulk}$  toggled between 800  $\mu$ s with the application of the CHP and 1.4 ms with the application of the AHP (see Fig. 3.11(b)). On other B-CZ wafers with a lower initial  $\tau_{bulk}$  of 250  $\mu$ s, the  $\tau_{bulk}$  toggled between 700  $\mu$ s with the application of the CHP and 1.3 ms with the application of the AHP, almost reaching the same final value (not shown). Similarly, on CB-CZ wafers, the  $\tau_{bulk}$  toggled between a value of approximately 100  $\mu$ s with the application of the CHP and over 300  $\mu$ s with the application of the AHP. However no such increase in  $\tau_{bulk}$  was observed for B-FZ or Ga-CZ wafers with the application of the AHP. For such wafers, the  $\tau_{bulk}$  typically suffered a slight degradation and hence there was no reversibility of passivation observed between the CHP and AHP for these wafers.

It should be noted that PL images did not indicate the presence of thermal donors after the CHP or AHP by processing at different temperatures. Fig. 3.11(c) shows the corresponding 1-sun  $iV_{OC}$  of the wafers with an improvement of approximately 15 mV and 70 mV for the B-CZ and CB-CZ wafers respectively between the CHP and AHP through a more effective passivation of the B–O defects, whilst no improvements were observed for the Ga-CZ and B-FZ wafers. For such wafers, a slight decrease was observed between the CHP and AHP, consistent with an enhancement in localised and/or edge recombination, which appears to be irreversible after the application of the initial AHP.

Therefore, in order to get effective hydrogenation of B–O defects, the hydrogen should be in the correct charge state to increase its mobility to allow it to move into and throughout the bulk of the silicon and subsequently deactivate the B–O complexes. Furthermore, during subsequent thermal processes, a sufficient concentration of hydrogen must be in the correct charge state such that any thermally reactivated B–O defects can be re-passivated by the atomic hydrogen, therefore not leading to a net reactivation of B–O defects during the process. It is also expected that it is



important to use a solar cell structure which avoids the formation of hydrogen sinks, and therefore reduce molecular hydrogen formation. Doing so, would retain larger concentrations of monatomic hydrogen available to passivate such defects.

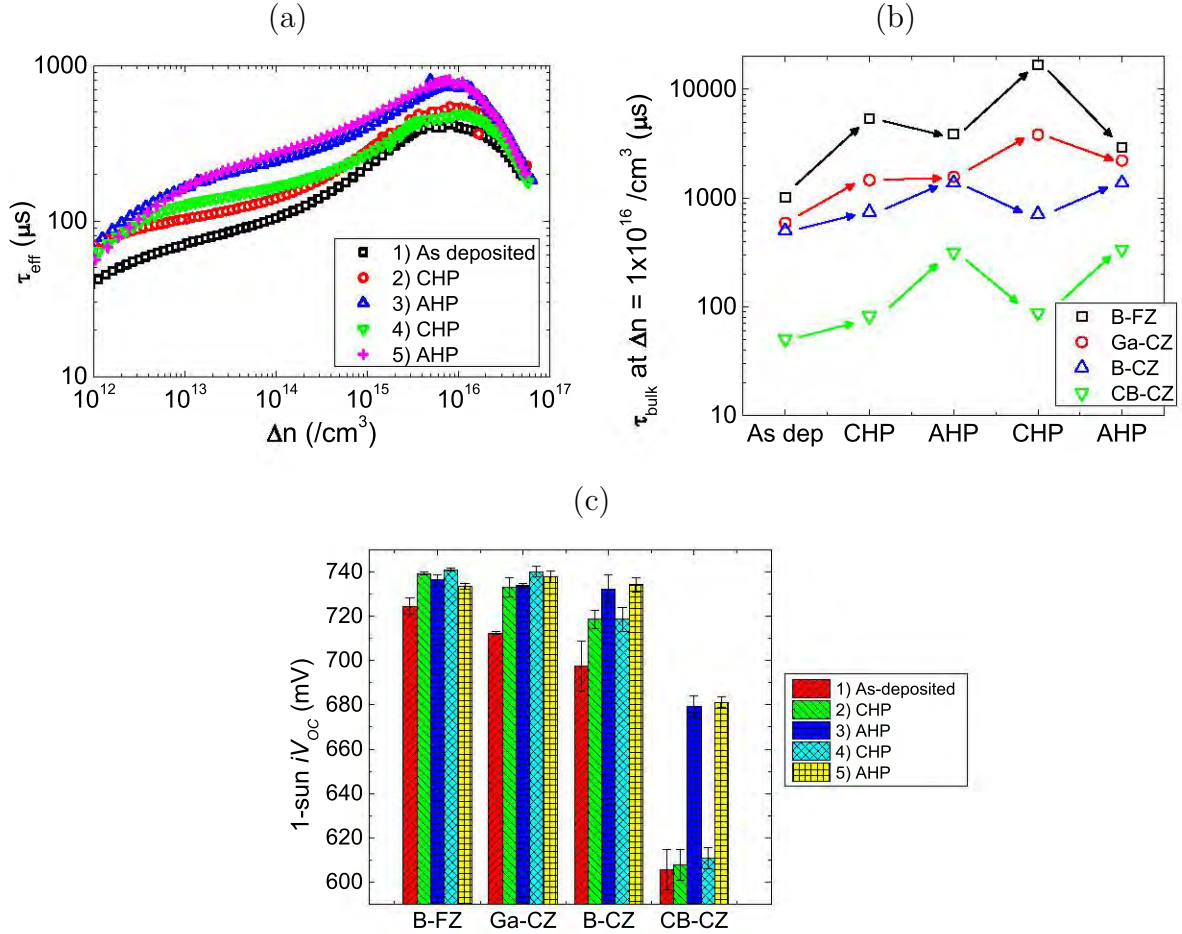


Figure 3.11: (a)  $\tau_{eff}$ , (b)  $\tau_{bulk}$  and (c) 1-sun  $iV_{OC}$  on B-FZ, Ga-CZ, B-CZ and CB-CZ wafers showing the reversibility of the passivation of B–O defects between a CHP and AHP.



### **3.2.1.5 Summary for Lifetime Test Structures for B–O Defect Passivation**

The use of hydrogen to passivate B–O defects was explored in this section. A CHP was shown to result in substantial improvements in lifetime on wafers not subject to the formation of B–O, however for industrially relevant wafers which are subject to the formation of B–O defects, an AHP was required. As a result, increases in  $\tau_{bulk}$  from initial values of 500  $\mu\text{s}$  to values of 1.4 ms were observed after an AHP. The passivation of the B–O was also reversible, if sufficient minority carrier injection was not applied during subsequent processes at elevated temperature. However solar cells undergo several high temperature processes during the fabrication sequence, and hence, the suitability of the AHP to passivate B–O defects in full solar cells must be explored.

## **3.2.2 Advanced Hydrogen Passivation for B–O Defects in Silicon Solar Cells**

### **3.2.2.1 Aim**

In this experiment, the AHP is applied to solar cells to investigate the suitability of the process for the solar cell fabrication sequence, and hence the relevance of hydrogen passivation of B–O defects in commercial silicon solar cells.

### **3.2.2.2 Experimental Procedures**

Second generation LDSE (LDSE2) solar cells with a rear surface passivation layer and localised rear contacts were fabricated on the standard commercial grade  $2\ \Omega\cdot\text{cm}$  B-CZ wafers and processed in an industrial environment using standard commercial production equipment. The wafers were anisotropically textured to expose the (111) planes followed by a phosphorus emitter diffusion in a  $\text{POCl}_3$  tube diffusion furnace. After the subsequent PSG removal and chemical edge junction isolation process to simultaneously planarise the rear surface and perform a slight etch back of the front surface to reduce the surface concentration of phosphorus, a resultant sheet resistance of  $100 - 150\ \Omega/\square$  was obtained. A thin thermal oxide layer was grown to reduce  $\text{LasID}$  generation,

before the front and rear  $\text{SiN}_x\text{:H}$  layers were deposited using an industrial Roth & Rau remote microwave PECVD system.

A commercially available boron spin on dopant source from Filmtronics (PBF1) was spun onto the rear surface at 2000 revolutions per minute (RPM) for 20 s. Laser doping was performed on the rear surface using a 532 nm CW Spectra Physics Millennia Prime laser with a Gaussian beam of approximately 20  $\mu\text{m}$  focus size ( $1/e^2$  diameter) and power of approximately 13.5 W reaching the wafer surface. Laser doping was performed at a processing speed of 0.5 m/s through the use of a galvanometer scanner and f-theta lens. Wafers then received a short HF dip and rinse to remove the SOD. The AHP was applied after the laser doping process to passivate LasID, B–O complexes and other defects within the device [Hall 13b]. The p-type metal contact was formed by Al sputtering and the n-type contacts were formed using the Pluto process [Shi 09] with self-aligned LIP contacts. Ni silicide formation was performed directly after Ni plating. Subsequently, copper LIP was used to thicken the contact followed by a silver immersion dip to prevent oxidation of the copper.

The process flow for the fabrication of solar cells in this section is shown in Fig. 3.12.

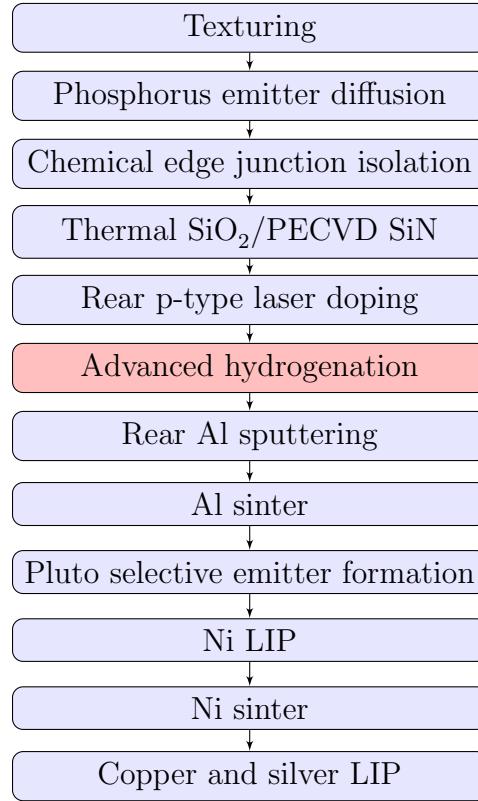


Figure 3.12: Process flow for solar cells fabricated to investigate the passivation of B–O defects.

#### 3.2.2.3 Application of the Advanced Hydrogenation Process for B-CZ Silicon Solar Cells

Hydrogen passivation of B–O defects appears to be a complex process with multiple interactions occurring within the device. The effectiveness of passivation depends on a number of factors, which for example can influence: (1) the release of atomic hydrogen from dielectric layers; (2) mobility of hydrogen throughout the device; (3) reactivity and ability of the atomic hydrogen to passivate B–O defects; (4) reactivation of defects during subsequent processing; or (5) the formation of molecular hydrogen and therefore loss of atomic hydrogen from the silicon.

Using the AHP based on controlling the charge state of the atomic hydrogen, large area industrial PERL solar cells were fabricated on standard commercial grade B-CZ silicon wafers. Through the

hydrogen passivation of B–O defects, greatly improved  $\tau_{bulk}$  in excess of 500  $\mu$ s and independently confirmed  $V_{OC}$  of 681 mV and  $J_{SC}$  of 40.0 mA/cm<sup>2</sup> were obtained with  $p$ - $\eta$  approaching 23 %. The light current density - voltage (J-V) parameters are shown in Table 3.7. Further results of such cells have been published in conjunction with Sugianto *et al.* 2012 [Sugi 12]. This suggests that efficiencies of devices in excess of 22 % should be feasible from solar cells fabricated on standard commercial grade B-CZ wafers.

Table 3.7: Light J-V data of the laser-doped PERL cell fabricated in this work as independently confirmed by the Solar Energy Research Institute of Singapore. The corresponding Suns- $V_{OC}$  data is also shown using the confirmed  $V_{OC}$  and  $J_{SC}$ .

$V_{OC}$	$J_{SC}$	$FF$	$\eta$	$p$ - $FF$	$p$ - $\eta$
(mV)	(mA/cm <sup>2</sup> )	(%)	(%)	(%)	(%)
681	40.0	72.2	19.7	84.1	22.9

#### 3.2.2.4 Summary of the Application of Advanced Hydrogen Passivation for B–O Defects in Silicon Solar Cells

The AHP was applied to LDSE2 solar cells fabrication on B-CZ wafers. Independently confirmed  $V_{OC} > 680$  mV and  $J_{SC}$  of 40.0 mA/cm<sup>2</sup> were obtained, with a pseudo efficiency of 23 %. The results demonstrate a large potential for efficiency enhancements on B-CZ wafers through the application of an AHP.

### 3.2.3 Summary of Hydrogen Passivation for B–O Defects

Hydrogen passivation of B–O defects depends on the hydrogen passivation used. An AHP was essential to increase the  $\tau_{bulk}$  of industrially relevant wafers subject to the formation of B–O defects.

Greatly increased lifetimes from 500  $\mu\text{s}$  to 1.4 ms were observed on test structures by using an AHP incorporating minority carrier injection to increase the minority fractional hydrogen charge state concentrations. When this AHP was incorporated into solar cells, independently confirmed  $V_{OC}$  over 681 mV and  $J_{SC}$  of 40.0 mA/cm<sup>2</sup> were obtained with a  $p\text{-}\eta$  approaching 23 %. This suggests a large potential efficiency improvement for solar cells fabricated on B-CZ wafers through a more effective passivation of B–O defects using an AHP.

## 3.3 Advanced Hydrogen Passivation for Upgraded Metallurgical Grade Silicon

There is a great need to reduce the cost of PV, so solar cells can produce electricity cheaper than conventional fossil fuel technologies. For wafer based silicon solar cells, there are many approaches which can assist in reducing the cost of PV. One approach is to focus on increasing the efficiency of the solar cells, without substantial increases in wafer to cell conversion costs, which enables a reduction in wafering and encapsulation costs (in terms of dollars per Watt). Other approaches opt for using lower-quality, cheaper silicon wafers, although solar cells fabricated on these types of wafers typically yield lower efficiencies, which effectively increases the costs of wafer to cell conversion and encapsulation. However there is substantial potential to treat lower-quality silicon wafers through advanced passivation techniques to improve the wafer quality, thereby allow higher efficiency devices to be fabricated on cheap, low-quality silicon wafers. Upgraded metallurgical grade (UMG) silicon is a low-cost, low-quality silicon material purified by processes other than the Siemens technique, with the potential to reduce cost of photovoltaics [Reut 10].

However, due to the purification methods used during the formation of UMG material, including plasma or Al purification, UMG silicon typically shows the significant presence of both n- and p-type dopants and various contaminants such as transition metals [De W 02; Brag 08; Yuge 94; Xu 10; Peri 02; Istr 03]. Therefore both n- and p-type UMG silicon may be subject to the formation of B–O complexes if sufficient quantities of oxygen are present in the silicon [Fisc 73; Reis 96; Lim 10b; Jung 11]. Due to the high recombination activity of transition metals and their precipitants, such impurities can also limit the  $\tau_{eff}$  in UMG silicon [Xu 10; Peri 02;

[Istr 03; Jung 11; Tais 07]. Furthermore, the presence of contaminants may lead to the formation of crystallographic defects during the crystal growth, leading to additional recombination sites [Macd 04a; Einh 06]. Due to the reduced  $\tau_{eff}$  in UMG silicon, solar cells fabricated from such material typically suffer from reduced efficiencies. Subsequently, the passivation of B–O complex defects, metallic impurities and crystallographic defects are of particular importance for solar cells fabricated using UMG silicon, to increase  $\tau_{eff}$  and therefore efficiency.

Variations in resistivity typically occur throughout ingots due to segregation during crystallisation. Such variations can greatly affect a large number of electrical parameters such as  $\tau_{eff}$ , conductivity, carrier profiles across the cell, bulk recombination and mobility, and therefore influence  $V_{OC}$ ,  $J_{SC}$ ,  $FF$  and  $\eta$  [McIn 03]. Subsequently, solar cell manufacturers often measure the resistivity of incoming wafers to reduce the risk of cell mismatch. It is common for silicon producers to reject approximately the last 25 % of CZ ingots, particularly that grown from UMG silicon due to the differences in wafer resistivity throughout the ingot and high defect densities. However, higher ingot utilisations may be realised through the use of more effective passivation of material from the bottom of CZ ingots through dopant compensation, even though such regions are typically prone to higher crystallographic defect densities caused by increased impurity concentrations. For solar cell manufacturers, incoming wafer inspection is also performed using techniques such as PL imaging to determine wafer lifetime, and material is rejected if the lifetime is deemed too low to make good devices. However this analysis is carried out before any phosphorus gettering and hydrogenation processes take place, which have been shown to lead to substantial changes in the  $\tau_{bulk}$  of the material [Haun 10; Rini 04]. If appropriate hydrogenation processes can ensure adequate passivation is retained on finished devices, it may allow high efficiency devices to be fabricated on wafers grown from UMG silicon.

### 3.3.1 Aim

In this experiment, the potential to passivate defects in low-cost, low-quality UMG silicon wafers through the use of advanced hydrogenation is explored. In particular, close attention was paid to the influence of wafer position within the ingot, and hence resistivity, on the response to hydrogen passivation.

### 3.3.2 Experimental Procedures

In this section, the same processing methods were used as described for the lifetime studies in Section 3.2.1. In this instance, a variety of  $125 \times 125$  mm UMG CZ silicon wafers were used throughout an experimental ingot, using 100 % UMG silicon from the PHOTOSIL project as produced by Apollon Solar [Einh 06; Fors 10; Fors 11]. Calibrated 1-sun  $iV_{OC}$  maps were obtained at various stages of processing [Hall 14h].

Approximate effective doping densities were obtained by measuring the conductivity of each wafer using a Sinton WCT-100 photoconductance tool. The intrinsic conductivity of the conductance unit was measured in the dark by obtaining an average signal voltage before the wafer was placed on the measuring coil. Subsequently, a wafer was placed onto the coil and the conductance was measured in the dark to determine the change in signal voltage ( $\delta$ ) due to the wafer. This change in signal voltage was then converted into an absolute conductance using Eq. 3.25, where  $S$  is the conductance in Siemens and  $\alpha$  and  $\beta$  are the system dependent calibration constants of  $3.72 \times 10^{-2}$  and  $3.98 \times 10^{-4}$  respectively [Hame 11a]. The bulk resistivity in  $\Omega \cdot \text{cm}$  was then obtained using Eq. 3.26 and converted to  $N_{eff}$  using PC1D [Baso 96]. It should again be noted that this did not take into account the minor effect of the reduction in mobility of the minority carriers due to compensation [Roug 10].

$$S = \alpha \cdot \delta + \beta \cdot \delta^2 \quad (3.25)$$

$$\rho_{bulk} = \frac{W}{S} \quad (3.26)$$

### 3.3.3 Resistivity Variation Throughout the UMG Ingot

Variations in wafer resistivity can alter the generation of  $H^0$ , and therefore influence hydrogenation processes. Prior to the deposition of  $\text{SiON}_x\text{:H}$ , a large variation in the normalised PL response ( $I_{PL}$ ) was observed throughout the UMG CB-CZ ingot (see Fig. 3.13(a)). Such variations could be due to a change in lifetime of the material and hence change in  $\Delta n$  and/or a change in the effective doping of the wafers [Trup 05a]. Dark conductance measurements obtained on the wafers after the

deposition of the  $\text{SiON}_x\text{:H}$  indicated a change in the resistivity of the wafers throughout the ingot as shown in Fig. 3.13(b), where a value of  $x_n = 0$  for the normalised wafer position in the ingot corresponds to the top of the ingot and a value of  $x_n = 1$  corresponds to the bottom of the ingot.

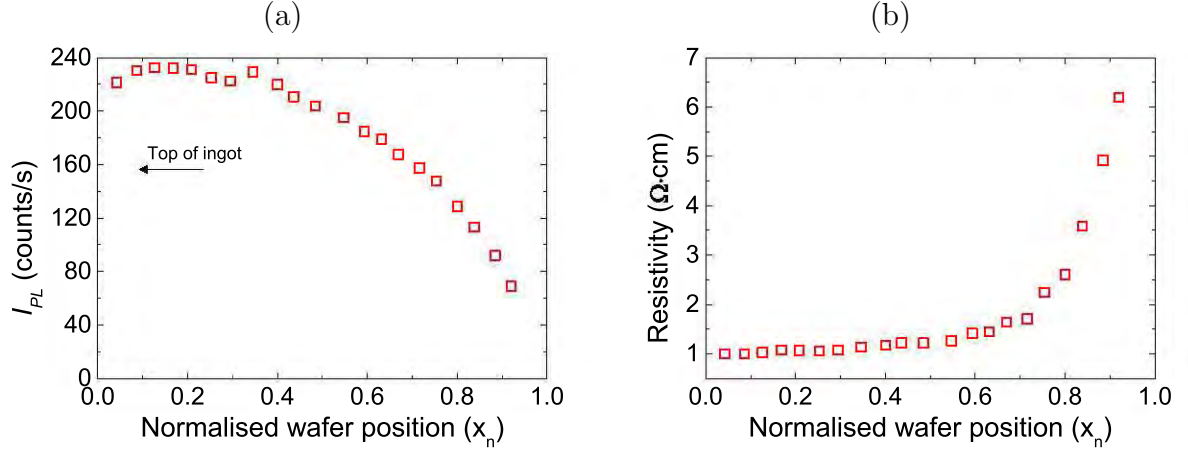


Figure 3.13: (a) Normalised PL response of raw UMG CZ wafers and (b) resistivity as measured by dark conductance, highlighting variations throughout the ingot.

Variations in resistivity throughout CZ ingots are typical due to the segregation coefficients of the dopants according to the Scheil equation (see Eq. 3.27), where  $f_S$  is the fraction of solidified silicon during ingot growth,  $C(f_S)$  is the concentration of the impurity at position  $f_S$ ,  $C_0$  is the initial concentration of the impurity in the silicon melt and  $k_{eff}$  is the effective segregation coefficient of the impurity in silicon [Sche 42]. A value of  $f_S = 0$  corresponds to the first silicon to solidify during the CZ growth process at the top of the ingot, and a value of  $f_S = 1$  corresponds to the last silicon to solidify at the bottom of the CZ ingot assuming that all silicon within the crucible is incorporated into the ingot. However due to the pot scrap which remains in the crucible after ingot growth and the silicon at the ends of the ingot which are discarded, there are differences in



the  $x_n$  and  $f_S$  values. It is assumed that  $f_S = 0.07$  at  $x_n = 0$  and  $f_S = 0.81$  at  $x_n = 1$ .

$$C(f_S) = C_0 \cdot k_{eff} (1 - f_S)^{k_{eff}-1} \quad (3.27)$$

For the case of solar grade Si, typically only one type of dopant is present in the silicon melt, and hence in CZ ingots,  $N_{eff}$  increases with increasing  $f_S$ . However UMG purified silicon may contain many different types of dopant atoms. The CZ ingot used in this work is typical of UMG silicon wafers grown using the 2010/11 version of the PHOTOSIL process, however this ingot had a phosphorus concentration of approximately 1 ppmw in comparison to the PHOTOSIL specifications of 0.5 ppmw. In certain situations, whilst the concentration of each given dopant increases throughout the CZ ingot, such variations can lead to an inversion of polarity of wafers throughout the ingot [Fors 10; Trup 11]. In order to increase  $N_{eff}$  throughout the ingot, other dopants such as gallium may be added in appropriate addition concentrations which can potentially prevent polarity inversion at the top of the ingot and therefore increase ingot utilisation [Fors 10; Fors 11]. Dark conductance measurements indicated that no such polarity inversion occurred for the wafers used in this work, however a large variation in resistivity was observed throughout the ingot which could affect solar cell performance. A simple segregation model including only boron and phosphorus closely matches the estimated  $N_{eff}$  (see Fig. 3.14). Differences in  $N_{eff}$  estimated by dark conductance and the model using the Scheil equation may be due to uncertainties in the actual  $f_S$  value for a given  $x_n$ .

### 3.3.4 Passivation of Slip Lines in UMG CZ Wafers

In addition to the segregation of dopants during CZ ingot growth, segregation also applies to other impurities. PL images of the wafers before and after the deposition of  $\text{SiON}_x\text{:H}$  indicate that slip-lines were present in wafers near the bottom of the ingot, for  $x_n > 0.65$ . It is likely that such defects were due to increased stresses during crystal growth resulting from higher concentrations of dopants and contaminants in these parts of the ingot (see Fig. 3.15). The slip-lines appeared to propagate throughout the ingot following the crystal planes, becoming more predominant towards the bottom of the ingot. The slip-lines greatly reduced the minority carrier lifetime, suggesting

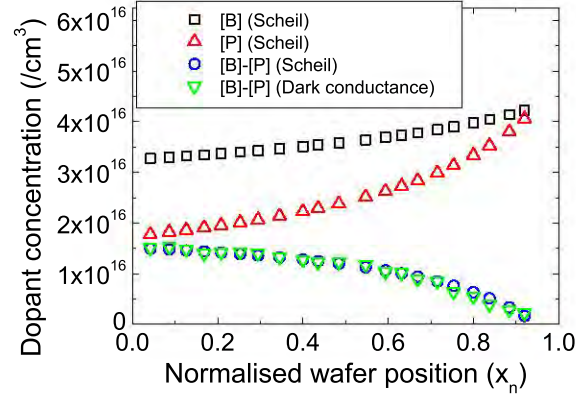


Figure 3.14: Effective dopant profile determined from dark conductance measurements and hypothetical doping profiles in a UMG CZ ingot from segregation during crystal growth showing close agreement.

that such defects could limit cell performance. Hence such defects should be passivated.

After a CHP, the PL image in Fig. 3.15 indicated the complete passivation of the slip-line defects. The application of an AHP did not appear to result in any benefit for the passivation of the slip-lines over the passivation provided by a CHP, as no remaining recombination activity was observed after the CHP. At this stage, it is unclear whether the passivation of such slip-lines can readily occur using a CHP in non-compensated material or whether the compensation aids in the passivation of the slip-lines by increasing the minority hydrogen charge state concentrations. For example, at the maximum process temperature for the CHP, a reduction in  $N_{eff}$  of one order of magnitude would lead to an enhancement in the concentration of  $H^0$  and  $H^-$  by a factor of two and five respectively. During cool down this enhancement becomes larger, and at a temperature of 200 °C the  $H^0$  and  $H^-$  concentrations would be enhanced by one- and two-orders of magnitude respectively (see Fig. 3.6), and could therefore have a large impact on hydrogen passivation. If the compensation does assist in the passivation, then impurities such as phosphorus, which are present in increasing concentrations towards the bottom of the ingot and potentially increase the defect concentration, may actually assist with the passivation of such defects.

It was also evident that prior to the CHP, substantially higher PL counts were observed in regions

### 3.3. ADVANCED HYDROGEN PASSIVATION FOR UPGRADED METALLURGICAL GRADE SILICON

of the wafer without slip-lines than the corresponding regions after the CHP. Hence, whilst a CHP was sufficient to passivate slip-lines, the CHP was detrimental to other defects in the material. This reduction in  $\tau_{bulk}$  will be discussed later in this section.

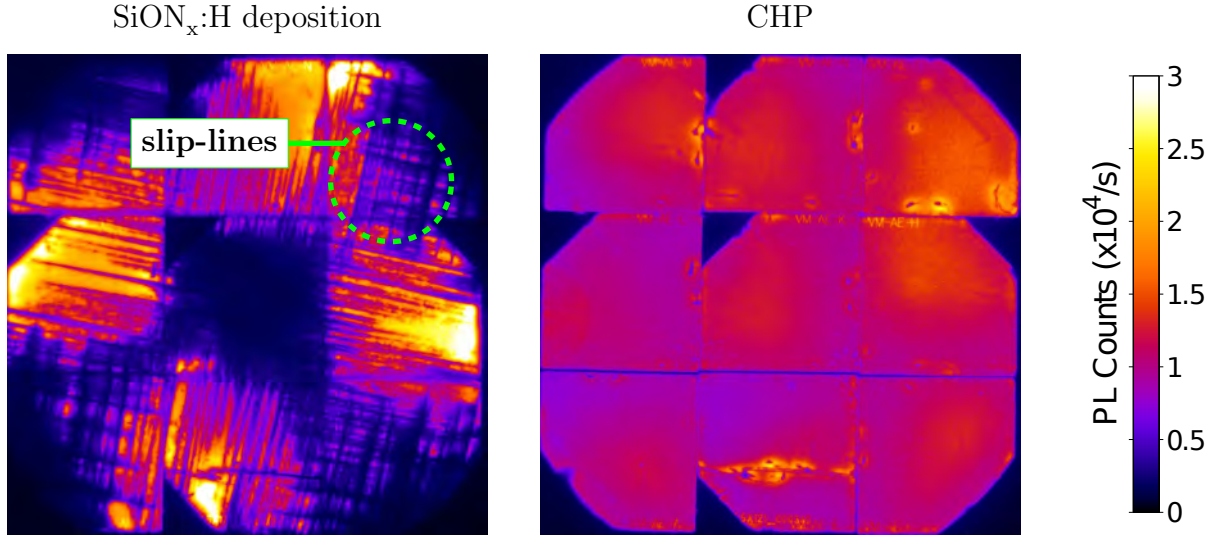


Figure 3.15: PL images of the passivation of slip-lines on a UMG CZ wafers with a normalised wafer position of  $x_n = 0.72$ , showing complete passivation after a CHP.

#### 3.3.5 Improved Bulk Passivation for UMG Silicon through Advanced Hydrogenation

The response of UMG silicon wafers to hydrogenation was shown to greatly depend on the wafer position in the ingot given the increase in contaminants towards to bottom of the ingot. A summary of the results of wafers from the top and bottom of a UMG CZ silicon after various hydrogenation processes is shown in Table 3.8, highlighting the different response of wafers from different parts of the ingot.

Table 3.8: Summary of the benefits obtained from wafers at the top and bottom of a UMG CZ silicon ingot for a CHP and AHP, highlighting substantial improvements for all wafers using an AHP.

Region of Ingot	Top ( $x_n = 0.04$ )	Bottom ( $x_n = 0.92$ )
Wafer resistivity ( $\Omega \cdot \text{cm}$ )	1	6.2
Significant benefit from a CHP	✗	✓
Significant benefit from an AHP	✓	✓

#### 3.3.5.1 Response of Wafers at the Top of the Ingot to Hydrogenation

Wafers from near the top of the UMG CZ silicon ingot ( $x_n = 0.04$ ) have lower total impurity concentrations and lower resistivity than wafers at the bottom of the ingot. Directly after the deposition of  $\text{SiON}_x\text{:H}$ , the wafers displayed 1-sun  $iV_{OC}$  of approximately 610 mV, with no evidence of slip-lines observed in the PL images (see Fig. 3.16(a)). After a CHP, a slight reduction in  $iV_{OC}$  to approximately 600 mV was observed due to the unfavourable hydrogenation conditions used, in conjunction with the higher  $N_{eff}$  of the wafers from the top of the ingot, which resulted in a reduced  $f_0$ . After the AHP, the  $iV_{OC}$  was greatly enhanced to over 650 mV, highlighting the importance of the AHP, although these wafers still displayed substantially lower  $iV_{OC}$  than wafers at the bottom of the ingot. This may be due to the lower wafer resistivities at the top of the ingot in reducing the lifetime as well as reducing the generation of  $\text{H}^0$ .

#### 3.3.5.2 Response of Wafers at the Bottom of the Ingot to Hydrogenation

Wafers from near the bottom of the UMG CZ silicon ingot ( $x_n = 0.92$ ) have higher total impurity concentrations and higher resistivity than wafers at the top of the ingot. Directly after the deposition of  $\text{SiON}_x\text{:H}$ , the wafers displayed 1-sun  $iV_{OC}$  of approximately 520 mV, due to the high concentrations of contaminants and defects such as slip-lines. After a CHP, the  $iV_{OC}$  of all regions of the wafers increased substantially to 620 mV and indicated the complete passivation of

### 3.3. ADVANCED HYDROGEN PASSIVATION FOR UPGRADED METALLURGICAL GRADE SILICON

the slip-lines. After an AHP, significant further enhancements in  $iV_{OC}$  were observed, with values approaching 700 mV. This increase in  $iV_{OC}$  of approximately 180 mV through hydrogenation represented a three order of magnitude reduction in the recombination activity of the material, suggesting a significant level of passivation of the defects in the material at the bottom of the ingot.

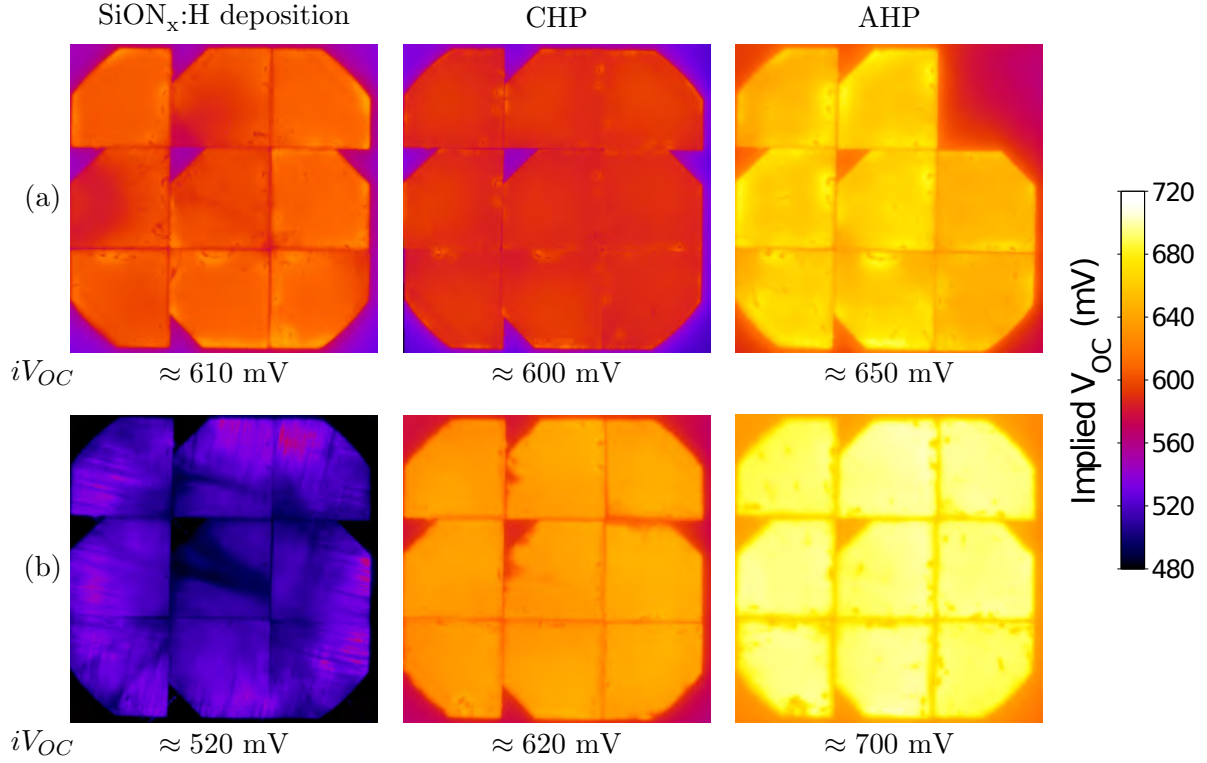


Figure 3.16: Calibrated 1-sun  $iV_{OC}$  maps of a wafer with (a)  $x_n = 0.92$  (near the top of the ingot with a resistivity of  $1 \Omega \cdot \text{cm}$ ) and (b)  $x_n = 0.04$  (near the bottom of the ingot with a resistivity of  $6 \Omega \cdot \text{cm}$ ) after a CHP and an AHP. Note that the top-right ninth of the wafer in (a) was broken during the AHP.

### 3.3.5.3 Response of Wafers to Hydrogenation Processes Throughout a UMG CZ Ingot

On closer inspection of the lifetimes of the UMG wafers, much lower  $\tau_{eff}$  and  $iV_{OC}$  values were observed compared to that shown on B-FZ and commercial grade B-CZ wafers as presented in Section 3.2. It should again be noted, that due to the reduced mobility of minority carriers in compensated silicon, lifetimes of wafers at the bottom of the ingot may be underestimated by a larger extent than that of wafers at the top of the ingot with lower doping densities of both boron and phosphorus, and therefore higher mobilities of the charge carriers.

**SiON<sub>x</sub>:H deposition:** Directly after the deposition of the SiON<sub>x</sub>:H a substantial difference in  $iV_{OC}$  was observed throughout the ingot from 520 – 630 mV, with higher values occurring at the top of the ingot (see Fig. 3.17(a)). When compared with a graph of  $x_n$  versus  $\tau_{bulk}$ , the similarities indicate that the difference in  $iV_{OC}$  throughout the ingot was due to changes in  $\tau_{bulk}$ , with values of 10 – 80  $\mu$ s (see Fig. 3.17(b)). The strong decrease in  $\tau_{bulk}$  and  $iV_{OC}$  for  $x_n > 0.7$  coincided with the increasing presence of slip-lines in the wafers due to increasing contaminant and defect concentrations with increasing  $x_n$  values. Furthermore, the response of the UMG wafers to hydrogen passivation processes greatly depended on the position of the wafer within the ingot (see Fig. 3.17).

**CHP:** After a CHP, wafers from the top 60 % of the ingot ( $x_n < 0.6$ ) saw a slight reduction in  $\tau_{bulk}$  and  $iV_{OC}$ , whilst large improvements were observed on wafers from lower regions of the ingot ( $x_n > 0.6$ ). This was despite such wafers from the bottom of the ingot only having an initial  $\tau_{bulk}$  of approximately 8  $\mu$ s, well below that of wafers from higher regions in the ingot of approximately 60 – 70  $\mu$ s. The enhanced response to hydrogenation of the wafers at the bottom of the ingot was consistent with a reduced  $N_{eff}$ , and hence higher resistivity, from increased levels of compensation and therefore higher  $f_0$  and  $f_-$ , even when using a CHP (see Fig. 3.17(c)). This resulted in such regions of the ingot showing substantially higher  $\tau_{bulk}$  than wafers from regions of the ingot with higher  $N_{eff}$ .

### 3.3. ADVANCED HYDROGEN PASSIVATION FOR UPGRADED METALLURGICAL GRADE SILICON

---

**AHP:** By intentionally controlling the charge state of hydrogen through the AHP, the  $\tau_{bulk}$  of all wafers throughout the ingot increased substantially, again with an enhanced response of wafers with higher resistivities at the bottom of the ingot. For wafers with  $x_n < 0.5$ , the  $\tau_{bulk}$  increased to approximately 200  $\mu\text{s}$  whilst for wafers with  $x_n = 0.92$  the  $\tau_{bulk}$  was over 550  $\mu\text{s}$ . The corresponding improvement in 1-sun  $iV_{OC}$  was on average approximately 160 mV, from 540 mV before hydrogenation to 700 mV after the AHP and the increase in 1-sun  $\tau_{eff}$  was from 2  $\mu\text{s}$  to 440  $\mu\text{s}$ , suggesting a great level of passivation of the defects occurred in the material at the bottom of the ingot.

**Reversibility:** Fig. 3.17(d) shows the reversibility of the  $\tau_{bulk}$  on UMG wafers with a  $x_n$  value of 0.72 in more detail than that presented in Fig. 3.11(b). Little spread was observed in the data for the 9 samples measured at each stage of processing indicating reproducibility of the data and a consistent change in the  $\tau_{bulk}$  between the CHP and AHP. This clearly demonstrated the benefits of an AHP for the UMG silicon material in improving  $\tau_{bulk}$ .



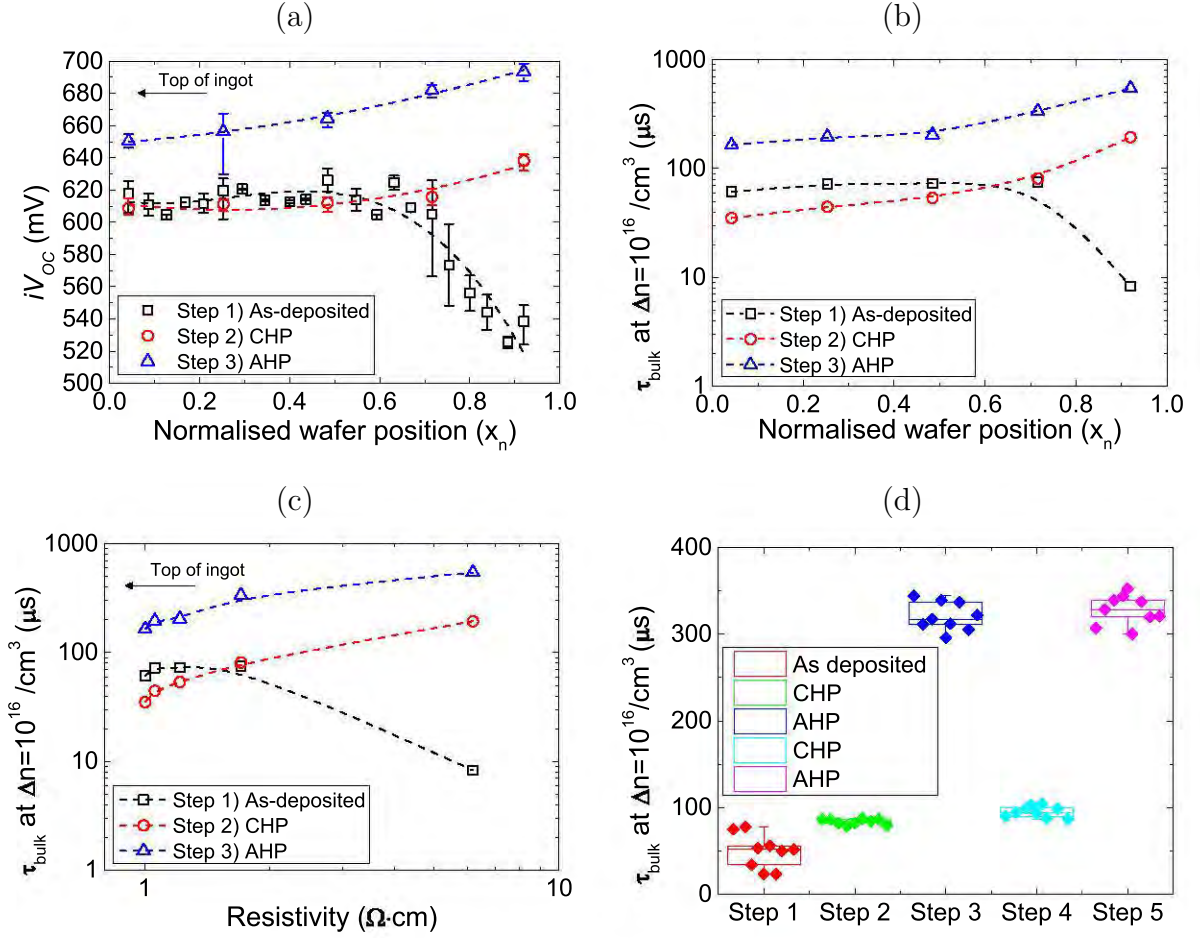


Figure 3.17: Effect of wafer position within the ingot on (a) 1-sun  $iV_{OC}$  and  $\tau_{bulk}$ . (c) Effect of wafer resistivity on the response to hydrogen passivation and (d) the reversibility of hydrogen passivation of  $2 \Omega \cdot \text{cm}$  CB-CZ wafers ( $x_n = 0.72$ ). Dashed lines are intended as visual aids only.

### 3.3.6 Summary for the Passivation of UMG Silicon

UMG silicon typically suffers from high impurity concentrations and lower lifetimes than silicon feedstock purified using the Siemens process. An experimental UMG CZ ingot was used in this section which suffered from the formation of slip-lines at the bottom of the ingot due to high impurity concentrations. The slip-lines were completely passivated by hydrogen, suggesting that



such defects may not be of concern for silicon solar cells if the passivation is stable. The UMG wafers showed a differing response to hydrogenation processes, with highly defected wafers at the bottom of the ingot responding the best, due to increased compensation and hence a high wafer resistivity which can enhance  $H^0$  and  $H^-$  generation. The benefits of an AHP over a CHP were clearly noted for all wafers throughout the ingot. As a result wafers with an initial  $\tau_{bulk}$  of 8  $\mu s$  were greatly improved through the use of an AHP to a  $\tau_{bulk}$  of 550  $\mu s$ .

### 3.4 Passivation of Oxidation-Induced Stacking Faults

Due to the incorporation of oxygen from the crucible in CZ silicon growth, variations in pulling speed during crystallisation can cause interstitial and vacancy rich regions to form in the silicon. Such regions can assist oxygen precipitation, although to differing extents [Voro 99], and may form oxidation-induced stacking faults (OSF) [Quei 64]. OSF typically occur at the seed end of the ingot due to the high concentrations of  $O_i$  and a slow cooling rate, leading to the agglomeration of oxygen within the solidified CZ crystal [Cous 10; Sond 13]. Depending on the type of defect present in the as-cut wafers, defects may either be annealed or activated during subsequent processing [Haun 11b]. The recombination activity of OSF can appear as ring-like patterns in PL images of CZ grown wafers [Haun 11b; Cous 10; Simm 97]. Thermal donors can also generate ring-like recombination patterns in PL images, however the thermal donors are eliminated by annealing above 450 °C. In contrast, during processes such as emitter formation and oxidation [Drec 13; Toku 89; Haun 11b], temperatures around 400 – 750 °C can result in the formation of oxygen precipitate nuclei, which then grow during subsequent high temperature processing and form OSF [Fals 97; Free 77; Voro 99]. Hence OSF can form after emitter diffusion and oxidation [Haun 11a].

For the fabrication of Sunpower rear contact solar cells, OSF present in the wafer have been observed to further develop throughout cell fabrication during high temperature processes [Cous 10], and can lead to a relative loss of 12 % in efficiency, meaning that a 24.2 % efficient device in the absence of OSF could be reduced to 21.3 % efficiency if subjected to OSF. Other papers report efficiency reductions of up to 5 % absolute due to the presence of OSF, however the recombination activity was reported to greatly depend on the size and strain state of the precipitates

[Murp 10; Sond 13; Haun 11a; Chen 11]. Hence OSF represent a large potential limitation for the efficiencies of solar cells fabricated using both n- and p-type CZ grown silicon.

To reduce the effect of OSF, thermal treatments such as tabula rasa can be applied, a high temperature process around 1000 °C to dissolve the grown-in oxygen precipitate nuclei [Walt 13; Fals 97]. Such brief high temperature processes above 950 °C result in the initial grown-in cluster distribution relaxing to a narrow high temperature distribution consisting primarily of monomers. Furthermore, with rapid cooling, no major deviation from this distribution was observed [Fals 97]. However for this method to be effective, there should not be sufficient quantities of pre-existing oxygen clusters or that which can form during the ramp up, large enough to be stable during the process. Hence performing the tabula rasa process directly before thermal processing around 800 °C can avoid precipitate formation due to the absence of nuclei large enough to survive the process and grow. In contrast, performing a low temperature process such as annealing at 500 °C after the tabula rasa process can result in a broadening of the size distribution of the clusters and form precipitate nuclei, which can then grow during subsequent processing at 800 °C [Fals 97]. However, in solar cell processing, it is challenging to perform such high temperature processes, due to a potential degradation of the silicon material, particularly for multi-crystalline silicon.

For solar cell applications, another method to reduce the recombination activity of precipitates is phosphorus gettering. This process can avoid the decoration of the OSF with metallic impurities such as iron [Murp 14].

### 3.4.1 Aim

In this experiment, the passivation of OSF is explored using an AHP at substantially lower temperatures than that used for the tabula rasa process.

### 3.4.2 Experimental Procedures

LDSE2 solar cells were fabricated on commercial grade  $2 \Omega \cdot \text{cm}$  B-CZ wafers using an industrial production line. After alkaline texturing, a phosphorus emitter was formed in a  $\text{POCl}_3$  tube

diffusion furnace. PSG removal and chemical edge junction isolation were performed in an in-line single sided etching tool. A thin thermal  $\text{SiO}_2$  layer was grown before the deposition of the front and rear  $\text{SiN}_x\text{:H}$  layers using an industrial Roth & Rau remote microwave PECVD system. After thermal oxidation, the resultant sheet resistance of the emitter was approximately  $150 \, \Omega/\square$ . The AHP was performed in an industrial in-line belt furnace with a peak set temperature of  $700 \, ^\circ\text{C}$  to increase  $\text{H}^0$  generation.

Laser doping was performed using the same CW laser system as detailed in Section 3.2. For n-type laser doping on the front surface, 85 %  $\text{H}_3\text{PO}_4$  was spun at 6000 RPM for 40 s. Laser doping was performed using a scan speed of 5 m/s in a typical cell front pattern, followed by a short HF dip. On the rear surface, Filmtronics PBF1 SOD was applied at 2000 RPM for 20 s followed by baking at  $130 \, ^\circ\text{C}$  for 10 min. Point-like contacts were formed by using a physical mask and scanning the CW laser beam at a speed of 0.5 m/s perpendicular to the openings in the mask using a pitch of  $500 \, \mu\text{m}$ . Point-like contacts had a length of approximately  $40 \, \mu\text{m}$  and width of  $10 \, \mu\text{m}$ . Wafers then received a short HF dip and rinse to remove the SOD. The AHP was again applied after the laser doping process to passivate LasID and avoid reactivation of B–O complexes and other defects in the device.

The p-type metal contacts were formed by Al sputtering, followed by a low temperature sinter. The n-type contacts were formed using self-aligned LIP contacts. For plating, silicide formation was performed after the Ni plating process, before continuing to LIP copper and a silver immersion dip to prevent oxidation of the copper.

PL imaging was performed at various stages of cell fabrication using a BTi R1 luminescence imaging system. Images were calibrated to obtain 1-sun  $iV_{OC}$  maps.

The process flow for solar cells fabricated in this section is shown in Fig. 3.18.

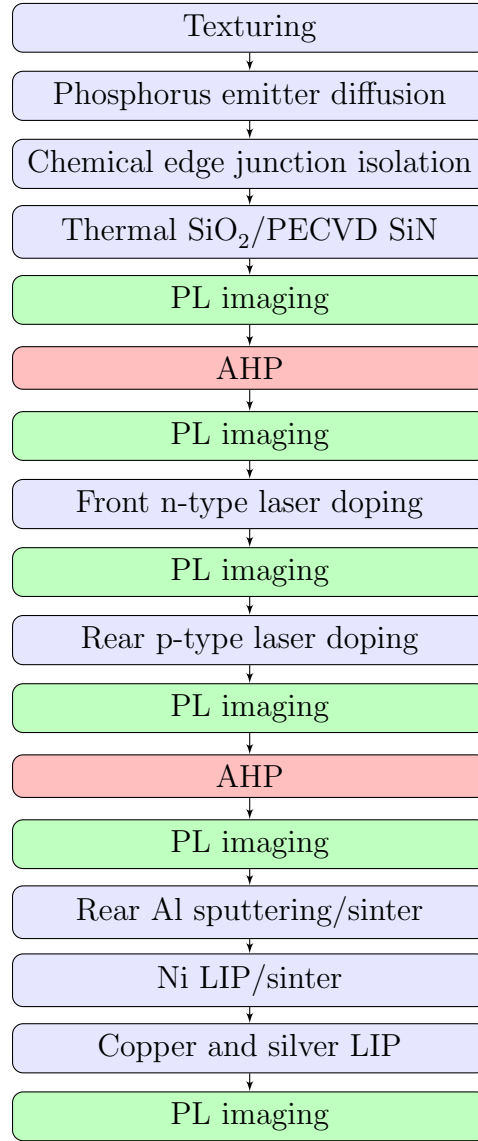


Figure 3.18: Process flow for LDSE2 solar cells to investigate hydrogen passivation of OSF.

### 3.4.3 Results of Hydrogen Passivation of Oxidation-Induced Stacking Faults

OSF can be observed using characterisation techniques such as PL imaging. Fig. 3.19 shows calibrated 1-sun  $iV_{OC}$  maps of an LDSE2 solar cell at various stages of fabrication. Directly after

the deposition of the PECVD  $\text{SiN}_x\text{:H}$ , OSF were observed in ring-line patterns on some wafers, which had grown during emitter diffusion and oxidation (see Fig. 3.19(a)). Such defects reduced the local  $iV_{OC}$  down to as low as 620 mV in heavily defected regions in the centre of the wafer, whilst in non affected areas a higher  $iV_{OC}$  of approximately 660 mV was observed. The presence of these ring-line patterns after emitter diffusion/oxidation and deposition of  $\text{SiN}_x\text{:H}$  indicated that these defects were OSF, rather than thermal donors which would have been annealed during the thermal processes above 450 °C.

Post the AHP, the recombination activity of the OSF had been eliminated (see Fig. 3.19(b)). As the AHP only subjects wafers to a temperature of approximately 620 °C for a few seconds (substantially lower than that of the emitter diffusion/oxidation at a temperature of 1000 °C in the tabula rasa process to dissolve oxygen precipitates), the results suggest that the OSF were passivated by hydrogen. Furthermore, the finished device did not show any evidence of OSF, demonstrating that the passivation was retained on the finished device (see Fig. 3.19(c)). Hence, whilst previous publications report a reduction in efficiency for screen-printed solar cells where the OSF were enhanced by emitter diffusion and oxidation [Haun 11a], it appears that hydrogen passivation can subsequently be used to eliminate the recombination activity of the defects. Therefore, hydrogen passivation could be used to avoid performance degradation from OSF in solar cells without the need for high temperature tabula rasa processes.

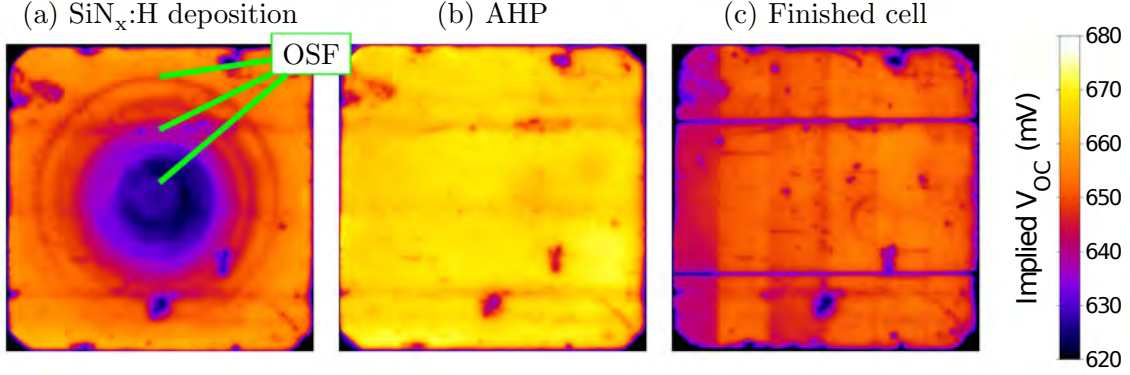


Figure 3.19: Calibrated  $iV_{OC}$  maps of a B-CZ wafer containing OSF (a) after the deposition of SiN<sub>x</sub>:H, (b) after an AHP and (c) on the finished LDSE2 device.

### 3.4.4 Summary of OSF Passivation

OSF were observed on partially fabricated solar cells after emitter diffusion/oxidation and the deposition of SiN<sub>x</sub>:H. However, after an AHP was applied, no such evidence of the OSF were observed in the PL images. Hence hydrogen passivation was shown to be very effective at avoiding performance degradation from OSF, without the need to use high processing temperatures as are used in the tabula rasa process. These results are particularly important for low quality silicon material, which can degrade during high temperature processes.

## 3.5 Hydrogen Passivation for Defected n-type Silicon

Whilst hydrogenation processes are often used for solar cells fabricated on p-type silicon wafers, a large benefit can also be obtained for silicon solar cells fabricated on n-type wafers. Hydrogen passivation has played a critical role in the fabrication of high efficiency passivated emitter, rear and totally diffused (PERT) solar cells fabricated on n-type FZ wafers. However for PERT solar cells, hydrogen passivation was not used to improve bulk passivation for the wafers, which have inherent multi-millisecond bulk lifetimes, but was instead used to improve passivation at both the

front and rear surface. Similar to the processes used for the fabrication of PERL solar cells, n-type PERT cells employ an alneal process, through which Al is evaporated onto both the front and rear surface of the devices, to allow hydrogen passivation of both surfaces, before the front Al layer is removed to define the active cell area [Zhao 96; Zhao 00].

For commercial solar cell technologies fabricated on n-type wafers, high bulk lifetimes are typically required due to the p-n junction being located at the rear of the solar cell [Mull 04]. As a result, either FZ or high lifetime CZ wafers are typically used. For the production of HIT solar cells, Sanyo has reported that in order to achieve finished devices with  $V_{OC} > 700$  mV,  $\tau_{eff}$  greater than 1 ms are required, implying that bulk lifetimes must also be larger than 1 ms [Kann 08]. For the Sunpower rear contact solar cell, due to the interdigitated nature of the contacts, further restrictions on lifetime are required to achieve high efficiencies [Mull 04; Cous 10]. Whilst earlier publications required lifetimes  $> 1$  ms for the fabrication of the Sunpower technology to achieve efficiencies of 21.5 %, more recent publications demonstrated efficiencies of 22 – 23 % from wafers with bulk lifetimes of 1 – 2 ms, whilst wafers with bulk lifetimes of 2 – 5 ms produced solar cells of up to 24.2 % efficiency [Smit 12].

To avoid the formation of B–O defects in commercially produced solar cells, n-type CZ wafers are often used. However commercial grade CZ grown n-type wafers are still subject to oxygen-related defects as mentioned in Section 3.4, as well as defects associated with various other impurities present in the silicon after crystal growth or introduced during a variety of processing steps.

### 3.5.1 Aim

This experiment explores the use of hydrogen passivation on commercial grade n-type CZ wafers to increase bulk lifetimes. In particular, the potential of low quality wafers is explored, which could allow the fabrication of high efficiency devices without the need for expensive, high-quality wafers.

### 3.5.2 Experimental Procedures

In this experiment a range of wafers were used to investigate the passivation of defected n-type CZ silicon. The following wafers were used: (1)  $2 \Omega \cdot \text{cm}$  standard commercial grade n-type CZ wafers; (2)  $2 \Omega \cdot \text{cm}$  standard commercial grade Ga-CZ wafers; and (3)  $1 \Omega \cdot \text{cm}$  n-type FZ wafers.

Each pseudo square  $125 \times 125 \text{ mm}$  n-type CZ and Ga-CZ wafer was cleaved into 9 pieces with dimensions of approximately  $42 \times 42 \text{ mm}$  with one diagonal corner to assist with laboratory processing. The round  $100 \text{ mm}$  n-type FZ wafers were also cleaved into 4 pieces of similar dimensions. Prior to the deposition of the dielectric passivation layer, wafers were saw-damage etched (SDE) (to create wafers with a resultant thickness of approximately  $150 \mu\text{m}$ ), given the Radio Corporation of America (RCA) clean and HF dipped.

Hydrogenated silicon oxynitride ( $\text{SiON}_x\text{:H}$ ) layers with a refractive index of 2.3 and hydrogen content of approximately 14.2 % [Hall 12b] were deposited using a laboratory type Roth & Rau AK400 remote microwave PECVD system. Subsequently, the passivation quality was determined through photoluminescence (PL) imaging [Trup 05a; Trup 06] obtained using a BTi luminescence imaging system. The quasi-steady-state photoconductance (QSS-PC) and quasi-steady-state PL (QSS-PL) measurement techniques [Sint 96b; Sint 96a; Trup 05b] were used to obtain injection-level-dependent  $\tau_{eff}$  curves, 1-sun  $\tau_{eff}$  and 1-sun  $iV_{OC}$ .

To eliminate surface effects from the QSS-PC and QSS-PL measurements, the minority carrier bulk lifetime ( $\tau_{bulk}$ ) was extracted at  $\Delta n = 1 \times 10^{14} / \text{cm}^3$  and  $\Delta n = 1 \times 10^{14} / \text{cm}^3$  by removing the Auger and  $J_{0d}$  lifetime components associated with the surfaces [Cuev 04]. For Auger correction, the simplified Richter model for the intrinsic lifetime with enhancement factors was used [Rich 12a; Rich 12b].

A CHP was used which consisted of  $400^\circ\text{C}$  for 5 min in the dark, in nitrogen ambient. On selected n-type CZ samples, an AHP was also used to investigate benefits of an advanced hydrogenation process for the n-type CZ silicon. The AHP was performed in a conventional fast firing furnace with a peak set temperature of  $700^\circ\text{C}$  and belt speed of  $4600 \text{ mm/min}$  with a modification of power distribution throughout the furnace and incorporation of illumination into the cooling zone. Following the AHP, an additional (and identical) CHP was applied.



The process flow for this section is given in Fig. 3.20.

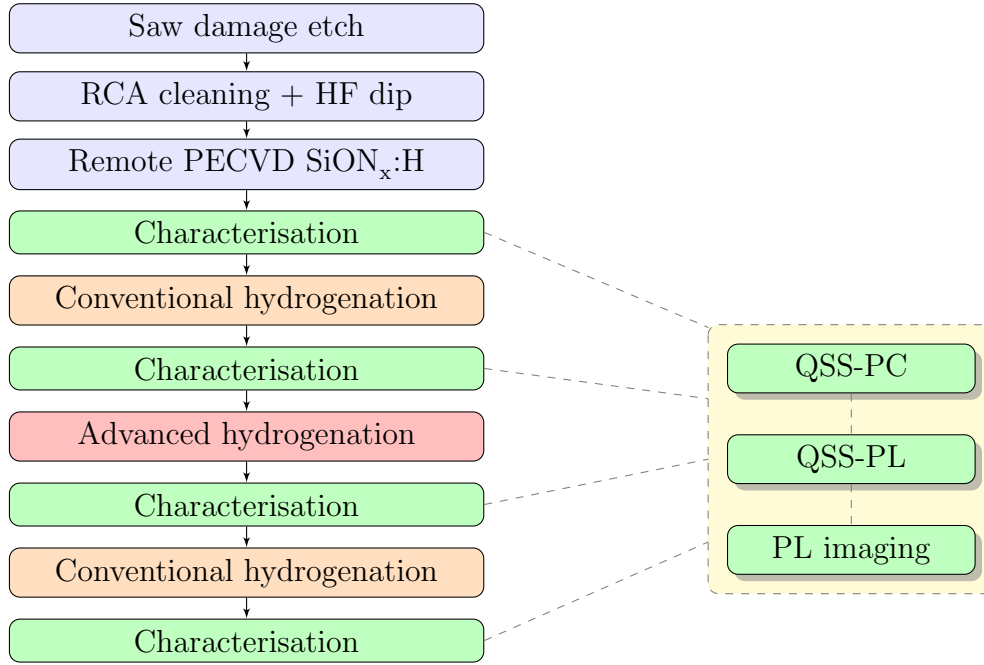


Figure 3.20: Process flow for lifetime studies on the hydrogen passivation of defected n-type silicon.

### 3.5.3 Results of the Passivation of Defected n-type Silicon Wafers

Directly after the deposition of the SiON<sub>x</sub>:H, a highly defected region was observed around the perimeter of the n-type CZ wafer approximately 25 mm into the wafer from the ingot edge (see Fig. 3.21(a)). The radial symmetry of the defected region in the PL image suggests that the increased recombination around the perimeter of the wafer was due to impurities incorporated into the silicon during crystal growth. In addition, the PL response throughout the remainder of the CZ wafer was substantially reduced from that seen in other commercial grade Ga-CZ wafers (see Fig. 3.21(c)), B-CZ wafers from previous experiments, or indeed other n-type CZ wafers obtained from the same wafer supplier. The regions marked ‘W1’ and ‘W2’ represent regions of the wafers in which QSS-PC and QSS-PL measurements were obtained and will be discussed shortly. In

comparison, for the Ga-CZ wafer shown in Fig. 3.21(c), directly after the deposition of the  $\text{SiON}_x\text{:H}$ , a much narrower defected region around the edge of the wafer was observed, and the remainder of the wafer exhibited a higher PL response.

After a CHP, the quality of the n-type CZ wafers increased greatly as indicated by the large enhancement in the PL response (see Fig. 3.21(b)), with corresponding improvements in  $iV_{OC}$  in the central regions of the wafer from 690 mV, to values of approximately 740 mV. In particular, the highly defected region around the edge of the n-type CZ wafer showed the most substantial improvement after the CHP, such that the wafer exhibited a much more uniform PL response across the wafer. The improvements in  $iV_{OC}$  in such regions were from values of approximately 640 mV to values approaching 740 mV. As shown in Fig. 3.21(d), the Ga-CZ wafers demonstrated a smaller, but still significant enhancement in the PL response. Subsequently, both the n-type and gallium-doped wafers displayed similar PL responses with corresponding increases in  $iV_{OC}$  from 710 mV to approximately 740 mV.

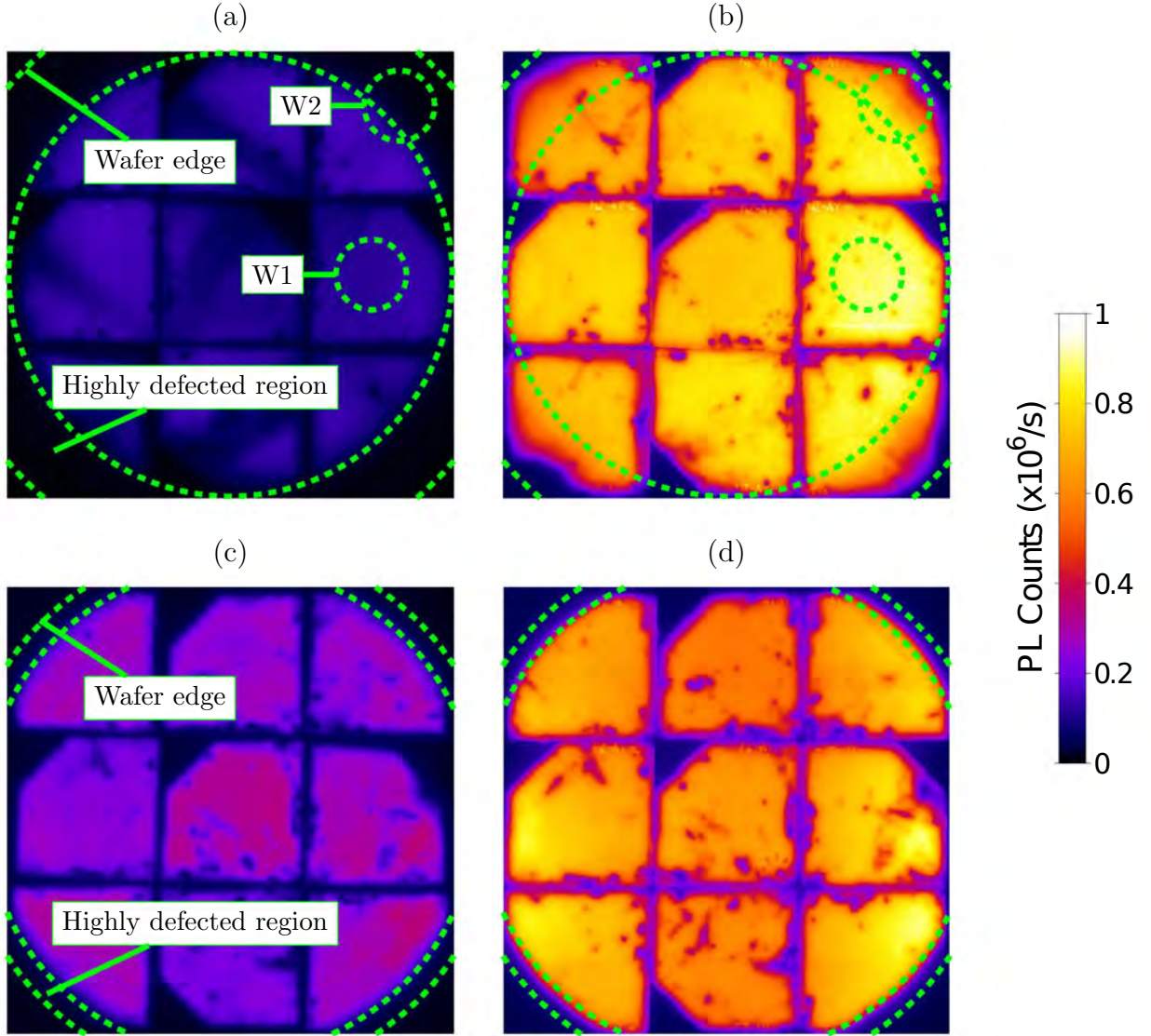


Figure 3.21: PL images of a highly defected n-type CZ wafer (a) after the deposition of SiON<sub>x</sub>:H and (b) after hydrogenation highlighting significant improvements, particularly in the highly defected regions. The corresponding PL images of a Ga-CZ wafer processed in parallel are shown in (c) and (d). The dashed green area indicates the region used for lifetime measurements for wafers W1 and W2 in Fig. 3.22 as well as the highly defected region before hydrogenation and the wafer edge at the full width of the CZ ingot.

Curves of  $\Delta n$  versus  $\tau_{eff}$  are often used to highlight the presence of defects in solar cells which have an injection-level dependence such as SRH recombination. Fig. 3.22(a) shows the corresponding injection-level dependent  $\tau_{eff}$  curves for the regions of the wafer highlighted in Fig. 3.21(a). Prior to annealing, relatively low lifetimes were obtained compared to that of n-type FZ wafers processed in parallel. In particular, the  $\tau_{bulk}$  at  $\Delta n = 1 \times 10^{14} / \text{cm}^3$  was 190  $\mu\text{s}$  for W1, whilst the highly defected region for W2 only showed a corresponding value of approximately 90  $\mu\text{s}$ , compared to that of the FZ wafer at 1.5 ms. Furthermore, a large reduction in  $\tau_{eff}$  was observed for the n-type CZ wafers at low-injection, which indicated the presence of SRH recombination.

Upon annealing, very impressive increases in  $\tau_{bulk}$  were observed for the n-type CZ wafers, along with a reduction in  $J_{0d}$ . For W1, the  $\tau_{bulk}$  at  $\Delta n = 1 \times 10^{14} / \text{cm}^3$  increased to 4.9 ms whilst the  $\tau_{bulk}$  in the initially highly defected region (W2) increased to 3.4 ms. In addition, the injection-level dependence  $\tau_{eff}$  in low-injection for the n-type CZ wafers was eliminated, which indicated the effective passivation of the SRH recombination centres. In contrast, no substantial change to the injection-level dependent  $\tau_{eff}$  curve was observed for the FZ wafer due to the high starting quality of the material, which was predominately free of defects, and only a small enhancement in lifetime in high injection was observed due to a slight reduction in  $J_{0d}$ . The low  $J_{0d}$  of 4 – 20 fA/cm<sup>2</sup> after the deposition of the SiON<sub>x</sub>:H and subsequent improvement upon annealing down to 3 – 8 fA/cm<sup>2</sup> indicates a high quality surface passivation was realised by hydrogen and charge effects from the dielectric layer, with similar values obtained on p-type wafers using the same layers. The multi-millisecond  $\tau_{bulk}$  of the defected wafers after hydrogenation would now appear to be compatible for use with the fabrication of the most efficient commercial silicon solar cells over 24 % [Smit 12].

On additional n-type CZ wafers (NCZ1) the AHP developed for p-type silicon was also applied (see Fig. 3.22(b)). However no additional benefit for bulk passivation was observed directly after the application of the AHP through increasing the temperature and minority carrier injection. In fact, these samples saw a slight reduction in lifetime over low to mid injection-levels, with a decrease in  $\tau_{bulk}$  from 2.4 ms to 1.7 ms. This poorer quality level of passivation may be due to the increased minority carrier injection which on n-type silicon can act to reduce  $\text{H}^0$  concentrations in the material. However the sample demonstrated a slight improvement in the surface passivation through a reduction in  $J_{0d}$  which may be attributed to an enhanced release of hydrogen from the dielectric layer at the elevated temperature. The release of hydrogen may also be assisted by

minority carrier injection. With a subsequent CHP,  $\tau_{bulk}$  was again increased to a substantially higher level of 2.9 ms, than that observed with the initial CHP (2.4 ms). This also suggests the intermediate AHP enhanced the release of hydrogen from the dielectric layers which could then be manipulated during subsequent processing to enhance defect passivation. Such increases in hydrogen release from  $\text{SiN}_x\text{:H}$  layers with increasing annealing temperatures has previously been observed [Boeh 00]. Lifetime parameters for the sample are shown at the bottom of Table 3.9 in sequential order of processing.

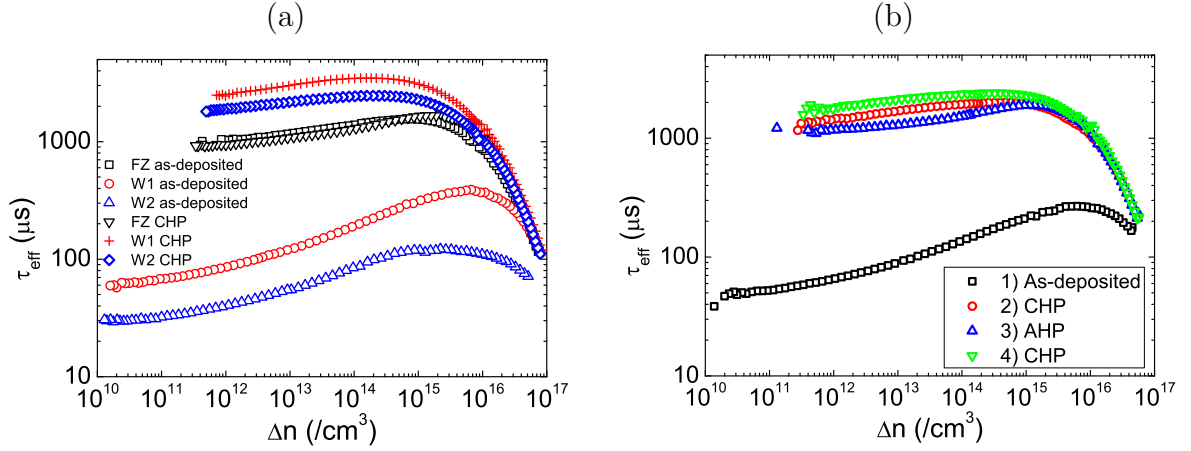


Figure 3.22:  $\tau_{eff}$  curves of (a) two parts of the n-type CZ wafer with PL images shown in Fig. 3.21 (W1 and W2) and an n-type FZ wafer processed in parallel, and (b) an n-type CZ wafer (NCZ1), highlighting significant improvements in  $\tau_{bulk}$  after hydrogenation.

Table 3.9: Lifetime parameters extracted from various n-type wafers highlighting signification improvements in bulk and surface passivation from hydrogenation.

Sample	Process step	1-sun $iV_{OC}$ (mV)	$J_{0d}$ (fA/cm <sup>2</sup> )	$\tau_{bulk_{\Delta n=1 \times 10^{14} / \text{cm}^3}}$ ( $\mu\text{s}$ )	$\tau_{bulk_{\Delta n=1 \times 10^{15} / \text{cm}^3}}$ ( $\mu\text{s}$ )
CZ-W1	SiON deposition	694	12	190	294
CZ-W1	CHP	742	5	4880	5000
CZ-W2	SiON deposition	642	20	87	124
CZ-W2	CHP	734	7	3350	3560
FZ	SiON deposition	729	4	1510	1940
FZ	CHP	736	3	1410	1910
NCZ1	SiON deposition	677	18	140	237
NCZ1	CHP (1)	737	8	2400	2690
NCZ1	AHP	738	7	1730	2370
NCZ1	CHP (2)	740	7	2970	3220

### 3.5.4 Summary for the Passivation of Defected n-type Silicon

Substantial improvements in  $\tau_{bulk}$  from 100 – 300  $\mu\text{s}$  to values of 3.4 – 4.9 ms were demonstrated on defected n-type CZ silicon wafers through the use of a CHP. This suggests that such wafers could be used to fabricate high efficiency devices, without the need to use expensive, high quality wafers, hence highlighting the importance of hydrogen passivation for n-type solar cell technologies. In addition, enhancements in  $\tau_{bulk}$  were achieved from 2.4 ms to 2.9 ms through the use of an intermediate AHP to enhance the release of hydrogen, even though directly after the AHP a substantially lower  $\tau_{bulk}$  of 1.7 ms was observed.

## 3.6 Hydrogenation for Multi-Crystalline and Seeded-Cast Quasi Mono-Crystalline Silicon

In recent years, multi-crystalline silicon solar cells have dominated the PV market. This is largely due to the lower cost of the casting process used to crystallise the silicon. However this method results in a reduced material quality when compared to CZ or FZ processes. Multi-crystalline silicon is prone to many types of impurities and defects, which are incorporated into the material during the casting process. These include the boundaries between adjacent grains and dislocation clusters within the grains. Impurities such as oxygen and iron can accumulate at structural defects including grain boundaries and dislocations [Schu 06; Schr 00; Sopo 97].

On the other hand, one benefit for multi-crystalline silicon solar cells is a reduced susceptibility to LID when compared to B-CZ solar cells, due to a reduced level of oxygen incorporation during the casting process [Cunn 08; Schm 04; Schm 03]. Whilst impressive efficiencies of over 20 % with  $V_{OC}$  up to 660 mV have been demonstrated using multi-crystalline silicon, such devices only had cell areas of 1 cm<sup>2</sup>, and substantial reductions in efficiency and  $V_{OC}$  were observed by increasing cell areas to 4 cm<sup>2</sup>. Furthermore, cell efficiencies varied by more than 2 % absolute across a given wafer on which the small area devices were fabricated [Schu 06]. This variability greatly limits the effective quality of the material.

Several approaches have been developed in recent years to improve the crystalline quality of cast material. One approach is to use the seeded-cast method to grow ingots largely comprising of quasi mono-crystalline (QM) silicon [Stod 08]. QM solar cells can show up to 1% absolute increase in efficiency over their multi-crystalline counterparts [Gu 12]. However, like conventional multi-crystalline silicon cast ingots, QM material also suffers from a large variability in crystalline quality. Dislocations may be nucleated by particles, and the dislocation clusters can spread in area throughout the ingot growth due to thermal stresses. This can also result in the growth of multi-crystalline material, particularly around the edge of the ingot [Stod 08; Guer 12; Gu 12]. The multi-crystalline areas can also spread in area as the crystallisation of the cast continues.

Directional solidification is another method for growing multi-crystalline silicon wafers through

the control of grains and grain boundaries to enhance crystalline quality and hence solar cell efficiency [Lan 12]. Grain orientations, grain boundaries and dislocation densities have been shown to be closely correlated, and play a vital role in determining the electrical properties of the material [Fuji 06; Usam 10; Wurz 10]. For example, the  $\Sigma 3$  grain boundary shows a higher resistance to cutting stresses and is electrically inactive, whilst twin grains can reduce dislocation densities [Wurz 10; Mart 93; Chen 05c; Chen 05a; Chen 05b]. Small angle grain boundaries have also proven to be more difficult to passivate using hydrogen [Chen 05a; Chen 05b]. With improved nucleation control and cooling, increases in the number of grains with  $\Sigma 3$  or twin boundaries can be obtained, with reduced dislocation generation and recombination activity [Chen 05c].

Phosphorus gettering and hydrogen passivation have a profound influence on the electrical properties of solar cells fabricated on multi-crystalline silicon substrates [Tan 08]. During the PECVD process, atomic hydrogen is dissociated from the precursor gases of  $\text{SiH}_4$  and  $\text{NH}_3$  used to deposit the  $\text{SiN}_x\text{:H}$ , and can be incorporated into the dielectric layer and/or diffuse into the silicon. Wafers are typically held at elevated temperatures of around 400 °C whilst the vacuum chamber is evacuated in preparation for the deposition, and during the actual deposition. If the composition of  $\text{SiN}_x\text{:H}$  allows, hydrogen can also be released from the dielectric layer at these temperatures and diffuse into the silicon. When depositing  $\text{SiN}_x\text{:H}$  onto both the front and rear surface of the device, the processing at elevated temperature in preparation for the deposition of the second surface could therefore release hydrogen from the  $\text{SiN}_x\text{:H}$  layer on the first surface of the solar cell. Subsequently, hydrogen either released from the dielectric layer or already within the silicon can be redistributed throughout the device for defect passivation. Hence directly after the deposition of  $\text{SiN}_x\text{:H}$  onto both surfaces of the device, a certain level of hydrogen passivation can be achieved within the bulk silicon material. However further improvements can be obtained from dedicated hydrogen passivation processes to release additional hydrogen from the dielectric layers and distribute it throughout the bulk silicon.

### 3.6.1 Aim

In this experiment, the effectiveness of the AHP is explored for multi-crystalline silicon material used to fabricate of LDSE2 solar cells due to the relevance of multi-crystalline silicon for commercial



### 3.6. HYDROGENATION FOR MULTI-CRYSTALLINE AND SEEDED-CAST QUASI MONO-CRYSTALLINE SILICON

---

silicon solar cells. The effectiveness of CHP and AHP are also investigated for QM silicon to explore the potential of QM silicon as a high efficiency multi-crystalline silicon material. The effect of phosphorus gettering for the QM silicon is also explored.

#### 3.6.2 Experimental Procedures

Standard commercial grade  $1.5 \Omega \cdot \text{cm}$  p-type multi-crystalline wafers ( $125 \times 125 \text{ mm}$ ) from the edge of a cast ingot were processed in an industrial environment with acidic texturing using the same LDSE2 process flow as shown in Fig. 3.18 in Section 3.4. Rear point-like contacts were formed with a contact pitch of  $500 \times 500 \mu\text{m}$ . Solar cells were also fabricated in parallel on commercial grade  $2 \Omega \cdot \text{cm}$  B-CZ wafers using alkaline texturing.

Test structures were also fabricated on QM silicon wafers from the central regions and edge region of the seeded-cast ingot were used with a bulk resistivity of approximately  $1 \Omega \cdot \text{cm}$ . Standard commercial grade  $2 \Omega \cdot \text{cm}$  B-CZ grown silicon wafers were also processed in parallel. Wafers were cleaved into 9 smaller area pieces of  $45 \times 45 \text{ mm}$  and  $42 \times 42 \text{ mm}$  for the QM and B-CZ wafers respectively due to limitations in wafer processing capabilities in the laboratory. Subsequently, the wafers received a SDE (with a resultant thickness of approximately  $150 \mu\text{m}$ ) and were RCA cleaned. Further samples from the edge of the seeded-cast ingot were processed in an industrial facility for alkaline texturing,  $\text{POCl}_3$  diffusion and chemical edge junction isolation, before cleaving and receiving an RCA clean. A HF dip was performed on all samples prior to the deposition of  $\text{SiON}_x\text{:H}$  using a laboratory type Roth & Rau AK400 remote microwave PECVD system. A CHP and AHP was then used as detailed previously. The passivation quality was determined by PL imaging, QSS-PC and QSS-PL measurements [Sint 96b; Sint 96a; Trup 05b].

The process flow is shown in Fig. 3.23.

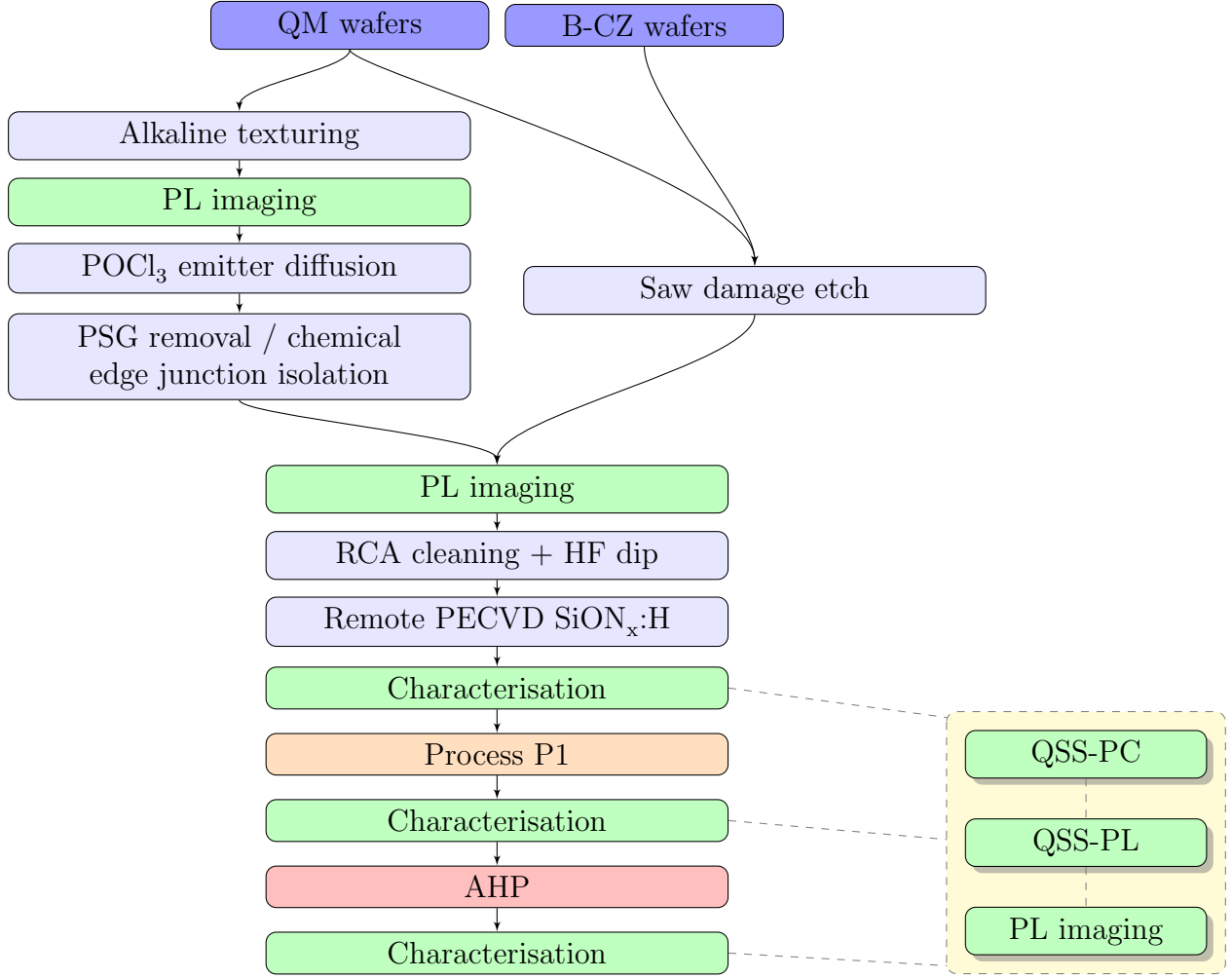


Figure 3.23: Process flow for lifetime studies on QM and B-CZ wafers.

### 3.6.3 Multi-Crystalline Silicon Solar Cells with Advanced Hydrogenation

The large improvements in  $iV_{OC}$  achieved through hydrogenation on the phosphorus gettered cell structures on multi-crystalline silicon wafers is shown in Fig. 3.24. Directly after the deposition of the  $\text{SiN}_x\text{:H}$ , the partially processed multi-crystalline solar cell in Fig. 3.24(a) demonstrated an  $iV_{OC}$  of approximately 645 mV. This value is consistent with values expected for a conventionally processed multi-crystalline solar cell after taking into account the reduction in  $V_{OC}$  due to the full area Al-BSF, whereby the bulk material and the Al-BSF both have a strong influence on the

### 3.6. HYDROGENATION FOR MULTI-CRYSTALLINE AND SEEDED-CAST QUASI MONO-CRYSTALLINE SILICON

---

resultant  $V_{OC}$  values (in the range of 610 – 620 mV). In contrast, the B-CZ solar cell shown in Fig. 3.24(b) had a much higher  $iV_{OC}$  of approximately 680 mV due to the higher quality of the silicon material. For conventional solar cells fabricated on B-CZ wafers, the full area Al-BSF largely limits the  $V_{OC}$  to 640 – 650 mV.

It was also observed that the best regions of the multi-crystalline wafer, free of dislocations, showed  $iV_{OC}$  of up to 680 mV. These values are comparable with that displayed by the B-CZ wafer (690 mV) indicating that at 1-sun illumination, a similar quality of material was observed within certain grains of the multi-crystalline silicon as that observed in the B-CZ silicon. A region of reduced  $iV_{OC}$  was also observed along the bottom of the wafer, associated with an impurity affected region (IAR) from the incorporation of impurities along the edge of the cast silicon ingot.

After the AHP, a greatly enhanced level of passivation was observed, with an improvement in spatially averaged  $iV_{OC}$  of approximately 60 mV and a substantial reduction in the recombination activity of dislocation clusters and grain boundaries, whereby many grain boundaries could no longer be observed in the PL image (see Fig. 3.24(b)). Similarly, the B-CZ wafer showed improvements in  $iV_{OC}$  of approximately 50 mV. Again, the best regions of the multi-crystalline wafer of up to 735 mV showed similar values as that of the B-CZ wafers (741 mV) as shown in Fig. 3.24(f). The IAR of the multi-crystalline silicon wafer from the edge of the cast silicon ingot still suffered from a reduced  $iV_{OC}$  in comparison to that displayed in the centre of the wafer, however these values were still  $> 645$  mV suggesting that hydrogen passivation had greatly enhanced the material quality in this region.

It is likely that this significant passivation improvement was caused by an enhanced release of hydrogen from the dielectric layer, increased hydrogen diffusivity and changes in charge state concentrations of hydrogen within the device. In addition, the charge state control is thought to have enabled higher concentrations of the minority hydrogen charge species, which are required to enhance defect passivation. This is particularly important during the latter stages of the hydrogenation process and cool down, in order to minimise the reactivation of the passivated defects.

During the formation of both n- and p-type laser-doped contacts, a large amount of LasID were introduced into the material, predominately independent of the wafer material. However a substantial portion of the recombination activity associated with the defects was passivated by hydrogen

through a second AHP, leading to an increase in  $iV_{OC}$  of approximately 20 mV. The passivation of LasID by hydrogen will be discussed in more detail in Chapter 5. Subsequently, the spatially averaged  $iV_{OC}$  of the large area multi-crystalline cell prior to metallisation was approximately 660 mV with large regions displaying  $iV_{OC} > 680$  mV. The B-CZ wafers processed in parallel displayed an  $iV_{OC}$  of approximately 685 mV. The values on both the multi-crystalline and B-CZ material were predominately limited by the p-type laser doping process.

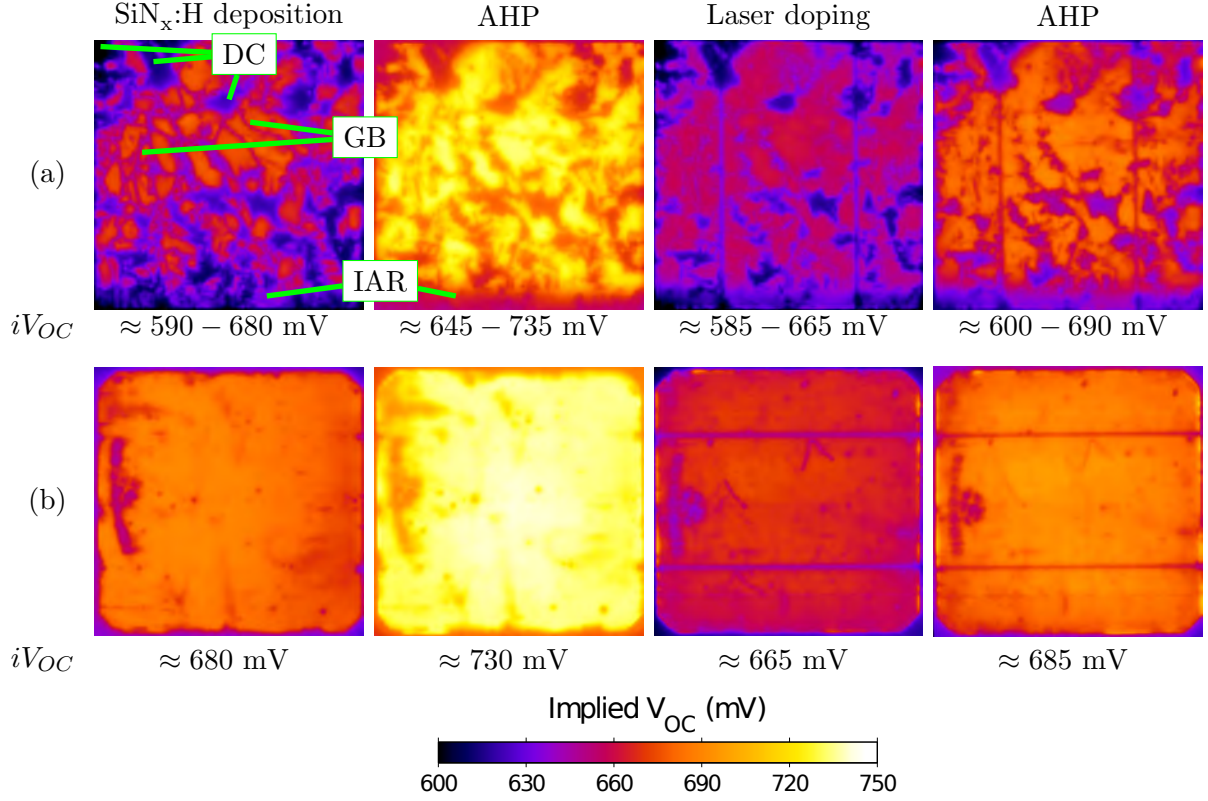


Figure 3.24: Calibrated  $iV_{OC}$  maps of a partially processed solar cells fabricated using (a) multi-crystalline silicon and (b) B-CZ silicon highlighting significant improvements after hydrogenation. In (a) some dislocation clusters (DC), grain boundaries (GB) and the impurity affected region (IAR) are highlighted. Note that for (b), a different wafer processed in parallel (of similar quality) is shown before and after laser doping.

### 3.6. HYDROGENATION FOR MULTI-CRYSTALLINE AND SEEDED-CAST QUASI MONO-CRYSTALLINE SILICON

A summary of the  $iV_{OC}$  from the multi-crystalline and B-CZ solar cells for each stage of processing are shown in Fig. 3.25, including the spatially average, minimum and maximum values observed across the device. Variations in  $iV_{OC}$  across the multi-crystalline wafers between the regions of highest and lowest quality were around 90 mV whilst on B-CZ wafers a smaller variation of approximately 50 mV was observed, as expected with an inherently lower variability in the quality of B-CZ material when compared to multi-crystalline silicon material.

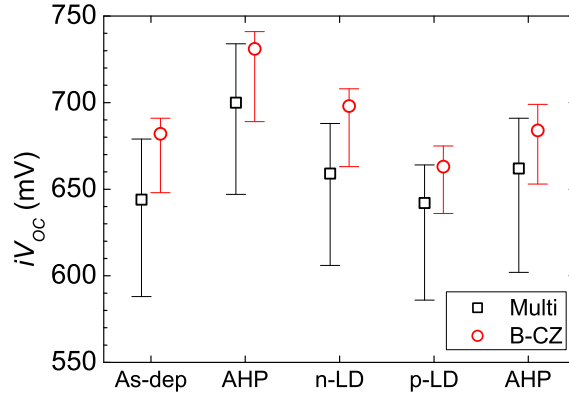


Figure 3.25: Range in  $iV_{OC}$  on B-CZ and multi-crystalline silicon wafers from the edge of a cast ingot as shown in Fig. 3.24 after the deposition of  $\text{SiON}_x\text{:H}$  (As-dep), an AHP, n-type laser doping (n-LD), p-type laser doping (p-LD) and a subsequent AHP to passivate LasID.

After the deposition of the rear Al layer on both the multi-crystalline and CZ substrates, a substantial reduction in  $iV_{OC}$  was observed due to a variety of defects forming (such as pinholes in the dielectric layer formed during the rear laser doping process), which allowed the Al to contact the bulk p-type material (see Fig. 3.26). Subsequently, the final  $V_{OC}$  and other electrical parameters of the solar cells were reduced substantially as shown in Table 3.10. The electrical parameters of a first generation LDSE (LDSE1) solar cell is also shown, highlighting the low shunt resistance ( $R_{SH}$ ) of the second generation LDSE (LDSE2) solar cells which may partially be attributed to the defect generation at the rear surface around the laser-doped point-like contacts. Subsequently, the  $FF$  of the LDSE2 cells were substantially reduced compared to that of the LDSE1 cells.

An improved process for the formation of the p-type laser-doped contacts has since resulted in substantial increases to the  $V_{OC}$  of 15 – 30 mV on the B-CZ material [Sugi 12], however this improved process has not yet been applied to the multi-crystalline material.

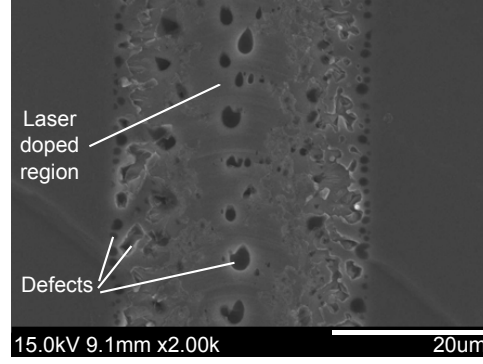


Figure 3.26: SEM image of a p-type laser-doped line processed at 0.5 m/s displaying the same defect types as a similarly processed point-like contact.

Table 3.10: Light J-V measurements of the multi-crystalline and B-CZ LDSE2 solar cells shown in Fig. 3.24 (measured in-house).

Wafer	Process	$J_{SC}$	$V_{OC}$	$FF$	$\eta$	$R_{SH}$
		(mA/cm <sup>2</sup> )	(mV)	(%)	(%)	( $\Omega \cdot \text{cm}^2$ )
Multi-crystalline	2 <sup>nd</sup> Gen LDSE	35.5	634	72.2	16.2	1090
B-CZ	2 <sup>nd</sup> Gen LDSE	38.4	652	70.7	17.7	1430
B-CZ	1 <sup>st</sup> Gen LDSE	37.2	628	79.0	18.5	7600

In conclusion, a massive potential exists for standard multi-crystalline silicon material featuring improved hydrogenation. From the preliminary results obtained, the  $iV_{OC}$  approached 680 mV on test structures prior to contact formation.

### 3.6.4 The Potential of Quasi Mono-Crystalline Silicon Wafers

#### 3.6.4.1 QM Wafers from the Central Region of a Seeded-Cast Ingot

As previously mentioned, a significant issue associated with the use of QM silicon wafers grown by the seeded-cast method is the variability in wafer quality, and high dislocation and defect densities which can occur [Stod 08]. Fig. 3.27(a) shows a PL image of a heavily dislocated QM wafer from the central region of a seeded-cast ingot comprising of mono-crystalline silicon. The corresponding PL image of a B-CZ wafer in Fig. 3.27(b) did not show any dislocations. However the image indicated the presence of oxygen-related defects in ring-line patterns such as OSF or thermal donors.

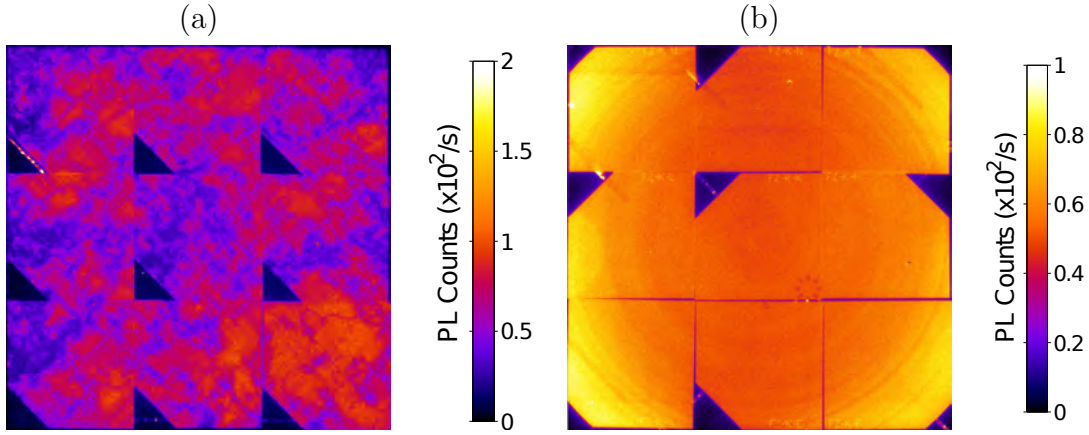


Figure 3.27: PL images after a SDE of (a) a heavily dislocated QM wafer from the central region of a seeded-cast ingot and (b) a B-CZ wafer that does not display dislocations but indicates the presence of oxygen-related defects.

**SiON<sub>x</sub>:H deposition:** After the deposition of SiON<sub>x</sub>:H, the calibrated  $iV_{OC}$  map of the QM wafer highlighted  $iV_{OC}$  values as low as 550 mV in heavily dislocated regions, whilst values of up to 640 mV were observed in dislocation-free regions. In contrast, the B-CZ wafer demonstrated

an  $iV_{OC}$  of approximately 710 mV. A slight decrease in wafer resistivity and the absence of the ring-line patterns in the PL image after  $\text{SiON}_x\text{:H}$  deposition indicated that the defects seen in the B-CZ wafer were thermal donors.

**CHP:** After the CHP, a substantial reduction in the recombination activity over the entire QM wafer was observed, particularly in heavily dislocated areas, resulting in an  $iV_{OC}$  of approximately 630 mV whilst dislocation free areas displayed  $iV_{OC}$  of up to 720 mV, approaching that of the B-CZ wafers.

**AHP:** Whilst the CHP resulted in an average improvement of approximately 100 mV from 585 mV to 685 mV, a substantial further improvement was observed after the AHP, particularly in dislocated regions. The  $iV_{OC}$  of certain heavily dislocated regions increased from 630 mV to 695 mV, which represented a further one order of magnitude reduction in the recombination activity of the area by using the AHP compared to a CHP. The total effect of the hydrogen process was more than a 120 mV improvement, representing more than two orders of magnitude reduction in the recombination activity of the material, with the higher quality material approaching 740 mV. On the B-CZ wafers, only a modest improvement in 1-sun  $iV_{OC}$  of 30 mV was observed through the CHP, however a larger increase in  $iV_{OC}$  was obtained after the AHP, highlighting the improved effectiveness of the AHP in passivating defects.



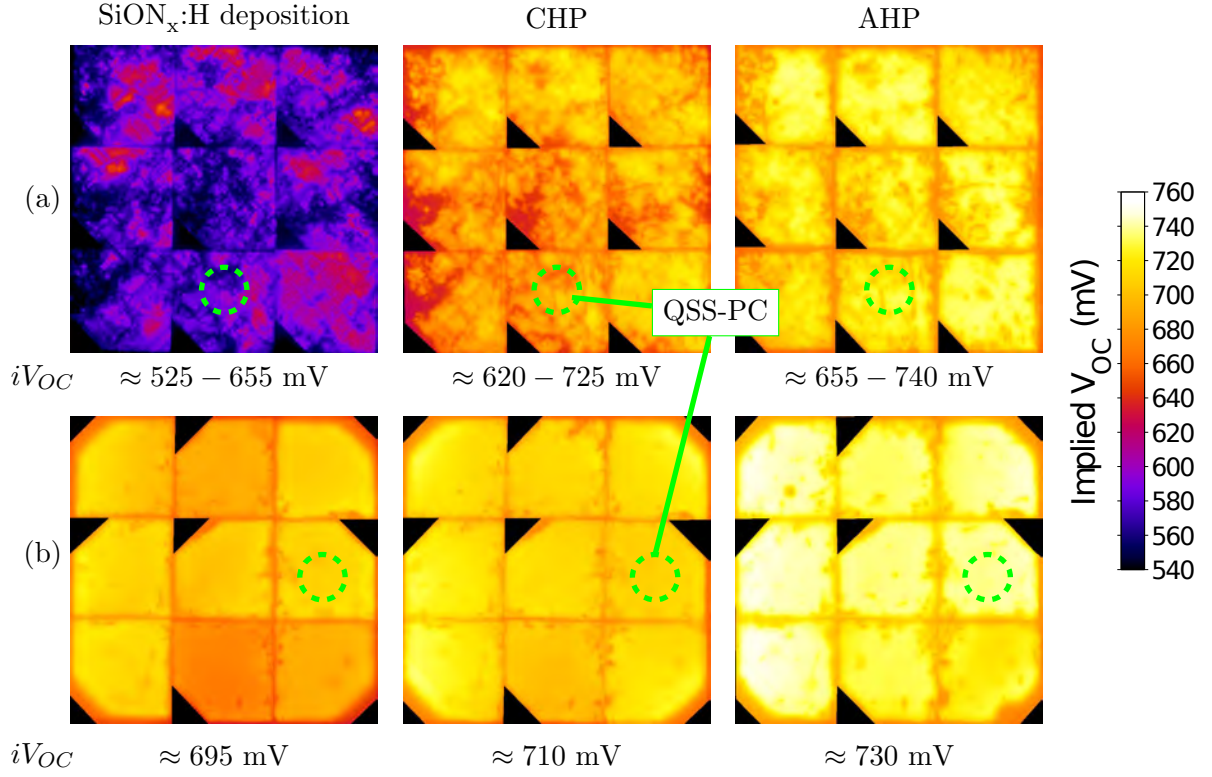


Figure 3.28: Calibrated  $iV_{OC}$  maps of a partially processed (a) QM wafer from the central region of a seeded cast ingot and (b) B-CZ wafer highlighting significant improvements in the quality and uniformity of the QM silicon. The area used for the QSS-PC measurements are highlighted by the dashed green circles.

Many recombination centres affecting the bulk silicon have an injection-level dependence and become more pronounced at low injection levels. Hence improvements in bulk passivation may be more pronounced at lower injection-levels. Fig. 3.29 highlights the substantial improvements in  $\tau_{eff}$  at low injection-levels ( $\Delta n = 1 \times 10^{14} / \text{cm}^3$ ) from 8  $\mu\text{s}$  on the QM wafers before hydrogen passivation to over 160  $\mu\text{s}$  with the AHP, with substantial increases in  $\tau_{eff}$  for all injection-levels observed using the AHP compared to that observed after the CHP. For the B-CZ wafers, almost no increase in  $\tau_{eff}$  was observed from 130  $\mu\text{s}$  to 155  $\mu\text{s}$  with the application of the CHP, whilst the AHP greatly enhanced the  $\tau_{eff}$  to 270  $\mu\text{s}$ . It was also observed that for higher injection-levels, the  $\tau_{eff}$  of the QM wafer approached that of the B-CZ wafer. The large enhancements in  $\tau_{eff}$  clearly highlight the importance and effectiveness of hydrogen passivation to greatly enhance the quality of this material without any phosphorus gettering.

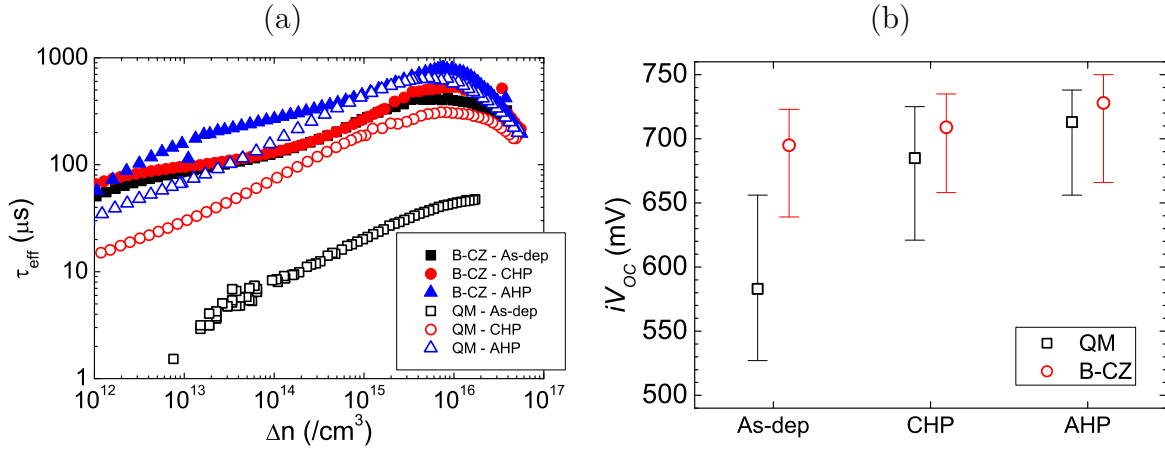


Figure 3.29: (a)  $\tau_{eff}$  curves and (b) range in  $iV_{OC}$  of B-CZ and QM wafers from the central region of a seeded-cast ingot shown in Fig. 3.28 after the deposition of  $\text{SiON}_x\text{:H}$  (As-dep), a CHP and an AHP highlighting significant improvements after hydrogenation.

#### **3.6.4.2 QM Wafers from the Edge Region of a Seeded-Cast Ingot**

Bricks from the edge of cast silicon ingots typically have substantially lower lifetimes than that of the central bricks due to the inclusion of impurities. Fig. 3.30 shows PL images of sister QM wafers from the edge of the seeded-cast ingot prior to the deposition of PECVD  $\text{SiO}_x\text{N}_x\text{:H}$  after (a) SDE, (b) texturing and (c) emitter diffusion and rear-etch, highlighting the effect of processing on the PL response. The sister wafers displayed regions of large multi-crystalline grains and smaller grains towards the bottom of the wafer at the edge of the ingot, particularly evident in Fig. 3.30(b) after alkaline texturing, with a reduced PL response in the multi-crystalline section. Bright regions in the PL images along the grain boundaries of the small multi-crystalline grains at the bottom of the images indicated a decoration of the grain boundaries with metallic impurities, however these were not evident after phosphorus emitter diffusion suggesting the impurities were effectively gettered (see Fig. 3.30(c)). Slightly different areas of the  $156 \times 156$  mm wafer were used in (a) to that in (b) and (c) whereby only  $135 \times 135$  mm were used to process the 9 small  $45 \times 45$  mm wafers for laboratory processing. As a result, the dislocated region along the left side of the wafer in Fig. 3.30(a) was unintentionally cut off from the samples in (b) and (c).

It should be noted that the PL image of the sample in Fig. 3.30(a) after SDE was obtained using a shorter exposure time which resulted in more noise in the PL signal and hence image. However the SDE process appears to highlight more structural defects within the material including slip-lines (as observed in Section 3.3). A heavily dislocated region was also observed along the edge of the wafer which received a SDE. The dislocated region may have formed due to slight changes in the alignment of the crystals from different seed wafers at the bottom of the cast. The PL response of the phosphorus gettered sample shown in (c) were much higher than that of (a) and (b), which may be attributed to having a reasonably well passivated front surface due to the field effect induced by the phosphorus emitter on the front surface, only leaving one poorly passivated surface of the wafer. In contrast, both surfaces of the the other two wafers in (a) and (b) were poorly passivated with non-diffused bulk p-type silicon at the surface.

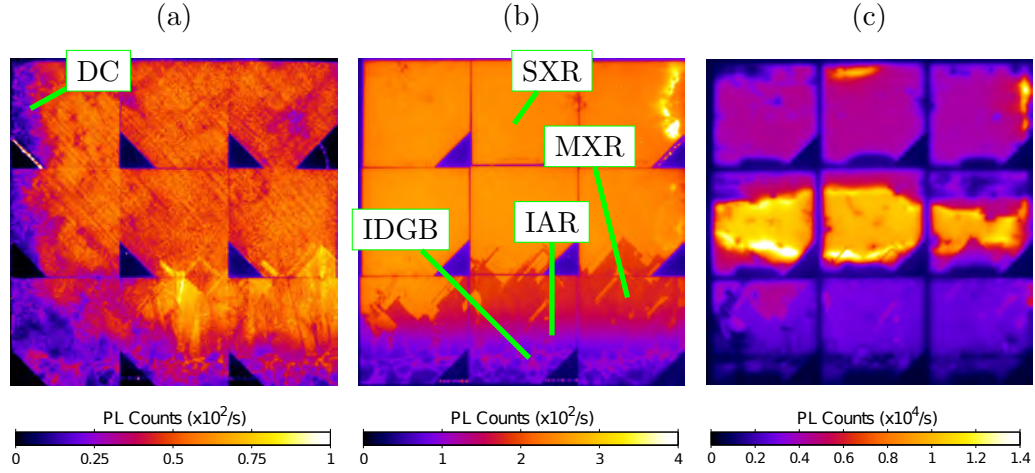


Figure 3.30: PL images of QM wafers from the edge of a seeded cast ingot after (a) SDE, (b) a sister wafer after alkaline texturing and (c) another sister wafer after alkaline texturing and subsequent phosphorus diffusion/chemical edge junction isolation. Dislocation clusters (DC), the single-crystalline region (SXR), multi-crystalline region (MXR), impurity affected region (IAR) and impurity decorated grain boundaries (IDGB) are also shown.

**SiON<sub>x</sub>:H deposition:** Phosphorus gettering is an essential process for multi-crystalline silicon, which is naturally incorporated into the fabrication sequence for screen-printed solar cells. As shown in Fig. 3.31(a), after the deposition of the SiON<sub>x</sub>:H a large difference was observed in the  $iV_{OC}$  between samples through phosphorus gettering. For the sample without gettering, slip-lines were still evident along the crystal planes along with a greatly reduced  $iV_{OC}$  in the highly dislocated region along the left side of the wafer. In addition, the impurities decorating the grain boundaries were still recombination active. In contrast, at the same stage of processing, the phosphorus gettered samples shown in Fig. 3.31(b) had a much higher and more uniform  $iV_{OC}$  across the wafer with the most significant reductions in  $iV_{OC}$  occurred in dislocated regions and a slight reduction was observed along the grain boundaries at the bottom of the image. In addition, differences in the  $iV_{OC}$  between multi-crystalline grains of the gettered samples were not evident, highlighting the importance of phosphorus gettering.

### 3.6. HYDROGENATION FOR MULTI-CRYSTALLINE AND SEEDED-CAST QUASI MONO-CRYSTALLINE SILICON

---

**CHP:** After receiving a CHP, the  $iV_{OC}$  of the sample without phosphorus gettering displayed a large improvement in  $iV_{OC}$  in all regions of the wafer by approximately 60 mV representing one order of magnitude reduction in the recombination of the wafer. However the CHP had limited effectiveness in passivating impurities along the bottom of the wafer where there was the highest density of defects. In this region, a clear reduction in  $iV_{OC}$  was observed between the large single-crystalline region and the multi-crystalline region along the bottom of the wafer. In addition, the dislocated region along the left side of the wafer displayed a substantially reduced  $iV_{OC}$  indicating a higher rate of recombination in this region.

**AHP:** By using an AHP, a difference in material quality purely due to the different crystalline grains was no longer evident, and only the edge region of the wafer with high impurity concentrations had a reduced  $iV_{OC}$ . The AHP also reduced the recombination activity in dislocated regions on the phosphorus gettered samples. It should be noted that the presence of two large regions of reduced  $iV_{OC}$  after the AHP (see Fig. 3.31(a)) was due to the formation of blisters in the  $\text{SiON}_x\text{:H}$  present after the deposition of the dielectric layer, which were exacerbated by thermal processing, particularly after the AHP due to the elevated temperature. However, the AHP provided superior passivation when compared to a CHP.

**Discussion:** The improvements in  $\tau_{eff}$  at low injection on the multi-crystalline samples highlight the importance of both hydrogen passivation and phosphorus gettering for the multi-crystalline material. Fig. 3.32 demonstrates large improvements in  $\tau_{eff}$  of three separate regions from the multi-crystalline wafers through hydrogen passivation. Without gettering, in the mono-crystalline section (R1 and R2) large improvements in  $\tau_{eff}$  were observed through hydrogen passivation from approximately 3  $\mu\text{s}$  to 30  $\mu\text{s}$ , whilst much lower lifetimes were observed in the multi-crystalline section (R3) and indicated the presence of trapping. However with hydrogen passivation, the  $\tau_{eff}$  increased and the effect of trapping was reduced, indicating that the hydrogen may have passivated the traps. All non-gettered wafers showed a larger improvement in  $\tau_{eff}$  after the application of the AHP compared to that displayed after a CHP. For gettered samples, the  $\tau_{eff}$  was substantially higher than that of non-gettered samples directly after the deposition of  $\text{SiON}_x\text{:H}$ , and the QSS-PC measurements from the multi-crystalline region did not indicate the presence of trapping. P1 was

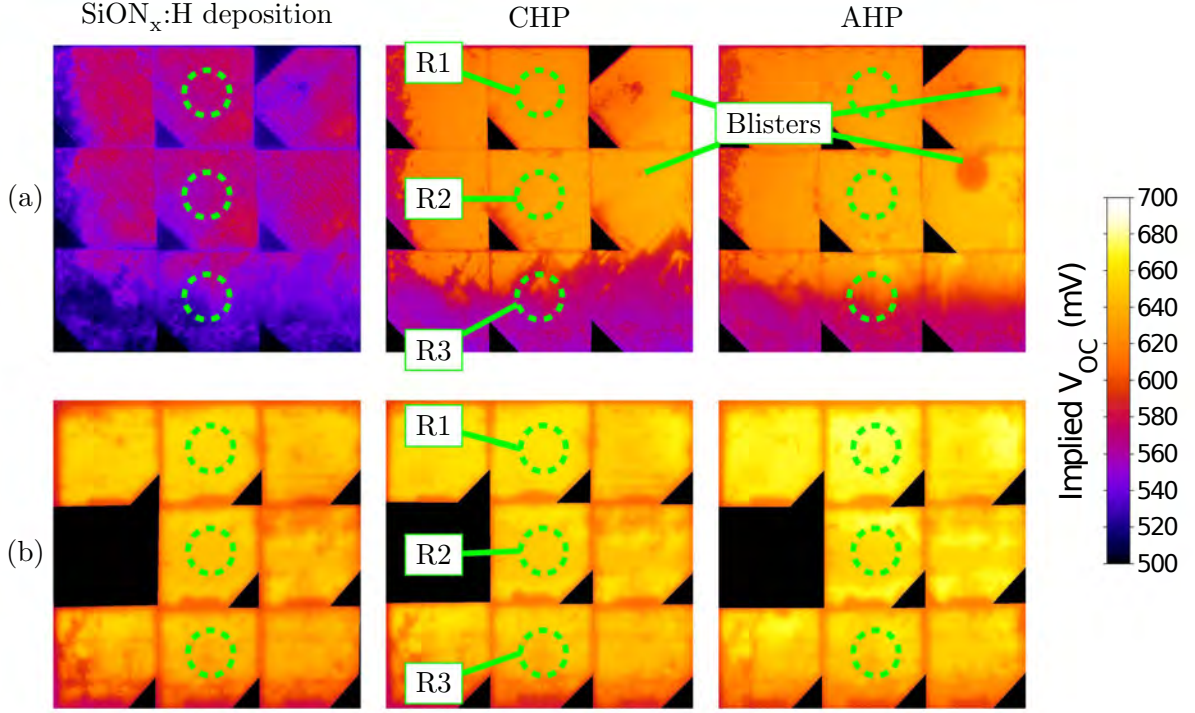


Figure 3.31: Calibrated 1-sun  $iV_{OC}$  maps before and after a conventional hydrogenation process (CHP) and an advanced hydrogenation process (AHP) of a QM wafer from the edge of a seeded-cast ingot (a) without phosphorus gettering and (b) with phosphorus gettering. ‘R1’, ‘R2’ and ‘R3’ indicate the areas used for the QSS-PC measurements presented in Fig. 3.32.

observed to have little or no effect on the  $\tau_{eff}$  in both the single-crystalline and multi-crystalline regions, indicating this CHP was ineffective for the material. However by using the AHP, substantial improvements were observed for regions in the centre of the ingot, and resulted in  $\tau_{eff}$  up to 80  $\mu$ s, whilst edge regions show  $\tau_{eff}$  up to 30  $\mu$ s. In some instances, hydrogen passivation alone was observed to result in higher  $\tau_{eff}$  than the phosphorus gettered samples (R2), however this may have been due to the phosphorus emitter remaining on the surface, resulting in an higher  $J_{0d}$  of the gettered samples.

The large increases in lifetimes on the QM silicon highlight the suitability of the material to



### 3.6. HYDROGENATION FOR MULTI-CRYSTALLINE AND SEEDED-CAST QUASI MONO-CRYSTALLINE SILICON

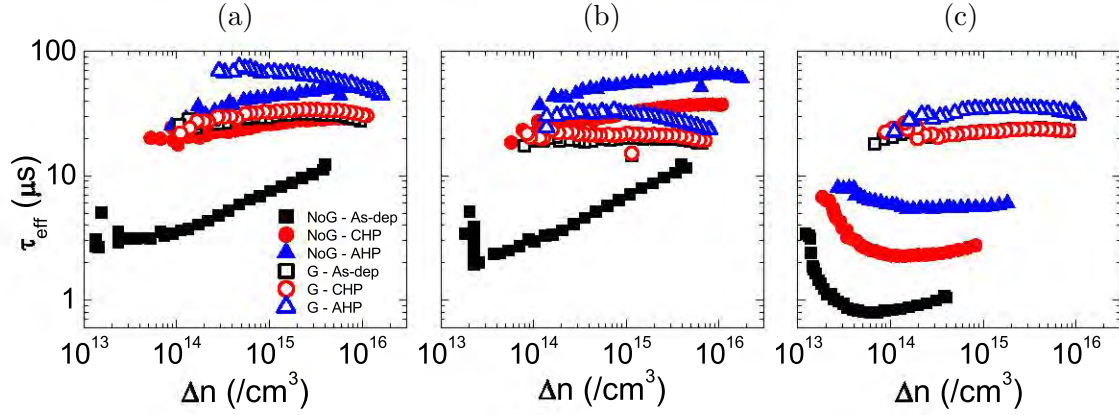


Figure 3.32:  $\tau_{eff}$  curves of (a) R1, (b) R2 and (c) R3 as indicated in Fig. 3.31 after the deposition of  $\text{SiON}_x\text{:H}$  (As-dep), a CHP and an AHP highlighting significant improvements. “G”=gettered, “NoG”=no gettering.

achieve high lifetimes if advanced passivation processes are used. The benefits of using an AHP were clear, with substantial improvements in  $\tau_{eff}$  from 8  $\mu\text{s}$  to 160  $\mu\text{s}$ , and the reduced recombination activity of structural defects such as dislocation clusters. However, in addition to hydrogen passivation, phosphorus gettering must be incorporated into the processing sequence to achieve the highest lifetimes.

#### 3.6.5 Summary of Hydrogenation for Multi-crystalline and Seeded-Cast QM Silicon

Large increases in the material quality of multi-crystalline and seeded-cast QM silicon were achieved through hydrogenation. On standard multi-crystalline silicon material,  $iV_{OC}$  values approaching 680 mV were obtained after contact formation, suggesting a large potential of multi-crystalline silicon material when used in conjunction with improved hydrogenation. The benefits of using an AHP were clearly noted on the QM silicon material, in leading to higher and more uniform lifetimes across wafers, resulting in  $iV_{OC}$  of more than 725 mV and passivation of structural defects such as

dislocation clusters. Hence, a large potential exists for such material to be used for low-cost, high efficiency silicon solar cells. However further opportunities in increase the quality of silica material could be gained through hydrogen passivation processes on finished solar cells.

## 3.7 Hydrogenation for Finished Solar Cells

While the benefits associated with hydrogen passivation of various silicon materials and solar cells have been explored in the preceding sections of this chapter, it is important to note that hydrogen passivation is not always beneficial for solar cells. As briefly discussed in Section 2.2.2 hydrogen can lead to the formation of structural defects in crystalline silicon. The passivation of dopants and/or defect states in the vicinity of the metal/Si interface can also affect the ohmic contact between the metal and silicon, increase barrier height and affect tunneling properties of the interface [Shum 12; Schr 84; Chad 97].

When performing hydrogen passivation processes on finished cells, there are substantial limitations to the subsequent thermal processes that can be used without having adverse effects on the solar cell, particularly in relation to the metal contacts. For solar cells featuring a local or full area Al-BSF, subsequent thermal processing must be below the eutectic temperature of Al and silicon (577 °C) to avoid remelting the  $p^+$  layer [Murr 84]. For front surface Ni/Cu/Ag plated contacts on solar cells, Ni sintering is usually performed below the eutectic temperature of Al and silicon in the range of 250 – 500 °C [Wolf 00; Tous 14; Wenh 02]. Hence to avoid further modifications to both the Al-BSF and Ni silicide, subsequent thermal processes should be below the temperature used for Ni silicide formation.

### 3.7.1 Aim

In this experiment, the effect of additional hydrogenation processes on the electrical performance of finished devices is explored. In particular, changes to the  $V_{OC}$ ,  $FF$ ,  $R_S$  and efficiency of the devices all be observed after various hydrogenation processes.



### 3.7.2 Experimental Procedures

To investigate the potential for hydrogen passivation to improve the efficiency of fully fabricated solar cells, second generation LDSE solar cells were fabricated on standard commercial grade  $2\ \Omega\cdot\text{cm}$  B-CZ wafers ( $125\times 125\ \text{mm}$ ) and standard commercial grade  $1.5\ \Omega\cdot\text{cm}$  boron-doped multi-crystalline wafers ( $125\times 125\ \text{mm}$ ). Processing for these solar cells was the same as that used from Fig. 3.18 in Section 3.4 whereby acidic texturing was performed on the multi-crystalline wafers. Ni sintering was performed at approximately  $375\ ^\circ\text{C}$  for 2 min in nitrogen ambient to form Ni silicide and avoid oxidation of the Ni prior to plating the Cu/Ag.

On the finished devices, light J-V measurements were obtained using a xenon flasher with AM1.5G spectrum on a Halm CetusPV XF2 tester (Class AAA) in accordance with IEC60904-9. Calibrated 1-sun  $iV_{OC}$  maps and  $R_S$  PL images were obtained using a BTi R1 luminescence imaging system [Kamp 08].

Subsequently, hydrogen passivation was performed in oxygen ambient in the range of  $200\text{--}250\ ^\circ\text{C}$  in various stages of either 5 min or 10 min duration. After each hydrogen passivation process, light J-V measurements, calibrated  $iV_{OC}$  maps and  $R_S$  PL images were obtained. The process flow is shown in Fig. 3.33.

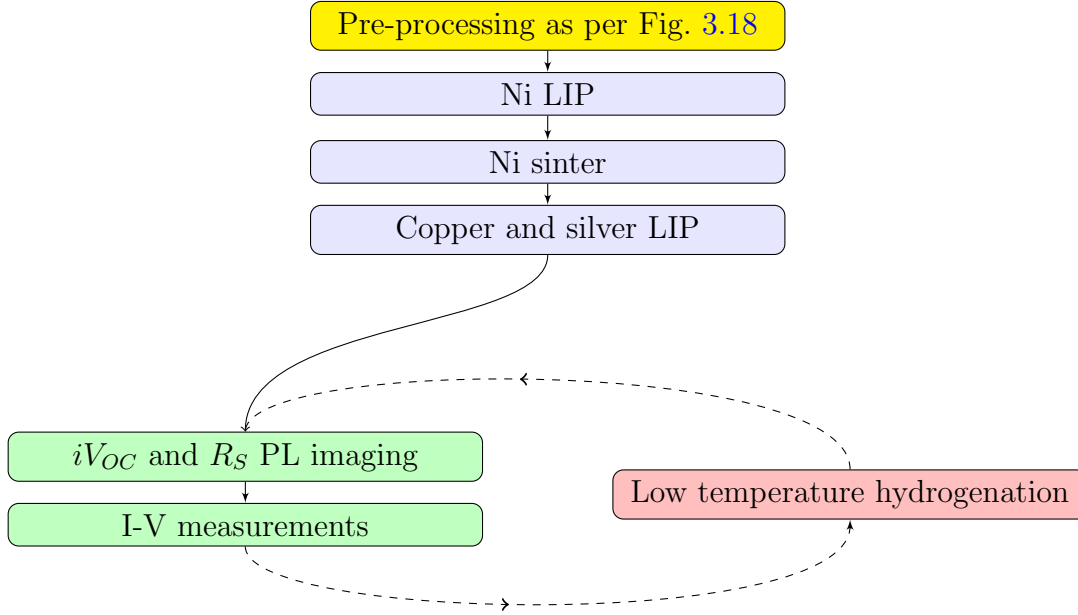


Figure 3.33: Process flow for LDSE2 solar cells fabricated to investigate the reactivation of dopants on finished devices.

## Efficiency Enhancements for Finished Devices

For the finished devices fabricated in this section, cells suffered from high  $R_S$  losses and a low  $R_{SH}$ . As a result, cells suffer from low  $FF$  and low efficiencies (see Table 3.11). After receiving hydrogenation processes at either 200 °C or 250 °C incorporating minority carrier injection, improvements were observed in almost all electrical parameters, suggesting that several different effects may have occurred in parallel. Substantial increases in  $V_{OC}$  were observed of up to 16 mV for mono-crystalline solar cells (B-CZ8) and 9 mV for multi-crystalline silicon solar cells (MX14).

Samples showing the largest improvement in  $FF$  of up to 7.7 % absolute also exhibited substantial increases in  $R_{SH}$  which may have been due to improved isolation between the localised p-type contacts on the rear of the device and the surrounding inversion layer formed due to the fixed positive charge in the  $\text{SiO}_2/\text{SiN}_x\text{:H}$  dielectric stack. For samples showing smaller improvements in  $FF$  of approximately 2 % absolute (B-CZ8 and MX19), substantial reductions in  $R_S$  were observed. On some samples, increases in  $J_{SC}$  may have also occurred, however for B-CZ8 and MX19, the  $J_{SC}$  appeared to toggle between different values which may indicate the difference was simply noise

due to slight differences in the calibration when measuring after each hydrogenation step. Subsequently, improvements in efficiency of up to 2.2 % absolute were observed for mono-crystalline silicon solar cells (B-CZ5) and up to 1.7 % absolute for multi-crystalline silicon solar cells (MX14) from a 10 min hydrogenation step at 250 °C.

In some instances a reduction in  $V_{OC}$  was observed between the value obtained after 10 min annealing and 20 min annealing (B-CZ8) which could suggest damage to the lifetime in some regions of the device. This decrease was observed on several identically processed samples and coincides with a substantial improvement in  $FF$ . In contrast, the PL images indicated a further improvement in the  $iV_{OC}$  with the additional hydrogenation treatment.

$\tau_{eff}$  values are often monitored throughout solar cell fabrication to investigate the effect of individual processes on solar cell performance. But many changes in the  $\tau_{eff}$  of silicon wafers and the solar cells fabricated on such materials can be interpreted in different ways. For example, low temperature processes in the range of 300 – 500 °C have been reported to lead to iron precipitation in the bulk of mono- and multi-crystalline silicon which results in reduction in the interstitial iron concentration  $Fe_i$  by more than one order of magnitude [Krai 09]. However the reported technique for determination of  $Fe_i$  was based on QSS-PC measurements and hence  $\tau_{eff}$ . The  $Fe_i$  was extracted by differences in the  $\tau_{eff}$  before and after illumination to dissociate  $Fe_i-B_s$  pairs [Macd 04b]. The process to perform the gettering in the work by Krain *et al.* 2009 was after the deposition of hydrogenated PECVD  $SiN_x:H$ . An alternative explanation for the reduced concentrations of  $Fe_i$  measured after the low temperature process is due to the passivation of  $Fe_i$  by hydrogen. Once hydrogen passivates the  $Fe_i$ , the recombination activity is altered and would no longer be able to pair with  $B_s$ . Hence with the passivation of the  $Fe_i$ , higher lifetimes could be observed with a reduced change in the lifetimes measured before and after dissociation of  $Fe_i-B_s$  pairs. The paper also reported on a reduced rate of the internal gettering process for samples with higher oxygen concentrations, attributed to a reduction iron diffusivity. However hydrogen diffusivity has also been observed to be reduced in the presence of oxygen [Sopo 92; Estr 90; Newm 91; Capa 99; Elga 98].

The changes in  $iV_{OC}$  and hence  $\tau_{eff}$  reported in this section could also potentially be described by many different effects, some contradictory, or indicate many different processes are occurring in parallel. The increased PL response of the device with each additional hydrogenation process

Table 3.11: Light J-V measurements of the multi-crystalline (denoted as MX below) and B-CZ solar cells before and after hydrogenation on the finished devices (measured in-house).

Cell	Process	$J_{SC}$ (mA/cm <sup>2</sup> )	$V_{OC}$ (mV)	$FF$ (%)	$\eta$ (%)	$R_S$ ( $\Omega \cdot \text{cm}^2$ )	$R_{SH}$ ( $\Omega \cdot \text{cm}^2$ )
B-CZ8	0 min at 200 °C	39.08	648.6	66.72	16.91	2.67	1080
	5 min at 200 °C	39.24	654.6	68.01	17.47	2.51	1190
	10 min at 200 °C	39.01	664.9	67.70	17.56	2.26	1300
	20 min at 200 °C	39.25	656.4	68.84	17.74	2.01	1300
MX19	0 min at 200 °C	35.38	622.8	67.72	14.92	2.44	1190
	5 min at 200 °C	35.61	628.7	68.02	15.23	2.15	1250
	10 min at 200 °C	35.44	631.0	68.29	15.27	1.91	1270
	20 min at 200 °C	35.61	631.3	67.97	15.28	1.94	1280
B-CZ6	0 min at 200 °C	39.03	653.8	59.51	15.19	-	460
	10 min at 200 °C	39.00	657.5	66.23	16.98	-	940
	20 min at 200 °C	38.99	657.9	66.70	17.11	-	980
B-CZ5	0 min at 250 °C	39.16	649.5	57.06	14.51	-	600
	10 min at 250 °C	39.16	657.6	64.80	16.68	-	1060
MX14	0 min at 250 °C	35.35	623.5	63.31	13.96	-	940
	10 min at 250 °C	35.47	632.7	68.20	15.30	-	1320

would suggest increases in  $\Delta n$  and/or increases in the  $N_{eff}$  of the device (see Fig. 3.34). Increases in the  $\Delta n$  could be due to increased  $\tau_{eff}$  of the solar cell, whilst increased  $N_{eff}$  could be due to a reactivation of boron (passivated during previous hydrogenation processes such as the AHP applied both before and after laser doping), the sintering of the Al contact, or Ni sintering. The corresponding reduction in  $R_S$  with subsequent hydrogenation processes could also indicate the increase in  $N_{eff}$  and hence reduced  $R_S$  in the bulk of the wafers. Changes in  $R_S$  and hence  $FF$

may also be due to changes in both the current and voltage of the device, or changes in the contact resistance at the metal/Si interface areas through changes in the structure of NiSi or improved contact at the  $p^+$ /Al interface. However changes to the structure of the metal contacts would appear unlikely given that the Al and Ni sintering processes were performed at substantially higher temperatures.

In addition to the blanket improvements in PL images across the wafers in Fig. 3.34, the PL images also indicated localised improvements in given areas suggesting the passivation of localised defect centres on the CZ solar cells as well as dislocation clusters and the IAR in the multi-crystalline solar cells. The increase in PL response and hence  $iV_{OC}$  of the finished devices and corresponding decrease in actual  $V_{OC}$  between certain hydrogenation steps may indicate the passivation of dopants and/or defect states at the metal/Si interface. However the passivation of dopants at the metal/Si interface would likely result in an increase in  $R_S$  and contradict the reduction in  $R_S$  observed in the PL images. Hence it appears the multiple passivation processes are occurring simultaneously such as the passivation of impurities within the bulk silicon, and the passivation of dopants and/or defect states in the vicinity of the metal/Si interface.

The substantial changes in the recombination properties of the finished devices through hydrogen passivation give further evidence that hydrogen passivation is not necessarily a one-step process. Hydrogen can be incorporated into the silicon in a given process, and can be dispersed through the silicon during that process, or during subsequent processes. In addition, the hydrogen can be retained in the device for later manipulation to activate the passivation of given defects by performing additional hydrogenation processes during subsequent processing steps or on the finished device. However, the hydrogen passivation processes must be controlled to passivate recombination active defects in the device which lead to performance degradation, whilst avoiding the passivation of defects at the metal/Si interface required for solar cell operation. This may require changes to the solar cell structure to reduce the ability of hydrogen to diffuse to the metal/Si interface by using structures such as localised deep and heavily diffused regions formed by laser doping. In addition, the fabrication process for the solar cell may need to be changed to allow the diffusion of hydrogen all throughout the device and passivation of certain defects, prior to the formation of the heavily diffused regions, to minimise the time in which hydrogen can reach the metal/Si interface during subsequent thermal treatments aimed at enhanced hydrogen diffusivity. However

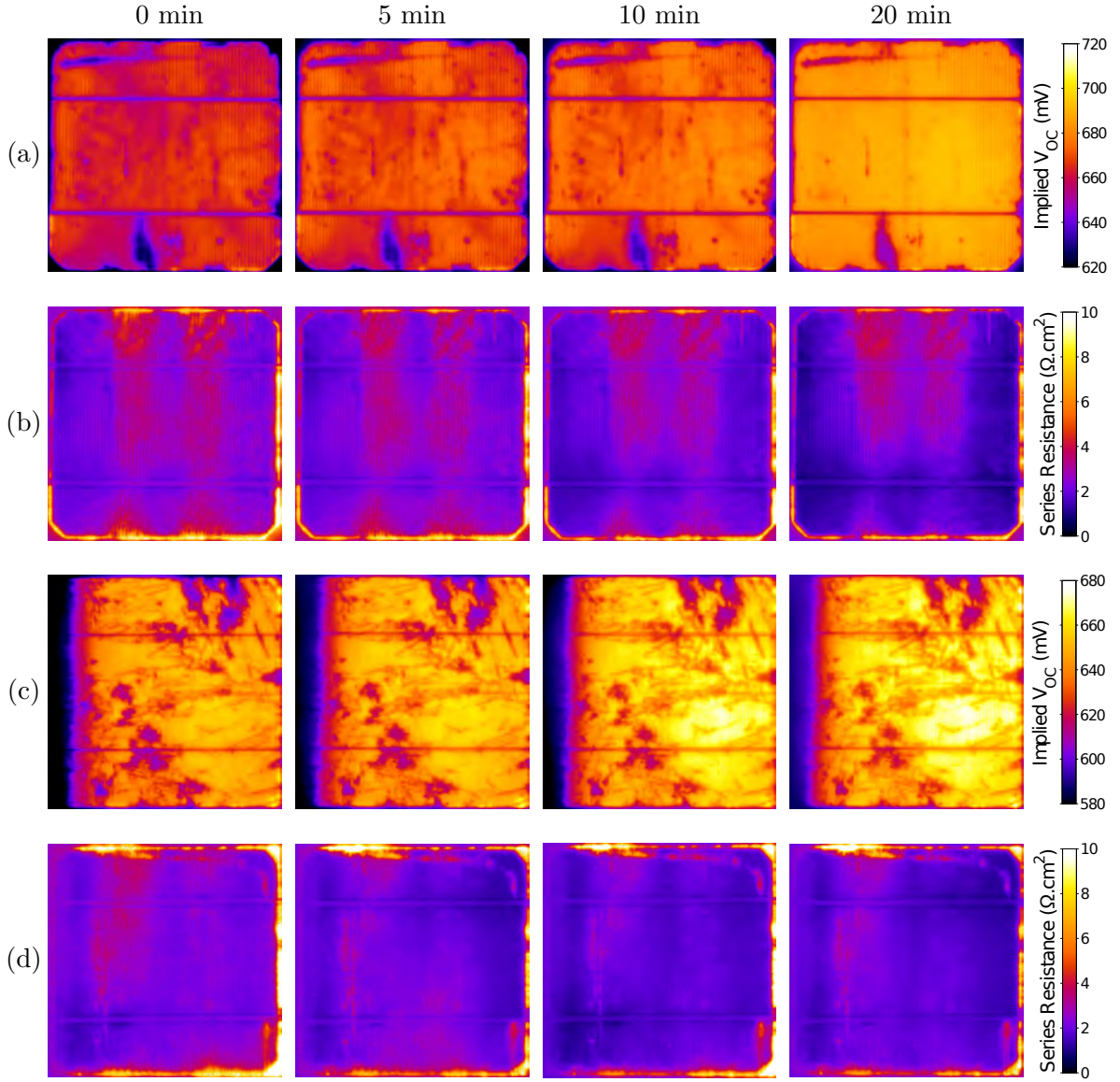


Figure 3.34: (a) 1-sun  $iV_{OC}$  maps and (b) PL  $R_S$  images on B-CZ solar cells after various hydrogenation steps at 200 °C highlighting improvements in  $iV_{OC}$  and  $R_S$ . The corresponding images of multi-crystalline silicon solar cells are shown in (c) and (d).

for contacts formed by laser doping, due to the large density of LasID introduced during the process, subsequent hydrogen passivation steps will be required as discussed in Chapter 5.

Hence it is proposed that hydrogen passivation for silicon solar cells could be broken up into several key areas including the following:

- Release of hydrogen from a source such as PECVD  $\text{SiN}_x\text{:H}$  and incorporation into the silicon
- Diffusion of hydrogen throughout the solar cell
- Activation of the hydrogen to allow the passivation of recombination sites
- Trapping the hydrogen in the silicon to ensure it does not escape during subsequent processing
- Control of subsequent processes to avoid a net reactivation of performance degrading recombination centres
- Deliberate reactivation of passivated recombination sites required for solar cell operation

The mechanisms of hydrogen passivation for silicon solar cells are extremely complicated and poorly understood, requiring a significant amount of further research to understand and utilise its full potential. Many attributes of hydrogen passivation may be influenced by the charge states of hydrogen, such as hydrogen diffusivity, and the passivation and reactivation of defects within the device.

Hydrogen passivation is not necessarily permanent. It is a two-way process. Defects can be passivated by hydrogen to form a hydrogen-defect complex and change the recombination activity of the defect. However, certain conditions can allow the hydrogen to escape from the hydrogen-defect complex, thus reactivating the recombination activity of the isolated defect. Therefore, the recombination active concentration of a given defect type will depend on the rate of passivation to form new hydrogen-defect complexes, as well as the rate of reactivation of the defect by the release of hydrogen from the hydrogen-defect complex. In addition, due to the large array of crystallographic defects and impurities present in silicon solar cells, the passivation of one given defect or impurity type may be occurring alongside to the reactivation of a different defect or impurity type.

Whilst stability of hydrogen passivation has not been studied in this work, this is of vital importance for the long-term performance of solar cells. The stability of hydrogen passivation for all kinds of defects need to be studied in great detail, including the influence of the hydrogenation

process used and hence hydrogen charge state responsible for the passivation of each defect and/or impurity type.

### 3.7.3 Summary of Hydrogenation for Finished Solar Cells

Hydrogen passivation was performed on finished devices, highlighting substantial improvements in  $iV_{OC}$  and the  $R_S$  of the devices. This led to efficiency enhancements of up to 1.9 % absolute. The results give further evidence that hydrogenation is not a one-step process, but can involve separate steps for the release of hydrogen from dielectric layers, to the distribution of hydrogen throughout the solar cell and activation of the hydrogen to allow passivation to occur.

## 3.8 Chapter Summary

In this chapter, theory for the fractional charge state concentrations of hydrogen in silicon and their relevance for silicon solar cells was presented. Minority carrier injection was shown to play a crucial role in determining the fractional charge state concentrations of hydrogen in silicon. For p-type silicon, regardless of the  $N_{eff}$ , an optimum function ( $\Delta n_{opt}(T)$ ) was shown to exist to maximise  $H^0$  generation in the silicon. This became increasingly important for heavily doped p-type silicon. With appropriate minority carrier injection throughout the thermal process,  $H^0$  and  $H^-$  concentrations were shown to be increased by several orders of magnitude.

A process modification was developed for existing fast firing furnaces, with a change in power distribution in the furnace resulting in higher illumination intensities in the peak firing zones and cool down section, particularly for wafers with a fully metallised rear whereby illumination can only enter the wafer from one surface. This AHP was applied to various types of wafers to passivate:

- B–O defects in B-CZ silicon
- Slip-lines and other defects in UMG silicon
- OSF in B-CZ silicon



- Defected n-type CZ silicon
- Grain boundaries, impurities and dislocations in multi-crystalline and QM silicon
- Defects in finished devices

**B–O defect passivation:** Improvements to the passivation of B–O defects in B-CZ and CB-CZ wafers grown from UMG silicon over a CHP in the dark at 400 °C. However the passivation was reversed if the charge state was not adequately controlled during subsequent processing, resulting in a net reactivation of defects throughout the process. Subsequently, after an initial  $\tau_{bulk}$  of 500  $\mu$ s on B-CZ wafers, the value toggled between 800  $\mu$ s on the application of the CHP to 1.4 ms with the application of the AHP, despite previous literature suggesting a complete passivation of B–O defects should have been obtained by performing a thermal process in the dark above 170 °C. Incorporating the AHP to solar cells, resulted in independently confirmed  $V_{OC}$  and  $J_{SC}$  over 680 mV and 40 mA/cm<sup>2</sup> respectively with a  $p$ -FF of 23 %, demonstrating a large potential for high efficiency solar cells to be fabricated on B-CZ wafers.

**Passivation of UMG CZ silicon:** For UMG CZ silicon wafers, a large variation in the  $\tau_{bulk}$  and response to hydrogenation processes was observed throughout the ingot. Whilst wafers in the last section of the ingot suffered from increased impurity concentrations due to segregation, which increase defect concentrations and can lead to the formation of slip-lines, the increasing presence of phosphorus in such regions led to a higher resistivity of the wafers. Subsequently the phosphorus compensation enabled higher  $f_0$  and  $f_-$ , allowing more effective hydrogenation to take place in such regions of the ingot. This was observed for the CHP as well as for the AHP by incorporating minority carrier injection through illumination due to a more favourable  $E_{Fn}$  in relation to the  $E_m$ . However a CHP did not result in any improvement in  $\tau_{bulk}$  throughout a large section of the ingot. In contrast, applying minority carrier injection during hydrogenation through an AHP, greatly improved the  $\tau_{bulk}$  of wafers throughout the entire ingot, resulting in improvements from 8  $\mu$ s to 550  $\mu$ s. If such improvements in passivation can be retained on finished devices, larger fractions of ingots grown from UMG silicon could be used, helping to bring down the cost of UMG Si and improve the efficiency of finished devices.

**Passivation of OSF:** OSF present a significant problem for silicon solar cells fabricated on CZ grown silicon wafers, which may be present in as-cut wafers and exacerbated during high temperature processing. Such defects can reduce cell efficiencies by up to 5 % absolute. However by applying an AHP incorporating minority carrier injection, the recombination activity associated with OSF present after emitter diffusion/oxidation on standard commercial grade B-CZ wafers were completely eliminated. Furthermore, the passivation was retained on finished devices, suggesting that rather than using high temperature tabula rasa processes (around 1000 °C) which can reduce the lifetime in solar-grade silicon, lower temperature hydrogenation processes could be used to passivate OSF and avoid the associated performance degradation.

**Passivation of n-type CZ silicon:** Whilst high efficiency devices are often fabricated on n-type wafers to avoid LID, n-type wafers can suffer from other oxygen related defects such as OSF and other impurities present in the silicon after crystal growth, or introduced during a variety of processing steps. On highly defected commercial grade n-type CZ material with inherent bulk lifetimes in low injection  $\tau_{bulk}$  in the range of 90 – 190  $\mu$ s, very substantial improvements in  $\tau_{bulk}$  to 3.4 – 4.9 ms were achieved from a CHP at 400 °C only utilising hydrogen released from PECVD SiON<sub>x</sub>:H. These lifetime values are compatible with the wafer lifetimes used for the most efficient solar cells in commercial production. Furthermore, the n-type material still demonstrated a benefit (from 2.4 ms to 2.9 ms) using an AHP to enhance the release of hydrogen from the dielectric layer before the activation of passivation for bulk defects during a subsequent low temperature hydrogenation process.

**Passivation of multi-crystalline and QM silicon:** Hydrogen passivation and phosphorus gettering are essential processes for low quality material such as multi-crystalline and QM silicon. CHP was shown to have limited effectiveness in defect passivation, however substantial improvements were obtained through an AHP incorporating minority carrier injection. Through the AHP,  $iV_{OC}$  over 700 mV were demonstrated on full cell structures prior to contact formation using standard commercial grade multi-crystalline wafers. This suggests a significant potential for improvements in solar cell efficiencies on such substrates with more effective hydrogen passivation than is currently achieved using conventional solar cell technologies. For QM silicon, large vari-

ations in wafer quality can also occur. In mono-crystalline regions in the central regions of the seeded-cast ingot, substantial improvements in  $\tau_{eff}$  from 8  $\mu\text{s}$  to 270  $\mu\text{s}$  were obtained with an AHP, whilst for the edge regions of the ingot it was essential to perform phosphorus gettering to reduce impurity concentrations as well as perform the AHP to passivate the remaining defects.

**Hydrogen passivation for finished devices:** Hydrogen passivation can be incorporated into any thermal processing where a hydrogen source exists within the silicon or is introduced into the silicon. Hence hydrogen passivation can be performed on finished devices, and initial results demonstrated increases in efficiencies of 2 % absolute. However several passivation mechanisms appeared to be taking place, such as: (1) the passivation of local recombination centres leading to an increase in  $iV_{OC}$  due to improved bulk defect passivation; and (2) the passivation of dopants and/or defect states at the metal/Si interface leading to a reduction in measured  $V_{OC}$ . This requires further investigation to understand the mechanisms taking place.

**Summary of hydrogen passivation in silicon:** The mechanisms of hydrogen passivation for silicon solar cells are extremely complicated and poorly understood, requiring an immense amount of further research to understand and utilise its full potential. Hydrogen passivation is not necessarily permanent. It is a two-way process in which passivated defect sites can be reactivated during subsequent processes. Hence, future work must include studies on the stability of hydrogen passivation for different defects using different hydrogenation processes (with different hydrogen charge states for the passivation process). To retain the benefits of hydrogen passivation in finished devices, new and novel contacting approaches are required to improve the effectiveness of hydrogen passivation and reduce recombination losses at the metal/Si interface. In Chapter 4 new laser-doped structures are presented.

## Chapter 4

# Advanced Laser-Doped Structure Formation

To date, a vast array of lasers with substantially different properties have been used for laser doping in silicon solar cells, with wavelengths ranging from the ultraviolet to near infrared. The frequency of Q-switched lasers have varied from low frequencies up to values approaching 1 MHz. The pulse-lengths of such lasers are typically in the range of nanoseconds, however some work using the LCP method has investigated the use of pulse lengths in the order of microseconds.

Conventional approaches for fabricating laser-doped solar cells can result in a significant introduction of LasID to the solar cell. Thermal stress appears to be one of the most likely causes of LasID in silicon [Aror 96], which can create cracks at the silicon surface [Kray 05] and extend defects well into the bulk of the device [Moon 78; Abbo 05]. Increasing the number of pulses supplied to a laser-doped region can result in a larger defect density along the edge of the laser-doped region leading to further performance degradation [Sugi 07]. One approach to avoid defect generation is to perform laser doping prior to dielectric deposition and to use an aligned metallisation process [Rode 10; Kray 10a]. This may require the use of linear beam focusing to suppress defect generation [Amet 05]. Another approach is to modify the dielectric stack to reduce thermal expansion mismatch between the dielectric layer and silicon by incorporating a thin layer of SiO<sub>2</sub> between the silicon surface and the SiN [Wenh 11; Tjah 07; Sugi 07; Hame 11b]. However such approaches add

---

complexities and expense to the fabrication sequence.

Alternatively, thermal cycling can be greatly reduced through the use of modified Q-switched lasers, or more preferably the use of continuous wave (CW) or quasi CW (Q-CW) lasers [Wenh 12]. A further potential benefit of CW and Q-CW lasers is that due to the long effective pulse-length of the lasers, deep molten regions may be formed. By extending the duration in the molten phase, the thermal conductivity of the silicon may be used to enhance both the depth and width of the molten region. Therefore, lateral melting of the silicon could occur well beyond the effective laser spot size and opening in the dielectric layer. As a result, defected regions of silicon at the edge of the laser illuminated area, which typically hurt laser-doped solar cell performance, would undergo melting and resolidification throughout the laser doping process. During the recrystallisation process, liquid phase epitaxial growth would likely reduce the defect concentration remaining after the laser doping process. The heavy doping within the molten region could also ensure that any defects remaining after resolidification lie within a heavily doped region, further reducing the recombination activity. Additional benefits of deep junction formation can also result from an improved shielding of minority carriers underneath the metal/Si interface through a reduction in the  $J_{0d}$ .

This chapter focuses on the use of mode-locked 355 nm UV Q-CW and 532 nm CW lasers to fabricate deep molten regions in silicon. Such deep molten regions will then be used to create advanced laser-doped structures formed through: the use of dopants in dielectric layers such as aluminium oxide; the manipulation of diffusion coefficients of multiple impurity types to contact buried layers within the solar cell for interdigitated back contacts; and form junctions within the laser-doped region to form transistors. In addition, a model is developed to understand the influence of a solid/liquid interface in affecting the resulting dopant profiles.

## 4.1 Continuous Wave Laser Doping for Deep Junction Formation

To form deep junctions using laser doping, close attention should be paid to the laser properties. Silicon has a band gap of approximately 1.12 eV, corresponding to light with a wavelength of approximately 1.1  $\mu\text{m}$ . Hence, in order for the laser emission to be absorbed by the silicon, the wavelength of the laser must be shorter than this. However, even for wavelengths which are absorbed by silicon, there are more than five orders of magnitude of difference in the absorption coefficient and hence penetration depth of wavelengths in the near visible spectrum at room temperature [Sze 07]. Therefore, a wavelength with an appropriate absorption depth should be chosen to allow the formation of deep molten regions.

Industrial applications using diode pumped solid-state lasers typically involve wavelengths generated by neodymium-doped media and frequency-conversion optics [Bova 11]. Infrared light such as the fundamental laser emission wavelength of 1064 nm for such lasers is only weakly absorbed in silicon at room temperature, with a penetration depth of more than 100  $\mu\text{m}$  [Sze 07]. For this wavelength, the penetration depth is approaching the thickness of the wafer, and hence would not appear to be favourable. On the other hand, the third harmonic is in the UV range with a wavelength of 355 nm. Such light is absorbed very rapidly, with a penetration depth of 10 – 100 nm [Sze 07]. Subsequently, it would appear that this penetration depth is too shallow for the feature sizes desired in this work, which are in the order of several microns.

The second harmonic of the Nd:YAG laser is in the green range and has a wavelength of 532 nm. This wavelength has a penetration depth in silicon in the order of 1  $\mu\text{m}$ , and hence it would appear that to form molten regions with depths of more than 5  $\mu\text{m}$ , wavelengths greater than approximately 750 nm would be required [Sze 07]. However as the silicon heats up, the absorption depth within the silicon is substantially shortened, and again shortened as the silicon moves into the liquid state [Jell 87], resulting in a positive feedback mechanism. Hence care should be taken to ensure the energy of laser pulses, or average power in the case of a Q-CW or CW laser beam, is not so high that it causes ablation of the silicon at the surface.

By allowing the silicon itself to conduct the absorbed energy, substantially deeper molten regions can be obtained than when simply relying on the instantaneous absorption of the laser energy to melt the silicon. To do so, it is preferable that energy is supplied to the silicon over a time frame that allows the thermal conductivity of the silicon to heat adjacent regions of silicon and hence expand the molten region. It is difficult to achieve this using a conventional pulsed laser, as successive pulses of energy are too infrequent. This results in the resolidification of the entire molten silicon region between successive pulses with the silicon essentially returning to room temperature after each pulse. Hence, each successive pulse is only able to re-melt the same small volume of silicon. To compensate for this effect, extended pulse-lengths may be used to increase the time in the molten phase and enhance the depth of the molten region. Higher power levels may also be used, however if the power levels are too high the silicon material may be ablated [Hame 11b]. To eliminate these losses, energy can be supplied without interruption using a CW laser, allowing the silicon to remain molten for a desired length of time, resulting in the formation of deeper junctions [Bova 11]. Subsequently, the thermal conductivity of the silicon can be used to enhance the depth of the molten silicon region, and junction depths can simply be controlled by varying the scan speed and hence time for which the laser illumination is supplied.

As an alternative approach to increase the effective laser illumination time, is to increase the frequency of the laser to shorten the time between successive pulses. This ensures that the silicon is not able to entirely solidify before the next pulse arrives, however this technique still results in a certain amount of energy being lost through the repeated heating/cooling of the silicon between successive pulses. For lasers with extremely high repetition frequencies such as mode-locked UV Q-CW lasers, the energy is supplied to a given area by a large number of pulses over a very short period of time. For example, using such a laser with: a beam size of 20  $\mu\text{m}$  ( $1/e^2$  diameter); equivalent CW power of 8 W; repetition frequency of 80 MHz; and processing speed of 10 m/s, 160 pulses are supplied within a 2  $\mu\text{s}$  time interval. Whilst the energy delivered by each pulse is typically very small (100 nJ), heat loss between successive pulses can be greatly reduced, as each pulse is only 12.5 ns apart. As a result, an accumulation effect can result with further increases in temperature after each additional pulse, until the silicon reaches a quasi-steady-state. Hence if the power is sufficient to avoid the solidification of the silicon between successive pulses, the 160 pulses supplied to a given area can be considered as one continuous effective pulse which keeps the silicon

molten for the 2  $\mu\text{s}$  duration.

### **4.1.1 Aim**

Deep junction formation is explored in this experiment using CW lasers. Both n- and p-type dopants are investigated for the laser doping process to explore differences in the junction depths obtainable due to the different diffusion coefficients of dopants such as boron and phosphorus. Planar and textured surfaces are also used to explore differences in the laser doping process that arise from optical differences in the morphology of the silicon surface, relevant for processing the front and rear of mono-crystalline solar cells.

### **4.1.2 Experimental Procedures**

Test structures were fabricated on standard commercial grade  $0.5 - 3 \Omega \cdot \text{cm}$  n- and p-type CZ wafers with both planar and textured surfaces. Samples on p-type wafers with textured surfaces were pre-processed on an industrial production line following the standard processing for LDSE solar cells including: alkaline texturing with small pyramids  $2 - 5 \mu\text{m}$ ; a light phosphorus emitter diffusion with a sheet resistance of approximately  $120 \Omega/\square$ ; edge junction isolation (EJI); standard PECVD of  $\text{SiN}_x\text{:H}$ ; and Al rear screen-printing and firing.

Test structures fabricated on n-type wafers (with textured surfaces) were alkaline textured at an industrial facility with pyramids  $2 - 5 \mu\text{m}$ , and coated on both sides by  $\text{SiON}_x\text{:H}$  using a laboratory type remote microwave Roth & Rau AK400 PECVD system. No thermal diffusions were applied to the n-type textured wafers.

Test structures fabricated on p-type wafers with planar surfaces were saw-damaged etched and diffused to sheet resistances in the range of  $100 \Omega/\square$  using phosphorous solid sources. Samples were then coated with PECVD  $\text{SiON}_x\text{:H}$  on both surfaces. Samples fabricated on n-type wafers with planar surfaces were saw-damaged etched and coated with PECVD  $\text{SiON}_x\text{:H}$ . No thermal diffusions were applied to the n-type planar wafers.



---

#### 4.1. CONTINUOUS WAVE LASER DOPING FOR DEEP JUNCTION FORMATION

---

Prior to laser doping, wafers used for n-type laser doping investigations were spin coated with  $\text{H}_3\text{PO}_4$  at 3000 RPM for 20 s. Wafers used for p-type laser doping investigations were spin coated with a boron-dopant source (Filmtronics PBF1) at 2000 RPM for 40 s. The wafers with p-type dopants were then dried at 90 °C for 10 min.

Laser doping was performed using a 15 W 532 nm CW laser with a Gaussian beam distribution and scanning optics. Unless otherwise stated, the average power of the laser reaching the stage was approximately 13 W, with a focus size of 10  $\mu\text{m}$  at the  $1/e^2$  radius ( $w_0$ ). The peak average intensity,  $I(0)$ , of the laser was approximately 8.2 MW/cm<sup>2</sup>, with a corresponding intensity at the focus size radius,  $I(w_0)$  of approximately 1.1 MW/cm<sup>2</sup>. Laser-doped lines were formed with various scan speeds ranging from 0.1 – 10 m/s to vary illumination time, and therefore energy supplied to the silicon. On selected samples laser-doped point contacts were also formed to investigate the potential of forming rear contacts on PERL cells. In addition, on selected samples laser doping was performed using a 355 nm mode-locked UV Q-CW laser with a repetition frequency of 80 MHz, pulse-length of 60 ps and focus size of 10  $\mu\text{m}$  at the  $1/e^2$  radius to investigate the use of a pulsed laser with an extremely short time between successive pulses.

To make electrical contact on samples for electron beam induced current (EBIC) measurements [Leam 82; Piro 01], n- and p-type contact tabs were created on all samples using laser doping and/or the existing screen-printed Al rears. The area of the contact pads was 1 cm<sup>2</sup>, with full laser-doped coverage achieved by overlapping laser-doped lines on a 15  $\mu\text{m}$  pitch. After each laser process, the dopant source was removed using a short, weak HF dip.

To enable analysis of the junction, prior to the EBIC measurements, samples were cleaved across the laser-doped lines from the side of the wafer without the laser-doped lines of interest (with the assistance of a Nd:YAG 1064 nm Q-switched laser) to expose the junction on a high recombination velocity surface. The samples were cleaved approximately 1 mm from the edge of the laser-doped contact pad.

Cross-sectional scanning electron microscope (SEM) and EBIC measurements were obtained on a Hitachi S3400 SEM imaging tool. For the SEM technique, a focused beam of electrons is used to raster over the surface of the samples and create an image [Gold 03].

For EBIC, the energetic electron beam of the SEM is scanned across the sample, and absorbed near the surface generating electron-hole pairs. This generates an electron beam induced current, which is detected by probes. The recorded signal is converted into an image, with the brightness in each pixel being proportional to the collection probability of the carrier for the corresponding region of the device [Leam 82]. The freshly cleaved surface on the test structures fabricated for this experiment has a high SRV and as a result, only carriers generated within the depletion region of the p-n junction, or within a diffusion length of the p-n junction could contribute to the measured EBIC signal. Hence this method was used to highlight the location of the p-n junction, denoted by bright regions in the EBIC image, and therefore indicate the depth to which dopants diffused to during the laser doping process.

Focused ion beam (FIB) imaging enabled a high resolution image to be obtained of the surface structure of the laser doped samples with point contacts in this work. The FIB imaging technique is similar in principle to SEM imaging, however FIB uses a focused beam of ions (in this case gallium), compared to electrons for SEM. Secondary ions are collected to form an image of the sample surface. In this instance, low beam currents were used to produce an image, rather than high currents which can be used to mill a sample [Gold 03].

An extremely accurate method to determine the doping profile of a diffused region in silicon is secondary ion mass spectroscopy (SIMS). For this technique, the silicon surface is sputtered with a primary ion beam. The beam of ejected secondary ions is collected and analysed using a mass spectrometer to determine the elemental composition of the surface [Benn 69]. As the surface is gradually removed by the sputtering process, this technique therefore provides a technique to determine the concentration of dopant atoms as a function of depth from the surface.

Fig. 4.1 shows the process flow for the work in this section.

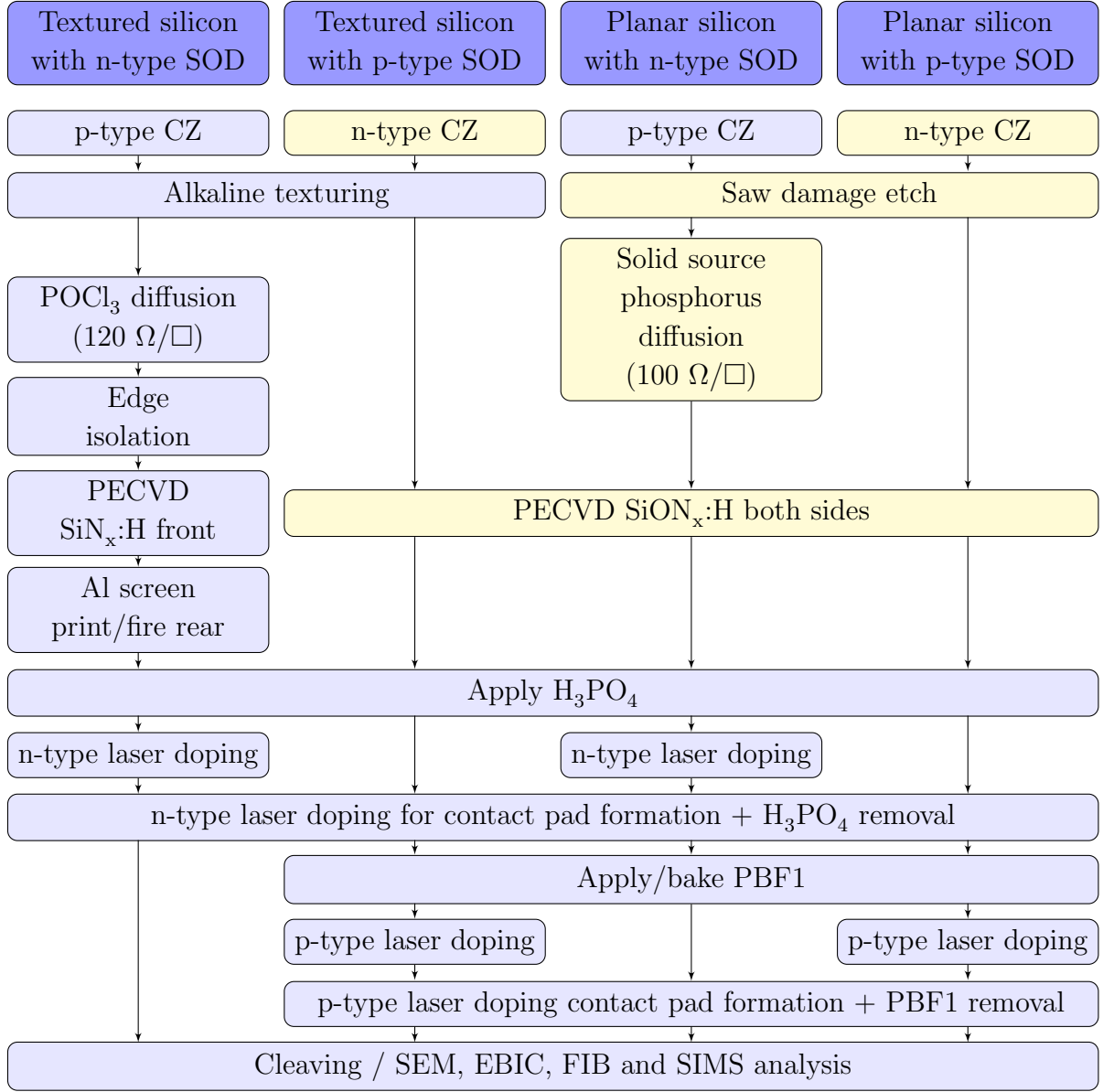


Figure 4.1: Process flow for deep junction formation using laser doping.

### 4.1.3 Deep Junction Laser Doping

#### 4.1.3.1 Surface Morphology and Influence of n-type/p-type Dopants

Laser doping for the various surface morphologies with either n-type or p-type dopants indicated that greatly enhanced junction depths could be obtained in localised regions, compared to that

achieved using conventional methods. Fig. 4.2(a) shows a combined SEM/EBIC image of a sample with a textured surface and an n-type laser-doped line processed at 0.2 m/s. The introduced white regions (EBIC signal) in the image represent the device junction highlighting: (1) the junction formed during the thermal diffusion which follows the textured surface of the wafer; and (2) the well-defined semicircular junction formed during the laser doping process, which extends to depths of 10  $\mu\text{m}$ . The junction induced by the laser doping process also extends approximately 8  $\mu\text{m}$  laterally from the clearly opened region in the  $\text{SiN}_x\text{:H}$ . It was also observed that the surface had been modified in the majority of this region, with the textured surface structure only being retained within 1 – 2  $\mu\text{m}$  from the edge of the laser-doped region. The textured surface may have been retained in these peripheral regions of the melt due to the short duration held in the molten phase.

The junction depth appeared to be primarily independent of surface morphology and dopant type. Fig. 4.2(b) shows a combined SEM/EBIC image of an n-type laser-doped line on a planar surface processed at 0.2 m/s, with a junction depth of 11  $\mu\text{m}$ . Similarly, Fig. 4.2(c) shows a combined SEM/EBIC image of a p-type laser-doped line on a planar surface for a processing speed of 0.2 m/s with a junction depth of 11  $\mu\text{m}$ , with lateral doping extending 9  $\mu\text{m}$  beyond the opening in the dielectric layer. For the sample shown in Fig. 4.2(c), there was no thermal diffusion and hence the junction in this sample was only formed by laser doping. In addition to the semicircular junction observed on the cleaved surface of the wafer, an EBIC signal was observed along the top surface of the wafer, illustrating the wide lateral doping achieved by laser doping, well beyond the opening in the dielectric layer. These results indicate that essentially the same junction depths and lateral width of doping can be achieved by laser doping with n- or p-type dopants on a textured or planar surface.

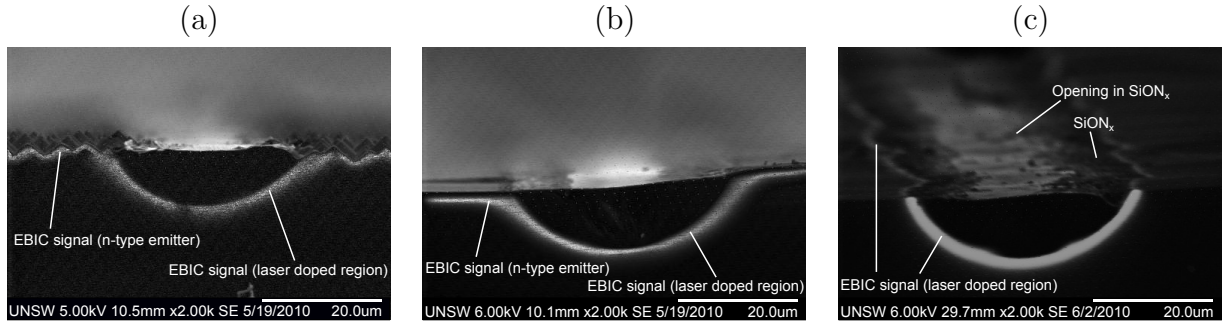


Figure 4.2: Combined SEM/EBIC images at x2000 magnification of lines processed at 0.2 m/s for (a) n-type laser doping on a textured surface, (b) n-type laser doping on a planar surface and (c) p-type laser doping on a planar surface.

#### 4.1.3.2 Influence of Laser Speed

By varying the speed at which the laser scans over the wafer surface, the duration the silicon remains molten for can be controlled, which in turn, affects the depth and width of the junction. The results of varying speed from 0.5–10 m/s are shown through the combined SEM/EBIC images in Fig. 4.3(a) of n-type laser-doped lines on a textured surface. For these samples, increasing processing speed lead to a reduction in the junction depth as expected, due to the shorter laser illumination time and hence reduced duration in the molten phase. Similarly, Fig. 4.3(b) and (c) show the corresponding images on a planar surface for n- and p-type dopants respectively, for laser-doped lines processed from 0.5 m/s – 10 m/s, demonstrating a reduction in junction depth with increasing processing speeds. It should also be noted in Fig. 4.3(c) that on the sample processed at 10 m/s no junction was observed, however hot probe measurements indicated that the surface was indeed p-type with other samples processed using the same conditions yielding similar junction depths to that observed when using n-type dopants. It is expected that no junction was detected in this sample during the EBIC measurements due to a break in the laser-doped line.

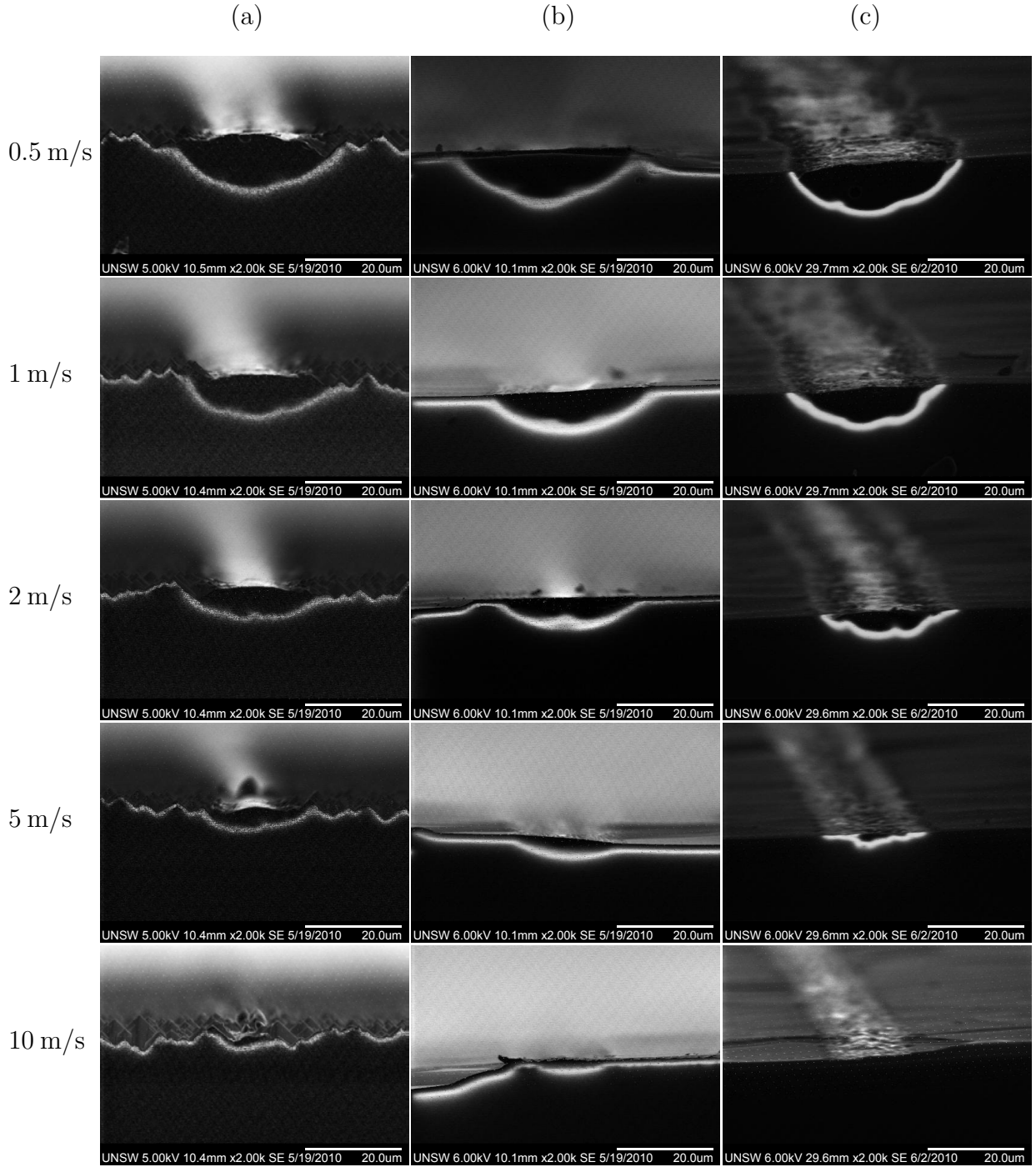


Figure 4.3: Combined SEM/EBIC images of (a) n-type laser doping on a textured surface, (b) n-type laser doping on a planar surface and (c) p-type laser doping on a planar surface for various processing speeds.

#### 4.1. CONTINUOUS WAVE LASER DOPING FOR DEEP JUNCTION FORMATION

The junction depths obtained after laser doping greatly depend on the laser parameters. Fig. 4.4(a) shows junction depths as extracted from the EBIC profiles, using a beam power of 13 W ( $I(0)$  of  $8 \text{ MW/cm}^2$ ) for various scan speeds. It was observed that even by using a speed of 10 m/s, junction depths of more than approximately  $2 \text{ }\mu\text{m}$  can be obtained. However for slower speeds, the junction depth could be greatly enhanced, with junction depths of more than  $10 \text{ }\mu\text{m}$  obtained for processing speeds below  $0.5 \text{ m/s}$  regardless of the dopants or surface morphology. By forming a deep molten region, the distance for which doping extends beyond the opening in the dielectric layer on each side of the laser-doped line could also be greatly enhanced. This effect is highlighted in Fig. 4.4(b), with distances of more than  $10 \text{ }\mu\text{m}$  demonstrated for a processing speed of  $0.5 \text{ m/s}$ . As a result, it appears that forming a deep junction can assist with wide lateral doping, and could potentially be used to isolate heavily doped regions from the surrounding silicon surface, thereby reducing recombination. The slightly reduced junction depth and lateral doping widths for processing speeds below  $0.5 \text{ m/s}$  may be due to ablation of silicon and a wider opening occurring in the dielectric layer from the increase in energy supplied to the wafer.

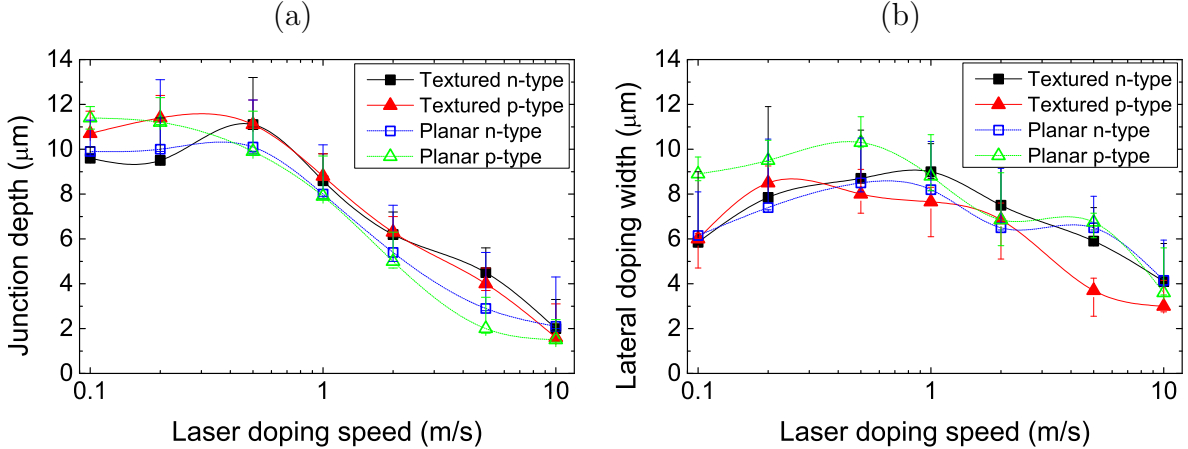


Figure 4.4: (a) Junction depths and (b) distance of lateral doping extending beyond the opening in the dielectric layer for laser doping with n- and p-type dopants on planar and textured surfaces for processing speeds between  $0.1 \text{ m/s} - 10 \text{ m/s}$ .

#### **4.1.3.3 Point Contact Formation with Deep Junctions**

Point contacts have a benefit of reducing metal/Si interface and resistive losses, when compared to line contacts, and have been used for the world record PERL cell [Zhao 96]. Hence, the formation of deep junctions was also explored with point contacts to investigate such contacts on a textured surface. A focused ion beam (FIB) image of the surface of a laser-doped point contact with a length of approximately 40  $\mu\text{m}$  is shown in Fig. 4.5(a). It was observed that small mounds developed at the end of the point contact as the laser illumination was removed from the silicon surface. Such mounds may be caused by the Marangoni effect through surface tension pulling the molten silicon from hotter to cooler regions [Grig 97], resulting in a deformation of the wafer surface which is retained in the crystal structure after rapid solidification [Brow 10; Schw 01]. Fig. 4.5(b) shows a combined SEM/EBIC image of the cross section along a laser-doped point contact, with the mounds of many point contacts closely spaced behind the front point contact. As shown, impressive junction depths of more than 8  $\mu\text{m}$  were obtained from point contacts with an opening in the dielectric layer 25  $\mu\text{m}$  long and 15  $\mu\text{m}$  wide when processed at a speed of 0.5 m/s, demonstrating that deep junctions can also be formed for small point contacts using laser doping, with doping also extending several microns beyond the opening in the dielectric layer.



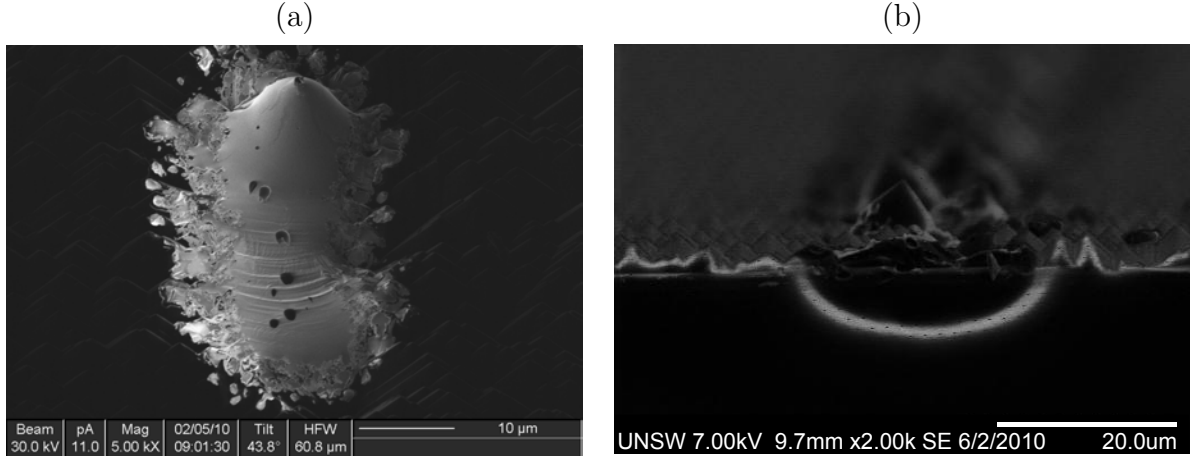


Figure 4.5: (a) FIB image of the surface of a laser-doped point contact on a textured surface processed at 0.5 m/s and (b) combined SEM/EBIC image of the cross section of an n-type laser-doped point contact on a textured surface processed at 0.5 m/s.

#### 4.1.3.4 SIMS Analysis of Laser Doped Regions

SIMS can also be used to investigate junction depths of laser-doped regions, however more information is gained on the actual profile of the dopants within the laser doped region. SIMS measurements for n- and p-type laser-doped contacts on a textured surface were in good agreement with the EBIC images, highlighting the deep junction formation using CW laser doping (see Fig. 4.6). In this figure, all laser doping was performed using an optical power of 13 W (apart from the sample processed at 2 m/s which used an optical power of 12 W due to a power fluctuation in the laser). For a processing speed of 10 m/s a relatively shallow diffusion was obtained with a junction depth of approximately 2.5 μm and typical Gaussian diffusion profile. When reducing the processing speed from 10 m/s to 2 m/s, a large enhancement in junction depth was observed, along with increases in the dopant surface concentration, with the doping profile still resembling a Gaussian profile. It is expected that whilst the sample processed at 2 m/s used a lower power than that for all the other speeds, due to the Gaussian profile of dopants obtained, the reduced power did not affect the dopant profile. However, when reducing the processing speed further, an enhancement in junction depth was observed, but the resultant doping profile deviated from a

Gaussian diffusion profile typical of conventional solid-state diffusions. An understanding of the discrepancies between the diffusion profiles for the various processing conditions will be presented in Section 4.2.

For sufficiently high repetition frequencies in pulsed lasers, such as mode-locked UV Q-CW lasers with a repetition frequency of 80 MHz, deep junction formation can also be observed in a similar fashion to pure CW lasers. Whilst individual pulses are typically 15 – 60 ps, the accumulation effect caused by the high repetition frequency allows the expansion of the molten region. Fig. 4.6(c) shows SIMS profiles of laser doping performed using a 532 nm CW laser and 355 nm mode-locked UV Q-CW laser for an optical power of 12 W and processing speed of 2 m/s. Both profiles indicated junction depths of approximately 5  $\mu\text{m}$  despite the differences in the absorption depth for the illumination of the two lasers. However, certain differences in the dopant profiles were apparent, such as increased dopant concentrations for the Q-CW laser between depths of 2 – 3.5  $\mu\text{m}$  and a slightly reduced junction depth. These differences will be discussed in Section 4.2.

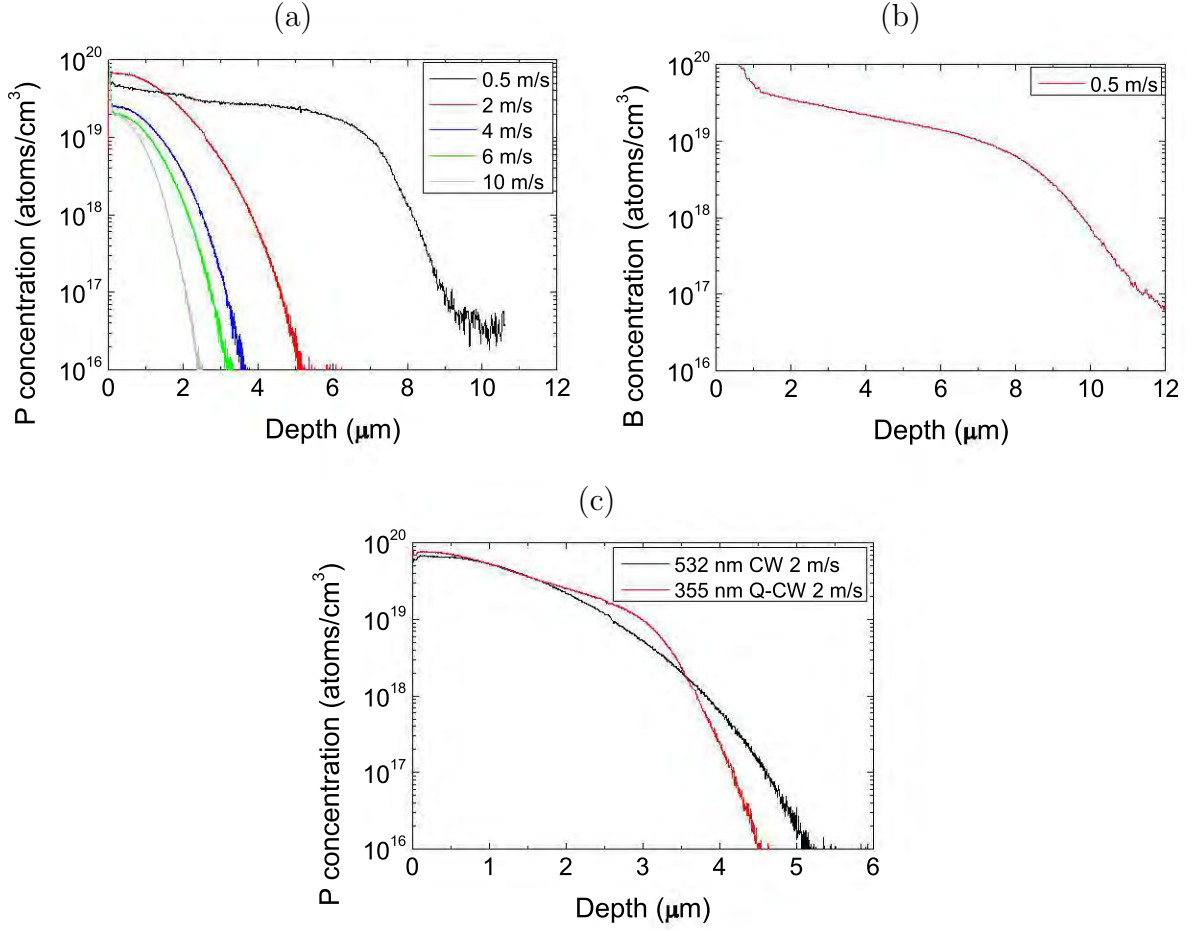


Figure 4.6: SIMS profiles of 532 nm CW laser doping with (a) phosphorus and (b) boron. (c) SIMS profiles of phosphorus laser doping using a 532 nm CW and 355 nm mode-locked UV Q-CW laser. An optical power of 12 W was used for a processing speed of 2 m/s. All other speeds were processed with an optical power of 13 W.

#### 4.1.3.5 Deep, Heavily Diffused Regions for Pluto-PERL

Similarly to the deep, heavily diffused regions obtainable using laser doping, the next generation Pluto-PERL cells feature deep and localised heavily diffused boron-doped  $p^{++}$  regions. However unlike the laser-doped regions formed in this work, which simultaneously open the dielectric and form a heavily diffused region, for the Pluto-PERL cells, the heavily diffused regions are formed

after dielectric opening of the rear surface [Wang 12]. Due to the enhanced doping underneath the rear metal/Si interface, Pluto-PERL cells have demonstrated an improved shielding of minority carriers. Hence the cells have a lower rear SRV than that of Pluto-PERC cells fabricated using a local Al-BSF region. This has resulted in improved values for  $J_{SC}$  approaching 41 mA/cm<sup>2</sup> with a record efficiency of 20.3 %. However, the increased metal/Si interface area has outweighed the potential  $V_{OC}$  increase from the reduction in SRV. The developments of improved hydrogen passivation and incorporation of the locally heavily diffused boron-doped regions for the Pluto-PERL technology could result in radically improved efficiencies with production cell efficiencies on standard commercial grade B-CZ material likely to approach 23 %. The results of pilot production of Pluto-PERC and Pluto-PERL cells are shown in Table 4.1, as fabricated in conjunction with Wang *et al* 2012 [Wang 12].

Table 4.1: Light J-V measurements of the Pluto-PERC and Pluto-PERL solar cells sourced from [Wang 12]. \*Best cell independently confirmed by the Solar Energy Research Institute of Singapore.

		$J_{SC}$	$V_{OC}$	$FF$	$\eta$	$p-FF$	$p-\eta$
		(mA/cm <sup>2</sup> )	(mV)	(%)	(%)	(%)	(%)
<b>Pluto-PERC</b>	Best cell*	674	39.3	73.9	19.7		-
	Best $V_{OC}$	683	39.3	72.1	19.4		-
	Average	674	39.0	73.6	19.3	81.1	21.3
<b>Pluto-PERL</b>	Best cell*	665	40.9	74.4	20.3		-
	Best $V_{OC}$	668	40.5	73.3	19.9		-
	Average	662	40.7	74.3	20.2	83.3	22.4

---

#### 4.1.4 Summary for CW Laser Doping for Deep Junction Formation

Deep junction formation with depths over 10  $\mu\text{m}$  were demonstrated independently of the surface morphology and dopant choice (n-type or p-type). The depth of the diffused regions could be varied simply by altering the processing speed with the laser. Point contact structures with junction depths  $> 8 \mu\text{m}$  were also demonstrated, which could allow the simple fabrication of localised heavily doped contacts for PERL cells. Localised deep and heavily-diffused regions were implemented into a Pluto-PERL cell structure in pilot production, resulting in a record efficiency of 20.3 %.

To gain an improved understanding of deep junction formation, modelling is required for the resultant dopant profiles from the laser doping process. This could allow further improvements to dopant profiles for contact formation.

## 4.2 Modelling Diffusion in Laser-Doped Regions

The diffusion of impurities plays an important role in crystalline silicon photovoltaics. Diffusion of undesired metal atoms in the silicon such as copper, gold and iron can have devastating effects on the performance of such devices due to the introduction of energy levels near the middle of the band-gap [Conw 58; Istr 03; Sze 07; Sze 68]. On the other hand, diffusion processes are commonly used to intentionally incorporate dopants into the silicon lattice to create a p-n junction, allowing the collection of minority carriers, and increasing the conductivity of the silicon. Such processes may occur in the solid state, as is typical for emitter formation, or in the liquid state when performing laser doping.

In order to understand these effects better, a model was developed to investigate the diffusion of dopants during the laser doping process, and the influence of the solid/liquid interface on the diffusion process.

### 4.2.1 Diffusion in Silicon

For photovoltaic devices, it is essential to form a p-n junction to allow the collection of light-generated minority carriers. This is typically achieved using thermal diffusions. These diffusions can involve a single diffusion/drive-in step, or a two-step process in which after an initial process that introduces dopants into the silicon, the dopant source is removed and a drive-in step is performed. In two-step processes, it is often assumed that all dopants incorporated into the silicon within a unit area of the surface ( $Q$ ) prior to the drive-in step are located at the surface of the silicon. Subsequently, during the drive-in step, the doping concentration ( $C_{(z,t)}$ ) is given by a Gaussian function shown in Eq. 4.1 below, where  $D$  is the diffusion coefficient,  $t$  is the time and  $z$  is the distance from the surface of the silicon.

$$C_{(z,t)} = \frac{Q}{\sqrt{\pi Dt}} e^{-\frac{z^2}{4Dt}} \quad (4.1)$$

Diffusion coefficients greatly depend on temperature, impurities and the state which the diffusion process occurs in. Fig. 4.7 shows theoretical dopant profiles assuming a fixed  $Q$  value of  $1 \times 10^{21}/\text{cm}^2$  with various characteristic diffusion lengths ( $L_D$ ), given as  $2\sqrt{Dt}$ . The characteristics of all curves show a more rapid reduction in dopant concentration with increasing depth into the silicon due to the diffusion process being driven by concentration gradients. Given the nature of Eq. 4.1, enhancements in the  $L_D$  of impurities may be achieved by increasing time for the diffusion process, or increasing the diffusion coefficient by either increasing the temperature of the diffusion or by selecting an appropriate dopant.

Table 4.2 shows the diffusion coefficients of various impurities common in crystalline silicon solar cells. It should be noted that the diffusion coefficients in the liquid phase at the melting point of silicon (1414 °C) are substantially higher than that in the solid phase, even when approaching the melting temperature. For example the diffusion coefficient of boron in liquid silicon is approximately eight orders of magnitude higher than that of boron in solid silicon. Furthermore, by reducing the temperature to approximately 980 °C, the diffusion coefficient of silicon reduces an extra two orders of magnitude. Subsequently, by performing diffusions in the liquid state, as occurs during laser doping, diffusion processes which may take several hours to perform at conventional diffusion

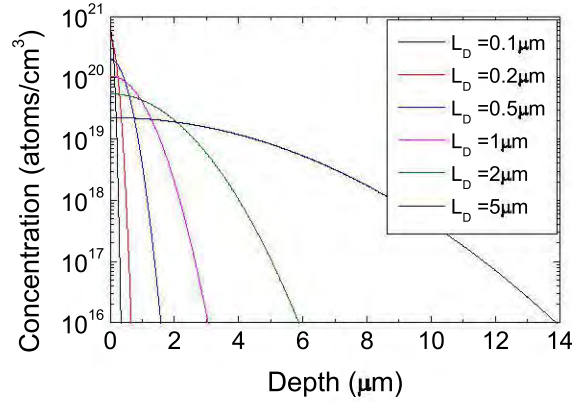


Figure 4.7: Theoretical Gaussian diffusion profiles for a  $Q = 1 \times 10^{21} / \text{cm}^2$ , highlighting the effect of the characteristic diffusion lengths ( $L_D = 2\sqrt{Dt}$ ) on the resultant dopant profile.

temperatures between 800 °C – 1000 °C for solid state diffusions, can take place in the order of microseconds. It should also be noted that the diffusion coefficients between different elements in the liquid state are much more uniform with less than two orders of magnitude variation, compared to more than five orders of magnitude variation in the solid state at 1393 °C. A temperature dependence also exists for the diffusion coefficients of impurities in liquid silicon, however the differences in diffusivity for impurities in liquid silicon are much smaller than that in the solid state [Tang 09].

Due to the large range in laser parameters used for laser doping, significant variations in the resultant dopant profiles have been reported in the literature. For example, using pulse-lengths between 10 ns – 25 ns with a pulse spacing of 1.4 μm for a 60 μm beam diameter gives a total illumination time ranging from 430 ns – 1.1 μs. The resultant doping profile approximated a Gaussian curve with a junction depth of 1 μm [Fell 11]. Sugianto *et al.* 2010 have demonstrated junction depths of up to 4 μm yielding typical Gaussian distributions using a CW laser with a phosphorus dopant source for illumination times of up to 5 μs [Sugi 10].

In contrast, uniform doping profiles with junction depths of 0.2 μm have been demonstrated using multiple pulses each with a duration of 10 ns to take the total illumination time to over 1 μs [Wong 93]. Such uniform dopant profiles have been assumed for deeper laser-doped regions when

Table 4.2: Diffusion coefficients of impurities in liquid silicon ( $D_l$ ) at the melting temperature of silicon (1414 °C) and in solid silicon ( $D_s$ ) near the melting temperature (1393 °C) and at a reduced temperature of 977 °C highlighting substantial differences in  $D$  of impurities common in diffusion processes for solar cells.

Impurity	$D_l$ at 1414 °C (cm <sup>2</sup> /s)	$D_s$ at 1393 °C (cm <sup>2</sup> /s)	$D_s$ at 977 °C (cm <sup>2</sup> /s)	References
Al	$6.8 \times 10^{-4}$	$3.6 \times 10^{-6}$	$1.1 \times 10^{-9}$	[Tang 09]
P	$5.7 \times 10^{-4}$	$3.3 \times 10^{-7}$	$1.2 \times 10^{-10}$	[Tang 09]
Ga	$3.6 \times 10^{-4}$	$2.7 \times 10^{-11}$	$4.1 \times 10^{-14}$	[Gara 07; Tang 09]
As	$2 \times 10^{-4}$	$3.0 \times 10^{-12}$	$4.1 \times 10^{-15}$	[Tang 09]
B	$1.2 \times 10^{-4}$	$8.6 \times 10^{-12}$	$7.4 \times 10^{-14}$	[Tang 09]
Cu	$8.1 \times 10^{-5}$	$2.7 \times 10^{-5}$	$1.6 \times 10^{-6}$	[Tang 09]
Fe	$3 \times 10^{-5}$	$1.1 \times 10^{-5}$	$2.5 \times 10^{-6}$	[Tang 09]
Ni	$3.8 \times 10^{-5}$	—	—	[Tang 09]

the silicon remains molten for periods in the order of 10  $\mu$ s [Wang 11]. However this assumption is not necessarily correct. Dopant profiles are dependent on the diffusion coefficient and the time the silicon remains molten for, which varies across the width of the laser-doped line and with the depth of the molten region. For sufficiently deep molten regions, diffusion profiles resemble Gaussian profiles [Hall 13d; Grov 67]. It is only when the characteristic diffusion length is long enough to enable dopants to reach the solid/liquid interface, that the dopants start to create a more box-like diffusion profile, due to the diffusion coefficients being orders of magnitude lower in the solid state and hence not able to penetrate further into the silicon [Tang 09].

For a given impurity, the resultant dopant profile after a diffusion greatly depends on the duration of the process. Fig. 4.8(a) shows the time required to obtain a ratio between the phosphorus concentration ( $C_{(z,t)}$ ) at a given depth ( $z$ ) from the silicon surface and the phosphorus concentration



at the surface ( $C_{(S,t)}$ ) (assuming Eq. 4.1 and neglecting changes to the diffusion process which occur around the solid/liquid interface). It is observed that for silicon at a depth of 1  $\mu\text{m}$  to have a concentration one order of magnitude lower than that of the surface requires a duration of 1  $\mu\text{s}$ , whilst for silicon at a depth of 10  $\mu\text{m}$ , approximately 100  $\mu\text{s}$  is required. The more general case related to the characteristic diffusion length ( $2\sqrt{Dt}$ ) is shown in Fig. 4.8(b), with the equation shown in Eq. 4.2 below. Hence, in order to have at least one order of magnitude variation between the concentration at the surface and a given depth, the depth must be at least twice the  $L_D$ , whilst for depths less than half the  $L_D$ , the concentration is essentially the same as that at the surface. Therefore, neglecting interactions of dopants at the solid/liquid interface, for a laser-doped region to exhibit a Gaussian-like profile, the depth of the molten region should be at least twice the  $L_D$ .

$$\frac{C_{(z,t)}}{C_{(S,t)}} = e^{-\frac{z^2}{4Dt}} \quad (4.2)$$

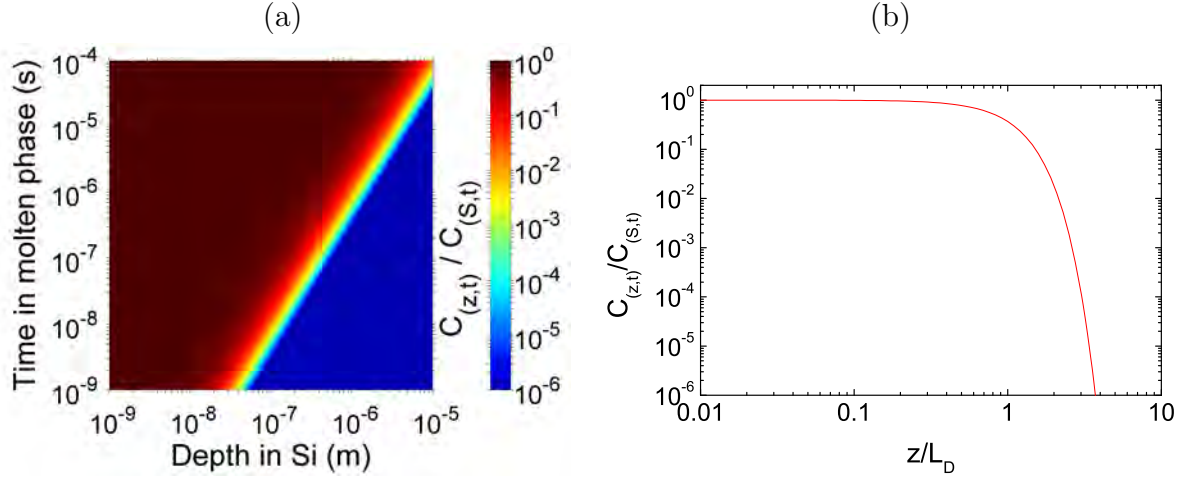


Figure 4.8: Ratio of the dopant concentration at depth  $z$  ( $C_{(z,t)}$ ) to that at the surface ( $C_{(s,t)}$ ) for (a) phosphorus as a function of the depth and the time of the diffusion process, and (b) an arbitrary dopant as a function of the ratio between the depth  $z$  and characteristic diffusion length ( $L_D$ ), highlighting the effect of  $L_D$  on the resultant dopant profile. For simplicity any values of  $C_{(z,t)}/C_{(s,t)}$  below  $1 \times 10^{-6}$  are shown as  $1 \times 10^{-6}$ .

#### 4.2.1.1 Simple Gaussian Modelling of SIMS Profiles

**High speed dopant profiles:** For the phosphorus diffusion profiles in Fig. 4.6(a) from a CW laser, Gaussian diffusion theory was able to closely approximate the diffusion profile for high processing speeds of 2 m/s – 10 m/s, although slightly higher concentrations were observed in the mid-range depths of each profile than a pure Gaussian profile (see Fig. 4.9). In addition, larger discrepancies were observed for slower processing speeds. Due to the SIMS profiles being obtained on laser-doped boxes formed by overlapping laser-doped lines, the effective time for which the silicon was molten may be increased over that experienced for a single line. In this image, modelling assumed a single time-step with an effective spot size ranging between 28 – 35  $\mu\text{m}$  at the correct scan speed, with no lateral or vertical variation in the time for which the silicon remained molten during the laser doping process. Furthermore, the  $Q$  value was adjusted for each processing speed to conserve the total number of dopants obtained from SIMS analysis of the respective samples, with

the values given in Table 4.3. The increasing  $Q$  values for decreasing processing speeds suggested a more effective incorporation of the dopants into the silicon with reduced processing speed, which would favour the creation of a heavily doped region underneath the metal contacts which can shield against recombination.

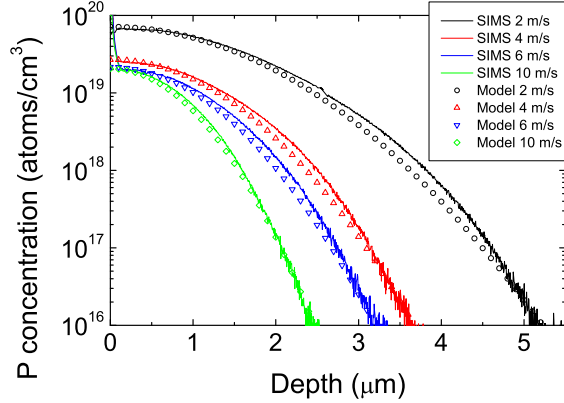


Figure 4.9: SIMS profiles as shown in Fig. 4.6 and modelled Gaussian profiles for phosphorus (P) laser doping at various processing speeds for a 532 nm CW laser displaying Gaussian-like diffusion profiles. Effective spot sizes and  $Q$  values are given in Table 4.3.

**Low speed dopant profiles:** Whilst doping profiles obtained at higher speeds closely match Gaussian diffusion theory, the profiles of samples processed at a reduced speed of 0.5 m/s for both phosphorus and boron displayed a substantial deviation from theoretical Gaussian diffusions, with the actual dopant concentration measured using SIMS at mid range depths (4–8  $\mu\text{m}$  for phosphorus and 5 – 10  $\mu\text{m}$  for boron) being substantially higher and more uniform than that of a Gaussian profile (see Fig. 4.10). A distinct kink was evident in both SIMS profiles, before a sharper decay in dopant concentration at the larger depths.

Even though the diffusion coefficient of boron is smaller than that of phosphorus, the dopant profile for boron was deeper than that of phosphorus. This may be due to a number of factors such as: a larger number of passes over the laser-doped region for boron; slight increases to the power of

the laser after re-alignment of the beam in the laser system; differences in the optical properties of the wafers, dielectrics and dopant source and subsequent interactions with the laser beam; and/or differences between the theoretical and actual diffusion coefficient of boron.

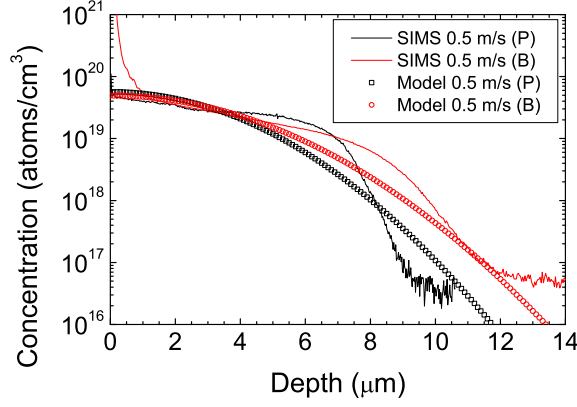


Figure 4.10: SIMS profiles as shown in Fig. 4.6 and modelled Gaussian profiles for phosphorus (P) and boron (B) laser doping at 0.5 m/s using a 532 nm CW laser showing a large deviation from Gaussian profiles. Effective spot sizes and  $Q$  values are given in Table 4.3.

**Q-CW or CW laser doping:** Deep junctions were demonstrated in Section 4.1 using both CW and Q-CW lasers. Fig. 4.11 shows a comparison between SIMS profiles from Fig. 4.6(c) for laser doping at 2 m/s using either a CW or Q-CW laser, and a theoretical Gaussian diffusion profile for the CW laser. Due to the similar  $Q$  values of the CW and Q-CW SIMS profiles, only the theoretical profile for the CW laser is shown. It was observed that whilst the profile from the CW laser closely matches the theoretical profile, the profile from the Q-CW laser deviated from the theoretical profile, again with higher concentrations in the mid-range depths, a distinct kink, and a sharper decay at larger depths with a shallower junction depth than expected. A hypothetical Gaussian diffusion profile is also shown for the Q-CW laser assuming the same 28  $\mu\text{m}$  effective spot size, and 1120 pulses each of 60 ps duration delivered over the 14  $\mu\text{s}$  time for which the area is potentially illuminated by the laser. Furthermore, for the 60 ps duration of each pulse the silicon was assumed to be molten sufficiently deep such that the resultant dopant profile is unaffected

by the solid/liquid interface and completely solidifies immediately after each pulse, hence giving a total diffusion time of approximately 67 ns. As shown, for the same  $Q$  value this would only result in a junction depth of 0.4  $\mu\text{m}$ . Hence it is clear that the pulses of the Q-CW laser do indeed interact together to greatly enhance the time for which the silicon remains molten.

The reduced junction depth and larger deviation from a pure Gaussian profile for the Q-CW laser would suggest a stronger influence of the solid/liquid interface in determining the resultant dopant profile than that for a pure CW laser. The sharp decrease in dopant concentration at the larger depths of the Q-CW profile is typical of a shortened  $L_D$ , presumably due to a reduced duration in the molten phase at these larger depths. In addition, increases in the dopant concentrations in the mid-range depths would suggest that the solid/liquid interface is limiting the diffusion of dopants at certain times during the laser doping process. This may be due to a certain amount of energy being lost from the molten region between successive pulses, resulting in the solidification of the deepest molten regions, and hence reducing the time for which the diffusion process occurs at such depths and therefore the junction depth. This may also reduce the maximum melt depth of the silicon compared to that possible for a pure CW laser, further reducing the junction depth.

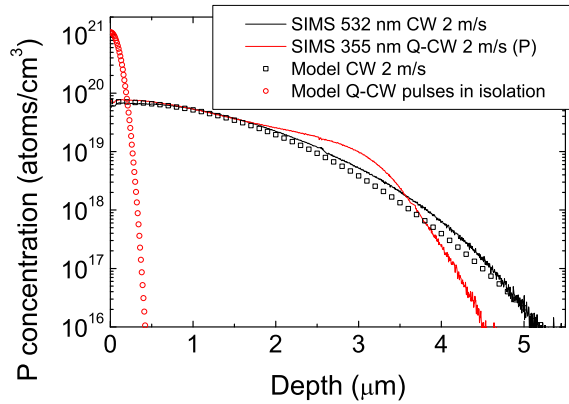


Figure 4.11: SIMS profiles as shown in Fig. 4.6 and modelled Gaussian profiles for phosphorus (P) laser doping at 2 m/s for a 532 nm CW and 355 nm mode-locked UV Q-CW laser highlighting similar junction depths but very different dopant profiles. Effective spot sizes and  $Q$  values are given in Table 4.3.

**Gaussian diffusion in the largest depths of molten silicon:** In Fig. 4.12, hypothetical Gaussian diffusion profiles were seeded from within the silicon to model the diffusion at larger depths for the laser-doped profiles of phosphorus and boron at 0.5 m/s using a CW laser and phosphorus laser doping at 2 m/s using a Q-CW laser, which could not be modelled by a single Gaussian diffusion profile over the entire dopant profile. For these profiles, a reduced effective spot size was assumed to represent the reduced time which the silicon remains molten for, with the  $Q$  value, effective spot size and depth which the Gaussian diffusion profile was seeded from (see Table 4.3). It was observed that excellent agreement could be obtained between the dopant profiles obtained from SIMS and the modified Gaussian profile for the deepest regions of the respective SIMS profile. This suggests that for such laser processing conditions, a Gaussian diffusion process is taking place, but another factor, such as the influence of a solid/liquid interface, is resulting in the SIMS profiles showing a substantial deviation from a Gaussian diffusion profile.

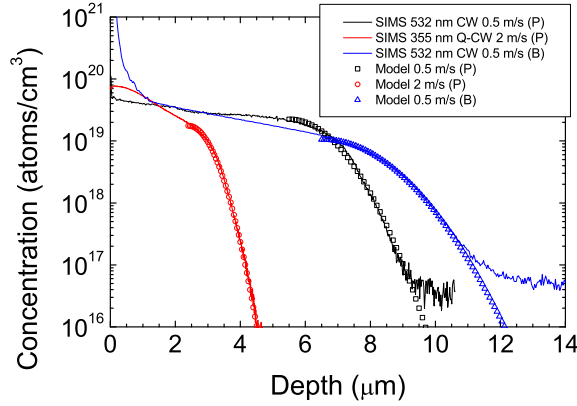


Figure 4.12: SIMS profiles as shown in Fig. 4.6 and modelled Gaussian profiles for phosphorus (P) and boron (B) laser doping at 0.5 m/s using a 532 nm CW laser and P laser doping at 2 m/s for a 355 nm mode-locked UV Q-CW laser in the deepest laser-doped regions. Effective spot sizes and  $Q$  values are given in Table 4.3.

A summary of the values used to model the diffusion profiles in this section for Fig. 4.9 - Fig. 4.12 is shown in Table 4.3.

Table 4.3: Total number of dopants within the laser-doped region ( $Q$ ) from SIMS profiles shown in Fig. 4.9-Fig. 4.12 for various laser doping processes for phosphorus (P) and boron (B) along with the effective spot of the modelled Gaussian diffusion. For laser processes highlighted in red, the dopant profile at the larger depth was modelled starting from a different depth ( $z$ ) in the silicon and using a different  $Q$  value and effective spot size.

Laser	Speed (m/s)	$Q$ (/cm <sup>2</sup> )	Effective spot size ( $\mu\text{m}$ )
532 nm CW (P)	0.5	$2.04 \times 10^{16}$	35
532 nm CW (P)	0.5	$3 \times 10^{13}$	5 seeded at $z = 5.5 \mu\text{m}$
532 nm CW (B)	0.5	$2.03 \times 10^{16}$	220
532 nm CW (B)	0.5	$2 \times 10^{13}$	47.5 seeded at $z = 6.5 \mu\text{m}$
532 nm CW (P)	2	$1.14 \times 10^{16}$	28
355 nm Q-CW (P)	2	$1.26 \times 10^{16}$	28
355 nm Q-CW (P)	2	$1.2 \times 10^{13}$	5.2 seeded at $z = 2.4 \mu\text{m}$
1120 $\times$ 60 ps pulses (P)	N/A	$1.26 \times 10^{16}$	N/A
532 nm CW (P)	4	$3.25 \times 10^{15}$	31
532 nm CW (P)	6	$2.31 \times 10^{15}$	35
532 nm CW (P)	10	$1.73 \times 10^{15}$	35

---

**Summary of a simple Gaussian model of SIMS profiles:** A simple Gaussian model was able to describe laser doped profiles processed at speeds  $> 2$  m/s reasonably well. For slower speeds, no such agreement was obtained with Gaussian diffusion theory. The increasing discrepancy for reducing processing speeds and Gaussian-like profiles at larger depths for dopant profiles processed at slow speeds could suggest a stronger influence of the solid/liquid interface in determining the resultant dopant profile.

#### 4.2.1.2 Advanced Modelling of SIMS Profiles

In this section, an advanced model was developed to incorporate the influence of a solid liquid interface on the dopant profiles and investigate the discrepancies of the SIMS profiles of dopant profiles processed at high speeds, to theoretical Gaussian diffusion profiles.

Whilst the lasers used in this work had a spot size of approximately  $20\text{ }\mu\text{m}$  diameter at the  $1/e^2$  intensity, thermal conduction greatly increased the diameter and volume of the molten region. As a first approximation, the shape of the molten region can be assumed to be similar to that of the junction profile. Due to the Gaussian beam profile, the profile of the molten region was also assumed to be approximately symmetrical in the  $x - y$  plane, where  $x$  is the direction along the wafer surface perpendicular to the direction of scanning of the laser beam,  $y$  is the direction along the wafer surface parallel to the direction of scanning of the laser beam and  $z$  is the depth into the silicon, as shown in Fig. 4.13.

Approximate cross sectional junction profiles based on the EBIC measurements from Fig. 4.2-4.3 were estimated as shown in Fig. 4.14. The profiles were assumed to have the general form of Eq. 4.3 where  $z_J$  is the localised junction depth,  $x$  is the distance from the central axis of the laser beam and  $a_1$ ,  $a_2$  and  $a_3$  are constants, the values of which are given in Table 4.4 for the various laser speeds ( $v$ ). It was observed that no increase in junction depth occurred for speeds below 0.2 m/s suggesting that for such speeds, despite the additional energy being supplied to the molten region, no further enhancement to the volume of the molten region were obtained. Furthermore, for such speeds dopants had diffused in sufficient quantities to the solid/liquid interface. Subsequently, the time which the silicon remains molten for at each depth along the  $x = 0$  axis could be obtained



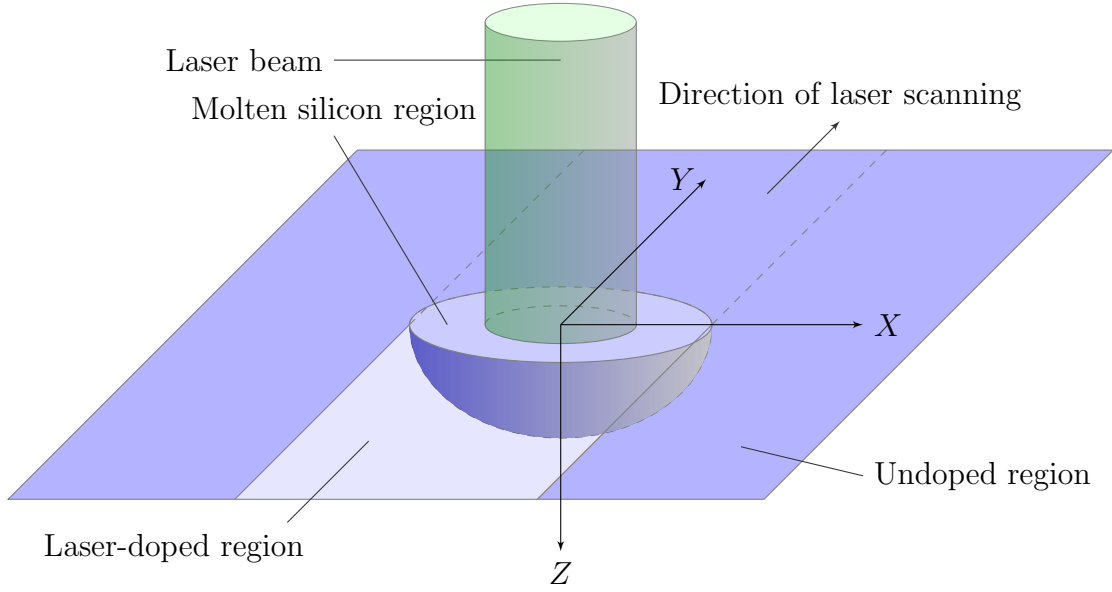


Figure 4.13: Diagrammatic representation of a laser-doped region.

from the cross sectional junction profiles through the simple relationship in Eq. 4.4, where  $t$  is the time and  $v$  is the velocity of the laser scan. For high processing speeds yielding Gaussian like diffusion profiles, it is expected that the depth of the molten region was deeper than the maximum junction depth, with the solid/liquid interface only exerting a small influence on the doping profiles at larger depths. For such speeds, the depth of the molten region may simply be stretched from the junction depth by a depth factor ( $Z_F$ ) as shown in Eq. 4.5. Similarly, due to the laser-doped area potentially being exposed to multiple passes, a time dilation factor ( $T_F$ ) was also introduced.

$$z_J = a_1 x^4 + a_2 x^2 + a_3 \quad (4.3)$$

$$t = \frac{y \cdot T_F}{v} \quad (4.4)$$

$$z_M = z_J \cdot Z_F \quad (4.5)$$

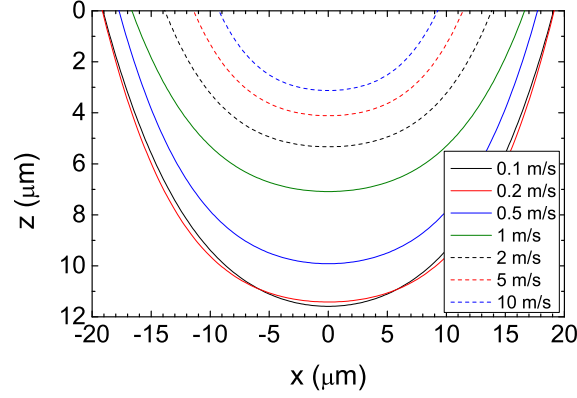


Figure 4.14: Cross sectional junction profiles of laser-doped regions extracted from the combined SEM/EBIC images in Fig. 4.2-4.3

Table 4.4: Values of  $a_i$  for Eq. 4.3 for the junction profile of various laser processing speeds shown in Fig. 4.14.

Speed (m/s)	$a_1$	$a_2$	$a_3$
0.1	$-3.696 \times 10^{-5}$	$-1.836 \times 10^{-2}$	$1.159 \times 10^1$
0.2	$-4.996 \times 10^{-5}$	$-1.293 \times 10^{-2}$	$1.142 \times 10^1$
0.5	$-5.097 \times 10^{-5}$	$-1.555 \times 10^{-2}$	$9.917 \times 10^0$
1	$-4.407 \times 10^{-5}$	$-1.343 \times 10^{-2}$	$7.087 \times 10^0$
2	$-7.477 \times 10^{-5}$	$-1.352 \times 10^{-2}$	$5.331 \times 10^0$
5	$-1.185 \times 10^{-4}$	$-1.622 \times 10^{-2}$	$4.113 \times 10^0$
10	$-1.942 \times 10^{-4}$	$-1.975 \times 10^{-2}$	$3.126 \times 10^0$

**Development and verification of a Gaussian diffusion time-step model:** To create an enhanced model for the Gaussian diffusion process, a time-step model was developed in MATLAB, by seeding Gaussian profiles from each element in silicon at each time-step. At time  $t = 0$ , a total number of phosphorus atoms ( $Q = 3.25 \times 10^{15} / \text{cm}^2$ ) is introduced into the element of silicon a sufficient distance from the surface with a depth of  $z_\alpha = 5 \text{ } \mu\text{m}$  with thickness  $\Delta z = 1 \times 10^{-8} \text{ m}$  to result in an initial phosphorus concentration of  $C_{(z=z_\alpha, t=0)} = 3.25 \times 10^{21} / \text{cm}^3$ . Assuming the diffusion process takes place over a duration of  $2 \text{ } \mu\text{s}$ , with the silicon molten to a depth of  $10 \text{ } \mu\text{m}$  for the entire process, at the  $j^{\text{th}}$  time-step ( $t_j$ ), the Gaussian profile seeded from the  $k^{\text{th}}$  silicon element ( $z_k$ ) is given by  $\delta C_{(k,z,t_j)}$  in Eq. 4.6, where  $C_{(z_k,t_j)}$  is the concentration of dopants in the  $k^{\text{th}}$  element of silicon at the beginning of the  $j^{\text{th}}$  time-step. Subsequently at the  $(j+1)^{\text{th}}$  time-step ( $t_{j+1}$ ), the new concentration for the  $i^{\text{th}}$  element of silicon ( $C_{(z_i,t_{j+1})}$ ) in the absence of any solid/liquid interface is given by Eq. 4.7, where  $N_z$  is the number of elements of silicon, each of thickness  $\Delta z$  and each time-step of duration  $\Delta t$ .

$$\delta C_{(k,z,t_j)} = \frac{C_{(z_k,t_j)} \Delta z}{2\sqrt{\pi D \Delta t}} e^{-\frac{(z-z_k)^2}{4D \Delta t}} \quad (4.6)$$

$$C_{(z_i,t_{j+1})} = \sum_{k=1}^{N_z} \delta C_{(k,z_i,t_j)} \quad (4.7)$$

The superposition approximation allowed for the time-step model to be created to simulate the complex process of laser doping. As shown in Fig. 4.15, in the absence of any solid/liquid interface or boundary excellent agreement was observed between a single theoretical Gaussian profile seeded at time  $t=0$  for the  $2 \text{ } \mu\text{s}$  duration, to that of the simple model with the superposition of Gaussian profiles seeded from each element of silicon for each time-step.

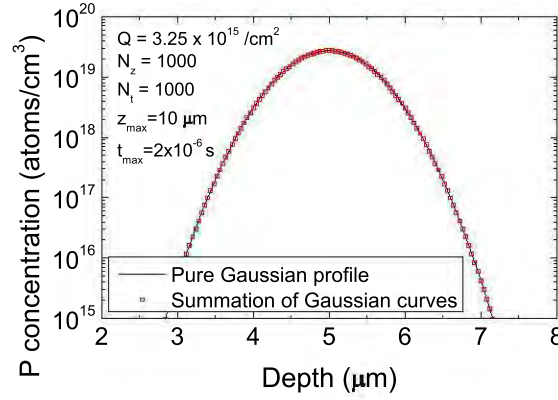


Figure 4.15: Simulated profile for a pure Gaussian profile seeded from a depth of 5  $\mu\text{m}$  over a single time-step compared to that of Gaussian profiles seeded from each element of silicon for each time-step in the absence of a solid/liquid interface demonstrating excellent agreement.

**Modelling the influence of a solid/liquid interface:** To develop a realistic model of the junction depth through laser doping, a potential influence of the solid/liquid interface on the diffusion process was incorporated.

The interactions of dopants within close proximity to boundaries are unclear, and hence the three alternative models (A, B and C) were developed to include interactions around the solid/liquid interface, with slightly different assumptions based on the conservation of dopants at each time-step. For all three models, assuming an air/silicon boundary at  $z = 0$ , a solid/liquid interface is introduced in the silicon, and Eq. 4.6 is replaced by Eq. 4.8 where  $L_{(z,t_j)}=1$  for any element of silicon at time  $t_j$  which is liquid and 0 otherwise. Hence  $\delta C_{(k,z,t_j)}=0$  for all  $z$  whereby the  $k^{th}$  element of silicon is solid, and is locally reduced to 0 for an element of silicon which is solid (see Eq. 4.9), where  $Z_{L(t_j)}$  includes all elements of liquid silicon and  $Z_{S(t_j)}$  includes all elements of solid silicon at time  $t_j$ . In addition,  $Z_{I(t_j)}$  includes the elements of silicon which are the last elements of liquid silicon before either a boundary or solid silicon element, and hence the two silicon elements at the end of the  $Z_{L(t_j)}$  domain.

$$\delta C_{(k,z,t_j)} = L_{(z_k,t_j)} \cdot L_{(z,t_j)} \cdot \frac{C_{(z_k,t_j)} \Delta z}{2\sqrt{\pi D \Delta t}} e^{-\frac{(z-z_k)^2}{4D\Delta t}} \quad (4.8)$$

$$L_{(z,t_j)} = \begin{cases} 1 & \forall z : z \in Z_{L(t_j)} \\ 0 & \forall z : z \in Z_{S(t_j)} \end{cases} \quad (4.9)$$

**Model A:** For Model A, Eq. 4.7 is replaced by Eq. 4.10 through the introduction of a symmetric linear scaling factor ( $\alpha_{(k,t_j)}$ ) to conserve the number of dopants in the Gaussian curve seeded from the  $k^{th}$  silicon element at time  $t_j$  (see Eq. 4.11-4.11). Hence for each Gaussian profile seeded, a net movement of dopants away from the solid/liquid and air/liquid interfaces results.

$$C_{(z_i,t_{j+1})} = \alpha_{(k,t_j)} \cdot \sum_{k=1}^{N_z} \delta C_{(k,z_i,t_j)} \quad (4.10)$$

$$\alpha_{(k,t_j)} = \begin{cases} 0 & \forall k : \sum_{i=1}^{N_z} \delta C_{(k,z_i,t_j)} = 0 \\ \frac{C_{(z_k,t_j)}}{\sum_{i=1}^{N_z} \delta C_{(k,z_i,t_j)}} & \text{otherwise} \end{cases} \quad (4.11)$$

**Model B:** For Model B, Eq. 4.7 was replaced by Eq. 4.12 through the introduction of an asymmetric linear scaling factor ( $\beta_{(k,z_i,t_j)}$ ) to conserve the number of dopants in the Gaussian curve seeded from the  $k^{th}$  silicon element at time  $t_j$  (see Eq. 4.12-4.15). In these equations,  $\beta_{l(k,t_j)}$  and  $\beta_{u(k,t_j)}$  are the scaling factors for depths on the lower and upper side of  $z_k$  respectively. For the case where the Gaussian profile is seeded from  $Z_{I(t_j)}$ ,  $\beta_{(k,z_i,t_j)}$  collapses to the symmetric linear scaling factor ( $\alpha_{(k,t_j)}$ ) as shown previously in Eq. 4.11. Hence apart from Gaussian profiles seeded from  $Z_{I(t_j)}$ , Model B equalises the movement of dopants either side of the seed location for each Gaussian profile.

$$C_{(z_i, t_{j+1})} = \sum_{k=1}^{N_z} \beta_{(k, z_i, t_j)} \cdot \delta C_{(k, z_i, t_j)} \quad (4.12)$$

$$\beta_{(k, z_i, t_j)} = \begin{cases} 0 & \forall k : \sigma_{\delta C(k, t_j)} = 0 \\ \alpha_{(k, t_j)} & \forall k : z_k \in Z_{I(t_j)} \\ \beta_{l(k, t_j)} & \forall i : (i < k) \cap (z_i \in Z_{L(t_j)}) \\ \beta_{u(k, t_j)} & \forall i : (i > k) \cap (z_i \in Z_{L(t_j)}) \\ \frac{1}{2} (\beta_{l(k, t_j)} + \beta_{u(k, t_j)}) & \forall i : (i = k) \cap (z_i \notin Z_{I(t_j)}) \end{cases} \quad (4.13)$$

$$\beta_{l(k, t_j)} = \begin{cases} 0 & \forall k : \delta C_{(k, z_k, t_j)} + 2 \cdot \sum_{i=1}^{k-1} \delta C_{(k, z_i, t_j)} = 0 \\ \frac{C_{(z_k, t_j)}}{\delta C_{(k, z_k, t_j)} + 2 \cdot \sum_{i=1}^{k-1} \delta C_{(k, z_i, t_j)}} & \text{otherwise} \end{cases} \quad (4.14)$$

$$\beta_{u(k, t_j)} = \begin{cases} 0 & \forall k : \delta C_{(k, z_k, t_j)} + 2 \cdot \sum_{i=k+1}^{N_z} \delta C_{(k, z_i, t_j)} = 0 \\ \frac{C_{(z_k, t_j)}}{\delta C_{(k, z_k, t_j)} + 2 \cdot \sum_{i=k+1}^{N_z} \delta C_{(k, z_i, t_j)}} & \text{otherwise} \end{cases} \quad (4.15)$$

**Model C:** For Model C, Eq. 4.7 was replaced by Eq. 4.16 through the introduction of an asymmetric linear excess concentration increase ( $\gamma_{(k, z_i, t_j)}$ ) to conserve the number of dopants in the Gaussian curve seeded from the  $k^{th}$  silicon element at time  $t_j$  (see Eq. 4.16-4.20). Hence in Model C, excess dopants from either side, which in the absence of the solid/liquid interface would fall into the actual solid silicon, are redistributed throughout the liquid silicon elements on the given side of the seeded Gaussian profile. In these equations,  $\lambda_{(k, t_j)}$  is a correction factor for the case where the Gaussian curve is seeded from a boundary or interface. In these equations,  $\gamma_{l(k, z_i, t_j)}$  and  $\gamma_{u(k, z_i, t_j)}$  represent the excess dopants on either side of the seed location when the curve is seeded from a silicon element other than at a boundary or interface.

$$C_{(z_i, t_{j+1})} = \sum_{k=1}^{N_z} \left( \lambda_{(k, t_j)} \cdot \delta C_{(k, z_i, t_j)} + \gamma_{(k, z, t_j)} \right) \quad (4.16)$$

$$\lambda_{(k, t_j)} = \begin{cases} 2 & \forall k : z_k \in Z_{I(t_j)} \\ 1 & \text{otherwise} \end{cases} \quad (4.17)$$

$$\gamma_{(k, z, t_j)} = \begin{cases} \frac{C_{(z_k, t_j)} - \lambda_{(k, t_j)} \cdot \sum_{i=1}^{N_z} \delta C_{(k, z_i, t_j)}}{\sum_{i=1}^{N_z} L_{(z_i, t_j)}} \cdot L_{(z, t_j)} & \forall k : \left( \sum_{i=1}^{N_z} L_{(z_i, t_j)} \neq 0 \right) \cap \left( z_k \in Z_{I(t_j)} \right) \\ 0 & \forall k : \sum_{i=1}^{N_z} L_{(z_i, t_j)} = 0 \\ \gamma_l(k, z, t_j) + \gamma_u(k, z, t_j) & \text{otherwise} \end{cases} \quad (4.18)$$

$$\gamma_l(k, z, t_j) = \begin{cases} 0 & \forall k : \sum_{i=1}^k L_{(z_i, t_j)} = 0 \\ \frac{\frac{1}{2} C_{(z_k, t_j)} - \lambda_{(k, t_j)} \cdot \sum_{i=1}^{k-1} \delta C_{(k, z_i, t_j)}}{\sum_{i=1}^k L_{(z_i, t_j)}} \cdot L_{(z, t_j)} & \text{otherwise} \end{cases} \quad (4.19)$$

$$\gamma_u(k, z, t_j) = \begin{cases} 0 & \forall k : \sum_{i=k}^{N_z} L_{(z_i, t_j)} = 0 \\ \frac{\frac{1}{2} C_{(z_k, t_j)} - \lambda_{(k, t_j)} \cdot \sum_{i=k+1}^{N_z} \delta C_{(k, z_i, t_j)}}{\sum_{i=k}^{N_z} L_{(z_i, t_j)}} \cdot L_{(z, t_j)} & \text{otherwise} \end{cases} \quad (4.20)$$

**Predictions of Models A, B and C at the solid/liquid interface:** The simple model developed in the previous section which neglected any influence of a solid/liquid interface on the diffusion process had limited agreement with dopant profiles obtained from laser doped regions.

The predictions of Models A, B and C for a single time step are shown in Fig. 4.16(a), which highlight the different assumptions based on the conservation of dopants within the silicon. For these predictions, a single time-step of duration  $\Delta t = 2 \mu s$  of the model was used for a Gaussian curve seeded at a depth of  $2.3 \mu m$ , with the silicon only molten between depths of  $2 \mu m$  and  $3 \mu m$ . The black curve in this image indicates a pure Gaussian curve in the absence of a solid/liquid interface that continues into the solid silicon region (dashed line). The other curves show the modified Gaussian curves to reflect the potential influence of the solid/liquid interface of the three models yielding very different dopant distributions.

Similarly, Fig. 4.16(b) shows the resultant dopant profiles for dopants seeded at the silicon surface, after  $N_z = 1000$  time-steps of Models A, B and C, for a total duration of  $2 \mu s$  with a solid/liquid interface at a depth of  $z = 1.5 \mu m$ . For this image, the black curve indicates a pure Gaussian curve assuming a single time-step in the absence of a solid/liquid interface. A very good

agreement between the dopant profiles from all models with a pure Gaussian profile was observed over the majority of the dopant profile, however differences were apparent near the silicon surface and solid/liquid interface due to interactions of the dopants in the vicinity of the boundaries. Inset (i) shows a close-up of the dopant profiles at the surface and indicated a reduced dopant concentration for Model A, whilst Model B and Model C displayed a slightly higher dopant concentration than the pure Gaussian curve in the absence of a solid/liquid interface.

The depletion of dopants at the silicon surface for Model A was due to the net movement of dopants towards the centre of the laser-doped region from the use of a symmetric linear scaling factor to conserve the number of dopants. In contrast, through the use of asymmetric modifications to the Gaussian profiles, Model B and Model C ensured a higher retention of dopants around the boundary. Similarly, inset (ii) shows a close up of the dopant profiles around the solid/liquid interface with all models leading to increased concentrations compared to the pure Gaussian curve, again with Model A indicating a reduced concentration at the interface compared to Model B and Model C. Despite the depletion of dopants at the surface for Model A, the use of the symmetric linear scaling still resulted in an increase in dopant concentration near the solid/liquid interface in the silicon. Furthermore, Model B and Model C displayed an unrealistic increase in the dopant profiles in the very close vicinity of the silicon surface or the solid/liquid interface.

Given these findings, Model A was used for all subsequent models, as the model was a simpler computational model and results in a more realistic reduction in dopant concentration in close vicinity of the solid/liquid interface.



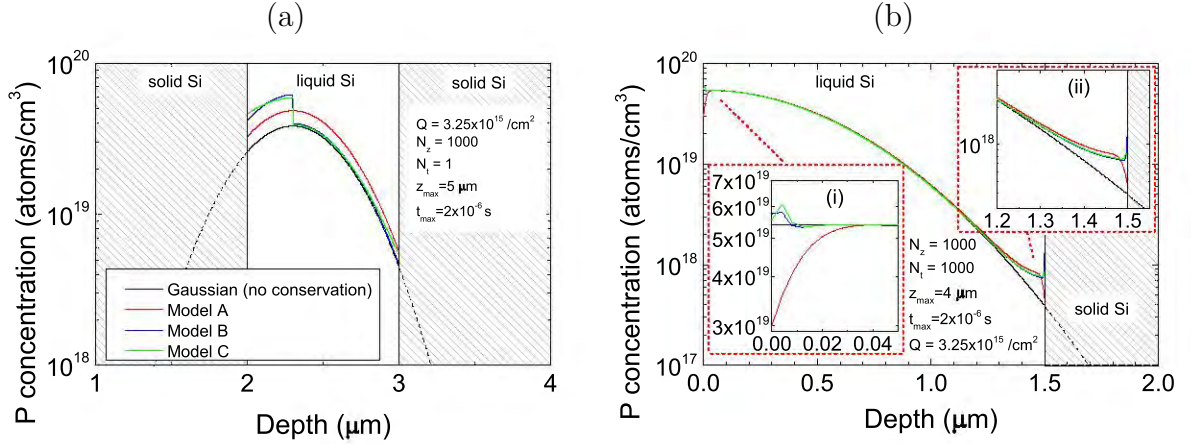


Figure 4.16: (a) Predictions from models A, B and C of a single time-step with the influence of a solid/liquid interface compared to a pure Gaussian curve in the absence of a solid/liquid interface with dopants seeded from at depth of 2.3  $\mu\text{m}$ . (b) Predictions of models A, B and C for 1000 time-steps with dopants seeded at the silicon surface showing general consensus between the influence of a solid/liquid interface on the dopant profile. Inset (i) shows a zoomed-in profile of the surface/liquid interface. Similarly, inset (ii) shows that for a solid/liquid interface at  $z = 1.5 \text{ μm}$ .

**Application of Model A to laser-doped SIMS profiles:** Changing the location of the solid/liquid interface throughout the laser doping process, could greatly influence the dopant profile. In Fig. 4.17 a SIMS profile of phosphorus laser doping at a process speed of 4 m/s is shown. In addition, various modelled profiles are shown with different  $Z_F$ , highlighting a profound influence of the time-dependent location of the solid/liquid interface on the dopant profile. For depths of up to approximately 1.5  $\mu\text{m}$ , the profiles of all models were essentially identical. However at the larger depths, decreasing the  $Z_F$  and hence reducing the melt depth had a greater influence on limiting the dopants ability to move further into the silicon, resulting in a sharper reduction in dopant concentration with increasing depth, and hence a reduced junction depth. It should be noted that as no EBIC images were obtained for a processing speeds of 4 m/s and 6 m/s, and no SIMS profile was measured for a speed of 5 m/s, the function for the solid/liquid interface of a sample processed

at 5 m/s was used to model to the SIMS profiles processed at 4 m/s and 6 m/s.

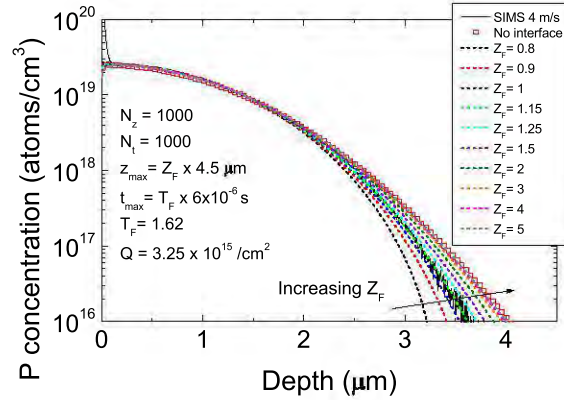


Figure 4.17: Predictions from Model A showing the influence of  $Z_F$  on the dopant profile for a SIMS profile of phosphorus laser doping at 4 m/s.

Including the influence of a solid/liquid interface allowed a more accurate representation of the measured dopant profiles to be obtained from the model. Fig. 4.18(a) shows predicted dopant profiles of various processing speeds for phosphorus laser doping with relevant modelling parameters given in Table 4.5. It was observed that the given model can accurately describe all dopant profiles measured by SIMS in this image with an enhanced reduction of the dopant concentrations at the larger depths due to the influence of the solid/liquid interface during the laser doping process. As a result, the junction depths were greatly reduced compared to that of a Gaussian profile in the absence of a solid/liquid interface as denoted by the dashed line of the respective colour. In Fig. 4.18(b), the influence of the  $Z_F$  is shown against the junction depth for each speed (assumed to be at  $N_D=1 \times 10^{16} /\text{cm}^3$ ). A substantial reduction in junction depth was observed for all profiles even when the maximum depth of the molten region throughout the laser doping process was twice the junction depth as observed in EBIC images. The reduction in junction depth was more pronounced for lower laser doping speeds due to the increased time for the diffusion process. It was observed that even for a time dependent solid/liquid interface which has a maximum depth of twice the junction depth observed in EBIC images, the solid/liquid interface can result in a substantial reduction in junction depth. The modelled diffusion profiles assuming no influence of the solid/liquid interface are shown by the dashed lines of the respective colours.

Table 4.5:  $T_F$  and  $Z_F$  values for the predictions shown in Fig. 4.18 for Model A.

Speed (m/s)	$Q$ (/cm <sup>2</sup> )	$t_{max}$ ( $\mu$ s)	$z_{max}$ ( $\mu$ m)	$T_F$	$Z_F$
2	$1.14 \times 10^{16}$	$T_F \times 14.5$	$Z_F \times 5.5$	1.2	1.29
4	$3.25 \times 10^{15}$	$T_F \times 6$	$Z_F \times 4.5$	1.62	1.1
6	$2.31 \times 10^{15}$	$T_F \times 4$	$Z_F \times 4.2$	1.8	1.29
10	$1.73 \times 10^{15}$	$T_F \times 1.9$	$Z_F \times 3.2$	2.15	1.2

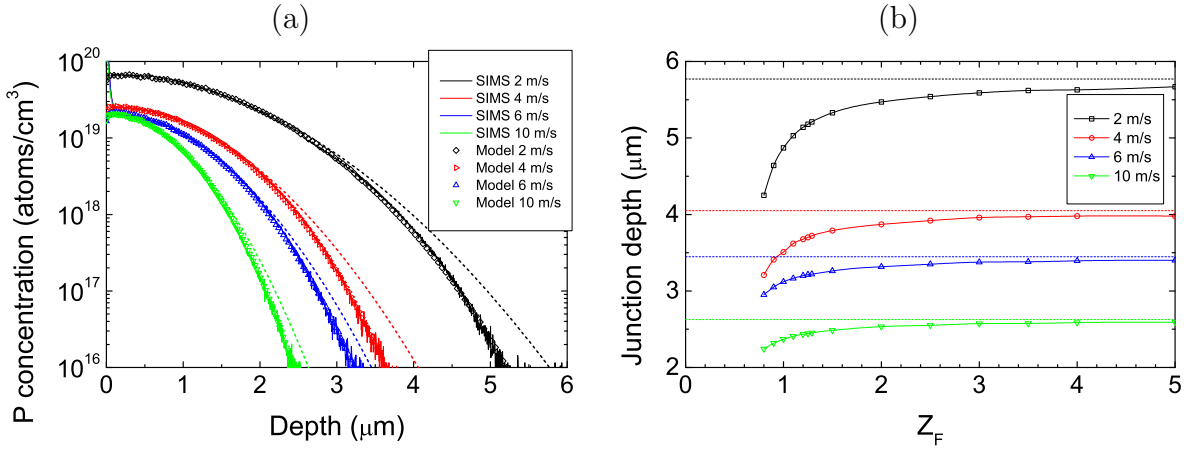


Figure 4.18: (a) Modelled diffusion profiles for various laser doping speeds of phosphorus laser doping showing excellent agreement and (b) junction depths (assumed to be at  $N_D=1 \times 10^{16}$  /cm<sup>3</sup>) for various  $Z_F$ . Relevant modelling parameters are shown in Table 4.5 unless stated otherwise in (b). All calculations were performed for  $N_Z=1000$  and  $N_T=1000$ . Dashed lines indicate the expected values in the absence of a solid/liquid interface.

The model predictions indicate that the solid/liquid interface has a profound influence on the resultant dopant profile for laser-doped regions with processing speeds of 2 – 10 m/s. However the

model should also be used to assess the influence of a solid/liquid interface of samples processed at slower speeds or using a Q-CW laser, which all displayed significant differences from theoretical Gaussian diffusion profiles.

**Partial solidification between successive pulses for Q-CW lasers:** Whilst the model could accurately describe the doping process for a CW laser with a processing speed of  $2 - 10$  m/s, using the same assumptions the model failed to show the characteristic kink in the SIMS profile introduced by the Q-CW laser. Even though the pulsing frequency is extremely high, due to the pulsed nature of the laser it is expected that a certain fraction of silicon within the molten region would resolidify between successive pulses. To model this, a modification was made to the time dependent melt depth throughout the laser doping process. In reality, variations would occur between each pulse and a very large number of time-steps and high spatial resolution would be required to accurately model the process. However to simplify the computational model, the laser process was simplified to have one effective pulse in which the duration of silicon in the molten phase at the larger depths was greatly reduced compared to that for the pure CW laser.

The depth at which the kink in the dopant profile occurs is thought to be due to a substantial reduction in time which the silicon remains molten for at depths larger than the given value, hence limiting the diffusion of dopants which can occur beyond this depth (see Fig. 4.19). Hence dopants start to increase in concentration around this depth, with little diffusion occurring beyond. As a result, the model shows a substantial reduction in the dopant concentration beyond this depth, and a greatly reduced junction depth compared to an identical system with no partial solidification of silicon between successive pulses. The model suggests that for the case of the Q-CW laser, the silicon was only molten to a depth of approximately  $5\text{ }\mu\text{m}$ , rather than  $7\text{ }\mu\text{m}$  when using a pure CW laser (see Fig. 4.19(b)).

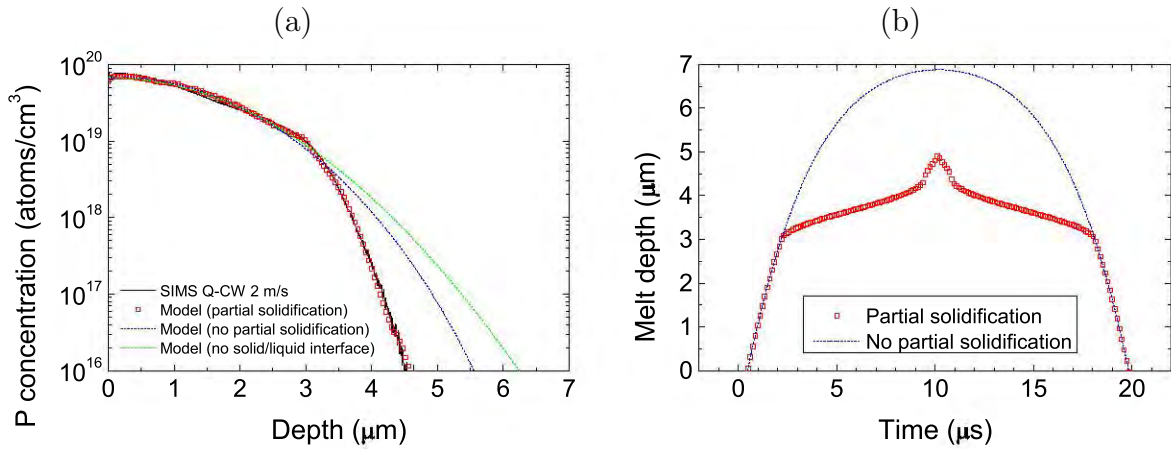


Figure 4.19: (a) Modelled diffusion profile for phosphorus laser doping at a scan speed of 2 m/s using a Q-CW laser assuming the partial solidification of the silicon between successive pulses showing good agreement and (b) the simplified time-depth profile of the molten region used for the model assuming a single pulse.

**Influence of overlapping passes on laser-doped regions:** A similar methodology to the partial solidification of silicon between successive pulses when using Q-CW lasers, can be used to describe the resulting deep CW dopant profiles (such as that processed at 0.5 m/s using either boron or phosphorus which both show kinks in the diffusion profile). For a CW laser, only a single ‘pulse’ is applied as the laser scans over a given region. However to fabricate laser-doped regions for SIMS measurements, overlapping laser-doped lines are formed and hence a given area may become molten during multiple passes of the laser depending on the line pitch used. Fig. 4.20 shows a hypothetical dopant profile obtained from three overlapping pulses which melt the silicon to different depths. Whilst a perfect fit is by no means obtained, the model does suggest that the kink in the dopant profile for CW lasers at such slow speeds could be described by such a mechanism. However, it may also be that the variations in the doping process for these deep molten regions at different depths when using a CW laser, which could not be described by the 1-dimensional model developed in this work.

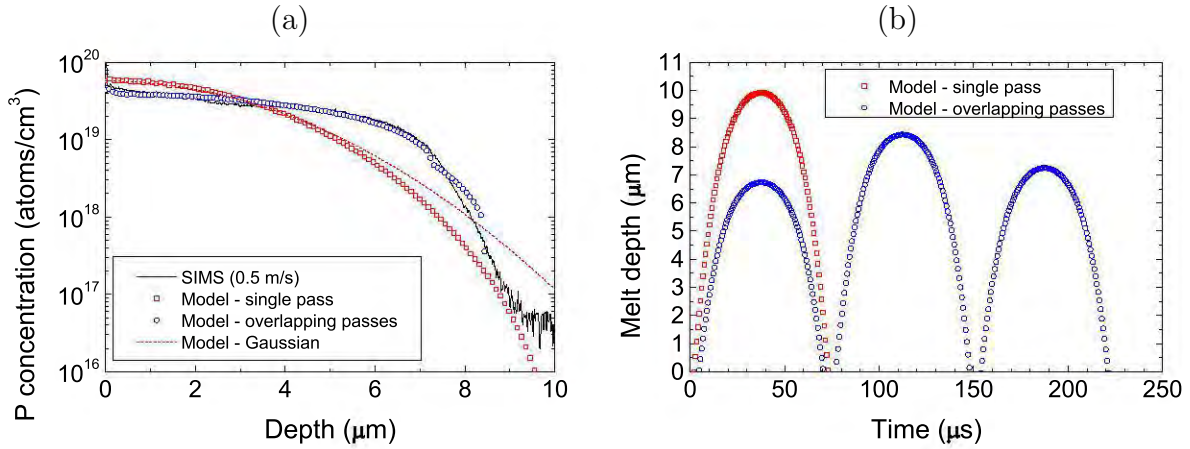


Figure 4.20: (a) Modelled diffusion profile for phosphorus laser doping at a scan speed of 0.5 m/s using a CW laser assuming three passes of the laser over a given region each of which melt the silicon to a different depth. (b) The simplified time-depth profile of the molten region used for the model assuming multiple spatially overlapping passes by the laser.

#### 4.2.2 Summary for Modelling Diffusion in Laser-Doped Regions

A Gaussian diffusion time-step was developed to model the laser doping process which included a time-dependent solid/liquid interface. Excellent agreement was observed between the model and SIMS profiles for processing speeds of 2 – 10 m/s using a CW laser. For a Q-CW laser, a characteristic kink in the dopant profile could be described using the model by assuming partial solidification in between successive pulses of the laser, which reduced the time in the molten state for the larger depths, and also the maximum melt depth. The dopant profiles processed at slow speeds which also featured a characteristic kink could be described by a partial overlap of successive passes of a laser beam, however these could also indicate other factors are involved which are not taken into account by the 1-dimensional model.

## 4.3 Laser Doping with Aluminium Oxide

In recent years there has been significant interest in the use of  $\text{AlO}_x$  as a passivating dielectric layer for p-type surfaces due to the high density of fixed negative charge in the layer [Agos 06]. The fixed negative charges in the dielectric layer result in an accumulation effect for p-type surfaces, therefore reducing minority carrier recombination at the surface [Heze 89; Agos 06; Sain 09]. In contrast, films such as  $\text{SiN}_x\text{:H}$ ,  $\text{SiON}_x\text{:H}$  and  $\text{SiO}_2$  have fixed positive charge which can result in a depletion of majority carriers at p-type surfaces therefore increasing recombination at the p-type surface, or a weak inversion of the surface polarity which can induce shunting on finished devices with localised contacts [Aber 92; Dauw 02a].

In addition to the benefits of field effect passivation provided by  $\text{AlO}_x$  layers for p-type surfaces, Al atoms within the layer can be used as a source of p-type dopants for laser doping [Lu 11; Hard 13; Mart 13]. Hence using  $\text{AlO}_x$  in conjunction with laser doping could avoid the need to coat solar cells with additional dopant sources and the subsequent removal of the dopant source prior to the formation of localised, heavily diffused p-type contact regions.

### 4.3.1 Aim

To investigate the use of  $\text{AlO}_x$  as a dopant source for laser doping localised p-type contacts in a self-aligned manner to avoid the formation of local BSF using high temperature processes. The effect of laser processing speed will be explored for line widths and  $\tau_{eff}$ . Subsequently, the laser doping process will be incorporated into a solar cell fabrication sequence for proof of concept devices.

### 4.3.2 Experimental Procedures

#### 4.3.2.1 Laser-Doped Test Structures

Test structures using  $\text{AlO}_x$  as a passivating dielectric layer were formed on commercial grade  $2\ \Omega\cdot\text{cm}$  n-type CZ wafers. Wafers received alkaline texturing in an industrial environment. Subsequently,

wafers were cleaned and HF dipped prior to the deposition of approximately 75 nm  $\text{AlO}_x$  onto both surfaces using an industrial Roth & Rau remote microwave PECVD tool. No thermal diffusions were applied to the wafers.

Laser doping was performed at various speeds using a 532 nm wavelength CW laser with a Gaussian beam distribution and scanning optics as detailed previously with approximately 13 W reaching the wafer surface. No additional dopant source was applied to the wafers to form  $p^+$  regions. Contact pads for the EBIC measurements were formed as detailed previously using the  $\text{AlO}_x$  as a dopant source for the rear p-type contact pad, and  $\text{H}_3\text{PO}_4$  as a dopant source for the n-type contact pad on the front surface of the wafer. Subsequently wafers were HF dipped to remove the  $\text{H}_3\text{PO}_4$  and cleaved in preparation for the EBIC measurements using the same method as detailed in Section 4.1. Fig. 4.21 shows the process flow for the investigation in this section.

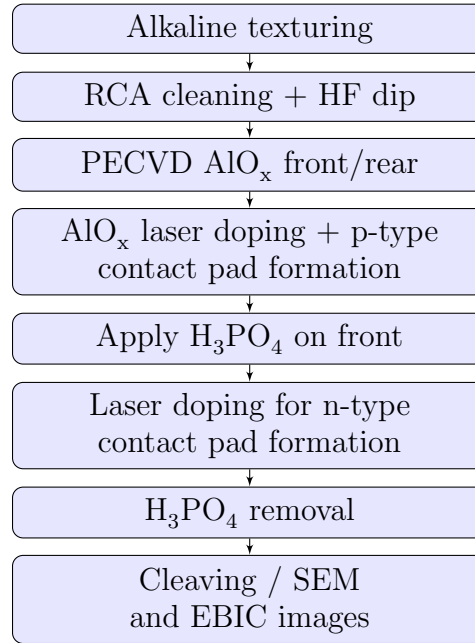


Figure 4.21: Process flow for EBIC analysis of laser doping using  $\text{AlO}_x$ .



#### 4.3.2.2 Lifetime Test Structures

To investigate the suitability of the local BSF formed using  $\text{AlO}_x$  as a dopant source for laser-doping, lifetime test structures were formed on  $2 \Omega \cdot \text{cm}$  boron-doped p-type magnetically confined CZ (MCZ) wafers. Wafers were processed in an industrial environment with alkaline texturing, followed by planarisation on the front surface, then rear surface, using an inline single-sided rear etch system, to make symmetrical test structures resembling the rear surface of the solar cell. Subsequently, samples were cleaned and had a 10 nm layer of stoichiometric  $\text{AlO}_x$  ( $\text{Al}_2\text{O}_3$ ) grown onto both surfaces using an industrial SolayTec spatial atomic layer deposition (ALD) tool at a temperature of  $200^\circ\text{C}$  using trimethyl-aluminium (TMA) and  $\text{H}_2\text{O}$  previously shown to provide excellent passivation for the rear p-type surface with low TMA consumption [Corn 13], as PECVD  $\text{AlO}_x$  was not available in the facility used for this experiment. The ALD  $\text{Al}_2\text{O}_3$  was capped by either 150 nm of  $\text{SiO}_x\text{:H}$ , 50 nm of  $\text{SiO}_x\text{:H}$  or 120 nm of  $\text{SiN}_x\text{:H}$  using an industrial direct PECVD system to increase firing stability [Dull 12]. The passivation was then activated by annealing in FG (FGA) at  $450^\circ\text{C}$ .

Laser doping was performed using a mode-locked UV (355 nm) Q-CW laser with an optical power of approximately 8.3 W at the wafer and a focus size of approximately 20  $\mu\text{m}$  diameter (as a 532 nm CW laser was not available in the facility for which these experiments were performed). High-speed fabrication was achieved through the use of a galvanometer scanner and f-theta lens with processing speeds of 0.5 – 20 m/s using lines with a pitch of 500  $\mu\text{m}$ . The scan field of the scanning optics allows rapid processing of a full  $156 \times 156$  mm wafer without moving the wafer. After laser doping, wafers received another FGA to passivate LasID. QSS-PC measurements were obtained on a BTi R1 luminescence imaging system at various stages. The process flow for the fabrication of lifetime test structures is shown in Fig. 4.22.

SIMS measurements were obtained on small laser-doped regions using overlapping lines with a pitch of 15  $\mu\text{m}$  for a processing speed of 1 m/s and 10  $\mu\text{m}$  for 8 m/s. Measurements were obtained using a Cameca system with an  $\text{O}_2^+$  primary beam at an incidence angle of  $40^\circ$ , impact energy of 5 keV, crater size of  $400 \times 400 \mu\text{m}^2$  and beam size of  $50 \times 50 \mu\text{m}^2$ . The analysis was performed on a dielectric stack of 10 nm ALD  $\text{Al}_2\text{O}_3$  and 120 nm PECVD  $\text{SiN}_x\text{:H}$  to improve stability of the passivation layers. Prior to the SIMS measurements, the samples received a HF dip to remove the

dielectric and residues from the surface.

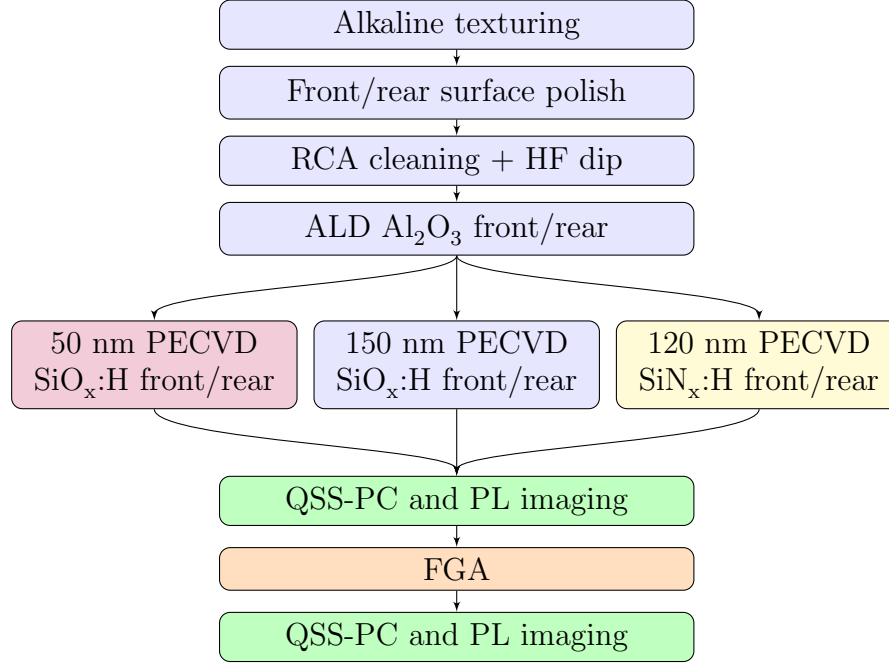


Figure 4.22: Process flow for fabrication of lifetime test structures for laser doping using AlO<sub>x</sub> to investigate the compatibility of different dielectric stacks.

#### 4.3.2.3 Solar Cell Structures

Two solar cell structures are investigated in this section: (1) as a control, cells are fabricated with a conventional PERC rear featuring local Al-BSF formation (i-PERC), which represents the current state-of-the-art process for solar cells on p-type CZ substrates [Metz 14]. (b) cells with a PERL rear featuring laser-doped contacts using the Al<sub>2</sub>O<sub>3</sub> as a dopant source (i-PERL) are also fabricated. The solar cell structures are shown in Fig. 4.23

Solar cells were fabricated on 156 × 156 mm boron-doped p-type MCZ wafers with a nominal bulk resistivity of 1.5 – 2 Ω · cm. Wafers were etched in a KOH-alkaline solution to remove saw damage and simultaneously texture the wafer surface anisotropically to expose the (111) planes in

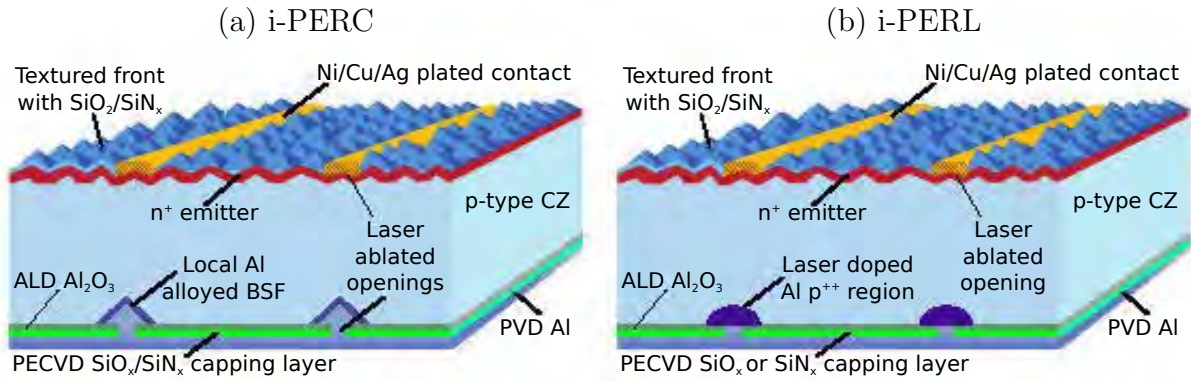


Figure 4.23: Structure of (a) a i-PERC solar cell with local Al-BSF and (b) i-PERL solar cell with laser-doped Al  $p^{++}$  contacts.

an in-line tool. Following acidic neutralisation in hot HCl, the rear side of the wafers received a single-side in-line chemical rear etch tool in a Si-etchant, resulting in a wafer thickness of 180  $\mu\text{m}$ .

After chemical cleaning, a  $\text{POCl}_3$  tube diffusion furnace was performed followed by PSG removal. Subsequently the emitter on the rear was chemically removed in the same single-sided rear etch tool. Approximately 15 nm of  $\text{SiO}_2$  was grown during thermal oxidation to assist with surface passivation and act as a drive-in for the emitter, followed by the deposition of an antireflection coating of  $\text{SiN}_x\text{:H}$  on the front surface. After the thermal oxidation, the sheet resistance of the phosphorus emitter was approximately 120  $\Omega/\square$ . Wafers then received a short HF dip to remove the thin thermal  $\text{SiO}_2$  layer from the rear prior to the deposition of 10 nm of ALD  $\text{Al}_2\text{O}_3$  in the same ALD system as previously described.

Subsequently the capping dielectric layers for the  $\text{Al}_2\text{O}_3$  layer were deposited using a direct PECVD system. For the i-PERC solar cells, a capping dielectric stack consists of > 100 nm  $\text{SiO}_x\text{:H}/\text{SiN}_x\text{:H}$ . For the i-PERL solar cells, the capping layer either consisted of 150 nm  $\text{SiO}_x\text{:H}$  or 120 nm  $\text{SiN}_x\text{:H}$ .

Laser processing of the rear surface was then performed on all samples. For samples with local Al-BSF formation, openings in the rear dielectric stack were formed by UV (355 nm) nanosecond laser ablation with a fixed pitch of 500  $\mu\text{m}$  for batches 1 and 2 (600  $\mu\text{m}$  for batch 3), resulting in

an opened diameter of approximately 60  $\mu\text{m}$  prior to firing. Laser doping of the  $\text{Al}_2\text{O}_3$  layers was performed on the other wafers to form local Al  $\text{p}^{++}$  doped regions with the Q-CW laser system used for the lifetime test structures in this section. An optical power of approximately 8.3 W and processing speed of 8 m/s were used, resulting in an opened line width of approximately 9  $\mu\text{m}$  for samples with a capping layer of  $\text{SiN}_x\text{:H}$  and 8  $\mu\text{m}$  for samples with a capping layer of  $\text{SiO}_x\text{:H}$ . The line pitch for batches 1 and 2 was 1 mm and 1.2 mm for batch 3.

2  $\mu\text{m}$  of Al was grown on the rear surface by sputtering followed by a thermal treatment. Samples with local Al-BSF formation were fired  $> 800^\circ\text{C}$  in an industrial belt furnace, whilst laser-doped samples received a FGA at  $450^\circ\text{C}$ . Laser-ablated contact openings were formed on the front surface using a UV (355 nm) picosecond laser resulting in an opened line width of approximately 12  $\mu\text{m}$ , which retained the homogenous emitter structure and front surface texturing in the contact area. Prior to plating, a short HF dip was performed to remove any native oxide in the contact openings. Approximately 1  $\mu\text{m}$  of Ni was deposited by LIP followed by approximately 10  $\mu\text{m}$  of electroplated Cu and immersion Ag to prevent oxidation of the Cu. All plating was performed in a commercial in-line plating tool from Meco. Sintering was then performed on the fully plated stack in  $\text{N}_2$  ambient to form a Ni silicide layer to reduce contact resistance and act as a diffusion barrier for the Cu [Tous 13; Russ 12].

Light current-voltage (J-V) measurements were obtained at 1-sun illumination on a WXS-200S-20 Wacom Electric Co. class AAA tester with a AM1.5G spectrum conforming to IEC 60904-9. Values for series resistance ( $R_S$ ) at maximum power point were obtained from J-V measurements at an illumination intensity of 1-sun and approximately 0.07-suns [Bowd 01].  $p\text{-}FF$  were extracted from curves of Suns versus  $V_{OC}$  using a Sinton Instruments SunsVoc tester [Sint 00]. The process flow for these cells is shown in Fig. 4.24

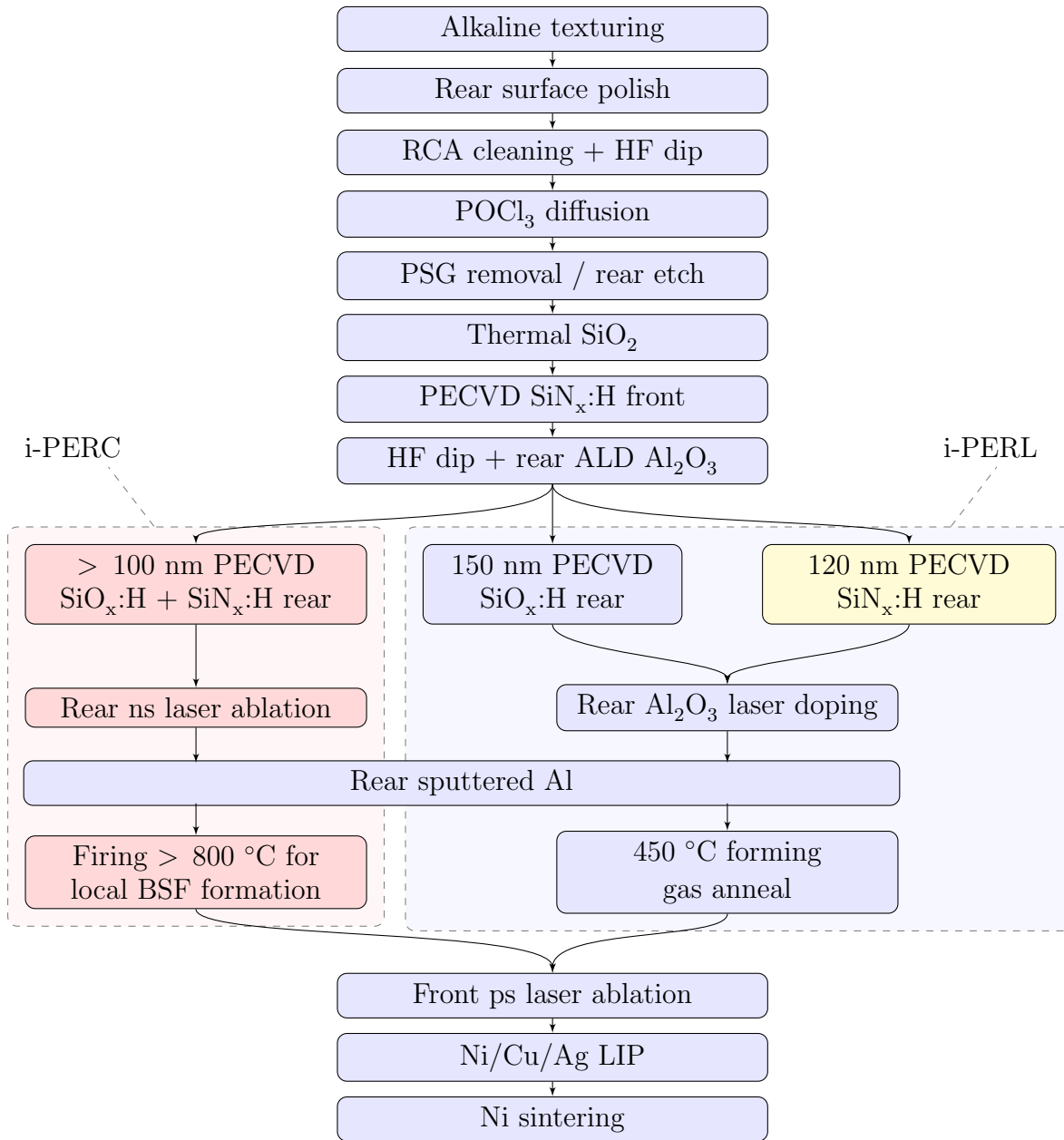


Figure 4.24: Process flow for fabrication of lifetime test structures for laser doping using  $\text{AlO}_x$ .

### 4.3.3 Demonstration of Laser Doping using Aluminium Oxide

The ability to utilise dopant atoms within the existing  $\text{AlO}_x$  passivation layers could greatly increase the importance of such layers for silicon solar cells. The formation of deep, heavily diffused silicon

in localised regions without the need for additional dopant applications such as SOD layers and/or the subsequent SOD removal could greatly simplify the process sequence and reduce costs.

SEM/EBIC images in Fig. 4.25 demonstrate deep junction formation using the PECVD  $\text{AlO}_x$  layers as a dopant source for the laser doping process. Similar to the cross sectional junction profiles obtained when using either phosphorus or boron dopants, a large variation in the shape and depth of the profiles was observed when using Al dopants.

At slow speeds, such as  $0.2 - 0.5$  m/s, semi-circular profiles were obtained suggesting the doping profiles and hence junction depths were largely determined by the depth and shape of the molten silicon region. For higher speeds in the range of  $1 - 10$  m/s, relatively uniform junction depths were observed directly below the opening in the  $\text{AlO}_x$  layers. This may indicate that the junction depth was limited by the diffusion coefficient of Al rather than the depth of the molten silicon region. It should be noted that for the higher speeds of  $5 - 10$  m/s, the silicon surface in the laser-doped region was no longer flat, but rather exhibited a raised and rounded surface. It is expected that this was due to the same effect which produced mounds at the ends of the point contacts in Section 4.1.3 with the abrupt removal of the laser source when using a physical mask. In this instance, the mound which travels along with the laser-doped line is crystallised in place to differing degrees, depending on the processing speed and hence crystallisation rate. For the higher speeds, the silicon does not have enough time to flatten the mound prior to crystallisation. Hence for such speeds, the junction profile also exhibited a raised region in the middle of the laser-doped region, due to the increased height of the silicon surface in this region, following a line of equidistance from the silicon surface.

In addition, it appeared that an additional diffusion mechanism occurred on samples processed with higher speeds. This is clearly shown in the sample processed at 2 m/s. Directly adjacent to the region with a flattened junction depth, the junction depth transitioned towards the peripheral areas, similar to what occurred in the samples with slower laser doping speeds (due to the junction depth being determined by the shape of the molten region). However, beyond this, a shallow Al  $p^{++}$  region was observed. This may be due to solid-state diffusion in the peripheral regions where the energy of the laser beam is insufficient to melt the silicon. As shown previously in Table 4.2, for solid state diffusion of Al in Si near the melting temperature, the diffusion coefficient

is approximately 200 times smaller than that of Al in molten Si at 1414 °C, which would result in a greatly reduced diffusion of Al in regions of silicon still in the solid phase to that in the liquid phase.

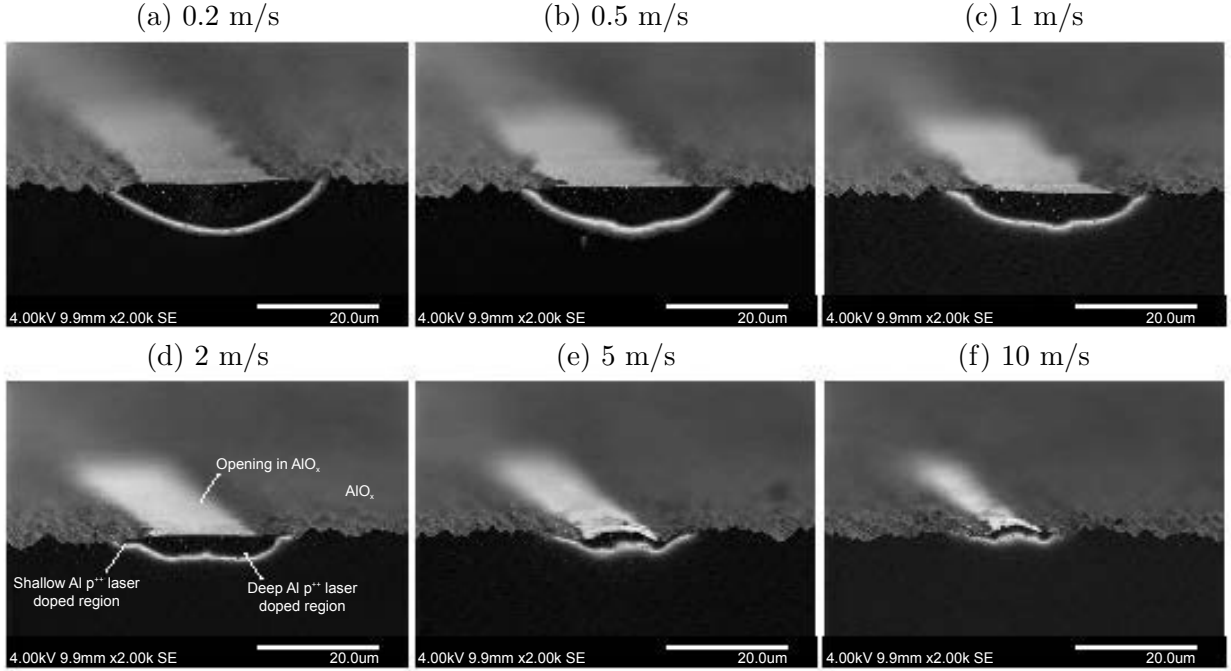


Figure 4.25: Combined SEM/EBIC images of Al p<sup>++</sup> laser doping using PECVD AlO<sub>x</sub> at (a) 0.2 m/s, (b) 0.5 m/s, (c) 1 m/s, (d) 2 m/s, (e) 5 m/s and (f) 10 m/s.

In contrast to the junction depths observed using boron dopants, the junction depths produced using  $\text{AlO}_x$  were greatly reduced, particularly for slower processing speeds. Fig. 4.26(a) shows a comparison of the junction depths achieved using Al dopants from PECVD  $\text{AlO}_x$  and boron dopants from a SOD layer (as presented in Section 4.1.3). This result was inconsistent with differences in the diffusion coefficients reported for boron and Al at 1414 °C in the literature. However this discrepancy may be due to the use of different dielectric layers and/or SOD layers which could influence the process. It would appear that from the junction profile obtained for 0.1 m/s, the molten region of silicon formed using the PECVD  $\text{AlO}_x$  was substantially shallower than that obtained when using a boron SOD on PECVD  $\text{SiON}_x\text{:H}$ .

In addition to the benefits of deep, heavily diffused regions situated below the metal contacts (which help reduce recombination at the metal/Si interface), wide lateral doping extending beyond the opening in dielectric layers and defected region alongside the opening in the dielectric layer, could assist in the avoidance of recombination at the defect sites. The apparent solid-state diffusion in the peripheral regions when using  $\text{AlO}_x$  greatly enhanced the width of the heavily doped region extending beyond the opening in the  $\text{AlO}_x$  layer compared to when using a boron SOD (see Fig. 4.26(b)). The enhanced doping in the lateral areas is likely due to the natural incorporation of the dopants into the dielectric layer, rather than being located in an applied dopant source and therefore needing to diffuse through the existing dielectric layers in order to reach the silicon.

As indicated by the EBIC images shown above in Fig. 4.25, for PECVD  $\text{AlO}_x$ , SIMS measurements confirm the deep and heavily doped regions formed using Al atoms from aluminium containing dielectric layers such as ALD  $\text{Al}_2\text{O}_3$ . Fig. 4.27 shows that for a processing speed of 8 m/s, a junction depth of approximately 2.5  $\mu\text{m}$  was obtained, whilst using a reduced speed of 1 m/s resulted in a junction depth of approximately 5  $\mu\text{m}$ . The SIMS profiles displayed similar features to those observed for the phosphorus profiles shown in Section 4.1.3, with a Gaussian like diffusion profile for a high process speed of 8 m/s, whilst a kink was observed in the dopant profile at a depth of approximately 2.5  $\mu\text{m}$  (similar to that for the dopant profile of phosphorus at 2 m/s when using a Q-CW laser, due to the duration in the molten phase at the larger depths). However due to the reduced power of 8.3 W used for the  $\text{Al}_2\text{O}_3$  laser doping, the silicon presumably resolidifies to a shallower depth. Interestingly, both Al dopant profiles had similar surface dopant concentrations of approximately  $4 \times 10^{19} \text{ /cm}^3$ , although the profile at 1 m/s exhibited much higher



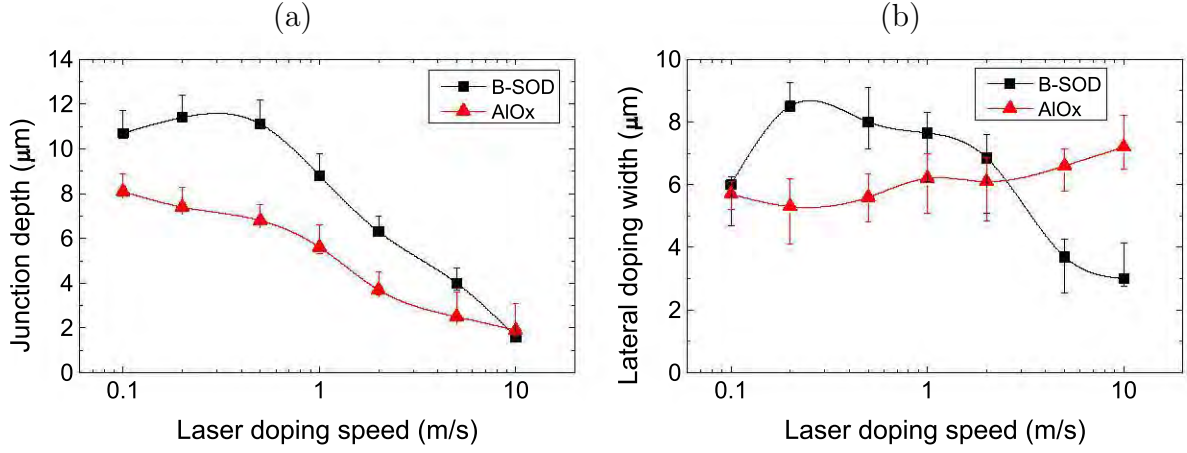


Figure 4.26: (a) Junction depths and (b) distance of lateral doping extending beyond the opening in the dielectric layer for laser doping with PECVD AlO<sub>x</sub> for processing speeds between 0.1 m/s – 10 m/s using a 532 nm CW laser showing enhanced lateral doping for AlO<sub>x</sub> laser doping at high speeds.

doping densities approximately 0.5 μm from the surface of the silicon. The origin for the depletion of Al dopants near the surface is unclear. Table 4.6 highlights some of the key attributes of the dopant profiles as measured by SIMS. The utilisation of dopant atoms from the Al<sub>2</sub>O<sub>3</sub> greatly depends on the processing speed with a reduced incorporation of the Al atoms using a higher speed. Whilst only 5 % of Al atoms from the Al<sub>2</sub>O<sub>3</sub> layer are incorporated in the silicon at 8 m/s, a very significant number of dopants can be incorporated into the silicon and result in a profile well suited to shield minority carriers from a metal/Si interface. In contrast, up to 35 % of Al atoms were utilised using slower speeds.

The results suggest a very effective level of doping could be achieved by using AlO<sub>x</sub> layers as a dopant source, with junction depths approaching 8 μm for slow processing speeds and a dopant utilisation of up to 34 %. However for solar cell applications, the influence of the laser process on  $\tau_{eff}$  through defect generation should also be explored.

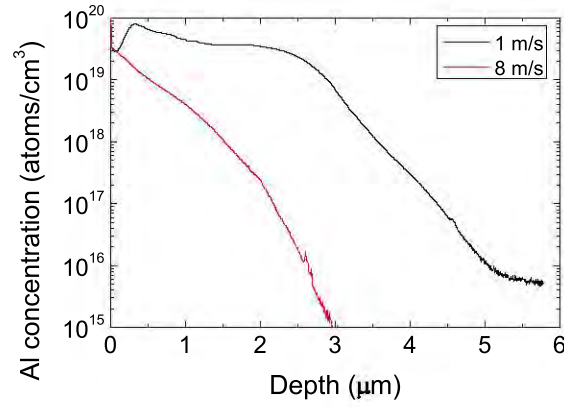


Figure 4.27: SIMS profiles of aluminium laser-doped regions formed through a stack of 10 nm ALD  $\text{Al}_2\text{O}_3$ /120 nm PECVD  $\text{SiN}_x\text{:H}$  using a Q-CW laser with optical power of 8.3 W showing deep, heavily doped regions.

Table 4.6: Doping properties of laser-doped regions using  $\text{AlO}_x$  extracted from the SIMS profiles shown in Fig. 4.27.

Laser speed	(m/s)	1	8
Surface concentration	(/cm <sup>3</sup> )	$4 \times 10^{19}$	$3.5 \times 10^{19}$
BSF depth	(μm)	5.1	2.6
Al atoms in 10 nm ALD $\text{Al}_2\text{O}_3$	(/cm <sup>2</sup> )	$3.5 \times 10^{16}$	$3.5 \times 10^{16}$
Al atoms in SIMS profile	(/cm <sup>2</sup> )	$1.2 \times 10^{16}$	$1.6 \times 10^{15}$
Al atoms from $\text{Al}_2\text{O}_3$ incorporated in Si	(%)	34	5

#### 4.3.4 Lifetime Test Structures for Laser-Doped Regions from Aluminium Oxide Layers

Processing speeds for laser doping can greatly affect many attributes of the process such as width of line openings, dopant profiles, defect generation and the removal of the overlying dielectric layers.

Fig. 4.28 shows microscope images of resulting line openings in various dielectric stacks featuring  $\text{Al}_2\text{O}_3$  at processing speeds of 0.5–20 m/s. For slow processing speeds of 0.5–5 m/s, a heat affected zone was observed directly adjacent to and more than 10  $\mu\text{m}$  from the clearly defined openings in the dielectric stack. This suggests that the damage may be occurring well beyond the doped region, which could lead to increased recombination.

At higher speeds of 10 – 20 m/s, no such heat affected zone was observed in the microscope images, however the opening in the dielectric layers was greatly dependent on both the speed and the capping layer of the  $\text{Al}_2\text{O}_3$ . Using high speeds > 10 m/s in conjunction with a PECVD  $\text{SiN}_x\text{:H}$  capping layer resulted in the incomplete removal of the dielectrics from the laser-doped region and would appear undesirable for a metal/Si interface, unless the residual dielectric layers can be removed during chemical processing prior to the deposition of the metal contacts.

When using a thick  $\text{SiO}_x\text{:H}$  layer of approximately 150 nm the laser was not able to open the dielectric layer at speeds of 8 – 20 m/s. This may have been due to optical interference with the dielectric stack, or because the laser power was not sufficient to open the dielectric layer at such high speeds. In contrast, a thinner 50 nm layer of identical composition could be clearly opened at processing speeds of 20 m/s and resulted in a very fine opening of less than 4  $\mu\text{m}$  width, whilst still melting the silicon, and resulted in an expected junction depth of approximately 1 – 2  $\mu\text{m}$ . The improved line quality compared to previous work using boron dopant source through PECVD  $\text{SiON}_x\text{:H}$  with the 532 nm CW laser system used in this work may be due to a combination of improved laser optics, different laser wavelengths, different dielectric layers and dopant source through which the laser must penetrate.

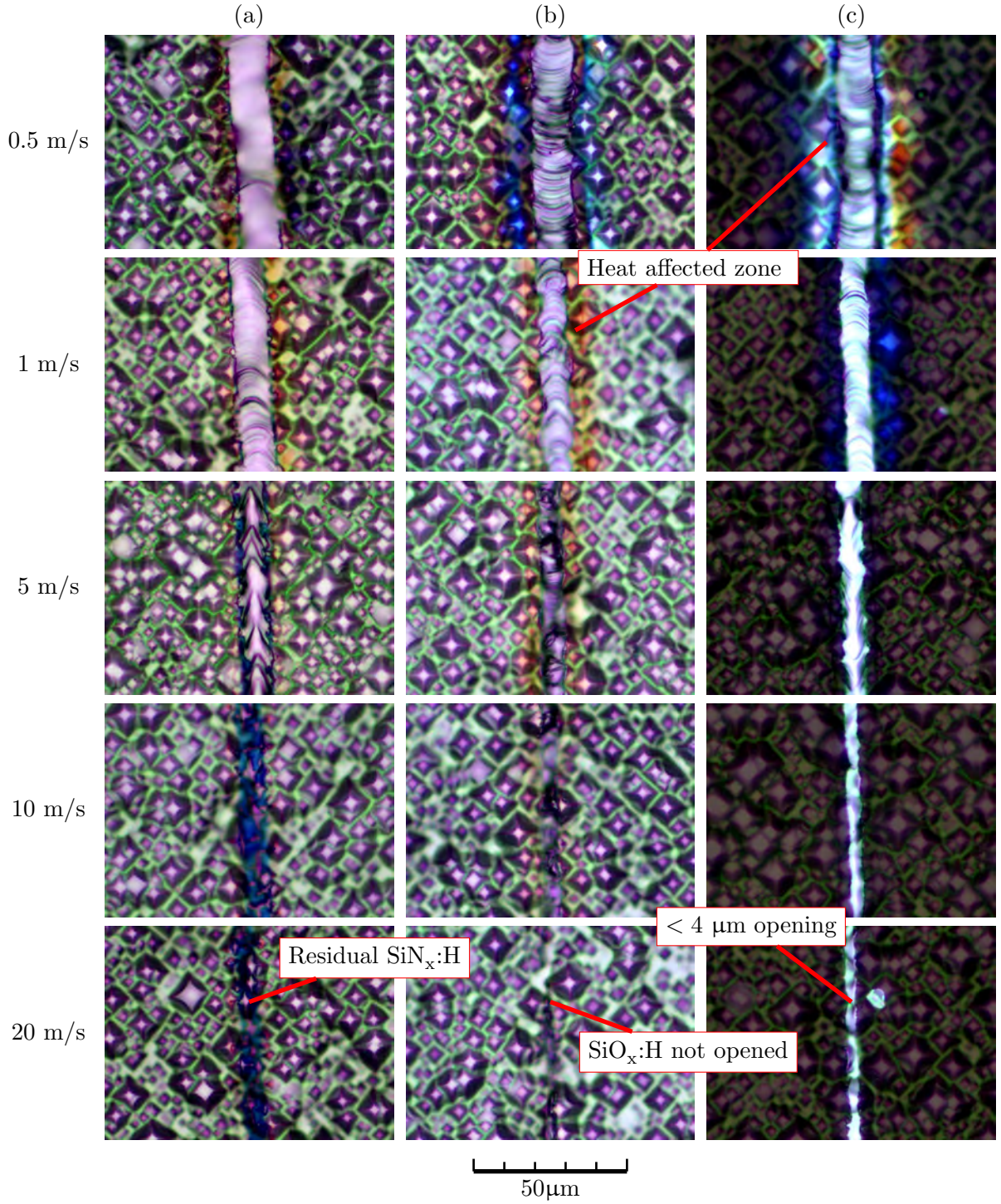


Figure 4.28: Microscope images at x500 magnification of Al  $p^{++}$  laser-doped lines from ALD  $\text{Al}_2\text{O}_3$  capped by PECVD layers of (a) 120 nm  $\text{SiN}_x\text{:H}$ , (b) 150 nm  $\text{SiO}_x\text{:H}$  and (c) 50 nm  $\text{SiN}_x\text{:H}$  at various speeds.

The investigation highlighted that the dielectric stack composition and processing speed used can have a large influence on the laser process and resultant width of the opening in the dielectric stack. Fig. 4.29 shows the opening line widths for the various dielectric stacks showing a substantial reduction in the opening widths with increasing processing speed. In addition, the line widths of cells with a capping layer of  $\text{SiO}_x\text{:H}$  were substantially narrower than that when using a  $\text{SiN}_x\text{:H}$  capping layer. These widths were also substantially smaller than the focus size of the laser beam which was  $20\text{ }\mu\text{m}$  in diameter, and can likely be attributed to the Q-CW nature of the laser (which uses the coupling of many pulses to generate one effective pulse) as opposed to a conventional nanosecond pulse-length Q-switched laser (whereby each pulse acts in isolation and clearly affects an area of a designated size for a given pulse energy independent of process speed).

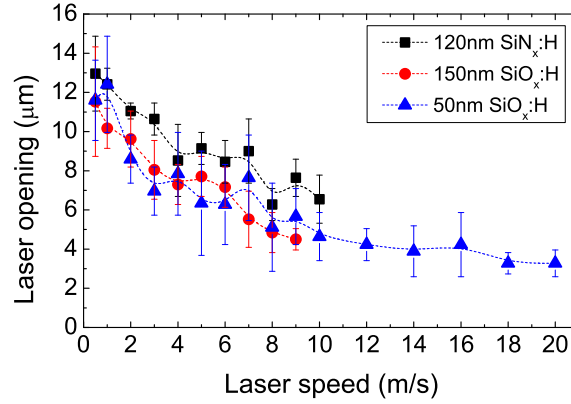


Figure 4.29: Opening line widths for laser-doped lines formed at speed of  $0.5 - 20\text{ m/s}$  using a Q-CW laser with optical power of  $8.3\text{ W}$  performed through a stack of  $10\text{ nm}$  ALD  $\text{Al}_2\text{O}_3$  and capping layer of either  $120\text{ nm}$  PECVD  $\text{SiN}_x\text{:H}$ ,  $150\text{ nm}$  PECVD  $\text{SiO}_x\text{:H}$  or  $50\text{ nm}$  PECVD  $\text{SiO}_x\text{:H}$  illustrating that the width of the laser opening decreases with increasing dielectric stack thickness and laser processing speeds.

In addition to line widths of the contact openings, it is also important to consider the generation of LasID and the ability of the heavily diffused region to shield minority carriers at the metal/Si interface. Fig. 4.30 shows the 1-sun  $iV_{OC}$  and  $\tau_{eff}$  curves extracted from lifetime test structures



with capping layers of  $\text{SiN}_x\text{:H}$  and  $\text{SiO}_x\text{:H}$ . For samples with a capping layer of 120 nm PECVD  $\text{SiN}_x\text{:H}$ , no significant trend was observed between the processing speed and the  $iV_{OC}$ . In contrast, cells with a capping layer of PECVD  $\text{SiO}_x\text{:H}$  displayed a strong relationship between the processing speed and  $iV_{OC}$ , with substantially higher values obtained after annealing using higher speeds. However before annealing, a significantly reduced  $iV_{OC}$  was observed for the higher speeds. It should be noted that for the samples shown with a capping layer of  $\text{SiO}_x\text{:H}$ , approximately the same  $\tau_{eff}$  and  $iV_{OC}$  were obtained by using either a 150 nm or 50 nm thick capping layer. Due to the inability of the laser to open the thick 150 nm  $\text{SiO}_x\text{:H}$  layer for processing speeds  $> 10$  m/s, for such speeds the values are shown for a 50 nm thick layer. Whilst higher  $iV_{OC}$  were obtained at speeds  $> 10$  m/s by using the thin  $\text{SiO}_x\text{:H}$  layer, similar values were obtained using either  $\text{SiN}_x\text{:H}$  or  $\text{SiO}_x\text{:H}$  capping layers at intermediate speeds of 5 – 10 m/s. For slower speeds, samples with a capping layer of  $\text{SiO}_x\text{:H}$  suffered from substantially reduced  $iV_{OC}$ .

In addition, no clear trend was observed between the processing speed and the  $\tau_{eff}$  curves when using a capping layer of  $\text{SiN}_x\text{:H}$ . However a clear trend was observed for the samples with a capping layer of  $\text{SiO}_x\text{:H}$ , with increasing lifetimes at all injection-levels when using increased processing speeds. For samples below 5 m/s substantially reduced lifetimes were observed likely due to an increase in bulk defect generation, which was not passivated by hydrogen using the applied process. In addition, increasing the processing speed increased the  $\tau_{eff}$  in high injection suggesting an improved  $J_{0d}$ . However due to the use of a paper wipe underneath the wafers during the QSS-PC measurements to avoid contamination, no lifetime curve fitting was performed. It should be noted that due to the use of the wipe, all  $\tau_{eff}$  and  $iV_{OC}$  values were underestimated.

For samples with  $\text{SiN}_x\text{:H}$  capping layers, substantially higher  $\tau_{eff}$  curves were obtained using slower speeds. This may be due to a difference in the generation of LasID in the bulk silicon, or an improved passivation of defects generated by hydrogen if the deposition of  $\text{SiN}_x\text{:H}$ , or subsequent thermal processing allowing for a more effective incorporation of hydrogen into the bulk than when using PECVD  $\text{SiO}_x\text{:H}$  layers.

In conclusion, when using slow processing speeds, a capping layer of  $\text{SiN}_x\text{:H}$  should be used to avoid performance degradation due to LasID generation in the bulk. However for faster speeds of 5 – 10 m/s, similar lifetime curves are obtained using either  $\text{SiN}_x\text{:H}$  or  $\text{SiO}_x\text{:H}$  capping layers

suggesting that either layer could effectively be used for cell fabrication.

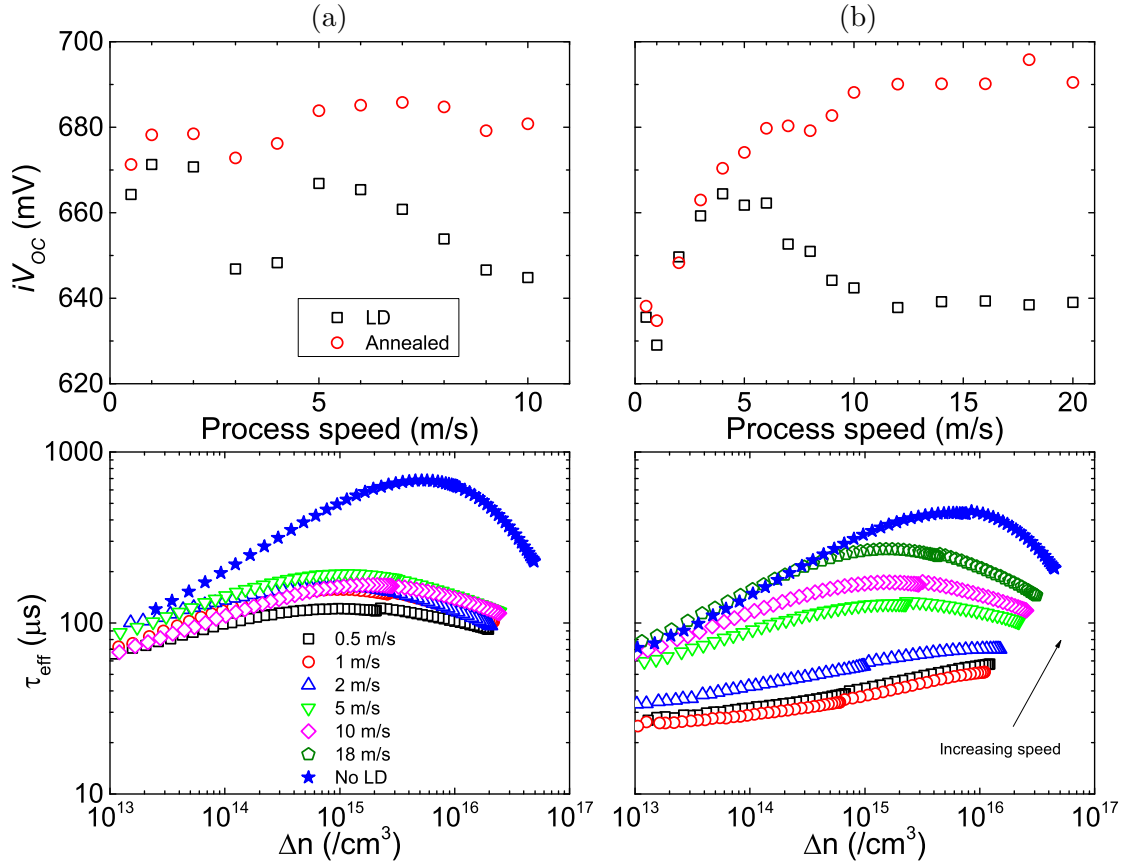


Figure 4.30: 1-sun  $iV_{OC}$  and  $\tau_{eff}$  curves of laser doping through 10 nm of ALD  $Al_2O_3$  and a capping layer of (a) 120 nm PECVD  $SiN_x:H$  or (b) 150 nm PECVD  $SiO_x:H$ . It should be noted, that for speeds higher than 10 m/s a thickness of 50 nm was used for the PECVD  $SiO_x:H$ .

### **4.3.5 Solar Cell Fabrication with Laser-Doped Contacts from Aluminium Oxide**

Whilst the fabrication of test structures is an important aspect of developing new processes for silicon solar cells, it is essential to fabricate full devices to demonstrate that the new processes are compatible with other conventional manufacturing processes. For full cells fabricated in this section, the average efficiency of all groups from each batch was over 20 % indicating a good overall performance of the cells (see Table 4.7). In addition, the results provided a proof of concept for the use of the application of Al based laser doping into silicon solar cell fabrication. Cells in this section were fabricated in conjunction with Cornagliotti *et al.* [Corn 13; Corn 14].



Table 4.7: Light J-V measurements of i-PERC and i-PERL solar cells (measured in-house). Dielectric layers in parentheses are the capping dielectric layers used. Values in red are for the highest i-PERL cell efficiency in each batch. \*Best cells independently confirmed at Fraunhofer ISE-CalLab, with AM 1.5G IEC60904-3.

	$J_{SC}$ (mA/cm <sup>2</sup> )	$V_{OC}$ (mV)	$FF$ (%)	$\eta$ (%)	$R_S$ ( $\Omega \cdot \text{cm}^2$ )	$p\text{-}FF$ (%)
<b>Batch 1</b>						
i-PERC	39.1 ± 0.1	651 ± 2	79.1 ± 0.4	20.1 ± 0.0	0.62 ± 0.08	-
i-PERL (SiN <sub>x</sub> :H)	38.8 ± 0.1	655 ± 1	79.4 ± 0.6	20.2 ± 0.1	0.57 ± 0.08	-
<b>i-PERL (SiN<sub>x</sub>:H)*</b>	<b>38.8</b>	<b>655</b>	<b>79.5</b>	<b>20.2</b>	<b>-</b>	<b>-</b>
<b>Batch 2</b>						
i-PERC	38.6 ± 0.3	653 ± 2	79.3 ± 0.6	20.0 ± 0.3	0.57 ± 0.05	82.3 ± 0.2
i-PERL (SiN <sub>x</sub> :H)	38.5 ± 0.2	658 ± 1	79.7 ± 0.4	20.2 ± 0.1	0.55 ± 0.08	82.4 ± 0.2
i-PERL (SiO <sub>x</sub> :H)	38.7 ± 0.1	657 ± 1	78.6 ± 0.4	20.0 ± 0.2	0.76 ± 0.03	82.6 ± 0.2
<b>i-PERL (SiN<sub>x</sub>:H)*</b>	<b>38.6</b>	<b>657</b>	<b>80.2</b>	<b>20.4</b>		
<b>Batch 3</b>						
i-PERC	39.4 ± 0.2	659 ± 3	78.7 ± 0.3	20.4 ± 0.2	0.46 ± 0.1	82.0 ± 0.2
i-PERL (SiN <sub>x</sub> :H)	39.5 ± 0.1	653 ± 3	79.2 ± 0.4	20.4 ± 0.2	0.48 ± 0.05	82.4 ± 0.1
<b>i-PERL (SiN<sub>x</sub>:H)*</b>	<b>39.4</b>	<b>657</b>	<b>79.9</b>	<b>20.7</b>		

#### 4.3.5.1 Proof of Concept

In batch 1, i-PERL cells (with SiN<sub>x</sub>:H and 1 mm pitch) were fabricated with the localised Al doped BSF formed by laser doping through the Al<sub>2</sub>O<sub>3</sub> layers demonstrated slightly higher efficiencies of 20.2 ± 0.1 % than that of the control group of i-PERC cells with the convention formation of Al-BSF through the alloying of Al/Si during the firing process (with efficiencies of 20.1 ± 0.1 %). The increased efficiency was attributed to slight increases in  $V_{OC}$ , and increases in  $FF$  through a

reduction in  $R_S$ . The reduced  $R_S$  (of  $0.57 \pm 0.08 \Omega \cdot \text{cm}^2$  versus  $0.62 \pm 0.08 \Omega \cdot \text{cm}^2$ ) was attributed to the different contact geometry used for the laser-doped samples, with lines rather than point contacts for the fired samples, therefore affecting the resistive losses holes are subjected to in order to reach the p-type metal contact. In addition, the heavy doping under the metal/Si interface could lead to reduced contact resistances, however further studies will be required to determine the contact resistance achieved using such contacts. On the other hand, the  $J_{SC}$  of the i-PERL laser-doped samples was reduced by  $0.3 \text{ mA/cm}^2$  compared to that of the i-PERC control group. The reduction in  $J_{SC}$  is unclear at this stage, but potentially due to a non-optimised texturing process or width of the Cu fingers, resulting in increased reflection. Subsequently, the highest efficiency cell with laser-doped local Al  $p^+$ + BSF contacts was 20.2 % with a  $FF$  of 79.5 %, which successfully demonstrates the suitability of the  $\text{AlO}_x$  laser doping process for solar cell fabrication.

#### 4.3.5.2 Rear Reflection

In batch 2 (also using a pitch of 1 mm comparing  $\text{SiN}_x\text{:H}$  and  $\text{SiO}_x\text{:H}$ ), efforts focused on the optimisation of the rear reflection properties of the solar cell structure. Due to the avoidance of the firing step to form the Al-BSF, a wider choice of dielectric capping layers becomes available. For example, when using  $\text{SiO}_x$  in direct contact with Al a substantial degradation of the rear reflector properties can result during the firing process due to spiking of the Al through  $\text{SiO}_x$ . However this can be overcome through the use of an intermediate capping layer such as  $\text{SiN}_x$  [Urue 12]. Furthermore, spiking of Al through  $\text{SiO}_2$  layers has been demonstrated at temperatures well below the eutectic temperature, leading to the formation of localised  $p^+$  regions [Ho 04]. The avoidance of the firing step can also eliminate thermal stability issues associated with the use of  $\text{Al}_2\text{O}_3$  such as crystallisation and blistering [Henn 12; Verm 11; Lude 12]. This can also lead to optical enhancements of the rear reflector properties due to the avoidance of parasitic Si absorption in non-active regions of the device [Urue 13].

In this batch the objective was to substitute the  $\text{SiN}_x\text{:H}$  capping layer (refractive index (RI) of approximately 2.03) with a lower RI film to boost the performance of the rear reflector [Holm 14]. A 150 nm thick layer of PECVD  $\text{SiO}_x\text{:H}$  (RI=1.52) was used for this purpose. In Table 4.8 the rear reflection  $R_b$  and number of light passes at 1200 nm ( $Z_0$ ) were calculated for different cell

architectures following the model described by Basore *et al.* 1993 [Baso 93]. When comparing the values for the firing processes, the impact of the intermediate  $\text{SiO}_x\text{:H}$  layer in improving the rear reflector is clear with an improvement in  $R_b$  from 82 % to 89 % and  $Z_0$  from 13.6 to 18.7. However for the laser-doped samples, even with use of a  $\text{SiN}_x\text{:H}$  capping layer and no intermediate low RI  $\text{SiO}_x\text{:H}$  layer, the  $R_b$  was increased to 90 % with a corresponding  $Z_0$  of 21.4 due to an absence of a firing process to induce Al spiking. If using a low RI  $\text{SiO}_x\text{:H}$  capping layer, further increases in optical performance were observed with  $R_b$  and  $Z_0$  of 93 % and 25.5 respectively due to the enhancement in rear reflector properties at the silicon/dielectric interface for low RI films. The influence of the contact geometry was also observed for laser-doped samples with a capping layer of  $\text{SiN}_x\text{:H}$  with a slight improvement in using a larger contact pitch, due to a lower deterioration of the rear reflection properties by laser doping a smaller coverage area.

Table 4.8: Calculated backside reflectance ( $R_b$ ) and the number of light passes at 1200 nm ( $Z_0$ ) for different cell architectures/rear dielectric stack/contact pitch highlighting enhanced backside reflectance for i-PERL. Calculations were performed according to [Baso 93]. Contact pitch for lines and point contacts are also shown.

Cell type	Contact geometry	$R_b$ (%)	$Z_0$
i-PERC ( $\text{Al}_2\text{O}_3/\text{SiO}_x\text{:H}/\text{SiN}_x\text{:H}$ )	Point contacts - 500 $\mu\text{m}$	89	18.7
i-PERC ( $\text{Al}_2\text{O}_3/\text{SiN}_x\text{:H}$ )	Point contacts - 500 $\mu\text{m}$	82	13.6
i-PERL ( $\text{Al}_2\text{O}_3/\text{SiN}_x\text{:H}$ )	Lines - 1 mm	90	21.4
i-PERL ( $\text{Al}_2\text{O}_3/\text{SiN}_x\text{:H}$ )	Lines - 1.5 mm	91	22.1
i-PERL ( $\text{Al}_2\text{O}_3/\text{SiO}_x\text{:H}$ )	Lines - 1 mm	93	25.5

Despite of the clear improvements in the properties of the rear reflector, such improvements did not explain the reduction in  $J_{SC}$  of the i-PERL cells in batch 1. However increases in  $J_{SC}$  of 0.2  $\text{mA}/\text{cm}^2$  were observed on i-PERL cells when using a  $\text{SiO}_x\text{:H}$  capping layer rather than  $\text{SiN}_x\text{:H}$ , although only a 0.1  $\text{mA}/\text{cm}^2$  increase in  $J_{SC}$  was observed compared to the i-PERC cells.

It should be noted that the  $J_{SC}$  values obtained in batch 2 were lower than that in batch 1 due to a non-optimal deposition of the front  $\text{SiN}_x\text{:H}$  anti reflection coating. An increase in  $V_{OC}$  was observed for both i-PERL cell groups compared to that of the i-PERC cells. i-PERL cells with a  $\text{SiN}_x\text{:H}$  capping layer also showed a significant increase in  $FF$  and similar  $R_S$  to that of i-PERC cells, however i-PERL cells with a  $\text{SiO}_x\text{:H}$  capping layer suffered from a greatly increased  $R_S$  and therefore have a reduced  $FF$ . The  $p\text{-}FF$  of all groups was over 82 % with slight increases in  $p\text{-}FF$  for i-PERL cells compared to i-PERC cells suggesting an improved contact structure compared to the conventional localised Al-BSF approach. For this batch, an increased efficiency of 20.4 % was achieved with  $FF$  over 80 %.

Although it was observed that cells with  $\text{SiO}_x\text{:H}$  capping layers were more likely to suffer from regions with reduced or an incomplete opening of the dielectric stack due to variations in dielectric thickness, the entire increase in  $R_S$  could not be attributed to this effect, since unaffected cells also presented higher  $R_S$  values than the cells with  $\text{SiN}_x\text{:H}$  capping layers. Hence differences may have been due to differences in the metal/Si interface area formed by using the various dielectric stack combinations or differences in the resultant dopant profiles after laser doping.

In conclusion, batch 2 showed that using a capping layer of  $\text{SiN}_x\text{:H}$  resulted in a more robust cell process with reduced  $R_S$  than when using a capping layer of  $\text{SiO}_x\text{:H}$ .

#### 4.3.5.3 Optimised i-PERL

In batch 3, the i-PERC process was again compared with the i-PERL process (only using a capping layer of  $\text{SiN}_x\text{:H}$ ). For this batch wafers from a different supplier were used and small variations were made to other processing steps to optimise efficiency such as Cu plating thickness, texturing, reduced polishing of the rear (7  $\mu\text{m}$  compared to 10  $\mu\text{m}$ ), and the use of pure Al sputtering source compared to Al-Si (1 %) for the previous batches. No modifications were made to the laser processes in this batch.

This optimisation led to efficiencies on i-PERL solar cells up to 20.7%. A substantial increase in  $J_{SC}$  was observed in this batch, attributed to improved texturing and optimised Cu finger width. Further improvements were due to a reduced polished depth resulting in a slightly higher

$Z_0$  [Corn 12]. It should be noted that whilst the  $V_{OC}$  for i-PERL cells was higher than that of i-PERC cells in batches 1 and 2, a slight reduction in  $V_{OC}$  was observed in this batch. This was due to the changes in the Al sputtering source. For batches 1 and 2, an Al target containing 1% Si was used in order to avoid spiking problems during contact annealing [Cohé 82]. It was later observed that the Al-Si target was degrading the  $V_{OC}$  of fired cells substantially (by 5 – 7 mV) with respect to a pure Al target. This may have been caused by the presence of impurities other than Si in the target being driven into the bulk silicon during Al-BSF formation.

In contrast, for batch 3, a pure Al target was used. Whilst this improved the performance of i-PERC cells, it is unclear whether or not this modification was detrimental to the i-PERL cells. At this stage, it is also unclear whether the laser doping process can improve the  $V_{OC}$  of the cells with respect to an optimised i-PERC cell process. However, the firing process which the i-PERC cells received did also act to release hydrogen from the  $\text{SiN}_x\text{:H}$  layers, distribute it throughout the device and passivate bulk and surface defects. As the i-PERL solar cells do not receive this firing step, hydrogen may not have been effectively released from the  $\text{SiN}_x\text{:H}$  layers, and hence suffered from reduced  $\tau_{bulk}$ .

The narrow contact openings demonstrated of  $< 10 \mu\text{m}$  for a speed of 8 m/s as used for cells fabricated in this section, were smaller than those used for the world record PERL cell using photolithography [Zhao 96]. For higher speeds  $> 8 \text{ m/s}$ , contact widths less than  $5 \mu\text{m}$  represent a significant reduction in metal/Si interface area for laser processed contacts, without the introduction of complex optics or limitations on the scan-field area. In addition, the self-aligned process with simultaneous patterning of the dielectric and the formation of a localised, heavily doped BSF region greatly simplifies processing. Furthermore, the utilisation of Al atoms from the  $\text{Al}_2\text{O}_3$  layer avoids the need for the application of a dopant source or its subsequent removal.

Hence these results are of significant commercial importance for the fabrication of high efficiency silicon solar cells, which typically require small metal/Si interfaces and heavy doping under the metal/Si interface to minimise recombination. For a processing speed of 20 m/s and line pitch of 1.2 mm as used in batch 3, the processing time for each wafer for laser processing was less than 1.2 s. Assuming a cell efficiency of 21 %, an overall cell fabrication yield of 95 % and production 360 days a year, neglecting automation, the process is capable of  $> 120 \text{ MW}$  using a single laser

head.

In conclusion, these results proved a proof of concept for the use of  $\text{AlO}_x$  as a dopant source for the self-aligned p-type contacts of industrial PERL cells. However further work is needed to incorporate improved hydrogen passivation processes into the cell process sequence. With such improvements to result in  $V_{OC} > 680$  mV and an optimisation of the contact geometries to yield  $FF > 81$  %, efficiencies of  $> 21.8$  % appear feasible.

### **4.3.6 Summary for Laser Doping with Aluminium Oxide**

Laser doping was performed using passivating  $\text{AlO}_x$  layers as a dopant source for a self-aligned formation of localised p-type contacts. Deep, heavily diffused regions were formed with junction depths of up to  $8\text{ }\mu\text{m}$  with a high utilisation of Al atoms from the  $\text{AlO}_x$  layer of up to 34 %. Narrow line widths  $< 5\text{ }\mu\text{m}$  were obtained for processing speeds  $> 8\text{ m/s}$  with little bulk damage. The process was incorporated into solar cells which provided a proof of concept, with efficiencies of up to 20.7 % and  $FF > 80$  %, in an industrially relevant manner with an anticipated throughput  $> 120\text{ MW}$ .

## **4.4 Contacting Buried Layers in Silicon Solar Cells**

A number of silicon solar cell technologies have been developed that utilise processes to either (1) contact buried layers in a solar cell, or (2) remove surface layers such that the underlying layers can be contacted. However due to fundamental constraints, there are substantial limitations as to what and how such solar cell structures can be realised. To date, such technologies require complex processing sequences, typically involving multiple high temperature diffusions with lengthy thermal oxidations. In addition, multiple patterning and alignment processes are required for the formation of the diffused regions and to define the metal/Si interface for the n- and p-type contacts. Such high temperatures and complex patterning process add significant cost to solar cell production. hence this section aims to highlight the processes used today, and investigate a new, simplified method to achieve such structures through the use of laser doping in a self-aligned manner.

#### 4.4.1 The Need to Contact Buried Layers in Solar Cells

The PERL solar cell has held the world record for small area 1-sun silicon solar cells since 1990 [Wang 90] with an efficiency of 25 % [Zhao 99; Gree 11; Gree 09]. However, one issue associated with the fabrication of PERL solar cells and indeed other solar cell technologies fabricated on p-type substrates is the passivation of the lightly doped p-type surface at the rear of the device. This is largely due to the high mobility of the minority carriers at the p-type surface, i.e. the electrons [Sze 07], as well as the low majority carrier concentration and hence high minority carrier concentration at the rear surface, both of which play a large role in determining the recombination rate [Wenh 01]. To overcome this, the PERL cell structure employs the use of high quality thermally grown  $\text{SiO}_2$  with trichloroethane, in conjunction with hydrogen passivation at the  $\text{Si}/\text{SiO}_2$  interface realised through the alneal process [Zhao 96].

Conventional screen-printed silicon solar cells effectively passivate the lightly doped p-type rear surface through the use of a full area Al-BSF through the alloying of Al and Si above the eutectic temperature to create a  $\text{p}^+$  layer, which has demonstrated relatively low SRV values below 200  $\text{cm/s}$  [Nara 99; Lolg 93]. In recent times, with the development of selective emitter structures to resemble the front surface of the PERL cell, yielding efficiencies of more than 19 % on large area devices fabricated in industrial environments, [Tjah 11; Hall 11d], it now appears that this Al/Si alloyed  $\text{p}^+$  layer is limiting the efficiency of screen-printed solar cells. Subsequently, the focus of research on p-type substrates has moved towards solar cells with a passivated rear and local contact formation [Gatz 11; Mack 10; Munz 11; Wang 12; Verm 12]. However this again raises the need to adequately passivate non-diffused p-type surfaces in a commercially applicable manner, such as by using negatively charged dielectrics like  $\text{AlO}_x$  [Agos 06]. Various other dielectric layers have been used to passivate the non-diffused p-type surfaces such as intrinsic a-Si, or dielectric stacks such as thermally stable a-Si/ $\text{SiN}_x\text{:H}$ ,  $\text{AlO}_x/\text{SiN}_x\text{:H}$ , thermal  $\text{SiO}_x\text{:H}/\text{SiN}_x\text{:H}$  and  $\text{AlO}_x/\text{SiO}_x\text{:H}/\text{SiN}_x\text{:H}$  [Gatz 11; Verm 12; Dauw 02b; Li 12a; Horz 12].

One potential way to avoid the need to passivate a lightly doped p-type surface is through the use of a floating junction [Ghan 91], as is used by the passivated emitter, rear floating junction (PERF) solar cell. Using a floating junction has multiple benefits for rear surface passivation including a reduction in minority carrier mobility and a reduced minority carrier concentration. In

addition, due to field effect passivation with commonly used dielectrics such as thermal  $\text{SiO}_2$  and PECVD  $\text{SiN}_x\text{:H}$  with fixed positive charge, n-type surfaces benefit from the passivation by such dielectrics through the accumulation of majority carriers at the surface which act to reduce the minority carrier concentration.

Other high efficiency approaches have opted for the use of interdigitated contacts to capitalise on reduced shading losses by having both contacts on the rear of the device. Such devices have typically been fabricated on n-type wafers due to the high diffusion lengths required. This also avoids the need to passivate lightly doped p-type surfaces. However all of the technologies using floating junction structures and interdigitated contacts require several patterning methods to effectively contact a buried layer within the solar cell.

Section 4.4.2 will explore some of these patterning methods in more detail.

## 4.4.2 Current Methods to Contact Buried Layers

Several methods have been developed to fabricate complex cell structures involving floating junctions and interdigitated contacts. Typically, all approaches for wafer-based technologies require patterning for at least one diffusion, and subsequent patterning steps to define the contact window of smaller dimensions than the diffused region. Hence we will explore the PERF, buried emitter solar cell, Sunpower A-300 and crystalline silicon on glass technologies to explore their suitability at forming contacts in a simple, self-aligned manner.

### 4.4.2.1 PERF Solar Cells

To fabricate PERF solar cells, several diffusion masks are required. For such solar cells, even the formation of the floating emitter over essentially the entire rear surface requires a patterning step, to mask the regions that will be boron-diffused from the phosphorous diffusion [Wenh 94; Alte 96]. After the phosphorus diffusion, the rear oxide layer is patterned to create openings for the boron diffusion ensuring a gap of undiffused p-type silicon is retained between the floating junction and the boron diffused contacts to prevent shunting between the  $n^+$  and  $p^+$  regions. Following the boron-



diffusion, an additional photolithographic step is required to define the metal contact windows in the centre of the boron-diffused regions to ensure the metal does not contact the lightly doped p-type substrate (see Fig. 4.31) [Wang 90].

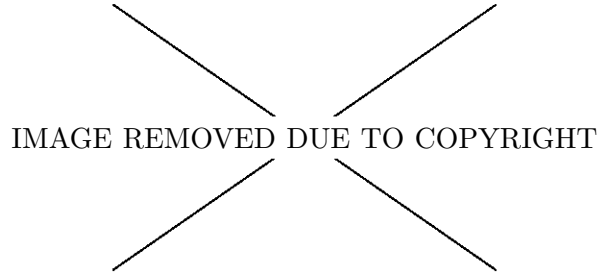


Figure 4.31: Structure of the PERF solar cell (image from [Alte 96]).

#### 4.4.2.2 Buried Emitter Solar Cell

The buried emitter solar cell concept was proposed by Harder *et al.* 2008, as an alternative approach to using a floating junction (which retains the passivation benefits of a diffused n-type surface) (see Fig. 4.32) [Hard 08]. This technology uses a similar approach to the PERF cell described above, whereby the boron emitter is created through a masked boron diffusion process with localised diffusion barriers [Hard 08]. Thereafter a phosphorous diffusion process is performed in the non-diffused areas to form heavily doped n-type silicon regions (allowing contact between the n-type base silicon and the n-type metal contact). During this phosphorus diffusion process, a diffusion mask is used to avoid the diffusion of phosphorous into regions which will later form the p-type contacts of the device [Mert 09].

However, unlike other approaches used to form interdigitated contacts, in the buried emitter solar cell, phosphorous is intentionally diffused over a large portion of the existing emitter. This diffusion process utilises the “push effect” [Hu 83], which drives the boron atoms further into the solar cell during the phosphorous diffusion, hence burying the emitter of the device. The concentration of phosphorous in the n-type layer is also higher than that of boron in the p-type

layer, which allows phosphorous to overcompensate any remaining boron at the surface [Hard 08]. Even though the cell structure results in more than 50 % of the back surface being covered by overlapping  $n^+$  and  $p^+$  regions,  $FF$  in excess of 80 % and efficiencies of almost 22 % have been achieved, indicating that tunneling of carriers between the  $n^+$  and  $p^+$  regions does not appear to be a significant recombination mechanism for this cell design [Mert 09; Hurk 92].

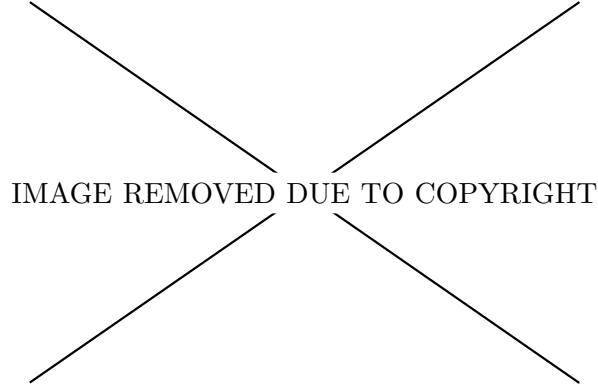


Figure 4.32: Structure of the buried emitter solar cell (image from [Hard 08]).

#### 4.4.2.3 Sunpower A-300 Solar Cell

Another approach which is widely used to contact buried layers in solar cells is the use of patterning and subsequent etching processes to remove the surface layer of the solar cell in precise locations. A commercial technology which uses this approach is the Sunpower A-300 solar cell, which until recently, had achieved the highest independently confirmed efficiency for a large area silicon solar cell at 24.2 % [Gree 11; Cous 10]. The A-300 solar cell used n-type silicon as the base wafer. A full area boron diffusion and subsequent oxidation is performed on the rear of the device to create the p-type regions. To contact the n-type base, the oxide is patterned and the exposed silicon regions are etched. After this structure has been created, a phosphorus diffusion is performed on the exposed regions as shown in Fig. 4.33 [Sint 90]. The use of the mesa/trench structure allows

a self-aligned separation of the n- and p-type metal contacts after the deposition of a single metal layer.

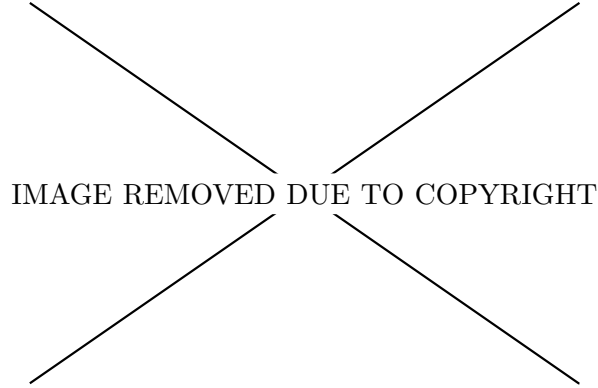


Figure 4.33: Structure of the Sunpower A-300 interdigitated rear contact solar cell (image from [Mull 04]).

##### 4.4.2.4 Crystalline Silicon on Glass Thin-Film Technology

The crystalline silicon on glass thin-film solar cell technology [Gree 04] uses a similar approach, however for these solar cells all layers are deposited onto a glass superstrate in amorphous form over the full area. Subsequently, several inkjet and laser patterning steps are employed to locally remove layers in different regions of the solar cell (see Fig. 4.34). The first of these patterning processes is used to etch through the entire device to the insulating  $\text{SiN}_x\text{:H}$  layer in order to isolate adjacent cells within the module. Following this, an insulating layer of resin is applied over the whole surface as a mask for the formation of the n- and p-type contacts. Subsequently inkjet technology is used to form “craters” in the device to etch through to the  $\text{n}^+$  silicon layer in localised regions, and “dimples” which etch through the resin and  $\text{SiO}_2$  to reach the  $\text{p}^+$  silicon [Gree 04]. This approach also relies on an additional process to allow the reflow of resin into the craters to isolate the metal contacting the  $\text{n}^+$  silicon from contacting the p or  $\text{p}^+$  silicon on the walls of the crater [Baso 05; Baso 06].

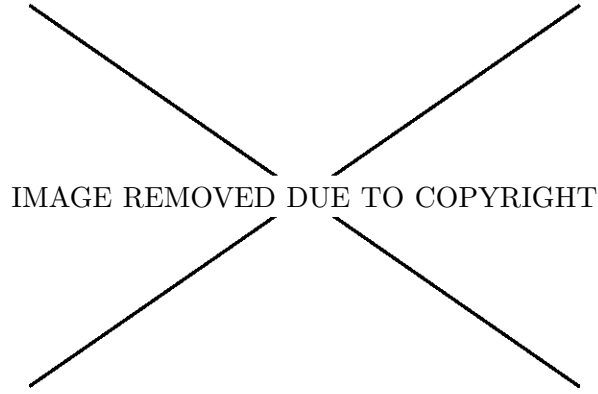


Figure 4.34: Structure of the crystalline silicon on glass thin-film solar cell (image from [[Gree 04](#)]).

#### 4.4.2.5 Summary of Existing Methods for Contacting Buried Layers

While the PERF, buried emitter solar cell, Sunpower A-300 solar cell and crystalline silicon on glass thin films technologies have many advantages associated with them, all technologies have significant processing complexities. For all of the wafer based silicon technologies, two separate thermal diffusions are required to form the interdigitated contact or floating junction structure, with diffusion masks being required for the formation of at least one of these diffusions. Subsequently, an additional patterning process is required to form the contact windows over smaller regions in the diffusion/s such that metal contacts of either polarity cannot come into direct contact with silicon of the opposite polarity. On the other hand, the approach adopted for the crystalline silicon on glass technology using the reflow of resin is essentially self-aligning, although this still requires an additional step.

Hence it would appear desirable to develop a self-aligning patterning approach to effectively expose a buried layer in the solar cell and thereby allow the formation of a contact of opposite polarity to that of the surrounding surface layer, whilst simultaneously providing adequate electrical insulation between the base and emitter contacts. The patterning process should also simultaneously form a heavily doped region of the appropriate polarity, to avoid the need for subsequent high temperature diffusion processes.

### 4.4.3 New Proposed Method for Contacting Buried Layers

#### 4.4.3.1 Overview

One potential method to develop a self-aligning heavy doping patterning approach to contact a buried silicon layer could be through laser doping. However, in order to fabricate a heavily diffused laser-doped region of opposite polarity to the existing surface layer without the removal of any part of the surface layer, several key features of the laser-doped structure are essential such as: (1) the depth of the diffused region; (2) width of doping beyond the opening in the dielectric layer; and (3) the thermal properties of the dielectric layer. Hence for the proposed method close attention should be given to the characteristics of the laser beam and thermal properties of the dielectric layer. In this section a new contacting scheme will be developed.

Firstly, in order to achieve such a contact, dopants in the existing surface layer must be overcome through the addition of sufficient dopants of the opposite polarity during the laser doping process in order to invert the polarity of the surface region. For the proposed method, the laser-doped region should be sufficiently deep to ensure the pre-existing dopants can be distributed over a large volume to greatly reduce the concentration of the dopants, whilst simultaneously incorporating dopants of the opposite polarity into the molten region. In comparison to thermal diffusions which typically form a diffused layer 200 nm – 2  $\mu$ m in depth, laser doping forms a molten region up to 10  $\mu$ m deep, which can lead to reductions in the average dopant density of pre-existing dopants throughout the laser-doped region of up to 50 times compared to that in the surrounding surface layer. Through doing so, the resultant dopant density of the introduced dopants can even be substantially less than that of the dopants in the surrounding surface, hence reducing the risk of parasitic shunting, whilst still inverting the polarity of this surface region [Hurk 92]. As a result, this process can be applied through full area surface layers formed without the use of patterning processes and the subsequent removal of dopants from the surface layer in any region.

Secondly, to allow adequate electrical isolation of the metal contact to the laser-doped region from the surrounding surface regions, it is desirable to dope a region that is wider than the resulting opening in the dielectric layer. This avoids the need to grow a subsequent dielectric layer over the laser-doped region and perform additional patterning steps to define a narrower contact window

than the laser-doped region. Hence for this work, the use of a laser beam with a non-uniform cross sectional intensity distribution with the fundamental transverse mode ( $\text{TEM}_{00}$ ) was adopted, which approximates a Gaussian distribution [Alda 03] (see Fig. 4.35), as this laser has been shown to generate a laser doped region well beyond the dielectric layer opening (see Secion 4.1). Such laser beams have an intensity at the radial spot size ( $w_0$ ) at a ratio of  $1/e^2$  to the peak intensity at the central part of the laser beam ( $I_0$ ) (see Fig. 4.35).

Further to this, it is desirable to use a dielectric layer with a substantially higher melting point than the underlying silicon which melts at  $1414^\circ\text{C}$  [Sze 07]. With these properties, it is expected that the dielectric layer will require a higher energy density to melt than will be required by the underlying silicon. Subsequently, the radial threshold at which the silicon melts can be larger than that of the dielectric layer as shown in Fig. 4.35.

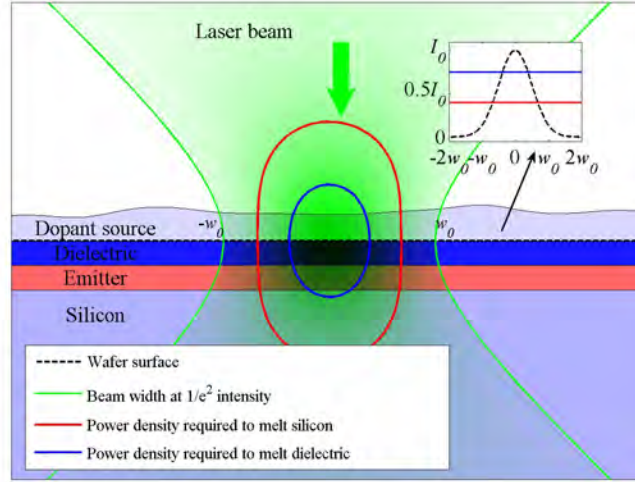


Figure 4.35: Schematic diagram of a  $\text{TEM}_{00}$  laser beam incident on a wafer surface. Indicated power density levels to melt silicon and the dielectric layer are arbitrary.

In addition, it is preferable to use dielectrics which have lower thermal conductivity and diffusivity, and a higher specific heat than silicon, such as  $\text{SiO}_2$  (see Table 4.9), to lead to an enhancement of the silicon melt front if the dwell time of the laser is sufficient.

Table 4.9: Thermal properties of silicon and silicon dioxide [Sze 07].

	Si	SiO <sub>2</sub>
<b>Melting point</b> (°C)	1414	1700
<b>Specific heat</b> (J/g · K)	0.713	1
<b>Thermal conductivity</b> (W/cm · K)	1.56	0.14
<b>Thermal diffusivity</b> (cm <sup>2</sup> /s)	0.9	0.006

By using these approaches, a substantially deep junction should be formed, (preferably more than 5  $\mu\text{m}$ ) and the heavily diffused region should extend several microns laterally from the edge of the opening in the dielectric layer.

#### 4.4.3.2 Proposed Processing Sequence

Fig. 4.36 shows the proposed processing sequence to contact the base p-type silicon in a silicon solar cell through an n-type emitter using laser doping. In the first step, a spin on dopant source containing a high concentration of p-type dopants such as boron is applied to the wafer surface (see Fig. 4.36(a)). A laser is then used to illuminate the surface of the wafer, which melts the silicon and overlying dielectric layer. At this time, dopants from the spin on dopant source mix with the molten silicon and dopants from the emitter, and begin to diffuse into the silicon (see Fig. 4.36(b)). As the laser illumination continues, the melt front of the silicon moves further into the wafer hence expanding the molten region. During this time, the dopants from the emitter and spin on dopant source diffuse further into the silicon (see Fig. 4.36(c)). After the illumination is removed, the molten silicon cools and resolidifies resulting in a contact formed through a surface layer, which makes direct contact to the underlying silicon, with a certain junction depth and lateral doping width extending beyond the opening in the dielectric layer (see Fig. 4.36(d)).

The method for redistributing dopants from an existing emitter and overcompensating such dopants with introduced dopants of the opposite polarity was first proposed by Hallam *et al.* 2013 [Hall 13a], with further experimentation performed in conjunction with Chan *et al.* 2012

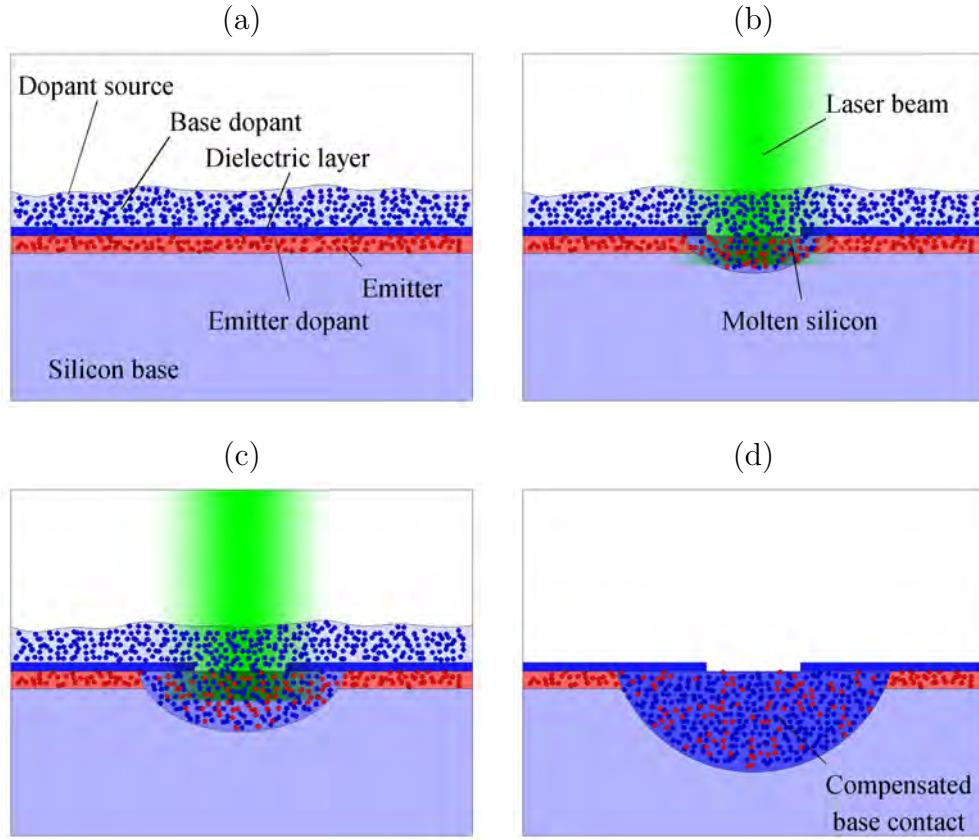


Figure 4.36: Process for penetrating contacts through an emitter using laser doping by (a) coating the silicon wafer with a spin on dopant source, (b) illuminating the surface with a laser and melting the silicon surface, (c) continuing the laser illumination to expand the molten region and incorporate dopants and (d) the finished structure.

[Chan 12]. At the same conference, the method was independently demonstrated by Gall *et al.* 2012 [Gall 12b; Gall 12a]. For the proposed method, such contacts could be formed through a surface layer of a silicon solar cell of opposite polarity in a self-aligned process that does not require typical diffusion masking processes or the removal of any part of the surface layer. In addition, the method can pattern the dielectric layer to define the contact area for the metal/Si interface whilst simultaneously forming a heavily doped region of opposite polarity to the surrounding surface layer in a single process, with a contact opening substantially narrower than the width of the doped



region, hence avoiding the need for patterning/alignment steps.

For interdigitated contact solar cells, the emitter of the device could essentially cover the entire rear of the solar cell, therefore essentially allow a one-dimensional transport of minority carriers, reducing the distance required for minority carrier collection by the p-n junction. As a result, constraints placed on wafer quality could be relaxed, whilst still achieving a high collection probability of minority carriers, and therefore  $J_{SC}$  [Hard 08; Hard 09]. This also avoids recombination losses above the base diffusion typical for interdigitated contact solar cells [DeCe 07]. This process could allow the formation of interdigitated back contact cells that only require one thermal diffusion. If fabricating such cells on p-type wafers, this could take advantage of the benefits of having n-type surfaces for ease of surface passivation. In addition, if contacts of the same polarity as the emitter are formed by laser doping, the emitter could be optimised for lateral series resistance losses and recombination losses from  $J_{0d}$ , with an independent optimisation of the contact resistance during the laser doping process.

In comparison to the fabrication of the previously outlined cell structures require two patterning/alignment steps with a self-aligning process for the separation of the metal contacts, the proposed method requires only one additional patterning/alignment process step to fabricate interdigitated back contact solar cells [Cous 10; DeCe 07].

#### 4.4.4 Aim

To investigate the use of laser doping to overcompensate a surface region of a solar cell to contact a buried layer in the device in a self-aligned process. The use of both planar and textured surfaces will be explored for the suitability of the process for monofacial and bifacial solar cell structures. Subsequently, the process will be applied for different solar cell applications including isolation of localised recombination sites, edge junction isolation and for IBC solar cell fabrication.

### 4.4.5 Experimental Procedures

In this section, test structures were fabricated on standard commercial grade  $0.5 - 3 \, \Omega \cdot \text{cm}$  p-type CZ wafers with both planar and textured surfaces.

Textured samples on p-type wafers with textured surfaces were pre-processed on an industrial production line following the standard processing sequence for LDSE solar cells outlined in Section 5.2. This included alkaline texturing with pyramids  $2 - 5 \, \mu\text{m}$ , a light phosphorus emitter diffusion with a sheet resistance of approximately  $120 \, \Omega/\square$ , chemical edge junction isolation, standard PECVD  $\text{SiN}_x\text{:H}$  and Al rear screen-printing and firing.

Test structures fabricated with planar surfaces were saw-damaged etched, RCA cleaned and diffused using phosphorous solid sources to a sheet resistance of either  $120 \pm 20 \, \Omega/\square$  or  $1200 \pm 100 \, \Omega/\square$ . Subsequently,  $\text{SiON}_x\text{:H}$  was deposited onto both surfaces using a laboratory Roth & Rau remote microwave PECVD system.

Filmtronics PBF1 SOD was then applied at 2000 RPM for 40 s and dried at  $90 \, ^\circ\text{C}$  for 10 min on the rear. The approximate dose for the SOD was  $1.0 \times 10^{16}/\text{cm}^2$ . Laser doping was performed using a 532 nm wavelength CW laser with an optical power of approximately 13.5 W (as previously described in Section 4.1), using processing speeds ranging from  $0.1 - 10 \, \text{m/s}$ . On selected samples, laser-doped point contacts were also formed by using a physical mask with small line openings and by scanning the laser beam perpendicular to the openings in the mask.

EBIC was used to determine the location of the p-n junction in the test structures, and therefore the ability of the laser doping process to overcompensate the surface diffused region. To make electrical contact to the samples for EBIC measurements, n-type contact tabs were created on the front surface of all samples using laser doping. For the n-type laser-doped contact pads, wafers were spin coated with  $\text{H}_3\text{PO}_4$  at 3000 RPM for 20 s on the front surface prior to laser doping. For the p-type contact pad, textured samples used the existing screen-printed Al rear surface as previously describe, whereas laser doping was used to form the p-type contact pad on planar samples using PBF1 applied at 2000 RPM followed by baking at  $130 \, ^\circ\text{C}$  for 10 min. After each laser doping process the dopant source was removed using a short, weak HF dip. Subsequently EBIC measurements were performed as discussed in Section 4.1. The process sequence for samples

in this section is shown in Fig. 4.37.

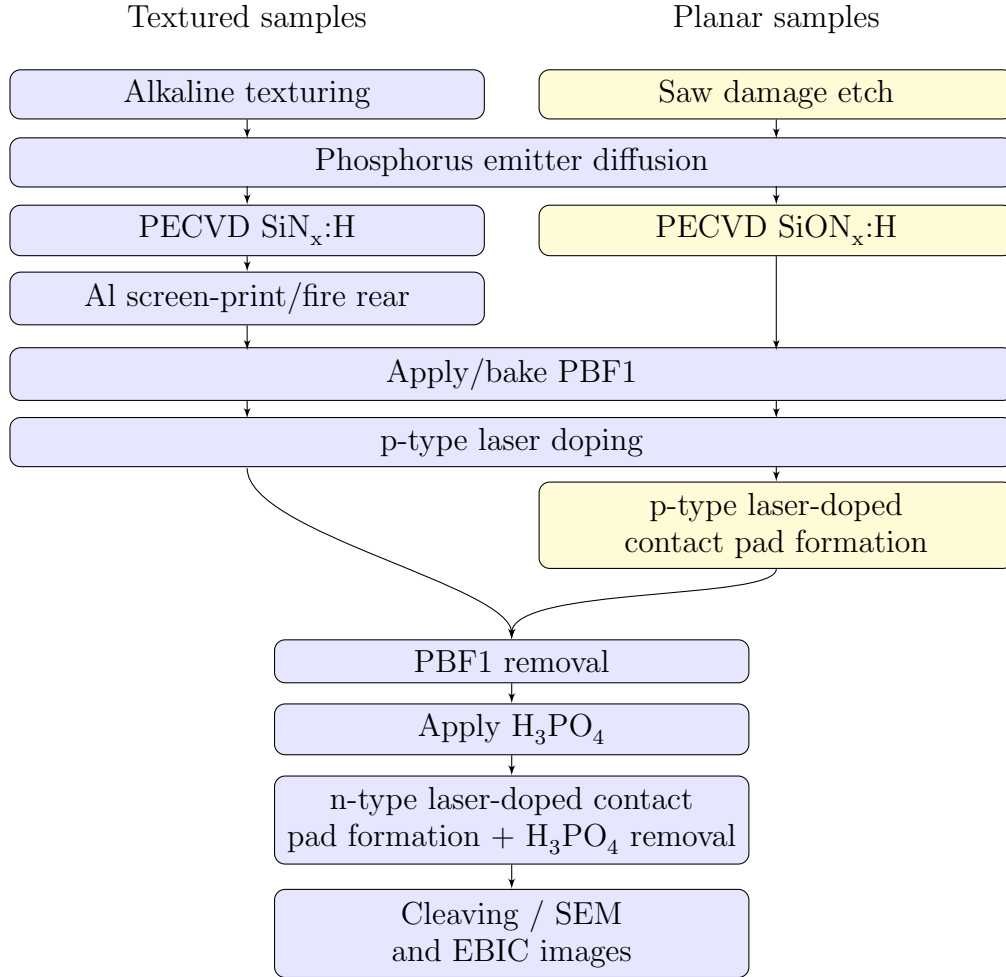


Figure 4.37: Process flow for p-type laser doping to contact buried layers in silicon solar cells.

#### 4.4.6 Results of Laser Doping to Contact Buried Layers

By performing p-type laser doping through a n-type surface layer, direct contact could be made to the underlying p-type silicon on both planar and textured surfaces.

#### 4.4.6.1 Slow Speeds

As shown by the combined SEM/EBIC images in Fig. 4.38, no p-n junction was observed in the laser-doped region of both textured and planar samples processed at the slow speed of 0.2 m/s. Importantly, this demonstrates that the p-type dopants incorporated into the silicon during the laser doping process have completely overcompensated the n-type dopants from the thermally diffused emitter to form a p-type region at the surface of the wafer, and that this p-type region continues uninterrupted to the p-type silicon base. Furthermore, the p-type doping extended well beyond the opening in the dielectric layer and hence it may be possible to form a p-type metal contact over the laser-doped region without contacting the surrounding n-type emitter.

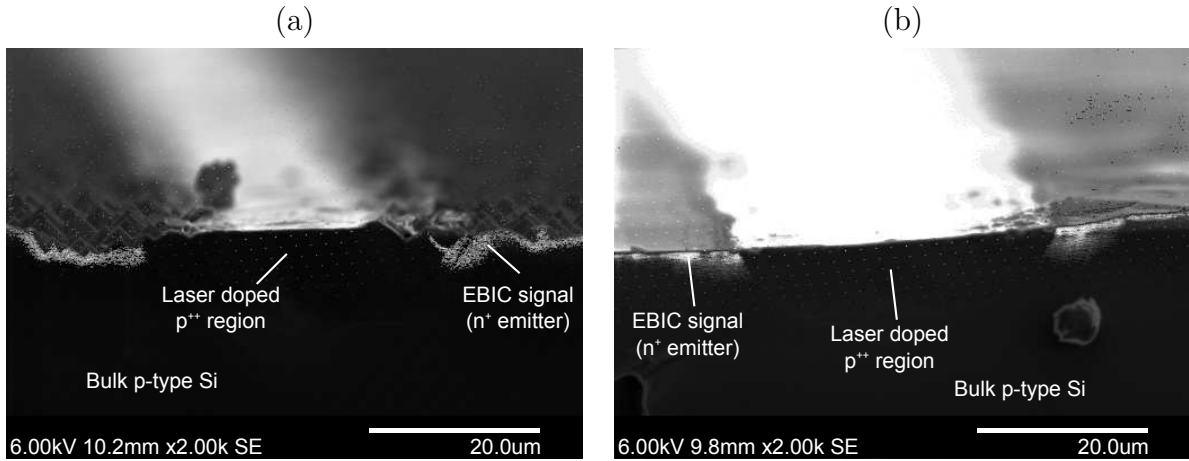


Figure 4.38: Combined SEM/EBIC image of a p-type laser-doped line processed at 0.2 m/s formed through a  $120 \Omega/\square$  phosphorus emitter on (a) a textured surface and (b) a planar surface.

#### 4.4.6.2 High Speeds

At higher processing speeds, the silicon within the laser-doped region remains molten for a shorter time and hence the dopants have less time to diffuse in the liquid state. As shown in Fig. 4.39, for speeds of  $0.5 - 2$  m/s regions of n-type silicon can remain in the laser-doped area, predominately along the edge of the laser-doped lines. This can result in the formation of localised transistor structures in which a region of n-type silicon exists between the p-type silicon base and the heavily diffused p-type laser-doped contact. This effect increases with increasing processing speeds, which results in the n-type regions penetrating further into the solar cell and reduces the area of contact between the heavily doped p-type region and the p-type silicon base. Furthermore, as the processing speed increases, the width of the n-type region at the surface becomes wider, such that the n-type silicon moves closer to the edge of the opening in the dielectric layer.

At high processing speeds of 5 m/s and 10 m/s, no p-type surface layer was evident when laser doping through a phosphorus emitter with a sheet resistance of  $120 \Omega/\square$ , and hence the surface of the wafer remained n-type, with the n-type region extending several microns from the silicon surface (see Fig. 4.39(a)-(b)). This was likely due to the short duration in the molten phase and hence the limited spread of the n-type dopants from the emitter, resulting in a high concentration of phosphorus dopants remaining at the surface. Subsequently the limited number of boron atoms diffusing into the molten silicon may not have been sufficient to overcompensate the concentration of the phosphorus in this surface region, particularly with the reduced incorporation of dopant atoms into the silicon when laser doping at higher processing speeds.

For the samples shown in Fig. 4.39(c), due to the reduced number of phosphorus atoms for the  $1200 \Omega/\square$  emitter, a p-type region could still be formed at the surface, however a fully formed transistor was observed, with the p-type surface completely surrounded by n-type silicon. Whilst this effect may be reduced by using appropriate concentrations of the dopants and selecting dopants for their diffusion coefficients, it is expected that using deeper laser-doped regions would be more desirable to allow a greater spread of the dopants within the emitter and hence allow p-type dopants to more readily overcome the concentration of the n-type dopants.

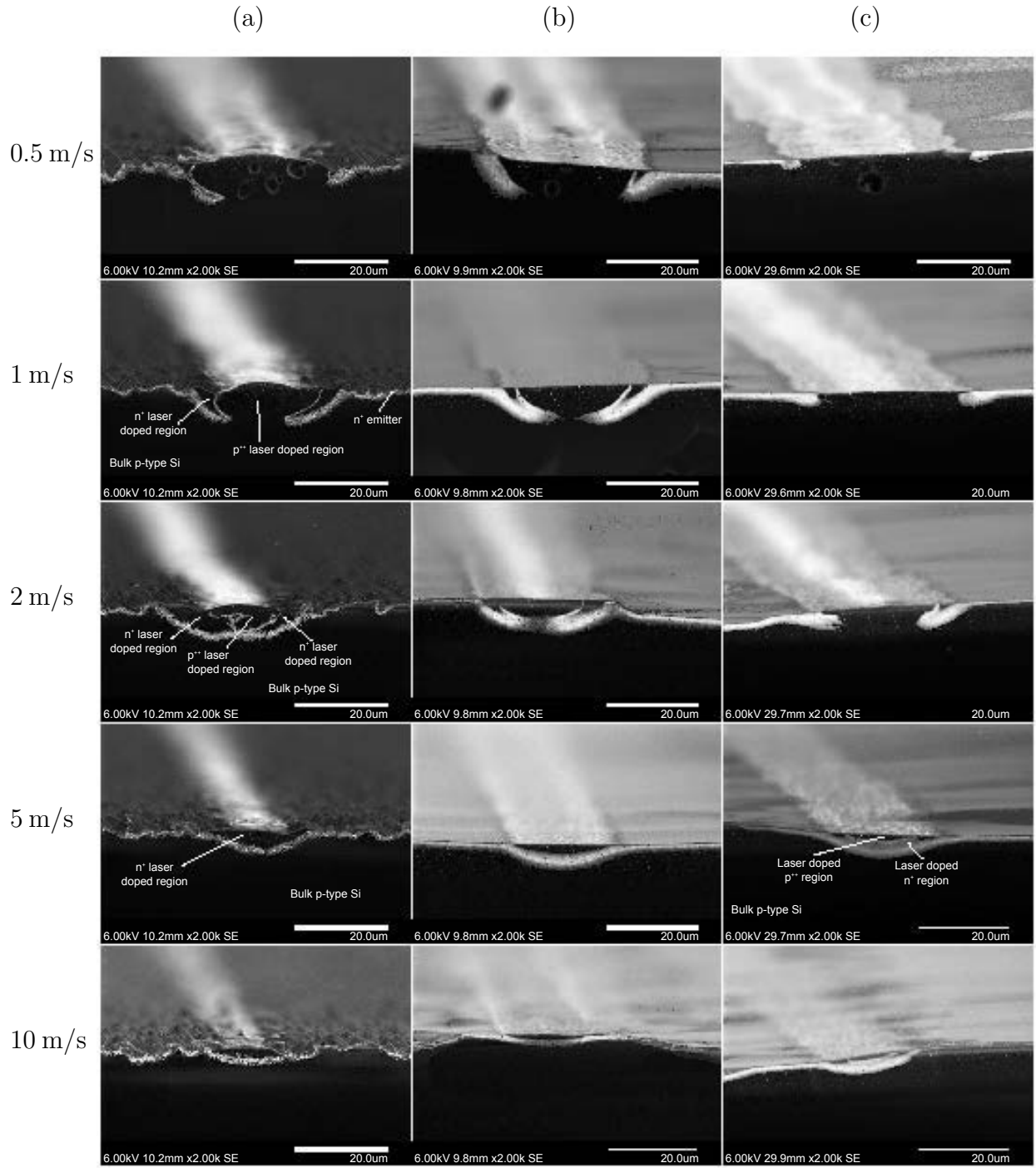


Figure 4.39: Combined SEM/EBIC images of p-type laser doping through a 120  $\Omega/\square$  phosphorus emitter on (a) a textured surface, (b) a planar surface and (c) a 1200  $\Omega/\square$  phosphorus emitter on a planar surface.

#### 4.4.6.3 Textured Surfaces

For the textured sample shown in Fig. 4.39(a) with a sheet resistance of  $120 \Omega/\square$  processed at 2 m/s, a somewhat random junction structure was observed, suggesting either a turbulent mixing of the dopants within the molten region or that the concentrations of boron and phosphorus within the molten region are similar, and hence slight spatial variations in doping concentrations resulted in a change of the polarity in localised areas. It was also observed that the heavily doped p-type region appears to be completely isolated from the underlying p-type silicon base by a thin layer of n-type silicon, and hence the laser doping process resulted in a fully formed transistor contact. However the n-type region on the left side of the laser-doped region at the surface is  $9 \mu\text{m}$  wide and extends all the way to the opening in the dielectric layer. This suggests that such a contact may be prone to shunting on finished devices.

#### 4.4.6.4 Planar Surfaces

In contrast, the planar sample shown in Fig. 4.39(b) with the same emitter sheet resistance of  $120 \Omega/\square$  and processed using the same laser conditions of 2 m/s, did not show a random structure of the junction. In addition, for this sample there was direct contact for a width of  $7 \mu\text{m}$  of heavily doped p-type silicon to the underlying p-type silicon base, although this was substantially less than the  $27 \mu\text{m}$  width of the entire laser-doped region at the surface. Furthermore, the n-type silicon at the surface of the laser-doped region was several microns from the opening in the dielectric layer suggesting that shunting may not result for such structures on finished devices between the heavily doped p-type silicon and surrounding n-type emitter. The difference response between the samples with planar and textured surfaces is expected to be caused by the difference in diffusion profiles used (an industrial emitter for the textured surfaces with a junction depth of  $\approx 0.2 \mu\text{m}$ , and a laboratory emitter with substantially deeper junction of  $\approx 0.5 - 1.0 \mu\text{m}$ ).

#### 4.4.6.5 Discussion of Issues at Higher Speeds

The formation of such structures could be due to the diffusion coefficient of boron in the liquid state ( $1.2 \times 10^{-8} \text{ m}^2/\text{s}$ ) being substantially lower than that of phosphorus ( $5.7 \times 10^{-8} \text{ m}^2/\text{s}$ ) [Gara 07; Tang 09]. Such differences become of increasing importance for higher processing speeds in which the time the silicon is molten for is reduced, and hence the spatial distribution of dopants within the molten region are more heavily determined by their respective diffusion coefficients. The partial transistor formation was reduced when a lighter  $1200 \text{ } \Omega/\square$  phosphorus emitter was used, due to the lower number of available phosphorus dopants, which meant the boron atoms introduced during the laser doping process could more readily overcompensate the phosphorus atoms and form a  $p^+$  region (see Fig. 4.39(c)).

In addition, the peripheral areas of the laser-doped regions, rely on the thermal conductivity and diffusivity of the silicon to melt such regions due to the Gaussian distribution of the laser beam and hence the intensity of the laser being too low to directly melt the silicon in such regions. It is expected that the silicon predominately solidifies towards the surface and hence shallow molten regions solidify more rapidly than deeper molten regions. Subsequently, the peripheral laser-doped areas become molten later, and resolidify before the central laser-doped regions. As a result, the spatial distributions of the doping concentrations in the peripheral areas of the laser-doped region are more strongly dependent on the diffusion coefficients of the dopants, further exacerbating the effect of the shortened time in the molten state due to the increased processing speed.

Given that the junction depths achieved when performing n- or p-type laser doping on a base silicon wafer of the opposite polarity were essentially the same, it can be assumed that the n-type silicon areas within the laser-doped regions (shown in Fig. 4.39), form due to a lack of sufficient boron dopants diffusing to the peripheral regions to overcompensate the phosphorus dopants which have reached the same area. In addition, this affect may also have been due to the initial distribution of phosphorus dopants throughout the surface of the silicon wafer. This would have allowed them to travel shorter distances to reach such areas, than the boron dopants which were only introduced through the opening in the dielectric layer and were hence required to travel larger distances.

While results at slow speeds are encouraging it is essential that faster speeds be investigated



further as they are critical for commercial viability.

#### 4.4.6.6 Potential Solutions

It is expected that several approaches could be used to reduce the effect of overlapping n- and p-type laser-doped regions and hence allow faster processing speeds to be used. By reducing the concentration of phosphorus and hence using a more lightly doped emitter, less boron dopants would be required to overcompensate the phosphorus dopants. Alternatively a higher concentration of boron dopants could be incorporated into the molten region. Choosing dopants for the contact with a higher diffusion coefficient than that of the dopants in the surface layers, such as using gallium instead of boron, with a diffusion coefficient of  $(3.6 \times 10^{-8} \text{ m}^2/\text{s})$  could also reduce the formation of peripheral n-type silicon regions [Gara 07].

This effect would also be reduced when creating phosphorus-doped contacts through a boron-diffused surface. In this case, the phosphorus would be able to more readily reach the peripheral regions and reduce formation of peripheral p-type regions. However this may result in higher phosphorus doping concentrations being required at the surface to overcompensate the remaining boron dopants, and hence could lead to the formation of a tunnel diode and induce shunting [Hurk 92]. On the other hand, it appears that the diffusion coefficients may be utilised to form complete transistor structures in which a complete n-type layer exists between the p-type surface layer and the underlying p-type silicon base by using an appropriate processing speed and appropriate concentrations of both dopants, however this would not appear desirable for solar cell applications.

#### 4.4.6.7 Summary

Direct contact could be established between the p-type laser doped region and the underlying p-type bulk by overcompensating the n-type surface region. However the laser processing speed had a large influence on the process whereby slow speeds ( $\approx 0.2 \text{ m/s}$ ) resulted in direct contact, whilst intermediate processing speeds ( $0.5 - 2 \text{ m/s}$ ) resulted in localised transistor formation and higher speeds ( $5 - 10 \text{ m/s}$ ) resulted in the formation of couple transistors. Moving to lighter diffusions helped avoid the formation of localised transistors through a reduction in phosphorus dopants in

the emitter.

#### 4.4.7 Results for Point Contact Formation

Point contacts processed at a speed of 0.5 m/s on a textured surface with a sheet resistance of  $120 \Omega/\square$  also demonstrated the potential for contacts to be formed through the use of laser doping through a surface layer of the opposite polarity. Fig. 4.40 shows a combined SEM/EBIC image of such a contact. It was observed that for this point contact, direct contact could be made between the p-type surface layer and the underlying p-type silicon base. Similarly to the line contacts processed at 0.5 m/s, this point contact displayed the formation of localised transistor structures extending into the bulk of the wafer, and hence a slower speed should have been used to avoid the formation of such transistor structures.

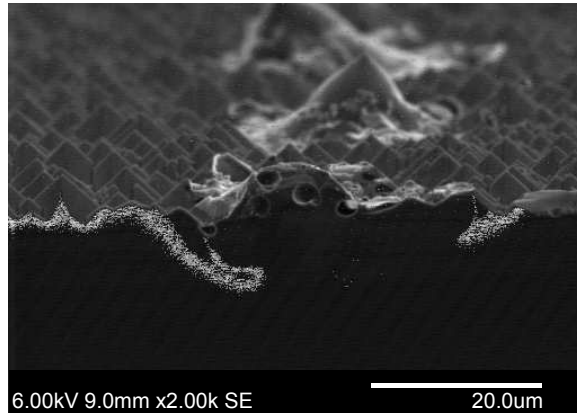


Figure 4.40: Combined SEM/EBIC images of the cross section of a p-type laser-doped point contact on a textured surface processed at 0.5 m/s through an n-type emitter with a sheet resistance of  $120 \Omega/\square$ .

Hence the proposed method could also be used to form contacts to buried layers in the solar cell using point contacts. However, such contacts must also be evaluated on real devices.

#### 4.4.8 Proof of Concept for Edge Junction Isolation and Interdigitated Rear Contact Devices

The proposed method of penetrating laser-doped contacts through surface layers of silicon solar cells has also proven to be effective for the isolation of sites with localised and/or edge recombination, with initial demonstrations performed in conjunction with Chan *et al.* 2013 [Chan 13a]. In addition, experiments were performed in conjunction with Chan *et al.* 2014, where screen-printed solar cells were fabricated which demonstrate the suitability of this process to perform EJI for silicon solar cells and allow the phosphorus emitter to remain on the rear surface [Chan 15].

First attempts to fabricate interdigitated rear contact solar cells on p-type CZ wafers with a single phosphorus thermal diffusion ( $150 \text{ } \Omega/\square$ ) using the proposed method were presented in conjunction with Chan *et al.* 2012, with efficiencies over 14 % achieved. J-V parameters shown in Table 4.10 indicated a substantially lower  $V_{OC}$  on the finished device than the  $iV_{OC}$  prior to metallisation due to shunting [Chan 12]. It is expected this shunting was due to the poor quality of the opened lines with defected regions adjacent to the laser-doped lines. It is expected that improvements to the laser optics and/or properties of the dielectric layers could reduce the shunting. In addition, the  $J_{SC}$  of the device was also affected by the use of a planar wafer surface and non-optimal dielectric layer for an anti-reflection coating.

Table 4.10: Light J-V data of a laser-doped IBC solar cell with a single thermal diffusion and p-type laser-doped contacts formed through the phosphorus emitter [Chan 12].

$V_{OC}$	$J_{SC}$	$FF$	$\eta$
(mV)	(mA/cm <sup>2</sup> )	(%)	(%)
625	35.7	64.8	14.5

#### 4.4.9 Summary for Contacting Buried Layers in Silicon Solar Cells

A novel contacting approach was presented whereby p-type laser-doped contacts were formed through an n-type surface layer (phosphorus emitter) to contact the underlying p-type bulk silicon. This process was achieved in a self-aligned manner, enabling a substantial simplification for IBC solar cell fabrication, with first attempts demonstrating efficiencies over 14 %. In addition, the process was used to perform edge junction isolation for screen printed solar cells, and for the isolation of localised recombination sites.

### 4.5 Chapter Summary

In this chapter, the formation of advanced laser-doped structures was presented.

**Deep junction formation:** Through the use of CW or Q-CW lasers, the volume of molten silicon formed during the laser doping process was shown to become substantially larger and deeper than that previously reported using conventional nanosecond pulse-length Q-switched lasers. Subsequently, deep junctions in excess of 10  $\mu\text{m}$  were demonstrated using both boron and phosphorus dopant sources. In addition, junction depths of more than 8  $\mu\text{m}$  were demonstrated using point contacts. A record efficiency of 20.3 % was also achieved for the Pluto-PERL technology.

**Modelling of the laser doping process:** Modelling of the SIMS profiles indicated a Gaussian diffusion mechanism for the liquid state diffusion. Slight differences were observed between theoretical Gaussian diffusion curves and the SIMS profiles when processing at speeds  $\geq 2$  m/s. Modelling highlighted that the differences were due to the influence of the solid/liquid interface in limiting the further diffusion of impurities into silicon, with the influence becoming stronger as the time in the molten phase is increased and dopants had more time to diffuse within close proximity of the solid/liquid interface. For Q-CW lasers, a characteristic kink was observed in the diffusion profiles and could be due to the partial solidification of the silicon between successive pulses. Kinks observed in the SIMS profiles of CW laser-doped regions formed at slow speeds (0.5 m/s) could

potentially be due to overlapping lines remelting laser-doped regions.

**Laser doping using  $\text{AlO}_x$ :** The potential to use Al containing dielectric layers as a dopant source for local BSF formation using laser doping was clearly demonstrated using both PECVD  $\text{AlO}_x$  and ALD  $\text{Al}_2\text{O}_3$ . Junction depths in excess of  $8\text{ }\mu\text{m}$  were achieved using a processing speed of  $0.5\text{ m/s}$ . A high incorporation of Al atoms from the dielectric layer of up to  $34\%$  was demonstrated, however this was reduced when using higher processing speeds. The processing speed had a clear influence on the generation of defects within the device and ability to shield minority carriers from recombining at the surface of the laser-doped region. On lifetime test structures, at speeds  $< 5\text{ m/s}$ , capping layers of  $\text{SiN}_x\text{:H}$  resulted in substantially higher  $\tau_{eff}$  and  $iV_{OC}$  than that achieved using  $\text{SiO}_x\text{:H}$ , which may have been due to a reduced generation of bulk defects or improved hydrogen passivation achieved when using  $\text{SiN}_x\text{:H}$ . At intermediate speeds of  $5 - 10\text{ m/s}$ , similar results were obtained using both capping layers. A clear influence of processing speed was observed using a capping layer of PECVD  $\text{SiO}_x\text{:H}$ , with increases in  $\tau_{bulk}$  and reduction in  $J_{0d}$  by using increased processing speeds. For a processing speed of  $18\text{ m/s}$ , extremely narrow contact openings of less than  $4\text{ }\mu\text{m}$  width were demonstrated with simultaneous local BSF formation. These contacts were smaller than that used for the world record PERL cells achieved through expensive laboratory processes such as photolithography, which required separate steps for the diffusion of the localised, heavily diffused regions underneath the metal/Si interface. On large area devices, independently confirmed efficiencies of  $20.7\%$  and  $FF$  over  $80\%$  were achieved, demonstrating the suitability of this process for the formation of industrial PERL solar cells. In addition, the process appears to have the potential of a  $120\text{ MW}$  throughput using a single laser head (neglecting automation). It is expected that even higher  $V_{OC}$  should be achieved through further optimisation of the processing sequence to incorporate a firing step to improve hydrogenation of the bulk.

**Contacting buried layers in silicon solar cells:** Laser doping was also demonstrated to have the ability to contact buried p-type layers in silicon solar cells with an n-type emitter. For processing speeds around  $0.2 - 0.5\text{ m/s}$  direct contact was achieved between the heavily doped  $p^{++}$  region and the bulk p-type silicon, whilst for higher speeds localised transistor structures along the edge of the laser-doped region could be formed which could result in shunting. However

optimisation involving modifications to the emitter diffusion and laser doping process should be able to overcome such issues. In addition, the penetration of the contacts through high sheet resistance emitters led to the formation of full transistor structures, particularly by using lightly doped phosphorus emitters. A proof of concept device was demonstrated for interdigitated back contact solar cells featuring a single conventional thermal diffusion, and no removal of any surface layers was required. Efficiencies over 14 % were achieved. It is expected that much higher efficiencies could be obtained through the optimisation of the dielectric layer, phosphorus emitter and laser parameters used. The same process was applied to avoid localised or edge recombination and demonstrated for use as an effective method for EJI in silicon solar cells.

To avoid performance degradation from the generation of LasID during the laser doping process, Chapter 5 investigates the use of hydrogen passivation to alter the recombination activity of such defects.

# Chapter 5

## Hydrogen Passivation of Laser-Induced Defects

LasID are widely reported to be a major limitation for the performance of laser-doped silicon solar cells, particularly when laser doping is used in conjunction with a self-aligned metallisation scheme [Sugi 07; Tjah 08; Hopm 09; Sugi 10; Tjah 10; Kray 10a; Kray 10b]. Whilst avoiding the generation of defects is preferable, various processing techniques exist to reduce the performance degradation associated with such defects. For example, defects generated during laser-groove formation for buried contact solar cells can be chemically removed after the laser process [Chon 88]. Hydrogen passivation can also be used to alter the recombination activity of the defects, as widely reported in the literature (see Chapter 2).

Hydrogen passivation of LasID is not a new topic [Bent 80], however the importance of hydrogen in passivating LasID for laser-doped silicon solar cells is often underestimated. Furthermore, for first generation LDSE (LDSE1) solar cells, laser doping is typically performed after the firing of the Al. As the Al firing process also acts as a hydrogen passivation process, passivation is typically performed before the introduction of LasID.

In Chapter 3, improved hydrogen passivation processes were developed for silicon solar cells to passivate various types of recombination centres, and in Chapter 4 new contacting approaches

were demonstrated using laser doping. In this chapter, the importance of hydrogen passivation for greatly reducing the electrically active recombination of LasID generated during the laser doping process is demonstrated. In Section 5.1, the generation of defects caused by laser doping using CW lasers is presented. In Section 5.2 the passivation of LasID by hydrogen is explored for laser-doped silicon solar cells.

## **5.1 Defects Generated during Continuous Wave Laser Doping**

### **5.1.1 Aim and Experimental Details**

To present defects which can form when using a CW laser to perform laser doping and highlight the importance of using correct laser conditions to avoid excessive defect generation. For processing details, see Section 4.1.

### **5.1.2 Results**

#### **5.1.2.1 Void Formation**

The highly localised heating and fast cooling of the silicon that occurs during laser doping inevitably introduces defects into the silicon material. In the development of advanced laser-doped structures outlined in Chapter 4, various defects were observed on the surface and within the bulk material. For example, when using both Q-CW and CW lasers at processing speeds below 5 m/s, voids were present in the laser-doped region below the surface. With decreasing speed, such voids were present in increasing concentrations with increased size. For speeds of approximately 0.5 m/s voids were observed with diameters up to 4  $\mu\text{m}$  both on the surface of the silicon, and submerged up to 5  $\mu\text{m}$  from the wafer surface (see Fig. 5.1).

For processing speeds below 0.2 m/s no voids were observed, presumably due to the gases within



the voids having sufficient time to diffuse to the surface and disperse prior to solidification of the laser-doped region. The density of such voids in laser-doped regions was highly dependent on the applied dopant source and dielectric layer, which would suggest that the voids may have been caused by the incorporation of atomic oxygen, hydrogen and nitrogen during the laser doping process [Hall 10a]. Evidence of crystallographic defects and silicon being splattered onto the textured silicon adjacent to the laser-doped region was also observed (see Fig. 5.1).

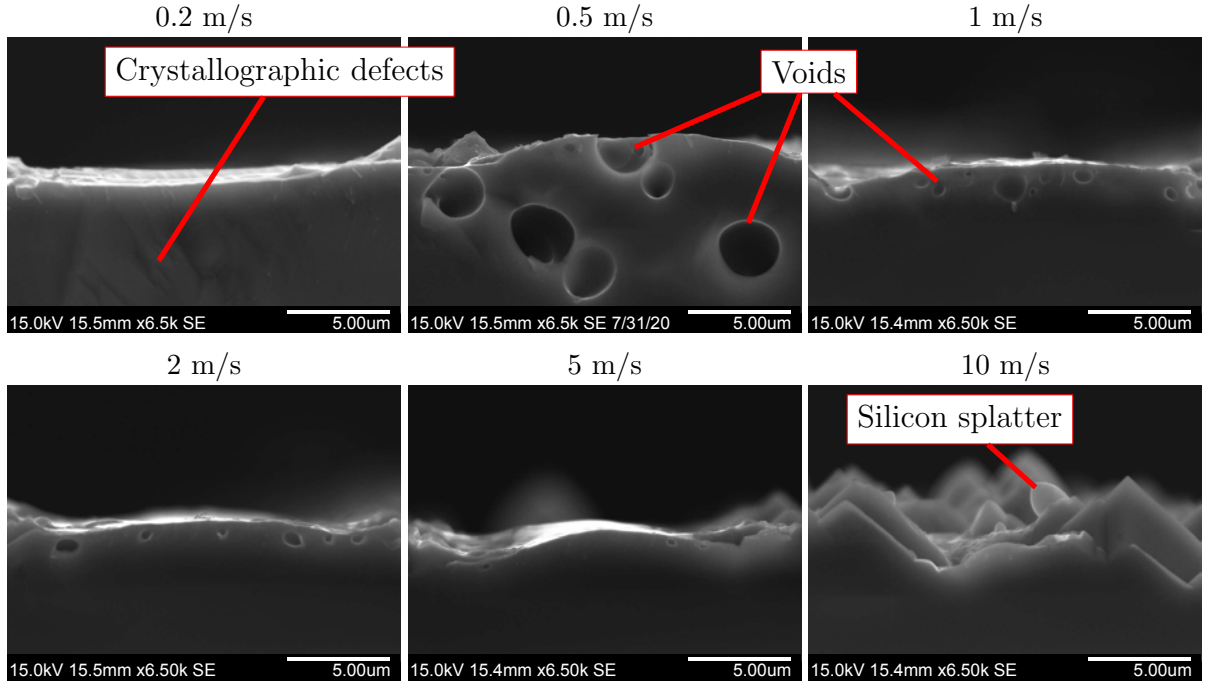


Figure 5.1: SEM images at x6.5k magnification of the cross section of laser-doped lines at various speeds using a 532 nm CW laser, optical power of 13 W and  $\text{H}_3\text{PO}_4$  dopant source showing voids.

### 5.1.2.2 Crack Formation

For speeds below 0.2 m/s, due to the large volume of molten silicon during the laser doping process, large thermal stresses can cause crystallographic defect formation. Such defects were visible

after cleaving the wafer perpendicular to the surface, extending beyond the doped region. The textured sample processed at 0.02 m/s in Fig. 5.2 highlights many crystallographic defects after cleaving whilst the corresponding laser-doped line processed at 0.5 m/s displayed no evidence of crystallographic defects in the SEM image. Similarly, for the planar sample processed at 0.1 m/s crystallographic defects were present predominately following the shape of the molten region indicated by the EBIC images presented in Chapter 4. In contrast, using speeds of 0.2 m/s did not highlight any crystallographic defects after cleaving. During the laser doping process, silicon in and surrounding the laser-doped region undergoes substantial expansion and contraction during the melting and resolidification. It is also possible that these defects were due to the laser doping process stressing the silicon and the subsequent cleaving process causing the extensive crystallographic defects to form. However, a clear trend was observed with these defects only evident for slow processing speeds, suggesting substantial defect generation when laser doping using such speeds.

Alternatively, when using slow speeds cracks were observed along or across the laser-doped region visible at the surface immediately after the laser doping process, confirming that the laser doping process could generate a large amount of crystallographic defects within the laser-doped region, and extend into the bulk of the silicon. In addition, cracks were observed along crystal planes which zig-zag along the laser-doped line and extend more than 25  $\mu\text{m}$  from the laser-doped region (see Fig. 5.3). As such defects can extend beyond the doped region, enhanced bulk recombination could result and it would therefore appear undesirable to use such processing conditions to fabricate silicon solar cells.

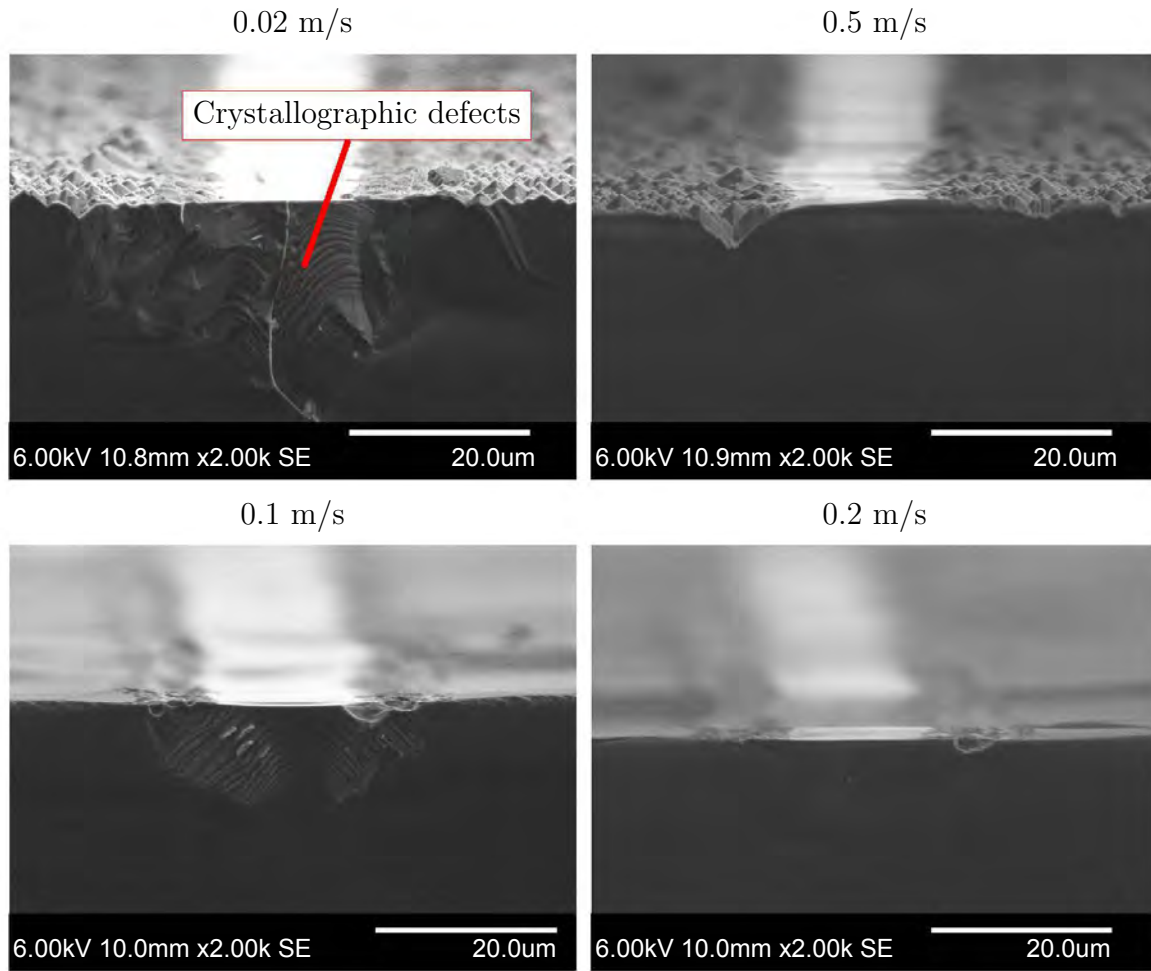


Figure 5.2: Cross sectional SEM images of laser-doped regions showing crystallographic defects directly after cleaving.

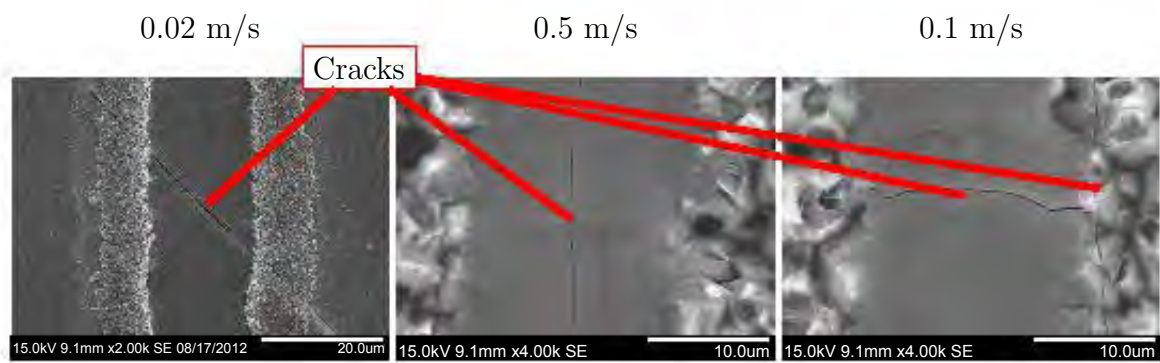


Figure 5.3: SEM images of the surface of laser-doped regions showing cracks along and across the surface.

### 5.1.2.3 $\text{SiN}_x\text{:H}$ Defects

On the surface, abnormalities to the  $\text{SiN}_x\text{:H}$  were observed, similar to that reported in literature using conventional laser doping approaches [Sugi 07]. Even using a processing speed of 0.5 m/s for p-type laser doping on planar surfaces and 5 m/s for n-type laser doping on textured surfaces as is used for the majority of cells fabricated in this thesis, caused a substantial generation of LasID. Fig. 5.4 highlights the defects present using these conditions such as pinholes in the  $\text{SiN}_x\text{:H}$  at the peaks of textured pyramids, or along the edge of the laser-doped line. The holes along the edge of the laser-doped line may have been caused by hydrogen effusion from the hydrogen rich dielectric layer. Further studies indicated that reducing the laser power well below that required to melt the underlying silicon could still generate such blisters to form in the  $\text{SiN}_x\text{:H}$ . In addition, molten silicon from the laser doping process was observed to splatter onto adjacent regions, therefore effectively increasing the conductive surface region. These can act as nucleation sites during the plating process, increasing the width of the metal plated fingers.

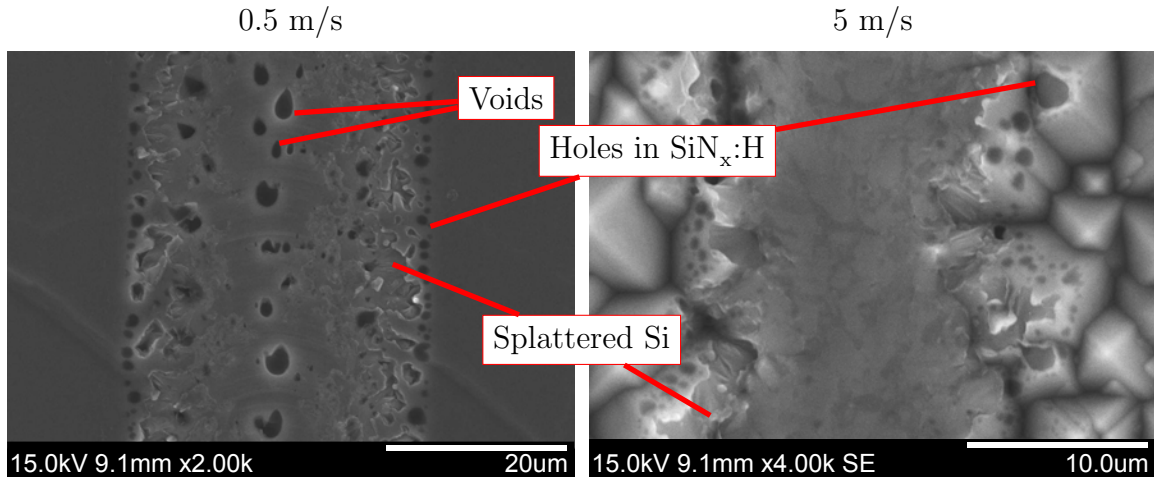


Figure 5.4: SEM images of surface defects on laser-doped lines processed at 0.5 m/s on a planar surface and 0.5 m/s on a textured surface.

### 5.1.3 Summary of Defects Generated during CW Laser Doping

Hence it is evident that a number of LasID are formed including voids, cracks and abnormalities in the  $\text{SiN}_x\text{:H}$  layers and that it would be beneficial to develop low-cost, commercially viable passivation techniques to neutralise these defects. This would improve the robustness of the laser doping technologies.

## 5.2 Hydrogen Passivation of LasID

In this section, the effectiveness of hydrogen passivation was explored to passivate recombination active defects introduced during the laser doping process.

### 5.2.1 Experimental Procedures

In this section LDSE1 solar cells with a full area Al-BSF, LDSE2 solar cells with a passivated rear surface and localised laser-doped contacts, and n-PERT solar cells were fabricated. The solar cell structures are shown in Fig. 5.5.

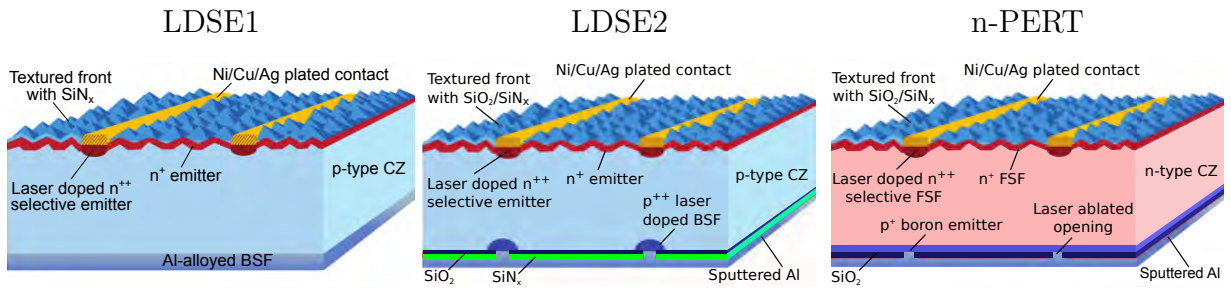


Figure 5.5: Cell structures of first generation LDSE (LDSE1), second generation LDSE (LDSE2) and n-PERT solar cells.

### 5.2.1.1 LDSE1

LDSE1 solar cells were fabricated on  $156 \times 156$  mm standard commercial grade  $0.5 - 3 \Omega \cdot \text{cm}$  p-type B-CZ wafers with a thickness of  $200 \pm 20 \mu\text{m}$ . Texturing was performed using a KOH based anisotropic etch to form random pyramids by exposing the (111) planes. A standard industrial HF/HCl clean was performed on the wafers prior to the emitter diffusion in a conventional  $\text{POCl}_3$  tube diffusion furnace with a resultant sheet resistance of  $120 \Omega/\square$  on both sides. Subsequently laser edge junction isolation (LEJI) was performed, followed by PSG removal and surface cleaning, prior to the deposition of  $\text{SiN}_x\text{:H}$  by direct PECVD. Al screen-printing was performed on a standard industrial screen-printing platform, with drying of the Al prior to fast firing. Fast firing was performed using an industrial belt furnace with 6 zones manufactured by Centrotherm.

Prior to the selective emitter formation using laser doping, 85 %  $\text{H}_3\text{PO}_4$  was spin-coated on the  $\text{SiN}_x\text{:H}$  layer at a spin speed of 4000 RPM for 40 s. Laser doping was performed using the CW laser system described in Chapter 4 with a scan speed of 5 m/s and optical power reaching the wafer of approximately 13.5 W, resulting in localised heavily doped regions with sheet resistances  $< 30 \Omega/\square$ . The laser-doped region of the cell had dimensions  $123 \times 123$  mm to overcome issues of EJI (which will be discussed in Chapter 6) and to highlight differences in the passivation of LasID to that of other defects within the device.

After laser doping, wafers were rinsed to remove the  $\text{H}_3\text{PO}_4$ . Subsequently the wafers were divided into two groups, whereby the first group received a belt furnace anneal (BFA) at  $400^\circ\text{C}$  in compressed dry air (CDA) for approximately 2 min to passivate LasID, and the second group proceeded directly to plating. The reduced temperature of  $400^\circ\text{C}$  in comparison to the AHP developed in Chapter 3 was used to avoid modifications to the Al-BSF. Subsequently the cells were dipped in a HF solution to clean the surface and remove any residual oxides before Ni/Cu LIP to form the front metal contact. No Ni sintering was applied to these cells due to limitations on wafer sizes in the equipment available. After plating, the cells were cleaved using a laser to a size of  $125 \times 125$  mm to perform EJI.

Additional LDSE1 solar cells were fabricated in a different industrial environment on  $125 \times 125$  mm standard commercial grade  $2 \Omega \cdot \text{cm}$  p-type B-CZ wafers to test the effectiveness of a Ni

sinter process for the passivation of LasID. For these solar cells, emitter diffusion was performed in a  $\text{POCl}_3$  tube diffusion furnace with a resultant sheet resistance of approximately  $60 \Omega/\square$ . Subsequently, chemical EJI was performed in an industrial inline wet-chemical processing tool to simultaneously remove the phosphorus emitter off the rear of the cell, planarise the rear surface and perform an emitter etch-back on the front surface using the fumes of the aggressive acids in direct contact with the rear surface. The subsequent sheet resistance of the phosphorus emitter was approximately  $90 \Omega/\square$ . On these cells, Al was screen-printed onto the rear surface to form a full area Al-BSF and dried, followed by screen-printing of Al/Ag tabs for interconnection. Subsequently, the wafers were fired in a Centrotherm belt furnace to form the Al-BSF.

Laser doping was performed in the same manner as for the other LDSE1 solar cells mentioned above. Subsequently the wafers were divided into two groups, the first received the BFA and the second did not. Cells then proceeded to plating in an industrial in-line LIP tool. After Ni plating, cells were sintered at  $375^\circ\text{C}$  for 2 min in nitrogen ambient to prevent the oxidation of the Ni. Subsequently the cells proceeded directly to the LIP copper baths before a silver immersion step to prevent oxidation of the copper and eliminate degradation of the encapsulant in the module.

PL images were taken at various stages of cell fabrication. Light J-V measurements were obtained using a xenon flasher with AM1.5G spectrum on a Halm CetisPV XF2 tester (Class AAA) in accordance with IEC60904-9. The processing sequence for the LDSE1 solar cells is shown in Fig. 5.6.



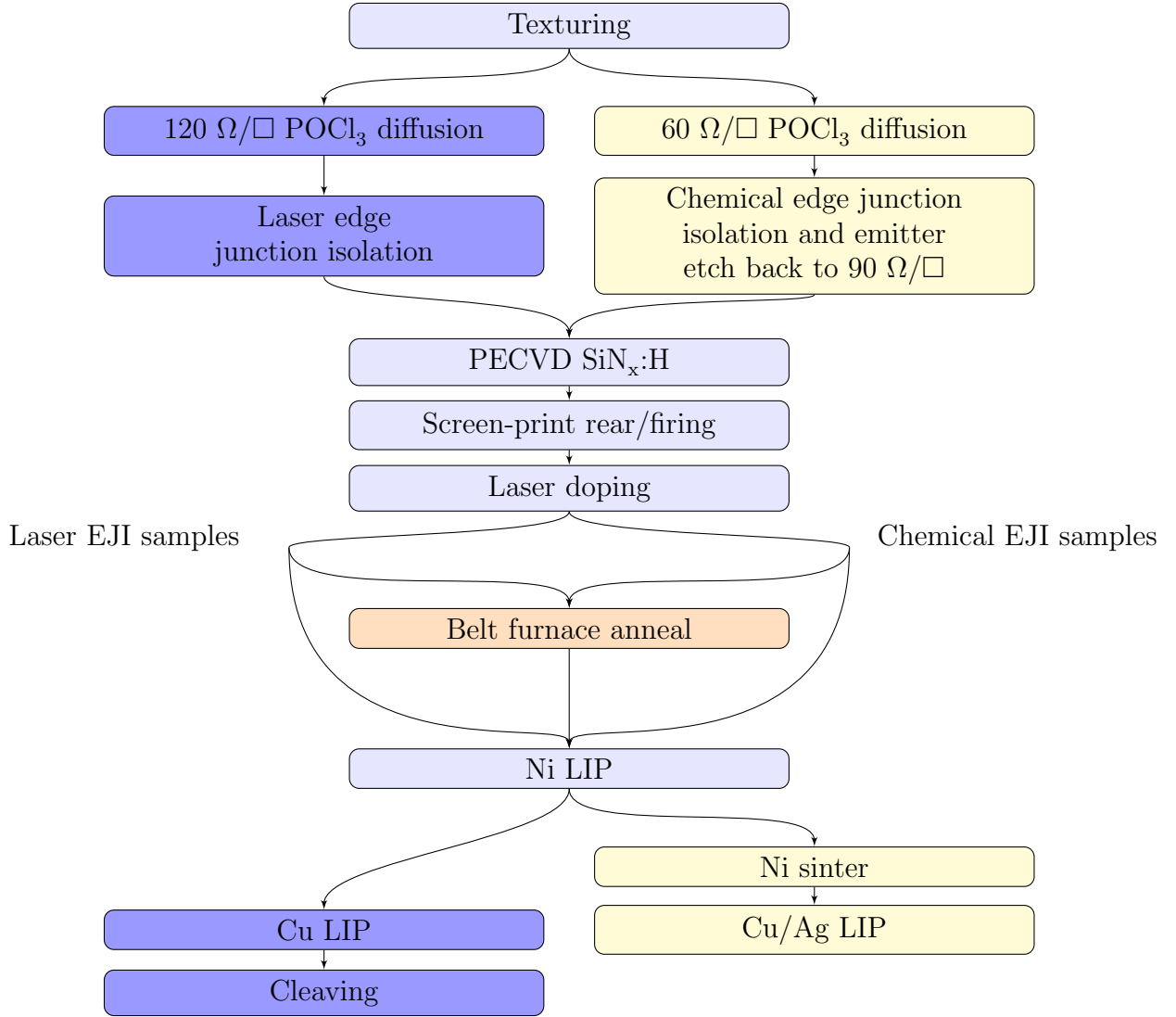


Figure 5.6: Process flow for LDSE1 solar cells to investigate hydrogen passivation of LasID.

### 5.2.1.2 LDSE2

LDSE2 solar cells were fabricated on  $125 \times 125$  mm standard commercial grade  $2 \Omega \cdot \text{cm}$  p-type B-CZ wafers. After alkaline texturing, emitter diffusion was performed in a conventional  $\text{POCl}_3$  tube diffusion furnace with a resultant sheet resistance of  $90 \Omega/\square$ . Subsequently, chemical EJI was performed in the same industrial inline wet-chemical processing tool. The sheet resistance of the emitter was approximately  $140 \Omega/\square$  after the chemical process. A thin thermal oxide layer

was grown before the front and rear  $\text{SiN}_x\text{:H}$  layers were deposited using an industrial Roth & Rau remote microwave PECVD system. The AHP was then applied (outlined in Section 3.2 in an industrial belt furnace with peak temperature of 620 °C and belt speed of 4600 mm/min) to passivate defects within the device.

For the formation of n-type laser-doped contacts, 85 %  $\text{H}_3\text{PO}_4$  was spun at 6000 RPM for 40 s. Laser doping was performed using a scan speed of 5 m/s in a typical cell front pattern using a 532 nm CW laser as previously described with an optical power of approximately 13.5 W, followed by a short HF dip. For the formation of p-type laser-doped contacts, PBF1 was spun onto the rear surface at 2000 RPM for 20 s followed by baking at 130 °C for 10 min.

To investigate the passivation of defects in p-type laser-doped regions, point-like contacts were formed by using a physical mask and scanning the CW laser beam at a speed of 0.5 m/s perpendicular to the openings in the mask with a pitch of  $300 \times 500 \mu\text{m}$ . Point-like contacts had a length of approximately 40  $\mu\text{m}$  and width of 10  $\mu\text{m}$ . Wafers then received a short HF dip and rinse to remove the SOD. The AHP was applied after the laser doping process to passivate LasID.

The p-type metal contacts were formed by Al sputtering, followed by a low temperature Al sinter. Front metal contacts were formed by LIP Ni/Cu/Ag with Ni sintering performed after the Ni plating. The process flow for the fabrication of solar cells in this section is shown in Fig. 5.7. PL images were obtained at various stages of fabrication.

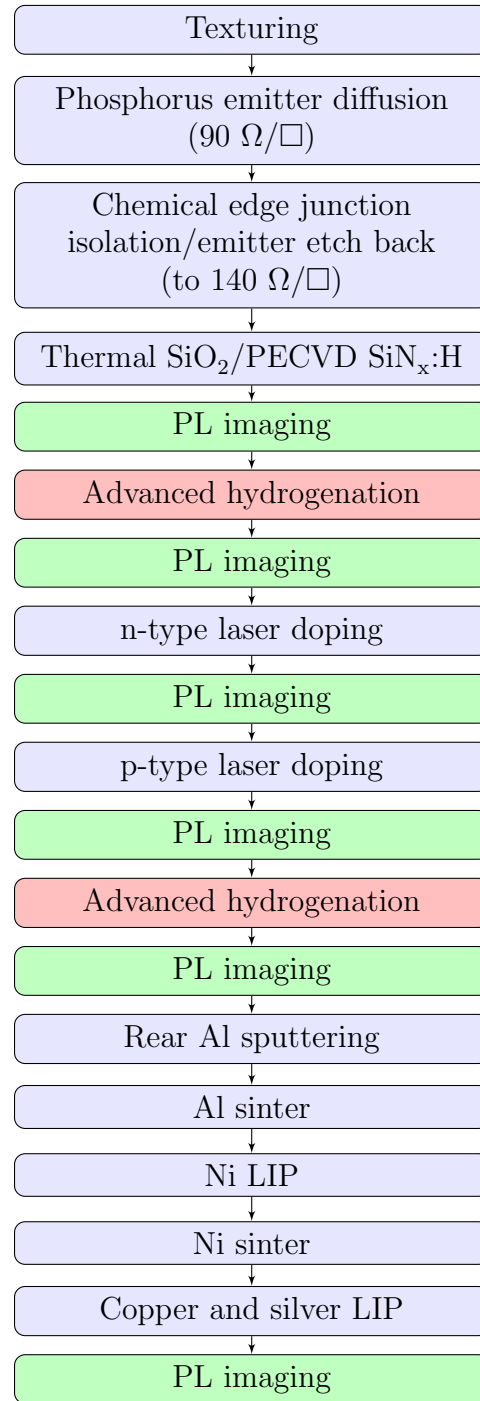


Figure 5.7: Process flow for LDSE2 solar cells to investigate the passivation of LasID.

To investigate the passivation of LasID for various laser processing speeds, additional lifetime test structures were fabricated on standard commercial grade  $2\ \Omega \cdot \text{cm}$  B-CZ wafers. Selected samples received alkaline texturing in an industrial facility before a  $120\ \Omega/\square$  emitter was formed using phosphorus solid source diffusion. Samples were then coated with  $\text{SiON}_x\text{:H}$  with a refractive index of 2.3 on both surfaces using a Roth & Rau AK400 remote microwave PECVD system. Prior to laser doping, a hydrogen passivation process was performed in nitrogen ambient for 5 min at  $400\ ^\circ\text{C}$ , to isolate improvements from the passivation of LasID to the passivation of other defects within the device. Some samples were also processed which did not receive the hydrogen passivation process prior to laser doping. The same CW laser system as previously described was then used to form n-type laser-doped contacts for various processing speeds ( $0.5 - 10\ \text{m/s}$ ) using a  $\text{H}_3\text{PO}_4$  dopant source. After laser doping and subsequent removal of the dopant source, the same hydrogenation process was applied. For both processes hydrogen released from the  $\text{SiON}_x\text{:H}$  was the only source of hydrogen for the passivation process.

To investigate the effect of performing the laser doping process before or after the deposition of the dielectric layer, on other samples, wafers were saw damage etched to a thickness of approximately  $150\ \mu\text{m}$ . Samples were then split into further groups, some wafers had p-type laser doping performed at various speeds from  $0.1 - 10\ \text{m/s}$  prior to RCA cleaning and the deposition of  $\text{SiON}_x\text{:H}$ , whilst others had the p-type laser doping performed after the  $\text{SiON}_x\text{:H}$  deposition for a conventional self-aligned approach. For samples with laser doping performed after the deposition of  $\text{SiON}_x\text{:H}$ , samples were laser processed with and without the application of a boron dopant source (PBF1) and hence that group only received a laser melting treatment with no addition of new dopants. After the laser doping/melting process, all groups were annealed at  $400\ ^\circ\text{C}$  for 5 min. Characterisation was performed at each stage of processing after the deposition of the PECVD using QSS-PC and QSS-PL to extract 1-sun  $iV_{OC}$ ,  $\tau_{bulk}$  and  $J_{0d}$  by removing Auger components (as described in Section 3.2). The processing sequence for the lifetime test structures is shown in Fig. 5.8.

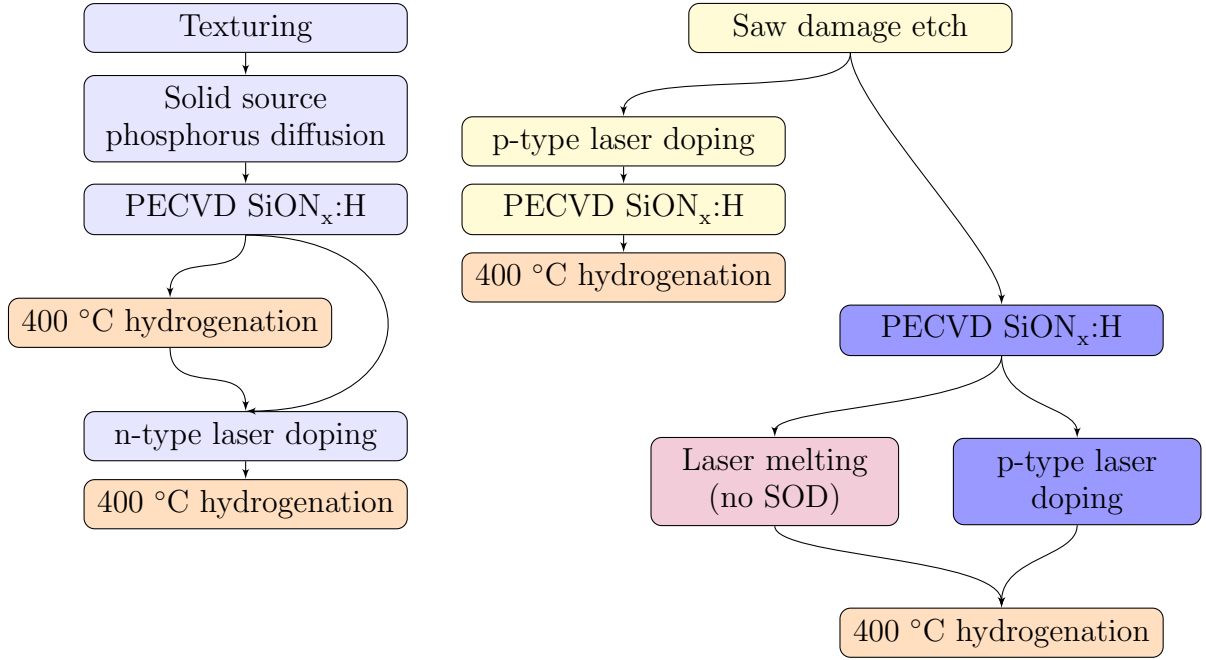


Figure 5.8: Process flow for lifetime test structures for avoiding performance degradation from LasID.

### 5.2.1.3 n-PERT

n-PERT solar cells were fabricated on  $3\ \Omega\cdot\text{cm}$  n-type CZ wafers ( $156\times 156\ \text{mm}$ ). After SDE removal the thickness of the wafers was approximately  $160\ \mu\text{m}$ . The boron emitter was formed using a  $\text{BBr}_3$  source. After the removal of the borosilicate glass (BSG) layer, the dopants were driven in using a high temperature wet oxidation step, which also provided the rear surface passivation layer for the solar cells. After oxidation the emitter sheet resistance was approximately  $95\pm 5\ \Omega/\square$ . Subsequently an FGA process was used at  $450\ ^\circ\text{C}$  for 30 min, with the wafers left in FG whilst the wafers were cooled down to below  $100\ ^\circ\text{C}$  in the tube furnace (following the standard Imec process). Single sided processing was then used to remove the  $\text{SiO}_2$  layer from the front surface and the wafers were then textured in a TMAH based solution to reduce reflection, with a resulting reflection of  $10\pm 0.5\ \%$  at  $700\ \text{nm}$ .

After texturing, the wafers were cleaned and a  $\text{POCl}_3$  diffusion was used to form the front surface field (FSF) followed by the growth of a thin thermal  $\text{SiO}_2$  layer in a dry oxidation process. The

recipe used for the FSF was adapted from that used to create a floating FSF on IBC cells. The resultant sheet resistance of the FSF was approximately  $1000 \Omega/\square$ .  $\text{SiN}_x\text{:H}$  was then deposited by direct PECVD onto the front surface for the antireflection coating. To define the rear contacts, picosecond laser ablation was performed to create small point contacts, followed by the deposition of  $2 \mu\text{m}$  of Al by sputtering. Subsequently, an Alneal process was performed on the wafers in FG at  $450^\circ\text{C}$  for 30 min.

A self-aligned laser doping process was then applied to form the n-type contacts of the solar cell. Dopants were applied using a phosphorus containing SOD source from Filmtronics (P509) at 7000 RPM for 20 s (due to the incompatibility of  $\text{H}_3\text{PO}_4$  with the spinner at Imec). Laser doping was performed using a Q-CW mode-locked UV (355 nm) laser with an optical power of 8.5 W reaching the wafer surface and a focus size of approximately  $20 \mu\text{m}$  ( $1/e^2$  diameter). High-speed fabrication was achieved through the use of a galvanometer scanner and f-theta lens with a processing speed of 5 m/s using a finger pitch of either 1 mm or 1.5 mm. Subsequently the dopant source was removed by a short HF dip. Selected samples then received a BFA in CDA at  $450^\circ\text{C}$  for approximately 3 min to incorporate minority carrier injection but avoid modifications to the Al rear.

Prior to plating, a short HF dip was performed to remove any native oxide in the contact openings. Subsequently the Imec plating sequence was then applied in a commercial in-line plating tool from Meco. The plating sequence consisted of the growth of  $1 \mu\text{m}$  of LIP Ni followed by the deposition of  $10 \mu\text{m}$  of electroplated Cu and immersion Ag. Sintering was then performed on the full Ni/Cu/Ag plated stack in  $\text{N}_2$  ambient at  $250^\circ\text{C}$  in a belt furnace [Russ 12].

Light (J-V) measurements were obtained at 1-sun illumination on a WXS-200S-20 Wacom Electric Co. class AAA tester with a AM1.5G spectrum conforming to IEC 60904-9. Values for series resistance ( $R_S$ ) at maximum power point were obtained from I-V measurements at an illumination intensity of 1-sun and approximately 0.07-suns [Bowd 01].  $p\text{-}FF$  were extracted from curves of Suns versus  $V_{OC}$  using a Sinton Instruments SunsVoc tester [Sint 00]. A BTi R1 luminescence imaging system was used to obtain calibrated  $iV_{OC}$  maps at various stages of fabrication.

After J-V measurements, one sample which did not receive a BFA after the laser doping process was then given a second sinter process at an elevated temperature of  $400^\circ\text{C}$  to test the effectiveness

of the standard Imec sintering process at passivating LasID. Various characterisation measurements were then obtained after the additional sinter process to check for changes to the electrical parameters caused by the potential passivation of LasID. The process sequence for the fabrication of the n-PERT solar cells in this section is shown in Fig. 5.9.

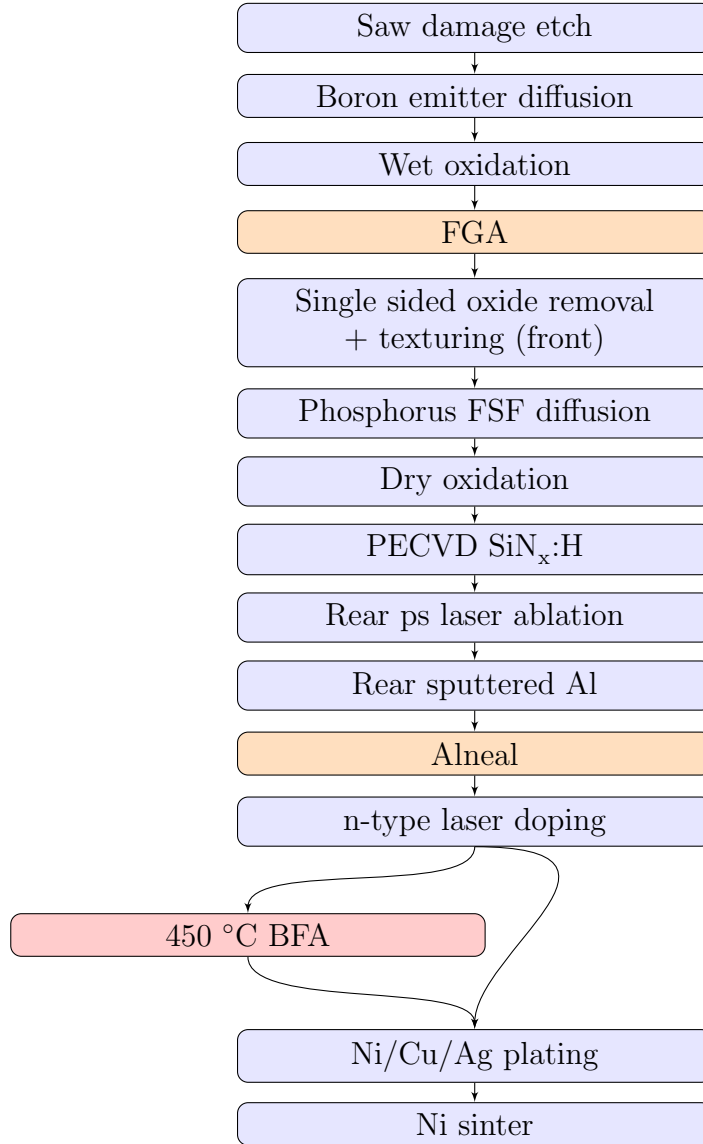


Figure 5.9: Process flow for n-PERT solar cells.

## 5.2.2 Results for Avoiding Performance Degradation of LasID by Hydrogen Passivation

### 5.2.2.1 LDSE1

The application of a low temperature anneal after the laser doping process, was found to substantially improve the electrical performance of the LDSE solar cells. The calibrated  $iV_{OC}$  maps shown in Fig. 5.10 indicated a substantial reduction in  $iV_{OC}$  after the laser doping process, particularly evident in the busbar regions with a high density of laser-doped lines, and hence high density of LasID. However almost all of the  $iV_{OC}$  loss induced by the laser doping process could be recovered through a subsequent 1 – 2 min anneal in CDA at 400 °C (as seen in Fig. 5.10(c)). In addition, control areas around the edge of the wafer which were not laser damaged show no substantial improvement in  $iV_{OC}$  with the anneal step, confirming that the improvement was due to the passivation of LasID rather than other defects within the device.

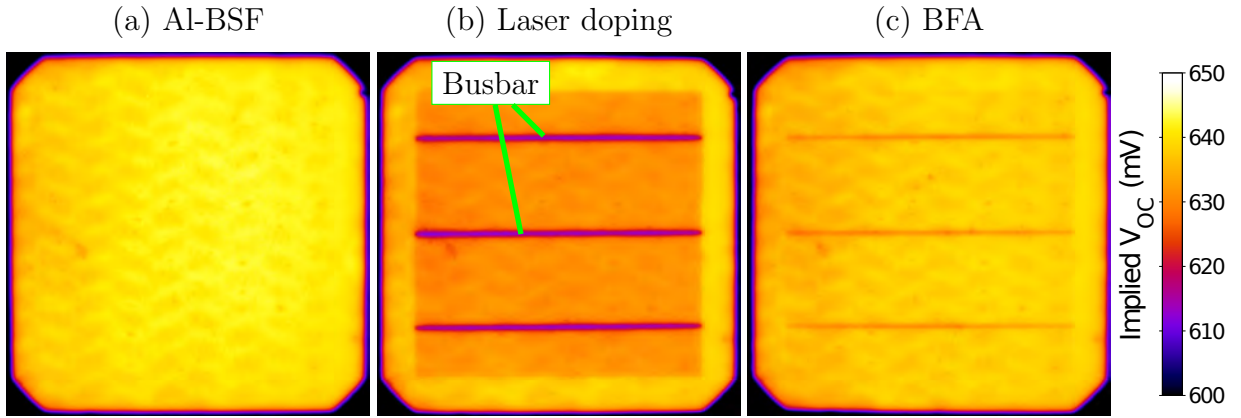


Figure 5.10: Calibrated 1-sun  $iV_{OC}$  maps of partially processed LDSE1 solar cells showing the passivation of LasID by hydrogen.

The effect of the LasID on electrical performance was compared on cells where no Ni sinter was performed, to highlight the importance of passivating LasID. The same annealing process was used directly after the laser doping process, and hence prior to plating. Cells which did not receive the



anneal had an average  $V_{OC}$  of 627 mV, whereas cells which received the anneal had a substantially higher average  $V_{OC}$  of 637 mV and an increase in the average  $p\text{-}FF$  of 0.4 % absolute, resulting in an improved efficiency of approximately 0.35 % absolute (see Table 5.1). This demonstrates the importance of applying a hydrogen passivation process after the LasID generation.

Table 5.1: Light J-V parameters for large area LDSE1 solar cells with hydrogen passivation of LasID.

<b>Process</b>	$J_{SC}$ (mA/cm <sup>2</sup> )	$V_{OC}$ (mV)	$FF$ (%)	$p\text{-}FF$ (%)	$\eta$ (%)
No anneal (Average)	37.78	627.4	77.42	83.2	18.35
Anneal (Average)	37.69	636.7	77.97	83.6	18.71

Effective annealing of the LasID can also be achieved during a Ni sinter process (at 375 °C), that also results in devices with a  $V_{OC}$  approaching 640 mV (small area). For such cells which did not receive a dedicated hydrogen passivation process prior to plating, a clear improvement in electrical performance was observed both in relation to a reduced contact resistance from the formation of NiSi as well as related to the  $V_{OC}$  and  $J_{SC}$  of the devices (attributed to the hydrogen passivation of LasID). This is of great benefit for the fabrication of LDSE1 solar cells, as it means that no extra processing steps are required for the passivation of the LasID, resulting in a more commercially viable process sequence.

For the full size 5-inch production cells, due to the absence of phosphorus on the back surface to assist in trapping hydrogen in the device during the Al-BSF formation and subsequent liquid-phase epitaxial growth which will be discussed in Chapter 6, the cells had lower  $V_{OC}$  and the improvements were less apparent. However on cells which had a BFA applied after the laser process a clear increase in  $iV_{OC}$  was observed (see Fig. 5.11) due to the passivation of the LasID. For the finished devices, no significant difference in the electrical performance or  $iV_{OC}$  was observed between cells which did or did not receive the BFA after laser doping, again showing the potential of the Ni sintering

process to simultaneously passivate LasID. Hence the Ni sintering process could become a valuable process to simultaneously perform enhanced bulk and surface defect passivation with appropriate thermal profiles and illumination (which could alter the equilibrium charge state concentrations of hydrogen throughout the process). The slight drop in  $iV_{OC}$  for cells at device level was due to an increase in  $J_{0d}$  after metallisation, and increased shading.

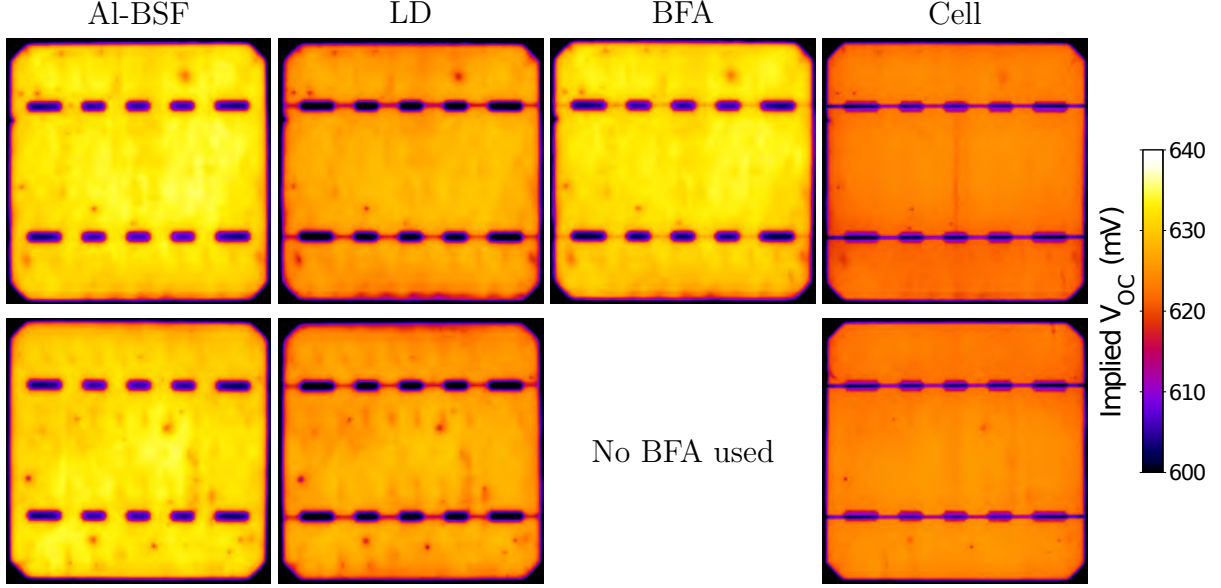


Figure 5.11: Calibrated 1-sun  $iV_{OC}$  maps of partially processed LDSE1 solar cells showing the effect of annealing and Ni sintering on the passivation of LasID.

### 5.2.2.2 LDSE2 Test Structures

It is likely that the low temperature anneal resulted in the redistribution of hydrogen within the bulk of the wafer; allowing it to passivate any crystallographic defects that were introduced during the laser doping process. Further evidence of this was demonstrated using test structures in which some parts of the cell that may change during an anneal step were removed. Extraction of  $\tau_{bulk}$  and  $J_{0d}$  from  $\tau_{eff}$  curves on the symmetrical phosphorus diffused test structures as shown in Fig. 5.12(a),

indicated that improvements in the  $iV_{OC}$  from the passivation process applied before laser doping were due to a substantial improvement in  $\tau_{bulk}$  as well as a large reduction in  $J_{0d}$  from 140 fA/cm<sup>2</sup> down to 30 fA/cm<sup>2</sup>.

**Anneal after laser doping:** For the annealing process applied after laser doping, improvements in  $iV_{OC}$  were primarily due to increases in  $\tau_{bulk}$  (see Table 5.2). Whilst on LDSE1 solar cells only a small increase in  $V_{OC}$  of 10 mV was observed, the  $V_{OC}$  of such cells was predominately limited by the Al BSF, and hence the increase actually represented a large reduction in the total  $J_{0d}$  of the device. As the  $J_{0d}$  of other attributes in such a device is reduced due to the incorporation of a passivated rear surface, the passivation of LasID will become of increasing importance to ensure the development of higher voltage devices. For the test structures with higher  $iV_{OC}$ , an increase of 25 mV was observed by applying the hydrogen passivation process after laser doping (see Table 5.2). The same effects of increase in  $J_{0d}$  and reduction in  $\tau_{bulk}$  have been observed on gallium-doped and phosphorus-doped wafers for both n- and p-type laser doping indicating that the changes were not completely due to B-O defect generation, however this may be occurring in parallel for the B-CZ wafers.

**Anneal before laser doping:** An anneal process applied before laser doping had no influence on the resultant  $iV_{OC}$  of the test structures, provided the same hydrogen passivation process was performed after the laser process to passivate LasID (see Fig. 5.12(b)). However differences were apparent directly after laser doping due to the passivation of other bulk and surface defects within the device from the prior annealing step. It should also be noted that there was a small difference in the quality from wafer to wafer in the  $iV_{OC}$  obtained directly after the SiON<sub>x</sub>:H deposition.

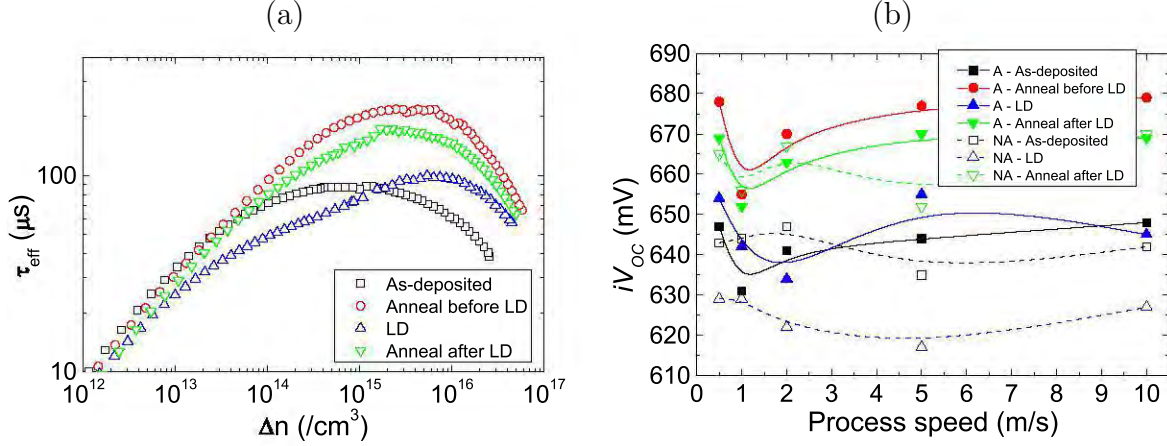


Figure 5.12: (a)  $\tau_{eff}$  curves for p-type CZ wafers with n-type laser doping (LD) and (b)  $iV_{OC}$  obtained for various speeds with and without an anneal process applied before LD. ‘A’ = annealed prior to LD, ‘NA’ = no anneal prior to LD.

Table 5.2: 1-sun  $iV_{OC}$ ,  $J_{0d}$  and  $\tau_{bulk}$  obtained at various stages of processing for a laser-doped sample on p-type CZ silicon using n-type laser doping with a processing speed of 5 m/s.  $\tau_{bulk}$  were extracted at  $\Delta n = 1 \times 10^{15} /cm^3$ .

Process step	1-sun $iV_{OC}$ (mV)	$J_{0d}$ (fA/cm <sup>2</sup> )	$\tau_{bulk}$ ( $\mu s$ )
SiON deposition	648	140	124
Anneal	679	30	239
Laser doping	645	40	82
Anneal	669	38	179

5.2.2.3 Passivation of LasID for  $\text{AlO}_x$  Laser Doping

Substantial improvements to  $iV_{OC}$  on lifetime test structures were also briefly presented for  $\text{AlO}_x$  laser doping in Section 4.3 with improvements of up to 50 mV demonstrated. Fig 5.13 shows the  $\tau_{eff}$  curve of a laser-doped region processed at 18 m/s through a dielectric stack of 10 nm ALD  $\text{Al}_2\text{O}_3$ /50 nm PECVD  $\text{SiO}_x\text{:H}$ . A low  $\tau_{eff}$  of 30 – 80  $\mu\text{s}$  was observed over all injection-levels in contrast to  $\tau_{eff}$  of almost 500  $\mu\text{s}$  at  $\Delta n = 1 \times 10^{16} / \text{cm}^3$  and over 100  $\mu\text{s}$  at  $\Delta n = 1 \times 10^{14} / \text{cm}^3$  for a region on the same wafer which did not receive the laser doping process. This indicates a substantial introduction of LasID into the bulk of the silicon. With the subsequent annealing process to passivate LasID, only a very slight improvement in  $\tau_{eff}$  was observed for the region without laser doping due to the wafer having an anneal process prior to laser doping to activate the passivation of the  $\text{Al}_2\text{O}_3$  layer. In contrast, a large increase in  $\tau_{eff}$  was observed over all injection-levels on laser-doped samples with no evidence of performance degradation in low injections from recombination active LasID. However this may be due to the wafers having a stronger reduction in  $\tau_{eff}$  associated with other defects within the device such as the B-O complex. Upon annealing the  $\tau_{eff}$  approached 300  $\mu\text{s}$  at  $\Delta n = 1 \times 10^{15} / \text{cm}^3$  and the curve appeared to be limited by the  $J_{0d}$  of the test structure.

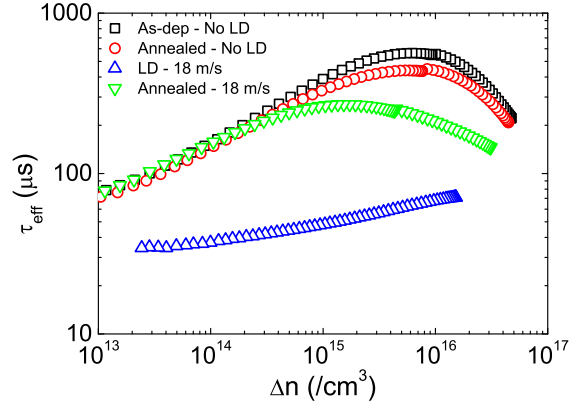


Figure 5.13: Injection-level-dependent  $\tau_{eff}$  curves for p-type CZ wafers with laser doping at 18 m/s through a 10 nm ALD  $\text{Al}_2\text{O}_3$ /50 nm PECVD  $\text{SiO}_x\text{:H}$  layer before and after hydrogen passivation of LasID.

#### 5.2.2.4 LDSE2 and n-PERT

Full cell structures employing rear surface passivation and localised contact formation were formed on both n- and p-type substrates (n-PERT and LDSE2 respectively), highlighting the importance of hydrogen passivation for LasID on these higher voltage devices, with much higher improvements in  $iV_{OC}$  observed than that of LDSE1 solar cells. This was due to the reduced total  $J_{0d}$  through the implementation of a rear passivated surface and improved bulk passivation.

Calibrated  $iV_{OC}$  maps of full cell structures are shown in Fig. 5.14 of both n-PERT and LDSE2 solar cells at various stages of fabrication. Both cell structures received a hydrogen passivation process prior to the introduction of LasID. For the n-PERT solar cells, this was a FGA process at 450 °C for 30 min whilst for the LDSE2 cells the AHP was applied with increased minority carrier injection, shown to be effective for passivating bulk defects such as B–O complexes [Hall 14f; Wenh 13b].

After laser doping, another hydrogen passivation process was performed at the same temperature for the respective cell structures, resulting in improvements in  $iV_{OC}$  of 15 – 25 mV. For the n-PERT solar cells, even after the passivation of the LasID the cells suffered from a large reduction in  $iV_{OC}$  in the busbar region due to an extremely high density of laser-doped lines, which were processed with a pitch of 10 µm to result in the complete opening of the dielectric layer for the 1 mm wide busbars (100 lines per busbar). In contrast, the LDSE2 solar cells had a busbar width of 1.6 mm featuring a larger pitch of 80 µm between each line (20 lines per busbar). It is expected that increasing the pitch of lines in the busbar for the n-PERT solar cells will greatly enhance the  $iV_{OC}$  of the cells and potentially lead to substantial increases in efficiency through reduced LasID generation and a reduced metal/Si interface. This is expected to result in higher  $J_{SC}$ , higher  $V_{OC}$  and higher  $p$ - $FF$  although the cells may also suffer from slightly higher resistive losses associated with the lateral transport of current in the busbar.

The effect of hydrogen passivation for LasID on the electrical performance of n-PERT solar cells is clearly shown in Table 5.3. The results indicated substantial increases in  $V_{OC}$ ,  $J_{SC}$  and  $p$ - $FF$  from the inclusion of a dedicated hydrogen passivation process after laser doping. Subsequently a 0.7 % absolute gain in efficiency was observed through hydrogen passivation of the LasID regardless

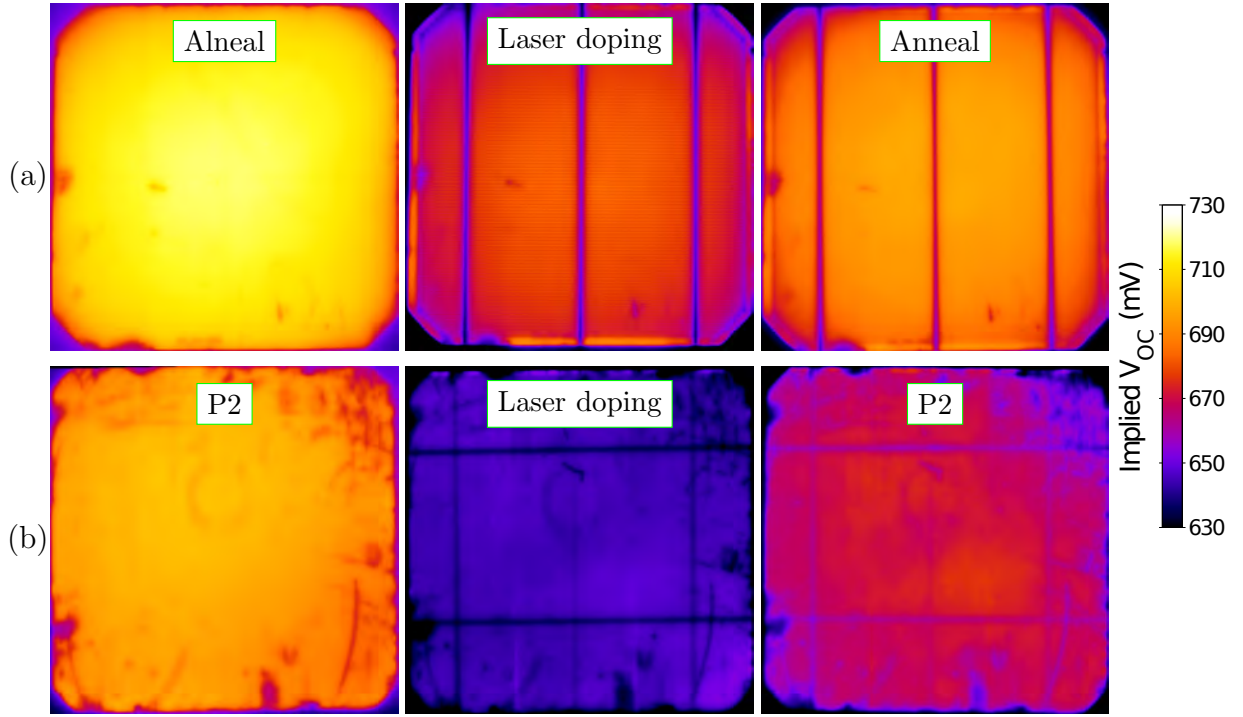


Figure 5.14: Calibrated PL 1-sun  $iV_{OC}$  maps of (a) n-PERT solar cells and (b) LDSE2 solar cells.

of finger pitch. A finger pitch of 1.5 mm resulted in higher efficiencies through increases in  $V_{OC}$  and  $J_{SC}$  through reduced defect generation and reduced shading, but suffered from higher resistive losses and therefore lower  $FF$ . The large differences between the  $p-FF$  and  $FF$  were due to the high sheet resistance of the FSF. Modelled resistive losses within the n-type bulk and FSF account for a 2.6 % loss in  $FF$ , compared to 1.45 % for a FSF of  $260 \Omega/\square$  as applied in Chapter 6, or 0.9 % for a  $110 \Omega/\square$  FSF as typically used for n-PERT cells at Imec with a homogenous FSF and laser-ablated contacts. Hence substantial improvements in  $FF$  should be gained by using a less resistive FSF.

Table 5.3: Light J-V parameters for large area n-PERT solar cells with hydrogen passivation of LasID.

<b>Process</b>	$J_{SC}$ (mA/cm <sup>2</sup> )	$V_{OC}$ (mV)	$FF$ (%)	$\eta$ (%)	$p\text{-}FF$ (%)
No anneal 1.5mm (Best cell)	39.24	649.1	77.87	19.83	82.23
Anneal 1.5mm (Best cell)	39.47	666.1	78.61	20.67	82.47
No anneal 1mm (Best cell)	38.26	643.9	79.59	19.60	82.11
Anneal 1mm (Best cell)	38.79	658.9	79.76	20.38	82.34
No anneal 1.5mm (Average)	39.19	648.4	77.97	19.81	82.18
Anneal 1.5mm (Average)	39.48	664.1	78.34	20.54	82.42
No anneal 1mm (Average)	38.23	643.2	79.56	19.56	82.13
Anneal 1mm (Average)	38.75	657.1	79.53	20.25	82.26
No anneal prior to extra 400 °C sinter	38.26	643.8	79.59	19.60	82.11
No anneal + extra 400 °C sinter	38.54	648.7	79.71	19.93	82.09

**Passivation during Ni sintering:** The effectiveness of hydrogen passivation during Ni sintering using Imec’s Standard Sintering process (SS) was also investigated (see Fig. 5.15(a)). On cells which did not receive a dedicated anneal for LasID, the SS process only resulted in an improvement in  $V_{OC}$  of 4 mV. Subsequently, an Extra Sintering (ES) process was applied to some samples which increased the effectiveness of hydrogen passivation, and demonstrated a further 4 mV improvement. However both the current SS and ES processes fell well short of the  $V_{OC}$  achieved through the enhanced annealing step, hence showing the limited effectiveness of hydrogen passivation during the SS and ES processes. It was also observed that for samples which received the defect anneal, subsequent Ni sintering using the SS process did not lead to any substantial gain in  $V_{OC}$  of the devices. Importantly, such defects were not reactivated during the subsequent SS process.

Quantum efficiency measurements were obtained which demonstrated a substantial improvement in the long-wavelength IQE and hence rear surface passivation or bulk of the device. This appears



to be responsible for the majority of the increase in  $J_{SC}$  in samples fabricated using a 1.5 mm finger pitch. Hence compared to an Alneal process which could be considered as state of the art for the fabrication of PERL solar cells, the hydrogenation process performed in CDA using only hydrogen already within the device, indicated an improved effectiveness for the hydrogen passivation of the bulk and/or rear surface of the device. This may have been due to changes in the actual temperature achieved with a set point of 450 °C in the belt furnace due to exothermic reactions between the oxygen in the ambient and the rear Al layer that may have led to: a further release of hydrogen from the  $\text{SiN}_x\text{:H}$  layer; or improved generation of atomic hydrogen from the Alneal process; or an enhanced cooling rate; or the addition of minority carrier injection during the hydrogenation process. The potential for improved hydrogen passivation of n-PERT solar cells will be explored further in Chapter 6.

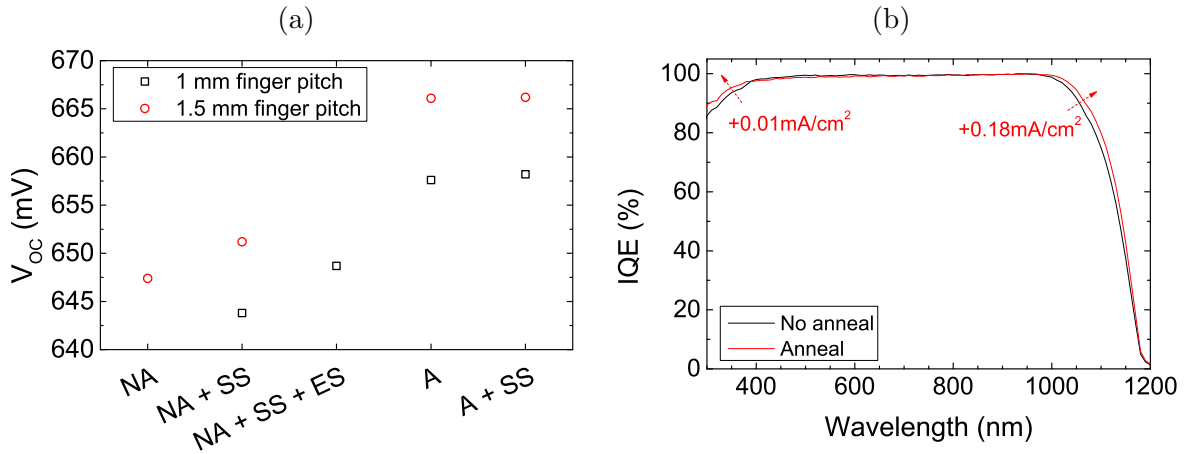


Figure 5.15: (a)  $V_{OC}$  of finished n-PERT solar cells with: ‘NA’ = no LasID anneal, ‘SS’ = Standard Imec Ni Sinter, ‘ES’ = Extra Sinter at increased temperature (400 °C) and ‘A’ = anneal after LD. (b) IQE for a cells with a finger pitch of 1.5 mm.

### 5.2.2.5 Summary

The importance of performing a hydrogen passivation process to passivate LasID was demonstrated in this section. For LDSE1 solar cells, this led to efficiency enhancements of 0.35 % absolute through increases in  $V_{OC}$ . On test structures, improvements in  $iV_{OC}$  of up to 50 mV were demonstrated, highlighting the importance of passivating LasID for high efficiency solar cells. For n-PERT solar cells, an efficiency enhancement of 0.7 % absolute was demonstrated through the incorporation of a hydrogen passivation process after laser doping.

## 5.2.3 Protection of Deep and High Doping against Performance Degradation from LasID

Laser doping using a CW laser can introduce an incredible amount of defects into the silicon both within the surface region, and well into the bulk of the silicon. To highlight this, the same laser doping process was used on wafers with and without the application of a p-type dopant source (outlined in Section 5.2.1.2 and Fig. 5.8). Hence for the samples without the SOD, the wafers merely saw a laser melting and recrystallisation process with no addition of new dopants into the molten silicon. As shown in Fig. 5.16, prior to laser doping the majority of samples had  $iV_{OC}$  of 710 – 720 mV indicating a high quality of bulk and surface passivation for the wafers.

### 5.2.3.1 After Laser Doping

A large loss in  $iV_{OC}$  was experienced by all wafers when subjected to the laser process for either laser doping (with an SOD) or laser melting (without an SOD). Fig. 5.16 highlights the 60 – 70 mV loss in  $iV_{OC}$  from the laser doping process when using a SOD (with  $iV_{OC}$  falling from an initial value of approximately 710 mV down to 615 – 650 mV). For these samples, a stronger decrease in  $iV_{OC}$  was observed for samples with laser doping performed with increasing speeds due to enhanced defect generation. Hence the highest  $iV_{OC}$  values were obtained for samples with the deepest junctions and highest incorporation of dopants into the silicon as shown in Chapter 4.

For samples without the application of a SOD, the  $iV_{OC}$  ranged from 615–640 mV. At speeds of 0.5–1 m/s these samples displayed a slightly reduced  $iV_{OC}$  compared to that of samples processed with the application of a SOD. In contrast, the higher speeds of 2–5 m/s yielded higher  $iV_{OC}$  than samples with an applied SOD. This may be partially due to a difference in the generation of LasID through changes in the optical properties of the wafer for the laser doping process.

### 5.2.3.2 After Annealing

After annealing, samples with an applied SOD layer displayed a strong dependence on processing speed with the highest  $iV_{OC}$  obtained for the slowest speeds. In contrast, little variation in  $iV_{OC}$  was observed for the samples processed without an applied SOD. This suggests that the deep, heavily diffused regions may act to enshroud the defects introduced through the laser doping process, and hence avoid performance degradation.

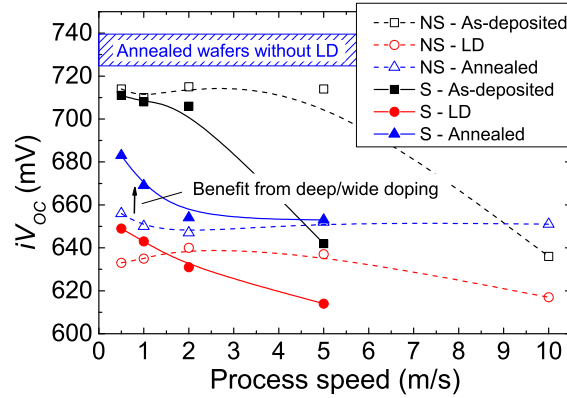


Figure 5.16: Effect of processing speed on the generation of LasID and ability of forming deep, heavily doped regions to protect against recombination with: ‘S’ an applied SOD, and ‘NS’ no applied SOD.

### 5.2.3.3 Impact of Performing Laser Doping Before or After $\text{SiN}_x\text{:H}$

Whilst performing laser doping prior to the deposition of a dielectric layer requires the subsequent alignment of metal contacts, doing so can be of benefit for several reasons. Firstly, it can assist in the avoidance of LasID generation through thermal expansion mismatch between the overlying dielectrics and silicon. Secondly, and perhaps just as importantly, it ensures a hydrogen passivation process will be performed after the laser doping process. For example,  $\text{SiN}_x\text{:H}$  is used on virtually all commercial silicon solar cells and a certain level of hydrogen passivation of the bulk and surface defects can be achieved during the deposition process. However further benefits are typically obtained during the firing step for screen-printed contacts which enhances the release of hydrogen from the  $\text{SiN}_x\text{:H}$ . For laser doping processes applied after the fast-firing process, with plated contacts and sintered at a low temperature, LasID may not be passivated. However, by ensuring the laser doping process on LDSE1 or PERC type solar cells is performed prior to the formation of the Al-BSF, adequate passivation of the LasID can be achieved. Differences in the  $V_{OC}$  of LCP cells have also been noted by performing the laser doping process before or after the rear Al metallisation process [Kyeo 12].

For this section, a comparison was made between p-type laser doping performed before and after the deposition of identical  $\text{SiN}_x\text{:H}$  dielectric layers. In contrast to the reduction in  $iV_{OC}$  observed for increasing speeds as shown in Fig. 5.16, by performing the laser doping process prior to dielectric deposition a substantial increase in  $iV_{OC}$  was observed with increasing speed due to a reduction in  $J_{0d}$  (see Fig. 5.17). Directly after the deposition of the  $\text{SiN}_x\text{:H}$  substantial reductions in  $iV_{OC}$  to 660 – 680 mV were observed compared to wafers processed in parallel without laser doping (710 mV). This suggests a large reduction in  $\tau_{eff}$  due to increased  $J_{0d}$  and/or the introduction of LasID. After annealing, a substantial increase in  $iV_{OC}$  was observed with values of 660 – 710 mV. This can partially be attributed to the improved bulk defect and surface passivation of other defects within the test structures, now yielding  $iV_{OC}$  of 730 mV without laser doping, however due to the substantial reduction in  $iV_{OC}$  of laser-doped samples prior to annealing, the majority of improvement comes from the passivation of LasID. Subsequently,  $iV_{OC}$  of up to 710 mV were demonstrated using a processing speed of 10 m/s. The higher  $iV_{OC}$  obtained by performing laser doping prior to the deposition of the  $\text{SiN}_x\text{:H}$  may also be due to enhanced surface passivation in

the laser-doped region, therefore reducing the  $J_{0d}$  of the laser-doped region.

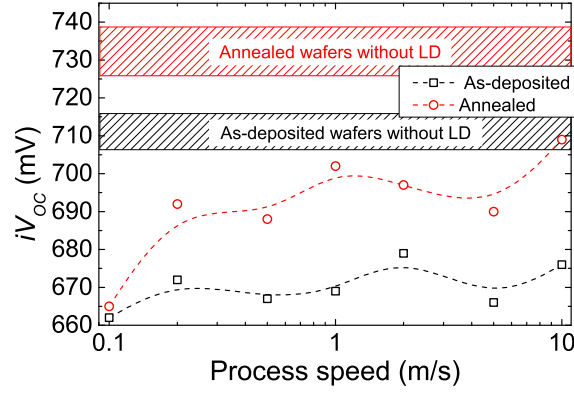


Figure 5.17: Effect of process speed for samples with laser doping performed prior to dielectric deposition.

Hence performing laser doping prior to dielectric deposition results in higher  $iV_{OC}$  through reduced defect generation and incorporation of hydrogen passivation of the LasID during the dielectric deposition and subsequent thermal processes.

#### 5.2.4 Summary for Hydrogen Passivation of LasID

The importance of performing a hydrogen passivation process to passivate LasID was clearly highlighted with efficiency enhancements of up to 0.7 % for n-PERT solar cells through the introduction of a hydrogen passivation process after laser doping. Importantly, defect passivation could be achieved for the LasID using a Ni sinter process when using sufficient temperature, and avoid the need for an additional process.

## 5.3 Chapter Summary

In this Chapter the passivation of LasID by hydrogen was presented. Even by using CW laser doping to avoid thermal cycling of the silicon between successive pulses of conventional Q-switched lasers, substantial defect generation was observed. Such defects include voids of more than 4  $\mu\text{m}$  diameter which may be partially exposed at the surface upon resolidification of the silicon, or completely hidden below the silicon surface. For excessively slow speeds below 0.5 m/s, that generate a large volume of molten silicon, thermal stress was shown to generate crystallographic defects in the laser-doped region and cause cracks to form across or along the laser-doped line (at times extending more than 25  $\mu\text{m}$  from the laser-doped region). In addition other defects such as pinholes in the nitride as previously observed for laser doping processes were also shown to be generated using the CW laser.

Hydrogen passivation was observed to be an essential attribute in the fabrication of laser-doped solar cells. LDSE1 solar cells with a full area Al-BSF saw a substantial reduction in  $iV_{OC}$  due to the introduction of LasID during the laser doping process. However a short, low temperature in-line belt furnace anneal in CDA was able to recover almost all  $iV_{OC}$  loss. For cells without Ni sintering, this resulted in an average 0.35 % efficiency enhancement predominately through increases in  $V_{OC}$  and  $p\text{-}FF$ . It was also demonstrated that effective hydrogen passivation of the LasID could be realised during the Ni sintering at 375  $^{\circ}\text{C}$ . This is of great importance as it avoids the need for additional processing steps, greatly increasing commercial viability.

For solar cells and test structures with higher  $V_{OC}$  and  $iV_{OC}$  (LDSE2 and n-PERT), the passivation of the laser induced defects becomes of increasing importance. As the  $J_{0d}$  of other attributes in the device is reduced due to the incorporation of a passivated rear surface, LasID can potentially become a dominant recombination mechanism. Test structures indicated improvements in  $iV_{OC}$  of up to 50 mV through hydrogen passivation of LasID. On n-PERT solar cells, an average efficiency gain of 0.7 % absolute was demonstrated through a 3 min belt furnace anneal in CDA at 450  $^{\circ}\text{C}$  which only used hydrogen within the device for defect passivation. This process was shown to improve the bulk and/or rear surface passivation more effective than that achieved using an Alneal process, a process considered as state of the art for the fabrication of the world record PERL cells. The improved passivation led to increases in  $J_{SC}$  of approximately 0.2 mA/cm<sup>2</sup>. Subsequently

an average efficiency of 20.54 % was achieved with peak efficiency of 20.67% for a finger pitch of 1.5 mm.

For the n-PERT solar cells, the sintering process used was relatively ineffective at passivating the LasID due to the low temperature of 250 °C used, with clear further improvements in  $V_{OC}$  and efficiency observed through a subsequent sintering process at 400 °C, however still well short of those cells with a dedicated hydrogen passivation process applied prior to plating.

The results suggested there may be more to gain from further improvements to the hydrogen passivation of the devices which will be presented in the latter part of Chapter 6, particularly after other performance limiting attributes of the solar cells are eliminated.

# Chapter 6

## Development of High Efficiency Laser-Doped Solar Cells with Advanced Hydrogenation

Until recently, the highest production cell efficiency on p-type CZ grown silicon wafers with a full area Al-BSF was produced by Suntech Power using the Pluto technology, with claimed efficiencies of up to 19.4 %. However the highest independently confirmed Pluto production cell efficiency at the time was 18.8 % [Shi 09]. In April 2011, Sunrise Global Solar Energy announced an independently confirmed cell result of 19.2% using the Schmid selective emitter approach [Tjah 11].

However a significant advantage of the LDSE technology over screen-printed selective emitter technologies is that it allows for an optimisation of the BSF formation to yield higher  $V_{OC}$  and independent optimisation for the formation of the front contacts.

In this Chapter, various solar cell processes are investigated to further optimise laser-doped silicon solar cells such as: (1) Al-BSF formation; (2) avoidance of parasitic plating through an emitter etch-back process; (3) edge junction isolation methods; (4) incorporation of an advanced hydrogenation process; (5) incorporation of LDSE into a PERC cell structure; and (6) improved hydrogen passivation for n-PERT solar cells.



## 6.1 An Improved Firing Process to Avoid Localised Recombination

Due to the use of LIP contacts, LDSE solar cells can be sensitive to localised recombination and defects introduced during a variety of processing steps. The LDSE1 solar cell structure was shown in Fig. 2.3 in Chapter 2.

### 6.1.1 Aim

In this section, an improved firing process is investigated on first generation LDSE (LDSE1) solar cells to avoid localised recombination which can affect the plating process. In particular the impact of forming the Al-BSF with the  $\text{SiN}_x\text{:H}$  surface face-up or face-down.

### 6.1.2 Experimental Procedures

The cells in this section were fabricated in the same manner as the LDSE solar cells in Section 5.2, diffused to a sheet resistance of  $120 \Omega/\square$  directly. The drying of the Al paste was performed on all cells prior to firing with the  $\text{SiN}_x\text{:H}$  surface face-down and hence in direct contact with the belt. In the first part of the experiment, one major difference in processing was used for the firing process, with samples processed with the  $\text{SiN}_x\text{:H}$  surface either face-down (in direct contact with the belt); or face-up (whereby the  $\text{SiN}_x\text{:H}$  was not in any direct contact with the belt). This was to highlight the effect of the belt being in intimate contact with the  $\text{SiN}_x\text{:H}$ .

In the second part of the experiment, the peak firing temperature of samples with face-up firing was varied in  $20^\circ\text{C}$  increments due to the changes from the standard firing process used on the production line using a face-down approach, to optimise the Al-BSF formation.

Independent cell measurements were performed by Fraunhofer ISE CalLab, in accordance with IEC60904 standards.

The process sequence for solar cells in this experiment is shown in Fig. 6.1.

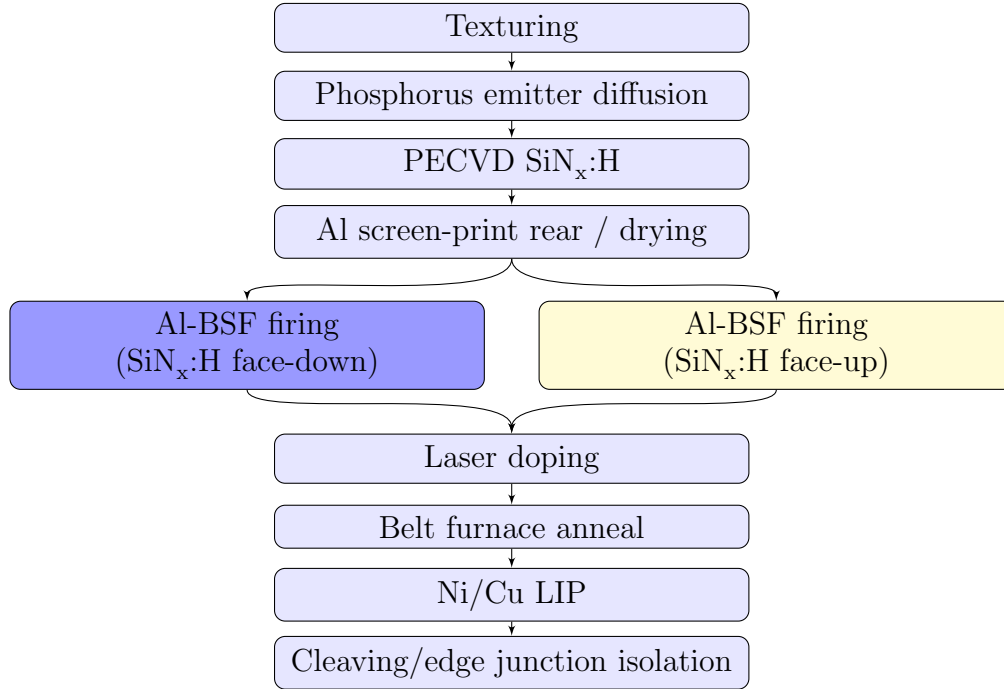


Figure 6.1: Process flow for LDSE1 solar cells with an improved firing process to avoid localised recombination.

### 6.1.3 Avoidance of Localised Recombination Site Formation During Al-BSF Firing

#### 6.1.3.1 Face-up versus Face-down

As previously mentioned, on the production line used in this section, the standard firing process is typically performed with the  $\text{SiN}_x\text{:H}$  surface face-down and as a result, the  $\text{SiN}_x\text{:H}$  surface is in direct contact with the metal belt in localised regions. In this experiment, a reduced  $iV_{OC}$  was observed in regions of the wafer directly above chain links of the belt, as indicated by the narrow lines in the PL image (see Fig. 6.2(a)). Due to the high thermal mass of the belt in comparison to that of the solar cells, as the wafer passes through the firing zones of the furnace the wafer would reach higher temperatures than that reached by the belt. In addition, regions of the wafer directly above physical parts of the belt would reach lower temperatures than other regions of the wafer which did not have such parts of the belt directly below. The PL images therefore indicated that the

temperature of firing was too low. Hence, for the optimal BSF formation using this configuration of firing with the  $\text{SiN}_x\text{:H}$  surface face-down, a higher peak firing temperature should be used.

In some locations, approximately in the centre of individual chain links (where the  $\text{SiN}_x\text{:H}$  surface was in direct contact with the belt), the  $iV_{OC}$  was reduced by up to 20 – 30 mV and influenced the local  $iV_{OC}$  for several millimeters (see Fig. 6.2(a)-(b)). One potential cause for the substantially reduced  $iV_{OC}$  was a lower temperature being reached for silicon in direct contact with the belt, in comparison to that of regions directly above but not in intimate contact with the belt, or regions of the wafer with no part of the belt directly below. As the temperature of firing was already lower than optimal, the even lower temperature reached in such areas had a further negative effect on the formation of the BSF.

It is possible that the regions of  $\text{SiN}_x\text{:H}$  in direct contact with the belt were damaged during the firing process (i.e. through scratching of the surface caused by vibrations in the belt). A higher rate of hydrogen effusion from the  $\text{SiN}_x\text{:H}$  may also occur in these regions, or contaminants such as Ag or Al from the belt may be introduced into the solar cell, and driven into the junction during the firing process, resulting in increased recombination and/or shunting.

In contrast, cells fired at the same temperature with the  $\text{SiN}_x\text{:H}$  surface face-up, were free of such localised regions with excessively reduced  $iV_{OC}$  (see Fig. 6.2(c)). This suggests that the Al firing step should be performed without the  $\text{SiN}_x\text{:H}$  contacting the metal belt.

However the PL images of these samples also suggest that the firing temperature was too low, and the wafers reached a lower temperature using the face-up approach than the face-down approach. The reduced temperature reduces the formation of the Al-BSF and therefore increases recombination at the rear surface and decreases  $V_{OC}$ . Hence further investigation is required to optimise Al-BSF formation.

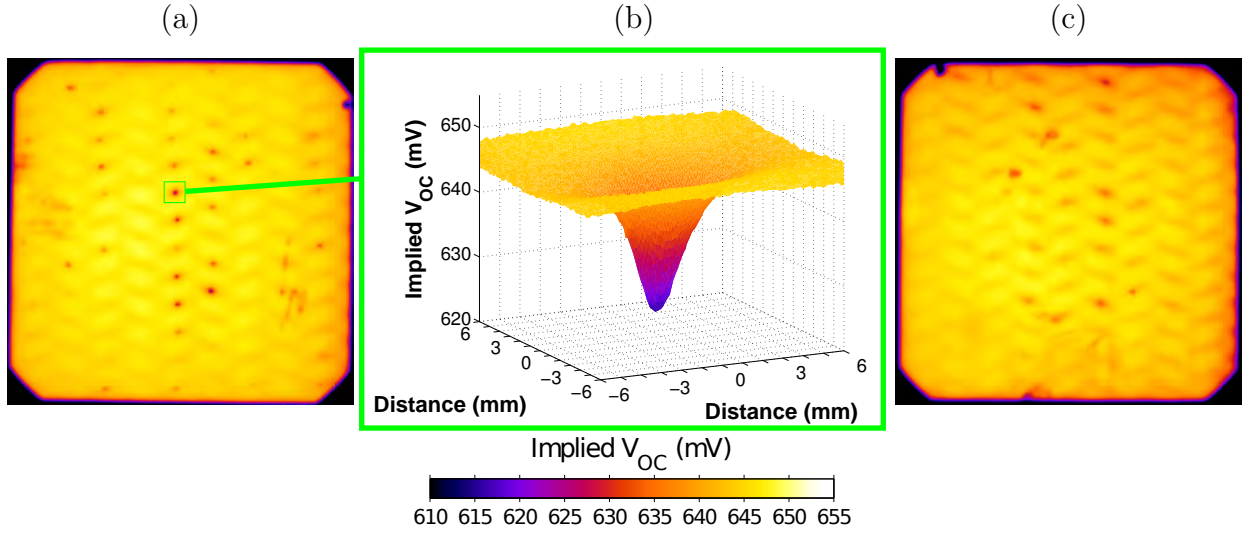


Figure 6.2: Calibrated  $iV_{OC}$  maps of a partially fabricated LDSE1 solar cell after the Al-BSF formation (a) which is performed with the  $\text{SiN}_x\text{:H}$  surface face-down on the belt showing localised recombination regions and (b) a zoomed-in 3D surface plot of the area highlighted in green, and (c) the corresponding image for a cell fired with the  $\text{SiN}_x\text{:H}$  face-up which reduced the formation of localised recombination regions. The peak firing temperature corresponding to group 3 in Fig. 6.3 was used on both samples.

### 6.1.3.2 Optimisation of Firing Temperature

To optimise the Al-BSF formation, 5 groups of wafers were fabricated with different belt furnace firing peak temperatures in zones 5 and 6 of the furnace. Temperature was increased in increments of 20 °C from group 1 to group 5 (but actual temperatures were not provided by the solar cell manufacturer due to commercial sensitivity). All samples were fired with the  $\text{SiN}_x\text{:H}$  surface face-up.

As shown in Fig. 6.3(a), for group 1 samples, the low  $iV_{OC}$  suggested a substantially reduced BSF formation compared to that of other groups, and particularly that of group 4. The lower  $iV_{OC}$

in regions of the wafer directly above the belt was similar to that observed in Fig. 6.2 suggesting the peak firing temperature was too low. The successive increases in  $iV_{OC}$  for groups 2 and 3 indicate that the temperature was indeed too low.

In contrast, samples in group 5 displayed a belt pattern in the  $iV_{OC}$  map which indicated an improved BSF field in regions of the wafer directly above the belt, suggesting that the peak firing temperature of group 5 was too high and the process started to damage the surface passivation on the front of the device. It was also noted, that in regions of the wafers not directly above the belt, small circular regions of reduced  $iV_{OC}$  were observed. Bubbles were visible on the rear Al layer in such regions, again suggesting the peak firing temperature was too high.

Wafers from group 4 displayed the highest spatially averaged  $iV_{OC}$  for any group of approximately 650 mV with high uniformity across the wafer, hence this was the best temperature investigated for the formation of the Al-BSF. These images clearly show the ability of the PL imaging for quality control during silicon solar cell fabrication. Even without specific knowledge of processing conditions such as actual peak firing temperature, valuable information can be obtained from the images to help determine the optimal processing conditions.

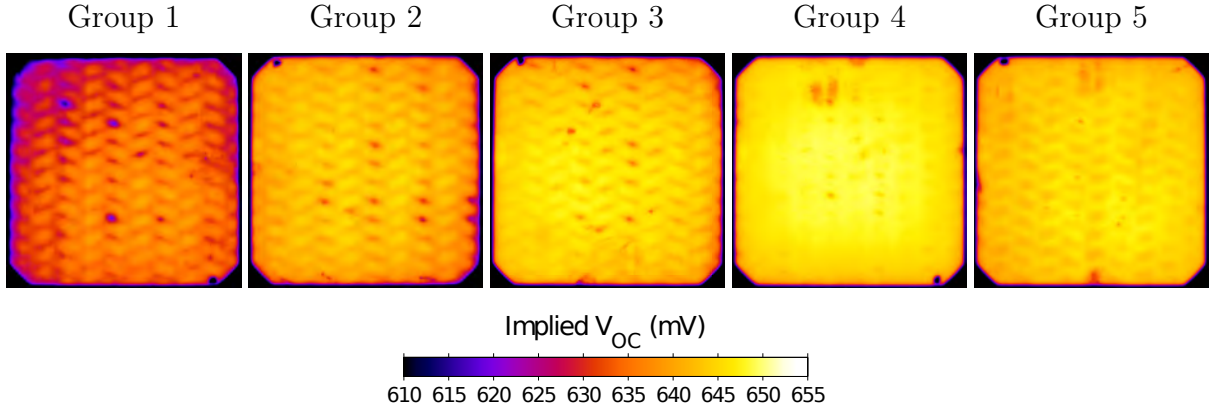


Figure 6.3: Calibrated  $iV_{OC}$  maps of partially fabricated LDSE1 solar cells after the Al-BSF formation with the  $\text{SiN}_x\text{:H}$  surface face-up on the belt for various processing temperatures with a 20 °C increment increasing from Group 1 to Group 5. Images highlight that the temperature for Groups 1-3 was too low, 5 was too high, and 4 was optimal.

### 6.1.3.3 Impact on Plating

Whilst such localised recombination sites are not an issue for the actual screen-printing process on screen-printed solar cells (as the metal deposition process occurs independently of wafer quality), when fabricating LDSE solar cells with self-aligned metal contacts using LIP, the local wafer quality can affect the process. For samples processed with the  $\text{SiN}_x\text{:H}$  face-down, the local reduction in  $iV_{OC}$  in the vicinity of regions of  $\text{SiN}_x\text{:H}$  in intimate contact with the belt during the firing process, resulted in a poor nucleation of plating (see Fig. 6.4), visible to the naked eye. This is due to the plating process depending on the localised  $iV_{OC}$  of a region.

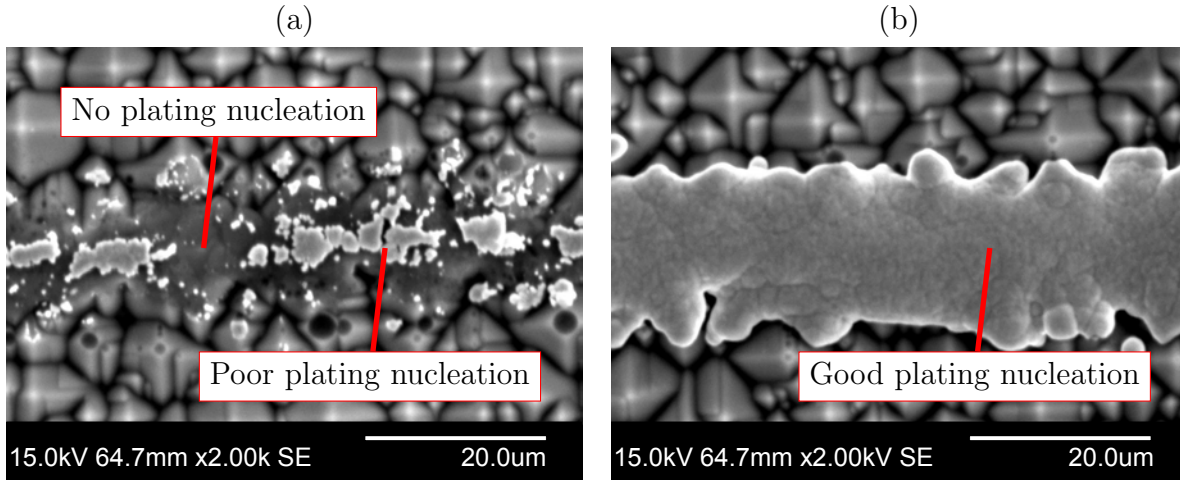


Figure 6.4: SEM images at x2000 magnification on finished LDSE1 solar cells where the Al-BSF was fired with the  $\text{SiN}_x\text{:H}$  surface face-down (a) in a region of reduced voltage caused by intimate contact between the  $\text{SiN}_x\text{:H}$  and belt during firing and (b) an unaffected area several mm away.

#### 6.1.3.4 Impact on Finished Devices

Although areas with reduced plating were expected to lead to substantial reductions in the efficiency of finished devices, the results in Table 6.1 indicated only a small increase in efficiency by forming the Al-BSF with the  $\text{SiN}_x\text{:H}$  face-up of 0.1 % absolute. This was due to a slight improvement in  $V_{OC}$  (3 mV) whilst no change was observed in  $FF$  or  $J_{SC}$ . This may be due to variations in the impact of defects within a batch across wafers, and variations between different batches.

Much larger increases in efficiency were observed through the use of a higher peak firing temperature (for group 4) compared to the standard process used (for group 3) of 0.3 % (both face-down) through a substantial increase in  $J_{SC}$  (0.6 mA/cm<sup>2</sup>). Using the improved firing conditions, an independently confirmed efficiency of 19.2 % was achieved. No cells were fabricated on wafers from groups 1, 2 and 5 due to the reduced  $iV_{OC}$ .

Table 6.1: Light J-V data of LDSE1 solar cells fabricated to improve the belt furnace firing process. Values in red were independently confirmed at Fraunhofer ISE-CalLab.

Group	Firing process	$V_{OC}$ (mV)	$J_{SC}$ (mA/cm <sup>2</sup> )	$FF$ (%)	$\eta$ (%)
3	SiN <sub>x</sub> :H face-down	635	38.0	78.1	18.8
4	SiN <sub>x</sub> :H face-down	636	38.6	77.9	19.1
4	SiN <sub>x</sub> :H face-up	639	38.6	77.9	19.2
4	SiN <sub>x</sub> :H face-up	638	38.4	78.3	19.2

#### 6.1.4 Summary of an Improved Firing process to Avoid Localised Recombination

In this experiment, firing with the SiN<sub>x</sub>:H surface face-down was shown to lead to the formation of localised recombination sites in regions of the wafer in intimate contact with the belt. Firing with the SiN<sub>x</sub>:H surface face-up avoided such localised recombination site formation. An optimisation of the peak firing temperature was then performed, taking the efficiency to 19.2 % (an improvement of 0.4 % absolute over the baseline process). However cells suffering from parasitic plating, which should be avoided to increase efficiencies further.

## 6.2 Avoidance of Parasitic Plating for LDSE Solar Cells

LDSE solar cells are susceptible to other issues associated with the use of plated contacts such as parasitic plating, which has been a widespread problem when forming contacts using electroless or LIP contacts, particularly on multi-crystalline silicon wafers in the vicinity of grain boundaries near the p-n junction. Parasitic plating can lead to shunting and increase shading losses.

However many techniques to avoid parasitic plating have been developed to address this issue



[Kray 10b; Wang 09; Wenh 11; Dumb 10]. Wang *et al.* 2009 have demonstrated several techniques to reduce parasitic plating. When using a remote PECVD tool, one such technique to reduce parasitic plating is to use a lower radio-frequency bias voltage that can lead to a more conformal coating of  $\text{SiN}_x\text{:H}$ . Hence this can result in a more adequate coverage of  $\text{SiN}_x\text{:H}$  in the grain boundaries and acidic textured wells, and avoid the formation of sites where parasitic plating can nucleate. Wang *et al.* 2009 also demonstrated that performing a rounding or NaOH etch after acidic texturing could assist in reducing parasitic plating, by removing features with sharp edges which can act as nucleation sites [Wang 09]. Other recent work performed by Wenham *et al.* 2011 and Dumbrell *et al.* 2010 have discussed the potential to avoid parasitic plating by performing a heavier thermal diffusion than required and subsequently etching back the emitter to reach the desired sheet resistance. Creating an emitter using this method reduces the surface dopant concentration compared to an emitter diffused directly to the same final sheet resistance. This effectively reduces the conductivity of the emitter region in relation to the laser-doped fingers. As a result, the nucleation of parasitic plating across the surface of the solar cell can be avoided in regions with pinholes in the  $\text{SiN}_x\text{:H}$  layer [Wenh 11; Dumb 10].

### 6.2.1 Aim

To incorporate an emitter etch-back process for LDSE solar cells as developed by Dumbrell *et al.* 2010 [Dumb 10], in an industrial environment to avoid parasitic plating and improve the efficiency of LDSE solar cells.

### 6.2.2 Experimental Procedures

LDSE1 solar cells fabricated in this section were fabricated in an industrial production environment on standard commercial grade  $2.0 - 2.5 \, \Omega \cdot \text{cm}$  p-type B-CZ silicon wafers ( $156 \times 156 \, \text{mm}$ ) with a thickness of  $200 \pm 20 \, \mu\text{m}$ . Alkaline texturing was performed using KOH prior to the emitter formation using a  $\text{POCl}_3$  tube diffusion furnace. In this section, two diffusion methods were used. In the first approach, a standard diffusion was performed directly to achieve a sheet resistance of approximately  $120 \, \Omega/\square$ . In the second approach, a slightly heavier diffusion was performed to

## CHAPTER 6. DEVELOPMENT OF HIGH EFFICIENCY LASER-DOPED SOLAR CELLS WITH ADVANCED HYDROGENATION

---

approximately  $90 \Omega/\square$  followed by an etch-back of the emitter to give a resultant sheet resistance of  $120 \Omega/\square$  using a solution comprising of 1:80:100:35 of 49 % HF: 70 %  $\text{HNO}_3$ : 98 %  $\text{CH}_3\text{COOH}$  and  $\text{H}_2\text{O}$  (HNA etch) [Robb 60].  $\text{SiN}_x\text{:H}$  with a thickness of 75 nm and refractive index of 2 was deposited using a direct PECVD system. Al was then screen-printed onto the rear of the device and fired using the improved firing conditions developed in Section 6.1 (for group 4).

In preparation for laser doping, the  $\text{SiN}_x\text{:H}$  surface of the wafers was coated with  $\text{H}_3\text{PO}_4$  (85 % w/v) at 4000 RPM for 40 s. Laser doping was performed using a 532 nm CW laser with a scan speed of 5 m/s. The dimensions of the laser-doped region of the cells was  $123 \times 123$  mm. After the removal of  $\text{H}_3\text{PO}_4$ , LasID were annealed using a BFA in oxygen ambient at 400 °C for approximately 2 min. LIP was then used to deposit Ni and Cu to form the front metal contacts in a self-aligned manner with subsequent laser cleaving. No Ni sinter was performed on the cells. The typical process sequence for the fabrication of LDSE1 solar cells in this section is shown in Fig. 6.5.

In house cell light J-V measurements in this section were obtained using a xenon flasher with AM1.5G spectrum on a Halm CetisPV XF2 tester (Class AAA) in accordance with IEC60904-9. Independently confirmed cell measurements were taken by Fraunhofer ISE CalLab, in accordance with IEC standards.

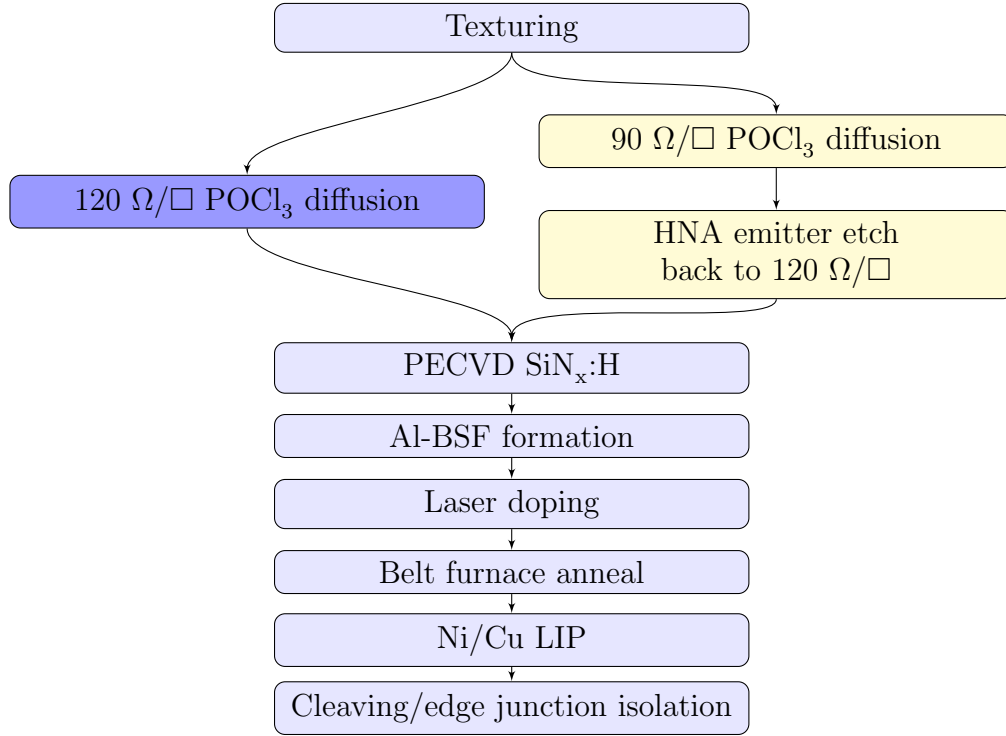


Figure 6.5: Process flow for LDSE1 solar cells fabricated to avoid parasitic plating.

### 6.2.3 Avoiding Parasitic Plating through the use of an Emitter Etch-back Process

For samples without an etch-back process, parasitic plating typically nucleated at the base of the textured pyramids, or on the peaks of the pyramids in close vicinity to the laser-doped region, due to the coupling of laser illumination. Fig. 6.6(a) shows an FIB image where parasitic plating had nucleated from abnormalities in the  $\text{SiN}_x\text{:H}$  at the base of a textured pyramid. The cause of such abnormalities in the  $\text{SiN}_x\text{:H}$  at the base of the pyramids is unclear, however this may be due to insufficient cleaning at the base of the pyramids prior to the deposition of  $\text{SiN}_x\text{:H}$ , or residual HF remaining near the base of the pyramids from the HF dip just prior to the LIP steps and hence attacking the  $\text{SiN}_x\text{:H}$  in these regions during the plating process.

The use of an emitter etch-back step greatly reduced parasitic plating. Fig. 6.6(b) shows the

textured surface of an LDSE1 solar cell with no emitter etch-back process and hence subject to parasitic plating. However on the sample shown in Fig. 6.6(c), the incorporation of an emitter etch-back process avoided parasitic plating. Particularly for heavily diffused emitters, the reduction in surface concentration realised through the emitter etch-back process can utilise the push effect in which the emitter comprises of a shallow heavily diffused region and a deeper, more lightly diffused region [Hu 83]. During the etch-back process, the shallow heavily diffused layer can be partially or entirely removed allowing the surface phosphorus concentration to be greatly reduced whilst still obtaining a low sheet resistance. Subsequently the lightly diffused emitter is less conductive at the surface relative to the heavily diffused laser-doped regions and hence less prone to parasitic plating.

In addition to the etch-back process, the  $\text{SiN}_x\text{:H}$  layer in this section was deposited using a direct PECVD system, which has been shown to assist in the avoidance of parasitic plating. Prior to the growth of  $\text{SiN}_x\text{:H}$  the direct PECVD system performs an ammonia plasma pre-etch process to clean the surface. This process also effectively performs a slight etch-back of the emitter to reduce the surface dopant concentration. This, in conjunction with the higher deposition temperature compared to remote PECVD systems, provides a tougher layer less prone to pinholes and hence more resistant to parasitic plating. The direct PECVD  $\text{SiN}_x\text{:H}$  layer also appears to provide superior surface passivation which could also be attributed to the pre-etch, by removing any native oxide prior to the deposition of the  $\text{SiN}_x\text{:H}$  layer [Hall 11d].

On finished devices, the avoidance of parasitic plating through the use of an emitter etch-back process resulted in an average increase in  $J_{SC}$  of more than  $0.3 \text{ mA/cm}^2$ , presumably due to lower shading losses. Increases to  $FF$  and  $V_{OC}$  were also observed, which may be due to reduced recombination mechanisms from the avoidance of regions of parasitic plating contacting the p-type base, or connecting the lightly doped emitter to the heavily doped contact through the metal. The average increase in  $FF$  from the inclusion of the etch-back process was  $0.9 \%$ , resulting in an average increase in efficiency of  $0.4 \%$  absolute (see Table 6.2). The difference between the light J-V parameters of the best cells from the batch of cells fabricated with and without an emitter etch-back process was smaller than the average difference between the batches, presumably due to variations in the levels of parasitic plating between the cells fabricated without an emitter etch-back process. However the highest efficiency of a cell fabricated using an emitter etch-back process was still  $0.3 \%$  absolute higher than that fabricated using the standard diffusion process. As shown in Table 6.2,

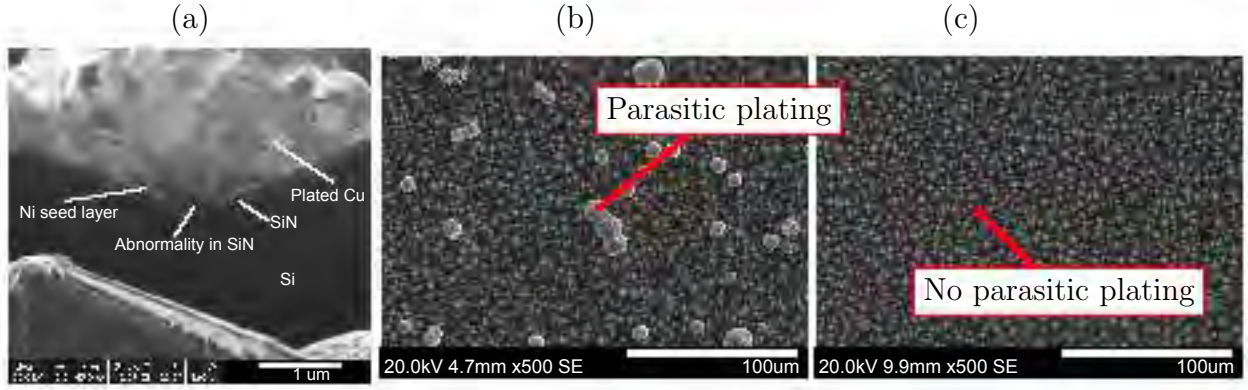


Figure 6.6: (a) FIB image of parasitic plating nucleating at the base of a textured pyramid at x65k magnification. SEM images at x500 magnification for an LDSE1 solar cell (b) without and (c) with an emitter etch-back process.

an increase in  $J_{SC}$  and  $V_{OC}$  of more than  $0.1 \text{ mA/cm}^2$  and  $2 \text{ mV}$  was observed respectively for the cell fabricated with an emitter etch-back process. An increase in  $FF$  of  $0.2 \%$  was also observed, resulting in an increase in efficiency of  $0.2 \%$  to a record of  $19.36 \%$  [Hall 11b].

The narrow line widths enabled through the use of laser doping can allow fine metal contact widths when used in conjunction with a self-aligned LIP process. This results in the lowest shading losses of any selective emitter technology in commercial production with contact widths of  $20 - 30 \text{ μm}$  in comparison to fine line screen-printing with a line width of  $70 \text{ μm}$  [Hall 11a; Sugi 10; Hofm 08]. Fig. 6.7 shows an FIB image of a Ni/Cu LIP contact with a total width of  $30 \text{ μm}$ . Whilst the width of the laser opening was approximately  $12 \text{ μm}$ , with the assistance of high aspect-ratio plating, the finger only plated  $8 \text{ μm}$  horizontally outwards in both directions. However a greatly enhanced plating rate was experienced in the vertical, resulting in a finger height of  $17 \text{ μm}$ . This results in greatly reduced shading losses whilst ensuring high conductivity of the metal fingers and hence low  $R_S$  losses. The image highlights the high crystalline quality of the plated copper, which assisted in reducing the bulk resistivity of the metal fingers, whilst reducing shading and enabling record efficiencies to be obtained.

Table 6.2: Light J-V data for small batches (less than 5) of 156 cm<sup>2</sup> LDSE1 solar cells, fabricated using a standard diffusion and a modified diffusion with an emitter etch-back process. The asterisk (\*) indicates Fraunhofer-ISE confirmed data for the highest efficiency cell fabricated in each batch.

Process		$V_{OC}$ (mV)	$J_{SC}$ (mA/cm <sup>2</sup> )	$FF$ (%)	$\eta$ (%)
Standard diffusion	Average	637.1	37.94	77.26	18.68
	Best cell	637.4	37.88	77.92	18.81
	Best cell*	638.1*	38.39*	78.29*	19.18*
Emitter etch-back	Average	638.1	38.22	78.16	19.06
	Best cell	638.4	38.24	78.46	19.15
	Best cell*	640.4*	38.52*	78.48*	19.36*

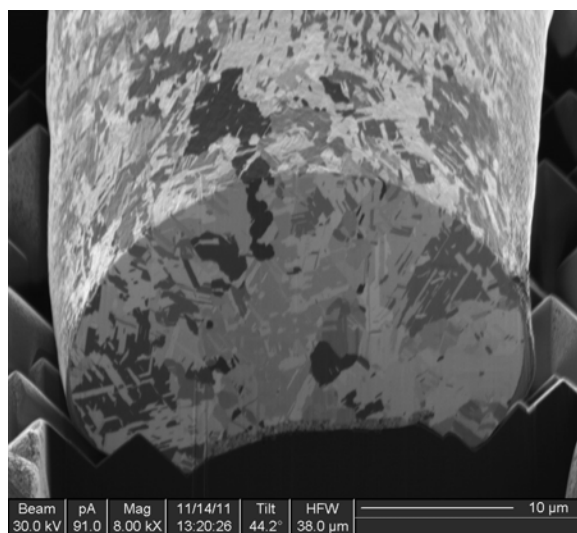


Figure 6.7: FIB image of a Ni/Cu LIP contact on a laser-doped finger with high aspect ratio plating. The image has been stretched in the vertical direction such that the scale bar also represents the scale in the vertical direction.

### 6.2.4 Summary for the Avoidance of Parasitic Plating for LDSE Solar Cells

In this section, the use of an emitter etch-back process was investigated to avoid parasitic plating on industrial laser-doped silicon solar cells. The etch-back process developed by Dumbrell *et al.* 2010 was observed to avoid parasitic plating [Dumb 10]. The etch-back process resulted in an efficiency enhancement of approximately 0.2 % absolute, to reach a record independently confirmed efficiency of 19.36 %.

## 6.3 Edge Junction Isolation Methods for LDSE Silicon Solar Cells

For LDSE1 solar cells, EJI plays a critical role in disconnecting the n-type emitter on the front of solar cells from the rear Al alloyed layer, and hence the p-type contact.

In transitioning from small area to large area devices, significant issues for the fabrication of LDSE1 solar cells were encountered in regards to the method of edge junction isolation (EJI) used. Typically, plasma EJI has been used for the commercial manufacture of screen-printed solar cells. However there are several issues associated with this technique. One such issue is that the wafers are required to be stacked; hence it is not an inline process. This disrupts the flow of the production line and increases wafer handling, which along with the mechanical stresses induced on the wafers during the plasma process, can adversely affect yields. The plasma process can also remove some of the  $\text{SiN}_x\text{:H}$  around the edge of the cell if the process is performed after the deposition of the antireflection coating, leading to further damage through the absence of surface passivation around the perimeter of the cells. This method of EJI also fails to remove the emitter from the rear side of the cells [Rena 07].

In recent times several alternative industrial approaches for EJI have been developed such as laser EJI (LEJI) or chemical EJI (CEJI). Commercial tools have been developed to perform EJI using these methods, and incorporated into turnkey solutions by PV equipment suppliers including



Schmid, Roth & Rau and Centrotherm. The LEJI and CEJI techniques overcome many of the limitations of the plasma EJI method. Both of these approaches allow an inline solution to the EJI process, and avoid the mechanical stresses induced by stacking the wafers and the plasma process. However, LEJI results in the loss of active emitter cell area caused by the formation of a laser groove, typically performed on the front of the cell. This has been found to cause a 0.2 % absolute efficiency loss when compared to cells fabricated using the CEJI method, which avoids the loss of any active emitter area. LEJI also fails to remove the emitter off the rear of the cell, limiting the compatibility with high efficiency cell technologies which require the removal of the rear phosphorus emitter [Rena 07].

In contrast, the CEJI process completely removes the diffusion from the rear of the cell. For standard screen-printed solar cells, this means that the Al alloyed rear no longer has to overcome the phosphorous diffusion on the rear of the solar cell to create an Al-BSF layer, as is the requirement for plasma EJI and LEJI. Hence a higher quality BSF can be obtained, leading to higher efficiencies. By removing the emitter from the rear of the cell, CEJI is compatible with the development of future cell technologies not utilising screen-printed rear contacts, and hence requiring the removal of the rear surface diffusion. One issue raised with the use of CEJI, is ensuring that the front emitter remains dry throughout this process while the rear is etched. Rena claims that to do so, precise wafer transport is required, which raises concerns as to the yields obtainable using this tool [Rena 07]. On the other hand, to overcome this issue, Kuttler designed a tool where the surface of the chemical lies well below the wafer, and an innovative pulse-spray technology is applied to locally raise the solution of the chemical to reach the wafer as it passes. Subsequently, surface tension spreads the solution over the entire rear of the device and ensures the front surface remains dry, hence avoiding the need for precise wafer transport [Ji 09].

### **6.3.1 Aim**

In this section, the suitability of CEJI and LEJI processes for the fabrication of LDSE1 solar cells are investigated. In particular, the compatibility of these processes with self-aligned contacts formed by LIP and the subsequent effect on the electrical performance of finished devices are compared.

### 6.3.2 Experimental Procedures

All LDSE1 solar cells fabricated in this section were produced on standard commercial grade  $0.5 - 3 \Omega \cdot \text{cm}$  p-type B-CZ silicon wafers ( $156 \times 156 \text{ mm}$ ) with a thickness of  $200 \pm 20 \mu\text{m}$ . The solar cells were produced using a standard industrial production line for screen-printed solar cells with the addition of laser doping and LIP steps.

Texturing was performed using a KOH based anisotropic etch to form random pyramids by exposing the (111) planes. Subsequently, a standard industrial HF/HCl clean was performed on the wafers. The diffusion was performed in a conventional tube furnace using a  $\text{POCl}_3$  source. Samples for LEJI were diffused to an emitter sheet resistance of  $120 \Omega/\square$  whilst CEJI samples (C6) were diffused to an emitter sheet resistance of approximately  $90 \Omega/\square$  (which would become higher after the subsequent CEJI process).

To investigate the effect of EJI on the performance of LDSE1 solar cells, industrially available LEJI and CEJI tools were used in this section. Following the CEJI process the emitter sheet resistance was approximately  $100 \Omega/\square$  due to the simultaneous gas-phase etch-back of the emitter which occurs on the front surface. After EJI,  $\text{SiN}_x\text{:H}$  was deposited using a direct PECVD system. Al was then screen-printed onto the rear of the device and the Al-BSF was formed during fast firing in a conventional belt furnace.

Prior to laser doping, the  $\text{SiN}_x\text{:H}$  surface of the wafers was spin coated with  $\text{H}_3\text{PO}_4$  (85% w/v) at 4000 RPM for 40 s. Laser doping was performed using a 532 nm CW laser with a power of 13 W and scan speed of 5 m/s. LasID were annealed in a belt furnace for 2 min at  $400^\circ\text{C}$  in CDA ambient.

For cells with LEJI, cells were laser-doped with either a full  $156 \times 156 \text{ mm}$  cell pattern (L6), or a  $123 \times 123 \text{ mm}$  cell pattern (L5) to highlight the effect of having a LEJI groove a large distance from the active cell area of the device during plating. LIP was then used to deposit Ni and Cu to form the front metal contact. After plating, cleaving was performed around the active cell area for L5 cells using a laser, which again performed EJI.

A BTi R1 luminescence imaging system was used extensively in this section. Calibrated  $iV_{OC}$

### 6.3. EDGE JUNCTION ISOLATION METHODS FOR LDSE SILICON SOLAR CELLS

maps were obtained at various stages of the fabrication sequence. PL  $R_S$  images were also obtained on the finished devices. All light J-V measurements in this section were obtained using a xenon flasher with AM1.5G spectrum on a Halm CetisPV XF2 tester (Class AAA) in accordance with IEC60904-9.

The processing sequence for the fabrication of the LDSE1 solar cells in this section is outlined in Fig. 6.8.

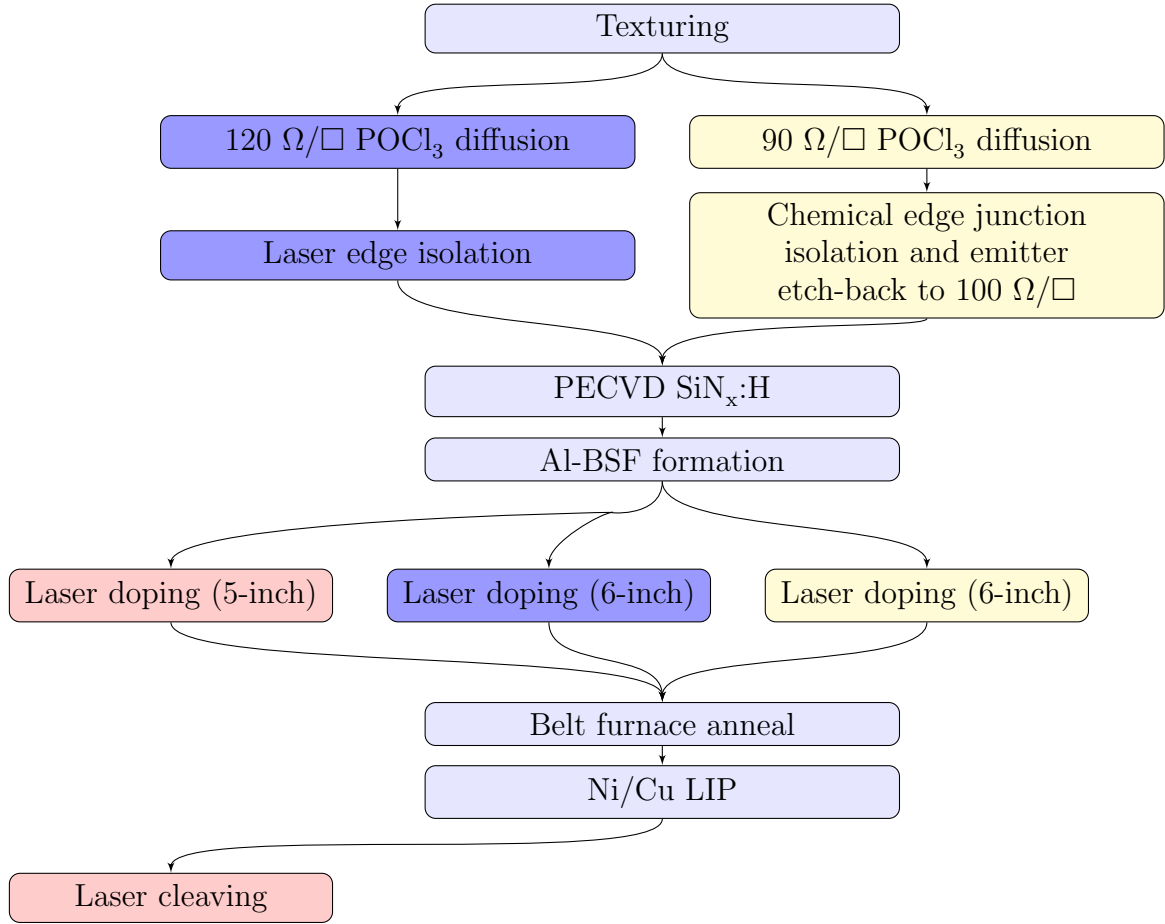


Figure 6.8: Process flow for solar cells fabricated to investigate edge junction isolation methods for LDSE1 solar cells.

### 6.3.3 Effect of Edge Junction Isolation Methods on the PL response of LDSE1 Solar Cells

The method used for EJI had a profound influence on both the  $iV_{OC}$  and  $R_S$  in the peripheral regions of the LDSE1 solar cells. Fig. 6.9 shows calibrated 1-sun  $iV_{OC}$  maps and  $R_S$  PL images of finished cells for L5, L6 and C6. The  $iV_{OC}$  of C6 was lower than that of the LEJI samples. This may be due to differences in processing such as a slightly lower emitter sheet resistance of  $100 \Omega/\square$  in comparison to the LEJI samples  $120 \Omega/\square$  as well as the non-optimal processing sequence used for these samples. As the production facility used to fabricate these solar cells does not have CEJI capabilities, for C6, directly after emitter diffusion the samples were packaged and transported to the location with CEJI equipment. After CEJI and PSG removal, the samples were repackaged and transported back to the screen-print production line. No additional chemical processing steps were given to these wafers prior to the deposition of  $\text{SiN}_x\text{:H}$ . Whilst the direct PECVD used to fabricate these cells performs an ammonia plasma pre-etch treatment which cleans the surface of the cell, this process only cleans the front surface of the cell. The PL images indicate that the rear of these cells may not have been sufficiently clean prior to the Al screen-printing process, and marks were observed which corresponded to the  $\text{SiN}_x\text{:H}$  carrier (see Fig. 6.9). Hence in conclusion, more tests are needed to investigate improved cleaning regimes.

In contrast, samples with LEJI moved directly from diffusion to LEJI, PSG removal and subsequently to the  $\text{SiN}_x\text{:H}$  deposition, with no time lag in between processes. For these samples, no such marks were observed from the PECVD carrier, but all samples suffered from additional low lifetime regions due to the suction cap loading mechanism for the PECVD carrier. This would suggest that either the suction cap was contaminating the samples prior to the deposition of the  $\text{SiN}_x\text{:H}$ , or the pressure used by the suction cap was too high and damaged the  $\text{SiN}_x\text{:H}$  surface during the unloading step. Directly after Al-BSF formation, PL images indicated a definite decrease in cell area with reasonable voltages for cells with LEJI. This suggests that substantial damages occurred during the LEJI process, resulting not only in the loss of active emitter area from the region outside the laser groove, but also reducing the localised voltage a considerable distance into the active emitter region.

For finished cells, the  $R_S$  PL image of L6 in Fig. 6.9 shows regions of high  $R_S$  around the perimeter of the cell with some of the regions in excess of  $2 \Omega \cdot \text{cm}^2$  due to the absence of plating in such regions. In contrast, the PL image of C6 shown in Fig. 6.9 is free of such high series resistance regions around the perimeter of the cell, apart from a small region of high series resistance corresponding to the low  $iV_{OC}$  region observed after laser doping. The central regions of both cells show slightly elevated series resistance, however this was due to measurement limitations of the BTi luminescence imaging system used in this section which is configured to measure the series resistance of cells using two busbars. Hence for these cells with a three busbar configuration, the  $R_S$  was measured by connecting the cell via the two outer busbars, leading to a higher apparent series resistance in the centre of the cell.

Hence, CEJI should be used to avoid regions of high series resistance around the edge of the solar cells which occurs when using LEJI. However the reason for the absence of plating in the peripheral regions should be explored.

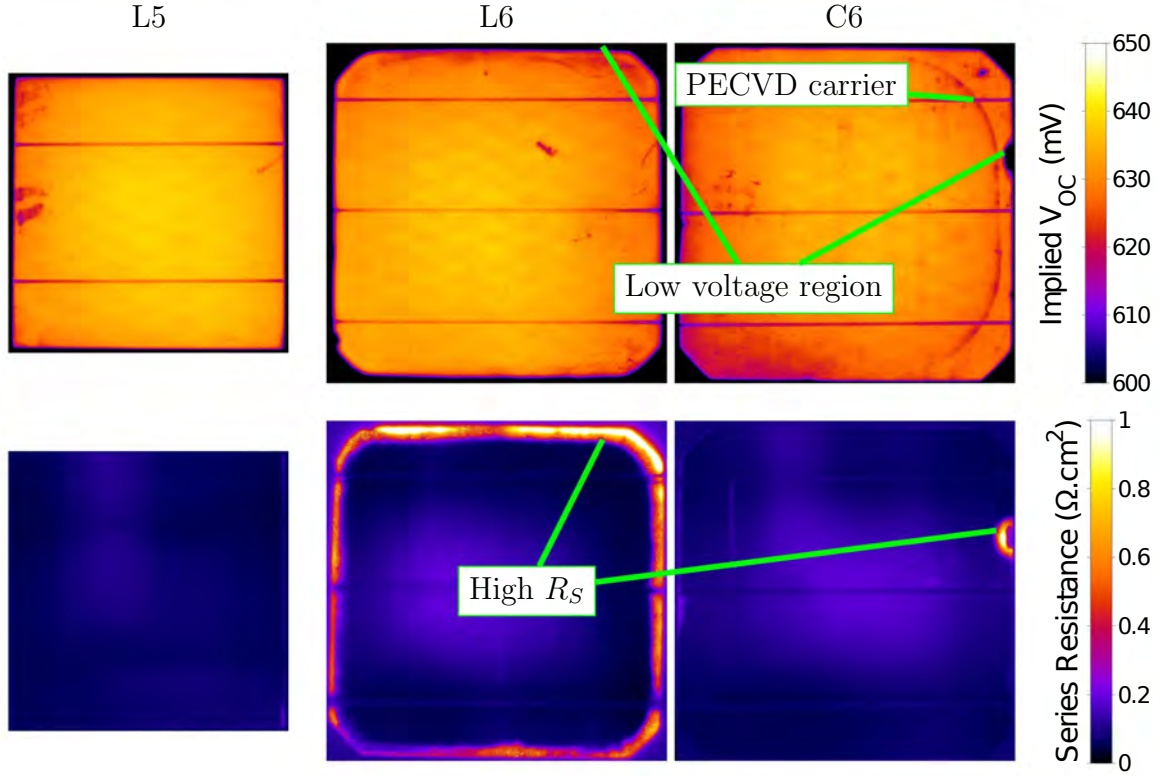


Figure 6.9: Calibrated 1-sun  $iV_{OC}$  maps and PL  $R_S$  images of finished solar cells with a 5-inch cell fabricated on a 6-inch wafer using laser edge junction isolation (L5), a full 6-inch cell with laser edge junction isolation (L6) and full 6-inch cell with chemical edge junction isolation (C6).

### 6.3.4 Evidence for Parasitic Plating Induced by Laser Edge Junction Isolation

The PL images shown in the previous section suffered from a dramatic increase in  $R_S$  around the perimeter of the LEJI samples. This was due to a significant reduction in plating around the perimeter of the cell, which in some areas extended distances of more than 1 cm into the active emitter area from the laser groove. The SEM images in Fig. 6.10 highlight the varying nature of the plating along a laser-doped line in the vicinity of the LEJI groove. On the finger investigated, at distances of less than 3 mm from the LEJI groove essentially no plating was observed, indicating

shunting and/or regions of high recombination which completely inhibited plating in this region.

At a distance of 3 mm from the laser groove, limited nucleation of plating was observed and confined to local nucleation sites along the edge of the laser-doped line and the surrounding areas. When comparing the location of the nucleation sites in this image to the location of LasID visible in the images without any plating nucleation, it appears that the LasID may assist with the nucleation of the plating along the laser-doped line by increasing roughness and exposing silicon. 4 mm from the LEJI groove, whilst the laser-doped line was completely covered by plated metal, the metal appears to have still nucleated in localised regions which have merged together as the plating process continued. It is possible that in these regions, the metal may only be in contact with the silicon in small areas, which would lead to high contact resistance. It was also observed that the width of the finger at a distance of 4 mm from the LEJI groove was substantially wider than that in the central region of the cell, where the plated line appears to be predominately continuous.

Assuming the plating is uniform around the perimeter of the cell, if little or no plating occurs within 3 mm of the edge of the wafer such areas can become completely isolated from the rest of the cell and not contribute towards the  $J_{SC}$  of the device. On a  $156 \times 156$  mm wafer used, this would lead to a reduction in  $J_{SC}$  of approximately 7.5 % relative. The lack of plating around the perimeter of the cell was partially due to a lower voltage in the perimeter region, caused by the LEJI groove. However the distance at which plating was inhibited suggests some form of shunting occurred, or that the heavily diffused laser-doped lines assisted with carrier transport to the localised recombination sites [Chan 13a]. The photograph of a 6-inch plated cell with LEJI clearly highlights the absence of plating around the edge of the cell, extending more than 1 cm from the cell edge.

For cells with LEJI, parasitic plating can nucleate within the laser groove itself. Fig. 6.11 shows an FIB image of a LEJI groove on a finished cell. It is noted that plating had occurred along the right hand side of the groove, corresponding to the active emitter area. Upon closer examination of the groove in the highlighted area of Fig. 6.11(a), plating was observed both on the textured surface as well as in the roughened area caused by the laser groove (see Fig. 6.11(b)). In some locations, plating on both of these surfaces was connected. It appears that even though the EJI was performed prior to the deposition of  $\text{SiN}_x\text{:H}$ , the roughened and damaged area in and around

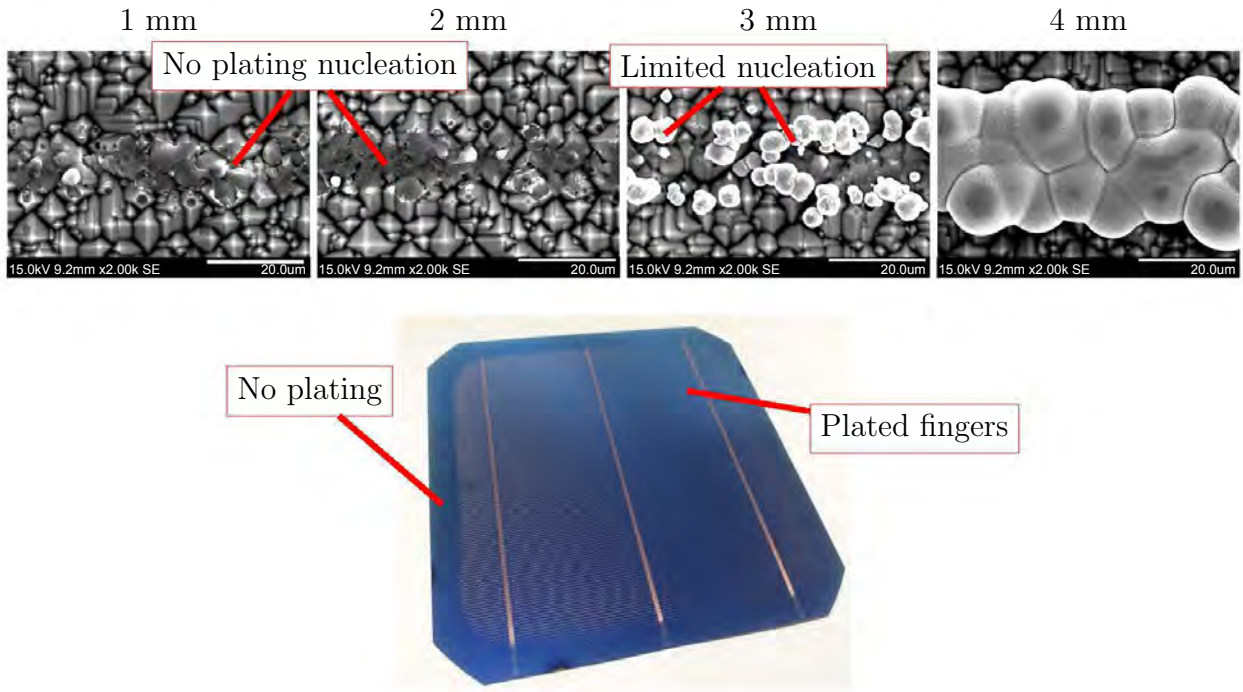


Figure 6.10: SEM images of a laser-doped finger after plating at various distances from the laser edge junction isolation groove and a photograph of a finished cell with laser edge junction isolation highlighting the absence of plating for approximately 1 cm from the edge.

the laser groove acted as a nucleation site for parasitic plating. During this process, plated regions connected to the n-type emitter can come into physical contact with the p-type base and hence induce a shunt. This lowers the voltage, and inhibits further plating in the surrounding areas.

### 6.3.5 Effect of Edge Junction Isolation on the Electrical Performance of LDSE Solar Cells

However, the different methods used can greatly impact the performance of finished devices. Table 6.3 summarises the performance of the 6-inch cells fabricated using CEJI (C6) and LEJI (L6). The light J-V data is also included for a 5-inch cell processed in parallel on a 6-inch wafer with



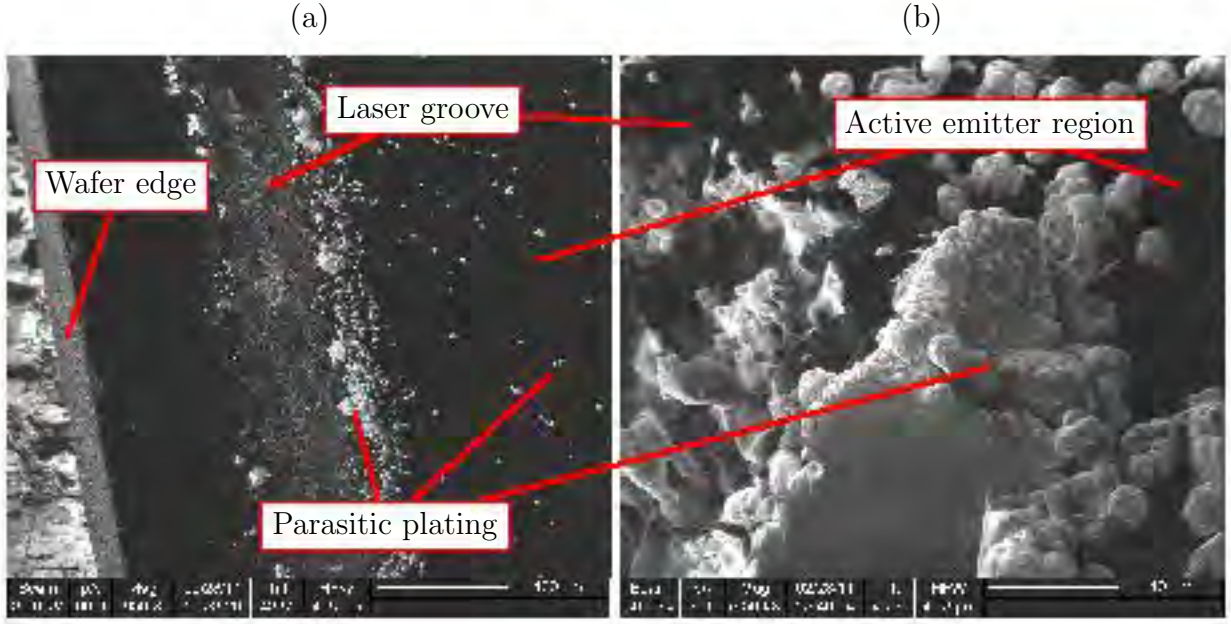


Figure 6.11: FIB images of parasitic plating in the active emitter region alongside the laser edge junction isolation groove at (a) x650 magnification and (b) x6500 magnification.

LEJI (L5). After Cu plating, L5 was cleaved down to a size of  $125 \times 125$  mm. The electrical parameters of L5 clearly highlighted the adverse effect of the LEJI process on the performance of LDSE1 solar cells when a full area cell was fabricated on a wafer using LEJI. Fig. 6.12 shows the light J-V curves of the three aforementioned cells.

For L5, whilst the wafer itself was subject to the same issues during plating as L6, the peripheral regions of the wafer which are affected by  $R_S$  were outside the laser-doped region, and hence outside the active cell area which was subsequently cleaved. Hence cell L5 avoids the series resistance issues displayed by full 6-inch cells processed using LEJI on a 6-inch wafer. Whilst C6 had a reasonable  $FF$  in excess of 78 %, sample L6 had a substantially reduced  $FF$  of 72.2 %, with a 20 % relative increase in series resistance. L6 also suffered more than a 5 % reduction in  $J_{SC}$  compared to C6. This is presumably due to the loss of active emitter area caused by the LEJI process, as well as the high series resistance region around the perimeter of the cell which if high enough, could isolate regions of the cell and therefore not allow such areas to contribute to the  $J_{SC}$  of the finished device.

## CHAPTER 6. DEVELOPMENT OF HIGH EFFICIENCY LASER-DOPED SOLAR CELLS WITH ADVANCED HYDROGENATION

---

L6 also suffered from a reduction in  $R_{SH}$  of  $460 \Omega \cdot \text{cm}^2$ , almost a factor of 10 lower than that of C6 at  $3970 \Omega \cdot \text{cm}^2$ , presumably due to the shunting induced by parasitic plating in the LEJI groove. These factors resulted in a 2.1 % absolute reduction in efficiency for 6-inch cells fabricated using LEJI compared to that of cells processed in parallel with CEJI, and limited the performance of the cell to an efficiency of 15.8 %.

In contrast, L5 displayed an almost identical  $FF$  and similar  $R_S$  to C6, yielding an efficiency of 18.5 % whilst the  $R_{SH}$  was an order of magnitude higher than that of C6 at  $69300 \Omega \cdot \text{cm}^2$ . The higher  $R_{SH}$  suggests that laser cleaving of the cell after plating was a superior method for EJI than CEJI. However this process did not appear to be viable for production due to the high wastage of the silicon wafer, particularly when CEJI is capable of achieving  $FF > 78$  %. The laser cleaving process can also introduce new defects into the newly defined edge region. The  $J_{SC}$  of L5 was significantly higher than that of the C6, although substantially reduced from that of LDSE1 solar cells produced on the same production line with Fraunhofer ISE confirmed conversion efficiencies in excess of 19.2 % [Lee 11a]. It is expected that the lower  $J_{SC}$  and  $V_{OC}$  of C6 was due to non-optimal processing conditions for the CEJI samples, and upon optimisation of the process similar  $J_{SC}$  and  $V_{OC}$  values and hence efficiencies will be obtainable. However another key difference between the CEJI and LEJI samples was the removal of the phosphorus emitter off the rear of CEJI cells. This will be discussed in Section 6.4. Directly comparing the light J-V data of the two LEJI cells (L6 and L5) can imply the difference obtainable for LDSE solar cells fabricated using LEJI and CEJI as full area cells. Hence the reduction in  $J_{SC}$  for L6 was 8 % relative. This, in conjunction with the corresponding decrease in  $FF$ , reduced the efficiency of such cells by 2.7 % absolute compared to those processed using CEJI.

The difference in efficiency between LDSE1 solar cells with LEJI and CEJI was far greater than the 0.2 % absolute reduction in efficiency for conventional screen-printed solar cells fabricated using LEJI [Rena 07]. This suggests that the choice of suitable equipment for edge junction isolation of LDSE solar cells with LIP contacts is far more critical than for conventional screen-printed solar cells, whereby the deposition of the screen-printed contacts does not rely on the spatial distribution of quality of the solar cell. Based on the results obtained, it would appear that the use of LEJI is not compatible with the production of LDSE1 solar cells on an industrial level when using self-aligned LIP contacts.

Table 6.3: Electrical parameters for 6-inch cells ( $239 \text{ cm}^2$ ) fabricated using CEJI (C6) and laser edge junction isolation (L6) and a 5-inch cell ( $156 \text{ cm}^2$ ) fabricated on a 6-inch wafer using LEJI (L5).

Sample	$V_{OC}$ (mV)	$J_{SC}$ (mA/cm <sup>2</sup> )	$FF$ (%)	$\eta$ (%)	$R_S$ ( $\Omega \cdot \text{cm}^2$ )	$R_{SH}$ ( $\Omega \cdot \text{cm}^2$ )
C6	632	36.4	78.1	18	1.36	3970
L6	636	34.5	72.2	15.8	1.64	460
L5	638	37.2	78.0	18.5	1.39	69300

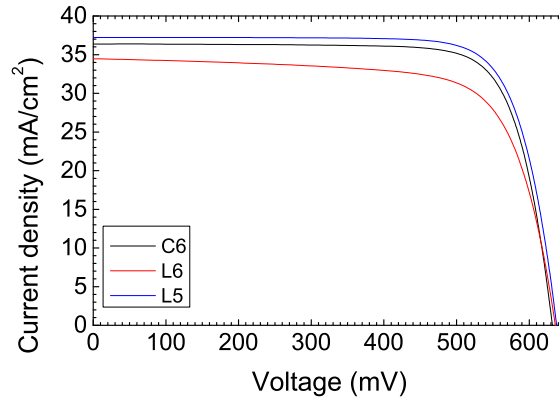


Figure 6.12: Light J-V curves of 6-inch LDSE1 solar cells with chemical edge junction isolation (C6), laser edge junction isolation (L6) and a 5-inch cell processed on a 6-inch wafer with laser edge junction isolation (L5).

However, it could be possible to fabricate LDSE1 solar cells using LEJI and avoid the regions of high series resistance around the perimeter of the cells fabricated using LIP, through the use of aligned screen-printed contacts to the heavily doped regions. This process has been proven and used for the turnkey selective emitter solutions offered by the Centrotherm and Schmid groups [Laue 09;

[Chun 03](#)], but defeats many of the benefits of using an LDSE structure over the conventional screen-printed solar cell and bring added process complexities to the fabrication sequence. The use of screen-printed front contacts requires precise alignment to the heavily doped region and therefore higher yield losses would be expected! Additional shading losses would also result even if using fine-line printing techniques capable of line widths of 50  $\mu\text{m}$  in comparison to line widths of 25  $\mu\text{m}$  achievable with LIP. Using screen-printing would also require either the use of glass-frit free pastes such as not to penetrate the  $\text{SiN}_x\text{:H}$  alongside the laser-doped region, or extending the laser-doped region wider to ensure the screen-printed contact only contacts the heavily doped silicon. However the latter approach leads to lower voltages on finished devices due to increased  $J_{0d}$  and an increased metal/Si interface area. For both of these approaches, the use of screen-printed front contacts means the ability to independently optimise firing conditions for the Al-BSF is lost, and the cells would still suffer from the loss of active emitter area from the LEJI process.

### 6.3.6 Summary of EJI Methods for LDSE Silicon Solar Cells

The results in this section highlight the importance of using CEJI for LDSE solar cell fabrication, which can result in efficiency enhancements of  $> 2\%$  absolute to that obtained using LEJI. Hence it would appear that using the LDSE structure with self-aligned LIP front contacts in conjunction with CEJI would be a superior way of fabricating selective emitter solar cells.

## 6.4 Advanced Hydrogenation for LDSE1 Solar Cells

Many processes for silicon solar cells have complex interactions with other processes in the fabrication sequence and can often introduce trade-offs. For example, the emitter doping profile and finger pitch used for the metallisation scheme introduce trade-offs between: contact resistance at the metal/Si interface; lateral resistive losses within the emitter; shading losses from the coverage of metal contacts; and optical losses associated with any formation of a dead-layer within the emitter. As another example, the formation of the Al-BSF has been reported to change the optimal temperature for hydrogen passivation of the bulk [\[Roha 02\]](#). Hence changes to the formation of the

Al-BSF formation could change the effectiveness of hydrogen passivation within the solar cell.

Following the substantial reduction in  $J_{SC}$  and  $V_{OC}$  observed for samples fabricated using CEJI in the previous section, a further investigation was performed to look at ways to enhance the  $J_{SC}$  and  $V_{OC}$  of such cells.

A key difference between the cells with LEJI and CEJI was that for the cells with LEJI the phosphorus emitter on the rear was retained. If a shallow phosphorus layer is retained ahead of the Al-BSF region during the firing process, the phosphorus could reduce the ability of hydrogen to reach the molten Al-Si alloyed region.

In this section the use of an alternative CEJI process was investigated which could retain the phosphorus emitter over the majority of the rear of the cell to increase hydrogen retention in the device. Cell structures are shown in Fig. 6.13. By comparing the two structures - one with a phosphorus emitter and one without, the impact of the phosphorus emitter can be further investigated.

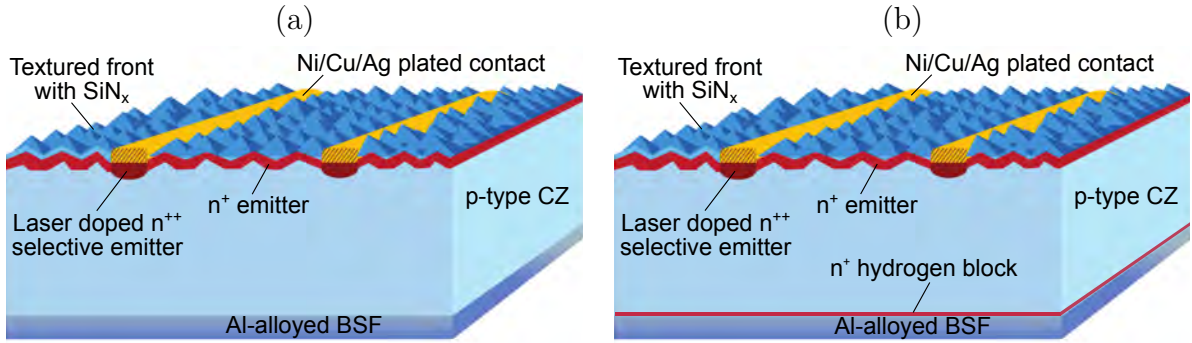


Figure 6.13: Structure of (a) a standard LDSE1 solar cell with chemical edge junction isolation to remove the phosphorus off the rear surface and (b) a modified cell structure to retain the phosphorus on rear of the cell.

### **6.4.1 Experimental Procedures**

Solar cells were fabricated on  $156 \times 156$  mm standard commercial grade  $0.5 - 3 \Omega \cdot \text{cm}$  p-type B-CZ wafers with a thickness of  $200 \pm 20 \mu\text{m}$ . Texturing was performed using a KOH based anisotropic etch to form random pyramids by exposing the (111) planes. A standard industrial HF/HCl clean was performed on the wafers prior to the emitter diffusion in a conventional  $\text{POCl}_3$  tube diffusion furnace followed by PSG removal, with a resultant sheet resistance of approximately  $120 \Omega/\square$  on both surfaces.

#### **6.4.1.1 Modified CEJI Process**

On selected samples, an oxide mask was deposited onto both surfaces and patterning was performed to remove the oxide from a strip approximately 5 mm wide from the perimeter of the cell. During the subsequent HNA etch, a local phosphorus emitter removal (LPR) occurred in the exposed regions on the perimeter of the cell, whilst the phosphorus and surface texture was retained on the remainder of the cell.

#### **6.4.1.2 Standard CEJI Process**

On other samples, an oxide mask was deposited onto the front surface. Subsequently the same chemical etch was used to remove the phosphorus emitter off the entire rear surface in a similar process to that in the previous section with CEJI. Hereafter, this process will also be referred to as CEJI.

#### **6.4.1.3 LEJI**

As a control, the conventional approach of fabricating a 5-inch cell on the 6-inch wafer with LEJI was also used with no removal of phosphorus from the rear surface.

Subsequently the oxide masks were removed and the wafers were cleaned prior to the deposition of  $\text{SiN}_x\text{:H}$  by direct PECVD.

Al screen-printing was performed on a standard industrial screen-printing platform with drying of the Al prior to fast firing. Fast firing was performed using an industrial belt furnace with 6 zones manufactured by Centrotherm. For cells with LPR, an advanced firing process (AFP) was used with the appropriate changes to the power distribution in the furnace as discussed in Section 3.2 to increase  $H^0$  generation. Other groups received a conventional firing process (CFP) with even power distribution between the top and bottom lamps.

Prior to selective emitter formation by laser doping, 85 %  $H_3PO_4$  was spin-coated on the  $SiN_x:H$  layer at a spin speed of 4000 RPM for 40 s. Laser doping was performed using the CW laser system described in Chapter 4 with a scan speed of 5 m/s and optical power reaching the wafer of approximately 13.5 W. After laser doping, wafers were rinsed to remove the  $H_3PO_4$  and then received a BFA at 400 °C in oxygen ambient for approximately 2 min to passivate LasID. Subsequently the cells were dipped in a HF solution to clean the surface and remove any residual oxides before Ni/Cu LIP to form the front metal contact. For the control LEJI samples, cleaving was then performed to isolate the cells.

The light J-V parameters of all cells fabricated in this section were measured using a Xenon flasher with AM1.5G spectrum on a WACOM cell tester (Class AAA). The best cells were independently measured by Fraunhofer ISE CalLab, in accordance with IEC60904 standards.

The cell processing sequence for CEJI and modified CEJI samples is shown in Fig. 6.14

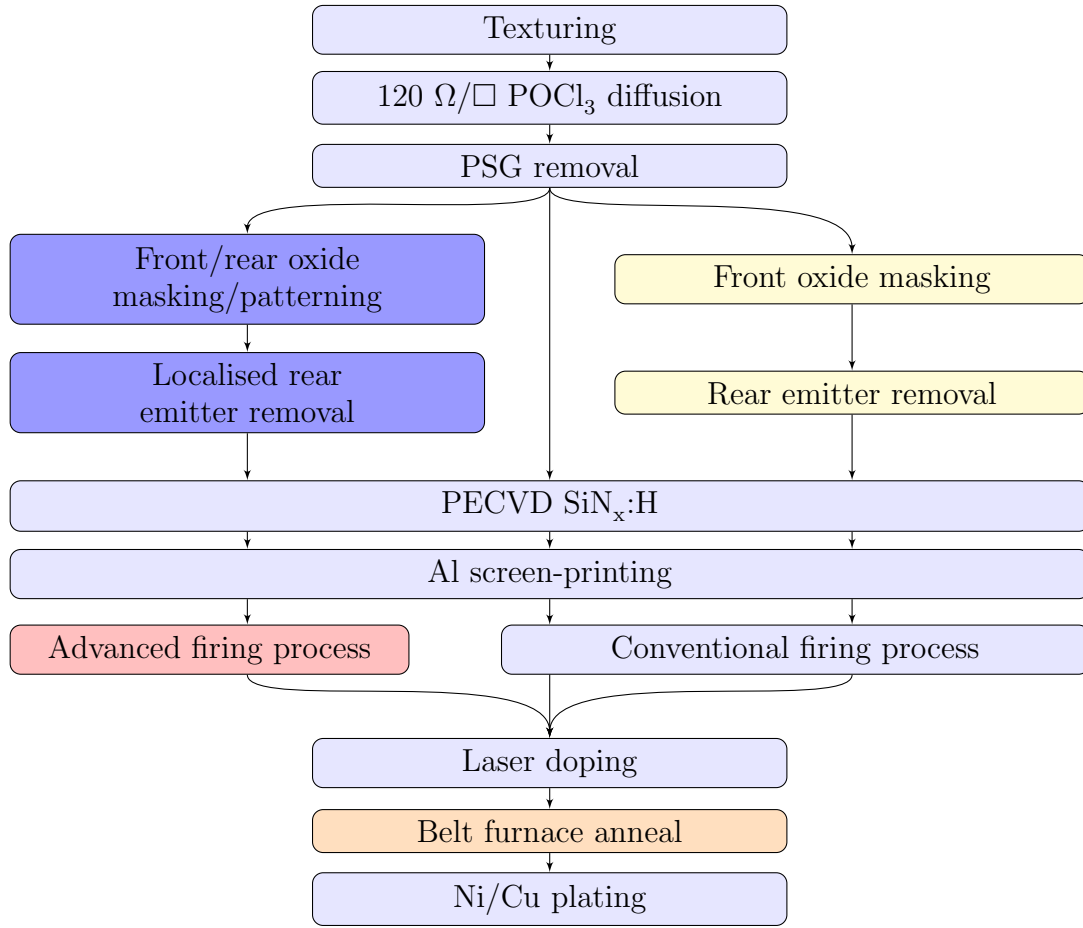


Figure 6.14: Process flow for LDSE1 solar cells with improved edge junction isolation methods.

### 6.4.2 Improved Performance of LDSE1 Solar Cells

Table 6.4 shows the light J-V data for cells fabricated in this section with and without phosphorus retained on the rear.



Table 6.4: Light J-V data for 6-inch LDSE1 solar cells ( $239 \text{ cm}^2$ ) fabricated using various methods to effectively perform edge junction isolation. ‘CEJI’ = chemical edge junction isolation, ‘SSD’ = single-sided diffusion (through oxide masking), ‘LEJI’ = laser edge junction isolation and ‘LPR’ = localised phosphorus emitter removal. Data in red was independently confirmed by Fraunhofer ISE CalLab. An asterisk (\*) denotes a 5-inch cell fabricated on a 6-inch wafer.

Emitter/edge junction isolation	Firing process	$V_{OC}$ (mV)	$J_{SC}$ (mA/cm <sup>2</sup> )	$FF$ (%)	$\eta$ (%)
CEJI	Conventional	636	36.7	78.5	18.3
SSD	Conventional	639	37.2	79.1	18.8
Ion implantation	Conventional	640	37.0	79.2	18.7
LEJI*	Conventional	640	38.5	78.0	19.4
LPR	Advanced	644	38.8	78.72	19.6

#### 6.4.2.1 Phosphorus Containing Rear Surfaces

Similarly to the results presented in Section 6.3, the results in Table 6.4 indicated a substantial improvement in  $J_{SC}$  for cells which retained the phosphorus diffusion on the rear of the cell prior to Al-BSF formation.

On the same production line used for this experiment, solar cells with alternative methods of forming a single sided diffusion such as oxide masking prior to emitter diffusion to result in a single sided diffusion (SSD) or ion implantation were processed in parallel. These approaches also resulted in a substantial reduction in the  $J_{SC}$  of  $36.7 - 37.0$  mA/cm<sup>2</sup> compared to cells with phosphorus remaining on the rear of the cell with  $J_{SC}$  of  $38.5 - 38.8$  mA/cm<sup>2</sup> [Kim 12; Cho 12a]. The results in this experiment also indicated that the AFP with a modification of power distribution in the lamps within the furnace, led to a further efficiency enhancement, primarily through increases in the  $V_{OC}$  and  $J_{SC}$  of the device.

It would appear that based on the results in this experiment and those performed in conjunction with Kim *et al.* 2012 and Cho *et al.* 2012, the changes in  $J_{SC}$  were not due to the change in surface morphology for the CEJI in planarising the rear surface. Therefore, one possible explanation for the increases in  $J_{SC}$  which occurs with the presence of phosphorus on the rear of the cell was that the phosphorus assisted with the formation of the BSF and lead to a lower rear SRV. Another possible explanation is that the presence of phosphorus assisted in the retention of hydrogen within the bulk of the device, and therefore led to enhanced bulk lifetimes.

When using Ni plated contacts on silicon solar cells, nickel silicide formation can result in the redistribution of dopants below the NiSi layer through segregation resulting in higher dopant concentrations at the Si/NiSi interface [Mori 95; Lenz 11]. For boron-doped Al-BSF pastes, a boron-doped region was also observed ahead of the Al-alloyed region after the BSF formation and similarly for phosphorus-doped Ag pastes [Du 12; Port 02]. Hence it is expected that the same, or a similar mechanism would occur during BSF formation with the presence of phosphorus on the rear surface. This phosphorus layer could then assist in blocking atomic hydrogen from reaching the molten Al-Si alloy through substantial reductions in hydrogen diffusivity, which occur in heavily doped silicon, particularly during the solidification of the Al-BSF region. An increased retention of

hydrogen within the solar cell could then allow more effective hydrogen passivation to be realised.

However the phosphorus could have also resulted in a modification to the BSF and hence improved rear SRV. This must be investigated further to determine the exact mechanism resulting in the improved  $J_{SC}$ . If the phosphorus on the rear surface assisted in trapping hydrogen in the device, other dopants such as boron may be used to result in further reductions in hydrogen diffusivity and hence increase the effectiveness of the hydrogen-blocking layer. Whilst not investigated in this section, it is expected that the EJI method based on laser doping to invert the surface polarity of the silicon could also be used to retain phosphorus on the rear surface and avoid the need for masking steps.

#### **6.4.2.2 Incorporation of an Advanced Firing Process**

For the cell with LPR and the AFP, an independently confirmed efficiency of 19.6 % was achieved with a  $V_{OC}$  of 644 mV. The independently confirmed current-voltage (I-V) curve of the 19.6 % cell is shown in Fig. 6.15. In contrast, the equivalent cell structure with phosphorus on the rear and a CFP had a reduced efficiency of 19.4 %.

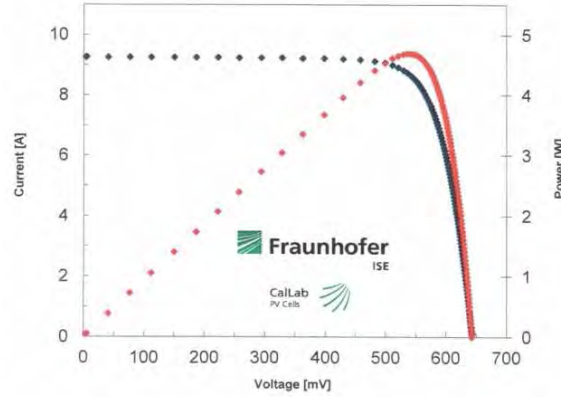


Figure 6.15: Independently confirmed light I-V curve of the 19.6 % LDSE1 solar cell with full area Al-BSF fabricated with a hydrogen block at the rear of the cell and the advanced firing process to increase minority carrier injection.

### 6.4.3 Summary for Advanced Hydrogenation for LDSE1 Solar Cells

In this section the effect of phosphorus on the rear of LDSE1 solar cells was explored. Cells which retained phosphorus on the rear prior to Al-BSF formation had  $J_{SC}$  of  $1.1 - 1.8 \text{ mA/cm}^2$  higher than that of cells with the phosphorus emitter removed prior. The improvements were attributed to an increased retention of hydrogen in the device due to the presence of phosphorus at the rear surface, which reduces the ability of hydrogen to reach the molten Al/Si region during the firing process. An AFP was used, which resulted in a 0.2 % absolute increase in efficiency when compared to cells with a CFP, resulting in an independently confirmed efficiency of 19.6 %.

## 6.5 Efficiency Enhancements for Passivated Emitter and Rear Cell Through the Addition of an LDSE Structure

For conventional large area solar cells fabricated on p-type CZ grown silicon wafers with a full area Al-BSF, carrier recombination and parasitic light absorption at the rear surface has been reported to be the dominant loss mechanisms, limiting efficiencies to below 20 % [Metz 14]. Subsequently, in recent years there have been substantial efforts to develop p-type solar cells with rear surface passivation and localised BSF through the alloying of Al/Si above the eutectic temperature [Gatz 11; Mack 10; Munz 11; Wang 12; Verm 12].

Recent work on p-type solar cells with local BSF formation has focused on industrial applications using a wide variety of dielectric layers at the rear, including: thin thermally grown  $\text{SiO}_2$ ; layers of  $\text{SiO}_x$ ,  $\text{SiN}_x$  and  $\text{AlO}_x$  grown by PECVD; and ALD of  $\text{AlO}_x$ . These dielectrics were often used in stacked arrangement such as  $\text{AlO}_x/\text{SiN}_x$ , thermal  $\text{SiO}_2/\text{SiN}_x$ ,  $\text{AlO}_x/\text{SiO}_x/\text{SiN}_x$  and thermal  $\text{SiO}_2/\text{SiO}_x/\text{SiN}_x$  to improve the stability of the dielectric layers, passivation and rear reflection [Gatz 11; Verm 12; Agos 06; Horz 12].

For local BSF contacts formed through the alloying of Al/Si, a variety of methods have been used to pattern the dielectrics such as: localised etching or laser ablation [Glun 00a]; two-step screen-printing processes (in which a first localised fire-through Al layer is deposited followed by a full area non-penetrating Al layer [Thai 13]); and the laser-fired contact approach [Schn 02]. Using such approaches, various groups have reported efficiencies on large area devices over 20 %, with Metz *et al.* 2013 reporting efficiencies up to 21.3 % [Metz 14; Wang 12; Mohr 11; Tous 13].

The implementation of p-type solar cells with local BSF formation at Imec is the industrial PERC (i-PERC) solar cell platform. i-PERC solar cells are fabricated using laser ablation to form contact openings in the rear dielectric stack [Urue 09], which consists of a thin thermally grown  $\text{SiO}_2$  layer capped by PECVD  $\text{SiO}_x/\text{SiN}_x$  [Urue 12]. For i-PERC solar cells, laser ablation is used on the front surface to form contact openings on a homogenous emitter and enable a self-aligned plating process. The plating sequence for i-PERC solar cells consists of plating the full stack of

Ni/Cu/Ag prior to Ni sintering [Russ 12], in contrast to conventional approaches in which the Ni sintering process is performed prior to copper plating [Wenh 88]. The approach developed by Imec avoids the need for two separate pieces of equipment for the plating sequence and the drying of wafers in between the plating baths. By plating the full metal stack prior to Ni sintering, it may also allow a relaxation of the oxygen levels during Ni sintering to prevent oxidation of the Ni prior to copper plating.

### 6.5.1 Aim

In this section, an optimisation of the laser doping process is performed using a 355 nm mode-locked UV laser at Imec including an investigation of sheet resistance, line widths and effect on  $\tau_{eff}$  for different processing conditions. Subsequently, a comparison is made between PERC solar cells fabricated using either the standard i-PERC process with a homogenous emitter and laser-ablated contacts (LA-PERC), or an LDSE structure (LD-PERC). Hence this experiment compares the use of a homogenous or selective emitter for PERC cells. The structure of the LD-PERC solar cells fabricated in this section is shown in Fig. 6.16(a) which highlight the deep selective emitter formed using the laser doping process through melting of the silicon, which removes the surface texture below the metal contacts. In contrast, using laser ablation merely removes with dielectric with little or no modification of the doping profile or the textured surface on the LA-PERC cells (see Fig. 6.16(b)).

### 6.5.2 Experimental Procedures

#### 6.5.2.1 Sheet Resistance Samples

2  $\Omega \cdot \text{cm}$  boron-doped MCZ grown silicon wafers (156 mm  $\times$  156 mm) were used for the sheet resistance measurements in this section. Wafers were etched in a KOH-alkaline solution to remove saw damage and simultaneously texture the wafer surface anisotropically to expose the (111) planes in an in-line tool. Following acidic neutralisation in hot HCl, the rear side of the wafers received a single-side in-line chemical polish in a Si-etchant, with a resultant thickness of 180  $\mu\text{m}$ .

## 6.5. EFFICIENCY ENHANCEMENTS FOR PASSIVATED EMITTER AND REAR CELL THROUGH THE ADDITION OF AN LDSE STRUCTURE

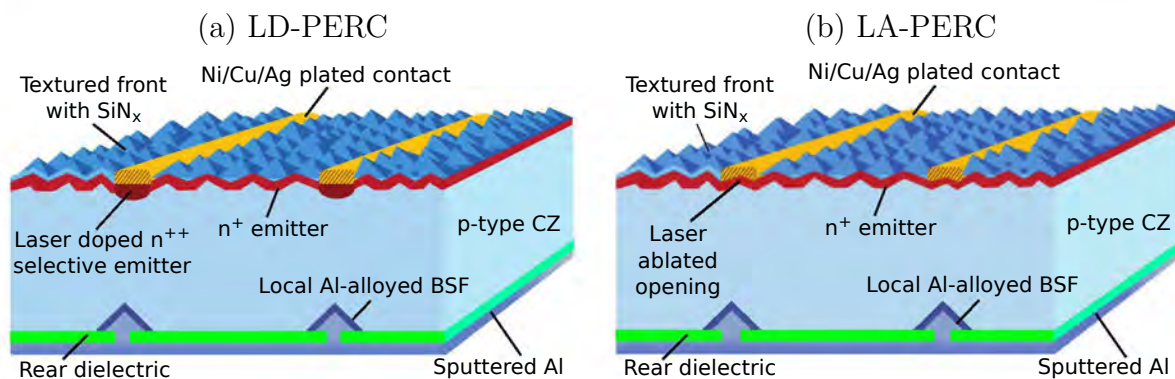


Figure 6.16: Structure of PERC solar cells with (a) an LDSE front and (b) a homogenous emitter with laser-ablated contact openings.

After chemical cleaning, a  $\text{POCl}_3$  tube diffusion furnace was performed followed by PSG removal and CEJI in a single-sided in-line tool. Approximately 15 nm of  $\text{SiO}_2$  was grown during thermal oxidation to assist with surface passivation and act as a drive-in for the emitter. This was followed by the deposition of an antireflection coating of  $\text{SiN}_x\text{:H}$  on the front surface, and a stack of  $\text{SiO}_x/\text{SiN}_x\text{:H}$  on the rear surface by PECVD. After the thermal oxidation the sheet resistance of the phosphorus emitter was approximately  $100 \Omega/\square$ .

For the LD-PERC test structures, dopants were applied using Filmtronics P509 at either 3000 RPM or 7000 RPM to vary the thickness of the applied SOD and hence the number of dopants and optical properties of the SOD. Laser doping was performed using a mode-locked UV Q-CW laser with a power density of approximately  $2.6 \text{ MW}/\text{cm}^2$  and a focus size of approximately  $20 \mu\text{m}$  ( $1/e^2$  diameter). High-speed fabrication was achieved through the use of a galvanometer scanner and f-theta lens with processing speeds of 1 – 10 m/s, corresponding to a range of laser fluences of  $5.3 - 53 \text{ J}/\text{cm}^2$ . Sheet resistance boxes were made to investigate the incorporation of electronically active dopants in the silicon from the laser doping process, by performing line scans across a  $3.5 \text{ cm} \times 3.5 \text{ cm}$  region and varying the spacing of the lines for the different scan speeds and SOD layers to account for differences in the width of the line openings. One box was laser-doped for each processing speed. Wafers then received a short HF dip and rinse to remove the SOD prior to sheet resistance measurements. Nine measurements were obtained on each sheet resistance box at different locations within the box whilst ensuring at least a 5 mm distance from the edge of the

box.

### 6.5.2.2 Lifetime Test Structures

Lifetime test samples were fabricated to minimise recombination induced by the laser doping process. The samples were processed as above, but with symmetrical surfaces representing the front surface of the solar cell. Dopants were applied using Filmtronics P509 at 7000 RPM for 80 s. Laser doping was performed using the same Q-CW laser system with processing speeds of 1 – 10 m/s and a power of 8.3 W. Lifetime test areas of 4.5 cm  $\times$  4.5 cm were processed with lines on a 500  $\mu$ m pitch to increase defect generation and therefore enhance differences between the resultant  $\tau_{eff}$  values obtained for different processing speeds. Similar tests were performed using laser ablation contact openings using a UV (355 nm) picosecond laser (without SOD application).

After SOD removal, wafers were annealed in FG for 30 min at 450 °C. Lifetime measurements were obtained using the QSS-PC method [Sint 96b] on a BTi R1 luminescence imaging system. Surface and bulk lifetime components were then extracted from the QSS-PC measurements.  $\tau_{bulk}$  were extracted at  $\Delta n = 1 \times 10^{14}$  /cm<sup>3</sup> by removing the Auger and  $J_{0d}$  lifetime components [Cuev 04]. For Auger correction, the simplified Richter model for the intrinsic lifetime with enhancement factors was used [Rich 12a; Rich 12b].

### 6.5.2.3 Solar Cell Fabrication

The solar cells in this work were fabricated on 2  $\Omega \cdot$ cm boron-doped MCZ grown silicon (156 mm  $\times$  156 mm) wafers. Wafers followed the same process up to the end of front and rear SiN<sub>x</sub>:H deposition as described for the sheet resistance samples above. Whilst laser doping for the n-type contacts for the LDSE solar cell in previous work at UNSW has typically been performed after the formation of the rear electrode to simplify the processing sequence, allowing laser doping and plating processes to be completed after the conventional screen-printing process sequence [Hall 11d; Bova 11]. However, the laser doping process can be performed prior to rear electrode formation. For the spinner system used in this work, if the rear electrode was formed prior to SOD application, wafers would break during the spinning process. Subsequent tests confirmed that this was due to balling of Al on



## 6.5. EFFICIENCY ENHANCEMENTS FOR PASSIVATED EMITTER AND REAR CELL THROUGH THE ADDITION OF AN LDSE STRUCTURE

---

the rear of the wafer during firing, causing a loss of sufficient vacuum suction during the spinning process. In contrast, no breakage was observed when the SOD was applied on wafers with unfired rear Al layers. Hence in this experiment, the SOD application, laser doping process and subsequent removal of the SOD were performed prior to deposition of the rear Al. Commercial equipment for dopant source application would likely involve the use of in-line spray-coaters and avoid this issue.

Dopants were applied using Filmtronics P509 at 7000 RPM for 80 s. Laser doping was performed using the same Q-CW laser system as used for the lifetime test structures in the previous section, but now limiting the range of scan speeds to 3 – 10 m/s, and using a power of 8.3 W. Wafers then received a short HF dip and rinse to remove the SOD. Cells with laser-ablated contact openings on the front surface receive the same SOD application and dopant removal prior to laser ablation to ensure the wafers had the same exposure to HF. Laser-ablated contact openings for the front surface were formed using a UV (355 nm) picosecond laser resulting in an opened line width of approximately 12  $\mu\text{m}$  using a process speed of 0.8 m/s.

Openings in the rear dielectric stack were formed on all cells by UV (355 nm) nanosecond laser ablation with a fixed pitch of 500  $\mu\text{m}$ , resulting in an opened diameter of approximately 30  $\mu\text{m}$ . Subsequently 2  $\mu\text{m}$  of Al was sputtered onto the rear surface and the localised BSF was formed in an in-line belt furnace, followed by the deposition of an additional 2  $\mu\text{m}$  of Al following the standard Imec process.

Prior to plating, a short HF dip was performed to remove any native oxide in the contact openings. Approximately 1  $\mu\text{m}$  of Ni was deposited by LIP followed by approximately 10  $\mu\text{m}$  of electroplated Cu and immersion Ag to prevent oxidation of the Cu. All plating was performed in a commercial in-line plating tool from Meco. Sintering was then performed on the full plated stack in nitrogen ambient to form a nickel silicide layer to reduce contact resistance and act as a more effective diffusion barrier for the copper.

Light J-V measurements were obtained at 1-sun illumination on a WXS-200S-20 Wacom Electric Co. class AAA tester with a AM1.5G spectrum conforming to IEC 60904-9. Cells were measured on a temperature controlled Cu block in full contact with the rear surface. Values for  $R_S$  at maximum power point were obtained from light J-V measurements at an illumination intensity of 1-sun and approximately 0.07-suns [Bowd 01].  $p\text{-}FF$  were extracted from curves of Suns versus  $V_{OC}$  using a

Sinton Instruments SunsVoc tester [Sint 00]. The fabrication sequence for solar cells in this work is shown in Fig. 6.17.

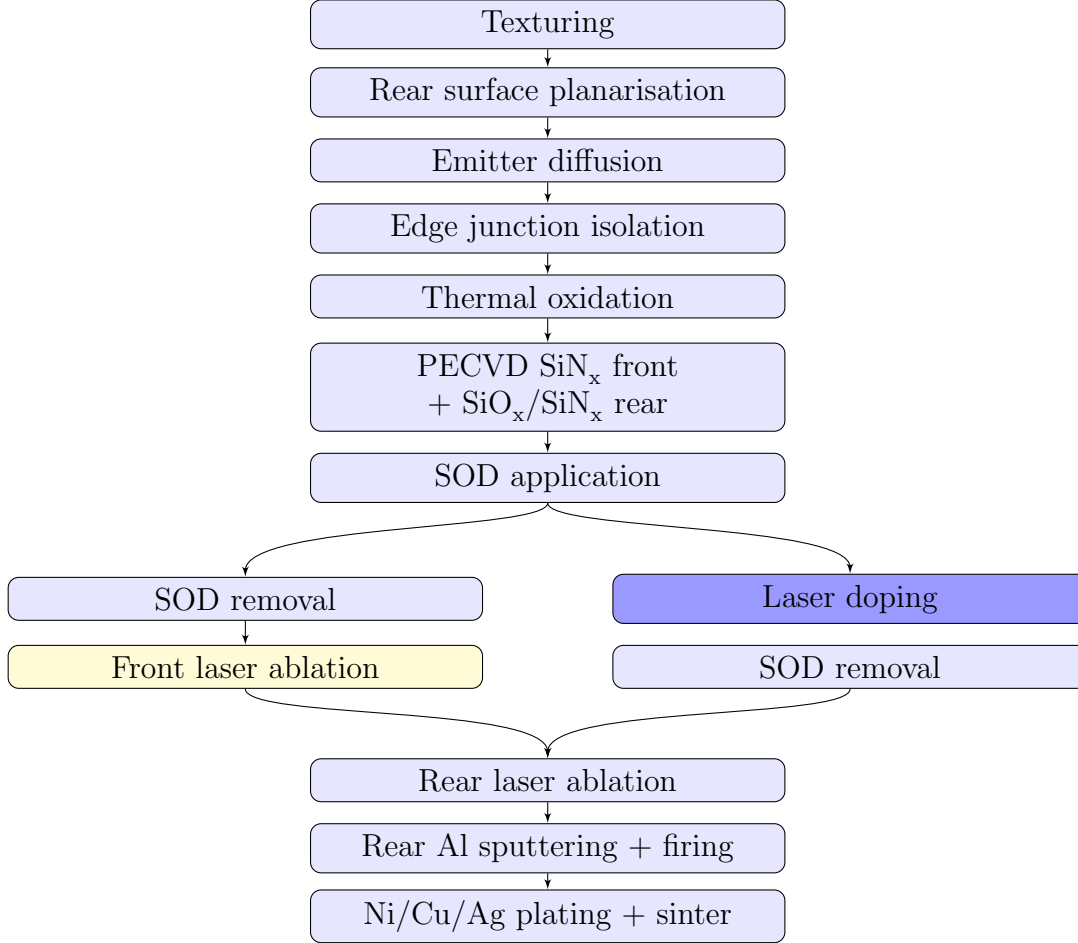


Figure 6.17: Process flow for PERC solar cells with laser-ablated and laser-doped contacts.

### 6.5.3 Sheet Resistance Results

The results of the characterisation of the sheet resistance test staples are summarised in Fig. 6.18. The figure plots the impact of laser speed on three different dopant sources for the laser doping process.

## 6.5. EFFICIENCY ENHANCEMENTS FOR PASSIVATED EMITTER AND REAR CELL THROUGH THE ADDITION OF AN LDSE STRUCTURE

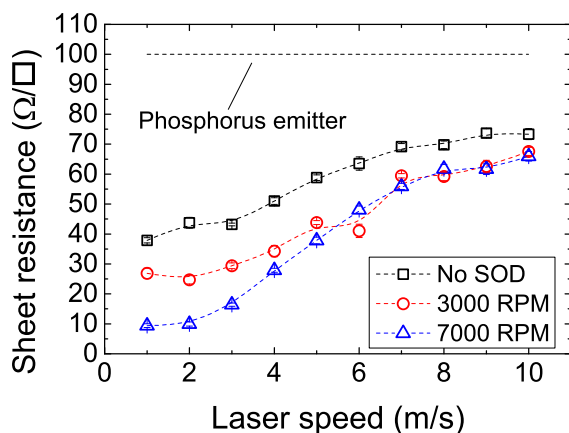


Figure 6.18: Sheet resistances obtained from laser doping by applying an SOD source or redistributing dopants from a phosphorus emitter.

For the case where no SOD was applied, no additional dopants were introduced into the silicon and hence the laser process only redistributed dopants from the thermally diffused phosphorus emitter and potentially activated non-electrically active dopants in the emitter. In the other two cases, additional dopants were introduced into the silicon by means of a SOD either spun at 3000 RPM or 7000 RPM.

A substantial reduction in sheet resistance was observed from an initial value of  $100 \Omega/\square$  down to  $40 - 70 \Omega/\square$  without the application of an SOD. Based on estimated junction depths from Chapter 4, modelling using PC1D and a freely available sheet resistance calculator from PV Lighthouse suggested that such reductions were simply due to dopant redistribution [Baso 96; PVsp 14b]. However much lower sheet resistances were obtained through the addition of a SOD layer. Whilst initial thoughts may suggest that thicker SOD layers may be of benefit to provide more dopants for the laser doping process, laser doping is a process complicated by interactions between the laser beam and the dopant sources, dielectric layers and surface morphology. As a result, when using the same laser power, a thicker SOD can result in more absorption and/or reflection of the illumination by the SOD layer, which can make it more difficult to melt and effectively dope the underlying silicon. In this work, it was observed that using a thinner SOD layer spun at 7000 RPM was more effective at forming a continuous line opening in the dielectric at high scan speeds than that obtained at 3000 RPM. Furthermore, at lower scan speeds a significant reduction in sheet

resistance was observed by using 7000 RPM. This indicates that too much laser illumination was being absorbed by the thicker layer, and hence a spin speed of 7000 RPM should be used.

However the effectiveness of the doped regions in avoiding recombination at the metal/Si interface should also be explored.

### 6.5.4 The Effect of Dopant Profiles on Recombination

To assess the theoretical suitability of a laser-doped region to be used as a solar cell contact it is necessary to learn as much as possible about the doping profile created. Both the contact resistance and recombination properties will be affected by the peak concentration at the surface and the depth and shape of the doped region. To reduce recombination at the metal/Si interface, it is desirable to create a deep, heavily doped region underneath the metal contact with relatively high surface dopant concentrations. Hence laser doping provides a valuable tool to achieve this, whilst leaving the surrounding areas with more favourable doping profiles for the passivated regions of the device.

Increasing the surface dopant concentration can reduce contact resistance and increase the tunnelling of carriers across the NiSi/Si Schottky barrier, leading to increased  $J_{SC}$ . A broad range of surface dopant concentrations from  $5 \times 10^{18} - 2 \times 10^{19} / \text{cm}^3$  with associated junction depths of  $0.5 - 4 \mu\text{m}$  have been modelled as ideal emitter profiles for Ni plated contacts [Thib 13]. However during nickel silicide formation, Ni is consumed by the silicon which results in the Si/Ni<sub>x</sub>Si interface moving below the surrounding silicon surface [Wolf 00]. For microelectronics, a 1 nm layer of Ni can result in approximately 2 nm of NiSi if all Ni is consumed. For different phases of Ni<sub>x</sub>Si such as Ni<sub>2</sub>Si and NiSi<sub>2</sub>, the consumption rate differs. However, due to the shifting of the Si/Ni<sub>x</sub>Si interface, the near surface dopant concentrations should also be considered for contact resistance and tunnelling properties. In this work, only a small fraction of the Ni was consumed, resulting in a Ni<sub>x</sub>Si layer of less than 50 nm thickness [Tous 14].

$J_{0d}$  values were simulated on hypothetical dopant profiles for laser-ablated and laser-doped samples using a freeware 1D emitter model developed by McIntosh *et al.* 2010 (EDNA 2 beta version 2.4.3 on PV Lighthouse) [McIn 10; McIn 13; PVsp 14a]. All settings were the default values unless otherwise specified, and hence Fermi-Dirac statistics were used with the SRH recombination

## 6.5. EFFICIENCY ENHANCEMENTS FOR PASSIVATED EMITTER AND REAR CELL THROUGH THE ADDITION OF AN LDSE STRUCTURE

---

at the surface determined by the effective SRV. Samples with laser-ablated contacts were assumed to have a  $100 \text{ } \Omega/\square$  complimentary error function profile with  $0.5 \text{ } \mu\text{m}$  junction depth, and all laser-doped profiles were assumed to be Gaussian with a sheet resistance value taken from Fig. 6.18 and junction depth 90 % of that obtained by a CW laser from Chapter 4, to account for the Q-CW nature of the laser ( $7.2 \text{ } \mu\text{m}$  deep at a speed of  $1 \text{ m/s}$  down to  $1.8 \text{ } \mu\text{m}$  for a speed of  $10 \text{ m/s}$ ) [Bova 11; Hall 13d].

Fig. 6.19 shows the modelled  $J_{0d}$  assuming full coverage of the surface by the given dopant profile as a function of SRV was shown. It was observed that deep heavily doped silicon such as that achieved by laser doping at  $1 \text{ m/s}$  was dominated by Auger recombination in the emitter with a very small dependence of the total  $J_{0d}$  on the SRV. However, for shallower, more lightly doped profiles from higher processing speeds and laser ablation, a much stronger dependence on the SRV through enhanced SRH recombination at the surface. For an SRV of  $1 \times 10^5 \text{ cm/s}$  the  $J_{0d}$  of the laser-ablated profile was substantially lower than that of the higher processing speeds. However for higher SRV values such as  $> 1 \times 10^6 \text{ cm/s}$  as expected after metallisation, the simulated  $J_{0d}$  value of all laser-doped profiles were lower than that of the laser-ablated sample. In addition, each laser process resulted in a different opening line width which would affect the percentage area exposed after the laser process, with higher processing speeds resulting in narrower line widths which would reduce the total  $J_{0d}$ .

Hence, under a metal/Si interface, a deep, heavily doped region results in the lowest  $J_{0d}$ . Laser doping provides the opportunity to form such contacts, without leading to excessive  $J_{0d}$  in the passivated regions, which should be lightly diffused.

### 6.5.5 Narrow Line Width Capability of Q-CW and CW Lasers

When using lasers to define front contacts, it is desirable to achieve line widths that are as narrow as possible. This is to minimise shading and avoid the loss of photo-generated current, and also reduce the metal/Si interface area and hence reduce recombination. Historically Q-switched lasers have been used for laser processing of silicon solar cells. The repetition frequency for conventional Q-switched lasers is  $< 1 \text{ MHz}$ . Due to the low repetition frequency of such lasers, including the

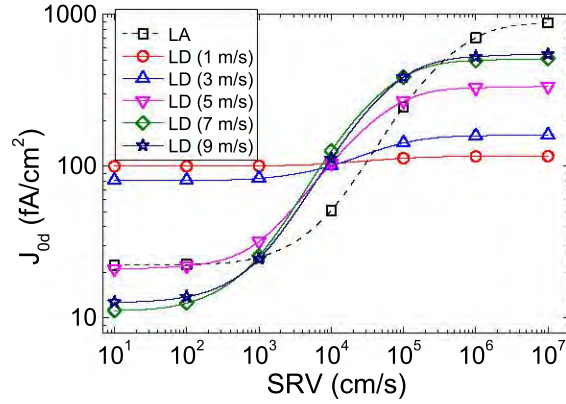


Figure 6.19: Simulated  $J_{0d}$  for hypothetical dopant profiles of laser doping at various speeds, and laser ablation (LA) performed on a  $100 \Omega/\square$  emitter with  $0.5 \mu\text{m}$  junction depth.

laser in this work used for laser ablation, pulses act in isolation with a relatively short pulse-length in relation to the time in between successive pulses. Hence for such lasers, when altering the scan speed of the laser beam, the line width of openings is essentially unchanged. In order to reduce line widths using such lasers, either a smaller focus or reduced power is required.

In contrast, for pulsed lasers with higher repetition frequencies, line widths can be reduced by increasing the scan speed of the laser beam. For such lasers, including the Q-CW laser used in this section with a repetition frequency of 80 MHz, the high repetition frequency resulted in the energy being supplied to a given area by a large number of pulses and an accumulation of heating effects with subsequent pulses as described in Chapter 4. Therefore increasing the scan speed decreased the energy of the effective pulse by reducing the number of actual pulses supplied to the area. Similarly, the energy delivered to a given area by a CW laser is reduced when increasing the scan speed, with both types of lasers resulting in narrower line openings.

Fig. 6.20 shows the widths after line opening by either laser ablation using a low frequency pulsed laser or laser doping using a Q-CW laser as well as the final contact finger widths after LIP ranging from  $22 \mu\text{m}$  to  $28 \mu\text{m}$ , showing the reduced widths with increasing processing speeds. Hence higher processing speeds can reduce the metal/Si interface area and shading losses, whilst also resulting in higher throughput processes.

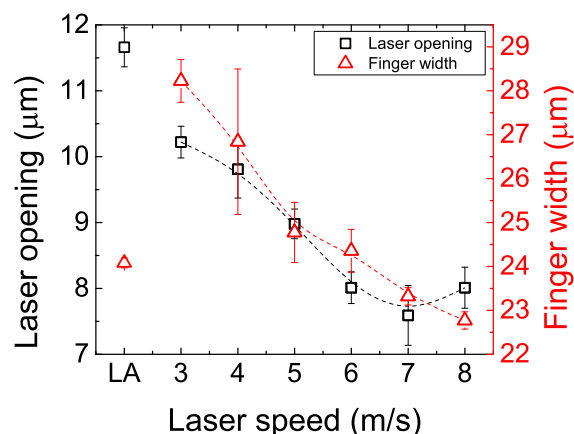


Figure 6.20: Widths of the laser contact openings and final contact finger widths for laser ablation (LA) and laser doping at various speeds.

### 6.5.6 Lifetime analysis

The highly localised heating and rapid cooling of the silicon that occurs during laser processing inevitably introduces defects into the substrates. The plot of  $\tau_{eff}$  against  $\Delta n$ , shown in Fig. 6.21(a), indicates that the laser processing had a significant impact on recombination. It was observed that prior to laser processing, the wafers for laser ablation tests had a higher  $\tau_{eff}$  than those used for laser doping tests due to a random variability in processing between wafers prior to laser processing. After laser processing and the subsequent passivation of LasID, the  $\tau_{eff}$  obtained by laser ablation was higher than that obtained for all laser-doped regions however this may be partially due to the higher initial lifetime of the wafers (see Fig. 6.21(a)).

It was also observed that the lifetimes obtained at low processing speeds for laser doping such as 0.5 – 2 m/s was substantially lower than that at higher processing speeds such as 2.5 – 8 m/s which all yielded similar  $\tau_{eff}$  (see Fig. 6.21(b)).

Upon extraction of the  $J_{0d}$  and  $\tau_{bulk}$ , Fig. 6.21(c) and Fig. 6.21(d) indicate that the reduced  $\tau_{eff}$  at slow processing speeds was due to a reduced  $\tau_{bulk}$ . At the slower speeds, the reduction in  $\tau_{bulk}$  came from both a reduction in  $\tau_{bulk0}$  used in the lifetime model, and the introduction of SRH recombination. The  $J_{0d}$  values obtained indicated that the additional  $J_{0d}$  induced by either laser doping or laser ablation was smaller than that of the surrounding passivated thermally

diffused emitter regions. Furthermore, in real devices the finger pitch is expected to be substantially larger than 500  $\mu\text{m}$  and hence the  $J_{0d}$  induced by the laser processes are expected to be reduced. Many of the processing speeds demonstrated  $J_{0d}$  of similar values or lower than that of the laser-ablated samples, however at speeds of approximately 5 m/s the  $J_{0d}$  of the laser-doped samples were substantially higher than that of the laser-ablated samples. Whilst the  $J_{0d}$  of laser-doped regions may be expected to be lower than that of laser-ablated regions due to enhanced doping, factors such as the SRV can influence the  $J_{0d}$  measured as previously discussed.

Hence the processing speed greatly influence the recombination properties of the laser doped regions, with high processing speeds resulting in the most effective shielding of minority carriers from the Si surface.



## 6.5. EFFICIENCY ENHANCEMENTS FOR PASSIVATED EMITTER AND REAR CELL THROUGH THE ADDITION OF AN LDSE STRUCTURE

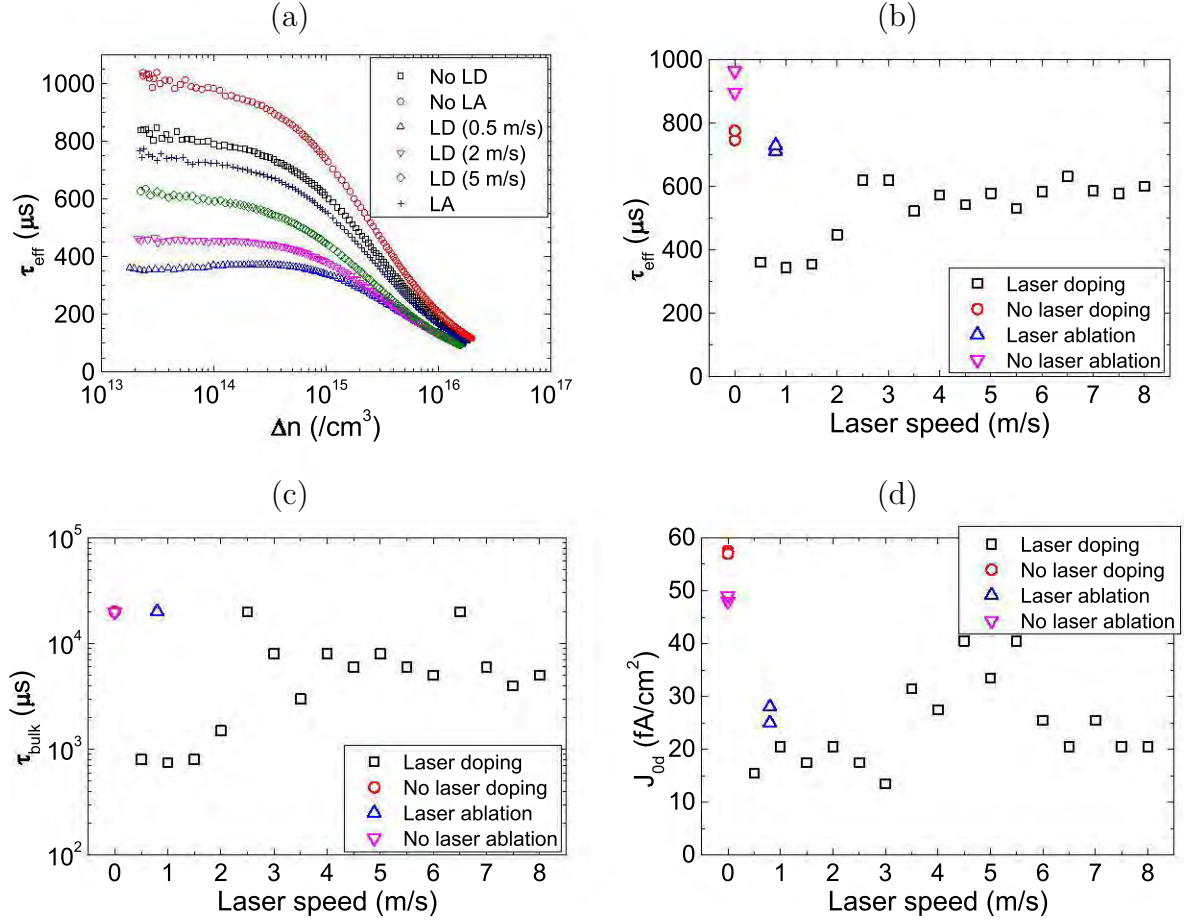


Figure 6.21: (a) Injection-level-dependent  $\tau_{eff}$  curves for various speeds, (b)  $\tau_{eff}$  at  $\Delta n = 1 \times 10^{14} / \text{cm}^3$ , (c)  $\tau_{bulk}$  at  $\Delta n = 1 \times 10^{14} / \text{cm}^3$  and (d)  $J_{0d}$  extracted for all processing speeds in this work. For (d), the  $J_{0d}$  of samples prior to laser processing is that per side, and the  $J_{0d}$  of the laser processed samples is the extra  $J_{0d}$  induced by the laser process for lines on a 500 μm pitch.

### 6.5.7 Efficiency Enhancements for i-PERC with an LDSE Structure

Whilst it is important to look at test structures in order to gain an understanding of the effect of individual processes on minority carrier lifetime, such test structures do not always give an accurate representation of the effect of such processes on solar cell performance. As discussed previously, changes in the effective SRV upon the deposition of the metal contacts can lead to substantial differences in the  $J_{0d}$  of the doped regions at the metal/Si interface. Fig. 6.22 and Table 6.5 show the light J-V data from the LA-PERC and LD-PERC solar cells fabricated in this work, highlighting the effect of the laser process on final cell performance.

Table 6.5: Light J-V measurements of the best cell in each group of laser-ablated (LA) and laser-doped (LD) cells (measured in-house). Cells highlighted in red were from the second batch with very poor adhesion.

Laser process	Speed (m/s)	Finger pitch (mm)	$J_{SC}$ (mA/cm <sup>2</sup> )	$V_{OC}$ (mV)	$FF$ (%)	$\eta$ (%)	$p\text{-}FF$ (%)	$R_S$ ( $\Omega \cdot \text{cm}^2$ )
LA	0.8 m/s	1.00	38.9	656	78.9	20.1	82.8	0.71
LA	0.8 m/s	1.00	38.6	663	79.5	20.3	-	-
LD	3 m/s	0.92	38.7	658	79.0	20.1	82.6	0.65
LD	4 m/s	0.92	38.7	662	79.1	20.3	82.6	0.61
LD	5 m/s	0.92	38.8	662	79.7	20.5	82.9	0.54
LD	5 m/s	1.00	38.6	670	79.8	20.6	-	-
LD	6 m/s	0.92	38.7	660	79.1	20.2	82.7	0.62
LD	7 m/s	0.92	38.9	656	78.5	20.1	82.5	0.69
LD	8 m/s	0.92	39.1	661	79.0	20.4	82.9	0.67

## 6.5. EFFICIENCY ENHANCEMENTS FOR PASSIVATED EMITTER AND REAR CELL THROUGH THE ADDITION OF AN LDSE STRUCTURE

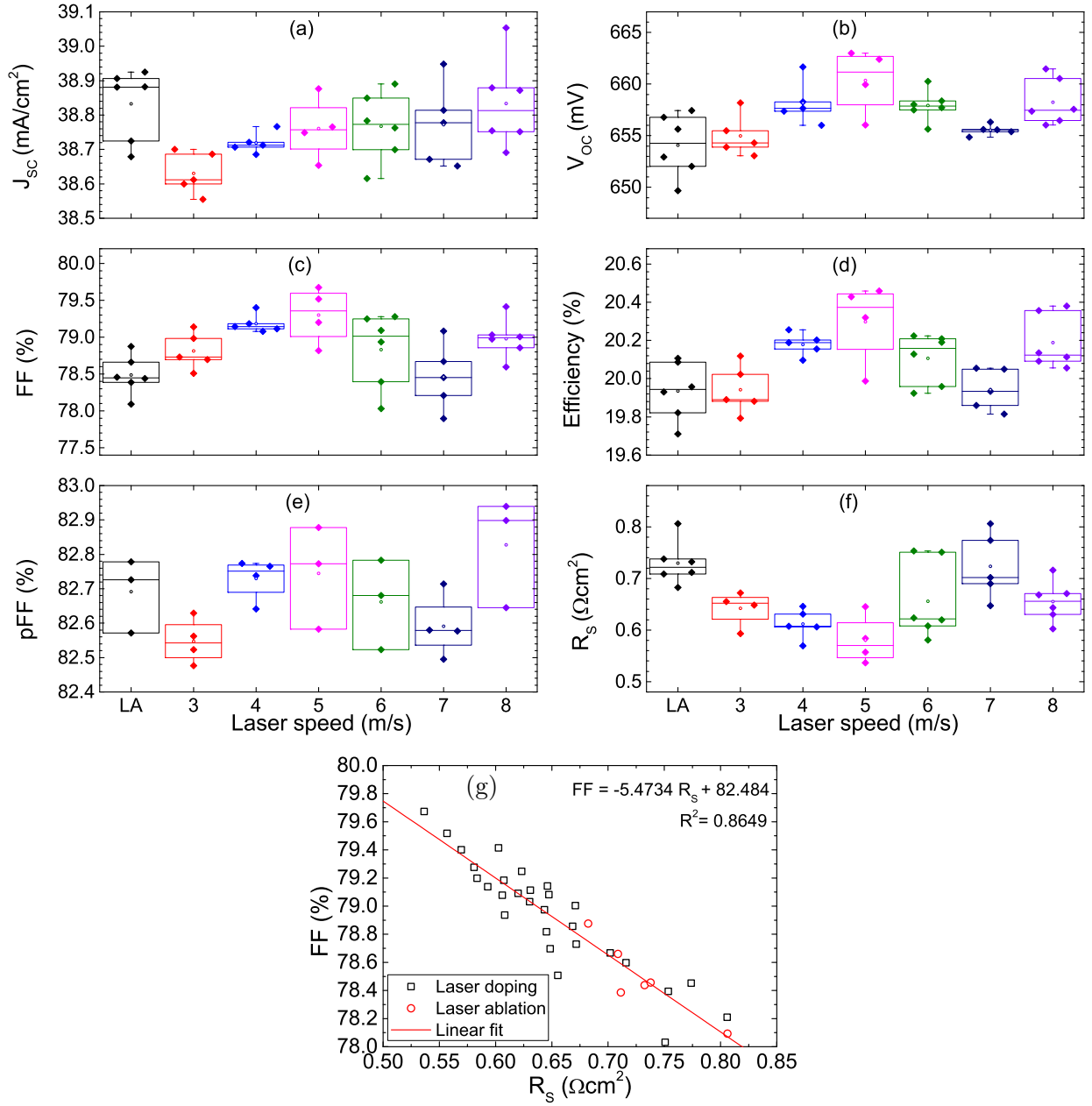


Figure 6.22: (a)  $J_{SC}$ , (b)  $V_{OC}$ , (c)  $FF$ , (d)  $\eta$ , (e)  $pFF$  and (f)  $R_s$  values for the solar cells fabricated in this work. LA-PERC cells are represented by “LA” whilst other values on the x-axes represent the process speed for laser doping. (g) Correlation between  $R_s$  and  $FF$ .

### 6.5.7.1 Efficiency

The average efficiency of each group of solar cells in this work was over 20 % indicating a good overall performance of the batch (see Fig. 6.22(d)). In addition, each group of LD-PERC (with different processing speeds) had an average efficiency as high as that of the baseline group with laser ablation, with efficiency gains of up to 0.4 % absolute from 20.1 % to 20.5 % for a speed of 5 m/s. Furthermore, apart from the group of cells with laser doping performed at 3 m/s and 7 m/s, the peak efficiency in each laser-doped group was higher than that of the laser-ablated cells.

### 6.5.7.2 $FF$

A significant part of the improved efficiency for cells with laser doping was due to a substantial increase in  $FF$ , of up to 0.8 % for the average  $FF$  of cells within a given group compared to the baseline laser ablation process, peaking at 79.7 % for cells with laser doping performed at 5 m/s. However a large difference in  $FF$  was observed between the different laser-doped groups of 1.2 % absolute. The single biggest improvement for the increase in  $FF$  was due to a reduced  $R_S$ .

### 6.5.7.3 $p$ - $FF$

Essentially no change in  $p$ - $FF$  was observed between the best laser-ablated and laser-doped cell (0.1 %), whilst slightly larger differences of up to 0.4 % were observed between the laser-doped groups (see Table 6.5). One explanation for this is that damage introduced at the metal/Si interface under the busbar was a limiting factor in determining the  $p$ - $FF$  of the devices. Alternatively, the  $p$ - $FF$  may have been limited by other aspects of the device such as the localised BSF on the rear surface. The much larger variations in  $FF$  observed between the different groups would suggest that  $R_S$  had a dominant effect in determining the  $FF$  of the devices.

## 6.5. EFFICIENCY ENHANCEMENTS FOR PASSIVATED EMITTER AND REAR CELL THROUGH THE ADDITION OF AN LDSE STRUCTURE

---

### 6.5.7.4 $R_S$

Fig. 6.22(g) indicates that there was a strong correlation between the  $R_S$  and  $FF$  of the devices, with the  $FF$  reducing for increased  $R_S$ . The reduced  $R_S$  on the laser-doped samples can partially be explained by the reduced finger pitch on these cells of 0.92 mm compared to 1 mm for the laser-ablated samples. The reduction in power loss associated between differences in the lateral transport of majority carriers within the emitter and transport within the fingers and busbar for the reduced pitch accounted for a 0.14 % increase in  $FF$ . Slight increases in  $FF$  may have also been observed for some laser-doped groups which feature wider metal plated lines than laser-ablated samples, but this only represented a 0.03 % variations in  $FF$  loss between the different laser-doped groups. Reductions may have also been due to enhanced doping underneath the metal contacts leading to a reduced contact resistance.

The much larger difference in  $FF$  observed between the laser-doped groups suggests a strong influence of the laser doping process in determining the  $R_S$  of the devices. Changes in the scan speed can change the dopant profile and hence surface dopant concentration, which can affect contact resistance. In addition, the changes in processing speed cause changes to the opening width of the dielectrics and hence the metal/Si interface area.

### 6.5.7.5 $V_{OC}$

Despite the closer finger spacing of the laser-doped cells, the  $V_{OC}$  of the best laser-doped group (5 m/s) was approximately 6 mV higher than that of the laser-ablated cells due to an improved shielding of minority carriers below the metal contacts from the incorporation of the selective emitter structure. The  $V_{OC}$  of samples processed with a processing speed of 8 m/s appears higher than that of samples processed at 7 m/s. At this stage it is unclear whether this was due to a reduction in metal/Si interface area, a more effective doping profile below the metal contacts or reduced defect generation.

### 6.5.7.6 $J_{SC}$

Despite the reduced finger spacing for laser-doped samples, no significant change in  $J_{SC}$  was observed. Changes in  $J_{SC}$  due to differences in the increased shading on laser-doped samples from using a reduced pitch of 0.92 mm were only estimated to account for approximately 0.1 mA/cm<sup>2</sup> reduction in  $J_{SC}$  compared to cells with a 1 mm finger pitch. Changes in the finger width for different scan speeds could also account for a 0.2 mA/cm<sup>2</sup> variation in  $J_{SC}$  between the samples, in close agreement between the average values shown for each group in Fig. 6.22(a).

### 6.5.7.7 Further Optimisation

In contrast to the laser-ablated cells (in which the thermally diffused emitter was optimised to balance: contact resistance; series resistance in the emitter; and recombination losses at the metal/Si interface), the incorporation of a selective emitter structure through the use of laser doping allows for a re-optimisation of the emitter profile. Whilst the initial implementation of the LDSE structure used the same emitter as for laser-ablated cells, the use of a higher sheet resistance emitter for LDSE cells is expected to yield substantially higher  $V_{OC}$  and  $J_{SC}$  values on finished devices through a more suitable doping profile in passivated regions and a reduction in free carrier absorption. Whilst such cells would then suffer increased series resistance losses within the emitter, it is expected that due to the selective doping, contacts of the laser-doped cells could be placed closer together than that for laser-ablated contacts due to less recombination below the contacts. Hence such cells would have a different balance between recombination losses and resistive losses at the front surface for optimum performance than that for the laser-ablated cells. In addition, the incorporation of the LDSE structure could allow the use of a more industrial shallow emitter, as deep heavily doped regions would still exist below the metal contacts to avoid metal coming within close proximity of the junction, or penetrating through the emitter to reach the underlying p-type silicon bulk during nickel silicide formation.

The increased processing speed used for the laser-doped cells compared to the laser ablation cells in this work allowed for substantial increases in throughput. Using the current cell pattern, a processing speed of 5 m/s resulted in a processing time of 15 s per wafer. However this is

## 6.5. EFFICIENCY ENHANCEMENTS FOR PASSIVATED EMITTER AND REAR CELL THROUGH THE ADDITION OF AN LDSE STRUCTURE

---

predominately due to the large number of lines in the busbar. By increasing the busbar line pitch from 10  $\mu\text{m}$  to 80  $\mu\text{m}$ , the processing time could be 6.5 s. Furthermore, moving to a busbar free approach would result in a processing time of approximately 5 s. Additional reductions would be obtained from increases to the processing speeds beyond 10 m/s (feasible based on the results of this present work and from previous work), to yield processing times of approximately 2 s per wafer. This may be assisted through the use of a higher laser beam power density to ensure adequate and continuous opening of the processed lines at elevated speeds. Increases to the throughput for laser-ablated solar cells may also be achieved by reducing the number of lines in the busbar, and/or increasing the repetition frequency of the laser pulses. Decreasing the processing time is important to increase throughput and hence the commercial viability of the process.

### 6.5.7.8 Optimised Finger Pitch

A second batch was identically processed with laser-doped and laser-ablated contacts with a finger pitch of 1 mm, however all cells suffered severe adhesion issues with the fingers of many cells peeling off during the plating process. Subsequently the cell results of this batch were extremely variable. However, peak efficiencies of 20.6 % and 20.3 % were achieved for laser doping at 5 m/s and laser ablation respectively despite poor metal adhesion with several fingers peeling off the cell, and localised regions of high  $R_S$  observed in PL images. The  $V_{OC}$  of both cells was approximately 7 mV higher than that obtained on cells fabricated in the first batch suggesting improved processing conditions. Other than changes in the finger pitch from 0.92 mm to 1.00 mm for the laser-doped cells, all processes were identical between the two batches of cells. The light J-V data of the best cells are also shown in Table 6.5 in red.

Hence a finger pitch of 1 mm resulted in higher efficiencies than when using a finger pitch of 0.92 mm, however cell results in this experiment were severely hampered by plating adhesion.

### 6.5.7.9 Optimisation of Busbar Pitch

To explore the effect of the metal/Si interface in the busbar on the performance of the LD-PERC cells, an additional batch was fabricated with variations in the pitch of laser-doped lines in the

busbar regions. Calibrated 1-sun  $iV_{OC}$  maps indicated a strong influence of the line pitch within the busbar on the localised  $iV_{OC}$  (see Fig. 6.23(a)). PL images obtained using a reduced illumination intensity show a pronounced reduction of  $iV_{OC}$  with decreasing line pitch, suggesting that the decreased line pitch caused a greater introduction of LasID into the silicon bulk. The PL images also indicated a large spatial variation in the remaining area of the wafers and may suggest that the firing temperature used on these wafers was too high. Due to a higher resolution, zoom PL images can highlight individual laser-doped lines on the front surface and point contacts on the rear surface. Due to the high illumination intensities used to obtain the images, the images predominately highlighted differences in the  $J_{0d}$  of the different regions in the device. It was also observed that several point contacts showed substantial reductions in the PL response, suggesting a reduced BSF formation in localised regions. A reduced BSF formation may have been due to rapid cooling or an enhanced diffusion of silicon into the Al which could result in void formation in localised areas [Urre 11].

Whilst a reduced metal/Si interface area would be expected to lead to increases in  $V_{OC}$  through a reduction in  $J_{0d}$ , practically no difference in  $V_{OC}$  was observed in this experiment by varying the line pitch in the busbar. Table 6.6 shows the light J-V data with a negligible variation in all electrical parameters for the different groups. For all groups, efficiencies of 20.6 – 20.7 % were obtained with a pseudo-efficiency ( $p\text{-}\eta$ ) of 21.7 – 21.8 %. The small variations between the different groups may suggest that other regions of the device were limiting the overall cell performance such as the localised rear Al-BSF regions, particularly with relatively low  $p\text{-}FF$  of 82.6 – 82.8 % in contrast to an expected  $p\text{-}FF$  of 84.0 % for a cell with  $V_{OC} = 665$  mV [Gree 81].



## 6.5. EFFICIENCY ENHANCEMENTS FOR PASSIVATED EMITTER AND REAR CELL THROUGH THE ADDITION OF AN LDSE STRUCTURE

---

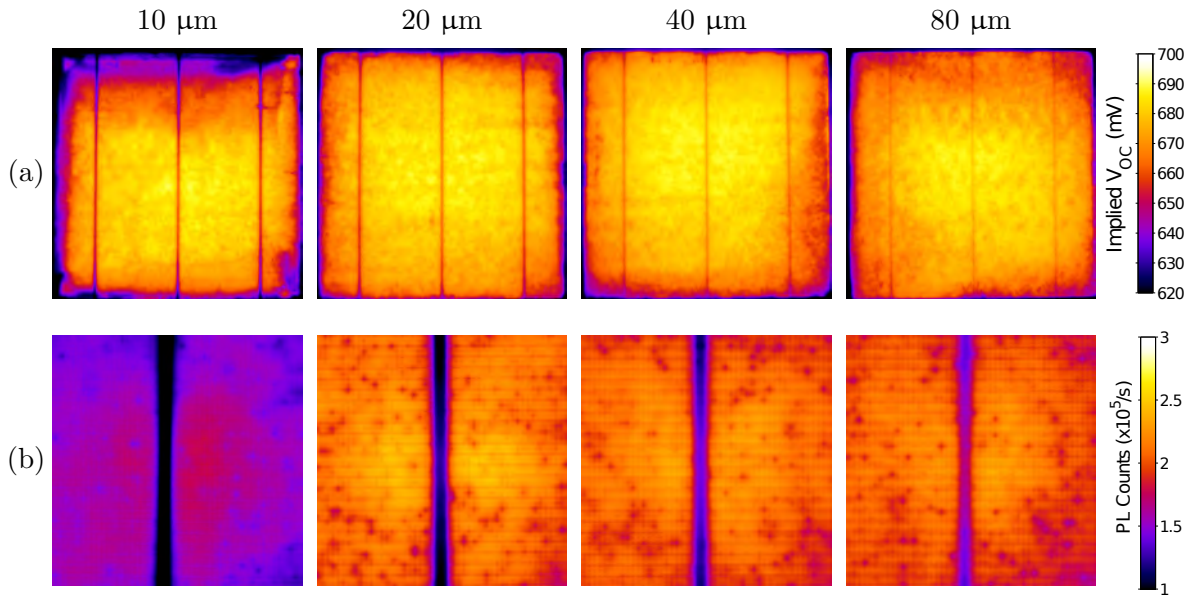


Figure 6.23: (a) 1-sun  $iV_{OC}$  maps on LDSE PERC solar cells for various laser-doped line pitches in the busbar and (b) corresponding uncalibrated zoom PL images taken with an illumination intensity of approximately 15 suns.

Table 6.6: Light J-V measurements of PERC solar cells with laser-doped n-type contacts featuring different line pitches for the busbar.

Pitch ( $\mu\text{m}$ )	$J_{SC}$ (mA/cm <sup>2</sup> )	$V_{OC}$ (mV)	$FF$ (%)	$\eta$ (%)	$p\text{-}FF$ (%)	$p\text{-}\eta$ (%)
10	$39.21 \pm 0.05$	$664.9 \pm 1.3$	$79.17 \pm 0.22$	$20.64 \pm 0.06$	—	—
10	39.18	664.9	79.41	20.69	—	—
20	$39.16 \pm 0.10$	$664.2 \pm 1.3$	$78.75 \pm 0.23$	$20.48 \pm 0.08$	$82.78 \pm 0.12$	$21.67 \pm 0.04$
20	39.22	664.4	79.02	20.59	82.87	21.71
40	$39.29 \pm 0.05$	$666.4 \pm 0.9$	$78.77 \pm 0.42$	$20.62 \pm 0.09$	$82.79 \pm 0.12$	$21.82 \pm 0.06$
40	39.26	665.8	79.20	20.70	82.75	21.76
80	$39.25 \pm 0.07$	$665.6 \pm 0.6$	$79.06 \pm 0.23$	$20.65 \pm 0.03$	$82.76 \pm 0.16$	$21.79 \pm 0.05$
80	39.33	664.9	79.09	20.68	82.57	21.80

Hence in this experiment, very little difference in efficiency was observed by changing the pitch of laser-doped lines in the busbar, but  $p$ -FF tended to increase with increasing pitch. The results also suggested that the rear PERC structure may have limited cell performance.

### 6.5.8 Summary for Efficiency Enhancements for PERC Cells Through the addition of an LDSE Structure

The use of a homogenous emitter (through laser ablation) or a selective emitter (through laser doping) was compared for PERC cells in this section. Laser doping was shown to provide superior throughputs and efficiencies for the solar cells, with increases in efficiency of 0.4 % absolute, with a maximum efficiency of 20.3 % realised for LA-PERC cells and 20.7 % realised for LD-PERC cells. However further optimisation is expected to lead to further efficiency enhancements. An alternative high efficiency solar cell technology is n-PERT, which uses n-type base wafers. This will be discussed in detail in Section 6.6.

## 6.6 The Pathway to Improved Hydrogen Passivation for n-PERT Cells

Forming gas annealing (FGA) processes and in particular, the alneal process are considered state of the art for hydrogen passivation in silicon solar cells, and were used to fabricate the world record PERL cells. However FG is relatively expensive and typically only contains 4 % diatomic hydrogen in argon. To be useful for defect passivation in silicon solar cells, the hydrogen must diffuse into the silicon and dissociate to form individual hydrogen atoms. On the other hand, the PECVD process for the deposition of dielectrics such as  $\text{SiN}_x$  and  $\text{SiON}_x$  naturally incorporates hydrogen into the dielectrics, which are already dissociated from the precursor gases, typically  $\text{SiH}_4$  and  $\text{NH}_3$ . Subsequently the PECVD could in a sense, be thought of as a hydrogen plasma, which also deposits a dielectric layer on the solar cell. This dielectric layer is effectively a store of hydrogen for subsequent processing and can contain more than 20 % hydrogen. A large benefit of the PECVD

process is that due to the high energy dissociation of the precursor gases in the plasma, hydrogen can enter the solar cell or be incorporated into the dielectric layer in atomic form, and therefore be of much more significance for passivation of defects in silicon solar cells.

For n-PERT solar cells, the Alneal process is typically performed after the deposition of Al on the rear of the cell. However, due to the presence of Al on the rear of the cell at this stage of processing, temperatures used for the BFA process must be low enough to avoid the formation of a molten Al-Si region.

### 6.6.1 Aim

In this section, the effectiveness of FGA processes for n-PERT solar cells are compared to simple, short BFA processes in oxygen ambient and the hydrogen passivation achieved directly after the deposition of  $\text{SiN}_x\text{:H}$  by direct PECVD, to assess whether the same level of passivation can be achieved at a lower cost. Different sheet resistances were tested to explore the processes for n-PERT solar cells with laser-ablated and laser-doped contacts. Different BFA processes are used to investigate the effectiveness of the process to release hydrogen from the  $\text{SiN}_x\text{:H}$ , and therefore passivation.

### 6.6.2 Experimental Procedures

#### 6.6.2.1 Lifetime Test Structures

Lifetime test structures were fabricated on  $3\ \Omega \cdot \text{cm}$  n-type CZ wafers ( $156 \times 156\ \text{mm}$ ). After saw damage etch removal and alkaline texturing the thickness of the wafers was approximately  $160\ \mu\text{m}$ . Subsequently, the wafers were cleaned and a  $\text{POCl}_3$  diffusion was used to form the FSF followed by the growth of a thin thermal  $\text{SiO}_2$  layer in a dry oxidation process. Three separate combinations of  $\text{POCl}_3$  diffusion and thermal oxidation recipes were used resulting in sheet resistances of  $110\ \Omega/\square$  (for contacting by laser ablation) and  $260\ \Omega/\square$  (for contacting by laser doping to avoid excessive  $R_S$  losses within the silicon as was observed in Section 5.2.2 when using an FSF with a sheet resistance

## 6.6. THE PATHWAY TO IMPROVED HYDROGEN PASSIVATION FOR N-PERT CELLS

---

of  $1000 \Omega/\square$ ), and an additional diffusion profile with a sheet resistance of approximately  $400 \Omega/\square$  (for contacting by laser doping). Symmetrical lifetime test structures were also fabricated on  $2 \Omega \cdot \text{cm}$  B-CZ wafers processed identically, however after emitter diffusion and PSG removal, the wafers received a surface polish on both surfaces of the wafer by passing the wafers through an in-line CEJI rear etch system twice.

After the growth of a thin thermal  $\text{SiO}_2$  layer for surface passivation, selected samples received an FGA at  $450^\circ\text{C}$  for 30 min with the wafers left in FG whilst the wafers were cooled down to below  $100^\circ\text{C}$  in the tube furnace, which lasts for several hours. Subsequently,  $\text{SiN}_x\text{:H}$  was deposited by direct PECVD onto both surfaces of all the wafers. An FGA process at  $450^\circ\text{C}$  for 30 min was then applied on the group of wafers which received the initial FGA after the  $\text{SiO}_2$  growth, as well as selected other samples. Following this process, all wafers received several BFA treatments, initially at  $450^\circ\text{C}$  with a belt speed of 20 in/min, followed by  $450^\circ\text{C}$  with a belt speed of 220 in/min. Additional BFA treatments were performed successively on all samples in  $100^\circ\text{C}$  increments from  $500 - 900^\circ\text{C}$  using a belt speed of 220 in/min, followed by a final thermal BFA at  $450^\circ\text{C}$  at 220 in/min to simulate the FGA process applied after the deposition of the Al rear of the n-PERT cells.

QSS-PC measurements were obtained on a BTi R1 luminescence imaging system at each stage of processing after the growth of thermal  $\text{SiO}_2$ . The process flow for the lifetime test structures is shown in Fig. 6.24.

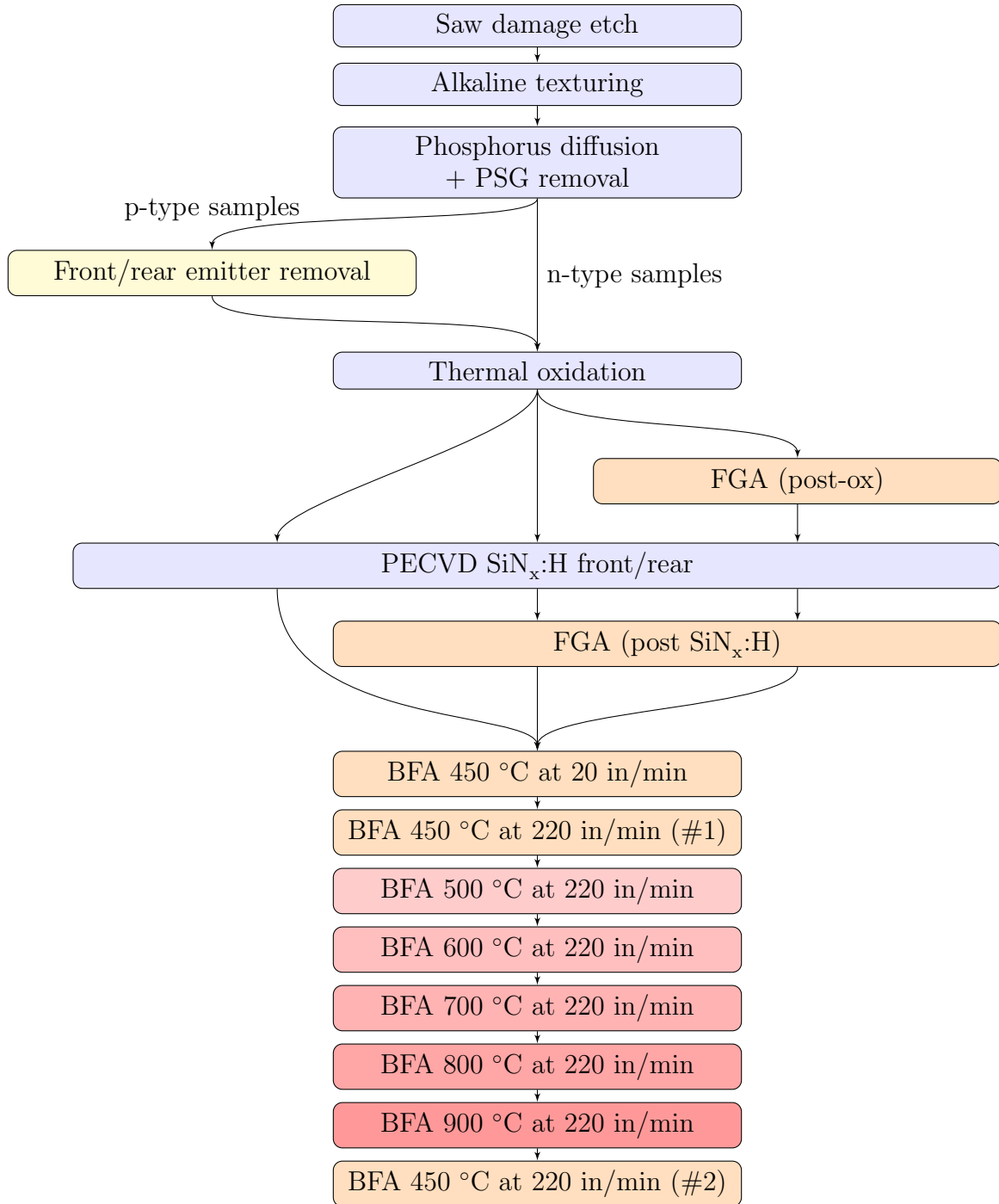


Figure 6.24: Process flow for the lifetime test structures to compare the effectiveness of different hydrogenation processes for n-PERT solar cells .

### 6.6.2.2 n-PERT Solar Cells

n-PERT solar cells were fabricated on  $3 \Omega \cdot \text{cm}$  n-type CZ wafers ( $156 \times 156 \text{ mm}$ ). Four different groups of solar cells were processed, with: (1) the conventional process sequence (control samples) using an FGA process directly after oxidation (OxFGA), as well as an Alneal process in FG prior to laser processing (FGAlneal); (2) Only an FGAlneal prior to laser processing; (3) a FGAlneal prior to laser processing and a BFA after laser processing; and (4) only a BFA after laser processing. The different groups were used to assess the influence of the FGA process (OxFGA and FGAlneal), and whether a simple BFA process applied after laser processing could replace the FGA processes.

After saw damage etch removal the thickness of the wafers was approximately  $160 \mu\text{m}$ . Four different groups of n-PERT solar cells were fabricated. The boron emitter was formed using a boron tribromide source ( $\text{BBr}_3$ ) followed by the removal of the borosilicate glass (BSG) layer. Subsequently, the dopants were driven-in using a high temperature wet oxidation step which also provided the rear surface passivation layer for the solar cells, with a resultant emitter sheet resistance of approximately  $95 \pm 5 \Omega/\square$ .

The cells in group 1 received the conventional Imec n-PERT fabrication sequence with an FGA at  $450^\circ\text{C}$  for 30 min with the wafers left in FG whilst the wafers were cooled down to below  $100^\circ\text{C}$  in the tube furnace. No other groups received the FGA after the thermal oxidation. Single sided processing was then used to remove the  $\text{SiO}_2$  layer off the front surface and the wafers were then textured in a TMAH based solution with a resulting reflection of  $10 \pm 0.5 \%$ .

After texturing, the wafers were cleaned and a  $\text{POCl}_3$  diffusion was used to form the FSF followed by the growth of a thin thermal  $\text{SiO}_2$  layer in a dry oxidation process. The resultant sheet resistances of the FSF were approximately  $110 \Omega/\square$  for contact by laser ablation and  $290 \Omega/\square$  for contact by laser doping.  $\text{SiN}_x\text{:H}$  was then deposited by direct PECVD. To define the rear contacts, picosecond laser ablation was performed, followed by the deposition of  $2 \mu\text{m}$  of Al by sputtering.

Subsequently, an alneal process was performed in FG at  $450^\circ\text{C}$  for 30 min on group 1 wafers. In addition, two of the three remaining groups also received the alneal process (groups 2 and 3).

For cells with laser-ablated contacts, a UV picosecond laser was used. For laser-doped samples,

## CHAPTER 6. DEVELOPMENT OF HIGH EFFICIENCY LASER-DOPED SOLAR CELLS WITH ADVANCED HYDROGENATION

---

Filmtronics P509 was applied at 7000 RPM for 20 s. Laser doping was performed using a Q-CW mode-locked UV (355 nm) laser as previously described with an optical power of 8.5 W reaching the wafer surface and a process speed of 5 m/s. Subsequently, the SOD source was removed by a short HF dip. The finger pitch for all cells was 1.5 mm with a busbar line pitch of 10  $\mu\text{m}$  for the laser-doped cells and 12.5  $\mu\text{m}$  for the laser-ablated cells. Selected samples then received a BFA in oxygen ambient at 450  $^{\circ}\text{C}$  for approximately 3 min which included group 3 (which only received the alneal process), and group 4 (which had not received any prior FGA).

Prior to plating, a short HF dip was performed to remove any native oxide in the contact openings. Subsequently the Imec plating sequence was then applied in a commercial in-line plating tool from Meco. The plating sequence consisted of the growth of 1  $\mu\text{m}$  of LIP Ni followed by deposition of 10  $\mu\text{m}$  of electroplated Cu and immersion Ag. Sintering was then performed on the full Ni/Cu/Ag plated stack in  $\text{N}_2$  ambient at 250  $^{\circ}\text{C}$  in a belt furnace [Russ 12].

Light J-V measurements were obtained at 1-sun illumination on a WXS-200S-20 Wacom Electric Co. class AAA tester with a AM1.5G spectrum conforming to IEC 60904-9.  $p\text{-}FF$  were extracted from curves of Suns versus  $V_{OC}$  measurements using a Sinton Instruments SunsVoc tester [Sint 00]. A BTi R1 luminescence imaging tool was used to obtain calibrated  $iV_{OC}$  maps at various stages of fabrication. The process sequence for the fabrication of the n-PERT solar cells in this section is shown in Fig. 6.25.



## 6.6. THE PATHWAY TO IMPROVED HYDROGEN PASSIVATION FOR N-PERT CELLS

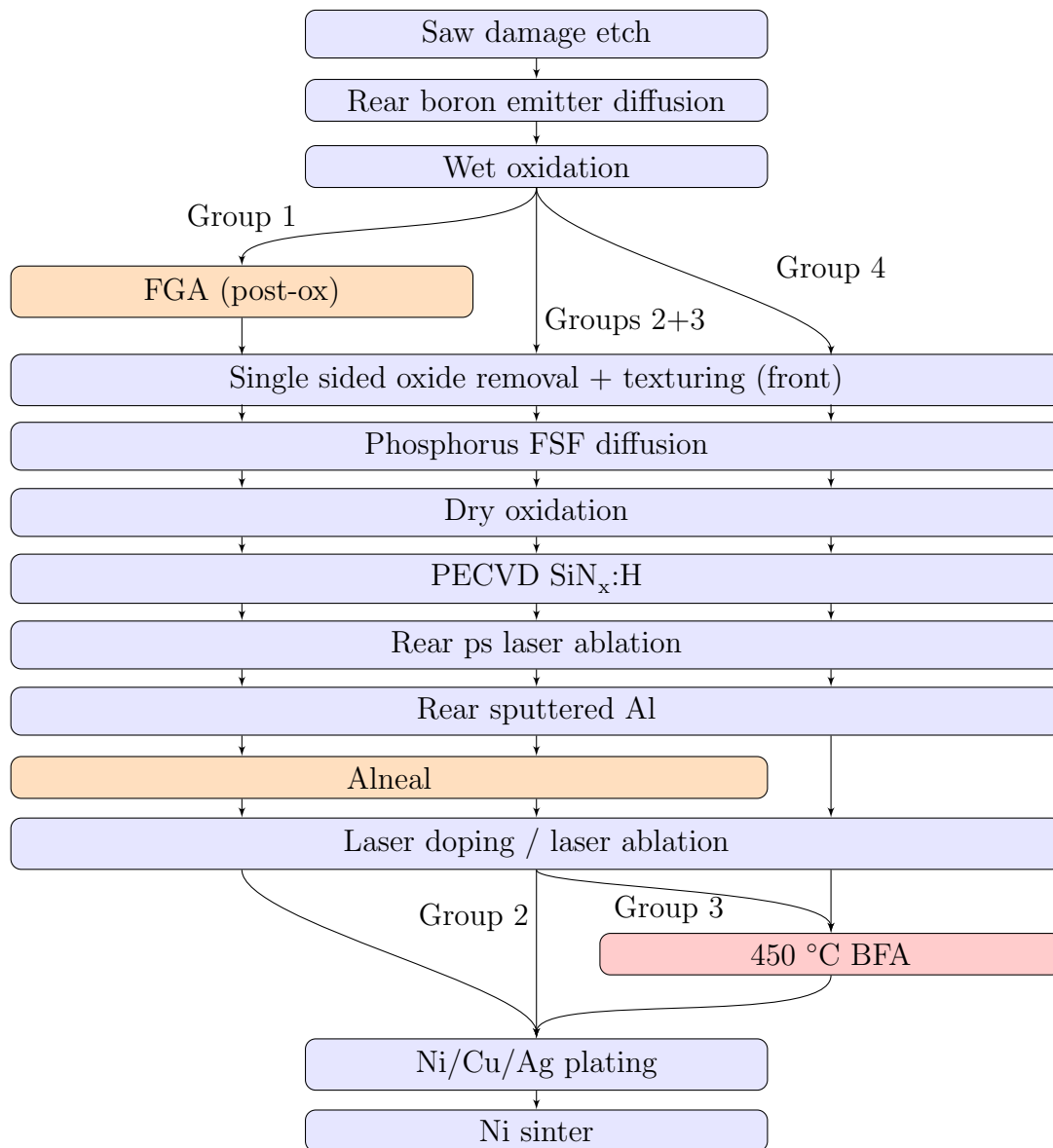


Figure 6.25: Process flow for n-PERT solar cells with simplified hydrogen passivation processes.

### 6.6.3 Results on Lifetime Test Structures

#### 6.6.3.1 Passivation After Thermal Oxidation

After the growth of thermal  $\text{SiO}_2$ , a very poor level of surface passivation was expected on non-diffused samples for two primary reasons. Firstly, many dangling bonds exist at the  $\text{Si}/\text{SiO}_2$  interface creating energy levels within the band-gap, which results in a high SRV. Secondly, the low majority carrier concentrations at the surface result in high minority carrier concentrations near the surface. This is exacerbated for p-type samples due to the higher minority carrier mobility of electrons. Diffused samples also have  $J_{0d}$  components associated with the diffusion profile which adds various recombination mechanisms such as Auger, radiative and SRH recombination. However for a high SRV, SRH recombination at the surface typically dominates the total  $J_{0d}$  of diffusion profiles. Hence, diffusion profiles with a lower surface dopant concentration, or worse, a non-diffused surface will result in increased SRH recombination at the surface and higher  $J_{0d}$ . As expected, Fig. 6.26(a) highlights the low lifetimes observed on the lifetime test structures directly after the thermal oxidation. The graph indicated a higher lifetime for the samples with the heaviest phosphorus diffusion, whilst wafers with non-diffused surfaces had very low  $\tau_{eff}$  over all injection-levels.

#### 6.6.3.2 Influence of FGA Prior to $\text{SiN}_x\text{:H}$ Deposition:

An FGA applied directly after the thermal oxidation was observed to greatly enhance the  $\tau_{eff}$  of the test structures (see Fig. 6.26(b)). This was largely due to hydrogen from the FG ambient diffusing through the  $\text{SiO}_2$  layer to passivate defect states at the  $\text{Si}/\text{SiO}_2$  interface. When hydrogen atoms satisfy the dangling bonds, SRH recombination at the surface and hence the effective SRV can be greatly reduced. This can result in the  $J_{0d}$  being dominated by Auger recombination within the emitter and hence heavier diffusions typically lead to higher  $J_{0d}$ . Hydrogen atoms can also diffuse into the silicon to passivate bulk defects, however the diffusivity is affected by the hydrogen charge state and is influenced by the presence of dopants in the silicon. Hence heavy diffusions can limit the diffusion of hydrogen into the bulk silicon. In contrast, the absence of a surface diffusion can allow a much more effective diffusion of hydrogen into the bulk.

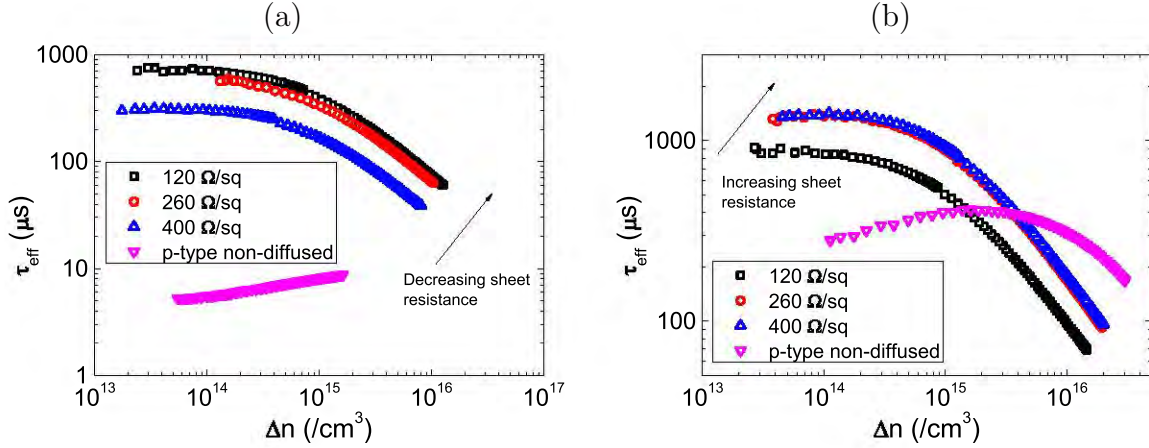


Figure 6.26: Extracted  $\tau_{eff}$  curves after (a)  $\text{SiO}_2$  growth and (b) the subsequent FGA.

### 6.6.3.3 Influence of the $\text{SiN}_x\text{:H}$ Deposition:

As discussed previously, the deposition of  $\text{SiN}_x\text{:H}$  is a highly effective hydrogen passivation process due to the hydrogen incorporated into the dielectric layer, which can immediately passivate defects at the  $\text{Si}/\text{SiO}_2$  interface or diffuse into the bulk. This is particularly the case when  $\text{SiN}_x\text{:H}$  is deposited onto both surfaces, when hydrogen from the first deposited layer can diffuse into the silicon during the deposition of the second layer. Improved passivation can also potentially be attributed to a much thicker dielectric stack if the  $\text{SiO}_2$  layer is too thin to achieve full field effect passivation. All samples displayed a substantial increase in  $\tau_{eff}$  directly after the deposition of  $\text{SiN}_x\text{:H}$  (see Fig. 6.27). However a substantial difference was evident between samples which received the FGA prior to the  $\text{SiN}_x\text{:H}$  deposition. Samples which received the FGA prior to the deposition of  $\text{SiN}_x\text{:H}$  show a substantial reduction in  $\tau_{eff}$  over all injection-levels. This is particularly evident at lower injections and on the p-type wafers suggesting the extended thermal processing during the FGA is detrimental to the bulk material. One possible explanation for the reductions in lifetime of such samples was due to the nucleation of oxygen precipitates during the extended FGA.

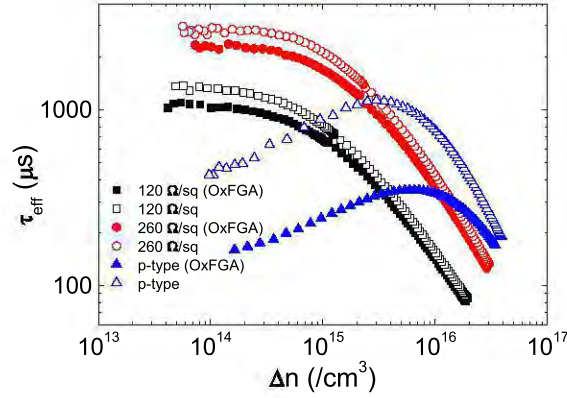


Figure 6.27: Extracted  $\tau_{eff}$  curves after  $\text{SiN}_x\text{:H}$  deposition for samples with and without a FG process applied directly after  $\text{SiO}_2$  growth (OxFGA).

#### 6.6.3.4 Impact of FGA and BFA post $\text{SiN}_x\text{:H}$ deposition

FGA processes are often used to incorporate hydrogen into the silicon solar cell to improve surface passivation of high efficiency silicon solar cells. However upon the application of an FGA after the deposition of  $\text{SiN}_x\text{:H}$ , no difference in  $\tau_{eff}$  was observed for n-type samples, and only a minor improvement was observed for p-type samples. Similarly, the use of a BFA at the same temperature proved ineffective for improved hydrogen passivation over that obtained directly after the  $\text{SiN}_x\text{:H}$  deposition.

On the p-type samples, a slight reduction in  $\tau_{eff}$  was often observed with additional thermal processing with non-FGA based processes. One possible explanation for this reduction is due to the effective loss of hydrogen from within the silicon if the temperature is too low to facilitate the release of hydrogen from the  $\text{SiN}_x\text{:H}$  layer. On the other hand, using FG allows for a replenishment of hydrogen within the device during the process. The evolution of the  $\tau_{eff}$  curves is shown for several samples in Fig. 6.28(a)-(c). The absence of any substantial changes in  $\tau_{eff}$  with either an FGA or BFA process applied after the  $\text{SiN}_x\text{:H}$  could suggest that a temperature of 450 °C was not sufficient to facilitate the release of atomic hydrogen from the  $\text{SiN}_x\text{:H}$ . This will be explored in Section 6.6.5.

## 6.6. THE PATHWAY TO IMPROVED HYDROGEN PASSIVATION FOR N-PERT CELLS

Different  $\tau_{eff}$  curves are also shown for two samples where QSS-PC measurements were obtained with and without a wipe underneath the wafers. Wipes were used for lifetime measurements after the BFA to avoid contamination in the BTi tool. As shown in Table 6.7, substantially higher  $\tau_{eff}$  were obtained over all injection-levels for measurements taken without the wipe and hence all  $\tau_{eff}$  measurements in this section were underestimated. However the values obtained still provide important information on the relative changes in  $\tau_{eff}$  for each process. In addition, the  $J_{0d}$  on the samples was substantially higher for the cells with a wipe underneath the wafer during the QSS-PC measurement, up to a factor of two higher for the lighter  $260 \Omega/\square$  FSF used for the laser-doped solar cells. A substantial difference was also observed between the different FSF with  $J_{0d}$  values of approximately  $45 \text{ fA}/\text{cm}^2$  and  $11 \text{ fA}/\text{cm}^2$  obtained for a sheet resistance of  $120 \Omega/\square$  and  $260 \Omega/\square$  respectively, per side. The reduced  $J_{0d}$  obtained for the lighter FSF results in substantially higher 1-sun  $\tau_{eff}$  and  $iV_{OC}$ .

Table 6.7: 1-sun  $\tau_{eff}$  and  $J_{0d}$  for the FSF used for the laser-doped and laser-ablated cells with and without a wipe underneath the wafer during QSS-PC measurements.

FSF	QSS-PC measurement	1-sun $\tau_{eff}$ ( $\mu\text{s}$ )	$J_{0d}$ per side ( $\text{fA}/\text{cm}^2$ )
$120 \Omega/\square$	no wipe	314	45.2
$120 \Omega/\square$	with wipe	250	68.7
$260 \Omega/\square$	no wipe	590	11.1
$260 \Omega/\square$	with wipe	471	21.8

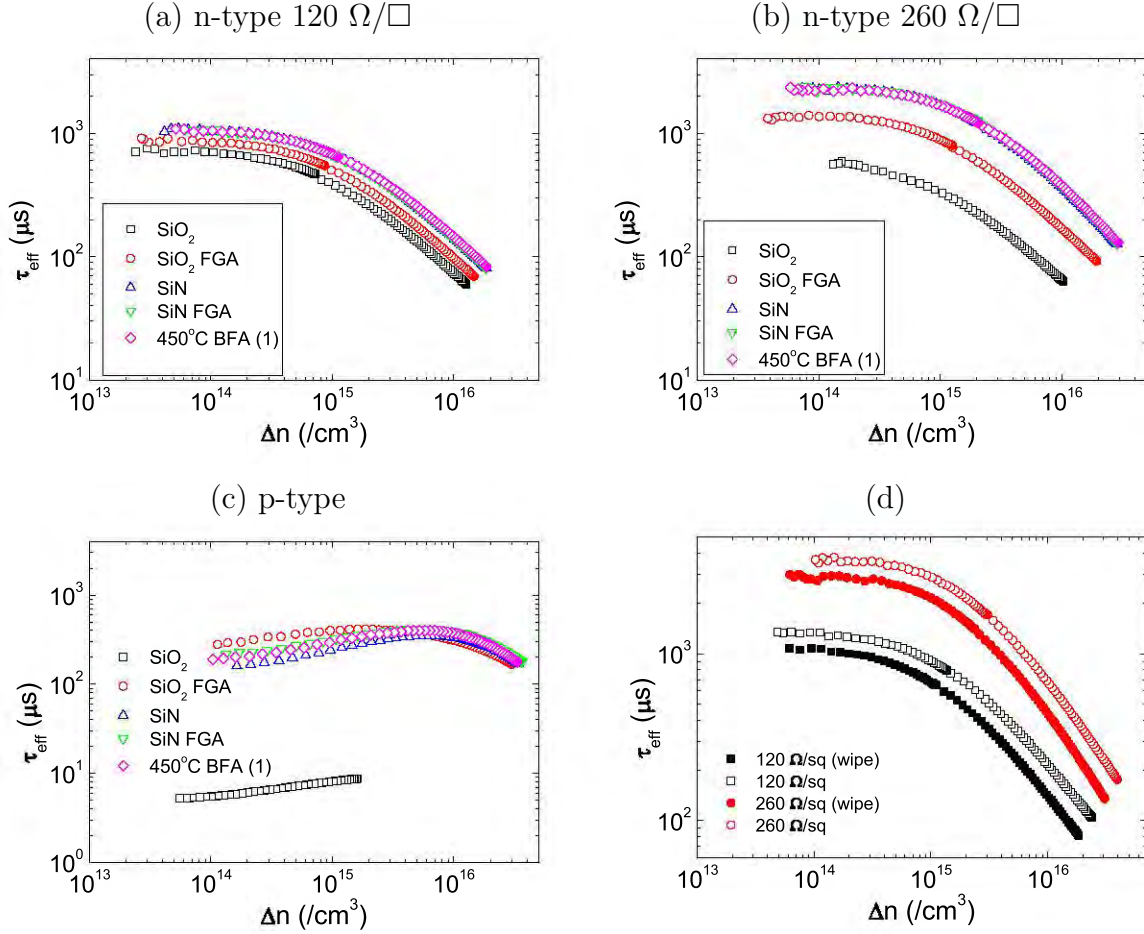


Figure 6.28:  $\tau_{eff}$  curves after various processes for (a) n-type wafers with a 120  $\Omega/\square$  FSF, (b) 260  $\Omega/\square$  FSF and (c) p-type wafers with the emitter diffusion removed. (d) The difference in  $\tau_{eff}$  for samples with and without a wipe underneath the wafer during the QSS-PC measurements. The legend in (a) - (c) indicates the process after which the QSS-PC measurements were performed.

### 6.6.3.5 Summary

Lifetime test structures indicated that the use of an extended FGA process directly after the growth of thermal SiO<sub>2</sub> was detrimental to the  $\tau_{bulk}$  of both n-type and p-type wafers. The deposition of

$\text{SiN}_x\text{:H}$  proved an effective process to incorporate hydrogen passivation into the structures, with no further improvement in  $\tau_{eff}$  observed by applying a subsequent FGA process or BFA process at the same temperature (450 °C). However investigations must also be conducted on full devices.

#### 6.6.4 n-PERT Cell Results

It has been shown that by using hydrogen naturally incorporated into the device structure from processes such as deposition of  $\text{SiN}_x\text{:H}$ , or the subsequent release of hydrogen from  $\text{SiN}_x\text{:H}$  and wet thermal oxides, the use of FG for hydrogenation processes can be avoided.

Table 6.8 shows the light J-V data for n-PERT solar cells with laser-ablated contacts with various hydrogenation processes. No significant variations in the light J-V parameters were observed between the different groups. This would suggest that the FGA applied directly after the thermal oxidation could be removed (see Section 6.6.3). In addition, essentially the same efficiency can be achieved by simply using a BFA process after laser ablation without a prior FGA. On additional test structures it was observed that performing a second BFA process led to a very slight improvement in  $iV_{OC}$  of approximately 1 – 2 mV. Slight improvements were also observed by using a single BFA anneal at 500 °C. This suggested that the time and/or temperature used for the BFA process was not sufficient to achieve effective hydrogen passivation.

Whilst a substantial difference in efficiency was observed for laser-doped solar cells by the use of a hydrogen passivation process after the introduction of LasID, no significant difference was observed for the laser-ablated cells in this section. The reduced generation of bulk defects using laser ablation may allow effective passivation of any LasID to occur during the Ni sinter. Differences in the recombination active concentration of LasID with and without a hydrogen passivation process may have also been masked by other limiting recombination mechanisms, which reduced the efficiency of cells fabricated in this batch to 20.0 – 20.2 % compared to 20.7 – 20.9 % in other batches processed in parallel. The reduced efficiency in this batch was due to a substantial reduction in  $J_{SC}$  and  $V_{OC}$ , however the reasons for the reduced performance is unclear.

Table 6.8: Light J-V measurements of n-PERT solar cells (average of less than 10 cells per group) with laser-ablated n-type contacts fabricated using different hydrogenation processes. Data for the best cells in each group are shown in red.

Group	Hydrogenation Process	$J_{SC}$ (mA/cm <sup>2</sup> )	$V_{OC}$ (mV)	$FF$ (%)	$\eta$ (%)	$p-FF$ (%)	$p-\eta$ (%)
1	OxFGA+	37.91 ± 0.09	656.0 ± 0.3	80.75 ± 0.47	20.08 ± 0.11	83.60 ± 0.08	20.91 ± 0.04
	FGAlneal	37.78	655.8	81.51	20.19	83.84	20.84
2	FGAlneal	37.89 ± 0.09	655.7 ± 0.7	80.34 ± 0.49	19.96 ± 0.18	83.48 ± 0.05	20.82 ± 0.09
		38.01	656.3	80.87	20.18	83.50	20.95
3	FGAlneal+	37.95 ± 0.15	656.7 ± 0.8	80.75 ± 0.37	20.12 ± 0.08	83.52 ± 0.21	20.91 ± 0.12
	BFAIneal	37.91	656.4	81.15	20.20	0.84	20.92
4	BFAIneal	37.90 ± 0.07	656.3 ± 0.23	80.48 ± 0.27	20.02 ± 0.07	83.40 ± 0.10	20.85 ± 0.05
		37.98	656.6	80.64	20.11	83.46	20.91



#### 6.6.4.1 Varied Line Pitch in Busbar

A subsequent batch of cells was fabricated with both laser doping and laser ablation for the front n-type contacts by varying the line pitch in the busbar regions to explore the effect of busbar metal/Si interface area on the performance of n-PERT solar cells. All other processing details were the same. All cells in this batch received an aneal process in FG after Al sputtering and a BFA after laser processing to passivate LasID. No FGA was applied directly after the thermal oxidation.

During plating, substantial issues were encountered with poor adhesion and a reduced nucleation of plating particularly around the peripheral region of the cells. This was due to shunting from a wrap-around of the Al during the sputtering process onto the front surface. Fig. 6.29 shows calibrated 1-sun  $iV_{OC}$  maps of an n-PERT solar cell with localised shunts around the perimeter of the cell. The extent of the shunts in reducing local minority carrier concentrations were exacerbated at lower illumination intensities (not shown). The shunting appeared to cause more issues for laser-doped samples during the plating process which may be due to enhanced conductivity in the laser-doped lines, assisting in the transport of carriers to the localised regions with high recombination [Chan 13a]. The shunting evident in PL images was extremely variable between samples with some cells relatively free of localised shunts, whilst other cells suffered from severe shunts around a significant fraction of the perimeter.

The line pitch used for the busbars of the laser-ablated and laser-doped cells had a significant influence on the localised voltage within the busbar region. Fig. 6.30 shows the  $iV_{OC}$  extracted from a  $5 \times 5$  cm area in the central region of the solar cells after laser processing and after the subsequent BFA. This area was chosen to give an approximate value for the solar cell, without effects of shunting around the perimeter of the cells, and to ensure a similar coverage area of the busbar within the measurement area to that on a full cell. An increase of approximately 10 mV was observed on both laser-ablated and laser-doped samples by increasing the line pitch in the busbar from 10  $\mu\text{m}$  to 80  $\mu\text{m}$ . Doing so greatly reduced the number of lines in the busbar region, greatly reducing the metal/Si interface in the busbar region, and led to substantially improved processing times. After a BFA, the  $iV_{OC}$  in the busbar region of the laser-ablated cells increased by approximately 5 mV whilst an increase of 15 – 20 mV was observed on the laser-doped cells. The larger increase on the laser-doped cells after the BFA process was due to the increased introduction

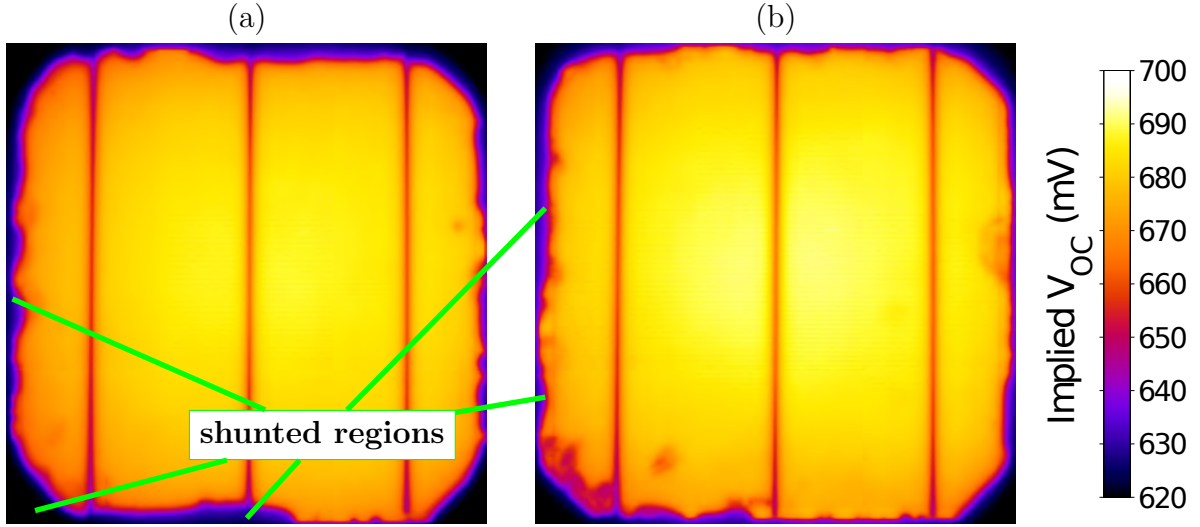


Figure 6.29: Calibrated 1-sun  $iV_{OC}$  maps of n-PERT solar cells after laser processing with a busbar line pitch of 20  $\mu\text{m}$  for (a) laser-ablated contacts and (b) laser-doped contacts.

of LasID compared to that introduced during laser ablation.

Whilst a significant difference in the  $iV_{OC}$  of the busbar region was observed by varying the line pitch in the busbars, only a small difference of approximately 2 mV was observed by spatially averaging the  $iV_{OC}$  within the  $5 \times 5$  cm area. The smaller spatially averaged increase in  $iV_{OC}$  was due to the relatively small coverage area of the busbar compared to that of the surrounding regions. In the surrounding regions, substantially higher  $iV_{OC}$  were observed both before and after the BFA. From the applied BFA process, an increase in the surrounding areas of 2 mV and 10 mV was observed for the laser-ablated and laser-doped cells respectively with corresponding  $iV_{OC}$  of up to 692 mV and 702 mV obtained. It appeared that the larger improvements of the  $iV_{OC}$  for laser-doped cells were due to the lighter FSF of approximately  $290 \Omega/\square$  which resulted in a higher effective diffusion coefficient of hydrogen within the diffused layer when compared to that when using a  $120 \Omega/\square$  FSF. This result was consistent with the observation on the lifetime test structures presented earlier in this section. Hence to improve the effectiveness of hydrogen passivation processes, lightly diffused surfaces should be used.

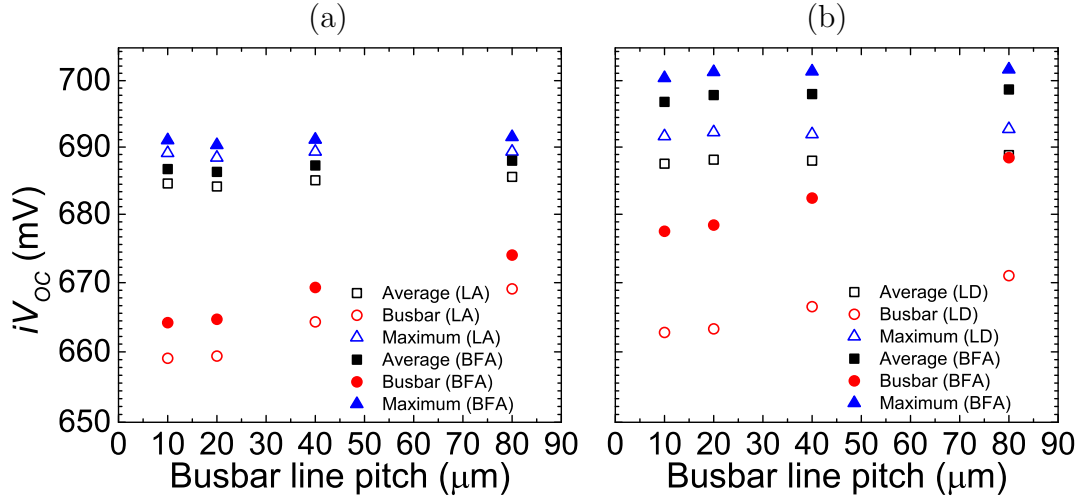


Figure 6.30: Effect of hydrogen passivation of LasID on the  $iV_{OC}$  values of n-PERT solar cells in various regions of the device with (a) laser-ablated and (b) laser-doped contacts.

Due to the severe shunting present after the sputtering of Al in this batch, very few samples survived the plating process with reasonable plating and many cells were excluded from light J-V measurements. As a result, light J-V measurements were only performed on one laser-doped sample. For the plating process, several wafers were plated as a trial before the remainder of the cells in this experiment. After the failure of many cells in the initial trial, a second HF dip was performed on the remainder of the cells to assist in the removal of the shunts by etching off any Al wrap-around onto the front surface. Table 6.9 shows the light J-V data for this experiment with laser-ablated and laser-doped contacts. The number of HF dips applied to the cell is also given in the table.

Despite the issues with shunting from the Al, efficiencies of 20.6 – 21.2 % were obtained in this batch with the aid of a laser cleaving process after plating. The cleaving process removed the shunt path from the peripheral regions of the wafers caused by the wrap-around of the Al and plating onto the edge of the wafers. Due to the low number of cells with light J-V measurements, it was difficult to obtain conclusive evidence on the effect of the line pitch in the busbar on overall cell efficiency. The only parameter with a distinct trend for the cells was the  $V_{OC}$  with a 4 mV

## CHAPTER 6. DEVELOPMENT OF HIGH EFFICIENCY LASER-DOPED SOLAR CELLS WITH ADVANCED HYDROGENATION

---

increase for a busbar line pitch increasing from 10  $\mu\text{m}$  to 80  $\mu\text{m}$ . The variations in actual  $V_{OC}$  of the finished laser-ablated cells were larger than the variations in spatially averaged  $iV_{OC}$  of the cells after the BFA. This is most likely due to the increased SRV of the contact region after the plating process and therefore larger absolute differences in the  $J_{0d}$  within the busbar regions for the different line pitches. In some instances the  $p\text{-}FF$  and  $FF$  also indicated an increasing trend from 20 – 80  $\mu\text{m}$ , however due to the small number of cells, only a limited number of  $p\text{-}FF$  measurements were obtained.

The busbar line pitch did not appear to affect the  $J_{SC}$  of the cells, however a substantial difference in  $J_{SC}$  of approximately 0.2 – 0.3  $\text{mA}/\text{cm}^2$  was observed between cells which had one HF dip to those which had two HF dips. Due to the excessive thinning of the  $\text{SiN}_x\text{:H}$  layer which occurred during the second HF dip, the  $J_{SC}$  of such cells was lower than that of cells which only received one HF dip. Despite receiving two HF dips and a visibly non-optimal thickness of the  $\text{SiN}_x\text{:H}$  layer, the single laser-doped solar cell in this section displayed a substantially higher  $J_{SC}$  of 39.6  $\text{mA}/\text{cm}^2$  than any laser-ablated cell (39.3  $\text{mA}/\text{cm}^2$ ). Hence further increases in  $J_{SC}$  are expected by reprocessing such cells without shunting issues and the requirement for a second HF dip. This cell had a substantially higher  $V_{OC}$  and efficiency than any of the laser-ablated samples of 673 mV and 21.2 % respectively. The improved electrical parameters were attributed to the use of a lighter FSF with reduced  $J_{0d}$  which also allowed more effective hydrogen passivation, and the improved shielding of minority carriers from the metal/Si interface due to the inclusion of the selective FSF structure.

The results highlight the importance of avoiding excessive metal/Si interface areas in the busbar regions and the potential improvements in moving towards busbar free or floating busbar structures. In addition, the importance of using light diffusions to improve the ability of hydrogen to enter the bulk silicon, and therefore enhance bulk defect passivation was demonstrated. However, further studies are required to determine the full effect of busbar line pitch on electrical performance.

Table 6.9: Light J-V measurements of n-PERT solar cells with laser-ablated (LA) and laser-doped (LD) n-type contacts featuring different line pitches for the busbar. Data for the best cells in each group are shown in red.

Busbar pitch ( $\mu\text{m}$ )	Laser Process	Number of HF dips	$J_{SC}$ (mA/cm <sup>2</sup> )	$V_{OC}$ (mV)	$FF$ (%)	$\eta$ (%)	$p\text{-}FF$ (%)	$p\text{-}\eta$ (%)
10	LA	1	$39.20 \pm 0.04$	$662.3 \pm 0.8$	$79.80 \pm 0.15$	$20.72 \pm 0.03$	$82.92 \pm 0.19$	$21.55 \pm 0.06$
	LA	1	39.22	661.7	79.91	20.74	83.06	21.59
	LA	2	38.93	661.7	79.37	20.44	—	—
	LD	2	39.60	672.9	79.61	21.21	83.31	21.92
20	LA	1	$39.17 \pm 0.07$	$662.8 \pm 0.1$	$79.60 \pm 0.12$	$20.66 \pm 0.00$	83.29	21.61
		1	39.12	662.8	79.69	20.66	83.29	21.61
		2	38.94	663.9	80.02	20.69	83.01	21.56
40	LA	1	$39.22 \pm 0.11$	$664.2 \pm 0.6$	$79.40 \pm 0.05$	$20.68 \pm 0.06$	$83.11 \pm 0.28$	$21.62 \pm 0.05$
		1	39.25	664.7	79.42	20.72	83.35	21.68
		2	$38.93 \pm 0.06$	$664.0 \pm 0.2$	$79.84 \pm 0.91$	$20.64 \pm 0.27$	$83.16 \pm 0.18$	$21.59 \pm 0.11$
		2	38.92	664.2	80.40	20.82	83.22	21.65
80	LA	1	39.13	666.1	79.90	20.82	83.18	21.60
		2	$38.80 \pm 0.17$	$664.6 \pm 3.5$	$80.05 \pm 0.55$	$20.64 \pm 0.31$	$83.09 \pm 0.32$	$21.63 \pm 0.17$
		2	38.92	665.5	80.56	20.87	83.35	21.70

### 6.6.5 Enhanced Passivation Through an Intermediate Hydrogen Release Process

For conventional silicon solar cell technologies, hydrogen passivation is performed during the co-firing process used to form the Al-BSF rear and front Ag contacts. This process is performed at temperatures above 800 °C and the  $\text{SiN}_x\text{:H}$  is often tuned to release hydrogen at such temperatures. However, with the move away from screen-printed contacts and Al-BSF formation, most high efficiency technologies do not expose wafers to temperatures above 450 °C after the growth of the dielectric layers. Subsequently, if the  $\text{SiN}_x\text{:H}$  layers are not modified to allow a more effective release of hydrogen at lower temperatures, any attempts at hydrogenation may be of limited effectiveness. Therefore, either the dielectric layers for high efficiency technologies must be modified to release hydrogen at lower temperatures, or a high temperature process must be incorporated to release hydrogen from the layer.

Fig. 6.31 shows the evolution in the  $\tau_{eff}$  measured at an injection-level of  $\Delta n = 1 \times 10^{15} \text{ /cm}^3$  for lifetime test structures after various BFA processes. On n-type samples, no substantial increases in  $\tau_{eff}$  were observed until the samples received a BFA with a peak temperature of at least 700 °C. However the additional thermal treatments were detrimental to the bulk lifetime if the wafers received the extended FGA after the growth of the  $\text{SiO}_2$ , most likely due to the nucleation of oxygen precipitates . The degradation in lifetime was most pronounced for the sample with a  $120 \text{ } \Omega/\square$  FSF which may indicate a reduced ability of hydrogen to passivate defects generated in such wafers due to the heavier diffusions on the surfaces, or that the differences in the thermal processes for the FSF diffusion and subsequent oxidation had a large influence on the subsequent generation of bulk defects during the FGA.

For p-type samples, a large increase in  $\tau_{eff}$  was observed for temperatures of 600 °C and above. The lower temperature at which the p-type wafers started to see increases in  $\tau_{eff}$  may have been due to the improved ability of hydrogen to penetrate into the bulk of the wafer, due to the absence of a phosphorus diffusion on the wafer surface.

For many of the lifetime test samples in this section, a reduction in  $\tau_{eff}$  was observed after the BFA process with a peak temperature of 900 °C. PL images also highlighted a belt pattern after the

## 6.6. THE PATHWAY TO IMPROVED HYDROGEN PASSIVATION FOR N-PERT CELLS

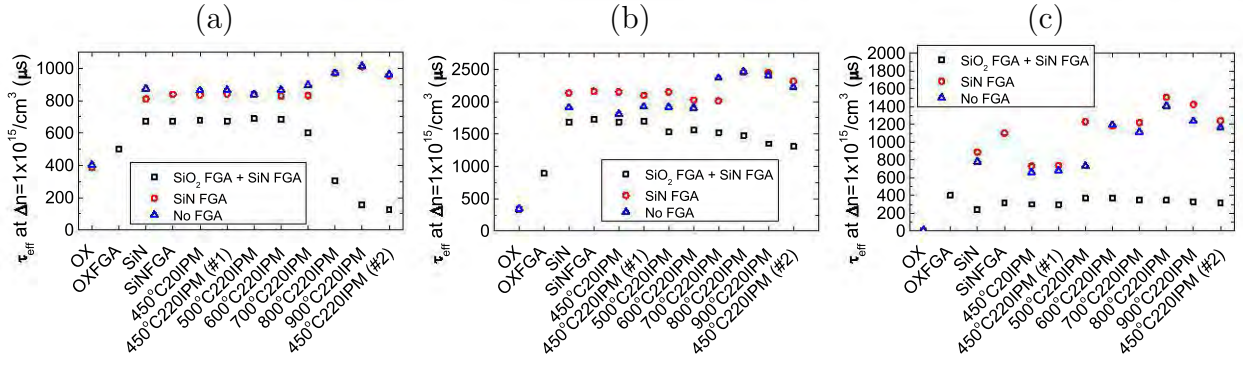


Figure 6.31: Evolution in  $\tau_{eff}$  at  $\Delta n = 1 \times 10^{15} / \text{cm}^3$  for (a) n-type wafers with a  $120 \Omega/\square$  FSF, (b)  $260 \Omega/\square$  FSF and (c) p-type wafers with the emitter diffusion removed highlighting improved  $\tau_{eff}$  for wafers after a high temperature hydrogen release process.

900 °C with regions directly above the belt showing a higher PL response than regions of the wafer without parts of the metal belt directly under the wafer. Hence it would appear that such a high temperature should not be used as an intermediate hydrogen release step. However, wafers in this experiment were subjected to a high number of thermal processes and further experiments should be undertaken to establish whether this was also the case for a single thermal process performed at an elevated temperature of 900 °C. Despite the reductions in  $\tau_{eff}$  which occurred by the 900 °C process, all samples displayed substantial improvements in  $\tau_{eff}$  after the subsequent 450 °C BFA treatment compared to that achieved when an identical BFA treatment was performed without any high temperature hydrogen release processes (see Fig. 6.32). These results suggest that even for solar cell structures which do not require high temperature processes for the formation of the metal contacts, substantial benefits may be obtained by the introduction of a high temperature process to enhance the release of hydrogen from the dielectric layers and diffusion of hydrogen throughout the device. Further enhancements may also be achieved through the use of an improved hydrogen source on the rear surface such as PECVD  $\text{SiN}_x\text{:H}$  in conjunction with a thinner thermal oxide layer to improve hydrogen diffusivity into the silicon.

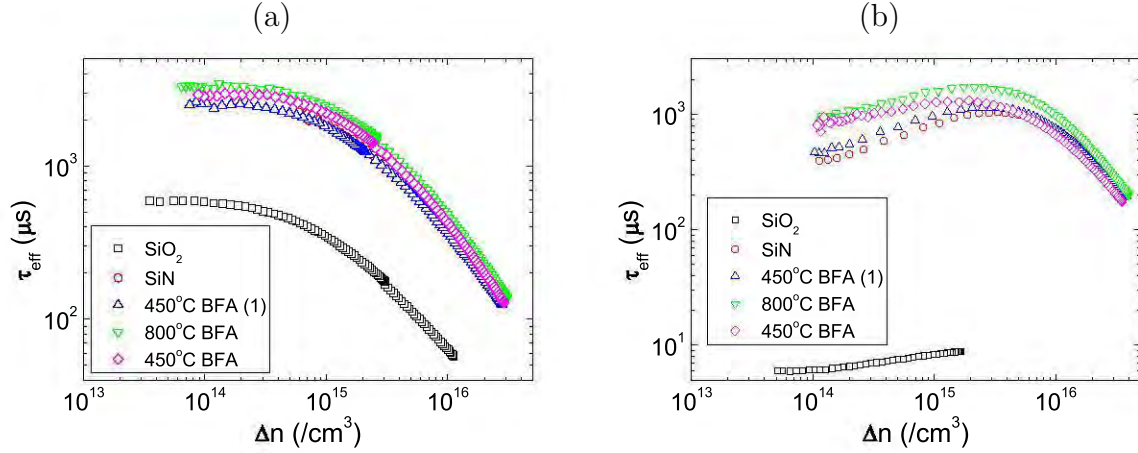


Figure 6.32: Simplified evolution of  $\tau_{eff}$  curves after selected processes for (a) n-type wafers with a  $260 \Omega/\square$  FSF and (b) p-type wafers with the emitter diffusion removed, highlighting improved  $\tau_{eff}$  through the application of a high temperature hydrogen release process. The legend indicates sequential order of the selected processes.

### 6.6.6 Summary for the Pathway to Improved Hydrogen Passivation for n-PERT

In this section, the effectiveness of FG based hydrogen passivation processes for n-PERT solar cells were compared to simple BFA processes in CDA ambient. It was observed that extended FGA processes resulted in a substantial reduction in  $\tau_{bulk}$ , which may have been due to the formation of oxygen precipitants. The results indicated that all FGA processes could be removed from the processing sequence for n-PERT solar cells and replaced with a BFA applied after laser processing, with no loss in performance. A peak efficiency of 21.2 % was demonstrated for an n-PERT solar cell with a selective FSF formed by laser doping with an FGA process applied after the deposition of the rear Al electrode, and a BFA applied after laser doping. Lifetime test structures indicated that further efficiency enhancements are possible through the use of an intermediate high temperature BFA to release hydrogen from the dielectric layer, prior to the deposition of the Al rear.



## 6.7 Chapter Summary

In this chapter, the development of high efficiency silicon solar cells with advanced hydrogenation was presented.

**Avoidance of localised recombination site formation during firing:** On LDSE1 solar cells, an improved firing process was used to reduce the formation of localised recombination sites. This was achieved by firing the Al-BSF with the  $\text{SiN}_x\text{:H}$  surface face-up.

**Avoidance of parasitic plating through the use of an emitter etch-back:** The use of an emitter etch-back process to reduce the surface phosphorus concentration was observed to avoid parasitic plating. Subsequently a record efficiency of 19.36 % was obtained.

**Edge junction isolation for LDSE cells:** CEJI was deemed essential to allow the use of self-aligned plated contacts by avoiding shunting during the plating process which occurred when using LEJI. However CEJI resulted in lower  $J_{SC}$  and  $V_{OC}$  than cells fabricated as a 5-inch cell on a 6-inch wafer with LEJI. Further experimentation suggested that this was due to the removal of the phosphorus off the rear of the cell.

**Advanced hydrogenation for LDSE cells:** The presence of phosphorus on the rear of the cell during Al-BSF formation may have blocked hydrogen in the wafer and led to improved hydrogen passivation of the bulk of the device. This, in conjunction with the AFP to enhance minority carrier injection led to independently confirmed efficiencies of 19.6 % on large area devices with a full area Al-BSF.

**Incorporation of LDSE into PERC cells:** The LDSE technology was also incorporated into a solar cell with local rear Al-BSF contacts. Efficiency enhancements of approximately 0.4 % absolute were demonstrated compared to using a homogenous emitter with laser-ablated contacts. The increases were attributed to an improved shielding from minority carriers at the metal/Si

interface with higher  $V_{OC}$ , and higher  $FF$ . Differences in  $FF$  of all laser-ablated and laser-doped groups were related to  $R_S$ , which could be attributed to a number of factors such as different dopant profiles in the selective emitter region and different widths of the plated metal contacts. Efficiencies of up to 20.7 % were demonstrated using an LDSE structure, but again suggest the rear local Al-BSF contact structure was limiting cell performance.

**Improvement hydrogenation for n-PERT cells:** to the fabrication sequence for n-PERT solar cells were realised through the avoidance of FGA processes, particularly before the deposition of PECVD  $\text{SiN}_x\text{:H}$ . This process was determined to reduce the bulk lifetime of the wafers which may have been due to the nucleation of oxygen precipitates from the prolonged exposure to elevated temperatures. The deposition of  $\text{SiN}_x\text{:H}$  was observed to be an effective process for improving surface passivation with no further improvements in bulk or surface passivation gained on symmetrical n-type wafers with a phosphorus FSF through the use of subsequent FGA or BFA processes applied at 450 °C. However minor improvements were observed on p-type wafers processed in parallel and were attributed to the ease of hydrogen diffusion into the bulk due to the absence of surface diffusions. To improve the effectiveness of hydrogen passivation, a higher temperature firing process was required to release atomic hydrogen from the  $\text{SiN}_x\text{:H}$  layers used. Even with subsequent processes at 450 °C, an improved level of passivation could be attained than that without an intermediate hydrogen release process. This suggests that for high efficiency solar cells, even if a high temperature process is not required for the formation of the metal contacts, a substantial benefit could be gained through exposure to high temperatures to improve bulk defect passivation. An efficiency of 21.2 % was achieved for an n-PERT solar cell with a laser-doped selective FSF, however further improvements are expected by reducing the metal/Si interface area in the busbar region and incorporation of a high temperature hydrogen release process before the formation of the metal contacts.

The results in this chapter suggest that substantial further improvements in efficiency could be gained for silicon solar cells fabricated on both n-type and p-type substrates with further improvements to hydrogen passivation.

# Chapter 7

## Conclusions and Outlook

The work presented in this thesis explored hydrogen passivation mechanisms in silicon solar cells. The importance of hydrogen charge states in the passivation process was demonstrated for a range of commercial grade silicon wafers, leading to substantial improvements in the electrical qualities of all materials investigated. The formation of advanced contacting structures was also demonstrated using laser doping.

In Chapter 2, a review of B–O defect formation, hydrogen in silicon and the laser doping process for silicon solar cells was presented.

A study of hydrogen passivation for silicon wafers and solar cells as presented in Chapter 3, showed that:

1. The charge state of hydrogen plays a vital role in the passivation process. Certain defects require a specific charge state of hydrogen in order to be passivated. The concentration of  $H^0$  can be maximised by ensuring an  $E_{Fn}$  of approximately 0.15 eV above  $E_m$ . This may be realised by changes to temperature, minority carrier injection and  $N_{eff}$ . By maximising the concentration of  $H^0$ , relatively high concentrations of  $H^+$ ,  $H^0$  and  $H^-$  can be obtained in the silicon which can therefore passivate a wider array of defects with different hydrogen charge state requirements.

2. Hydrogen passivation processes are reversible. For B-O defects, a net reactivation of recombination active defects was observed if subsequent processes were performed at elevated temperatures without sufficient minority carrier injection. This resulted in insufficient minority charge state concentrations of hydrogen required to once again passivate the defect. However further processing with the appropriate minority carrier injection could again increase lifetimes through increased charge state concentrations of  $H^0$  and  $H^-$ . Independently confirmed  $V_{OC} > 680$  mV and  $p\text{-}\eta$  of 23 % were obtained with the AHP on standard commercial grade B-CZ.
3. Appropriate charge state control was vital in improving the electrical quality of UMG silicon, with improvements in  $iV_{OC}$  of approximately 60 mV throughout the entire ingot compared to that obtained using conventional hydrogenation processes. The effectiveness of hydrogen passivation was also dependent on the  $N_{eff}$  of the wafer, whereby wafers with the lowest  $N_{eff}$  responded most positively to defect passivation, despite having higher impurity and defect concentrations in the last section of the ingot to solidify. As a result, it may be possible to have higher ingot utilisations for solar cell fabrication, therefore reducing costs.
4. OSF present after the emitter diffusion/oxidation were successfully passivated by an AHP incorporating minority carrier injection on B-CZ wafers. In addition, the defect passivation was retained on finished devices.
5. Hydrogen passivation resulted in a substantial improvement in  $\tau_{bulk}$  of standard commercial grade n-type CZ wafers from 90  $\mu$ s to 3.4 ms. This improvement, suggests that the material is compatible with the fabrication of 24 % efficient solar cells in commercial production provided the passivation can be retained on the finished device. The benefit of an intermediate firing step to enhance hydrogen release from the dielectric layer was observed on the n-type wafers, with passivation activated during a subsequent low temperature hydrogenation process.
6. Both phosphorus gettering and hydrogen passivation are essential processes for low quality materials such as multi-crystalline and QM silicon. The AHP was shown to lead to substantial improvements over a CHP, with improvements in  $\tau_{eff}$  from 8  $\mu$ s to 270  $\mu$ s on seeded-cast material demonstrated through hydrogen passivation alone. The AHP also displayed an improved effectiveness in the passivation of impurity related defects around the edge of cast

---

ingots. Using standard multi-crystalline material,  $iV_{OC} > 700$  mV were demonstrated on large area full cell structures prior to contact formation.

7. Hydrogen passivation can be incorporated during a number of thermal processes throughout the fabrication sequence or on the finished device. Hydrogen passivation processes performed on finished devices demonstrated efficiency enhancements of 2 % absolute. However the results also indicated a potential passivation of the metal/Si interface leading to a reduction in actual  $V_{OC}$  measured whilst the  $iV_{OC}$  continued to improve through the passivation of other defects within the device.
8. The mechanisms of hydrogen passivation were shown to be extremely complicated and significant further work is required to fully understand and exploit its full potential. Future work should focus on determining which charge states of hydrogen are required for defect passivation for a variety of defects present in typical commercial grade silicon wafers used for PV. In addition, stability and durability testing is required to investigate the long-term viability of efficiency enhancements through hydrogen passivation.

In Chapter 4 the formation of advanced contact structures was presented using laser doping. Using the unique properties of CW and Q-CW lasers, a number of laser-doped structures were shown to be formed for the fabrication of silicon solar cells including:

1. Deep junction formation was demonstrated with depths  $> 10$   $\mu\text{m}$  for both n- and p-type dopant sources. For point contacts with dimensions of  $10 \times 40$   $\mu\text{m}$ , junction depths  $> 8$   $\mu\text{m}$  were obtained.
2. A numerical model was developed to simulate the laser doping process. Modelling of the SIMS profiles obtained from CW laser-doped regions suggested that the laser doping process follows Gaussian diffusion theory, however the resultant dopant profiles were influenced by the presence of a solid/liquid interface during the process which acted to reduce the junction depth. Q-CW lasers could also be used to form deep junction depths, however the partial solidification of silicon between successive pulses and resulted in a more box-like profile.
3. Laser-doped p-type regions were formed using Al atoms from passivating dielectric layers of PECVD  $\text{AlO}_x$  and ALD  $\text{Al}_2\text{O}_3$  with an incorporation of up to 34 % Al into the silicon.

Narrow line widths as low as 4  $\mu\text{m}$  were obtained, comparable with dimensions used for the fabrication of PERL solar cells using expensive photolithographic processes. For processing speeds over 5 m/s almost no detriment to the bulk was observed after subsequent hydrogen passivation, and increasing speeds resulted in lower  $J_{0d}$  contributions. EBIC images suggested two separate diffusion mechanisms in the laser-doped region, with solid state diffusion occurring in the peripheral laser-doped regions which may assist in the avoidance of performance degradation from LasID. On finished devices,  $FF > 80\%$  were demonstrated with independently confirmed efficiencies of 20.7 %. Further efficiency enhancements are expected by ensuring an effective release of hydrogen from the  $\text{SiN}_x\text{:H}$  layers and the incorporation of an AHP.

4. p-type laser doping was shown to be able to penetrate through surface phosphorus emitters to form direct contact to buried layers in the silicon solar cell (such as the p-type bulk) without the removal of any region of the phosphorus diffusion. As a result, interdigitated rear contact solar cells with a single thermal diffusion were fabricated with efficiencies over 14 % using this process, with the potential of significant efficiency enhancements through process optimisation.
5. By varying the surface phosphorus emitter and/or laser parameters, full transistor structures were demonstrated whereby a p-type surface layer was separated from the p-type bulk silicon by an n-type silicon region comprised of dopants from a pre-existing thermal diffusion.

In Chapter 5, the hydrogen passivation of LasID was presented, which resulted in efficiency enhancements of up to 0.7 % absolute for n-PERT solar cells. The passivation of LasID was deemed essential of laser-doped solar cells. The passivation process could also be incorporated into the Ni sinter process, therefore avoiding the need for an additional process.

In Chapter 6 improved hydrogen passivation processes were applied to laser-doped solar cells. Several aspects were investigated such as:

1. The hydrogen passivation of LasID avoided performance degradation caused by defects introduced when laser doping with CW or Q-CW lasers and deemed essential for laser-doped solar cells.

- 
2. Localised recombination for LDSE1 solar cells was avoided by firing the Al-BSF with the  $\text{SiN}_x\text{:H}$  surface facing upwards to ensure it was not in intimate contact with the belt.
  3. An emitter etch-back process was used to reduce the surface concentration of phosphorus and avoid parasitic plating due to a reduction in surface dopant concentration.
  4. CEJI was compared to LEJI for LDSE1 solar cells. For cells fabricated using LEJI, parasitic plating occurred in the laser grooved region which shunted the device. In contrast, CEJI samples did not show any sign of shunting and hence CEJI was deemed essential for laser-doped solar cells with plated contacts.
  5. The presence of phosphorus on the rear surface of LDSE1 solar cells was observed to greatly increase the  $V_{OC}$  and  $J_{SC}$  of finished devices. Results suggested that the phosphorus layer retained ahead of the Al/Si alloyed region may have blocked hydrogen from reaching the molten region during the firing process. This, in conjunction with the AFP, resulted in independently confirmed efficiencies of 19.6 % and  $V_{OC}$  of 644 mV.
  6. Improvements in efficiency of PERC solar cells of 0.4 % absolute were demonstrated by incorporating an LDSE structure. The improved efficiencies were attributed to an improved shielding of minority carriers at the metal/Si interface leading to higher  $V_{OC}$ , as well as improvements in  $FF$ . The improvements in  $FF$  were due to changes in  $R_S$  caused by a number of factors such as different dopant profiles for different laser doping conditions as well as the width of the resultant plated contacts.
  7. Simplified hydrogen passivation was incorporated into n-PERT solar cells through the elimination of FGA processes and implementation of a simple BFA at 450 °C, with efficiencies of up to 21.2 % obtained using a laser-doped selective FSF. Test structures indicated that further enhancements in hydrogen passivation could be realised through the use of an intermediate high temperature hydrogen release step prior to the formation of the metal contacts.

In this thesis, the aims specified in Chapter 1 have been achieved. An understanding of hydrogen passivation in silicon has been presented along with the development of an advanced hydrogenation process to increase minority hydrogen charge state concentrations, and therefore the effectiveness of hydrogen passivation processes. New contact structures were formed using laser doping featuring;

deep, and heavily diffused regions; utilising dopant atoms from AlO<sub>x</sub> dielectric layers; and allow contact to buried layers in silicon solar cells. An improved understanding of the diffusion process during laser doping was also presented. Methods to avoid performance degradation from LasID were presented using hydrogen passivation and the benefits of bulk hydrogen passivation were demonstrated on finished devices with laser-doped contacts. Improved device designs were also presented to increase the effectiveness of hydrogen passivation, and incorporated into solar cells. This work contributes new findings to the silicon solar cell research community which will hopefully lead to cost reductions for photovoltaic based electricity.



# Appendices

# Appendix A

## Physical Constants, Symbols and Abbreviations

### Physical Constants

Constant	Description	Value
$e$	base of the natural logarithm	2.71828
$h$	Planck constant	$6.62608 \times 10^{-34} \text{ J} \cdot \text{s}$
$k$	Boltzmann constant	$1.380648813 \times 10^{-23} \text{ J/K}$
$m_0$	electron mass	$9.11 \times 10^{-31} \text{ kg}$
$q$	elementary charge	$1.602 \times 10^{-19} \text{ C}$

# Symbols

Symbol	Description	Unit
$\alpha$	symmetric linear scaling factor	
$\beta$	asymmetric linear scaling factor	
$C$	impurity concentration	/cm <sup>3</sup>
$C_0$	initial impurity concentration in molten silicon	/cm <sup>3</sup>
$C_S$	impurity concentration at the surface	/cm <sup>3</sup>
$D$	diffusion coefficient	m <sup>2</sup> /s
$D_l$	diffusion coefficient in liquid silicon	m <sup>2</sup> /s
$D_s$	diffusion coefficient in solid silicon	m <sup>2</sup> /s
$\Delta n$	excess electron concentration	/cm <sup>3</sup>
$\Delta n_{opt}(T)$	optimal function of excess carrier concentration to maximise the generation of neutrally charged hydrogen	/cm <sup>3</sup>
$\Delta p$	excess hole concentration	/cm <sup>3</sup>
$E_a$	acceptor energy level	eV
$E_d$	donor energy level	eV
$E_F$	Fermi level	eV
$E_{Fn}$	electron quasi-Fermi level	eV
$E_{Fp}$	hole quasi-Fermi level	eV
$E_g$	band-gap energy	eV
$E_m$	energy level at mid band-gap	eV
$E_T$	recombination centre energy level	eV
$f_S$	fraction of solidified silicon during ingot growth	
$f_+$	fraction of monatomic hydrogen in the positive charge state	
$f_0$	fraction of monatomic hydrogen in the neutral charge state	
$f_-$	fraction of monatomic hydrogen in the negative charge state	
$FF$	fill factor	%
$G$	generation rate of electron-hole pairs	/cm <sup>3</sup>
$I$	laser beam intensity	MW/cm <sup>2</sup>
$iV_{OC}$	implied open circuit voltage	mV
$I_{PL}$	normalised photoluminescence response	counts/s
$J_{SC}$	short circuit current density	mA/cm <sup>2</sup>
$J_{0d}$	dark saturation current density	fA/cm <sup>2</sup>

---

## APPENDIX A. PHYSICAL CONSTANTS, SYMBOLS AND ABBREVIATIONS

---

Symbol	Description	Unit
$k_{eff}$	effective segregation coefficient	
$\lambda$	correction factor for a Gaussian profile seeded from a boundary or interface	
$L_D$	diffusion length	$\mu\text{m}$
$m_{de}$	density of states mass of electrons	kg
$m_{dh}$	density of states mass of holes	kg
$n$	electron concentration	$/\text{cm}^3$
$n_0$	electron concentration in thermal equilibrium	$/\text{cm}^3$
$n_1$	equilibrium concentration of electrons	$/\text{cm}^3$
$n_{n0}$	electron concentration in thermal equilibrium in n-type silicon	$/\text{cm}^3$
$n_{p0}$	electron concentration in thermal equilibrium in p-type silicon	$/\text{cm}^3$
$N_a$	acceptor dopant density	$/\text{cm}^3$
$N_C$	density of states in the conduction band	$/\text{cm}^3$
$N_d$	donor dopant density	$/\text{cm}^3$
$N_{eff}$	effective dopant density	$/\text{cm}^3$
$n_i$	intrinsic carrier concentration	$/\text{cm}^3$
$N_V$	density of states in the valence band	$/\text{cm}^3$
$N_z$	number of depth elements of silicon	
$p\text{-}\eta$	pseudo efficiency	%
$p\text{-}FF$	pseudo fill factor	%
$p$	hole concentration	$/\text{cm}^3$
$p_0$	hole concentration in thermal equilibrium	$/\text{cm}^3$
$p_1$	equilibrium concentration of holes	$/\text{cm}^3$
$p_{n0}$	hole concentration in thermal equilibrium in n-type silicon	$/\text{cm}^3$
$p_{p0}$	hole concentration in thermal equilibrium in p-type silicon	$/\text{cm}^3$
$Q$	flux of dopants incorporated into silicon during diffusion	$/\text{cm}^2$
$R_S$	series resistance	$\Omega \cdot \text{cm}^2$
$R_{SH}$	shunt resistance	$\Omega \cdot \text{cm}^2$
$t$	time	s
$T$	absolute temperature	K
$T_F$	time dilation factor	
$\tau_{bulk}$	minority carrier bulk lifetime	$\mu\text{s}$
$\tau_{bulk_0}$	injection-level-independent minority carrier bulk lifetime	$\mu\text{s}$
$\tau_{eff}$	effective minority carrier lifetime	$\mu\text{s}$

---

Symbol	Description	Unit
$\tau_{eff}^*$	effective minority carrier lifetime after removing Auger components	$\mu\text{s}$
$\tau_{J_{0d}}$	lifetime component related to the dark saturation current density	$\mu\text{s}$
$\tau_n$	electron lifetime associated with Shockley-Read-Hall recombination	$\mu\text{s}$
$\tau_p$	hole lifetime associated with Shockley-Read-Hall recombination	$\mu\text{s}$
$\tau_{SRH}$	lifetime component related to Shockley-Read-Hall recombination	$\mu\text{s}$
$\tau_{total}$	total lifetime excluding Auger contributions determined by modelling	$\mu\text{s}$
$V_{OC}$	open circuit voltage	mV
$W$	wafer thickness	cm
$w_0$	focus size of a laser beam at the $1/e^2$ radius	
$x_n$	normalised wafer position within the ingot	
$v_i$	number of possible configurations in the unit cell for hydrogen with charge state $i$ (+,0,-)	
$z$	distance from silicon surface	$\mu\text{m}$
$z_\alpha$	seeding location for a Gaussian diffusion process	$\mu\text{m}$
$z_J$	localised junction depth	$\mu\text{m}$
$Z_F$	depth factor	
$Z_L$	element of liquid silicon	
$Z_S$	element of solid silicon	
$Z_I$	element of silicon at a surface or solid/liquid interface	
$Z_i$	vibrational partition function for hydrogen charge state $i$ (+,0,-)	

## Abbreviations

Abbreviation	Description
AFP	advanced firing process
AHP	advanced hydrogenation process
ALD	atomic layer deposition
a-Si:H	hydrogenated amorphous silicon
AlO <sub>x</sub>	aluminium oxide
Al <sub>2</sub> O <sub>3</sub>	stoichiometric aluminium oxide
B-CZ	boron-doped Czochralski
B-FZ	boron-doped float-zone
B-MCZ	boron-doped magnetically confined Czochralski
BFA	belt furnace anneal
B <sub>i</sub>	interstitial boron
B <sub>s</sub>	substitutional boron
BSG	borosilicate glass
CB-CZ	compensated boron-doped Czochralski
CDA	compressed dry air
CFP	conventional firing process
CHP	conventional hydrogenation process
CEJI	chemical edge junction isolation
CW	continuous wave
CZ	Czochralski
e <sup>-</sup>	electron
EBIC	electron beam induced current
EJI	edge junction isolation
Fe <sub>i</sub>	interstitial iron
FG	forming gas
FGA	forming gas anneal
FIB	focused ion beam
FRC	fast-forming recombination centre
FSF	front surface field
FZ	float-zone
Ga-CZ	gallium-doped CZ

---

Abbreviation	Description
HNA	hydrofluoric / nitric / acetic acid (etching process)
IBC	interdigitated back contact
Imec	Inter-university microelectronics research centre
i-PERC	industrial passivated emitter and rear contact
i-PERL	industrial passivated emitter, rear and locally diffused
IQE	internal quantum efficiency
$h^+$	hole
$H^+$	positively charged atomic hydrogen
$H^0$	neutrally charged atomic hydrogen
$H^-$	negatively charged atomic hydrogen
IAR	impurity affected region
J-V	current density - voltage
LA	laser ablation
LasID	laser-induced defect
LCP	laser chemical processing
LD	laser doping
LDSE	laser-doped selective emitter
LDSE1	1 <sup>st</sup> generation laser-doped selective emitter
LDSE2	2 <sup>nd</sup> generation laser-doped selective emitter
LEJI	laser edge junction isolation
LID	light-induced degradation
LIP	light-induced plating
LIMPID	laser-induced melting of pre-deposited impurity doping
LPR	local phosphorus emitter removal
MCZ	magnetically confined Czochralski
n-PERT	n-type passivated rear, totally diffused boron emitter
$O_i$	interstitial oxygen
$O_{2i}$	interstitial oxygen dimer
OSF	oxidation-induced stacking fault
PECVD	plasma enhanced chemical vapor deposition
PERC	passivated emitter and rear contact
PERF	passivated emitter, rear floating junction
PERL	passivated emitter, rear and locally diffused

---

**APPENDIX A. PHYSICAL CONSTANTS, SYMBOLS AND ABBREVIATIONS**

---

<b>Abbreviation</b>	<b>Description</b>
PERT	passivated emitter, rear and totally diffused
PL	photoluminescence
PSG	phosphosilicate glass
PV	photovoltaic
QM	quasi mono-crystalline
Q-CW	quasi-continuous wave
QSS-PC	quasi-steady-state photoconductance
QSS-PL	quasi-steady-state photoluminescence
RCA	Radio Corporation of America
RPM	revolutions per minute
SEM	scanning electron microscope
SIMS	secondary ion mass spectroscopy
SiN <sub>x</sub>	silicon nitride
SiN <sub>x</sub> :H	hydrogenated silicon nitride
SiON <sub>x</sub>	silicon oxynitride
SiON <sub>x</sub> :H	hydrogenated silicon oxynitride
SiO <sub>x</sub>	silicon oxide
SiO <sub>x</sub> :H	hydrogenated silicon oxide
SOD	spin on dopant
SRC	slow-forming recombination centre
SSD	single-sided diffusion
SRV	surface recombination velocity
UMG	upgraded metallurgical grade
UNSW	University of New South Wales
UV	ultra violet

---



# Appendix B

## Publications List

### Refereed Journal Papers

1. B. Hallam, A. Sugianto, L. Mai, G. Xu, C. Chan, M. Abbott, S. Wenham, A. Uruena, E. Cornagliotti, and M. Aleman. “Hydrogen Passivation of Laser-Induced Defects for Laser-Doped Silicon Solar Cells”. *Photovoltaics, IEEE Journal of*, Vol. 4, No. 6, pp. 1413–1420, Nov 2014.
2. B. Hallam, B. Tjahjono, T. Trupke, and S. Wenham. “Photoluminescence imaging for determining the spatially resolved implied open circuit voltage of silicon solar cells”. *Journal of Applied Physics*, Vol. 115, No. 4, p. 044901, 2014.
3. B. Hallam, A. Urueña, R. Russell, M. Aleman, M. Abbott, C. Dang, S. Wenham, L. Tous, and J. Poortmans. “Efficiency enhancement of i-PERC solar cells by implementation of a laser doped selective emitter”. *Submitted to Solar Energy Materials and Solar Cells*, Vol. PP, p. 1, 2014.
4. D. Lin, M. Abbott, P. H. Lu, B. Xiao, B. Hallam, B. Tjahjono, and S. Wenham. “Incorporation of deep laser doping to form the rear localized back surface field in high efficiency solar cells”. *Solar Energy Materials and Solar Cells*, Vol. 130, pp. 83–90, 2014.
5. E. Cornagliotti, L. Tous, A. Urueña, A. Rothschild, R. Russell, V. Lu, S. Radosavjlevic, J. John, J. Toman, M. Aleman, F. Duerinckx, J. Poortmans, J. Szlufcik, B. Dielissen, F. Souren, X. Gay, R. Görtzen, and B. Hallam. “Large Area p-type PERC Cells Featuring Local p+ BSF Formed By Laser Processing of ALD AL<sub>2</sub>O<sub>3</sub> Layers”. *Submitted to Solar Energy Materials and Solar Cells*, Vol. PP, p. 1, 2014

## APPENDIX B. PUBLICATIONS LIST

---

6. P. Hamer, B. Hallam, S. Wenham, and M. Abbott. “Manipulation of Hydrogen Charge States for Passivation of p-type Wafers in Photovoltaics”. *IEEE Journal of Photovoltaics*, Vol. 4, No. 5, pp. 1252–1260, 2014
7. C. Chan, M. Abbott, B. Hallam, M. Juhl, D. Lin, Z. Li, Y. Li, J. Rodriguez, and S. Wenham. “Edge isolation of solar cells using laser doping”. *Solar Energy Materials and Solar Cells*, Vol. 132, pp. 535–543, 2015
8. B. Hallam, P. Hamer, S. Wenham, M. Abbott, A. Sugianto, A. Wenham, C. Chan, G. Xu, J. Kraiem, J. Degoulange, and R. Einhaus. “Advanced Bulk Defect Passivation for Silicon Solar Cells”. *IEEE Journal of Photovoltaics*, Vol. 4, No. 1, pp. 88–95, Jan 2014.
9. B. Hallam, C. Chan, A. Sugianto, and S. Wenham. “Deep junction laser doping for contacting buried layers in silicon solar cells”. *Solar Energy Materials and Solar Cells*, Vol. 113, pp. 124–134, 2013.
10. C. Chan, M. Abbott, M. Juhl, B. Hallam, B. Xiao, and S. Wenham. “Assessing the Performance of Surface Passivation Using Low-Intensity Photoluminescence Characterization Techniques”. *IEEE Journal of Photovoltaics*, Vol. PP, No. 99, pp. 1–7, 2013.
11. B. Hallam, B. Tjahjono, and S. Wenham. “Effect of PECVD silicon oxynitride film composition on the surface passivation of silicon wafers”. *Solar Energy Materials and Solar Cells*, Vol. 96, pp. 173 – 179, 2012.
12. B. Hallam, S. Wenham, H. Lee, E. Lee, H. Lee, J. Kim, J. Shin, K. Cho, and J. Kim. “Record Efficiency on Large Area P-Type Czochralski Silicon Substrates”. *Japanese Journal of Applied Physics*, Vol. 51, No. 10, p. 10NA08, 2012.
13. Z. Wang, P. Han, H. Lu, H. Qian, L. Chen, Q. Meng, N. Tang, F. Gao, Y. Jia, J. Wu, W. Wu, H. Zhu, J. Ji, Z. Shi, A. Sugianto, L. Mai, B. Hallam, and S. Wenham. “Advanced PERC and PERL production cells with 20.3% record efficiency for standard commercial p-type silicon wafers”. *Progress in Photovoltaics: Research and Applications*, Vol. 20, pp. 260–268, 2012.
14. B. Hallam, S. Wenham, H. Lee, E. Lee, H. Lee, J. Kim, and J. Shin. “Effect of edge junction isolation on the performance of laser doped selective emitter solar cells”. *Solar Energy Materials and Solar Cells*, Vol. 95, No. 12, pp. 3557–3563, 2011.
15. B. Hallam, S. Wenham, A. Sugianto, L. Mai, C. Chong, M. Edwards, D. Jordan, and P. Fath. “Record Large Area P-type CZ Production Cell Efficiency of 19.3% Based on LDSE Technology”. *IEEE Journal of Photovoltaics*, Vol. 1, pp. 43–48, 2011.
16. E. Lee, H. Lee, J. Choi, D. Oh, J. Shim, K. Cho, J. Kim, S. Lee, B. Hallam, S. R. Wenham, *et al.* “Improved LDSE processing for the avoidance of overplating yielding 19.2% efficiency on commercial

---

grade crystalline Si solar cell”. *Solar Energy Materials and Solar Cells*, Vol. 95, No. 12, pp. 3592–3595, 2011.

## Conference Proceedings

1. B. Hallam, A. Sugianto, L. Mai, G. Xu, C. Chan, M. Abbott, S. Wenham, A. Uruena, M. Aleman, and J. Poortmans. “Hydrogen Passivation of Laser-Induced Defects for Silicon Solar Cells”. *40th IEEE Photovoltaic Specialists Conference, Denver*, Vol. PP, p. 1, 2014. *Poster presentation*.
2. B. Hallam, W. S., A. Wenham, P. Hamer, C. Chan, M. Abbott, and S. Wenham. “Hydrogen passivation for highly defected commercial grade n-type CZ wafers and oxidation-induced stacking faults”. *29th European Photovoltaic Solar Energy Conference, Amsterdam*, Vol. 1, pp. 608–611, 2014. *Oral presentation*.
3. B. Hallam, S. Wang, M. Abbott, A. Wenham, C. Chan, P. Hamer, M. Eadie, and S. Wenham. “Hydrogen passivation for multi-crystalline and quasi-mono cast silicon wafers - A pathway to low cost, high efficiency solar cells?”. *29th European Photovoltaic Solar Energy Conference, Amsterdam*, Vol. 1, pp. 1292–1295, 2014. *Poster presentation*.
4. B. Hallam, P. Hamer, S. Wang, M. Abbott, A. Wenham, C. Chan, and S. Wenham. “Hydrogen Passivation for Commercial CZ Silicon Wafers and Solar Cells”. *24th Workshop on Crystalline Silicon Solar Cells & Modules*, Vol. PP, p. 1, 2014. *Invited oral presentation*.
5. A. Wenham, C. Chan, B. Hallam, M. Abbott, A. Lochtefeld, A. Gerger, S. Wenham, and A. Barnett. “Development of Metal-Less Monolithic Crystalline Silicon Solar Cells”. *29th European Photovoltaic Solar Energy Conference*, pp. 693–698, 2014. *Oral presentation*.
6. T. Pletzer, J. Mülken, S. Rißland, E. Cornagliotti, J. John, O. Breitenstein, and J. Knoch. “Quantitative local current-voltage analysis with different spatially-resolved camera-based techniques of silicon solar cells with cracks”. *Oral presentation*.
7. B. Xiao, L. Mai, D. Lin, B. Hallam, C. Chong, A. Lennon, and S. Wenham. “Study of P-type silicon laser doping with ALD AlO<sub>x</sub> as dopant source”. *Accepted poster presentation for the 40th IEEE Photovoltaic Specialists Conference, Denver*, Vol. PP, p. 1, 2014. *Poster presentation*.
8. B. Hallam, P. Hamer, S. Wenham, M. Abbott, A. Sugianto, A. Wenham, C. Chan, G. Xu, J. Kraiem, J. Degoulange, and R. Einhaus. “Advanced Bulk Defect Passivation for Silicon Solar Cells”. *Proceedings of the 39th IEEE Photovoltaic Specialists Conference, Tampa*, Vol. PP, pp. 1–8, 2013. *Oral presentation and best student presentation award for Section 4*.

## APPENDIX B. PUBLICATIONS LIST

---

9. B. Hallam, S. Wenham, P. Hamer, M. Abbott, A. Sugianto, C. Chan, A. Wenham, M. Eadie, and G. Xu. “Hydrogen passivation of B-O defects in Czochralski silicon”. *Energy Procedia*, Vol. 38, pp. 561–570, 2013. *Oral presentation and Silicon PV award for the 7<sup>th</sup> highest ranked abstract of the conference.*
10. B. Hallam, C. Chan, M. Eadie, P. Hamer, A. Sugianto, S. Wenham, K. Casalenuovo, J. Kraiem, D. Degoulange, R. Einhaus, and Z. Shi. “High Quality Passivation for p-Type CZ UMG Silicon Wafers”. *Proceedings of the 27th European Photovoltaic Solar Energy Conference, Frankfurt, Germany*, pp. 1942 – 1945, 2012. *Poster presentation.*
11. B. Hallam, S. Wenham, M. Edwards, H. S. Lee, E. Lee, H. W. Lee, J. Kim, and J. Shin. “Record Industrial Cell Efficiency Fabricated on Commercial Grade P-Type CZ Substrates”. *Proceedings of the 21st IEEE Photovoltaic Science and Engineering Conference, Fukuoka*, 2011. *Oral presentation.*
12. B. Hallam, S. Wenham, C. M. Chong, A. Sugianto, L. Mai, M. Edwards, D. Jordan, and P. Fath. “Record large area P-type CZ production cell efficiency of 19.3% based on LDSE technology”. *Proceedings of the 37th IEEE Photovoltaic Specialists Conference, Seattle*, pp. 47–47, 2011. *Oral presentation.*
13. B. Hallam, A. Sugianto, B. Tjahjono, N. Kuepper, N. Western, G. Xu, and S. Wenham. “Deep junction formation for silicon solar cells through the use of laser doping”. *Proceedings of the 2010 Annual Conference of the Australian Solar Energy Society*, p. 136, 2010. *Oral presentation.*
14. B. Hallam, N. Western, and S. Wenham. “Large increase in bulk lifetime of commercial grade CZ silicon wafers through hydrogenation”. *Proceedings of the 2010 Annual Conference of the Australian Solar Energy Society*, pp. 160–166, 2010. *Oral presentation.*
15. C. Chan, M. Abbott, M. Juhl, B. Hallam, B. Xiao, and S. Wenham. “Assessing the Performance of Surface Passivation Using Low-Intensity Photoluminescence Characterization Techniques”. *Proceedings of the 39th Photovoltaic Specialists Conference, Tampa*, Vol. PP, pp. 1–7, 2013. *Oral presentation.*
16. E. Cornagliotti, L. Tous, A. Urueña, A. Rothschild, R. Russell, V. Lu, S. Radosavjevic, J. John, J. Toman, M. Aleman, F. Duerinckx, J. Poortmans, J. Szlufcik, B. Dielissen, F. Souren, X. Gay, R. Görtzen, and B. Hallam. “Integration of spatial ALD aluminium oxide for rear side passivation of p-type PERC/PERL solar cells”. *Proceedings of the 28th European Photovoltaic Solar Energy Conference, Paris, France*, pp. 976 – 981, 2013. *Oral presentation.*
17. P. Hamer, B. Hallam, C. Chan, A. Wenham, A. Sugianto, M. Abbott, and S. Wenham. “Hydrogen passivation mechanisms in silicon solar cells”. *Proceedings of the 28th European Photovoltaic Solar Energy Conference, Paris, France*, pp. 982–987, 2013. *Oral presentation.*

- 
18. A. Wenham, C. Chan, B. Hallam, P. Hamer, S. Wang, D. Lu, A. Sugianto, B. Tjahjono, B. Newman, Z. Shi, A. Lochtefeld, A. Gerger, S. Wenham, and A. Barnett. “Novel metal-less monolithic crystalline silicon solar cells”. *Proceedings of the 28th European Photovoltaic Solar Energy Conference, Paris, France*, pp. 135–141, 2013. *Oral presentation*.
  19. B. Xiao, B. Hallam, L. Mai, D. Lin, C. Chong, A. Lennon, and S. Wenham. “Rear side laser doping through PECVD AlOx/SiNx passivation dielectrics on p-type CZ silicon solar cells”. *Proceedings of the 28th European Photovoltaic Solar Energy Conference, Paris, France*, pp. 1989–1993, 2013. *Poster presentation*.
  20. K. Cho, J. Kim, E. Lee, K. Hong, H. Lee, J. Shim, D. Oh, J. Shin, J. Kim, J. Seo, S. Lee, B. Hallam, S. Wenham, and H. Lee. “Shinsung Solar Energy high efficiency commercial crystalline Si solar cells”. *Proceedings of the 38th IEEE Photovoltaic Specialists Conference*, pp. 002145–002148, 2012. *Poster presentation*.
  21. M. Eadie, B. Hallam, O. Kunz, and S. Wenham. “Investigation into the Influence of Process Parameters on the Passivation on Commercial Grade Silicon Solar Cells”. *Proceedings of the 27th European Photovoltaic Solar Energy Conference, Frankfurt, Germany*, pp. 1574–1578, 2012. *Poster presentation*.
  22. J. Kim, K. Cho, E. Lee, K. Hong, H. Lee, J. Shim, D. Oh, J. Shin, J. Kim, J. Seo, S. Lee, B. Hallam, S. Wenham, and H. Lee. “The effect of emitter diffusion formation methods for laser doped selective emitter silicon solar cells”. *Proceedings of the 38th IEEE Photovoltaic Specialists Conference*, pp. 002178–002181, 2012. *Poster presentation*.
  23. A. Sugianto, B. Hallam, X. Bai, P. Han, H. Lu, L. Mai, S. Wenham, and Z. Shi. “Over 20%-Efficient Laser-Doped Passivated Rear Contact Solar Cells on Industrial-Sized Commercial Grade p-Type CZ Wafers”. *Proceedings of the 27th European Photovoltaic Solar Energy Conference, Frankfurt, Germany*, pp. 700–705, 2012. *Oral presentation*.
  24. G. Xu, B. Hallam, C. Chong, and S. Wenham. “Progress in Laser Doped PERL Solar Cell on p-Type CZ Silicon Wafer”. *Proceedings of the 27th European Photovoltaic Solar Energy Conference, Frankfurt, Germany*, pp. 1550–1552, 2012. *Poster presentation*.
  25. J. Bovatsek, A. Sugianto, B. Hallam, B. Tjahjono, S. Wenham, and R. Patel. “High-Speed Fabrication of Laser Doping Selective Emitter Solar Cells Using 532nm Continuous Wave (CW) and Modelocked Quasi-CW Laser Sources”. *Proceedings of the 26th European Photovoltaic Solar Energy Conference, Hamburg*, pp. 895–900, 2011. *Poster presentation*.
  26. Z. Hameiri, N. Gao, B. Hallam, R. Sinton, J. Weber, and T. Trupke. “Effective Doping Density Obtained from Combined Photoconductance and Photoluminescence Measurements”. *Proceedings*
-

## APPENDIX B. PUBLICATIONS LIST

---

- from the 26th European Photovoltaic and Solar Energy Conference, Hamburg, Germany, pp. 117–121, 2011. *Oral presentation.*
27. H. Li, B. Hallam, and S. Wenham. “Comparative study of PECVD deposited a-Si:H/SiNx:H double passivating layer on CZ crystalline si substrate”. *Proceedings of the 37th IEEE Photovoltaic Specialists Conference, Seattle, U.S.A.*, pp. 1481–1485, 2011. *Poster presentation.*
28. J.-S. Kim, H.-W. Lee, J.-E. Shin, E.-J. Lee, J.-Y. Choi, J.-M. Shim, D.-J. Oh, K.-Y. Cho, J. hyun Kong, J. keun Seo, J. soo Kim, S.-H. Lee, H.-S. Lee, B. Hallam, and S. Wenham. “Improved front side metallization for laser doped solar cells”. *Proceedings of the 37th IEEE Photovoltaic Specialists Conference, Seattle*, pp. 1091–1094, 2011. *Poster presentation.*
29. H. Lee, E. Lee, J. Kim, J. Shin, J. Kim, J. Choi, I. Kim, J. Shim, D. Oh, C. K, J. Kong, J. Seo, S. Lee, B. Hallam, S. Wenham, and H. Lee. “Production of 19.2% Efficient Large Area Commercial Grade P-Type CZ Silicon Solar Cells Based on the Laser Doped Selective Emitter Technology”. *Proceedings of the 26th European Photovoltaic Solar Energy Conference, Hamburg, Germany*, pp. 1390 – 1393, 2011. *Poster presentation.*
30. G. Xu, Y. Yao, C. Chong, B. Hallam, C. Yang, and S. Wenham. “Process Optimization and Device Characterization of Laser-Doped Selective Emitter Solar Cell on p-Type Czochralski Silicon Wafer”. *Proceedings of the 26th European Photovoltaic Solar Energy Conference, Hamburg, Germany*, pp. 1323 – 1328, 2011. *Poster presentation.*
31. E. Lee, H. Lee, I. Kim, J. Choi, D. Oh, J. Shim, K. Cho, J. Kim, H.-S. Lee, S. Lee, B. Hallam, and S. R. Wenham. “The potential efficiency of laser doped solar cells using photoluminescence imaging”. *Proceedings of the 35th IEEE Photovoltaic Specialists Conference, Honolulu, U.S.A.*, pp. 1436–1439, 2010. *Poster presentation.*
32. A. Sugianto, J. Bovatsek, S. Wenham, B. Tjahjono, G. Xu, Y. Yao, B. Hallam, X. Bai, N. Kuepper, C. Chong, and R. Patel. “18.5% laser-doped solar cell on CZ p-type silicon”. *Proceedings of the 35th IEEE Photovoltaics Specialist Conference, Hawaii*, pp. 689–694, 2010. *Oral presentation.*
33. P. Hamer, S. Wenham, X. Bai, and B. Hallam. “Application of Boron Depletion Techniques to Low Resistivity Silicon for Photovoltaics”. *Proceedings of the 2010 Annual Conference of the Australian Solar Energy Society*, p. 160, 2010. *Oral presentation.*

---

## Patents and Patent Applications

1. B. Hallam, C. Chan, S. Wenham, A. Sugianto, P. Lu, and V. Vais. *Formation of localised molten silicon regions in silicon containing multiple impurity types*. 2013. WO Patent No. 2013/142892 A1.
2. L. Mai, M. Edwards, M. Green, B. Hallam, Z. Hameiri, N. Kuepper, A. Sugianto, B. Tjahjono, S. Wang, A. Wenham, and S. Wenham. *Rear junction solar cell*. 2012. US Patent App. 2012/0048366 A1.
3. S. Wenham, P. Hamer, B. Hallam, A. Sugianto, C. Chan, L. Song, P. Lu, A. Wenham, L. Mai, C. Chong, G. Xu, and M. Edwards. *Advanced hydrogenation of silicon solar cells*. 2013. WO2013173867 A1.
4. Authors withheld. *High concentration doping in silicon*. 2013. Australian Provisional Patent Application No. 2013902773.
5. C. Chan, B. Hallam, A. Wenham, and S. Wenham. *A monolithically integrated solar cell system*. 2013. Australian Provisional Patent Application No. 2013900704.
6. Authors withheld. *Thermal processing in silicon*. 2013. Australian Provisional Patent Application No. 2013902774.

# Bibliography

- [Abbo 05] M. Abbott, P. Cousins, F. Chen, and J. Cotter. “Laser-induced defects in crystalline silicon solar cells”. *Proceedings of the 31st IEEE Photovoltaic Specialists Conference*, pp. 1241–1244, 2005.
- [Abbo 06a] M. D. Abbott, J. E. Cotter, T. Trupke, and R. A. Bardos. “Investigation of edge recombination effects in silicon solar cell structures using photoluminescence”. *Applied Physics Letters*, Vol. 88, p. 114105, 2006.
- [Abbo 06b] M. Abbott. *Advanced laser processing and photoluminescence characterisation of high efficiency silicon solar cells*. PhD thesis, University of New South Wales, 2006.
- [Aber 01] A. Aberle. “Overview on SiN surface passivation of crystalline silicon solar cells”. *Solar Energy Materials and Solar Cells*, Vol. 65, No. 1, pp. 239–248, 2001.
- [Aber 92] A. G. Aberle, S. Glunz, and W. Warta. “Impact of illumination level and oxide parameters on Shockley–Read–Hall recombination at the Si-SiO<sub>2</sub> interface”. *Journal of Applied Physics*, Vol. 71, No. 9, pp. 4422–4431, 1992.
- [Adey 04] J. Adey, R. Jones, D. Palmer, P. Briddon, and S. Öberg. “Degradation of boron-doped Czochralski-grown silicon solar cells”. *Physical review letters*, Vol. 93, No. 5, p. 55504, 2004.
- [Agos 06] G. Agostinelli, A. Delabie, P. Vitanov, Z. Alexieva, H. Dekkers, S. De Wolf, and G. Beaucarne. “Very low surface recombination velocities on p-type silicon wafers passivated with a dielectric with fixed negative charge”. *Solar Energy Materials and Solar Cells*, Vol. 90, No. 18, pp. 3438–3443, 2006.
- [Alda 03] J. Alda. “Laser and Gaussian beam propagation and transformation”. *Optical Engineering*, pp. 999–1013, 2003.
- [Alla 07] G. Allardyce, J. Cahalen, J. Rasch, T. Ridler, O. Weigel, H. Fröhlich, H. Kappler, F. Oberholtzer, C. Rattey, A. Mette, *et al.* “The commercial application of light induced electroplating for improving the efficiency of crystalline silicon solar cells”. *Proceedings of the 22nd European Photovoltaic Solar Energy Conference, Milan*, pp. 1578–1580, 2007.



- 
- [Alte 96] P. Altermatt, G. Heiser, X. Dai, J. Jürgens, A. Aberle, S. Robinson, T. Young, S. Wenham, and M. Green. “Rear surface passivation of high-efficiency silicon solar cells by a floating junction”. *Journal of Applied Physics*, Vol. 80, pp. 3574–3586, 1996.
- [Amet 05] M. Ametowabla, A. Esturo-Breton, J. Kohler, and J. Werner. “Laser processing of crystalline silicon solar cells”. *Proceedings of the 31st IEEE Photovoltaic Specialists Conference*, pp. 1277–1280, 2005.
- [Amet 07] M. Ametowabla, J. Kohler, and A. Esturo-Breton. “Improved laser doping for silicon solar cells”. *Proceedings of the 22nd European Photovoltaic Solar Energy Conference, Milan*, 2007.
- [Aror 96] V. Arora and A. Dawar. “Laser-induced damage studies in silicon and silicon-based photodetectors”. *Applied Optics*, Vol. 35, No. 36, pp. 7061–7065, 1996.
- [Auth 13a] Authors withheld. *High concentration doping in silicon*. 2013. Australian Provisional Patent Application No. 2013902773.
- [Auth 13b] Authors withheld. *Thermal processing in silicon*. 2013. Australian Provisional Patent Application No. 2013902774.
- [Baso 05] P. Basore. “Crystalline silicon on glass device optimization”. *Proceedings of the 31st IEEE Photovoltaic Specialists Conference*, pp. 967–970, 2005.
- [Baso 06] P. Basore. “CSG-1: manufacturing a new polycrystalline silicon PV technology”. *Proceedings of the 4th IEEE World Conference on Photovoltaic Energy Conversion*, Vol. 2, pp. 2089–2093, 2006.
- [Baso 93] P. A. Basore. “Extended spectral analysis of internal quantum efficiency”. *Proceedings of the 23rd IEEE Photovoltaic Specialists Conference*, pp. 147–152, 1993.
- [Baso 96] P. A. Basore and D. A. Clugston. “PC1D version 4 for windows: from analysis to design”. *Proceedings of the 25th IEEE Photovoltaic Specialists Conference*, pp. 377–381, 1996.
- [Bate 11] N. Bateman, P. Sullivan, C. Reichel, J. Benick, and M. Hermle. “High quality ion implanted boron emitters in an interdigitated back contact solar cell with 20% efficiency”. *Energy Procedia*, Vol. 8, pp. 509–514, 2011.
- [Beni 08] J. Benick, B. Hoex, M. van de Sanden, W. Kessels, O. Schultz, and S. Glunz. “High efficiency n-type Si solar cells on Al<sub>2</sub>O<sub>3</sub>-passivated boron emitters”. *Applied Physics Letters*, Vol. 92, p. 253504, 2008.
- [Benn 69] A. Benninghoven. “Analysis of submonolayers on silver by negative secondary ion emission”. *physica status solidi (b)*, Vol. 34, No. 2, pp. K169–K171, 1969.
- [Bent 80] J. Benton, C. Doherty, S. Ferris, D. Flamm, L. Kimerling, and H. Leamy. “Hydrogen passivation of point defects in silicon”. *Applied Physics Letters*, Vol. 36, pp. 670–671, 1980.
- [Bent 88] G. Bentini, M. Bianconi, and C. Summonte. “Surface doping of semiconductors by pulsed-laser
-

## BIBLIOGRAPHY

---

- irradiation in reactive atmosphere”. *Applied Physics A: Materials Science & Processing*, Vol. 45, No. 4, pp. 317–324, 1988.
- [Besu 97] U. Besu-Vetrella, L. Pirozzi, E. Salza, G. Ginocchietti, F. Ferrazza, L. Ventura, A. Slaoui, and J. Muller. “Large area, screen printed silicon solar cells with selective emitter made by laser overdoping and RTA spin-on glasses”. pp. 135–138, 1997.
- [Boeh 00] C. Boehme and G. Lucovsky. “H loss mechanism during anneal of silicon nitride: Chemical dissociation”. *Journal of Applied Physics*, Vol. 88, No. 10, pp. 6055–6059, 2000.
- [Bore 88] J. Borenstein, D. Angell, and J. Corbett. “Influence of Dopant type and Concentration on Hydrogen Diffusion in Silicon”. *MRS Proceedings*, Vol. 138, No. 1, 1988.
- [Bore 93] J. Borenstein, J. Corbett, and S. Pearton. “Kinetic model for hydrogen reactions in boron-doped silicon”. *Journal of Applied Physics*, Vol. 73, No. 6, pp. 2751–2754, 1993.
- [Both 02] K. Bothe, J. Schmidt, and R. Hezel. “Effective reduction of the metastable defect concentration in boron-doped Czochralski silicon for solar cells”. *Proceedings of the 29th IEEE Photovoltaic Specialists Conference*, pp. 194–197, 2002.
- [Both 03] K. Bothe, R. Hezel, and J. Schmidt. “Recombination-enhanced formation of the metastable boron–oxygen complex in crystalline silicon”. *Applied Physics Letters*, Vol. 83, pp. 1125–1127, 2003.
- [Both 05] K. Bothe, R. Sinton, and J. Schmidt. “Fundamental boron–oxygen-related carrier lifetime limit in mono-and multicrystalline silicon”. *Progress in Photovoltaics: Research and Applications*, Vol. 13, No. 4, pp. 287–296, 2005.
- [Both 06] K. Bothe and J. Schmidt. “Electronically activated boron-oxygen-related recombination centers in crystalline silicon”. *Journal of Applied Physics*, Vol. 99, No. 1, pp. 013701–013701, 2006.
- [Bour 00] J. Bourgoin, N. de Angelis, and G. Strobl. “Light Induced Degradation of Si Cells. Model of a Metastable Defect”. *Proceedings of 16th European Photovoltaic Solar Energy Conference, Glasgow*, p. 1356, 2000.
- [Bour 72] J. Bourgoin and J. Corbett. “A new mechanism for interstitial migration”. *Physics Letters A*, Vol. 38, No. 2, pp. 135–137, 1972.
- [Bova 11] J. Bovatsek, A. Sugianto, B. Hallam, B. Tjahjono, S. Wenham, and R. Patel. “High-Speed Fabrication of Laser Doping Selective Emitter Solar Cells Using 532nm Continuous Wave (CW) and Modelocked Quasi-CW Laser Sources”. *Proceedings of the 26th European Photovoltaic Solar Energy Conference, Hamburg*, pp. 895–900, 2011.
- [Bowd 01] S. Bowden and A. Rohatgi. *Rapid and accurate determination of series resistance and fill factor losses in industrial silicon solar cells*. Georgia Institute of Technology, 2001.
- [Brag 08] A. Braga, S. Moreira, P. Zampieri, J. Bacchin, and P. Mei. “New processes for the production of

- solar-grade polycrystalline silicon: A review”. *Solar Energy Materials and Solar Cells*, Vol. 92, No. 4, pp. 418–424, 2008.
- [Brow 10] M. Brown and C. Arnold. “Fundamentals of Laser-Material Interaction and Application to Multiscale Surface Modification”. *Laser Precision Microfabrication*, pp. 91–120, 2010.
- [Camp 87] P. Campbell and M. Green. “Light trapping properties of pyramidally textured surfaces”. *Journal of Applied Physics*, Vol. 62, p. 243, 1987.
- [Capa 99] R. Capaz, L. Assali, L. Kimerling, K. Cho, and J. Joannopoulos. “Mechanism for hydrogen-enhanced oxygen diffusion in silicon”. *Physical Review B*, Vol. 59, No. 7, p. 4898, 1999.
- [Capi 87] M. Capizzi and A. Mittiga. “Hydrogen in crystalline silicon: A deep donor?”. *Applied Physics Letters*, Vol. 50, No. 14, pp. 918–920, 1987.
- [Chad 97] D. Chadi, P. Citrin, C. Park, D. Adler, M. Marcus, and H.-J. Gossmann. “Fermi-Level-Pinning Defects in Highly n-Doped Silicon”. *Physical review letters*, Vol. 79, No. 24, p. 4834, 1997.
- [Chan 12] C. Chan, B. Hallam, and S. Wenham. “Simplified Interdigitated Back Contact Solar Cells”. *Energy Procedia*, Vol. 27, pp. 543–548, 2012.
- [Chan 13a] C. Chan, M. Abbott, M. Juhl, B. Hallam, B. Xiao, and S. Wenham. “Assessing the Performance of Surface Passivation Using Low-Intensity Photoluminescence Characterization Techniques”. *IEEE Journal of Photovoltaics*, Vol. PP, No. 99, pp. 1–7, 2013.
- [Chan 13b] C. Chan, M. Abbott, M. Juhl, B. Hallam, B. Xiao, and S. Wenham. “Assessing the Performance of Surface Passivation Using Low-Intensity Photoluminescence Characterization Techniques”. *Proceedings of the 39th Photovoltaic Specialists Conference, Tampa*, Vol. PP, pp. 1–7, 2013.
- [Chan 13c] C. Chan, B. Hallam, A. Wenham, and S. Wenham. *A monolithically integrated solar cell system*. 2013. Australian Provisional Patent Application No. 2013900704.
- [Chan 15] C. Chan, M. Abbott, B. Hallam, M. Juhl, D. Lin, Z. Li, Y. Li, J. Rodriguez, and S. Wenham. “Edge isolation of solar cells using laser doping”. *Solar Energy Materials and Solar Cells*, Vol. 132, pp. 535–543, 2015.
- [Chen 05a] J. Chen, T. Sekiguchi, R. Xie, P. Ahmet, T. Chikyo, D. Yang, S. Ito, and F. Yin. “Electron-beam-induced current study of small-angle grain boundaries in multicrystalline silicon”. *Scripta materialia*, Vol. 52, No. 12, pp. 1211–1215, 2005.
- [Chen 05b] J. Chen, D. Yang, Z. Xi, and T. Sekiguchi. “Electron-beam-induced current study of hydrogen passivation on grain boundaries in multicrystalline silicon: Influence of GB character and impurity contamination”. *Physica B: Condensed Matter*, Vol. 364, No. 1, pp. 162–169, 2005.
- [Chen 05c] J. Chen, D. Yang, Z. Xi, and T. Sekiguchi. “Recombination activity of  $\Sigma 3$  boundaries in boron-doped multicrystalline silicon: Influence of iron contamination”. *Journal of applied physics*, Vol. 97, No. 3, pp. 033701–033701, 2005.

## BIBLIOGRAPHY

---

- [Chen 07] F. Chen, J. Cotter, M. Abbott, A. Li Tsu-Tsung, and K. Fisher. “The Influence of Parasitic Effects on Injection-Level-Dependent Lifetime Data”. *IEEE Transactions on Electron Devices*, Vol. 54, No. 11, pp. 2960–2968, 2007.
- [Chen 08] F. Chen. *PhD. Thesis - PECVD SiN for n-type Silicon Solar Cells*. University of New South Wales, Australia, 2008.
- [Chen 11] L. Chen, X. Yu, P. Chen, P. Wang, X. Gu, J. Lu, and D. Yang. “Effect of oxygen precipitation on the performance of Czochralski silicon solar cells”. *Solar Energy Materials and Solar Cells*, Vol. 95, No. 11, pp. 3148–3151, 2011.
- [Chen 94] Z. Chen, A. Rohatgi, R. Bell, and J. Kalejs. “Defect passivation in multicrystalline-Si materials by plasma-enhanced chemical vapor deposition of SiO<sub>2</sub>/SiN coatings”. *Applied Physics Letters*, Vol. 65, No. 16, pp. 2078–2080, 1994.
- [Cho 12a] K. Cho, J. Kim, J. Kim, J. Kong, S. Cho, S. Lee, H. Lee, and E. Lee. “Shinsung Solar Energy over 19% Commercial Selective Emitter Solar Cells with Ni/Cu Plated Contact”. *Proceedings of the 27th European Photovoltaic Solar Energy Conference, Frankfurt*, pp. 1494–1497, 2012.
- [Cho 12b] K. Cho, J. Kim, E. Lee, K. Hong, H. Lee, J. Shim, D. Oh, J. Shin, J. Kim, J. Seo, S. Lee, B. Hallam, S. Wenham, and H. Lee. “Shinsung Solar Energy high efficiency commercial crystalline Si solar cells”. *Proceedings of the 38th IEEE Photovoltaic Specialists Conference*, pp. 002145–002148, 2012.
- [Chon 88] C. Chong, S. Wenham, and M. Green. “High-efficiency, laser grooved, buried contact silicon solar cells”. *Applied Physics Letters*, Vol. 52, pp. 407–409, 1988.
- [Chun 03] S. Chunduri. “Be Selective”. *Photon International, November 2009*, pp. 108–116, 2003.
- [Cohe 82] S. Cohen, G. Gildenblat, M. Ghezzi, and D. Brown. “Al-0.9% Si/Si Ohmic Contacts to Shallow Junctions”. *Journal of The Electrochemical Society*, Vol. 129, No. 6, pp. 1335–1338, 1982.
- [Colv 09] F. Colville. “Laser-assisted selective emitters and the role of laser doping”. *Photovoltaics International*, Vol. 5, p. 84, 2009.
- [Conn 11] D. Connolly, H. Lund, B. V. Mathiesen, and M. Leahy. “The first step towards a 100% renewable energy-system for Ireland”. *Applied Energy*, Vol. 88, No. 2, pp. 502–507, 2011.
- [Conw 58] E. Conwell. “Properties of silicon and germanium: II”. *Proceedings of the IRE*, Vol. 46, No. 6, pp. 1281–1300, 1958.
- [Corb 88] J. Corbett, J. Lindström, S. Pearton, and A. Tavendale. “Passivation in silicon”. *Solar cells*, Vol. 24, No. 1, pp. 127–133, 1988.
- [Corb 89] J. Corbett, P. Deák, C. Ortiz-Rodriguez, and L. Snyder. “Embrittlement of materials: Si (H) as a model system”. *Journal of Nuclear Materials*, Vol. 169, pp. 179–184, 1989.
- [Corn 12] E. Cornagliotti, A. Uruena, J. Horzel, J. John, L. Tous, D. Hendrickx, V. Prajapati, S. Singh, R. Hoyer, F. Delahaye, *et al.* “How much rear side polishing is required? A study on the impact

- of rear side polishing in PERC solar cells”. *Proceedings of the 27th European Photovoltaic Solar Energy Conference and Exhibition, Frankfurt*, pp. 561–566, 2012.
- [Corn 13] E. Cornagliotti, L. Tous, A. Urueña, A. Rothschild, R. Russell, V. Lu, S. Radosavjlevic, J. John, J. Toman, M. Aleman, F. Duerinckx, J. Poortmans, J. Szlufcik, B. Dielissen, F. Souren, X. Gay, R. Görtzen, and B. Hallam. “Integration of spatial ALD aluminium oxide for rear side passivation of p-type PERC/PERL solar cells”. *Proceedings of the 28th European Photovoltaic Solar Energy Conference, Paris, France*, pp. 976 – 981, 2013.
- [Corn 14] E. Cornagliotti, L. Tous, A. Urueña, A. Rothschild, R. Russell, V. Lu, S. Radosavjlevic, J. John, J. Toman, M. Aleman, F. Duerinckx, J. Poortmans, J. Szlufcik, B. Dielissen, F. Souren, X. Gay, R. Görtzen, and B. Hallam. “Large Area p-type PERL Cells Featuring Local p+ BSF Formed By Laser Processing of ALD AL<sub>2</sub>O<sub>3</sub> Layers”. *Submitted to Solar Energy Materials and Solar Cells*, Vol. PP, p. 1, 2014.
- [Cous 10] P. Cousins, D. Smith, H.-C. Luan, J. Manning, T. Dennis, A. Waldhauer, K. Wilson, G. Harley, and W. Mulligan. “Generation 3: Improved performance at lower cost”. *Proceedings of the 35th IEEE Photovoltaic Specialists Conference*, pp. 275–278, 2010.
- [Cuev 04] A. Cuevas and D. Macdonald. “Measuring and interpreting the lifetime of silicon wafers”. *Solar Energy*, Vol. 76, No. 1, pp. 255–262, 2004.
- [Cunn 08] D. W. Cunningham, A. Parr, J. Posbic, and B. Poulin. “Performance comparison between BP solar mono and traditional multicrystalline modules”. *Proceedings of the 23rd European Photovoltaic Solar Energy Conference Proceedings, Valencia*, pp. 2829–2833, 2008.
- [Dauw 02a] S. Dauwe, L. Mittelstädt, A. Metz, and R. Hezel. “Experimental evidence of parasitic shunting in silicon nitride rear surface passivated solar cells”. *Progress in Photovoltaics: Research and Applications*, Vol. 10, No. 4, pp. 271–278, 2002.
- [Dauw 02b] S. Dauwe, J. Schmidt, and R. Hezel. “Very low surface recombination velocities on p-and n-type silicon wafers passivated with hydrogenated amorphous silicon films”. *Proceedings of the 29th IEEE Photovoltaic Specialists Conference*, pp. 1246–1249, 2002.
- [Davi 80] J. Davis Jr, A. Rohatgi, R. Hopkins, P. Blais, P. Rai-Choudhury, J. McCormick, and H. Mollenkopf. “Impurities in silicon solar cells”. *IEEE Transactions on Electron Devices*, Vol. 27, No. 4, pp. 677–687, 1980.
- [Davi 96] E. Davis. “Hydrogen in silicon”. *Journal of non-crystalline solids*, Vol. 198, pp. 1–10, 1996.
- [De W 02] S. De Wolf, J. Szlufcik, Y. Delannoy, I. Perichaud, C. Häßler, and R. Einhaus. “Solar cells from upgraded metallurgical grade (UMG) and plasma-purified UMG multi-crystalline silicon substrates”. *Solar Energy Materials and Solar Cells*, Vol. 72, No. 1, pp. 49–58, 2002.
- [DeCe 07] D. DeCeuster, P. Cousins, D. Rose, D. Vicente, P. Tipones, and W. Mulligan. “Low cost, high

- volume production of  $> 22\%$  efficiency silicon solar cells”. *Proceedings of the 22nd European Photovoltaic Solar Energy Conference, Milan*, pp. 816–819, 2007.
- [Drec 13] F. Dreckschmidt, V. Osinniy, M. Herms, and N. J. “Minority Carrier Lifetime and Thermal Donors in n-Type Czochralski Silicon”. *Proceedings of the 28th European Photovoltaic Solar Energy Conference and Exhibition, Paris*, pp. 2056 – 2058, 2013.
- [Du 12] G. Du, B. Chen, N. Chen, and R. Hu. “Efficient boron doping in the back surface field of crystalline silicon solar cells via alloyed-aluminum–boron paste”. *Electron Device Letters, IEEE*, Vol. 33, No. 4, pp. 573–575, 2012.
- [Dube 84] C. Dube, J. Hanoka, and D. Sandstrom. “Hydrogen diffusion along passivated grain boundaries in silicon ribbon”. *Applied Physics Letters*, Vol. 44, No. 4, pp. 425–427, 1984.
- [Dubo 12] S. Dubois, F. Tanay, J. Veirman, N. Enjalbert, J. Stendera, S. Butté, P. Pochet, D. Caliste, Y. Mao, D. Timerkaeva, D. Blanc, K. Fraser, M. Lemiti, O. Palais, I. Périchaud, B. Dridi Rezgui, V. Mong-The Yen, M. Pasquinelli, M. Gerard, F. Madon, and N. Le Quang. “The BOLID Project: Suppression of the Boron-Oxygen Related Light-Induced-Degradation”. *Proceedings of the 27th European Photovoltaic Solar Energy Conference, Frankfurt, Germany*, pp. 749–754, 2012.
- [Duer 02] F. Duerinckx and J. Szlufcik. “Defect passivation of industrial multicrystalline solar cells based on PECVD silicon nitride”. *Solar Energy Materials and Solar Cells*, Vol. 72, No. 1, pp. 231–246, 2002.
- [Dull 12] T. Dullweber, M. Siebert, B. Veith, C. Kranz, J. Schmidt, R. Brendel, B. Roos, T. Dippell, A. Schwabedissen, and S. Peters. “High-efficiency industrial-type PERC solar cells applying ICP AlOx as rear passivation layer”. *Proceedings of the 27th European Photovoltaic Solar Energy Conference, Frankfurt, Germany*, pp. 672–675, 2012.
- [Dumb 10] R. Dumbrell, P. Hamer, A. Lennon, and B. Tjahjono. “Emitter Etch-Back Application for Selective Emitter Silicon Solar Cells”. *Proc. 2010 Australian Solar Energy Society Conf., Canberra, Australia*, p. 131, 2010.
- [Durk 79] L. Durkee. *Method of plating by means of light*. 1979. US Patent 4,144,139.
- [Eadi 12] M. Eadie, B. Hallam, O. Kunz, and S. Wenham. “Investigation into the Influence of Process Parameters on the Passivation on Commercial Grade Silicon Solar Cells”. *Proceedings of the 27th European Photovoltaic Solar Energy Conference, Frankfurt, Germany*, pp. 1574–1578, 2012.
- [Einh 06] R. Einhaus, J. Kraiem, F. Cocco, Y. Caratini, D. Bernou, D. Sarti, G. Rey, R. Monna, C. Trassy, J. Degoulange, Y. Delannoy, S. Martinuzzi, I. Périchaud, M. Record, and P. Rivat. “PHOTOSIL–Simplified production of solar silicon from metallurgical silicon”. *Proceedings of the 21st European Solar Energy Conference, Dresden, Germany*, pp. 580–584, 2006.

- 
- [Einh 99] R. Einhaus, F. Duerinckx, E. Van Kerschaver, J. Szlufcik, F. Durand, P. Ribeyron, J. Duby, D. Sarti, G. Goaer, and G. a. Le. “Hydrogen passivation of newly developed EMC-multi-crystalline silicon”. *Materials Science and Engineering: B*, Vol. 58, No. 1, pp. 81–85, 1999.
- [Eise 09] S. Eisele, T. Roder, J. Kohler, and J. Werner. “18.9% efficient full area laser doped silicon solar cell”. *Applied Physics Letters*, Vol. 95, No. 13, pp. 133501–133501, 2009.
- [Elga 98] H. Elgamel, J. Nijs, R. Mertens, M. Mauk, and A. M Barnett. “Hydrogen in polycrystalline silicon solar cell material: Its role and characteristics”. *Solar Energy Materials and Solar Cells*, Vol. 53, No. 3, pp. 277–284, 1998.
- [Elli 12] B. Elliston, M. Diesendorf, and I. MacGill. “Simulations of scenarios with 100% renewable electricity in the Australian National Electricity Market”. *Energy Policy*, Vol. 45, pp. 606–613, 2012.
- [Estr 90] S. Estreicher. “Interstitial O in Si and its interactions with H”. *Physical Review B*, Vol. 41, No. 14, p. 9886, 1990.
- [Fair 68] J. Fairfield. “Silicon diodes made by laser irradiation”. *Solid State Electronics*, Vol. 11, pp. 1175–1176, 1968.
- [Fals 97] R. J. Falster, D. Gambaro, M. Cornara, M. Olmo, and M. Pagani. “Effect of high temperature pre-anneal on oxygen precipitates nucleation kinetics in Si”. *Solid State Phenomena*, Vol. 57, pp. 123–128, 1997.
- [Fell 11] A. Fell, S. Hopman, and F. Granek. “Simulation supported description of the local doping formation using laser chemical processing (LCP)”. *Applied Physics A: Materials Science & Processing*, Vol. 104, No. 1, pp. 165–170, 2011.
- [Fisc 73] H. Fischer and W. Pschunder. “Investigation of photon and thermal induced changes in silicon solar cells”. *Proceedings of the 10th IEEE Photovoltaic Specialists Conference*, p. 404, 1973.
- [Foga 81] E. Fogarassy, R. Stuck, J. Grob, and P. Siffert. “Silicon solar cells realized by laser induced diffusion of vacuum-deposited dopants”. *Journal of Applied Physics*, Vol. 52, No. 2, pp. 1076–1082, 1981.
- [Foga 83] E. Fogarassy, R. Stuck, M. Toulemonde, D. Salles, and P. Siffert. “A model for laser induced diffusion”. *Journal of Applied Physics*, Vol. 54, No. 9, pp. 5059–5063, 1983.
- [Fors 10] M. Forster, E. Fourmond, R. Einhaus, H. Lauvray, J. Kraiem, M. Lemiti, *et al.* “Doping engineering to increase the material yield during crystallization of B and P compensated silicon”. *Proceedings of the 25th European Photovoltaic Solar Energy Conference*, pp. 1250–1253, 2010.
- [Fors 11] M. Forster, E. Fourmond, R. Einhaus, H. Lauvray, J. Kraiem, and M. Lemiti. “Ga co-doping in Cz-grown silicon ingots to overcome limitations of B and P compensated silicon feedstock for PV applications”. *physica status solidi (c)*, Vol. 8, No. 3, pp. 678–681, 2011.
-

## BIBLIOGRAPHY

---

- [Foss 09] S. Foss, H. Scarborough, K. Mangersnes, and J. Mayandi. “Optimisation of laser doped emitters for solar cells”. *Proceedings of the 24th European Photovoltaic Solar Energy Conference*, pp. 1879–1881, 2009.
- [Free 77] P. Freeland, K. Jackson, C. Lowe, and J. Patel. “Precipitation of oxygen in silicon”. *Applied Physics Letters*, Vol. 30, No. 1, pp. 31–33, 1977.
- [Fuji 06] K. Fujiwara, W. Pan, N. Usami, K. Sawada, M. Tokairin, Y. Nose, A. Nomura, T. Shishido, and K. Nakajima. “Growth of structure-controlled polycrystalline silicon ingots for solar cells by casting”. *Acta Materialia*, Vol. 54, No. 12, pp. 3191–3197, 2006.
- [Gall 12a] S. Gall, B. Paviet-Salomon, J. Lerat, and T. Emeraud. “High Quality Passivation Scheme Combined with Laser Doping from SiN: P and SiN: B Layer for Silicon Solar Cell”. *Energy Procedia*, Vol. 27, pp. 467–473, 2012.
- [Gall 12b] S. Gall, B. Paviet-Salomon, J. Lerat, and T. Emeraud. “Laser Doping Strategies Using SiN: P and SiN: B Dielectric Layers for Profile Engineering in High Efficiency Solar Cell”. *Energy Procedia*, Vol. 27, pp. 449–454, 2012.
- [Gara 07] J. Garandet. “New determinations of diffusion coefficients for various dopants in liquid silicon”. *International Journal of Thermophysics*, Vol. 28, No. 4, pp. 1285–1303, 2007.
- [Gatz 11] S. Gatz, H. Hannebauer, R. Hesse, F. Werner, A. Schmidt, T. Dullweber, J. Schmidt, K. Bothe, and R. Brendel. “19.4%-efficient large-area fully screen-printed silicon solar cells”. *physica status solidi (RRL)-Rapid Research Letters*, Vol. 5, No. 4, pp. 147–149, 2011.
- [Geer 03] L. Geerligs, A. Azzizi, D. Macdonald, and P. Manshanden. *Hydrogen passivation of iron in multicrystalline silicon*. Energy Research Centre of the Netherlands, 2003.
- [Ghan 91] M. Ghannam. “A new  $n^+pn^+$  structure with back side floating junction for high efficiency silicon solar cells”. *Proceedings of the 22nd IEEE Photovoltaic Specialists Conference*, pp. 284–289, 1991.
- [Glnu 00a] S. Glunz, R. Preu, S. Schaefer, E. Schneiderlochner, W. Pfleging, R. Ludemann, and G. Willeke. “New simplified methods for patterning the rear contact of RP-PERC high-efficiency solar cells”. *Proceedings of the 28th IEEE Photovoltaic Specialists Conference*, pp. 168–171, 2000.
- [Glnu 00b] S. Glunz, S. Rein, J. Knobloch, W. Wettling, and T. Abe. “Comparison of boron-and gallium-doped p-type Czochralski silicon for photovoltaic application”. *Progress in photovoltaics: Research and Applications*, Vol. 7, No. 6, pp. 463–469, 2000.
- [Glnu 01a] S. Glunz, S. Rein, J. Lee, and W. Warta. “Minority carrier lifetime degradation in boron-doped Czochralski silicon”. *Journal of Applied Physics*, Vol. 90, p. 2397, 2001.
- [Glnu 01b] S. Glunz, S. Rein, W. Warta, J. Knobloch, and W. Wettling. “Degradation of carrier lifetime in Cz silicon solar cells”. *Solar Energy Materials and Solar Cells*, Vol. 65, No. 1, pp. 219–229, 2001.



- [Gold 03] J. Goldstein, D. E. Newbury, D. Joy, and C. Lyman. *Scanning electron microscopy and x-ray microanalysis*. Springer, New York, USA, 2003.
- [Graf 81] K. Graff and H. Pieper. “The properties of iron in silicon”. *Journal of the Electrochemical Society*, Vol. 128, p. 669, 1981.
- [Gree 04] M. Green, P. Basore, N. Chang, D. Clugston, R. Egan, R. Evans, D. Hogg, S. Jarnason, M. Keevers, P. Lasswell, J. O’Sullivan, U. Schubert, A. Turner, S. Wenham, and T. Young. “Crystalline silicon on glass (CSG) thin-film solar cell modules”. *Solar Energy*, Vol. 77, No. 6, pp. 857 – 863, 2004.
- [Gree 09] M. Green. “The path to 25% silicon solar cell efficiency: history of silicon cell evolution”. *Progress in Photovoltaics: Research and Applications*, Vol. 17, No. 3, pp. 183–189, 2009.
- [Gree 11] M. Green, K. Emery, Y. Hishikawa, and W. Warta. “Solar cell efficiency tables (version 37)”. *Progress in Photovoltaics: Research and Applications*, Vol. 19, pp. 82–84, 2011.
- [Gree 81] M. A. Green. “Solar cell fill factors: General graph and empirical expressions”. *Solid-State Electronics*, Vol. 24, No. 8, pp. 788–789, 1981.
- [Gree 95] M. A. Green. *Silicon Solar Cells: Advanced Principles and Practice*. Centre for Photovoltaic Devices and Systems, Sydney, 1995.
- [Grig 97] C. Grigoropoulos, P. Baumgart, and A. Tarn. “Marangoni mechanism in pulsed laser texturing of magnetic disk substrates”. *Journal of Heat Transfer*, Vol. 119, p. 589, 1997.
- [Grov 67] A. Grove. *Physics and technology of semiconductor devices*. Vol. 143, Wiley New York, 1967.
- [Gu 12] X. Gu, X. Yu, K. Guo, L. Chen, D. Wang, and D. Yang. “Seed-assisted cast quasi-single crystalline silicon for photovoltaic application: Towards high efficiency and low cost silicon solar cells”. *Solar Energy Materials and Solar Cells*, Vol. 101, pp. 95–101, 2012.
- [Guer 12] I. Guerrero, V. Parra, T. Carballo, A. Black, M. Miranda, D. Cancillo, B. Moralejo, J. Jiménez, J.-F. Lelièvre, and C. Cañizo. “About the origin of low wafer performance and crystal defect generation on seed-cast growth of industrial mono-like silicon ingots”. *Progress in Photovoltaics: Research and Applications* doi=10.1002/pip.2344, 2012.
- [Hall 10a] B. Hallam, A. Sugianto, B. Tjahjono, N. Kuepper, N. Western, G. Xu, and S. Wenham. “Deep junction formation for silicon solar cells through the use of laser doping”. *Proceedings of the 2010 Annual Conference of the Australian Solar Energy Society*, p. 136, 2010.
- [Hall 10b] B. Hallam, N. Western, and S. Wenham. “Large increase in bulk lifetime of commercial grade CZ silicon wafers through hydrogenation”. *Proceedings of the 2010 Annual Conference of the Australian Solar Energy Society*, pp. 160–166, 2010.
- [Hall 11a] B. Hallam, S. Wenham, C. M. Chong, A. Sugianto, L. Mai, M. Edwards, D. Jordan, and P. Fath. “Record large area P-type CZ production cell efficiency of 19.3% based on LDSE technology”. *Proceedings of the 37th IEEE Photovoltaic Specialists Conference, Seattle*, pp. 47–47, 2011.

## BIBLIOGRAPHY

---

- [Hall 11b] B. Hallam, S. Wenham, M. Edwards, H. S. Lee, E. Lee, H. W. Lee, J. Kim, and J. Shin. “Record Industrial Cell Efficiency Fabricated on Commercial Grade P-Type CZ Substrates”. *Proceedings of the 21st IEEE Photovoltaic Science and Engineering Conference, Fukuoka*, 2011.
- [Hall 11c] B. Hallam, S. Wenham, H. Lee, E. Lee, H. Lee, J. Kim, and J. Shin. “Effect of edge junction isolation on the performance of laser doped selective emitter solar cells”. *Solar Energy Materials and Solar Cells*, Vol. 95, No. 12, pp. 3557–3563, 2011.
- [Hall 11d] B. Hallam, S. Wenham, A. Sugianto, L. Mai, C. Chong, M. Edwards, D. Jordan, and P. Fath. “Record Large Area P-type CZ Production Cell Efficiency of 19.3% Based on LDSE Technology”. *IEEE Journal of Photovoltaics*, Vol. 1, pp. 43–48, 2011.
- [Hall 12a] B. Hallam, C. Chan, M. Eadie, P. Hamer, A. Sugianto, S. Wenham, K. Casalenuovo, J. Kraiem, D. Degoulangue, R. Einhaus, and Z. Shi. “High Quality Passivation for p-Type CZ UMG Silicon Wafers”. *Proceedings of the 27th European Photovoltaic Solar Energy Conference, Frankfurt, Germany*, pp. 1942 – 1945, 2012.
- [Hall 12b] B. Hallam, B. Tjahjono, and S. Wenham. “Effect of PECVD silicon oxynitride film composition on the surface passivation of silicon wafers”. *Solar Energy Materials and Solar Cells*, Vol. 96, pp. 173 – 179, 2012.
- [Hall 12c] B. Hallam, S. Wenham, H. Lee, E. Lee, H. Lee, J. Kim, J. Shin, K. Cho, and J. Kim. “Record Efficiency on Large Area P-Type Czochralski Silicon Substrates”. *Japanese Journal of Applied Physics*, Vol. 51, No. 10, p. 10NA08, 2012.
- [Hall 13a] B. Hallam, C. Chan, S. Wenham, A. Sugianto, P. Lu, and V. Vais. *Formation of localised molten silicon regions in silicon containing multiple impurity types*. 2013. WO Patent No. 2013/142892 A1.
- [Hall 13b] B. Hallam, S. Wenham, P. Hamer, M. Abbott, A. Sugianto, C. Chan, A. Wenham, M. Eadie, and G. Xu. “Hydrogen passivation of B-O defects in Czochralski silicon”. *Energy Procedia*, Vol. 38, pp. 561–570, 2013.
- [Hall 13c] B. Hallam, P. Hamer, S. Wenham, M. Abbott, A. Sugianto, A. Wenham, C. Chan, G. Xu, J. Kraiem, J. Degoulangue, and R. Einhaus. “Advanced Bulk Defect Passivation for Silicon Solar Cells”. *Proceedings of the 39th IEEE Photovoltaic Specialists Conference, Tampa*, Vol. PP, pp. 1–8, 2013.
- [Hall 13d] B. Hallam, C. Chan, A. Sugianto, and S. Wenham. “Deep junction laser doping for contacting buried layers in silicon solar cells”. *Solar Energy Materials and Solar Cells*, Vol. 113, pp. 124–134, 2013.
- [Hall 14a] B. Hallam, P. Hamer, S. Wang, M. Abbott, A. Wenham, C. Chan, and S. Wenham. “Hydrogen Passivation for Commercial CZ Silicon Wafers and Solar Cells”. *24th Workshop on Crystalline Silicon Solar Cells & Modules*, Vol. PP, p. 1, 2014.

- 
- [Hall 14b] B. Hallam, W. S., A. Wenham, P. Hamer, C. Chan, M. Abbott, and S. Wenham. “Hydrogen passivation for highly defected commercial grade n-type CZ wafers and oxidation-induced stacking faults”. *29th European Photovoltaic Solar Energy Conference, Amsterdam*, Vol. 1, pp. 608–611, 2014.
- [Hall 14c] B. Hallam, A. Sugianto, L. Mai, G. Xu, C. Chan, M. Abbott, S. Wenham, A. Uruena, E. Cornagliotti, and M. Aleman. “Hydrogen Passivation of Laser-Induced Defects for Laser-Doped Silicon Solar Cells”. *Photovoltaics, IEEE Journal of*, Vol. 4, No. 6, pp. 1413–1420, Nov 2014.
- [Hall 14d] B. Hallam, A. Urueña, R. Russell, M. Aleman, M. Abbott, C. Dang, S. Wenham, L. Tous, and J. Poortmans. “Efficiency enhancement of i-PERC solar cells by implementation of a laser doped selective emitter”. *Submitted to Solar Energy Materials and Solar Cells*, Vol. PP, p. 1, 2014.
- [Hall 14e] B. Hallam, S. Wang, M. Abbott, A. Wenham, C. Chan, P. Hamer, M. Eadie, and S. Wenham. “Hydrogen passivation for multi-crystalline and quasi-mono cast silicon wafers - A pathway to low cost, high efficiency solar cells?”. *29th European Photovoltaic Solar Energy Conference, Amsterdam*, Vol. 1, pp. 1292–1295, 2014.
- [Hall 14f] B. Hallam, P. Hamer, S. Wenham, M. Abbott, A. Sugianto, A. Wenham, C. Chan, G. Xu, J. Kraiem, J. Degoulange, and R. Einhaus. “Advanced Bulk Defect Passivation for Silicon Solar Cells”. *IEEE Journal of Photovoltaics*, Vol. 4, No. 1, pp. 88–95, Jan 2014.
- [Hall 14g] B. Hallam, A. Sugianto, L. Mai, G. Xu, C. Chan, M. Abbott, S. Wenham, A. Uruena, M. Aleman, and J. Poortmans. “Hydrogen Passivation of Laser-Induced Defects for Silicon Solar Cells”. *40th IEEE Photovoltaic Specialists Conference, Denver*, Vol. PP, p. 1, 2014.
- [Hall 14h] B. Hallam, B. Tjahjono, T. Trupke, and S. Wenham. “Photoluminescence imaging for determining the spatially resolved implied open circuit voltage of silicon solar cells”. *Journal of Applied Physics*, Vol. 115, No. 4, p. 044901, 2014.
- [Hall 52] R. N. Hall. “Electron-hole recombination in germanium”. *Physical Review*, Vol. 87, No. 2, p. 387, 1952.
- [Hame 10] P. Hamer, S. Wenham, X. Bai, and B. Hallam. “Application of Boron Depletion Techniques to Low Resistivity Silicon for Photovoltaics”. *Proceedings of the 2010 Annual Conference of the Australian Solar Energy Society*, p. 160, 2010.
- [Hame 11a] Z. Hameiri, N. Gao, B. Hallam, R. Sinton, J. Weber, and T. Trupke. “Effective Doping Density Obtained from Combined Photoconductance and Photoluminescence Measurements”. *Proceedings from the 26th European Photovoltaic and Solar Energy Conference, Hamburg, Germany*, pp. 117–121, 2011.
- [Hame 11b] Z. Hameiri, T. Puzzer, L. Mai, A. Sproul, and S. Wenham. “Laser induced defects in laser doped
-

## BIBLIOGRAPHY

---

- solar cells”. *Progress in Photovoltaics: Research and Applications*, Vol. 19, No. 4, pp. 391–405, 2011.
- [Hame 13] P. Hamer, B. Hallam, C. Chan, A. Wenham, A. Sugianto, M. Abbott, and S. Wenham. “Hydrogen passivation mechanisms in silicon solar cells”. *Proceedings of the 28th European Photovoltaic Solar Energy Conference, Paris, France*, pp. 982–987, 2013.
- [Hame 14] P. Hamer, B. Hallam, S. Wenham, and M. Abbott. “Manipulation of Hydrogen Charge States for Passivation of p-type Wafers in Photovoltaics”. *IEEE Journal of Photovoltaics*, Vol. 4, No. 5, pp. 1252–1260, 2014.
- [Hans 84] W. Hansen, S. Pearton, and E. Haller. “Bulk acceptor compensation produced in p-type silicon at near-ambient temperatures by a H<sub>2</sub>O plasma”. *Applied Physics Letters*, Vol. 44, No. 6, pp. 606–608, 1984.
- [Hard 08] N. Harder and R. Mertens, V. Brendel. “Buried emitter solar cell structures: Decoupling of metallisation geometry and carrier collection geometry of back contacted solar cells”. *physica status solidi (RRL) Rapid Research Letters*, Vol. 2, No. 4, pp. 148–150, 2008.
- [Hard 09] N. Harder, V. Mertens, and R. Brendel. “Numerical simulations of buried emitter back-junction solar cells”. *Progress in Photovoltaics: Research and Applications*, Vol. 17, No. 4, pp. 253–263, 2009.
- [Hard 13] N.-P. Harder, Y. Larionova, and R. Brendel. “Al<sup>+</sup>-doping of Si by laser ablation of Al<sub>2</sub>O<sub>3</sub>/SiN passivation”. *physica status solidi (a)*, Vol. 210, No. 9, pp. 1871–1873, 2013.
- [Haun 10] J. Haunschild, M. Glatthaar, M. Demant, J. Nievendick, M. Motzko, S. Rein, and E. Weber. “Quality control of as-cut multicrystalline silicon wafers using photoluminescence imaging for solar cell production”. *Solar Energy Materials and Solar Cells*, Vol. 94, No. 12, pp. 2007–2012, 2010.
- [Haun 11a] J. Haunschild, J. Broisch, I. Reis, and S. Rein. “Quality control of czochralski grown silicon wafers in solar cell production using photoluminescence imaging”. *Proc 26th EU PVSEC*, pp. 5–9, 2011.
- [Haun 11b] J. Haunschild, I. E. Reis, J. Geilker, and S. Rein. “Detecting efficiency-limiting defects in Czochralski-grown silicon wafers in solar cell production using photoluminescence imaging”. *physica status solidi (RRL)-Rapid Research Letters*, Vol. 5, No. 5-6, pp. 199–201, 2011.
- [Henn 12] L. Hennen, E. Granneman, and W. Kessels. “Analysis of blister formation in spatial ALD Al<sub>2</sub>O<sub>3</sub> for silicon surface passivation”. *Proceedings of the 38th IEEE Photovoltaic Specialists Conference, 2012*, pp. 001049–001054, 2012.
- [Herg 06] A. Herguth, G. Schubert, M. Käs, and G. Hahn. “A new approach to prevent the negative impact of the metastable defect in boron doped Cz silicon solar cells”. *Proceedings of the 4th IEEE World Conference on Photovoltaic Energy Conversion*, Vol. 1, pp. 940–943, 2006.

- 
- [Herg 08] A. Herguth, G. Schubert, M. Käs, and G. Hahn. “Investigations on the long time behavior of the metastable boron–oxygen complex in crystalline silicon”. *Progress in Photovoltaics: Research and Applications*, Vol. 16, No. 2, pp. 135–140, 2008.
- [Herg 09] A. Herguth and G. Hahn. “Boron-oxygen related defects in Cz-silicon solar cells degradation, regeneration and beyond”. *Proceedings of the 24th European Photovoltaic Solar Energy Conference, Hamburg, Germany*, pp. 974–976, 2009.
- [Herg 10] A. Herguth and G. Hahn. “Kinetics of the boron-oxygen related defect in theory and experiment”. *Journal of Applied Physics*, Vol. 108, No. 11, pp. 114509–114509, 2010.
- [Herr 01] C. Herring, N. Johnson, and C. Van de Walle. “Energy levels of isolated interstitial hydrogen in silicon”. *Physical Review B*, Vol. 64, No. 12, p. 125209, 2001.
- [Heze 89] R. Hezel and K. Jaeger. “Low-temperature surface passivation of silicon for solar cells”. *Journal of the Electrochemical Society*, Vol. 136, No. 2, pp. 518–523, 1989.
- [Hira 09] K. Hirata, A. Ogane, T. Saitoh, A. Kitiyanan, E. Sugimura, and T. Fuyuki. “Optimization of CW laser doping in crystalline silicon solar cell fabrication process”. *Proceedings of the 24th European Photovoltaic Solar Energy Conference, Hamburg, Germany*, pp. 1708 – 1711, 2009.
- [Ho 04] A. W. Y. Ho and S. R. Wenham. “Buried contact solar cells with innovative rear localised contacts”. *Progress in Photovoltaics: Research and Applications*, Vol. 12, No. 4, pp. 297–308, 2004.
- [Hofm 08] M. Hofmann, D. Erath, L. Gautero, J. Nekarda, A. Grohe, D. Biro, J. Rentsch, and B. Bitnar. “Industrial type CZ silicon solar cells with screen-printed fine line front contacts and passivated rear contacted by laser firing”. *Proceedings of the 23rd European Photovoltaic Solar Energy Conference, Valencia*, pp. 1704–1707, 2008.
- [Holm 14] Z. C. Holman, M. Filipič, B. Lipovšek, S. De Wolf, F. Smole, M. Topič, and C. Ballif. “Parasitic absorption in the rear reflector of a silicon solar cell: simulation and measurement of the sub-bandgap reflectance for common dielectric/metal reflectors”. *Solar Energy Materials and Solar Cells*, Vol. 120, pp. 426–430, 2014.
- [Hong 03] J. Hong, W. Kessels, W. Soppe, A. Weeber, W. Arnoldbik, and M. Van de Sanden. “Influence of the high-temperature Al firing step on high-rate plasma deposited silicon nitride films used as bulk passivating antireflection coatings on silicon solar cells”. *Journal of Vacuum Science & Technology B: Microelectronics and Nanometer Structures*, Vol. 21, No. 5, pp. 2123–2132, 2003.
- [Hopm 09] S. Hopman, A. Fell, K. Mayer, C. Fleischmann, K. Drew, D. Kray, and F. Granek. “Study on laser parameters for silicon solar cells with LCP selective emitters”. *Proceedings of the 24th European Photovoltaic Solar Energy Conference, Hamburg*, pp. 1072–1076, 2009.
- [Horz 12] J. Horzel, P. Choulat, E. Cornagliotti, T. Janssens, J. John, I. Kuzma Filipek, V. Prajapati, A. Rothschild, R. Russell, S. Singh, E. Sleetx, L. Tous, A. Uruena De Castro, B. Ver-
-

## BIBLIOGRAPHY

---

- mang, M. Ngamo, P. Jaffrennou, J. Penaud, F. Duerinckx, A. Cacciato, and J. Poortmans. “Overview on Recent Improvement for Industrially Applicable PERL-Type Si Solar Cell Processing”. *Proceedings of the 27th European Photovoltaic Solar Energy Conference, Frankfurt, Germany*, pp. 1602–1608, 2012.
- [Hosh 80] K. Hoshikawa, H. Kohda, H. Hirata, and H. Nakanishi. “Low Oxygen Content Czochralski Silicon Crystal Growth”. *Japanese Journal of Applied Physics*, Vol. 19, No. 1, pp. 33–36, 1980.
- [Hosh 85] K. Hoshi, N. Isawa, T. Suzuki, and Y. Ohkubo. “Czochralski silicon crystals grown in a transverse magnetic field”. *Journal of The Electrochemical Society*, Vol. 132, No. 3, pp. 693–700, 1985.
- [Hu 83] S. Hu, P. Fahey, and R. Dutton. “On models of phosphorus diffusion in silicon”. *Journal Applied Physics*, Vol. 54, No. 12, pp. 6912–6922, 1983.
- [Hurk 92] G. Hurkx, D. Klaassen, and M. Knuvers. “A new recombination model for device simulation including tunneling”. *IEEE Transactions on Electron Devices*, Vol. 39, No. 2, pp. 331–338, 1992.
- [Ichi 68] T. Ichimiya and A. Furuichi. “On the solubility and diffusion coefficient of tritium in single crystals of silicon”. *The International Journal of Applied Radiation and Isotopes*, Vol. 19, No. 7, pp. 573–578, 1968.
- [IEA 13] IEA. *World Energy Outlook 2013- Renewable Energy Outlook*. International Energy Agency, IEA-OECD, 2013.
- [IPCC 13] IPCC. *Intergovernmental Panel on Climate Change (IPCC) Fifth Assessment Report (AR5)*. Intergovernmental Panel on Climate Change, 2013.
- [Istr 03] A. Istratov, T. Buonassisi, R. McDonald, A. Smith, R. Schindler, J. Rand, J. Kalejs, and E. Weber. “Metal content of multicrystalline silicon for solar cells and its impact on minority carrier diffusion length”. *Journal of Applied Physics*, Vol. 94, p. 6552, 2003.
- [ITRP 11] ITRPV Working Group and others. “International Technology Roadmap for Photovoltaics (ITRPV.net): Results 2010”. *ITRPV: Germany*, Vol. 15, 2011.
- [Jack 92] W. Jackson, N. Johnson, C. Tsai, I. Wu, A. Chiang, and D. Smith. “Hydrogen diffusion in polycrystalline silicon thin films”. *Applied Physics Letters*, Vol. 61, No. 14, pp. 1670–1672, 1992.
- [Jaeg 09] U. Jaeger, M. Okanovic, M. Hörteis, A. Grohe, and R. Preu. “Selective emitter by laser doping from phosphosilicate glass”. *Proceedings of the 24th European Photovoltaic Solar Energy Conference*, pp. 1740–1743, 2009.
- [Jell 87] G. Jellison and D. Lowndes. “Measurements of the optical properties of liquid silicon and germanium using nanosecond time-resolved ellipsometry”. *Applied Physics Letters*, Vol. 51, No. 5, pp. 352–354, 1987.

- 
- [Jeng 88] S. Jeng, G. Oehrlein, and G. Scilla. “Hydrogen plasma induced defects in silicon”. *Applied Physics Letters*, Vol. 53, No. 18, pp. 1735–1737, 1988.
- [Ji 09] J. Ji, Z. Shi, and Y. Qin. *A method for Processing a Semiconductor Substrate Surface and a Chemical Processing Device for the Semiconductor Substrate Surface*. 2009. WO Patent No. 2009/009,931.
- [Jian 03] F. Jiang, M. Stavola, A. Rohatgi, D. Kim, J. Holt, H. Atwater, and J. Kalejs. “Hydrogenation of Si from SiNx:H films: Characterization of H introduced into the Si”. *Applied Physics Letters*, Vol. 83, No. 5, pp. 931–933, 2003.
- [Job 98] R. Job, W. Fahrner, N. Kazuchits, and A. Ulyashin. “A Two-Step Low-Temperature Process For A PN Junction Formation Due To Hydrogen Enhanced Thermal Donor Formation In P-Type Czochralski Silicon”. *MRS Proceedings*, Vol. 513, No. 1, p. 337, 1998.
- [John 85] N. Johnson and M. Moyer. “Absence of oxygen diffusion during hydrogen passivation of shallow-acceptor impurities in single-crystal silicon”. *Applied Physics Letters*, Vol. 46, No. 8, pp. 787–789, 1985.
- [John 86] N. Johnson, C. Herring, and D. Chadi. “Interstitial hydrogen and neutralization of shallow-donor impurities in single-crystal silicon”. *Physical review letters*, Vol. 56, No. 7, pp. 769–772, 1986.
- [John 91] N. Johnson, C. Doland, F. Ponce, J. Walker, and G. Anderson. “Hydrogen in crystalline semiconductors: A review of experimental results”. *Physica B: Condensed Matter*, Vol. 170, No. 1, pp. 3–20, 1991.
- [John 92] N. Johnson and C. Herring. “Diffusion of negatively charged hydrogen in silicon”. *Physical Review B*, Vol. 46, No. 23, p. 15554, 1992.
- [Jour 08] J. Jourdan, Y. Veschetti, S. Dubois, T. Desrues, and R. Monna. “Formation of Boron-doped region using spin-on dopant: investigation on the impact of metallic impurities”. *Progress in Photovoltaics: Research and Applications*, Vol. 16, No. 5, pp. 379–387, 2008.
- [Jung 11] J. Junge, A. Herguth, G. Hahn, D. Kreßner-Kiel, and R. Zierer. “Investigation of degradation in solar cells from different mc-Si materials”. *Energy Procedia*, Vol. 8, pp. 52–57, 2011.
- [Kamp 08] H. Kampwerth, T. Trupke, J. Weber, and Y. Augarten. “Advanced luminescence based effective series resistance imaging of silicon solar cells”. *Applied Physics Letters*, Vol. 93, p. 202102, 2008.
- [Kann 08] H. Kanno, D. Ide, Y. Tsunomura, S. Taira, T. Baba, Y. Yoshimine, M. Taguchi, T. Kinoshita, H. Sakata, and E. Maruyama. “Over 22% efficient HIT solar cell”. *Proceedings of the 23rd EU-PVSEC, Valencia*, pp. 1136–1139, 2008.
- [Karz 09] P. Karzel, J. Junge, and G. Hahn. “Mapping of hydrogen bond energies in EFG silicon samples by analysis of spatially resolved minority charge carrier lifetimes after annealing steps”.
-

- Proceedings of the 24th European Photovoltaic Solar Energy Conference, Hamburg, Germany*, pp. 2023 – 2027, 2009.
- [Kerr 02] M. J. Kerr and A. Cuevas. “General parameterization of Auger recombination in crystalline silicon”. *Journal of Applied Physics*, Vol. 91, No. 4, pp. 2473–2480, 2002.
- [Kim 11] J.-S. Kim, H.-W. Lee, J.-E. Shin, E.-J. Lee, J.-Y. Choi, J.-M. Shim, D.-J. Oh, K.-Y. Cho, J. hyun Kong, J. keun Seo, J. soo Kim, S.-H. Lee, H.-S. Lee, B. Hallam, and S. Wenham. “Improved front side metallization for laser doped solar cells”. *Proceedings of the 37th IEEE Photovoltaic Specialists Conference, Seattle*, pp. 1091–1094, 2011.
- [Kim 12] J. Kim, K. Cho, E. Lee, K. Hong, H. Lee, J. Shim, D. Oh, J. Shin, J. Kim, J. Seo, S. Lee, B. Hallam, S. Wenham, and H. Lee. “The effect of emitter diffusion formation methods for laser doped selective emitter silicon solar cells”. *Proceedings of the 38th IEEE Photovoltaic Specialists Conference*, pp. 002178–002181, 2012.
- [King 90] R. King, R. Sinton, and R. Swanson. “Studies of diffused phosphorus emitters: saturation current, surface recombination velocity, and quantum efficiency”. *IEEE Transactions on Electron Devices*, Vol. 37, No. 2, pp. 365–371, 1990.
- [Kish 79] S. Kishino, M. Kanamori, N. Yoshihiro, M. Tajima, and T. Iizuka. “Heat-treatment behavior of microdefects and residual impurities in CZ silicon crystals”. *Journal of Applied Physics*, Vol. 50, No. 12, pp. 8240–8243, 1979.
- [Klee 06] S. Kleekajai, F. Jiang, M. Stavola, V. Yelundur, K. Nakayashiki, A. Rohatgi, G. Hahn, S. Seren, and J. Kalejs. “Concentration and penetration depth of H introduced into crystalline Si by hydrogenation methods used to fabricate solar cells”. *Journal of applied physics*, Vol. 100, No. 9, pp. 093517–093517, 2006.
- [Knob 95] J. Knobloch, S. Glunz, V. Henninger, W. Warta, W. Wettling, F. Schomann, W. Schmidt, A. Endros, and K. Münzer. “21% efficient solar cells processed from Czochralski grown silicon”. *Proceedings of the 13th European Photovoltaic Solar Energy Conference*, pp. 9–12, 1995.
- [Knob 96] J. Knobloch, S. Glunz, D. Biro, W. Warta, E. Schaffer, and W. Wettling. “Solar cells with efficiencies above 21% processed from Czochralski grown silicon”. *Proceedings of the 25th IEEE Photovoltaic Specialists Conference*, pp. 405–408, 1996.
- [Kohl 09] J. Köhler, P. Grabitz, S. Eisele, T. Röder, and J. Werner. “Laser doped selective emitters yield 0.5% efficiency gain”. *Proceedings of the 24th European Photovoltaic Solar Energy Conference, Hamburg, Germany*, pp. 1847–1850, 2009.
- [Krai 09] R. Krain, S. Herlufsen, and J. Schmidt. “Low-temperature gettering of iron in mono- and multicrystalline silicon”. *Proceedings of the 24th European Photovoltaic Solar Energy Conference*, pp. 965–968, 2009.



- 
- [Kray 05] D. Kray, S. Baumann, K. Mayer, A. Eyer, and G. Willeke. “Novel techniques for low-damage microstructuring of silicon”. *Proceedings of the 20th European Photovoltaic Solar Energy Conference*, pp. 156–159, 2005.
- [Kray 08a] D. Kray, M. Aleman, A. Fell, S. Hopman, K. Mayer, M. Mesec, R. Muller, G. Willeke, S. Glunz, and B. Bitnar. “Laser-doped silicon solar cells by laser chemical processing (LCP) exceeding 20% efficiency”. *Proceedings of the 33rd IEEE Photovoltaic Specialists Conference*, pp. 1–3, 2008.
- [Kray 08b] D. Kray, A. Fell, S. Hopman, K. Mayer, G. Willeke, and S. Glunz. “Laser chemical processing (LCP) A versatile tool for microstructuring applications”. *Applied Physics A: Materials Science & Processing*, Vol. 93, No. 1, pp. 99–103, 2008.
- [Kray 10a] D. Kray, N. Bay, G. Cimiotti, S. Kleinschmidt, N. Kösterke, A. Lösel, O. Lühn, M. Sailer, A. Träger, H. Kühnlein, *et al.* “High-efficiency large area industrial LCP selective emitter solar cells ready for production”. *Proceedings of the 25th European Photovoltaic Solar Energy Conference*, pp. 1896–1898, 2010.
- [Kray 10b] D. Kray, N. Bay, G. Cimiotti, S. Kleinschmidt, N. Kösterke, A. Lösel, M. Sailer, A. Träger, H. Kühnlein, H. Nussbaumer, *et al.* “Industrial LCP selective emitter solar cells with plated contacts”. *Proceedings of the 35th IEEE Photovoltaic Specialists Conference*, pp. 000667–000671, 2010.
- [Krug 11] G. Krugel, W. Wolke, J. Geilker, S. Rein, and R. Preu. “Impact of Hydrogen Concentration on the Regeneration of Light Induced Degradation”. *Energy Procedia*, Vol. 8, pp. 47–51, 2011.
- [Kyeo 12] D. Kyeong, S. Cho, J. Lim, K. Lee, M. Hwang, W. Lee, and E. Cho. “Approaching 20% efficient selective-emitter solar cells with copper front contacts on industrial 156 mm CZ Si wafers”. *Proceedings of the 27th European Photovoltaic Solar Energy Conference, Frankfurt, Germany*, pp. 600 – 603, 2012.
- [Lan 12] C. Lan, W. Lan, T. Lee, A. Yu, Y. Yang, W. Hsu, B. Hsu, and A. Yang. “Grain control in directional solidification of photovoltaic silicon”. *Journal of Crystal Growth*, Vol. 360, pp. 68–75, 2012.
- [Laue 09] T. Lauermann, A. Dastgheib-Shirazi, F. Book, B. Raabe, G. Hahn, H. Haverkamp, D. Habermann, C. Demberger, and C. Schmid. “InSECT : an inline selective emitter concept with high efficiencies at competitive process costs improved with inkjet masking technology”. *Proceedings of the 24th European Photovoltaic Solar Energy Conference, Hamburg*, 2009.
- [Leam 82] H. Leamy. “Charge collection scanning electron microscopy”. *Journal of Applied Physics*, Vol. 53, No. 6, pp. R51–R80, 1982.
- [Lee 01] Y. Lee, J. Von Boehm, M. Pesola, and R. Nieminen. “Aggregation kinetics of thermal double donors in silicon”. *Physical Review Letters*, Vol. 86, No. 14, pp. 3060–3063, 2001.
-

## BIBLIOGRAPHY

---

- [Lee 10] E. Lee, H. Lee, I. Kim, J. Choi, D. Oh, J. Shim, K. Cho, J. Kim, H.-S. Lee, S. Lee, B. Hallam, and S. R. Wenham. “The potential efficiency of laser doped solar cells using photoluminescence imaging”. *Proceedings of the 35th IEEE Photovoltaic Specialists Conference, Honolulu, U.S.A.*, pp. 1436–1439, 2010.
- [Lee 11a] E. Lee, H. Lee, J. Choi, D. Oh, J. Shim, K. Cho, J. Kim, S. Lee, B. Hallam, S. R. Wenham, *et al.* “Improved LDSE processing for the avoidance of overplating yielding 19.2% efficiency on commercial grade crystalline Si solar cell”. *Solar Energy Materials and Solar Cells*, Vol. 95, No. 12, pp. 3592–3595, 2011.
- [Lee 11b] H. Lee, E. Lee, J. Kim, J. Shin, J. Kim, J. Choi, I. Kim, J. Shim, D. Oh, C. K, J. Kong, J. Seo, S. Lee, B. Hallam, S. Wenham, and H. Lee. “Production of 19.2% Efficient Large Area Commercial Grade P-Type CZ Silicon Solar Cells Based on the Laser Doped Selective Emitter Technology”. *Proceedings of the 26th European Photovoltaic Solar Energy Conference, Hamburg, Germany*, pp. 1390 – 1393, 2011.
- [Lenz 11] M. Lenz, H. Windgassen, T. Pletzer, and J. Knoch. “Contacting Moderately doped Phosphorus-Emitters of Silicon Solar Cells with Dopant Segregation During Nickel Sintering”. *IEEE Journal of Photovoltaics*, Vol. 1, p. PP, 2011.
- [Li 11] H. Li, B. Hallam, and S. Wenham. “Comparative study of PECVD deposited a-Si:H/SiNx:H double passivating layer on CZ crystalline si substrate”. *Proceedings of the 37th IEEE Photovoltaic Specialists Conference, Seattle, U.S.A.*, pp. 1481–1485, 2011.
- [Li 12a] H. Li and S. Wenham. “Industrially Feasible Rear Passivation and Contact Scheme for High Efficiency Crystalline Silicon Solar Cells on p-Type CZ Substrate”. *Proceedings of the 27th European Photovoltaic Solar Energy Conference, Frankfurt, Germany*, pp. 883–887, 2012.
- [Li 12b] T. Li, C. Zhou, Z. Liu, W. Wang, Y. Song, Z. Gao, Y. Duan, and Y. Li. “Liquid-Phase Diffusion of Phosphorus Atoms in Laser-Doped Crystalline Silicon Solar Cells”. *Applied Mechanics and Materials*, Vol. 130, pp. 3316–3319, 2012.
- [Lim 08a] B. Lim, K. Bothe, and J. Schmidt. “Deactivation of the boron–oxygen recombination center in silicon by illumination at elevated temperature”. *physica status solidi (RRL)-Rapid Research Letters*, Vol. 2, No. 3, pp. 93–95, 2008.
- [Lim 08b] B. Lim, S. Hermann, K. Bothe, J. Schmidt, and R. Brendel. “Permanent deactivation of the boron-oxygen recombination center in silicon solar cells”. *Proceedings of the 23rd European Photovoltaic Solar Energy Conference, Valencia, Spain*, pp. 1018–1022, 2008.
- [Lim 08c] B. Lim, S. Hermann, K. Bothe, J. Schmidt, and R. Brendel. “Solar cells on low-resistivity boron-doped Czochralski-grown silicon with stabilized efficiencies of 20%”. *Applied Physics Letters*, Vol. 93, No. 16, pp. 162102–162102, 2008.

- [Lim 10a] B. Lim, K. Bothe, and J. Schmidt. “Impact of oxygen on the permanent deactivation of boron–oxygen-related recombination centers in crystalline silicon”. *Journal of Applied Physics*, Vol. 107, No. 12, pp. 123707–123707, 2010.
- [Lim 10b] B. Lim, F. Rougieux, D. Macdonald, K. Bothe, and J. Schmidt. “Generation and annihilation of boron–oxygen-related recombination centers in compensated p-and n-type silicon”. *Journal of Applied Physics*, Vol. 108, p. 103722, 2010.
- [Lin 14] D. Lin, M. Abbott, P. H. Lu, B. Xiao, B. Hallam, B. Tjahjono, and S. Wenham. “Incorporation of deep laser doping to form the rear localized back surface field in high efficiency solar cells”. *Solar Energy Materials and Solar Cells*, Vol. 130, pp. 83–90, 2014.
- [Liu 79] P. Liu, R. Yen, N. Bloembergen, and R. Hodgson. “Picosecond laser-induced melting and resolidification morphology on Si”. *Applied Physics Letters*, Vol. 34, No. 12, pp. 864–866, 1979.
- [Lol9 93] P. Lolgen, C. Leguijt, J. Eikelboom, R. Steeman, W. Sinke, L. Verhoef, P. Alkemade, and E. Algra. “Aluminium back-surface field doping profiles with surface recombination velocities below 200 cm/s”. *Proceedings of the 23rd IEEE Photovoltaic Specialists Conference*, pp. 236–242, 1993.
- [Lu 11] D. Lu, B. Xiao, Z. Lu, K. Wang, A. Lennon, and S. Wenham. “Laser Doping through Anodic Aluminium Oxide Layers Formed on Silicon Solar Cells”. *Proceedings of the 21st IEEE Photovoltaic Science and Engineering Conference, Fukuoka*, 2011.
- [Lude 12] T. Lüdera, T. Lauermann, A. Zuschlag, G. Hahn, and B. Terheiden. “Al<sub>2</sub>O<sub>3</sub>/SiN<sub>x</sub> Stacks at Increased Temperatures: Avoiding Blistering During Contact Firing”. *Energy Procedia*, Vol. 27, pp. 426–431, 2012.
- [Lude 99] R. Lüdemann. “Hydrogen passivation of multicrystalline silicon solar cells”. *Materials Science and Engineering: B*, Vol. 58, No. 1, pp. 86–90, 1999.
- [Lund 09] H. Lund and B. V. Mathiesen. “Energy system analysis of 100% renewable energy systems - The case of Denmark in years 2030 and 2050”. *Energy*, Vol. 34, No. 5, pp. 524–531, 2009.
- [Macd 00] D. Macdonald and A. Cuevas. “The trade-off between phosphorus gettering and thermal degradation in multicrystalline silicon”. *Proceedings of the 16th European Photovoltaic Solar Energy Conference*, pp. 1707–1710, 2000.
- [Macd 03] D. Macdonald and A. Cuevas. “Validity of simplified Shockley-Read-Hall statistics for modeling carrier lifetimes in crystalline silicon”. *Physical Review B*, Vol. 67, No. 7, p. 075203, 2003.
- [Macd 04a] D. Macdonald and L. Geerligs. “Recombination activity of interstitial iron and other transition metal point defects in p-and n-type crystalline silicon”. *Applied Physics Letters*, Vol. 85, No. 18, pp. 4061–4063, 2004.
- [Macd 04b] D. Macdonald, L. Geerligs, and A. Azzizi. “Iron detection in crystalline silicon by carrier lifetime

## BIBLIOGRAPHY

---

- measurements for arbitrary injection and doping”. *Journal of Applied Physics*, Vol. 95, No. 3, pp. 1021–1028, 2004.
- [Macd 09] D. Macdonald, F. Rougieux, A. Cuevas, B. Lim, J. Schmidt, M. Di Sabatino, and L. Geerligs. “Light-induced boron-oxygen defect generation in compensated p-type Czochralski silicon”. *Journal of Applied Physics*, Vol. 105, No. 9, pp. 093704–093704, 2009.
- [Macd 11] D. Macdonald, A. Liu, A. Cuevas, B. Lim, and J. Schmidt. “The impact of dopant compensation on the boron-oxygen defect in p-and n-type crystalline silicon”. *physica status solidi (a)*, Vol. 208, No. 3, pp. 559–563, 2011.
- [Mack 10] S. Mack, U. Jger, G. Kastner, E. Wotke, U. Belledin, A. Wolf, R. Preu, and D. Biro. “Towards 19% efficient industrial PERC devices using simultaneous front emitter and rear surface passivation by thermal oxidation”. *Proceedings of the 35th IEEE Photovoltaic Specialists Conference*, pp. 34–38, 2010.
- [Mai 12] L. Mai, M. Edwards, M. Green, B. Hallam, Z. Hameiri, N. Kuepper, A. Sugianto, B. Tjahjono, S. Wang, A. Wenham, and S. Wenham. *Rear junction solar cell*. 2012. US Patent App. 2012/0048366 A1.
- [Mart 13] I. Martín, P. Ortega, M. Colina, A. Orpella, G. López, and R. Alcubilla. “Laser processing of Al<sub>2</sub>O<sub>3</sub>/a-SiC<sub>x</sub>: H stacks: a feasible solution for the rear surface of high-efficiency p-type c-Si solar cells”. *Progress in Photovoltaics: Research and Applications*, Vol. 21, No. 5, pp. 1171–1175, 2013.
- [Mart 93] G. Martinelli and R. Kibizov. “Growth of stable dislocation-free 3-grain silicon ingots for thinner slicing”. *Applied physics letters*, Vol. 62, No. 25, pp. 3262–3263, 1993.
- [Math 89] D. Mathiot. “Modeling of hydrogen diffusion in n-and p-type silicon”. *Physical Review B*, Vol. 40, No. 8, pp. 5867–5870, 1989.
- [McIn 03] K. R. McIntosh, M. J. Cudzinovic, D. D. Smith, W. P. Mulligan, and R. M. Swanson. “The choice of silicon wafer for the production of low-cost rear-contact solar cells”. *Photovoltaic Energy Conversion, 2003. Proceedings of 3rd World Conference on*, Vol. 1, pp. 971–974, 2003.
- [McIn 10] K. R. McIntosh and P. P. Altermatt. “A freeware 1D emitter model for silicon solar cells”. *Proceedings of the 35th IEEE Photovoltaic Specialists Conference*, pp. 002188–002193, 2010.
- [McIn 13] K. R. McIntosh, P. P. Altermatt, T. Ratcliff, K. Fong, L. Black, and M. Abbott. “An examination of three common assumptions used to simulate recombination in heavily doped silicon”. *Proceedings of the 28th European Photovoltaic Science and Engineering Conference, Paris, France*, pp. 1672 – 1679, 2013.
- [Meem 06] V. Meemongkolkiat, K. Nakayashiki, A. Rohatgi, G. Crabtree, J. Nickerson, and T. Jester. “Resistivity and lifetime variation along commercially grown Ga-and B-Doped Czochralski Si

- ingots and its effect on light-induced degradation and performance of solar cells". *Progress in Photovoltaics: Research and Applications*, Vol. 14, No. 2, pp. 125–134, 2006.
- [Meis 10] A. Meisel, M. Burrows, M. Abbott, F. Lemmi, and H. Antoniadis. "Impact of metal contact misalignment in silicon ink selective emitter solar cells". *Proceedings of the 35th IEEE Photovoltaic Specialists Conference*, pp. 1456–1460, 2010.
- [Mert 09] V. Mertens, S. Bordihn, Y. Larionova, N. Harder, and R. Brendel. "The buried emitter solar cell concept: interdigitated back-junction structure with virtually 100% emitter coverage of the cell area". *Proceedings of the 24th European Photovoltaic Solar Energy Conference*, pp. 934–936, 2009.
- [Metz 14] A. Metz, D. Adler, S. Bagus, H. Blanke, M. Bothar, E. Brouwer, S. Dauwe, K. Dressler, R. Droessler, T. Droste, *et al.* "Industrial high performance crystalline silicon solar cells and modules based on rear surface passivation technology". *Solar Energy Materials and Solar Cells*, Vol. 120, pp. 417–425, 2014.
- [Mohr 11] A. Mohr, P. Engelhart, C. Klenke, S. Wanka, A. Stekolnikov, M. Scherff, R. Seguin, S. Tardon, T. Rudolph, M. Hofmann, F. Stenzel, J. Lee, S. Diez, J. Wendt, S. Schmidt, J. Müller, P. Wawer, M. Hofmann, P. Saint-Cast, J. Nekarda, D. Erath, J. Rentsch, and R. Preu. "20%-efficient rear side passivated solar cells in pilot series designed for conventional module assembling". *Proceedings of the 26th European Photovoltaic Solar Energy Conference, Hamburg, Germany*, pp. 2150–2153, 2011.
- [Moon 78] P. Mooney, R. Young, J. Karins, Y. Lee, and J. Corbett. "Defects in laser damaged silicon observed by DLTS". *physica status solidi (a)*, Vol. 48, No. 1, pp. K31–K34, 1978.
- [Mori 03] K. Morita and T. Miki. "Thermodynamics of solar-grade-silicon refining". *Intermetallics*, Vol. 11, No. 11, pp. 1111–1117, 2003.
- [Mori 95] T. Morimoto, T. Ohguro, S. Momose, T. Iinuma, I. Kunishima, K. Suguro, I. Katakabe, H. Nakajima, M. Tsuchiaki, M. Ono, *et al.* "Self-aligned nickel-mono-silicide technology for high-speed deep submicrometer logic CMOS ULSI". *IEEE Transactions on Electron Devices*, Vol. 42, No. 5, pp. 915–922, 1995.
- [Mull 04] W. P. Mulligan, D. H. Rose, M. J. Cudzinovic, D. M. De Ceuster, K. R. McIntosh, D. D. Smith, and R. M. Swanson. "Manufacture of solar cells with 21% efficiency". *Proceedings of the 19th European Photovoltaic Solar Energy Conference, Paris*, pp. 387–390, 2004.
- [Munz 09] K. Münzer. "Hydrogenated Silicon Nitride for Regeneration of Light Induced Degradation". *Proceedings of the 24th European Photovoltaic Solar Energy Conference, Hamburg*, pp. 1558–1561, 2009.
- [Munz 11] K. Münzer, J. Schöne, A. Teppe, M. Hein, R. Schlosser, M. Hanke, K. Varner, H. Mäckel,

## BIBLIOGRAPHY

---

- S. Keller, and P. Fath. “Physical properties of industrial 19% rear side passivated Al-LBSFR-solar cells”. *Energy Procedia*, Vol. 8, pp. 415–420, 2011.
- [Muri 11] L. I. Murin, E. A. Tolkacheva, V. P. Markevich, A. R. Peaker, B. Hamilton, E. Monakhov, B. G. Svensson, J. L. Lindstrom, P. Santos, J. Coutinho, and A. Carvalho. “The oxygen dimer in Si: Its relationship to the light-induced degradation of Si solar cells?”. *Applied Physics Letters*, Vol. 98, No. 18, p. 182101, 2011.
- [Murp 10] J. D. Murphy, K. Bothe, M. Olmo, V. V. Voronkov, and R. J. Falster. “Minority carrier lifetime in Czochralski silicon containing oxide precipitates”. *ECS Transactions*, Vol. 33, No. 11, pp. 121–132, 2010.
- [Murp 14] J. D. Murphy, R. McGuire, K. Bothe, V. Voronkov, and R. J. Falster. “Minority carrier lifetime in silicon photovoltaics: The effect of oxygen precipitation”. *Solar Energy Materials and Solar Cells*, Vol. 120, pp. 402–411, 2014.
- [Murr 84] J. Murray and A. McAlister. “The Al-Si (aluminum-silicon) system”. *Bulletin of Alloy Phase Diagrams*, Vol. 5, No. 1, pp. 74–84, 1984.
- [Nage 00] H. Nagel, A. Merkle, A. Metz, and R. Hezel. “Permanent reduction of excess-carrier-induced recombination centers in solar grade Czochralski silicon by a short yet effective anneal”. *Proceedings of the 16th European Photovoltaic Solar Energy Conference*, pp. 1197–1200, 2000.
- [Nara 78] J. Narayan, R. Young, R. Wood, and W. Christie. “p-n junction formation in boron-deposited silicon by laser-induced diffusion”. *Applied Physics Letters*, Vol. 33, No. 4, pp. 338–340, 1978.
- [Nara 99] S. Narasimha, A. Rohatgi, and A. Weeber. “An optimized rapid aluminum back surface field technique for silicon solar cells”. *IEEE Transactions on Electron Devices*, Vol. 46, No. 7, pp. 1363–1370, 1999.
- [Neuh 07] D. Neuhaus and A. Münzer. “Industrial Silicon Wafer Solar Cells”. *Advances in Opto-electronics*, Vol. 24, pp. 1–15, 2007.
- [Newm 91] R. Newman, J. Tucker, A. Brown, and S. McQuaid. “Hydrogen diffusion and the catalysis of enhanced oxygen diffusion in silicon at temperatures below 500 C”. *Journal of Applied Physics*, Vol. 70, No. 6, pp. 3061–3070, 1991.
- [Nick 93] N. Nickel, N. Johnson, and W. Jackson. “Hydrogen passivation of grain boundary defects in polycrystalline silicon thin films”. *Applied Physics Letters*, Vol. 62, No. 25, pp. 3285–3287, 1993.
- [Nick 98] N. Nickel and I. Kaiser. “Hydrogen migration in phosphorous doped polycrystalline silicon”. *MRS Proceedings*, Vol. 513, No. 1, p. 165, 1998.
- [Ogan 08] A. Ogane, K. Hirata, K. Horiuchi, A. Kitiyanan, Y. Uraoka, and T. Fuyuki. “Feasible control of laser doping profiles in silicon solar cell processing using multiple excitation wavelengths”. *Proceedings of the 33rd IEEE Photovoltaic Specialists Conference*, pp. 1–4, 2008.

- [Ohme 11] K. Ohmer, Y. Weng, J. Khler, H. Strunk, and J. Werner. “Defect Formation in Silicon During Laser Doping”. *IEEE Journal of Photovoltaics*, Vol. 1, No. 2, pp. 183–186, 2011.
- [Okan 09] M. Okanovic, U. Jager, M. Ahrens, U. Stute, A. Grohe, and R. Preu. “Influence of different laser parameters in laser doping from phosphosilicate glass”. *2009 Proceedings 24th European Photovoltaic Solar Energy Conference*, pp. 1771–1774, 2009.
- [Pain 01] J. P. Painuly. “Barriers to renewable energy penetration; a framework for analysis”. *Renewable energy*, Vol. 24, No. 1, pp. 73–89, 2001.
- [Pali 11] N. Palina, T. Mueller, S. Mohanti, and A. Aberle. “Laser assisted boron doping of silicon wafer solar cells using nanosecond and picosecond laser pulses”. *Proceedings of the 37th IEEE Photovoltaic Specialists Conference, Seattle*, pp. 2193–2197, 2011.
- [Pank 84] J. Pankove, R. Wance, and J. Berkeyheiser. “Neutralization of acceptors in silicon by atomic hydrogen”. *Applied Physics Letters*, Vol. 45, No. 10, pp. 1100–1102, 1984.
- [Pank 85] J. Pankove, P. Zanzucchi, C. Magee, and G. Lucovsky. “Hydrogen localization near boron in silicon”. *Applied Physics Letters*, Vol. 46, No. 4, pp. 421–423, 1985.
- [Pank 91] J. Pankove and N. Johnson. *Hydrogen in Semiconductors: Hydrogen in Silicon*. Vol. 34, Academic Press, 1991.
- [Park 83] D. Parker, F. Lin, S. Zhu, D. Zhang, and W. Porter. “A comparison of Nd: YAG fundamental and second-harmonic Q-switched laser-beam lifetime doping in single-crystal silicon”. *IEEE Transactions on Electron Devices*, Vol. 30, No. 10, pp. 1322–1326, 1983.
- [Paul 76] W. Paul, A. Lewis, G. Connell, and T. Moustakas. “Doping, Schottky barrier and p-n junction formation in amorphous germanium and silicon by rf sputtering”. *Solid State Communications*, Vol. 20, No. 10, pp. 969–972, 1976.
- [Pavi 11] B. Paviet-Salomon, S. Gall, R. Monna, S. Manuel, and A. Slaoui. “Experimental and analytical study of saturation current density of laser-doped phosphorus emitters for silicon solar cells”. *Solar Energy Materials and Solar Cells*, Vol. 95, No. 8, pp. 2536–2539, 2011.
- [Pear 91] S. Pearton, J. Corbett, and J. Borenstein. “Hydrogen diffusion in crystalline semiconductors”. *Physica B: Condensed Matter*, Vol. 170, No. 1, pp. 85–97, 1991.
- [Peri 02] I. Périchaud. “Gettering of impurities in solar silicon”. *Solar Energy Materials and Solar Cells*, Vol. 72, No. 1, pp. 315–326, 2002.
- [Piro 01] L. Pirozzi, G. Arabito, F. Artuso, V. Barbarossa, U. Besi-Vetrella, S. Loreti, P. Mangiapane, and E. Salza. “Selective emitters in buried contact silicon solar cells: Some low-cost solutions”. *Solar energy materials and solar cells*, Vol. 65, No. 1, pp. 287–295, 2001.
- [Plet] T. Pletzer, J. Mülken, S. Rißland, E. Cornagliotti, J. John, O. Breitenstein, and J. Knoch. “Quantitative local current-voltage analysis with different spatially-resolved camera-based techniques of silicon solar cells with cracks”.

## BIBLIOGRAPHY

---

- [Port 02] L. Porter, A. Teicher, and D. Meier. “Phosphorus-doped, silver-based pastes for self-doping ohmic contacts for crystalline silicon solar cells”. *Solar energy materials and solar cells*, Vol. 73, No. 2, pp. 209–219, 2002.
- [PVsp 14a] PV Lighthouse. *EDNA 2*. 2014. <<http://pvlighthouse.com.au>>.
- [PVsp 14b] PV Lighthouse. *Sheet resistance calculator*. 2014. <<http://pvlighthouse.com.au>>.
- [Quei 64] H. Queisser and P. Van Loon. “Growth of Lattice Defects in Silicon during Oxidation”. *Journal of Applied Physics*, Vol. 35, No. 10, pp. 3066–3067, 1964.
- [Quei 98] H. Queisser and E. Haller. “Defects in semiconductors: Some fatal, some vital”. *Science*, Vol. 281, No. 5379, pp. 945–950, 1998.
- [Rash 01] S. Rashkeev, M. Di Ventura, and S. Pantelides. “Hydrogen passivation and activation of oxygen complexes in silicon”. *Applied Physics Letters*, Vol. 78, No. 11, pp. 1571–1573, 2001.
- [Rein 03] S. Rein, S. Diez, R. Falster, and S. Glunz. “Quantitative correlation of the metastable defect in Cz-silicon with different impurities”. *Photovoltaic Energy Conversion, 2003. Proceedings of 3rd World Conference on*, Vol. 2, pp. 1048–1052, 2003.
- [Reis 96] J. Reiss, R. King, and K. Mitchell. “Characterization of diffusion length degradation in Czochralski silicon solar cells”. *Applied Physics Letters*, Vol. 68, No. 23, pp. 3302–3304, 1996.
- [REN2 13] REN21. *Renewables 2013: Global Status Report*. REN, 2013.
- [Rena 07] Rena. *Wet Chemical Edge Isolation for Solar Cells*. EuroAsia Semiconductor Magazine, Mid September, 2007.
- [Reut 10] B. Reuter. “Superior top dog. Is the classic Siemens process the winner of the silicon industry’s technology race?”. *Proceedings of the 8th Solar Silicon Conference*, pp. 134–137, 2010.
- [Rich 12a] A. Richter, F. Werner, A. Cuevas, J. Schmidt, and S. Glunz. “Improved parameterization of auger recombination in silicon”. *Energy Procedia*, Vol. 27, pp. 88–94, 2012.
- [Rich 12b] A. Richter, S. W. Glunz, F. Werner, J. Schmidt, and A. Cuevas. “Improved quantitative description of Auger recombination in crystalline silicon”. *Physical Review B*, Vol. 86, No. 16, p. 165202, 2012.
- [Rini 04] M. Rinio, C. Ballif, T. Buonassisi, and D. Borchert. “Defects in the deteriorated border layer of block-cast multicrystalline silicon ingots”. *Proceedings of the 19th European Photovoltaic Solar Energy Conference*, Vol. 7, p. 11, 2004.
- [Rmat 09] T. Röder, P. Grabitz, S. Eisele, C. Wagner, J. Kohler, and J. Werner. “0.4% absolute efficiency gain of industrial solar cells by laser doped selective emitter”. *Proceedings of the 34th IEEE Photovoltaic Specialists Conference*, pp. 000871–000873, 2009.
- [Robb 60] H. Robbins and B. Schwartz. “Chemical Etching of Silicon II. The System, and”. *Journal of the electrochemical society*, Vol. 107, No. 2, pp. 108–111, 1960.



- 
- [Rode 10] T. Röder, S. Eisele, P. Grabitz, C. Wagner, G. Kulushich, J. Köhler, and J. Werner. “Add-on laser tailored selective emitter solar cells”. *Progress in Photovoltaics: Research and Applications*, Vol. 18, No. 7, pp. 505–510, 2010.
- [Roha 02] A. Rohatgi, V. Yelundur, J. Jeong, A. Ebong, M. Rosenblum, and J. Hanoka. “Fundamental understanding and implementation of Al-enhanced PECVD SiNx hydrogenation in silicon ribbons”. *Solar Energy Materials and Solar Cells*, Vol. 74, No. 1, pp. 117–126, 2002.
- [Roha 86] A. Rohatgi, D. Meier, P. Rai-Choudhury, S. Fonash, and R. Singh. “Effect of low-energy hydrogen ion implantation on dendritic web silicon solar cells”. *Journal of Applied Physics*, Vol. 59, No. 12, pp. 4167–4171, 1986.
- [Roug 10] F. Rougieux, D. Macdonald, A. Cuevas, S. Ruffell, J. Schmidt, B. Lim, and A. Knights. “Electron and hole mobility reduction and Hall factor in phosphorus-compensated p-type silicon”. *Journal of Applied Physics*, Vol. 108, p. 013706, 2010.
- [Roug 11] F. Rougieux, B. Lim, J. Schmidt, M. Forster, D. Macdonald, and A. Cuevas. “Influence of net doping, excess carrier density and annealing on the boron oxygen related defect density in compensated n-type silicon”. *Journal of Applied Physics*, Vol. 110, p. 063708, 2011.
- [Ruhl 12] K. Rühle, M. Rauer, M. Rüdiger, J. Giesecke, T. Niewelt, C. Schmiga, S. Glunz, and M. Kasemann. “Passivation Layers for Indoor Solar Cells at Low Irradiation Intensities”. *Energy Procedia*, Vol. 27, pp. 406–411, 2012.
- [Russ 12] R. Russell, L. Tous, H. Philipsen, J. Horzel, E. Cornagliotti, M. Ngamo, P. Choulat, R. Labie, J. Beckers, J. Bertens, M. Fujii, J. John, J. Poortmans, and R. Mertens. “A simple copper metallization process for high cell efficiencies and reliable modules”. *Proceedings of the 27th European Photovoltaic Solar Energy Conference, Frankfurt, Germany*, pp. 538–543, 2012.
- [Sah 83] C. Sah, J. Sun, and J. Tzou. “Deactivation of the boron acceptor in silicon by hydrogen”. *Applied Physics Letters*, Vol. 43, No. 2, pp. 204–206, 1983.
- [Sain 09] P. Saint-Cast, D. Kania, M. Hofmann, J. Benick, J. Rentsch, and R. Preu. “Very low surface recombination velocity on p-type c-Si by high-rate plasma-deposited aluminum oxide”. *Applied Physics Letters*, Vol. 95, No. 15, pp. 151502–151502, 2009.
- [Sait 01] T. Saitoh, X. Wang, H. Hashigami, T. Abe, T. Igarashi, S. Glunz, S. Rein, W. Wettling, I. Yamasaki, H. Sawai, H. Ohtuka, and T. Warabisako. “Suppression of light degradation of carrier lifetimes in low-resistivity CZ-Si solar cells”. *Solar Energy Materials and Solar Cells*, Vol. 65, No. 1, pp. 277–285, 2001.
- [Same 87] T. Sameshima, S. Usui, and M. Sekiya. “Laser-induced melting of predeposited impurity doping technique used to fabricate shallow junctions”. *Journal of Applied Physics*, Vol. 62, No. 2, pp. 711–713, 1987.
- [Sche 42] E. Scheil. “Remarks on the crystal layer formation”. *Z. Metallkd.*, Vol. 34, p. 70, 1942.
-

## BIBLIOGRAPHY

---

- [Schm 03] J. Schmidt. “Light-induced degradation in crystalline silicon solar cells”. *Solid State Phenomena*, Vol. 95, pp. 187–196, 2003.
- [Schm 04] J. Schmidt and K. Bothe. “Structure and transformation of the metastable boron- and oxygen-related defect center in crystalline silicon”. *Physics Review B*, Vol. 69, p. 024107, Jan 2004.
- [Schm 06] C. Schmiga, H. Nagel, and J. Schmidt. “19% efficient n-type Czochralski silicon solar cells with screen-printed aluminium-alloyed rear emitter”. *Progress in Photovoltaics: Research and Applications*, Vol. 14, No. 6, pp. 533–539, 2006.
- [Schm 97] J. Schmidt, A. G. Aberle, and R. Hezel. “Investigation of carrier lifetime instabilities in Cz-grown silicon”. *Proceedings of the 26th IEEE Photovoltaic Specialists Conference*, pp. 13–18, 1997.
- [Schm 98] J. Schmidt, C. Berge, and A. Aberle. “Injection level dependence of the defect-related carrier lifetime in light-degraded boron-doped Czochralski silicon”. *Applied Physics Letters*, Vol. 73, No. 15, pp. 2167–2169, 1998.
- [Schn 02] E. Schneiderlöchner, R. Preu, R. Lüdemann, and S. Glunz. “Laser-fired rear contacts for crystalline silicon solar cells”. *Progress in Photovoltaics: Research and Applications*, Vol. 10, No. 1, pp. 29–34, 2002.
- [Schn 03] E. Schneiderlochner, A. Grohe, S. Glunz, R. Preu, and W. Willeke. “Scanning Nd: YAG laser system for industrially applicable processing in silicon solar cell manufacturing”. *Proceedings of the 3rd World Conference on Photovoltaic Energy Conversion*, Vol. 2, pp. 1364–1367, 2003.
- [Schr 00] W. Schröter, V. Kveder, M. Seibt, H. Ewe, H. Hedemann, F. Riedel, and A. Sattler. “Atomic structure and electronic states of nickel and copper silicides in silicon”. *Materials Science and Engineering: B*, Vol. 72, No. 2, pp. 80–86, 2000.
- [Schr 84] D. K. Schroder and D. L. Meier. “Solar cell contact resistancea review”. *IEEE Transactions on Electron Devices*, Vol. 31, No. 5, pp. 637–647, 1984.
- [Schu 06] O. Schultz, S. Glunz, S. Riepe, and G. Willeke. “High-efficiency solar cells on phosphorus gettered multicrystalline silicon substrates”. *Progress in Photovoltaics: Research and Applications*, Vol. 14, No. 8, pp. 711–719, 2006.
- [Schu 10] T. Schutz-Kuchly, J. Veirman, S. Dubois, and D. Heslinga. “Light-Induced-Degradation effects in boron–phosphorus compensated n-type Czochralski silicon”. *Applied Physics Letters*, Vol. 96, No. 9, pp. 093505–093505, 2010.
- [Schw 01] T. Schwarz-Selinger, D. Cahill, S. Chen, S. Moon, and C. Grigoropoulos. “Micron-scale modifications of Si surface morphology by pulsed-laser texturing”. *Physical Review B*, Vol. 64, No. 15, p. 155323, 2001.
- [Seag 87] C. Seager, R. Anderson, and J. Panitz. “The diffusion of hydrogen in silicon and mechanisms

- 
- for unintentional hydrogenation during ion beam processing”. *Journal of Materials Research*, Vol. 2, No. 01, pp. 96–106, 1987.
- [Seag 88] C. Seager and R. Anderson. “Real-time observations of hydrogen drift and diffusion in silicon”. *Applied Physics Letters*, Vol. 53, No. 13, pp. 1181–1183, 1988.
- [Seag 91] C. Seager and R. Anderson. “Two-step debonding of hydrogen from boron acceptors in silicon”. *Applied Physics Letters*, Vol. 59, No. 5, pp. 585–587, 1991.
- [Sheo 08] M. Sheoran, A. Upadhyaya, and A. Rohatgi. “Bulk lifetime and efficiency enhancement due to gettering and hydrogenation of defects during cast multicrystalline silicon solar cell fabrication”. *Solid-State Electronics*, Vol. 52, No. 5, pp. 612–617, 2008.
- [Shi 09] Z. Shi, S. Wenham, and J. Ji. “Mass production of the innovative PLUTO solar cell technology”. *Proceedings of the 34th IEEE Photovoltaic Specialists Conference*, pp. 1922–1926, 2009.
- [Shoc 52] W. Shockley and W. Read Jr. “Statistics of the recombinations of holes and electrons”. *Physical Review*, Vol. 87, No. 5, p. 835, 1952.
- [Shum 12] S. Shumate, D. A. Hutchings, H. Mohammed, G. Beilke, B. Newton, M. Young, H. Abu-Safe, S. ShiuYu, and H. Naseem. “Self aligned hydrogenated selective emitter for n-type solar cells”. *Proceedings of the 38th IEEE Photovoltaic Specialists Conference, 2012*, pp. 1110–1114, 2012.
- [Sing 86] R. Singh, S. Fonash, and A. Rohatgi. “Interaction of low-energy implanted atomic H with slow and fast diffusing metallic impurities in Si”. *Applied Physics Letters*, Vol. 49, No. 13, pp. 800–802, 1986.
- [Sinn 97] T. Sinno, R. A. Brown, W. von Ammon, and E. Dornberger. “On the dynamics of the oxidation-induced stacking-fault ring in as-grown Czochralski silicon crystals”. *Applied physics letters*, Vol. 70, No. 17, pp. 2250–2252, 1997.
- [Sint 00] R. Sinton and A. Cuevas. “A quasi-steady-state open-circuit voltage method for solar cell characterization”. *Proceedings of the 16th European Photovoltaic Solar Energy Conference*, pp. 1–5, 2000.
- [Sint 90] R. Sinton and R. Swanson. “Simplified backside-contact solar cells”. *IEEE Transactions on Electron Devices*, Vol. 37, No. 2, pp. 348–352, 1990.
- [Sint 96a] R. A. Sinton and A. Cuevas. “Contactless determination of the current-voltage characteristics and minority-carrier lifetimes in semiconductors from quasi-steady-state photoconductance data”. *Applied Physics Letters*, Vol. 69, No. 17, pp. 2510–2512, 1996.
- [Sint 96b] R. A. Sinton, A. Cuevas, and M. Stuckings. “Quasi-steady-state photoconductance, a new method for solar cell material and device characterization”. *Proceedings of the 25th IEEE Photovoltaic Specialists Conference*, pp. 457–460, 1996.
- [Smit 12] D. Smith, P. Cousins, A. Masad, A. Waldhauer, S. Westerberg, M. Johnson, X. Tu, T. Dennis, G. Harley, G. Solomon, S. Rim, M. Shepherd, S. Harrington, M. Defensor, A. Leygo, P. Tomada,
-

## BIBLIOGRAPHY

---

- J. Wu, T. Pass, L. Ann, L. Smith, N. Bergstrom, C. Nicdao, P. Tipones, and D. Vicente. “Generation III high efficiency lower cost technology: Transition to full scale manufacturing”. *Proceedings of the 38th IEEE Photovoltaic Specialists Conference*, pp. 001594–001597, 2012.
- [Sond 13] R. Søndena, Y. Hu, M. Juel, M. Syre Wiig, and H. Angelskår. “Characterization of the OSF-band structure in n-type Cz-Si using photoluminescence-imaging and visual inspection”. *Journal of Crystal Growth*, Vol. 367, pp. 68–72, 2013.
- [Sopo 01] B. Sopori, Y. Zhang, and N. Ravindra. “Silicon device processing in H-ambients: H-diffusion mechanisms and influence on electronic properties”. *Journal of Electronic Materials*, Vol. 30, No. 12, pp. 1616–1627, 2001.
- [Sopo 02] B. Sopori. “Silicon solar-cell processing for minimizing the influence of impurities and defects”. *Journal of Electronic Materials*, Vol. 31, No. 10, pp. 972–980, 2002.
- [Sopo 03] B. Sopori. “Silicon nitride processing for control of optical and electronic properties of silicon solar cells”. *Journal of Electronic Materials*, Vol. 32, No. 10, pp. 1034–1042, 2003.
- [Sopo 92] B. Sopori, K. Jones, and X. Deng. “Observation of enhanced hydrogen diffusion in solar cell silicon”. *Applied Physics Letters*, Vol. 61, No. 21, pp. 2560–2562, 1992.
- [Sopo 96] B. Sopori, X. Deng, J. Benner, A. Rohatgi, P. Sana, S. Estreicher, Y. Park, and M. Roberson. “Hydrogen in silicon: A discussion of diffusion and passivation mechanisms”. *Solar Energy Materials and Solar Cells*, Vol. 41, pp. 159–169, 1996.
- [Sopo 97] B. L. Sopori. “Defect clusters in silicon: impact on the performance of large-area devices”. *Materials Science Forum*, Vol. 258, pp. 527–534, 1997.
- [Sopp 05] W. Soppe, H. Rieffe, and A. Weeber. “Bulk and surface passivation of silicon solar cells accomplished by silicon nitride deposited on industrial scale by microwave PECVD”. *Progress in Photovoltaics: Research and Applications*, Vol. 13, No. 7, pp. 551–569, 2005.
- [Stoc 90] G. Stock, D. Bollmann, R. Buchner, G. Neumayer, and K. Habberger. “Ultra-flat pn junctions formed by solid source laser doping”. *Applied Surface Science*, Vol. 46, No. 1, pp. 348–351, 1990.
- [Stod 08] N. Stoddard, B. Wu, I. Witting, M. C. Wagener, Y. Park, G. A. Rozgonyi, and R. Clark. “Casting single crystal silicon: novel defect profiles from BP Solar’s mono2 TM wafers”. *Solid State Phenomena*, Vol. 131, pp. 1–8, 2008.
- [Sugi 07] A. Sugianto, B. Tjahjono, J. Guo, and S. Wenham. “Impact of laser induced defects on the performance of solar cells using localised laser doped regions beneath the metal contacts”. *Proceedings of the 22nd European Photovoltaic Solar Energy Conference*, p. 1759, 2007.
- [Sugi 10] A. Sugianto, J. Bovatsek, S. Wenham, B. Tjahjono, G. Xu, Y. Yao, B. Hallam, X. Bai, N. Kuepper, C. Chong, and R. Patel. “18.5% laser-doped solar cell on CZ p-type silicon”. *Proceedings of the 35th IEEE Photovoltaics Specialist Conference, Hawaii*, pp. 689–694, 2010.

- 
- [Sugi 12] A. Sugianto, B. Hallam, X. Bai, P. Han, H. Lu, L. Mai, S. Wenham, and Z. Shi. “Over 20%-Efficient Laser-Doped Passivated Rear Contact Solar Cells on Industrial-Sized Commercial Grade p-Type CZ Wafers”. *Proceedings of the 27th European Photovoltaic Solar Energy Conference, Frankfurt, Germany*, pp. 700–705, 2012.
- [Sze 07] Sze, S. M. and Ng. K. K. *Physics of Semiconductor Devices - Third Edition*. Wiley-Interscience, 2007.
- [Sze 68] S. Sze and J. Irvin. “Resistivity, mobility and impurity levels in GaAs, Ge, and Si at 300 K”. *Solid-State Electronics*, Vol. 11, No. 6, pp. 599–602, 1968.
- [Tais 07] T. Taishi, T. Hoshikawa, M. Yamatani, K. Shirasawa, X. Huang, S. Uda, and K. Hoshikawa. “Influence of crystalline defects in Czochralski-grown Si multicrystal on minority carrier lifetime”. *Journal of Crystal Growth*, Vol. 306, No. 2, pp. 452–457, 2007.
- [Tan 08] J. Tan, A. Cuevas, D. Macdonald, T. Trupke, R. Bardos, and K. Roth. “On the electronic improvement of multi-crystalline silicon via gettering and hydrogenation”. *Progress in Photovoltaics: Research and Applications*, Vol. 16, No. 2, pp. 129–134, 2008.
- [Tang 09] K. Tang, E. Øvrelid, G. Tranell, and M. Tangstad. “Thermochemical and kinetic databases for the solar cell silicon materials”. *Crystal Growth of Si for Solar Cells*, pp. 219–251, 2009.
- [Tave 00] A. Tavendale and S. Pearton. “Deep level, quenched-in defects in silicon doped with gold, silver, iron, copper or nickel”. *Journal of Physics C: Solid State Physics*, Vol. 16, No. 9, pp. 1665–1673, 2000.
- [Thai 13] B. Thaidigsmann, C. Kick, A. Drews, F. Clement, A. Wolf, and D. Biro. “Fire-through contacts: a new approach to contact the rear side of passivated silicon solar cells”. *Solar Energy Materials and Solar Cells*, Vol. 108, pp. 164–169, 2013.
- [Thib 13] S. Thibert, J. Jourdan, B. Bechevet, D. Chaussy, N. Reverdy-Bruas, and D. Beneventi. “Emitter Requirements for Nickel Contacts on Silicon Solar Cells-A Simulation Study”. *Energy Procedia*, Vol. 38, pp. 321–328, 2013.
- [Tjah 07] B. Tjahjono, J. H. Guo, Z. Hameiri, L. Mai, A. Sugianto, S. Wang, and S. R. Wenham. “High efficiency solar cell structures through the use of laser doping”. *Proceedings of the 22nd European Photovoltaic Solar Energy Conference, Milan*, pp. 965–969, 2007.
- [Tjah 08] B. Tjahjono, S. Wang, A. Sugianto, L. Mai, Z. Hameiri, N. Borojevic, A. Ho-Baillie, and S. R. Wenham. “Application of laser doped contact structure on multicrystalline solar cells”. *Proceedings of the 23rd European Photovoltaic Solar Energy Conference, Valencia*, pp. 1995–2000, 2008.
- [Tjah 10] B. Tjahjono, M. Yang, C. Lan, J. Ting, A. Sugianto, H. Ho, N. Kuepper, B. Beilby, T. Szpitalak, and S. Wenham. “18.9% Efficient laser Doped Selective Emitter Solar Cell on Industrial
-

## BIBLIOGRAPHY

---

- Grade p-type Czochralski Wafer”. *Proceedings of the 25th European Photovoltaic Solar Energy Conference, Valencia*, p. 1396, 2010.
- [Tjah 11] B. Tjahjono, H. Haverkamp, V. Wu, H. Anditsch, W. Jung, J. Cheng, J. Ting, M. Yang, D. Habermann, T. Sziptalak, C. Buchner, C. Schmid, B. Beilby, and K. Hsu. “Optimizing Selective Emitter Technology in One Year of Full Scale Production”. *Proceedings of the 26th European Photovoltaic Solar Energy Conference, Hamburg*, pp. 901 – 905, 2011.
- [Toku 89] Y. Tokuda, N. Kobayashi, A. Usami, Y. Inoue, and M. Imura. “Thermal donor annihilation and defect production in n-type silicon by rapid thermal annealing”. *Journal of Applied Physics*, Vol. 66, No. 8, pp. 3651–3655, 1989.
- [Tous 13] L. Tous, R. Russel, M. Debucquoy, F. Posthuma, N. Duerinckx, R. Mertens, and J. Poortmans. “Power-loss analysis of advanced PERC cells reaching 20.5% energy conversion efficiency”. *Energy Procedia*, Vol. 38, pp. 467–473, 2013.
- [Tous 14] L. Tous. *Nickel/Copper Plated Contacts as an Alternative to Silver Screen Printing for the Front Side Metallization of Industrial High Efficiency Silicon Solar Cells*. PhD thesis, KU Leuven, 2014.
- [Trup 05a] T. Trupke and R. Bardos. “Photoluminescence: A surprisingly sensitive lifetime technique”. *Proceedings of the 31st IEEE Photovoltaic Specialists Conference*, pp. 903–906, 2005.
- [Trup 05b] T. Trupke, R. Bardos, and M. Abbott. “Self-consistent calibration of photoluminescence and photoconductance lifetime measurements”. *Applied Physics Letters*, Vol. 87, No. 18, p. 184102, 2005.
- [Trup 06] T. Trupke, R. A. Bardos, M. C. Schubert, and W. Warta. “Photoluminescence imaging of silicon wafers”. *Applied Physics Letters*, Vol. 89, p. 044107, 2006.
- [Trup 11] T. Trupke, J. Nyhus, and J. Haunschild. “Luminescence imaging for inline characterisation in silicon photovoltaics”. *physica status solidi (RRL)-Rapid Research Letters*, Vol. 5, No. 4, pp. 131–137, 2011.
- [UNSW 07] UNSW ARC Photovoltaic Centre of Excellence. *ARC Photovoltaic Centre of Excellence, 2007 Annual Report*. School of Photovoltaic and Renewable Energy Engineering, UNSW, 2007.
- [UNSW 09] UNSW ARC Photovoltaic Centre of Excellence. *ARC Photovoltaic Centre of Excellence, 2009 Annual Report*. School of Photovoltaic and Renewable Energy Engineering, UNSW, 2009.
- [Urre 11] E. Urrejola, K. Peter, H. Plagwitz, and G. Schubert. “Silicon diffusion in aluminum for rear passivated solar cells”. *Applied physics letters*, Vol. 98, No. 15, p. 153508, 2011.
- [Urue 09] A. Uruena, J. John, G. Beaucarne, P. Choulat, P. Eyben, G. Agostinelli, E. Van Kerschaver, J. Poortmans, and R. Mertens. “Local Al-alloyed contacts for next generation Si solar cells”. *Proceedings of the 24th European Photovoltaic Solar Energy Conference, Hamburg*, pp. 1483–1486, 2009.

- [Urue 12] A. Uruena, J. Horzel, J. John, E. Cornagliotti, P. Eyben, M. Pfeiffer, W. Vandervorst, J. Poortmans, and R. Mertens. “Interaction between Al–Si melt and dielectric layers during formation of local Al-alloyed contacts for rear-passivated Si solar cells”. *physica status solidi (a)*, Vol. 209, No. 12, pp. 2615–2619, 2012.
- [Urue 13] A. Uruena, L. Tous, F. Duerinckx, I. Kuzma-Filipek, E. Cornagliotti, J. John, R. Mertens, and J. Poortmans. “Understanding the mechanisms of rear reflectance losses in PERC type silicon solar cells”. *Energy Procedia*, Vol. 38, pp. 801–806, 2013.
- [Usam 10] N. Usami, R. Yokoyama, I. Takahashi, K. Kutsukake, K. Fujiwara, and K. Nakajima. “Relationship between grain boundary structures in Si multicrystals and generation of dislocations during crystal growth”. *Journal of Applied Physics*, Vol. 107, No. 1, p. 013511, 2010.
- [Van 56] A. Van Wieringen and N. Warmoltz. “On the permeation of hydrogen and helium in single crystal silicon and germanium at elevated temperatures”. *Physica*, Vol. 22, No. 6, pp. 849–865, 1956.
- [Verb 10] A. Verbruggen, M. Fischedick, W. Moomaw, T. Weir, A. Nadai, L. J. Nilsson, J. Nyboer, and J. Sathaye. “Renewable energy costs, potentials, barriers: conceptual issues”. *Energy Policy*, Vol. 38, No. 2, pp. 850–861, 2010.
- [Verm 11] B. Vermang, H. Goverde, A. Lorenz, A. Uruena, G. Vereecke, J. Meersschaut, E. Cornagliotti, A. Rothschild, J. John, J. Poortmans, *et al.* “On the blistering of atomic layer deposited Al<sub>2</sub>O<sub>3</sub> as Si surface passivation”. *Proceedings of the 37th IEEE Photovoltaic Specialists Conference*, pp. 003562–003567, 2011.
- [Verm 12] B. Vermang, H. Goverde, L. Tous, A. Lorenz, P. Choulat, J. Horzel, J. John, J. Poortmans, and R. Mertens. “Approach for Al<sub>2</sub>O<sub>3</sub> rear surface passivation of industrial p-type Si PERC above 19%”. *Progress in Photovoltaics: Research and Applications*, Vol. 20, No. 3, p. 269, 2012.
- [Vesc 11] Y. Veschetti, R. Cabal, P. Brand, V. Sanzone, G. Raymond, and A. Bettinelli. “High Efficiency on Boron Emitter n-Type Cz Silicon Solar Cells With Industrial Process”. *IEEE Journal of Photovoltaics*, Vol. 1, No. 2, pp. 118–122, 2011.
- [Voro 10] V. V. Voronkov and R. Falster. “Latent complexes of interstitial boron and oxygen dimers as a reason for degradation of silicon-based solar cells”. *Journal of Applied Physics*, Vol. 107, No. 5, pp. 053509–053509, 2010.
- [Voro 11] V. Voronkov, R. Falster, K. Bothe, B. Lim, and J. Schmidt. “Lifetime-degrading boron-oxygen centres in p-type and n-type compensated silicon”. *Journal of Applied Physics*, Vol. 110, No. 6, pp. 063515–063515, 2011.
- [Voro 99] V. Voronkov and R. Falster. “Grown-in microdefects, residual vacancies and oxygen precipitation bands in Czochralski silicon”. *Journal of crystal growth*, Vol. 204, No. 4, pp. 462–474, 1999.

## BIBLIOGRAPHY

---

- [Wall 06] C. Van de Walle and J. Neugebauer. “Hydrogen in semiconductors”. *Annu. Rev. Mater. Res.*, Vol. 36, pp. 179–198, 2006.
- [Walt 13] D. Walter, B. Lim, R. Falster, J. Binns, and J. Schmidt. “Understanding Lifetime Degradation in Czochralski-Grown N-Type Silicon after High-Temperature Processing”. *Proceedings of the 28th European Photovoltaic Solar Energy Conference and Exhibition*, pp. 699–702, 2013.
- [Wang 09] S. Wang, T. Puzzer, B. Vogl, B. Tjahjono, B. Hallam, M. Eadie, N. Borojevic, Z. Hameiri, and S. Wenham. “Overcoming over-plating problems on acid textured multicrystalline wafers with silicon nitride coated surfaces”. *Proceedings of the 24th European Photovoltaic Solar Energy Conference, Hamburg, Germany*, pp. 1449–1452, 2009.
- [Wang 11] K. Wang, B. Tjahjono, A. Uddin, and S. Wenham. “A method to characterize the sheet resistance of a laser doped line on crystalline silicon wafers for photovoltaic applications”. *Applied Physics Letters*, Vol. 98, No. 9, pp. 094105–094105, 2011.
- [Wang 12] Z. Wang, P. Han, H. Lu, H. Qian, L. Chen, Q. Meng, N. Tang, F. Gao, Y. Jia, J. Wu, W. Wu, H. Zhu, J. Ji, Z. Shi, A. Sugianto, L. Mai, B. Hallam, and S. Wenham. “Advanced PERC and PERL production cells with 20.3% record efficiency for standard commercial p-type silicon wafers”. *Progress in Photovoltaics: Research and Applications*, Vol. 20, pp. 260–268, 2012.
- [Wang 90] A. Wang, J. Zhao, and M. Green. “24% efficient silicon solar cells”. *Applied Physics Letters*, Vol. 57, No. 6, pp. 602–604, 1990.
- [Wata 02] M. Watanabe, M. Eguchi, W. Wang, T. Hibiya, and S. Kuragaki. “Controlling oxygen concentration and distribution in 200mm diameter Si crystals using the electromagnetic Czochralski (EMCZ) method”. *Journal of Crystal Growth*, Vol. 237, pp. 1657–1662, 2002.
- [Week 75] J. Weeks, J. Tully, and L. Kimerling. “Theory of recombination-enhanced defect reactions in semiconductors”. *Physical Review B*, Vol. 12, No. 8, p. 3286, 1975.
- [Wenh 01] S. R. Wenham, J. Zhao, X. Dai, A. Wang, and M. A. Green. “Surface passivation in high efficiency silicon solar cells”. *Solar Energy Materials and Solar Cells*, Vol. 65, No. 1-4, pp. 377 – 384, 2001.
- [Wenh 02] S. R. Wenham and M. A. Green. *Self Aligning Method for Forming A Selective Emitter and Metallization in a Solar Cell*. 2002. US Patent No. 6429039.
- [Wenh 11] S. R. Wenham, B. Tjahjono, N. Kuepper, and A. Lennon. *Improved Metallization Method for Silicon Solar Cells*. 2011. World Patent 2011/050399.
- [Wenh 12] A. M. Wenham, Z. Hameri, J. J. Jia, L. Mai, S. Zhengrong, B. Tjahjono, and S. R. Wenham. *Photovoltaic device structure and method*. 2012. US Patent No. 2012/0125424 A1.
- [Wenh 13a] A. Wenham, C. Chan, B. Hallam, P. Hamer, S. Wang, D. Lu, A. Sugianto, B. Tjahjono, B. Newman, Z. Shi, A. Lochtefeld, A. Gerger, S. Wenham, and A. Barnett. “Novel metal-less



- monolithic crystalline silicon solar cells”. *Proceedings of the 28th European Photovoltaic Solar Energy Conference, Paris, France*, pp. 135–141, 2013.
- [Wenh 13b] S. Wenham, P. Hamer, B. Hallam, A. Sugianto, C. Chan, L. Song, P. Lu, A. Wenham, L. Mai, C. Chong, G. Xu, and M. Edwards. *Advanced hydrogenation of silicon solar cells*. 2013. WO2013173867 A1.
- [Wenh 14] A. Wenham, C. Chan, B. Hallam, M. Abbott, A. Lochtefeld, A. Gerger, S. Wenham, and A. Barnett. “Development of Metal-Less Monolithic Crystalline Silicon Solar Cells”. *29th European Photovoltaic Solar Energy Conference*, pp. 693–698, 2014.
- [Wenh 88] S. R. Wenham and M. A. Green. *Method of making buried contact solar cell*. 1988. US Patent 4,748,130.
- [Wenh 94] S. Wenham, S. Robinson, X. Dai, J. Zhao, A. Wang, Y. Tang, A. Ebong, C. Honsberg, and M. Green. “Rear surface effects in high efficiency silicon solar cells”. *Proceedings of the 24th IEEE Photovoltaic Specialists Conference*, pp. 1278 –1282, 1994.
- [Wern 07] J. Werner, J. Kohler, and A. Esturo-Breton. “Laser doping of solid bodies using a linear-focussed laser beam and production of solar-cell emitters based on said method”. 2007. US Patent App. 20080026550A1.
- [Whit 78] C. White, W. Christie, B. Appleton, S. Wilson, P. Pronko, and C. Magee. “Redistribution of dopants in ion-implanted silicon by pulsed-laser annealing”. *Applied Physics Letters*, Vol. 33, No. 7, pp. 662–664, 1978.
- [Wilk 13] S. Wilking, A. Herguth, and G. Hahn. “Influence of hydrogen on the regeneration of boron-oxygen related defects in crystalline silicon”. *Journal of Applied Physics*, Vol. 113, No. 19, p. 194503, 2013.
- [Wolf 00] S. Wolf and R. N. Tauber. “Silicon Processing for the VLSI ERA”. *Lattice Press, Volumes*, Vol. 1, pp. 265–277, 2000.
- [Wong 93] Y. Wong, X. Yang, P. Chan, and K. Tong. “Excimer-laser doping of spin-on dopant in silicon”. *Applied Surface Science*, Vol. 64, No. 3, pp. 259–263, 1993.
- [Wurz 10] S. Würzner, R. Helbig, C. Funke, and H. J. Möller. “The relationship between microstructure and dislocation density distribution in multicrystalline silicon”. *Journal of Applied Physics*, Vol. 108, No. 8, p. 083516, 2010.
- [Xiao 13] B. Xiao, B. Hallam, L. Mai, D. Lin, C. Chong, A. Lennon, and S. Wenham. “Rear side laser doping through PECVD AlOx/SiNx passivation dielectrics on p-type CZ silicon solar cells”. *Proceedings of the 28th European Photovoltaic Solar Energy Conference, Paris, France*, pp. 1989–1993, 2013.
- [Xiao 14] B. Xiao, L. Mai, D. Lin, B. Halam, C. Chong, A. Lennon, and S. Wenham. “Study of P-type

## BIBLIOGRAPHY

---

- silicon laser doping with ALD AlOx as dopant source”. *Accepted poster presentation for the 40th IEEE Photovoltaic Specialists Conference, Denver*, Vol. PP, p. 1, 2014.
- [Xu 10] H. Xu, R. Hong, B. Ai, L. Zhuang, and H. Shen. “Application of phosphorus diffusion gettering process on upgraded metallurgical grade Si wafers and solar cells”. *Applied Energy*, Vol. 87, No. 11, pp. 3425–3430, 2010.
- [Xu 11] G. Xu, Y. Yao, C. Chong, B. Hallam, C. Yang, and S. Wenham. “Process Optimization and Device Characterization of Laser-Doped Selective Emitter Solar Cell on p-Type Czochralski Silicon Wafer”. *Proceedings of the 26th European Photovoltaic Solar Energy Conference, Hamburg, Germany*, pp. 1323 – 1328, 2011.
- [Xu 12] G. Xu, B. Hallam, C. Chong, and S. Wenham. “Progress in Laser Doped PERL Solar Cell on p-Type CZ Silicon Wafer”. *Proceedings of the 27th European Photovoltaic Solar Energy Conference, Frankfurt, Germany*, pp. 1550–1552, 2012.
- [Youn 79] R. Young, J. Narayan, and R. Wood. “Electrical and structural characteristics of laser-induced epitaxial layers in silicon”. *Applied Physics Letters*, Vol. 35, No. 6, pp. 447–449, 1979.
- [Youn 81] R. Young, R. Wood, W. Christie, and G. Jellison. “Substrate heating and emitter dopant effects in laser-annealed solar cells”. *Applied Physics Letters*, Vol. 39, No. 4, pp. 313–315, 1981.
- [Yuge 94] N. Yuge, H. Baba, Y. Sakaguchi, K. Nishikawa, H. Terashima, and F. Aratani. “Purification of metallurgical silicon up to solar grade”. *Solar Energy Materials and Solar Cells*, Vol. 34, No. 1, pp. 243–250, 1994.
- [Zhao 00] J. Zhao, A. Wang, and M. A. Green. “Performance degradation in CZ (B) cells and improved stability high efficiency PERT and PERL silicon cells on a variety of SEH MCZ (B), FZ (B) and CZ (Ga) substrates”. *Progress in Photovoltaics: Research and Applications*, Vol. 8, No. 5, 2000.
- [Zhao 96] J. Zhao, A. Wang, P. P. Altermatt, S. R. Wenham, and M. A. Green. “24% efficient PERL silicon solar cell: recent improvements in high efficiency silicon cell research”. *Solar Energy Materials and Solar Cells*, Vol. 41, pp. 87–99, 1996.
- [Zhao 99] J. Zhao, A. Wang, and M. Green. “24.5% efficiency silicon PERT cells on MCZ substrates and 24.7% efficiency PERL cells on FZ substrates”. *Progress in Photovoltaics: Research and Applications*, Vol. 7, No. 6, pp. 471–474, 1999.
- [Zhu 90] J. Zhu, N. Johnson, and C. Herring. “Negative-charge state of hydrogen in silicon”. *Physical Review B*, Vol. 41, No. 17, p. 12354, 1990.
- [Zule 83] W. Zulehner. “Czochralski growth of silicon”. *Journal of Crystal Growth*, Vol. 65, No. 1, pp. 189–213, 1983.
- [Zund 91] T. Zundel and J. Weber. “Boron reactivation kinetics in hydrogenated silicon after annealing in the dark or under illumination”. *Physical Review B*, Vol. 43, No. 5, p. 4361, 1991.